# Exploring critical-state behaviour using DEM

By

Xin Huang

September, 2014

*Department of Civil Engineering*

*The University of Hong Kong*

*Department of Civil and Environmental Engineering*

*Imperial College London*

A thesis submitted to The University of Hong Kong and Imperial College London in partial fulfilment of the requirements for the degree of Doctor of Philosophy in the Faculty of Engineering

# Abstract

The critical state soil mechanics (CSSM) framework originally proposed by Schofield & Wroth (1968) has been shown to capture the mechanical behaviour of soils effectively. The particulate implementation of the discrete element method (DEM) can replicate many of the complex mechanical characteristics associated with sand. This research firstly shows that the CSSM framework is useful to assess whether a DEM simulation gives a response that is representative of a real soil. The research then explores the capacity of DEM to extend understanding of soil behaviour within the CSSM framework.

The influence of sample size on the critical-state response observed in DEM simulations that use rigid-wall boundaries was examined. The observed sensitivity was shown to be caused by higher void ratios and lower contact densities adjacent to the boundaries. When the void ratio ($e$) and mean stress ($p'$) of the homogeneous interior regions were considered, the influence of sample size on the position of the critical state line (CSL) in $e$-log($p'$) space diminished.

A parametric study on the influence of the interparticle friction ($\mu$) on the load-deformation response was carried out. The macro-scale stress-deformation characteristics were nonlinearly related to $\mu$ and the particle-scale measures (fabric, contact force distribution, etc.) varied systematically with $\mu$. The limited effect of increases in $\mu$ on the overall strength at high $\mu$ values ($\mu$>0.5) is attributable to transition from sliding-dominant to rolling-dominant contact behaviour. A $\mu$ value higher than 0.5 leads to a CSL in $e$-log($p'$) space that does not capture real soil response.

True-triaxial simulations with different intermediate stress ratios ($b$) were performed. The dependency of strength on $b$ agreed with empirical failure criteria for sands and was related to a change of buckling modes of the strong force chains as $b$ increased. DEM simulations showed that the position of the CSL in $e$-log($p'$) space depends on the intermediate stress ratio $b$. This sensitivity seems to be related to the dependency of the directional fabric anisotropy on $b$. The link between the state parameter and both soil strength and dilatancy proposed by Jefferies & Been (2006) was reproduced in DEM simulations.

A new rotational resistance model was proposed and it was shown that the new model can qualitatively capture the influence of particle shape on the mechanical behaviour of sand. However, it was shown that the effect of rotational resistance is limited and to quantitatively compare the DEM simulation results with laboratory testing data, e.g., the critical-state loci, it is necessary to use non-spherical particles.

# Declaration of Originality

I declare that the work presented in this thesis resulting from my own work and that references are given to the sources of any quotation, or description of the work of others. The simulations and analyses were carried out in the geotechnics section of the Department of Civil and Environmental Engineering at Imperial College London and the Department of Civil Engineering at the University of Hong Kong.

This dissertation is not the same as any other that has been submitted for any degree, diploma or other qualification at any other university.

# Copyright Declaration

The copyright of this thesis rests with the author and is made available under a Creative Commons Attribution Non-Commercial No Derivatives licence. Researchers are free to copy, distribute or transmit the thesis on the condition that they attribute it, that they do not use it for commercial purposes and that they do not alter, transform or build upon it. For any reuse or redistribution, researchers must make clear to others the licence terms of this work.

# Acknowledgements

My foremost and greatest thanks should be given to my supervisor at Imperial College, Dr Catherine O'Sullivan, who has been an inexhaustible source of ideas and inspiration for me in the past three years. Her patience, prudence and enthusiasm for scientific truth have had a great impact on me. I also would like to express my deep gratitude to my supervisors at the University of Hong Kong: Dr Chung-Yee Kwok for her constant encouragement and guidance, the freedom she offered to develop my own ideas is particularly appreciated; Professor Leslie George Tham from whom I benefited a lot regarding my research and future career.

I am in great debt to Dr Kevin John Hanley at Imperial College whose help has been enormous. Without his major input to the LAMMPS code, the project would have been prolonged. His prompt response to the implementation of the rotational resistance towards the end of the project is especially appreciated. The contribution of Dr George Marketos to the LAMMPS code is also acknowledged. I would like to thank Dr David M. G. Taborda at Imperial College for his instructive discussions on soil constitutive modelling. I am also grateful for the fruitful conversations with Dr Jun Yang and Dr Ryan Yan at the University of Hong Kong. Access to the HPC facility, cx1, provided by Imperial College is highly appreciated.

Being enrolled in the joint PhD program between the University of Hong Kong and Imperial College is fantastic as it doubled the number of friends that I have made acquaintance with. The list of names will be lengthy if I mention all of them. In particular, I would like to thank Dr Tom Shire for his encouragement and help. The short conversations with him every early morning were extremely useful to improve my oral English. I also would like to single out the following names: Xiaodong Luo, Xin Liu, Shuangye Zhu, Jingwei Chang, Xiaoyan Zhang, Jianmei Zhou, Kan Duan, Lu Jing, Juan Camilo Lopera Perez, Dr Liming Wei, Dr Xiaoqiang Gu and T.C. Chan at the University of Hong Kong and Qinghua Lei, Wenjie Cui, Bo Han, Masahide Otsubo and Sarah Tallett-Williams, Michael Wan Siu, Howard Taylor and Dr John O'Donovan at Imperial College. Without their company the PhD life would have been dull and less joyful.

My gratitude is also expressed to my examiners, Dr Jun Yang from HKU, Dr Jidong Zhao from HKUST and Dr Stavroula Kontoe from Imperial College.

I am in debt to my parents who always give me the best. I would like to thank my sister Wei Huang for her constant support. I owe too much to my wife, Lingying and my little boy, Zerui. The time I have spent with them is little. Now it is time to make up.

# Table of contents

**Abstract** ..... i

**Declaration of Originality** ..... ii

**Copyright Declaration** ..... ii

**Acknowledgements** ..... iii

**Table of contents** ..... v

**List of Figures** ..... ix

**List of Tables** ..... xxii

**List of Publications** ..... xxiv

**List of Notation** ..... xxvi

**Chapter 1 Introduction** ..... 1

1.1 Background and research objectives ..... 1

1.2 Scope of the research ..... 2

1.3 Organisation of the thesis ..... 3

**Chapter 2 Modification and Verification of the LAMMPS code** ..... 4

2.1 Introduction ..... 4

2.2 LAMMPS and new features added into LAMMPS ..... 5

2.3 Servo-control algorithms for different loading conditions using periodic boundaries ..... 6

2.3.1 Periodic boundaries (PB) ..... 6

2.3.2 The gain parameter ..... 7

2.3.3 Constant-$\sigma'_3$ loading condition (Conventional drained compression (CDC)) ..... 8

2.3.4 Constant-$p'$ drained loading condition (CP) ..... 9

2.3.5 Constant-volume loading condition (CV) ..... 9

2.3.6 Constant-$b$ drained true triaxial loading condition ..... 11

2.4 Validation of the modified LAMMPS code ..... 11

2.4.1 Failure conditions for a FCC sample comprising uniform rigid spheres ..... 11

2.4.2 Effect of sample size ..... 13

2.4.3 Effect of local damping ..... 14
2.4.4 Effect of contact stiffnesses ..... 15
2.4.5 Effect of loading conditions and interparticle friction ..... 15
2.5 Summary ..... 18
**Chapter 3 Effects of Sample Size in DEM Simulations** ..... 34
3.1 Introduction ..... 34
3.2 Prior studies on sample size effects and boundary effects ..... 34
3.3 DEM Samples ..... 35
3.4 Stress-strain Response ..... 38
3.5 Evaluation of Homogeneity ..... 40
3.6 Summary ..... 44
**Chapter 4 Influence of interparticle friction on critical-state behaviour** ..... 59
4.1 Introduction ..... 59
4.2 Overview of prior studies ..... 60
4.3 DEM simulations ..... 65
4.4 Isotropic consolidation ..... 66
4.5 Macro-scale behaviour under triaxial loading conditions ..... 69
4.5.1 Constant-$\sigma'_3$ loading ..... 69
4.5.2 Constant-$p'$ loading ..... 70
4.5.3 Critical-state characteristics ..... 71
4.6 Micro-structural measures ..... 73
4.6.1 Scalar parameter ..... 73
4.6.2 Mechanical redundancy ..... 74
4.6.3 Directional fabric ..... 76
4.7 Contact force characteristics ..... 81
4.7.1 Configuration of the contact forces ..... 81
4.7.2 Influence of $\mu$ on the bimodal force transmission character ..... 81
4.7.3 Influence of $\mu$ on the contributions of contact forces in the normal and tangential directions ..... 83

4.7.4 Tangential force characteristics ..... 84
4.8 Sliding and rolling ..... 86
4.8.1 Analysis of sliding fraction ..... 86
4.8.2 Influence of $\mu$ on the rotational behaviour ..... 87
4.8.3 Interplay between sliding and rolling ..... 87
4.9 A simple conceptual model of strong force chain buckling ..... 89
4.10 Summary ..... 90
**Chapter 5 Critical state behaviour of granular materials** ..... 154
5.1 Introduction ..... 154
5.2 Literature review ..... 155
5.2.1 Experimental investigations on critical state behaviour of sands ..... 155
5.2.2 DEM studies on the mechanical behaviour of granular materials under generalised loading conditions ..... 157
5.2.3 Parameters to describe the state-dependent nature of sands ..... 159
5.3 DEM simulations of three-dimensional loading conditions ..... 160
5.4 Mechanical response under three-dimensional loading conditions ..... 161
5.4.1 Mechanical response under triaxial loading conditions ..... 161
5.4.2 Triaxial Compression (TC) vs Triaxial Extension (TE) ..... 165
5.4.3 Influence of the intermediate stress ratio ..... 168
5.5 Uniqueness of the critical state ..... 174
5.5.1 Critical state line in $e$-log($p'$) and $q$-$p'$ space ..... 174
5.5.2 Critical state from the particle-scale perspective ..... 176
5.6 DEM analysis of the state parameter ..... 179
5.6.1 Correlations between the state parameter and strengths ..... 179
5.6.2 Correlations between the state parameter and dilatancy ..... 181
5.6.3 Micro-scaled equivalent of the state parameter ..... 182
5.7 Application of NorSand to model the DEM data ..... 183
5.7.1 NorSand Overview ..... 183
5.7.2 Calibration of NorSand ..... 186

5.7.3 Performance of NorSand under 3D general loading conditions ..... 187
5.8 Discussions and Conclusions ..... 188
**Chapter 6 Using rotational resistance to study the effect of particle geometry** ..... 241
6.1 Introduction ..... 241
6.2 Overview of prior rotational resistance models ..... 243
6.3 Description and formulation of the new model ..... 245
6.3.1 Basic assumptions and formulation ..... 245
6.3.2 The critical timestep ..... 253
6.3.3 Model verification and preliminary testing ..... 256
6.4 Influence of rotational resistance on the mechanical behaviour ..... 260
6.4.1 Packing density after isotropic compression ..... 260
6.4.2 Stress-strain behaviour during shearing ..... 262
6.4.3 Position of the CSL ..... 264
6.5 Summary ..... 265
**Chapter 7 Conclusions** ..... 287
7.1 Summary ..... 287
7.2 Major findings ..... 288
7.3 Limitations and Recommendations for further work ..... 291
7.3.1 Limitations ..... 291
7.3.2 Recommendations for further work ..... 291
**References** ..... 293

# List of Figures

Figure 2.1 The number of publications using DEM (O'Sullivan, 2014): (a) All disciplines; (b) Geomechanics-related ..... 19
Figure 2.2 Schematic of the spatial-partition parallel technique for a 2D problem : The simulation domain is divided into (a) four subdomains; (b) 16 subdomains (C denotes core) (After Munjiza, 2004) ..... 19
Figure 2.3 Scaling tests of the modified LAMMPS code on the UK's national high-performance-computing (HPC) facilities: (a) triaxial compression simulation on a face-centred-cubic sample composed of 125,000 uniform spheres, run for 100,000 time steps on HECToR Phase 3; (b) constant-volume simulation on a polydisperse sample comprising 351,248 spheres, run for 100,000 time steps on Hartree Blue Joule (O'Sullivan, 2014)..... 20
Figure 2.4 Comparing the simulation results using different numbers of processors (Toyoura sand PSD, $e_0$=0.533, $\sigma'_3$=100 kPa, drained triaxial compression) (a) Deviatoric stress; (b) Volumetric strain ..... 20
Figure 2.5 Illustration of periodic boundaries: (a) a sample composed of repeated structures; (b) remapping of particles across the periodic boundaries..... 21
Figure 2.6 Effectiveness of the servo-control algorithm for CDC simulations (Toyoura sand grading, $e_0$=0.533, $\sigma'_3$=100 kPa) ..... 21
Figure 2.7 Effectiveness of the servo-control algorithm for CP compression simulations (Toyoura sand grading): (a) $p'$=419.8 kPa; (b) $p'$=5000 kPa; (c) $p'$=20 MPa ..... 22
Figure 2.8 Evolution of volumetric strain during a CV simulation (Toyoura sand grading, $e_0$=0.606, $\sigma_{3,0}$=500 kPa)..... 22
Figure 2.9 Effectiveness of the servo-control algorithm for constant-$\sigma'_3$ true triaxial simulations in controlling the $b$ values. (Toyoura sand grading, $e_0$=0.646, $\sigma'_3$=500 kPa)..... 22
Figure 2.10 Geometry of a FCC assembly: (a) plane view; (b) view from the x axis; (c) view from the y axis; (d) contact distribution for a representative element sphere $A$..... 23
Figure 2.11 Illustration of FCC samples containing different numbers of particles..... 24
Figure 2.12 Effect of sample size on the response of FCC assemblies: (a) Evolution of the major principal stress ratio; (b) Effect of sample size on relative error in peak major principal stress ratio ..... 25
Figure 2.13 Illustration of the effect of local damping considering a single ball bouncing under gravity ..... 26

Figure 2.14 Effect of the local damping ratio on the response of FCC assemblies: (a) evolution of major principal stress ratio; (b) Influence of local damping ratio on the relative error in peak major principal stress ratio ..... 26
Figure 2.15 Effect of contact stiffness on the response of FCC assemblies using a simplified Hertz-Mindlin model: (a) evolution of the major principal stress ratio; (b) Effect of shear modulus on the relative error in peak major principal stress ratio ..... 27
Figure 2.16 Effect of contact stiffness on the response of FCC assemblies using a linear elastic model: (a) evolution of the major principal stress ratio; (b) Effect of contact stiffness on the relative error in peak major principal stress ratio ..... 28
Figure 2.17 Failure mechanisms under axisymmetric triaxial loading conditions ($\mu$=0.2): (a) Principal stresses; (b) Stress ratio; (c) Coordination number ..... 29
Figure 2.18 Contact force network under axisymmetric triaxial loading conditions ($\mu$=0.2) 29
Figure 2.19 Failure mechanisms under true triaxial loading conditions (a=0.2,b=0.8, $\mu$=0.2): (a) Principal stresses; (b) Stress ratio; (c) Coordination number ..... 30
Figure 2.20 Contact force network under true triaxial loading conditions (a=0.2,b=0.8, $\mu$=0.2) ..... 31
Figure 2.21 Failure mechanisms under plane strain loading conditions ($\mu$=0.2): (a) Principal stresses; (b) Stress ratio; (c) Coordination number ..... 32
Figure 2.22 Contact force network under plane strain loading conditions ($\mu$=0.2) ..... 32
Figure 2.23 Comparing the measured major principal stress ratios with the analytical solutions: (a) Major principal stress ratios vs $\mu$; (b) Relative errors vs $\mu$ ..... 33
Figure 2.24 Comparing the measured minor principal stress ratios with the analytical solutions: (a) Minor principal stress ratios vs $\mu$; (b) Relative errors vs $\mu$ ..... 33
Figure 3.1 Number of particles used in published DEM simulations (O'Sullivan, 2011) ..... 45
Figure 3.2 Sensitivity of the stress-strain response to the small perturbation in PSD (O'Sullivan *et al.*, 2002) ..... 45
Figure 3.3 Effect of number of particles on the bulk elastic properties (Collop *et al.,* 2006) 46
Figure 3.4 Sensitivity of the mechanical behaviour of granular materials to the number of particles under triaxial loading conditions (Belheine *et al.*, 2009): (a) Deviatoric stress; (b) Volumetric strain ..... 46
Figure 3.5 Observed localisation phenomena adjacent to the rigid wall boundaries: (a) Porosity; (b) Axial strain; (c) Normal contact force (Marketos & Bolton, 2010) ..... 47
Figure 3.6 Schematic diagrams of the four numerical samples: PB: periodically-bounded sample; RW-S: Small rigid-wall sample; RW-M: Medium rigid-wall sample; RW-L: Large rigid-wall sample ..... 47
Figure 3.7 Particle size distributions of numerical samples ..... 48

Figure 3.8 Effect of sample size on the void ratio after isotropic compression for the PB samples ($\sigma'_{3,0}$=500 kPa) ..... 48
Figure 3.9 Effect of sample size on the stress-strain behaviour for the PB samples: (a) Deviatoric stress; (b) Volumetric strain ..... 48
Figure 3.10 Comparing the stress-strain response of samples with different sizes..... 49
Figure 3.12 Effects of sample size on the critical-state response..... 50
Figure 3.13 The homogeneity of the samples at the initial state: (a) Solid volume within each zones, (b) cylindrical rigid-wall samples at vertical direction, (c) cylindrical zones (rings) extending from bottom rigid wall boundary to top boundary, and (d) sample PB at horizontal and vertical directions. ..... 51
Figure 3.14 Distributions of initial void ratio of rigid-wall samples in which the shading illustrates data values normalized by the mean void ratio ($e_0$ = 0.649) for each sample and the actual void ratio values in each region are given on the right side of each plot. ..... 52
Figure 3.15 Distributions of initial void ratio of the periodically-bounded sample in which the shading indicates void ratios normalized by the mean for the entire sample ($e_0$ = 0.646) and the actual void ratios in each region are given on the right side of each plot. ..... 52
Figure 3.16 Variation in void ratio in the radial direction of a cylindrical child volume: (a) Smaller Leighton Buzzard sand sample; (b) Larger Reigate sand sample (Ní Bhreasail, 2014) ..... 52
Figure 3.17 Illustration of the geometrical constraints at the boundary: (a) Rigid-wall boundaries; (b) Periodic boundaries ..... 53
Figure 3.18 Distribution of void ratio within rigid-wall samples along radial direction (Thickness of each ring approximates $D_{50}$.)..... 53
Figure 3.19 Distributions of initial contact density of rigid-wall samples in which the shading illustrates data values normalized by the mean contact density for each sample and the actual contact densities in each region are given on the right side of each plot. (The mean contact densities for RW-L, RW-M, and RW-S are 331, 346, and 361 $mm^{-3}$, respectively.)..... 54
Figure 3.20 Distributions of initial contact density of periodically-bounded sample in which the shading indicates contact densities normalized by the mean contact density for the entire sample and the actual contact densities in each region are given on the right side of each plot. (The mean contact density for PB sample is 301 $mm^{-3}$.)..... 54
Figure 3.21 The critical state of DEM samples plotted in the $e$ against $(p'/p'_a)^{\alpha}$ space considering homogeneous interior regions only ..... 55
Figure 4.1 Geometry of two particles (A and B) in contact: **n** is the contact normal; **t** represents a direction on the contact plane; $L$ and $L'$ are the traces of contact points when A and B move against each other (After Duran, 2000) ..... 93

Figure 4.2 The saw blades model of dilatancy (Newland & Allely, 1957)..... 93
Figure 4.3 Variation of stress ratios with the tilt angle (Oda et al., 1982)..... 94
Figure 4.4 Observed effect of interparticle friction on the strength of granular materials when particles are free to rotate (Yang et al., 2012)..... 95
Figure 4.5 Observed effect of interparticle friction on the strength of granular materials when particle rotation is not allowed: (a) 2D results (Morgan, 1999); (b) 3D results (Suiker & Fleck, 2004)..... 95
Figure 4.6 Influence of $\mu$ on the peak strength of granular materials under true triaxial conditions: (a) Peak angle of shearing resistance; (b) Normalised peak angle of shearing resistance (c) Influence of μ on the peak stress and fabric states for true triaxial compression in the generalised stress plane (Barreto & O'Sullivan, 2012)..... 96
Figure 4.7 Influence of μ on the cyclic stress-strain behaviour (Sazzad & Suzuki, 2011).... 97
Figure 4.8 Influence of μ on the micro-scale characteristics: (a) Ratio of sliding contacts; (b) Mechanical coordination number (Thornton, 2000)..... 97
Figure 4.9 Evolution of contact parameters' anisotropy with various inter-particle frictions for drained tests: (a) Contact normal anisotropy; (b) Contact normal force anisotropy; (c) Contact tangential force anisotropy; (d) Mobilised friction anisotropy (Yang et al., 2012).. 98
Figure 4.10 Influence of μ on the contribution of contact force components to macro stress components (Antony & Kruyt, 2009)..... 99
Figure 4.11 Force transmission within a photoelastic assembly : (a) isotropic state; (b) during pure shear (Majmudar & Behringer, 2005)..... 100
Figure 4.12 Evolution of contact force network within a granular assembly subjected to constant-volume triaxial shearing: (a) Initial state; (b) Phase transformation state (c) 16.75% axial strain; (d) Critical state. (Guo & Zhao, 2013)..... 100
Figure 4.13 Strong force chain buckling and shear band formations: (a) Experimental observation (Oda & Kazama, 1998) ; (b) DEM observation ( Mahmood & Iwashita, 2011) ..... 101
Figure 4.14 Boundary conditions, degrees of freedom, and contact models for an N-particle force chain:(a) prior to buckling; (b) after buckling;(c) enlarged views of (b). (Tordesillas & Muthuswamy, 2009)..... 101
Figure 4.15 Spring and link models analogous to strong force chain buckling: (a) 2D (Hunt et al., 2010) (b) 3D (O'Sullivan et al., 2013)..... 102
Figure 4.16 Comparing the numerical grading curves and the experimental grading curves (RW: rigid-wall samples using the Toyoura sand grading; PB: periodically-bounded samples using the Toyoura sand grading)..... 103
Figure 4.17 Variation of the initial void ratio after isotropic compression with $\mu$ ..... 104

Figure 4.18 Comparing the void ratio before and after set $\mu$ to $\mu_{targ}$ ($\mu_{targ}$ = 0.25 and $p'_0$=500kPa) ..... 104
Figure 4.19 Structural change due to the reduce of $\mu$ during isotropic compression ($\mu$ = 1.0, $\mu_{targ}$ = 0.25 and $p'_0$=500 kPa) ..... 105
Figure 4.20 Variation of the coordination number (Z) and mechanical coordination number ($Z_m$) with $\mu$ after isotropic compression ($p'_0$=500 kPa) ..... 106
Figure 4.21 Correlations between $Z$ and $e$ and $Z_m$ and $e$ after isotropic compression before changing $\mu$ to $\mu_{targ}$ ..... 106
Figure 4.22 Effect of $\mu$ on the macromechanical response for PB simulations under conventional drained condition (Toyoura PSD, $e_0$ = 0.533 and $\sigma'_3$ = 100 kPa) ..... 107
Figure 4.23 Effect of interparticle friction on the macromechanical response for RW simulations under conventional drained condition (Toyoura PSD, $e_0$ = 0.648 and $\sigma'_3$ = 500 kPa) ..... 108
Figure 4.24 Variation of angle of shearing resistance of PB samples with $\mu$ (Toyoura PSD, $e_0$ = 0.533 and $\sigma'_3$ = 100 kPa) ..... 109
Figure 4.25 Variation of angle of shearing resistance of RW samples with $\mu$ (Toyoura PSD, $e_0$ = 0.648 and $\sigma'_3$ = 500 kPa) ..... 109
Figure 4.26 Effect of interparticle friction on the macromechanical response for PB simulations under constant-$p'$ condition (Toyoura PSD, $p'$ = 5000 kPa) ..... 110
Figure 4.27 Effects of $\mu$ and rotation on the shear resistance at critical state: FR=rotation fixed; simulations not denoted as PFC3D used periodic boundaries PB and Toyoura PSD 111
Figure 4.28 Effect of $\mu$ and rotation on the CSL in $e$-log $p'$ space; FR=rotation fixed; simulations not denoted as PFC3D used periodic boundaries: (a) Toyoura PSD with HM contact model (b) Toyoura PSD with linear contact model ..... 112
Figure 4.29 CSL in e-log($p'$) space for samples using Dunkirk PSD and a HM contact model ..... 113
Figure 4.30 Influence of $\mu$ on the variation in $Z$ with axial strain ($e_0$ = 0.533, $\sigma'_3$ = 100 kPa) ..... 113
Figure 4.31 The effect of $\mu$ on the coordination number $Z$ at critical state for LAMMPS simulations with Toyoura PSD, HM contact model: (a) Variation in $Z$ with $p'$; (b) Variation in $Z_m$ with $p'$ ..... 114
Figure 4.32 The effect of $\mu$ on the relationship between Z and $e$ for LAMMPS simulations with Toyoura PSD, HM contact model: (a) Variation in $Z$ with $e$ at critical state ; (b) Variation in $Z$ with void ratio ($e_0$ = 0.533, $\sigma'_3$ = 100 kPa) ..... 115

Figure 4.33 Index of mechanical redundancy: (a) excluding particles with zero contacts (b) including all particles ($e_0$ = 0.533, $\sigma'_3$ = 100 kPa) ..... 116
Figure 4.34 Effect of $\mu$ on the number of rattlers for LAMMPS simulations using the Toyoura PSD ..... 117
Figure 4.35 CSL in e-log(p') space excluding rattlers: (a) Simulations using the Toyoura PSD (b) Simulations using the Dunkirk PSD ..... 118
Figure 4.36 Evolution of deviatoric fabric for LAMMPS simulations, Toyoura PSD ($e_0$ = 0.533, $\sigma'_3$ = 100 kPa) ..... 119
Figure 4.37 Influence of $\mu$ on the deviatoric fabric at critical state (Toyoura PSD, HM model): (a) Variation of deviatoric fabric with $\mu$ at critical state ($e_0$ = 0.533, $\sigma'_3$ = 100 kPa); (b) Relative anisotropy between the strong and weak contact network at critical state ($e_0$ = 0.533, $\sigma'_3$ = 100 kPa); (c) Relationship between the deviatoric fabric and mean effective stress ..... 120
Figure 4.38 Comparing the stress ratio calculated from stress components and the stress ratio calculated from the stress-force-fabric relationship ..... 121
Figure 4.39 Influence of $\mu$ on the variation of the structural anisotropy quantities with axial strain ..... 122
Figure 4.40 Influence of $\mu$ on the contribution of the structural anisotropy quantities to the stress ratio ..... 123
Figure 4.41 Contact rose diagram at critical states for LAMMPS simulations, Toyoura PSD ($e_0$ = 0.533, $\sigma'_3$ = 100 kPa) ..... 124
Figure 4.42 The effect of $\mu$ on the contact force configuration ($e_0$ = 0.533, $\sigma'_3$ = 100 kPa) 125
Figure 4.43 Bimodal force transmission for a representative set of simulations ($e_0$ = 0.533, $\sigma'_3$ = 100 kPa) ..... 126
Figure 4.44 Cumulative contribution of contact forces to the deviatoric stress ($e_0$ = 0.533, $\sigma'_3$ = 100 kPa) ..... 127
Figure 4.45 Variation of $f$* with shearing for an undrained simulation ($e_0$=0.612, $\sigma'_{3,0}$ =5000 kPa): (a) stress-strain curve; (b) cumulative contribution curves at three characteristic states ..... 128
Figure 4.46 Evolution of contact force contributions to the stress ratio ..... 129
Figure 4.47 Probability density distribution of the mobilised friction index for PB samples (Toyoura PSD, $e_0$=0.533 and $\sigma'_3$=100 kPa) ..... 130
Figure 4.48 Cumulative contribution of single contact to $q$ evaluated by $I_{mf}$ ..... 131
Figure 4.49 Spatial distribution of $I_{mf}$ (Toyoura PSD, $e_0$=0.533 and $\sigma'_3$=100 kPa) ..... 131

Figure 4.50 Probability density distribution of the shear force ratio for PB samples (Toyoura PSD, $e_0$=0.533 and $\sigma'_3$=100 kPa) ..... 132
Figure 4.51 Probability density distribution of the mobilised friction index for RW samples ($e_0$=0.648,$\sigma'_3$=500 kPa) ..... 133
Figure 4.52 Probability density distribution of shear force ratio for RW samples ($e_0$=0.648,$\sigma'_3$=500 kPa) ..... 134
Figure 4.53 Influence of loading conditions and initial packing density on the probability density distribution of shear force ratio for PB samples ($\mu$=0.25) ..... 135
Figure 4.54 Comparing the probability density distribution of shear force ratio of RW and PB samples ..... 136
Figure 4.55 Comparing the probability density distribution of shear force ratio of PB samples with different contact models: LE: linear elastic; HM: Hertz-Mindlin (Toyoura grading, $\mu$ = 0.5) ..... 137
Figure 4.56 Rose diagram on the x-z plane of the isolated contact force network with different shear force ratios (μ=0.25) ..... 138
Figure 4.57 Rose diagram on the x-z plane of the isolated contact force network with different shear force ratios ($\mu$=1.0) ..... 138
Figure 4.58 Structural anisotropy of two sub-networks with different shear force ratios considering all contacts (PB, Toyoura PSD, $e_0$=0.533,$\sigma'_3$=100 kPa and μ=0.25): (a) Overall; (b) Strong; (c) Weak ..... 139
Figure 4.59 Influence of $\mu$ on the sliding behaviour (PB samples, Toyoura PSD, $e_0$=0.533 and $\sigma'_3$=100 kPa): (a) Evolution of sliding fraction ; (b) Sliding fraction at critical state; (c) Configuration of sliding contact at critical state ..... 140
Figure 4.60 Effect of μ on the angular velocity for LAMMPS simulations, Toyoura PSD ($e_0$ = 0.533 and $\sigma'_3$ = 100 kPa): (a) variation in mean resultant angular velocity with μ at $\varepsilon_a$ = 50% and (b) cumulative distribution of resultant angular velocities at $\varepsilon_a$ = 50%. ..... 141
Figure 4.61 Study the sliding and rolling states of a simple model ..... 142
Figure 4.62 Transition between sliding dominant and rolling dominant behaviour ..... 143
Figure 4.63 Influence of $\mu$ on the peak force of a single column ..... 144
Figure 4.64 A typical force evolution during the simulation of strong force chain buckling (A straight column with a middle deflection, $\beta$=15°) ..... 145
Figure 5.1 Definitions of the CSL (After Schofield & Wroth, 1968) ..... 191
Figure 5.2 Evaluating the uniqueness of the CSL in *e*-log(*p'*) space (Been et al., 1991) .... 192
Figure 5.3 Positive evidence regarding the uniqueness of CSL in e-log(p') space ..... 193
Figure 5.4 Dependency of the position of the CSL on initial void ratio (Finno & Rechenmacher, 2003) ..... 194

Figure 5.5 Dependency of the CSL on the initial anisotropy: (a) indicates dependency ; (b)-(c) show no dependency ..... 194
Figure 5.6 Comparing the CSLs obtained from triaxial compression and triaxial extension tests ..... 195
Figure 5.7 A higher position of the CSL in *e*-log(*p'*) for plane strain tests than for triaxial tests ..... 195
Figure 5.8 Reported variation of angle of shearing resistance with *b* in sands (After Sayão & Vaid, 1996) ..... 196
Figure 5.9 DEM studies of the uniqueness of CSL in *e*-log(*p'*) space under triaxial loading conditions ..... 197
Figure 5.10 DEM studies on the influence of loading mode on the position of the CSL .... 198
Figure 5.11 Definition of the state parameter (Been & Jefferies, 1985) ..... 199
Figure 5.12 Illustration of the dilatancy state line (DSL) and associated parameters in the Anisotropy Crtical State Theory (ACST) (Li & Dafalias, 2012) ..... 199
Figure 5.13 Illustration of the three-dimensional loading conditions: (a) A DEM sample subjected to three-dimensional loading; (b) Total stress paths considered in this study ..... 200
Figure 5.14 Stress-deformation response under triaxial drained loading conditions ($\sigma'3 = 500\ kPa$) ..... 201
Figure 5.15 Evolution of coordination number and mechanical coordination number under triaxial drained loading conditions ($\sigma'_3$=500 kPa) ..... 202
Figure 5.16 Evolution of the index of mechanical redundancy under triaxial drained loading conditions ($\sigma'_3$=500 kPa) ..... 202
Figure 5.17 Probability density distribution of the coordination number under drained triaxial loading conditions ($\sigma'_3$=500 kPa): (a) Dense; (b) Medium dense; (c) Loose ..... 203
Figure 5.18 Evolution of anisotropy parameters under triaxial drained loading conditions ($\sigma'_3$=500 kPa) ..... 203
Figure 5.19 Stress-strain behaviour under constant-volume triaxial loading conditions ($\sigma_{3,0}$=500 kPa) ..... 204
Figure 5.20 Evolution of the coordination number (Z) and mechanical coordination number ($Z_m$) under constant-volume triaxial loading conditions ($\sigma_{3,0}$=500 kPa) ..... 205
Figure 5.21 Evolution of the index of mechanical redundancy under constant-volume triaxial loading conditions ($\sigma_{3,0}$=500 kPa) ..... 205
Figure 5.22 Probability density distribution of the coordination number under constant-volume triaxial loading conditions ($\sigma'_3$=500 kPa): (a) Dense; (b) Medium dense; (c) Loose ..... 206

Figure 5.23 Evolution of anisotropy quantities under constant-volume triaxial loading conditions ($\sigma_{3,0}$=500 kPa) ..... 206
Figure 5.24 Stress-strain behaviour of a DEM sample sheared under different loading paths ($e_0$=0.646,$\sigma'_3$=500 kPa) ..... 207
Figure 5.25 Comparing the stress-strain response of granular materials subjected to constant-volume compression (CVC) and constant-volume extension (CVE) ($e_0$=0.619, $\sigma_3$=500 kPa): (a) |q|; (b) stress path ..... 208
Figure 5.26 Coaxiality between the fabric direction and the loading direction: (a) Evolution of *A'* for DEM simulations; (b) Modelling values of FAV A for the experimental data of Yoshimine et al. (1998) (Li and Dafalias, 2012) ..... 209
Figure 5.27 Comparing the stress-strain response of granular materials subjected to constant-p' compression (CPC) and constant-p' extension (CPE) ($e_0$=0.594, $\sigma'_3$=20 MPa): (a) q/p'; (b) $\varepsilon_v$ ..... 210
Figure 5.28 Evolution of *A'* for constant-*p'* simulations ($e_0$=0.594, $\sigma'_3$=20 MPa) ..... 211
Figure 5.29 Variation of stresses with *b* during "drained" shearing ($\sigma'_{3,0}$ = 500 kPa, $e_0$ = 0.646): (a) Stress ratio *q*/*p'*; (b) Major principal stress $\sigma'_1$; (c) Intermediate stress $\sigma'_2$ ..... 212
Figure 5.30 Variation of strains with *b* during "drained" shearing ($\sigma'_{3,0}$ = 500 kPa, $e_0$ = 0.646): (a) Intermediate principal strain; (b) Minor principal strain; (c) Volumetric strain 213
Figure 5.31 Coaxiality between the fabric direction and the loading direction at various *b* values (($\sigma'_{3,0}$ = 500 kPa, $e_0$ = 0.646): (a) Evolution of *A'* during the course of shearing; (b) Variation of *A'* at critical state with *b* ..... 214
Figure 5.32 Deviation between the direction of the stress vector and that of the strain increment vector under true triaxial loading conditions ($\sigma'_{3,0}$ = 500 kPa, $e_0$ = 0.646): (a) Orientation of the strain increment vector (This study) ; (b) Orientation of the strain increment vector (Sazzad & Suzuki, 2013); (c) Angle of deviation between the direction of the strain increment vector and the direction of the stress vector (This study); (d) Experimental observation of the angle of deviation between the direction of the strain increment vector and the direction of the stress vector at failure: $\beta$ is the angle between the major principal stress direction and the deposition direction and $\kappa$ is the Lade-Duncan strength parameter (Suzuki & Yanagisawa, 2006) ..... 215
Figure 5.33 Evaluation of different failure criteria ..... 216
Figure 5.34 Evolution of Z with axial strain for drained shearing ($\sigma'_{3,0}$ = 500 kPa and $e_0$ = 0.646) ..... 217
Figure 5.35 Clustering of contacts along the principal stress directions ($\sigma'_{3,0}$ = 500 kPa and $e_0$ = 0.646): (a) $\Phi_1$; (b) $\Phi_2$; (c) $\Phi_3$ ..... 217
Figure 5.36 Spatial contact density distributions at the critical state ..... 218

Figure 5.37 Biaxially loaded plate ..... 219
Figure 5.38 Critical state characteristics ..... 220
Figure 5.39 Variation of $Z$ and $Z_m$ at critical state with $b$ ..... 221
Figure 5.40 Correlation between the deviatoric fabric and mean effective stress at the critical state ..... 221
Figure 5.41 Correlation between the dilatancy and the deviatoric fabric for three representative sets of simulations: loose ($\sigma'_{3,0}$ = 500 kPa, $e_0$ = 0.646); medium ($\sigma'_{3,0}$ = 1000 kPa, $e_0$ = 0.627); dense ($\sigma'_{3,0}$ = 100 kPa, $e_0$ = 0.533)) ..... 222
Figure 5.42 Rose diagram of the branch vector ($\sigma'_{3,0}$ = 500 kPa, $e_0$ = 0.646) ..... 222
Figure 5.43 Contact force network at critical state ($\sigma'_{3,0}$ = 500 kPa, $e_0$ = 0.646): (a) b=0.0; (b) Plane strain; (c) b=1.0 ..... 223
Figure 5.44 Correlations between $K_c$ and $p'$ at critical state: (a) Zhao and Guo (2013); (b) This study (dashed lines indicate the product of the $\Phi_d$-$p'$ relationship and M($b$)$p'$ for various b values) ..... 224
Figure 5.45 Initial state parameter ($\psi_0$) and peak angle of shearing resistance ($\phi'_{peak}$ DEM simulation results presented along with the experimental data reported in Jefferies and Been (2006) ..... 225
Figure 5.46 Initial state parameter ($\psi_0$) and stress dilatancy angle of shearing resistance ($\phi'_{peak}$- $\phi'_{cv}$), DEM simulation results presented along with the experimental data reported in Jefferies and Been (2006) ..... 225
Figure 5.47 Relationship between the stress ratio at instability state ($\eta_{IS}$) and initial state parameter ($\psi_0$) for undrained triaxial compression simulations ($b$=0) ..... 226
Figure 5.48 Relationship between the peak dilatancy ($D^p_{max}$) and the initial state parameter ($\psi_0$), DEM simulation results presented along with the experimental data reported in Jefferies and Been (2006) ..... 226
Figure 5.49 Relationships between the dilatancy at peak ($D^p_{max}$) and the state parameter at peak ($\psi_p$) ..... 227
Figure 5.50 Relationship between the peak strength and dilatancy at peak ..... 228
Figure 5.51 Comparison between the measured critical state strength and the critical state strength predicted from the strength and dilatancy relationship ..... 229
Figure 5.52 Relationships between micro-scale state measurement and macro-scale state measurement ..... 230
Figure 5.53 Relationships between the deviatoric fabric at peak and initial state parameter ..... 231

Figure 5.54 Correlations between the strong deviatoric fabric and initial state parameter .. 232
Figure 5.55 Definition of image condition on yield surface (Jefferies and Shuttle, 2002) .. 233
Figure 5.56 Variation of critical state stress ratio ($M_{cs}$) with Lode angle ($\theta$) ..... 233
Figure 5.57 Variation of N with b ..... 233
Figure 5.58 Comparison between the NorSand modelling results and the DEM data for a dense sample ($e_0 = 0.549$, $\sigma'_3 = 300$ kPa) ..... 234
Figure 5.59 Comparison between the NorSand modelling results and the DEM data for a loose sample ($e_0 = 0.646$, $\sigma'_3 = 500$ kPa) ..... 235
Figure 5.60 Variation of hardening modulus ($H$) with initial state parameter ($\psi_0$) ..... 236
Figure 6.1 Effect of particle shape on critical state parameters where S represents sphericity (Cho et al., 2006) ..... 267
Figure 6.2 Different techniques used to consider the effect of particle shape in DEM simulations: (a) Ellipsoids (Ng, 2009); (b) Polygons (Peña et al., 2008); (c) Polyhedrons (Langston et al., 2013); (d) Clumps (Kozicki et al., 2012) ..... 267
Figure 6.3 (a) Illustration of the concept of 'potential' particles (Houlsby, 2009); (b) Potential particles with different shapes ..... 268
Figure 6.4 Illustration of physical origin of rotational resistance: (a) Noncoincidence between the branch vector direction and the contact normal direction; (b) Interlocking effect ..... 268
Figure 6.5 Discretisation of the contact springs ..... 268
Figure 6.6 Assumed mechanism of rolling resistance: (a) 2D illustration; (b) 3D illustration of contact force redistribution due to rolling about the y axis; (c) Limit of the rolling resistance prior to the opening of the contact ..... 269
Figure 6.7 Illustration of pure rolling and pure sliding in the absence of rigid-body rotation ..... 269
Figure 6.8 Kinematics of two particles in contact over a single timestep projected in a local coordinate system (After Jiang et al. (2005)) ..... 270
Figure 6.9 Assumed mechanism for the twisting/torque resistance model: (a) Illustration of the annular shear stress flow on the contact plane; (b) Calculation of the annular shear stress ..... 270
Figure 6.10 Applying quaternions to perform spatial rotation: (a) Rotation of a single vector around an arbitrary axis; (b) Rotation of a coordinate system around an axis that is orthogonal to the z axes of the old and new coordinate system ..... 271
Figure 6.11 Illustration of the construction of the lumped mass matrix ..... 272
Figure 6.12 Illustration of the local and global coordinate system for two particles in contact ..... 272

Figure 6.13 A single particle spins on a flat rigid wall ..... 272
Figure 6.14 Comparison between the measured motion and the analytical harmonic motion (Δt = 1e-6, no limit on the rolling resistance): (a) between 0 and 1 s; (b) Small scale (between 0 and 0.2 s); (c) Difference between the measured $\omega_x$ and the predicted $\omega_x$ at the peak and the valley ..... 273
Figure 6.15 Comparison between the measured motion and the analytical harmonic motion (Δt = 1e-9, no limit on the rolling resistance): (a) between 0 and 0.1 s; (b) Difference between the measured $\omega_x$ and the predicted $\omega_x$ at the peak and the valley ..... 274
Figure 6.16 Comparison between the measured motion and the theoretically-derived motion when the rolling resistance is bounded by a limit (Δt = 1e-9, κ=0.5): (a) between 0 and 0.2 s; (b) between 0 and 0.02 s ..... 275
Figure 6.17 Effect of $\delta$ on the angular motion (Δt = 1e-9, no limit) ..... 275
Figure 6.18 Influence of κ on the angular motion (Δt = 1e-9) ..... 276
Figure 6.19 Comparing the influence of different options after the limiting value for the rolling resistance is attained (Δt = 1e-9, κ=0.5) (Option 1: the rolling resistance is maintained at the limiting value; Option 2: The rolling resistance drops to zero.) ..... 276
Figure 6.20 Influence of κ on the angular motion when Option 2 is adopted after the limit of the rolling resistance is attained ..... 277
Figure 6.21 The kinematics of a single ball moving along a flat wall with initial translational velocity: (a) Illustration of the model; (b) Translational velocity; (c) Rotational velocity .. 278
Figure 6.22 Influence of $\kappa$ on the packing density after isotropic compression ($\sigma'_3$=100 kPa, $\delta$ =1,$\mu$ = 0.25, dashed line indicates the value without limit set for the rotational resistance) ..... 279
Figure 6.23 Influence of $\delta$ on the packing density after isotropic compression ($\mu$ = 0.25, no limit for the rotational resistance) ..... 279
Figure 6.24 Comparing the packing density after isotropic compression for different post-limit options ($\sigma'_3$=100 kPa, $\kappa$ =0.5, $\mu$ = 0.25. Option 1: $Mr = Mrm$post limit; Option 2: $M_r$ = 0 post limit) ..... 279
Figure 6.25 Influence of particle shape on the packing density ($e_{max}$ and $e_{min}$) (Cho et al., 2006) ..... 280
Figure 6.26 Correlations between the void ratio and the coordination number ($Z$) and between the void ratio and the mechanical coordination number ($Z_m$) after isotropic compression: (a) 100 kPa; (b) 500 kPa (RR: With rotational resistance; NRR: No rotational resistance) ..... 280

Figure 6.27 Influence of $\kappa$ on the mechanical behaviour ($e_0$=0.646, $\sigma'_3$=100 kPa): (a) Deviatoric stress vs axial strain; (b) Angle of shearing resistance vs axial strain; (c) Volumetric strain vs axial strain ..... 281
Figure 6.28 Influence of $\kappa$ on the particle-scale measures ($e_0$=0.646, $\sigma'_3$=100 kPa): (a) Coordination number; (b) Mechanical coordination number; (c) Deviatoric fabric ..... 282
Figure 6.29 Influence of $\kappa$ on the fraction of the contacts that reach the plastic limit: (a) Sliding fraction; (b) Rolling fraction; (c) Twisting fraction ..... 283
Figure 6.30 Effects of $\kappa$ on the elastic and plastic configurations of the contacts: (a) $\kappa$=0.1; (b) $\kappa$=0.3; (c) $\kappa$=1 (**PR**: pure rolling; **PT**: pure twisting; **PS**: pure sliding; **Elastic**: no rolling, no twisting and no sliding; **R-T**: rolling and twisting; **R-S**: rolling and sliding; **T-S**: twisting and sliding; **R-S-T**: rolling, sliding and twisting)..... 284
Figure 6.31 Influence of $\delta$ on the mechanical behaviour ($e_0$=0.646, $\sigma'_3$=100 kPa, $\kappa$=1): (a) Deviatoric stress vs axial strain; (b) Angle of shearing resistance vs axial strain; (c) Volumetric strain vs axial strain ..... 285
Figure 6.32 Effect of rotational resistance on the position of the critical state lines: (a) *e*-log(*p'*) space; (b) *q*-*p'* space ..... 286

# List of Tables

Table 3.1 Initial characteristics of the prepared virtual samples of the representative set of simulations and a real Toyoura sand for comparison ..... 56
Table 3.2 Initial characteristics of the RW-S samples ..... 56
Table 3.3 Initial characteristics of the RW-M samples ..... 56
Table 3.4 Initial characteristics of the PB samples ..... 57
Table 3.5 Micro characteristics of the representative set of simulations at the critical state ..... 57
Table 3.6 Critical-state characteristics of the RW-S samples ..... 57
Table 3.7 Critical-state characteristics of the RW-M samples ..... 57
Table 3.8 Critical-state characteristics of the PB samples ..... 58
Table 3.9 Unbiased sample variance of initial void ratio ..... 58
Table 3.10 Unbiased sample variance of initial contact density ..... 58
Table 3.11 Characteristics of PSDs in different parts of the rigid-wall samples ..... 58
Table 4.1 Examples of prior research using spherical or elliptical particles and $\mu \geqslant 0.5$ ..... 146
Table 4.2 Summary of LAMMPS simulations with a simplified Hertz-Mindlin contact model, Toyoura PSD and periodic boundaries ..... 147
Table 4.3 Summary of PFC3D simulations with a simplified Hertz-Mindlin contact model, Toyoura PSD and rigid boundaries (RW=rigid wall boundaries using PFC3D code) ..... 149
Table 4.4 Summary of simulations with the LE contact model and Toyoura PSD (RW=rigid wall boundaries using PFC3D code) ..... 150
Table 4.5 Summary of LAMMPS simulations with the simplified Hertz-Mindlin contact model, Dunkirk PSD, and periodic boundaries ..... 151
Table 4.6 Fitting parameters for the power-law relationships between $Z$ and $p'$ and $Z_m$ and $p'$ at critical state ..... 152
Table 4.7 Fitting parameters for the power-law relationships between $N_R$ and $p'$ at critical state ..... 152
Table 4.8 Fitting parameters for the power-law relationships between $\Phi_d$ and $p'$ at critical state ..... 153
Table 4.9 Input parameters for the single column test ..... 153
Table 5.1 Summary of the true triaxial simulations (continued) ..... 238
Table 5.2 Fitting parameters for different failure criteria at peak state ($e_0$=0.646, $\sigma'_3$=500 kPa) ..... 239

Table 5.3 Fitting parameters for different failure criteria at critical state ..... 239
Table 5.4 Summary of the critical-state parameters..... 239
Table 5.5 Summary of fitting parameters for the $\Phi_d$–$p'$ relationship at critical state ..... 239
Table 5.6 Initial state parameter ($\psi_0$) and stress ratio at instability state ($\eta_{IS}$) for undrained simulations ..... 240
Table 5.7 Input modelling parameters for NorSand..... 240

# List of Publications

- **Papers published in peer-reviewed journals**

1. **Huang, X.,** Hanley, K.J., O'Sullivan, C. & Kwok, C.Y. (2014) Effect of sample size on the response of DEM samples with a realistic grading. *Particuology*, 15, 107-115
2. Hanley, K.J., **Huang, X.**, O'Sullivan, C. & Kwok, C.Y. (2014) Temporal variation of contact networks in granular materials. *Granular Matter*. 16(1), 41-54.
3. **Huang, X.**, Hanley, K.J., O'Sullivan, C. & Kwok, C.Y. (2014) Influence of inter-particle friction on critical state behaviour. *International Journal for Numerical and Analytical Methods in Geomechanics*. 38(12), 1276-1297
4. **Huang, X**., Hanley, K.J., O'Sullivan, C. & Kwok, C.Y. (2014) DEM analysis of the influence of the intermediate stress ratio on the critical-state behaviour of granular materials. *Granular Matter*. http://link.springer.com/article/10.1007/s10035-014-0520-6
5. **Huang, X**., O'Sullivan, C., Hanley, K.J. & Kwok, C.Y. (2014) DEM study of the state parameter. *Géotechnique*. (Accepted)
6. Lopera Perez, J.C., O'Sullivan, C., Kwok, C.Y., Hanley, K.J. & **Huang, X**. (2014) On the conditions for quasi-static shearing in granular media. *Géotechnique*. (Under review)
7. Hanley, K.J., O'Sullivan, C., Wadee, M.A. & **Huang, X.** (2014) Use of elastic stability analysis to explain the stress-dependent nature of soil strength. *Proceedings of The Royal Society A: Mathematical, Physical & Engineering Sciences*. (Under review)

- **Conference**

1. **Huang, X.**, O'Sullivan, C., Hanley, K. J., & Kwok, C. Y. (2014). Capturing the state-dependent nature of soil response using DEM. In *The International Symposium on Geomechanics from Micro to Macro (IS-Cambridge 2014)*. Cambridge, UK (Accepted)
2. Hanley, K. J., O'Sullivan, C., & **Huang, X.** (2014). Investigation of Christensen ' s two-parameter failure criterion for brittle materials. In *The International Symposium on Geomechanics from Micro to Macro (IS-Cambridge 2014)*. Cambridge, UK. (Accepted)
3. Lopera Perez, J. C., Kwok, C. Y., O'Sullivan, C., Hanley, K. J., & **Huang, X.** (2014). Instability in granular materials - A Micromechanical Investigation. In *The International Symposium on Geomechanics from Micro to Macro (IS-Cambridge 2014)*. Cambridge, UK. (Accepted)

4. **Huang, X**., Hanley, K.J., O'Sullivan, C., Kwok, C.Y. & Tham, L.G. (2013). Effects of inter-particle friction on critical state behaviour of granular materials: a numerical study. In *III International Conference on Particle-based Methods – Fundamentals and Applications*, Stuttgart, Germany
5. Hanley, K.J., **Huang, X**., O'Sullivan, C. & Kwok, C.Y. (2013). Challenges Of Simulating Undrained Tests Using The Constant Volume Method *In Powders and Grains*, Sydney, Australia, pp. 277-280 doi:http://dx.doi.org/10.1063/1.4811921
6. **Huang, X**., Hanley, K.J., O'Sullivan, C. & Kwok, C.Y. (2013). Micro-scale study on specimen size effects in DEM simulations of granular assemblies subjected to triaxial loading. In *Experimental Micromechanics for Geomaterials, Joint workshop of the ISSMGE TC101-TC105*. Hong Kong, China
7. **Huang, X**., Kwok, C.Y., O'Sullivan C. & Tham, L.G. (2012). A micro mechanical study on the critical-state behavior of a granular assemblage with a realistic grading. In *the International Conference on Geomechanics and Engineering*, Seoul, Korea

# List of Notation

The following table lists the symbols used in the text in alphabetical order, along with their brief definitions. Greek letters are given at the end of the table. Any symbol in bold is tensorial.

| Symbol/Abbreviation | Brief definition |
|---|---|
| $a_c$ | Contact orientation anisotropy |
| $a_b$ | Branch vector anisotropy |
| $a_n$ | Normal contact force anisotropy |
| $a_t$ | Tangential contact force anisotropy |
| $a_{ij}^c$ | Anisotropy tensor of contact orientation |
| $a_{ij}^b$ | Anisotropy tensor of branch vector |
| $a_{ij}^n$ | Anisotropy tensor of contact normal force |
| $a_{ij}^t$ | Anisotropy tensor of tangential contact force |
| $A$ | Scalar-valued fabric anisotropy variable |
| $A'$ | Relative orientation between fabric direction and stress direction |
| ACST | Anisotropic critical state theory |
| $b$ | Intermediate stress ratio $b = (\sigma'_2 - \sigma'_3)/(\sigma'_1 - \sigma'_3)$ |
| $B$ | Radius of the contact area |
| $C_c$ | Coefficient of curvature |
| $C_u$ | Coefficient of uniformity |
| CDC | Conventional drained compression |
| CP | Constant $p'$ |
| CV | Constant volume |
| CSL | Critical state line |

| | |
|---|---|
| CSSM | Critical state soil mechanics |
| $d$ | Local damping ratio |
| $[d]$ | Displacement vector |
| $D$ | Particle diameter |
| $D^p$ | Dilatancy $D^p = d\varepsilon^p_v / d\varepsilon^p_q$ |
| $D^p_{max}$ | Dilatancy at peak stress ratio |
| $D_{50}$ | Characteristic particle diameter |
| DEM | Discrete element method |
| DSL | Dilatancy state line |
| $e$ | Void ratio |
| $e_s$ | Inter-granular void ratio |
| $e_0$ | Void ratio after isotropic compression |
| $e_d$ | Dilatancy void ratio |
| $E(\Omega)$ | Probability density function of contact orientation |
| $\boldsymbol{f}$ | Contact force vector |
| $\bar{f}^0$ | Average normal contact force over the assembly |
| $f_n$ | Normal contact force |
| $\langle f_n \rangle$ | Mean normal contact force |
| $f_t$ | Tangential contact force |
| $\Delta f_t$ | Tangential contact force increment |
| $f^*$ | Characteristic normal contact force |
| $F_c$ | Second invariant of the deviatoric fabric tensor |
| $\boldsymbol{F_d}$ | Damping forces/moments |
| $\boldsymbol{F_u}$ | Unbalanced forces/moments |

| | |
|---|---|
| FDM | Finite difference method |
| FEM | Finite element method |
| $g$ | Gain parameter for the servo control in LAMMPS |
| $g$ | Gravity |
| $G$ | Shear modulus |
| hpc | High-performance computing |
| $H$ | Hardening modulus of the NorSand model |
| $I$ | Rotation moment of inertia |
| $I$ | Area moment of inertia |
| $I_{mf}$ | Friction mobilisation index |
| $I_R$ | Index of mechanical redundancy |
| $I_D$ | Relative packing density |
| $I^{NR}{}_R$ | Index of mechanical redundancy excluding rattlers |
| $I_r$ | Elastic rigidity of the NorSand model |
| IS | Instability state |
| $J$ | Polar moment of inertia |
| $J_2$ | Second invariant of the deviatoric stress tensor |
| $k_n$ | Normal contact stiffness |
| $k_r$ | Rolling stiffness |
| $k_s$ | Tangential contact stiffness |
| $k_{\theta,n}$ | Twisting stiffness |
| [K] | Stiffness matrix |
| $K_c$ | First joint invariant of the deviatoric stress tensor and the deviatoric fabric tensor |

| | |
|---|---|
| $\boldsymbol{l}$ | Branch vector |
| LAMMPS | Large-scale Atomic/Molecular Massively Parallel Simulator |
| LC | Loading compression |
| LE | Loading extension |
| $m$ | Particle mass |
| *maxrate* | The maximum allowable strain rate for simulations in LAMMPS |
| $M$ | Stress ratio at the critical state |
| $[M]$ | Mass matrix |
| $M_i$ | Stress ratio at the image state |
| $\boldsymbol{M^k}$ | Torque resulted from the tangential force at the $k^{\text{th}}$ contact |
| $\boldsymbol{M_r}$ | Rolling resistance |
| $M_t$ | Twisting resistance |
| $\boldsymbol{M_r^k}$ | Torque resulted from rotational resistance at the $k^{\text{th}}$ contact |
| $\boldsymbol{M_r^m}$ | Limit of the rotational resistance |
| $\boldsymbol{n}$ | Contact normal |
| $N$ | Volumetric coupling parameter in stress dilatancy of the NorSand model |
| $N_p$ | Number of particles |
| $N_c$ | Number of contacts |
| $p'$ | Mean effective stress $p' = (\sigma'_1 + \sigma'_2 + \sigma'_3)/3$ |
| $p_a$ | Atmospheric pressure |
| $p'_0$ | Mean effective stress after isotropic compression |
| $p'_{cv}$ | Mean effective stress at critical state |
| $P_{crit}$ | Peak buckling force |
| PB | Periodic boundary |

| | |
|---|---|
| PDF | Probability density function |
| PT | Phase transformation state |
| $q$ | Deviatoric stress $q = \sqrt{\frac{1}{2}((\sigma_1' - \sigma_2')^2 + (\sigma_1' - \sigma_3')^2 + (\sigma_2' - \sigma_3')^2)}$ |
| $q_{cv}$ | Deviatoric stress at critical state |
| $\boldsymbol{q}$ | Quaternion/Unit quaternion |
| $\tilde{R}$ | Equivalent radius of two touching particles, $\tilde{R} = \frac{r_i r_j}{r_i + r_j}$ |
| $R_r$ | Common radius of two touching particles in the rotational resistance model |
| $r$ | Particle radius |
| $\Delta s$ | Tangential displacement increment |
| $s_{1,2,3}$ | $s_1 = (2\sigma'_1 - \sigma'_2 - \sigma'_3)/3$, $s_2 = (2\sigma'_2 - \sigma'_3 - \sigma'_1)/3$ and $s_3 = (2\sigma'_3 - \sigma'_1 - \sigma'_2)/3$ |
| $s'_{ij}$ | Deviatoric stress tensor |
| $\Delta t_{crit}$ | Critical timestep |
| $\Delta t$ | Timestep |
| $T$ | Transformation matrix |
| UC | Unloading compression |
| UE | Unloading extension |
| $v$ | Specific volume |
| $V$ | Volume of an assembly |
| $V_{inter}$ | The intersection volume between two spheres |
| $V^p$ | Volume of a single particle |
| $\boldsymbol{V_{rel}}$ | Relative tangential velocity |

| | |
|---|---|
| $V_0$ | Initial volume of an assembly |
| $\boldsymbol{x}$ | Coordinates of particle centroid |
| $\boldsymbol{x^c}$ | Coordinates of contact point |
| $Z$ | Coordination number |
| $Z_0$ | Coordination number after isotropic compression |
| $Z_m$ | Mechanical coordination number |
| $\alpha$ | The power of the linear interpretation of the critical state line in $e$-log($p'$) space |
| $\chi$ | Dilatancy parameter of the NorSand model |
| $\delta_n$ | Contact overlap |
| $\delta$ | Shape parameter for the rotational resistance model |
| $\dot{\boldsymbol{\varepsilon}}$ | Strain rate tensor |
| $\varepsilon_a$ | Axial strain |
| $\varepsilon_1$ | Major principal strain |
| $\varepsilon_2$ | Intermediate principal strain |
| $\varepsilon_3$ | Minor principal strain |
| $\varepsilon_v$ | Volumetric strain $\varepsilon_v = \frac{\varepsilon_1+\varepsilon_2+\varepsilon_3}{3}$ |
| $\varepsilon_v^p$ | Plastic volumetric strain |
| $\varepsilon_q$ | Deviatoric strain $\varepsilon_q = \frac{s_1\varepsilon_1+s_2\varepsilon_2+s_3\varepsilon_3}{q}$ |
| $\varepsilon_q^p$ | Plastic deviatoric strain |
| $\eta$ | Stress ratio $q/p'$ |
| $\eta_{IS}$ | Stress ratio at the instability state |
| $\zeta$ | Dilatancy state parameter |

| | |
|---|---|
| $\phi'$ | Angle of shearing resistance (°) |
| $\phi'_p$ | Interparticle friction angle (°) |
| $\phi'_{cv}$ | Angle of shearing resistance at the critical state (°) |
| $\phi'_{max}$ | Maximum angle of shearing resistance (°) |
| $\phi'_{peak}$ | Peak angle of shearing resistance (°) |
| $\Phi_{ij}$ | Fabric tensor (See Eq. 3.1) |
| $\Phi'_{ij}$ | Deviatoric part of the fabric tensor |
| $\Phi_d$ | Deviatoric fabric $\Phi_d = \sqrt{\frac{1}{2}((\Phi_1 - \Phi_2)^2 + (\Phi_1 - \Phi_3)^2 + (\Phi_2 - \Phi_3)^2)}$ |
| $\Phi_{d,0}$ | Deviatoric fabric after isotropic compression |
| $\Phi_{\mathrm{d,cs}}$ | Deviatoric fabric at the critical state |
| $\Phi_d^s$ | Deviatoric fabric of the strong contacts |
| $\Phi_d^w$ | Deviatoric fabric of the weak contacts |
| $\kappa$ | Strength index for the rotational resistance model |
| $\boldsymbol{\omega}$ | Angular velocity |
| $\omega_{max}$ | Maximum natural frequency of the discrete system |
| $\omega_r$ | Resultant angular velocity |
| $\boldsymbol{\omega_{rel}}$ | Relative rotational velocity |
| $\Omega$ | Orientation of contact normal in spherical coordinate |
| $\mu$ | Interparticle friction coefficient |
| $\mu_r$ | Rotational friction coefficient |
| $\mu_{targ}$ | Interparticle friction coefficient during shearing |
| $\mu_{transition}$ | Transition friction coefficient |
| $v$ | Poisson's ratio |

| | |
|---|---|
| $\psi$ | State parameter |
| $\psi_0$ | Initial state parameter |
| $\psi_p$ | State parameter at peak stress ratio |
| $\lambda$ | Slope of the critical state line in the $e$-$(p'/p_a)^{\alpha}$ space |
| $\sigma_{ij}$ | Overall stress tensor |
| $\sigma_{ij}^{p}$ | Stress tensor of a single particle |
| $\bar{\sigma}_{ij}$ | Average stress tensor within the region of interest |
| $\boldsymbol{\sigma'}_{required}$ | Target stress tensor for the servo control in LAMMPS |
| $\boldsymbol{\sigma'}_{measured}$ | Measured stress tensor for simulations in LAMMPS |
| $\sigma'_1$ | Major effective principal stress |
| $\sigma'_2$ | Intermediate effective principal stress |
| $\sigma'_3$ | Minor effective principal stress |
| $\tau_{peak}$ | Maximum applied horizontal shear stress in direct shear box tests |
| $\Gamma$ | Intercept of the critical state line in the $e$-$(p'/p_a)^{\alpha}$ space with the axis $p' = 0$ |
| $\theta$ | Lode angle $\sin(3\theta) = -13.5 s_1 s_2 s_3 / q^3$ |
| $\theta$ | Rotation angle |
| $\ddot{\boldsymbol{\theta}}$ | Angular acceleration |
| $\boldsymbol{\theta_r}$ | Relative rotation angle |

# Chapter 1 Introduction

## 1.1 Background and research objectives

Soil is a granular material, and its granular or particulate nature underlies its complex responses to applied loads or deformations. Many natural hazards such as landslides and debris flows are induced by the failure of soils and the performance of many important elements of infrastructure (e.g., buildings, bridges and dams) during and after construction depends on the properties of the underlying soils. Therefore, understanding the mechanical behaviour of soil is of great interest to both the industrial and academic communities. However, the mechanical behaviour of soils is rather complex and can be affected by a number of factors, e.g., the initial packing density, the stress state, the initial anisotropy and the loading conditions. Consequently, prediction of soil response is not easy. Prior studies that have investigated soil behaviour tended to use laboratory experiments such as element tests and physical models or resorted to numerical approaches, e.g., the finite element method (FEM) and the finite difference method (FDM). Neither conventional laboratory testing nor the continuum analysis approaches used in FEM/FDM enable the fundamental particle-scale mechanisms that are responsible for the complexity of soil responses to be uncovered.

The advent of the discrete element method (DEM) (Cundall & Strack, 1979) enables more fundamental studies of soil behaviour. Despite its simplicity, the particulate implementation of DEM captures many of the unique mechanical characteristics of soils and other granular materials (Cundall, 2001; Iwashita & Oda, 1998; O'Sullivan & Cui, 2009; Thornton, 2000). Furthermore, DEM enables the micro structures within soil to be quantified and the particle-scale fundamentals to be investigated. There has been a dramatic increase in the number of DEM-related research papers across a variety of scientific disciplines including geomechanics in the past decade (O'Sullivan, 2014). With the development of computer capacity, there is potential to apply DEM to investigate large-scale practical problems.

The framework of critical state soil mechanics (CSSM) (Schofield & Wroth, 1968) has been shown to effectively capture the state-dependent nature of soil responses and thus has been routinely referred to in modern constitutive modelling of soil. The major objective of the current study is to investigate the capacity of DEM to reproduce real sand behaviour within the framework of CSSM so as to strengthen the confidence of the geotechnical community regarding the future application of DEM in practical issues.

This dissertation follows two lines: (1) To show that the framework of CSSM is useful to evaluate whether a DEM simulation reflects the real behaviour of sand; (2) To explore the extent to which DEM can extend understanding of soil behaviour within the framework of CSSM.

## 1.2 Scope of the research

The current research investigates the quasi-static behaviour of granular materials. The effect of initial anisotropy is excluded in the current study by considering initially isotropic samples. All the simulations were conducted with idealised perfectly spherical particles. The influence of particle shape is considered by applying rolling and twisting resistances at the contacts between spherical particles.

The simulations presented here were mainly carried out using a modified version of the open-source LAMMPS code (Plimpton, 1995), while some supplemental simulations were performed using the PFC3D software (Itasca Consulting Group, 2007) to confirm that observations arising from the current study are code-independent. Access to high-performance computing (hpc) facilities allowed reasonably large samples containing more than 20,000 particles to be considered and enabled simulations to be finished in a reasonably short time: normally it took four days to shear a sample to 50% axial strain. As a result, a large database could be established.

DEM provides an idealised numerical environment in which the loading conditions can be precisely controlled and the stress-strain response can be accurately measured. The current study considered the mechanical behaviour of granular materials under three-dimensional loading conditions. The influence of initial states and types of loading condition on the critical-state behaviour were considered in detail. The failure mechanism and the uniqueness of critical state for granular materials under three-dimensional loading conditions were investigated.

DEM also provides particle-scale data which are difficult to obtain in physical experiments, particularly particle data (e.g., position, velocities and stresses) and contact force data (e.g., orientation and magnitude). These data allow the evolution of micro structures and the force transmission mechanism within a granular assembly to be identified. In particular, the characteristics of particle-scale measures such as fabric at the critical state are analysed and linked to macro-scale observations. The micromechanical information is used to extend our understanding of the macro-scale stress-deformation response of granular materials and provides insight to the CSSM framework.

## 1.3 Organisation of the thesis

This thesis contains seven Chapters. There is not a separate chapter for general literature review; instead, where relevant each Chapter contains its own literature review. The thesis is structured as follows:

In Chapter 2, the servo-control schemes associated with different loading conditions simulated using the open-source LAMMPS code (Plimpton, 1995) are introduced. Verification work associated with the modified code is presented.

Chapter 3 investigates the effects of sample size on the critical-state behaviour of granular materials when rigid-wall boundaries are used. The dependency of the mechanical behaviour on the sample size is presented and the origin of the sample size effect is explored within the CSSM framework.

Chapter 4 studies the influence of the interparticle friction coefficient ($\mu$) on the behaviour of granular materials. The usefulness of the CSSM framework in assessing the validity of input $\mu$ values for a DEM simulation of soil behaviour is addressed. The origin of the nonlinear relationship between the macro-scale mechanical behaviour and $\mu$ is discussed.

In Chapter 5, the behaviour of granular materials under 3D generalised loading conditions is simulated using DEM. The influence of the intermediate stress ratio ($b$) on the strength as well as the positions of the critical state lines in both $q$-$p'$ and $e$-log($p'$) spaces is discussed. New insight into the critical state is presented from a particle-scale perspective. The effectiveness of DEM in capturing the state-dependent response associated with sand is highlighted.

Chapter 6 extends the work carried out in Chapter 5 by considering the effect of particle shape. The interlocking effect due to irregular shapes of sand grains is investigated by introducing both rolling and twisting resistances for spherical particles.

Finally, the major findings of preceding Chapters are summarised and some recommendations for further studies are given in Chapter 7.

# Chapter 2 Modification and Verification of the LAMMPS code

## 2.1 Introduction

The discrete element method (DEM) (Cundall & Strack, 1979) simulates the mechanical behaviour of granular materials by considering particle-scale interactions and motions. In DEM, particles are assumed to be rigid, and a small amount of overlap is allowed at the contact points. At each timestep, the interaction forces at the contact points are evaluated from the overlap using a prescribed force-displacement law. The resultant forces and moments acting on each particle at the current timestep are obtained by considering the contact forces and moments for all constitutive contacts. Newton's second law of motion is then applied to obtain both the translational and angular accelerations for individual particles, from which the velocities and then the displacement increments can be obtained using an explicit Verlet integration scheme. Thereby, the position of each particle after each integration timestep can be obtained.

As documented by O'Sullivan (2014), the number of DEM-related studies published each year has increased exponentially since the 1980s (Figure 2.1 (a)). The data in Figure 2.1 (a) relate to all of the various scientific disciplines where DEM is used. There is also an increasing trend for the application of DEM in geomechanics research (Figure 2.1 (b)). According to O'Sullivan (2014), despite the prevalence of the commercial codes PFC2D and PFC3D (an estimated 67% of the publications in geomechanics between 2010 and 2013 used either PFC2D or PFC3D), open-source codes are also available, e.g., LAMMPS (Plimpton, 1995) , Yade (Kozicki & Donzé, 2008) and TRUBAL is still commonly used (e.g., Magnanimo et al., 2008; Thornton & Antony, 1998). Perhaps the biggest advantage of an open-source code over a commercial code is that users can view the source code, make changes and add new features freely. This is particularly attractive for scientific researchers as new ideas can be implemented and examined promptly. Secondarily, the latest modifications distributed by the main-code developers can be easily exploited when an open-source code is used, whereas this is not necessarily possible for a commercial code without the cost of updating an earlier version to the latest one.

The open-source code LAMMPS was used throughout this research. The acronym LAMMPS stands for Large-scale Atomic/Molecular Massively Parallel Simulator. Some new functionality was incorporated into LAMMPS to enable simulations of geomechanical

problems. This Chapter introduces the implementation of new loading-control schemes and the validation work associated with the modified LAMMPS code.

## 2.2 LAMMPS and new features added into LAMMPS

LAMMPS was originally proposed as a molecular dynamics (MD) code. Molecular dynamics is a numerical method to study the interaction of atoms and molecules and it is algorithmically similar to DEM. LAMMPS is maintained and distributed by researchers at the Sandia National Laboratories in the US. LAMMPS is capable of running simulations on distributed or shared-memory, multi-processor computers. It is parallelised using Message Passing Interface (MPI). The parallel capacities of LAMMPS can be exploited on both multi-core desktop machines as well as massively-parallel high-performance computers. Simulations in LAMMPS are run by reading commands from an input script.

Spatial-decomposition techniques are used when a LAMMPS simulation is run on multiple processors. In this case, the simulation domain is divided into several subdomains (Figure 2.2), each of which is assigned to a single processor (core). Contact detection, contact force calculation and motion integration for particles within an individual subdomain are performed by the assigned processor. Information about particles on the border of two adjacent subdomains is communicated between corresponding processors using MPI. Therefore, the simulation time depends on both the capacity of individual processors and the communication speed between neighbouring cores. Hanley (2014) (as cited by O'Sullivan (2014)) did a series of scaling tests for the modified LAMMPS code on two UK national hpc facilities, HECToR Phase 3 and Blue Joule (Hartree) and the results are shown in Figure 2.3. It is clear that the running time for the same problem does not decrease linearly with increasing number of processors due to the increasing cost of communicating information between neighbouring processors. This agrees with Munjiza (2004).

Figure 2.4 compares the measured stress-strain behaviour for a drained triaxial compression simulation performed using different numbers of processors in the current study. Simulations were performed on cx1, a large "Beowulf"-type PC cluster at Imperial College (Imperial College High Performance Computing Service, 2012). The same simulation conditions and procedures were followed in each simulation but the simulation domain was divided into different numbers of subdomains which were assigned to different numbers of processors (one node with 12 cores, two nodes with 24 cores and four nodes with 48 cores) in each simulation. As illustrated in Figure 2.4, the measured stress-deformation behaviour is almost identical for all the simulations. Figure 2.4 indicates that the accumulated round-off errors

due to communications between different processors are negligible and parallel processing of the LAMMPS code has negligible effect on the overall material response.

The original LAMMPS code was modified by Dr Kevin Hanley and Dr George Marketos at Imperial College for simulations of soil element tests. The main new features of the modified version of LAMMPS used throughout this research include:

- The relative velocities of the particles prior to the contact force calculation are updated to account for deformation of the periodic boundaries
- A number of control algorithms were implemented for periodic boundaries to enable stress and strain-controlled simulations. These are detailed in Section 2.3 below
- Particle rotations may be fixed by zeroing angular velocities before the contact force and moment calculation
- A local damping option similar to PFC3D (Itasca Consulting Group, 2007) is available

Of these modifications, Dr Marketos contributed to the implementation of local damping, while the remainder were implemented by Dr Hanley. The current research was amongst the first to use these features and so validation and small modifications to refine the implementation arose during this study.

## 2.3 Servo-control algorithms for different loading conditions using periodic boundaries

To reproduce different laboratory loading conditions in a numerical experimental environment, different servo-control algorithms are required to achieve either a prescribed stress path or a prescribed deformation pattern.

### 2.3.1 Periodic boundaries (PB)

The PB condition envisages a real material to be a system composed of multiple repeated structures, i.e., representative volume elements (RVE) (Figure 2.5 (a)). The overall response of the large system can be represented by the response of a RVE when the same loading condition is applied. Application of periodic boundaries enables DEM simulations to be free from boundary effects which may significantly affect the material responses (Thornton, 2000). This issue will be addressed in Chapter 3. When the PB condition is applied in a DEM simulation, particles can move across the periodic boundaries, i.e., when a particle passes through one side of the periodic cell, it will reappear on the opposite side. Figure 2.5(b) gives a 2D illustration of the PB condition. If a particle is located at a corner of a

periodic cell (filled circle in black), it will be imaged to the other three corners (filled circles with dashed periphery), while if a particle intersects just one side of a periodic cell (open circle with solid periphery), it will be remapped to the opposite side of the periodic cell (open circle with dashed periphery). Similarly, three circumstances can be identified for 3D situations: (a) particles locating at the corner will be remapped to the other seven corners; (b) particles across one edge of a periodic cell will be remapped to the other three paralleled edges; (c) particles exceeding one face of a periodic cell will be imaged to the opposite face. These remapped virtual particles ('ghost' particles) will be in contact with particles adjacent to the opposite boundaries and must be considered in both the contact detection and contact force calculation procedures. Descriptions of the use of periodic boundaries are given in O'Sullivan (2011) and Thornton (2000). A more in-depth discussion, which considers the LAMMPS code used in the current study, is outlined below.

### 2.3.2 The gain parameter

Stress-controlled loading conditions in a DEM simulation are achieved by continuously adjusting the boundary positions following Eq. 2.1.

$$\dot{\boldsymbol{\varepsilon}} = -g(\boldsymbol{\sigma'}_{required} - \boldsymbol{\sigma'}_{measured}) \qquad \text{(Eq. 2.1)}$$

in which $\dot{\boldsymbol{\varepsilon}}$ is the strain rate, $g$ is the gain parameter which controls speed of the convergence of the current stresses within a numerical assembly, $\boldsymbol{\sigma'}_{measured}$, to the target stresses, $\boldsymbol{\sigma'}_{required}$. The current ensemble average stress tensor $\sigma_{ij}$ is calculated using Eq. 2.2 (Potyondy & Cundall, 2004a) in the modified version of LAMMPS.

$$\sigma_{ij} = \frac{1}{V}\sum_{1}^{N_p} \sigma_{ij}^{p} V^{p} \qquad \text{(Eq. 2.2)}$$

where $V$ is the volume of the periodic cell, $\sigma_{ij}^{p}$ is the stress tensor in particle (p), $N_p$ is the total number of particles within the periodic cell and $V^p$ is the volume of the particle (p).

The first challenge when implementing stress-controlled algorithms for periodic boundaries is the determination of the gain parameter, $g$. When rigid-wall boundaries are used, the change of boundary stresses ($\Delta\boldsymbol{\sigma^{w}}$) corresponding to the change of boundary positions can be estimated from the interaction force between the particles and rigid walls. However, no such relationship can be established when periodic boundaries are used. Therefore, the appropriate $g$ was determined through trial and error. In this study the gain parameter $g$ is defined as $g = \frac{2 \cdot maxerate}{\boldsymbol{\sigma'}_{required}}$. Thus the servo control algorithm for simulations using periodic boundaries becomes:

$$\dot{\boldsymbol{\varepsilon}} = -\frac{2 \cdot maxerate}{\boldsymbol{\sigma'}_{required}} (\boldsymbol{\sigma'}_{required} - \boldsymbol{\sigma'}_{measured}) \quad \text{(Eq. 2.3)}$$

where $maxerate$ is the maximum allowable strain rate which is an input parameter. A similar definition of $g$ was adopted by Thornton & Antony (2000), i.e., $g = \frac{\dot{\boldsymbol{\varepsilon}}_{initial}}{\boldsymbol{\sigma'}_{required} - \boldsymbol{\sigma'}_{initial}}$, where $\dot{\boldsymbol{\varepsilon}}_{initial}$ is the prescribed initial strain rate and $\boldsymbol{\sigma'}_{initial}$ indicates the initial stress state.

There are several advantages of using Eq. 2.3. Firstly, it converges rapidly when $\boldsymbol{\sigma'}_{measured}$ is much smaller than $\boldsymbol{\sigma'}_{required}$. Meanwhile, the strain rate is bounded by $maxerate$, avoiding dynamic effects. This constraint is extremely useful for the initial stage of the isotropic compression when particles have almost no contacts with each other and the sample is in a zero-stress state. Secondly, $\dot{\boldsymbol{\varepsilon}}$ decreases as the difference between $\boldsymbol{\sigma'}_{measured}$ and $\boldsymbol{\sigma'}_{required}$ becomes smaller and approaches zero when $\boldsymbol{\sigma'}_{measured}$ is closed to $\boldsymbol{\sigma'}_{required}$. Once an appropriate $maxerate$ has been found for one simulation in a parametric study, the same $maxerate$ can be used for other samples with different initial states, i.e., no further trial and error is necessary.

Any operation including boundary conditions that is applied to the system during timestepping in LAMMPS is invoked by the 'fix' command. A new fix style 'multistress' which allows different types of element tests to be simulated by adjusting the periodic boundary as well as particle movements was added into the original LAMMPS code. The implemented servo-control algorithms associated with the 'fix multistress' are detailed below.

### 2.3.3 Constant-$\sigma'_3$ loading condition (Conventional drained compression (CDC))

To achieve CDC loading conditions, the movement of periodic boundaries in the lateral directions (i.e., *x* and *y* directions) is controlled by

$$\dot{\varepsilon}_{i,t} = -\frac{2 \cdot maxerate}{\sigma'_{i,required}} (\sigma'_{i,required} - \sigma'_{i,t}) \quad \text{(Eq. 2.4)}$$

where $\dot{\varepsilon}_{i,t}$ is the strain rate of boundaries normal to the *i*th axis at the current timestep, $\sigma'_{i,required}$ is the target confining pressure, *i* denotes directions that are orthogonal to the loading direction. Figure 2.6 illustrates the evolution of the principal stress components for a representative CDC simulation in which a constant compressive strain rate was applied in the *z* direction considered in this research. It is evident in Figure 2.6 that the lateral stresses ($\sigma_{xx}$ and $\sigma_{yy}$) were almost identical to each other and were effectively maintained at the target confining pressure of 100 kPa with the maximum error below 0.006% .

### 2.3.4 Constant-*p'* drained loading condition (CP)

For the CP simulations, the target stresses for the next time step are estimated at each time step assuming axisymmetric conditions (e.g., if loading is applied in the *z* direction, $\sigma'_{xx} = \sigma'_{yy}$),

$$p' = \frac{1}{3}\left(\sigma'_{xx} + \sigma'_{yy} + \sigma'_{zz}\right) \rightarrow \sigma'_{xx} = \sigma'_{yy} = \frac{1}{2}(3p' - \sigma'_{zz}) \qquad \text{(Eq. 2.5)}$$

Since the simulation is strain-controlled in the $\sigma'_{zz}$ direction, given a very small time step, it is reasonable to assume that the change of $\sigma'_{zz}$ due to the axial loading from *t* to *t* + *Δt* is approximately equal to the change from *t*-*Δt* to *t*, and thus $\sigma'_{zz}$ at *t* + *Δt* can be estimated by:

$$\sigma'_{zz,t+\Delta t} = \sigma'_{zz,t} + (\sigma'_{zz,t} - \sigma'_{zz,t-\Delta t}) \qquad \text{(Eq. 2.6)}$$

Therefore, the target stresses in the *x* and *y* directions at *t* + *Δt* can be obtained by Eq. 2.7:

$$\sigma'_{xx,t+\Delta t} = \sigma'_{yy,t+\Delta t} = \frac{1}{2}(3p' - \sigma'_{zz,t+\Delta t}) \qquad \text{(Eq. 2.7)}$$

The strain rate in the *x* and *y* directions at the current time step can then be determined following the same steps used for the CDC simulations by substituting $\sigma'_{required}$ in Eq. 2.4 with $\sigma'_{xx,t+\Delta t}$ and $\sigma'_{yy,t+\Delta t}$ respectively. Note that the subscripts in Eq. 2.5 to Eq. 2.7 may be swapped when loading is progressed in different directions. Figure 2.7 shows examples of CP simulations considering three *p'* levels: *p'* = 419.8 kPa, 5000 kPa and 20 MPa. Despite some small 'bumps', overall *p'* was effectively maintained at its target values.

### 2.3.5 Constant-volume loading condition (CV)

The CV loading condition is routinely used in DEM simulations to simulate undrained triaxial tests on fully-saturated soils. Carrera et al. (2011) showed in laboratory tests that a sample sheared under the constant-volume drained loading condition gives a stress-strain behaviour that is close to that of a sample with similar initial state but subjected to undrained shearing. CV DEM simulations carried out without fluid coupling were found by Lamei & Mirghasemi (2011) to be consistent with fluid-coupled undrained simulations. Therefore, it is reasonable to link the stress-strain response observed in a DEM CV simulation to that observed in an undrained laboratory triaxial test.

The condition of constant volume is imposed at each timestep by requiring that:

$$V_t = V_0(1 + \dot{\varepsilon}_x dt)\left(1 + \dot{\varepsilon}_y dt\right)(1 + \dot{\varepsilon}_z dt) = V_0 \qquad \text{(Eq. 2.8)}$$

Let $V = V_0(1 + \dot{\varepsilon}_z dt)$, Eq. 2.8 becomes,

$$(1 + \dot{\varepsilon}_x dt)\left(1 + \dot{\varepsilon}_y dt\right) = \frac{V_0}{V} \quad \text{(Eq. 2.9)}$$

Two alternative conditions can be assumed to derive the corresponding lateral strain rates:

1. Assuming an identical strain rate for the lateral boundaries, which leads to

$$\dot{\varepsilon}_x = \dot{\varepsilon}_y = (\sqrt{\frac{V_0}{V}} - 1)/dt \quad \text{(Eq. 2.10)}$$

2. Assuming identical stress for the lateral boundaries, i.e., $\dot{\sigma}'_{xx,t+\Delta t} = \dot{\sigma}'_{yy,t+\Delta t}$

In the latter case, the change of stresses is assumed to be linearly related to the strain rate in the corresponding direction, i.e., $\sigma_{i,t+\Delta t} \approx \sigma_{i,t} + \frac{\sigma'_{i,t} - \sigma'_{i,t-\Delta t}}{\dot{\varepsilon}_{i,t-\Delta t}} \dot{\varepsilon}_{i,t}$ $(i = xx, yy, zz)$, which leads to,

$$\sigma'_{xx,t} + \frac{\sigma'_{xx,t} - \sigma'_{xx,t-\Delta t}}{\dot{\varepsilon}_{x,t-\Delta t}} \dot{\varepsilon}_{x,t} = \sigma'_{yy,t} + \frac{\sigma'_{yy,t} - \sigma'_{yy,t-\Delta t}}{\dot{\varepsilon}_{y,t-\Delta t}} \dot{\varepsilon}_{y,t} \quad \text{(Eq. 2.11)}$$

Combining Eq. 2.9 and Eq. 2.11 and ignoring the second-order product of differentials $(\dot{\varepsilon}_{x,t}\dot{\varepsilon}_{y,t})$, the strain rates in the lateral directions can be obtained.

$$\begin{cases} \dot{\varepsilon}_{x,t} = \dfrac{\frac{V_0 - V}{Vdt}(\sigma'_{yy,t} - \sigma'_{yy,t-\Delta t}) - \dot{\varepsilon}_{y,t-\Delta t}(\sigma'_{xx,t} - \sigma'_{yy,t})}{\sigma'_{yy,t} - \sigma'_{yy,t-\Delta t} + \frac{\sigma'_{xx,t} - \sigma'_{xx,t-\Delta t}}{\dot{\varepsilon}_{x,t-\Delta t}} \dot{\varepsilon}_{y,t-\Delta t}} \\ \dot{\varepsilon}_{y,t} = \dfrac{V_0 - V(1 + \dot{\varepsilon}_{x,t} dt)}{V(1 + \dot{\varepsilon}_{x,t} dt)dt} \end{cases} \quad \text{(Eq. 2.12)}$$

Both Eq. 2.10 and Eq. 2.12 can yield a CV loading condition. To be consistent with the axisymmetric triaxial tests, in which the radial confining pressure is maintained constant, Eq. 2.12 is adopted in the version of LAMMPS used in this study. When this CV servo-control scheme was implemented into LAMMPS, the subscripts in Eq. 2.12 alternate between the *x* and *y* directions on successive timesteps to avoid bias. Note that the subscripts in Eq. 2.9 to Eq. 2.12 may be alternated accordingly when the loading direction is changed. The effectiveness of Eq. 2.12 in maintaining a constant-volume condition during CV simulations is evident in Figure 2.8 which shows the evolution of the volumetric strain for a representative CV simulation carried out in the current study. The volumetric strain oscillated between $-2 \times 10^{-8}$% and $3 \times 10^{-8}$% which is small enough to be considered negligible.

### 2.3.6 Constant-*b* drained true triaxial loading condition

A servo-control mechanism that simulates constant-$\sigma'_3$ true triaxial loading conditions was also implemented in LAMMPS. The strain rate in $\sigma'_3$ direction follows Eq. 2.4. The intermediate stress $\sigma'_{2,t+\Delta t}$ for $t + \Delta t$ can be obtained by,

$$\sigma'_{2,t+\Delta t} = b\sigma'_{1,t+\Delta t} - (b-1)\sigma'_{3,t+\Delta t} \quad \text{(Eq. 2.13)}$$

in which $b = \frac{\sigma'_2 - \sigma'_3}{\sigma'_1 - \sigma'_3}$ is the intermediate stress ratio, $\sigma'_{1,t+\Delta t}$ follows Eq. 2.6 and $\sigma'_{3,t+\Delta t}$ is equal to the confining pressure. Therefore, the strain rate in the intermediate stress direction can be obtained by replacing $\sigma'_{required}$ in Eq. 2.4 by $\sigma'_{2,t+\Delta t}$ as defined by Eq. 2.13. Note that again the directions of the major, intermediate and minor principal stresses can be alternated between different Cartesian axes as the loading direction changes. As shown in Figure 2.9, the *b* values can be effectively controlled in simulations using the modified LAMMPS code.

A stress-controlled, constant-volume, cyclic loading servo-control algorithm was also implemented into the modified LAMMPS code. It is not relevant to this research and thus is not detailed here. Since none of these features are available in the original LAMMPS code, a key contribution in the current study is the verification of the modified LAMMPS code.

## 2.4 Validation of the modified LAMMPS code

A DEM code can be validated either experimentally or analytically. Comparing the DEM simulation results to analytical solutions for a particular problem is a more reliable approach as the experimental results can be affected by boundary effects and could also be very sensitive to small biases in particle geometry (O'Sullivan, 2011). In this study the LAMMPS simulation results are compared to analytical solutions derived by Thornton (1979) considering the peak stress ratios for a face-centred cubic (FCC) assembly composed of uniform rigid spheres following previous work of Barreto (2009) and PFC3D (Itasca Consulting Group, 2007).

### 2.4.1 Failure conditions for a FCC sample comprising uniform rigid spheres

Figure 2.10 illustrates the representative geometry of a FCC assembly. The initial contact points (P, Q, R, S, T and U) for a representative element sphere A are shown in Figure 2.10(d). The other six contact points can be identified diametrically opposite to P, Q, R, S, T and U.

The work of Thornton (1979) was based on previous contributions of Rennie (1958) and Parkin (1965). Parkin (1965) derived the normalised strain-increment tensor for an FCC assembly subjected to a uniform small strain field as:

$$S = \begin{bmatrix} d\varepsilon_{xx} & d\varepsilon_{xy} & d\varepsilon_{xz} \\ d\varepsilon_{yx} & d\varepsilon_{yy} & d\varepsilon_{yz} \\ d\varepsilon_{zx} & d\varepsilon_{zy} & d\varepsilon_{zz} \end{bmatrix} = \begin{bmatrix} -2a & 0 & 0 \\ 0 & -2b & 0 \\ 0 & 0 & a+b \end{bmatrix} \quad \text{(Eq. 2.14)}$$

in which $a$+$b$ is equal to one and $\dot{\varepsilon}_z = -\frac{1}{2}(\dot{\varepsilon}_x + \dot{\varepsilon}_y)$. The special case when $a = b = 0.5$ corresponds to the axisymmetric triaxial loading condition while $a \neq b$ refers to the true triaxial loading conditions. The most conservative failure mechanism of an FCC assembly subjected to a strain field defined by Eq. 2.14 was assumed to be characterised by the loss of two sets of contacts in both the $x$ (U) and $y$ (T) directions for triaxial loading or the loss of two sets of contacts in either the $x$ (U) or $y$ (T) direction for plane-strain loading.

Based on the following idealisations:

- The direction of the stress tensor coincides with the direction of the strain increment tensor
- The moment of each particle is in equilibrium by assuming an identical tangential force for all the contacts, i.e., an 'irrotational' condition is imposed
- The normal force contribution to $\sigma'_{xx}$ is scaled to unity
- The shear stresses are negligible compared to the normal stresses

The stress ratios for triaxial loading can be expressed by:

$$\begin{cases} \dfrac{\sigma'_{zz}}{\sigma'_{xx}} = \dfrac{2+2\mu/F}{1-2a\mu/F} \\ \dfrac{\sigma'_{yy}}{\sigma'_{xx}} = \dfrac{1-2b\mu/F}{1-2a\mu/F} \end{cases} \quad \text{(Eq. 2.15)}$$

where $F = \sqrt{\frac{3}{2}(a^2 + b^2) + ab}$.

The same approach can be applied to plane strain loading conditions which yield:

$$\begin{cases} \dfrac{\sigma'_{zz}}{\sigma'_{xx}} = \dfrac{2+2\mu/F}{1-2\mu/F} \\ \dfrac{\sigma'_{yy}}{\sigma'_{xx}} = \dfrac{1+t}{1-2\mu/F} \end{cases} \quad \text{for } a=1, b=0 \qquad \text{(Eq. 2.16(a))}$$

$$\begin{cases} \dfrac{\sigma'_{zz}}{\sigma'_{xx}} = \dfrac{2+2\mu/F}{1+u} \\ \dfrac{\sigma'_{yy}}{\sigma'_{xx}} = \dfrac{1-2\mu/F}{1+u} \end{cases} \quad \text{for } a=0, b=1 \qquad \text{(Eq. 2.16(b))}$$

where $F = \sqrt{3/2}$. Eq. 2.15 and Eq. 2.16 are of particular interest for the validation of a DEM code as they allow different types of loading conditions to be examined. Moreover the formulations are independent of contact models and controlling parameters, e.g., the damping ratios, used for a DEM simulation.

As indicated by Eq. 2.15 and Eq. 2.16, the peak stress ratio of a FCC assembly depends on both the interparticle friction $\mu$ and loading conditions (different combinations of $a$ and $b$). Before performing the main validation simulations, parametric studies were carried out to investigate the sensitivity of the simulation results to factors that are not considered in Eq. 2.15 and Eq. 2.16. These include the effect of sample size, the effect of local damping and effects of contact models and contact stiffnesses. Simulations presented below were run on cx1 using one node with 12 cores.

### 2.4.2 Effect of sample size

As shown in Figure 2.11, four FCC assemblies containing 250, 2000, 6750 and 16000 mono-disperse spheres with identical properties (diameter=0.01m, density=2670 kg/m$^3$, $G$=1×10$^{12}$Pa, $v$=0.22, $\mu$=0.3) were generated. These samples were isotropically compressed to a stress state of 100 kPa prior to shearing. A vertical strain rate of 5×10$^{-3}$ $s^{-1}$ was then applied and the horizontal stresses ($\sigma'_{xx}$ and $\sigma'_{yy}$) were maintained constant throughout shearing. Particle rotations were inhibited to simulate an 'irrotational' condition in accordance with the assumption of the analytical model. A local damping ratio of 0.3 was used for all the samples. A simplified Hertz-Mindlin (HM) contact model (Itasca Consulting Group, 2007; Thornton et al., 2011; Zhang & Makse, 2005) was used. This model combines the Hertzian theory for the normal direction (Eq. 2.17 (a)) and the 'no-slip' Mindlin theory for the tangential direction (Eq. 2.17 (b)).

$$f_n = \frac{4}{3}\frac{G}{1-v}\tilde{R}^{1/2}\delta_n^{3/2} \qquad \text{(Eq. 2.17 (a))}$$

$$\Delta f_t = \frac{4G}{(2-v)} \tilde{R}^{1/2} \delta_n^{1/2} \ \Delta s \qquad \text{(Eq. 2.17 (b))}$$

where $G$ is the shear modulus of particles, $v$ is the particle's Poisson's ratio, $\tilde{R} = \frac{R_i R_j}{R_i + R_j}$ is the equivalent radius, $\delta_n$ is the contact overlap and $\Delta s$ is the tangential displacement increment. The tangent normal contact stiffness for the HM model $k_n = \frac{2G}{1-v} \tilde{R}^{1/2} \delta_n^{1/2}$ and the tangent tangential contact stiffness $k_t = \frac{4G}{2-v} \tilde{R}^{1/2} \delta_n^{1/2}$ can be derived from Eq. 2.17, which indicates a stiffness ratio $\frac{k_t}{k_n} = \frac{2(1-v)}{2-v}$. The *maxerate* was set to be 0.01 during isotropic compression and 0.1 during shearing for the validation simulations presented below. Parametric studies show that the response of a FCC assembly is not sensitive to the *maxerate*; thus a relatively high value of *maxerate* was adopted to facilitate the speed of convergence between $\boldsymbol{\sigma'}_{required}$ and $\boldsymbol{\sigma'}_{measured}$. Figure 2.12 (a) compares the evolution of the major principal stress ratio ($\sigma'_{zz}/\sigma'_{xx}$) for samples composed of different numbers of spheres, while Figure 2.12 (b) compares the peak major principal stress ratios in terms of relative error compared to the analytical value. It is evident in Figure 2.12 that the number of particles has little effect on the overall response. Consistent results were obtained with the relative error of the peak major principal stress ratio being around 0.01072% for all the samples comparing to the analytical value of 3.7143 (Eq. 2.15). The assembly comprising 2000 particles were adopted in the following validation work.

### 2.4.3 Effect of local damping

A local damping option was implemented into the LAMMPS code following the approach of PFC3D (Itasca Consulting Group, 2007). Local damping is used to facilitate kinetic energy dissipation so that the system can reach an equilibrium state in a reasonable number of calculation cycles. When activated, a damping force/moment $\boldsymbol{F_d}$, which is proportional to the unbalanced force/moment $\boldsymbol{F_u}$, is applied to particles opposite to the corresponding velocity ($\boldsymbol{V}$) direction according to Eq. 2.18.

$$\boldsymbol{F_d} = d \cdot |F_u| \cdot sign(\boldsymbol{V}) \qquad \text{(Eq. 2.18)}$$

in which $d$ is the local damping ratio and *sign* denotes the signum function. To gain an initial understanding of the effect of local damping, Figure 2.13 considers a simple system with one degree of freedom. A ball rests on a horizontal wall. An initial downward velocity of 0.0001 m/s is applied and gravity is switched on at the beginning of simulations. Different damping ratios are applied and the corresponding velocity evolutions are recorded. As shown in Figure 2.13, in the absence of local damping, the ball bounces following a harmonic motion

without degradation in the velocity amplitude, while when local damping is introduced, the amplitude of velocity decreases gradually and the ball eventually becomes stationary. The dissipation of kinetic energy becomes more significant and the ball settles faster as $d$ increases.

The influence of the local damping ratio on the overall response of the FCC assemblies was examined by applying the sample loading condition described in Section 2.4.2 to the sample composed of 2000 spheres. $d$ values in the range from 0.0 to 0.5 were examined at intervals of 0.1 and the results are presented in Figure 2.14. The response is almost identical for all $d$ values considered. The insensitivity of mechanical response to $d$ is attributable to the kinematic constraints imposed by the high number of symmetrically-distributed neighbours processed by each individual sphere. In Section 2.4.4 and Section 2.4.5, a local damping ratio of 0.1 was adopted.

### 2.4.4 Effect of contact stiffnesses

The analytical solution for the FCC packing assumes the spheres to be rigid. Figure 2.15 shows the influence of the shear modulus ($G$) on the peak major principal stress ratio when the simplified HM model is used. The Poisson's ratio ($v$=0.22) is identical for all samples while $G$ is varied between $2.9\times10^{10}$ Pa and $1\times10^{13}$ Pa. As shown in Figure 2.15 (a), the sample is stiffer when $G$ is increased and the strain level at which the peak stress ratio occurs decreases with increasing $G$. The relative error decreases from 0.114% to 0.0023% as $G$ increases from $2.9\times10^{10}$ Pa to $1\times10^{13}$ Pa (Figure 2.15 (b)). The increase in accuracy with increasing contact stiffnesses when a linear elastic model is used is also confirmed as shown in Figure 2.16. The normal and tangential contact stiffnesses were taken to be identical and increased from $1\times10^{7}$ N/m to $1\times10^{11}$ N/m step-wise by an order of magnitude. The maximum relative error (0.044%) is observed for the case with the lowest stiffness ($k_n$=$k_s$=$1\times10^{7}$ N/m), while the minimum relative error $4.5\times10^{-6}$ % is found for the case with the highest stiffness ($k_n$=$k_s$=$1\times10^{11}$ N/m). Overall, the peak major principal stress ratios for simulations using the linear elastic model are closer to the analytical solutions than those for simulations using a simplified Hertz-Mindlin contact model. This agrees with the observations of Hanley (2012) (Personal communication).

### 2.4.5 Effect of loading conditions and interparticle friction

To comprehensively evaluate the validity of the modified code, three types of loading conditions were considered, i.e., conventional triaxial compression, plane strain compression and true triaxial compression. For the conventional triaxial compression simulations,

shearing was progressed by applying a constant strain rate in the $z$ direction whilst maintaining the horizontal stresses constant. The plane strain loading condition was simulated by fixing the position of one pair of the horizontal boundaries which are normal to the $y$ axis while the stresses in the $x$ direction were held constant. Two approaches can yield a true triaxial loading condition:

- Strain-controlled method

Different strain rates are applied in different directions, with the strain rate ratios ($2a = \dot{\varepsilon}_x/\dot{\varepsilon}_z$ and $2b = \dot{\varepsilon}_y/\dot{\varepsilon}_z$) adhering to $a + b = -1$ as implied by the analytical model.

- Stress-controlled method

After isotropic compression, one of the horizontal stresses is increased to the target stress for the selected $\mu$ and $a$ values according to Eq. 2.15. Then the sample is sheared in the $z$ direction while both horizontal stresses are maintained constant.

Hanley (2012) showed that both methods can give accurate approximation for the analytical solutions (Personal Communication). The first approach was adopted here as the loading procedure in such a case conforms to that associated with the proposed failure mechanism. $\mu$ values ranging from 0.0 to 0.8 were considered. A very large shear modulus ($G$=1e13 Pa) was used for all the simulations to fulfil the rigid-body assumption.

The typical behaviour of a FCC sample subjected to axisymmetric triaxial loading conditions is presented in Figure 2.17. Figure 2.17(a) shows the evolution of principal stress components, Figure 2.17(b) shows the evolution of the stress ratios and Figure 2.17(c) presents the variation in coordination number $Z(=2N_c/N_p)$, in which $N_c$ and $N_p$ are the total number of contacts and the total number of particles within the sample respectively. As Figure 2.17 shows, only a single failure event (F1) can be identified for axisymmetric triaxial loading. The coordination number drops directly from 12 to 8 (Figure 2.17 (c)). Planar views of the contact force network at different stages of loading are given in Figure 2.18. Each line in Figure 2.18 connects two touching particles and the thickness of each line is proportional to the magnitude of the normal contact forces normalised by the mean value. Two sets of contacts break instantaneously in both the $x$ and $y$ directions. The instant at which the peak major principal stress is reached coincides with F1. Both the major and minor principal stress ratios agree with the analytical value (3 for $\sigma_1/\sigma_3$ and 1 for $\sigma_2/\sigma_3$).

Figure 2.19 shows the typical behaviour of a FCC sample subjected to true triaxial loading. A compressive strain rate of 5e-3 was applied in the $z$ direction, while extensive strain rates

of 2e-3 and 8e-3 were imposed in the $x$ and $y$ directions respectively. Figure 2.19(a) shows the evolution of the principal stress components, Figure 2.19(b) shows the evolution of stress ratios and Figure 2.19(c) presents the variation of coordination number. Two distinct failure events can be identified in Figure 2.19(c), at which the coordination number drops from 12 to 10 and from 10 to 8 respectively. The maximum major principal stress ($\sigma_{zz}$) and the minimum minor principal stress ($\sigma_{yy}$) are attained at the first failure instant (F1) and maintained constant thereafter, while the intermediate principal stress ($\sigma_{xx}$) keeps decreasing until a minimum value is reached at the second failure instant (F2). The maximum major ($\sigma_1/\sigma_3$) and minor ($\sigma_2/\sigma_3$) principal stress ratios correspond to F1 and the former coincides with the analytical solution, while the minor principal stress ratio which is attained after F2 agrees with the analytical solution. It is evident in Figure 2.19 (c) and Figure 2.20 that the same failure mechanism that is indicated by the analytical model is captured by the modified LAMMPS code for true triaxial loading, i.e., gap formation along two sets of rows of contiguous spheres perpendicular to each other in both the intermediate and minor principal stress directions which induces a drop of the coordination number from 12 to 8. Failure is however progressive in two steps rather than instantaneous. Contact loss firstly occurs in the minor principal stress direction ($y$) at F1 and propagates to the intermediate principal stress direction ($x$) at F2.

Figure 2.21 presents the behaviour of a representative plane strain simulation. As shown in Figure 2.21 (c), the coordination number drops from 12 to 10 at around 0.0006% axial strain which is due to the loss of two sets of contacts in the minor principal stress direction ($x$) as revealed in Figure 2.22. This agrees with the analytical model. However, the failure point (F1) does not correspond to the peak strength. Both the major and intermediate principal stresses continue to increase after F1 and reach a constant value at around 0.00095% axial strain. The subsequent increase in the major principal stress after F1 is due to the increase in the intermediate principal stress which strengthens the lateral support for the strong force chains aligned closer to the vertical direction.

Figures 2.23 and 2.24 compare the measured variation in the major and minor principal stress ratios at failure with the analytical solutions. Note that the minor principal stress ratios after the second failure event (F2) rather than the peak minor principal stress ratios are considered in Figure 2.24. The minor principal stress ratios for the plane strain loading condition are not presented in Figure 2.24 as the normalised normal contact force ($t$) at contact T is not directly defined in the analytical model. As reflected in Figures 2.23 and 2.24, both the major and the minor principal stress ratios increase with increasing $\mu$. The major principal stress ratio increases with increasing $a$, while the opposite is true for the

minor principal stress ratio. In general, the simulation results closely match the analytical solutions for both the major and the minor principal stress ratios. The relative errors for plane strain simulations are larger than those for other loading conditions. For both the major and the minor principal stress ratios, the accuracy decreases with increasing $\mu$. A dramatic increase in relative error is observed when $\mu$ exceeds 0.6. This may be attributable to the transition from the sliding-dominant to rolling-dominant contact behaviour as $\mu$ increases. This issue will be addressed in Chapter 4. Considering the entire data set, the maximum relative error is 0.165% which is observed for the plane strain simulation using $\mu$=0.5.

## 2.5 Summary

The open-source LAMMPS code has been modified to make it capable of simulating the behaviour of soils. Many new features have been added into the original LAMMPS code. These include different types of servo-control schemes which enable simulation of various loading conditions encountered in laboratory tests of soils. The modified code has been validated by comparing the simulation results with the analytical solutions for the peak stress ratio at failure derived for a FCC assembly composed of mono-sized rigid spheres (Thornton, 1979). The proposed failure mechanisms were shown to be captured by the simulations using the modified LAMMPS code. The simulation results were shown to be in good agreement with the analytical solutions under various loading conditions and considering differing interparticle friction coefficients. Therefore, the modified LAMMPS code can be reliably applied throughout this research to investigate the critical-state behaviour of granular materials. Most of the simulations presented in the following Chapters were carried out on the Imperial College PC cluster cx1 using 1 node with 12 cores.

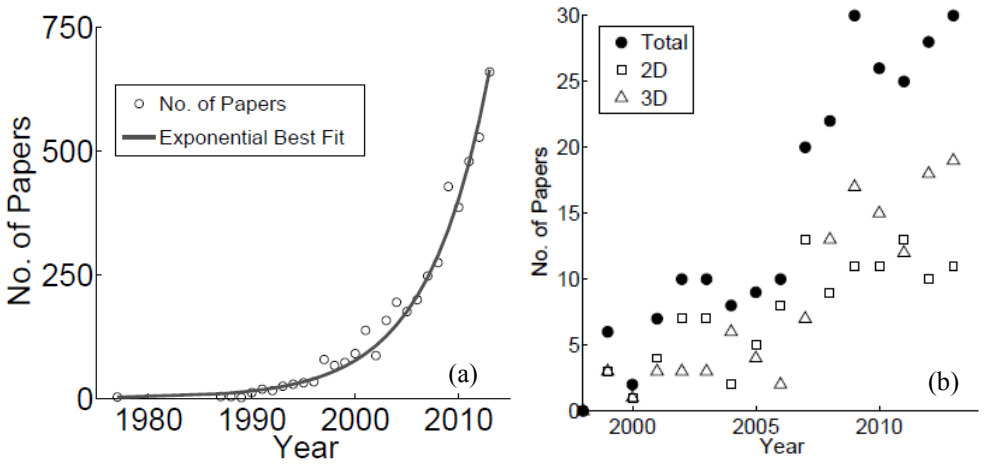
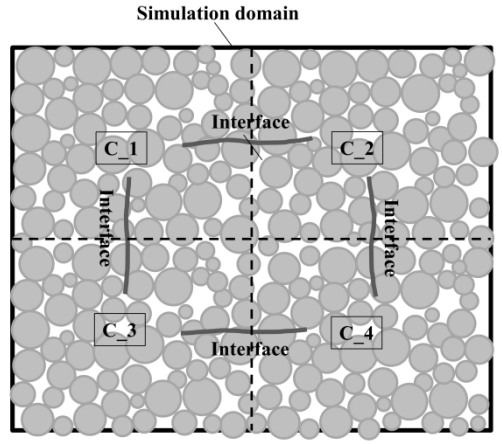
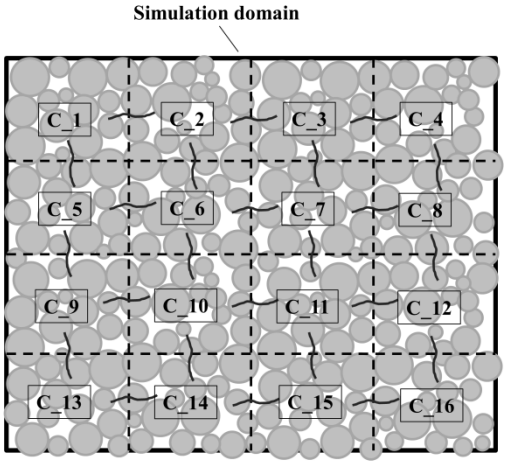



Figure 2.1 The number of publications using DEM (O'Sullivan, 2014): (a) All disciplines; (b) Geomechanics-related




(a)




(b)

Figure 2.2 Schematic of the spatial-partition parallel technique for a 2D problem : The simulation domain is divided into (a) four subdomains; (b) 16 subdomains (C denotes core) (After Munjiza, 2004)

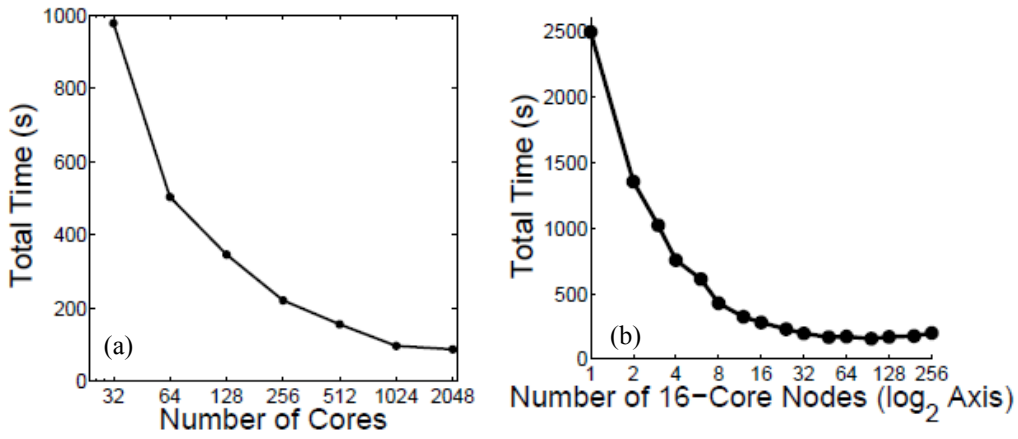



Figure 2.3 Scaling tests of the modified LAMMPS code on the UK's national high-performance-computing (HPC) facilities: (a) triaxial compression simulation on a face-centred-cubic sample composed of 125,000 uniform spheres, run for 100,000 time steps on HECToR Phase 3; (b) constant-volume simulation on a polydisperse sample comprising 351,248 spheres, run for 100,000 time steps on Hartree Blue Joule (O'Sullivan, 2014)

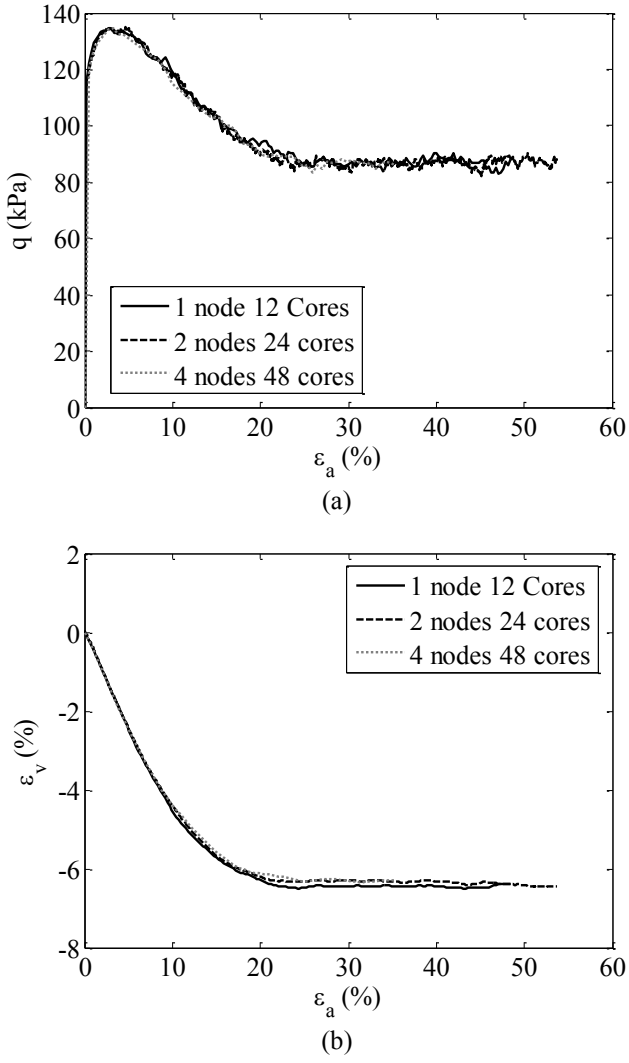



Figure 2.4 Comparing the simulation results using different numbers of processors (Toyoura sand PSD, $e_0$=0.533, $\sigma'_3$=100 kPa, drained triaxial compression) (a) Deviatoric stress; (b) Volumetric strain

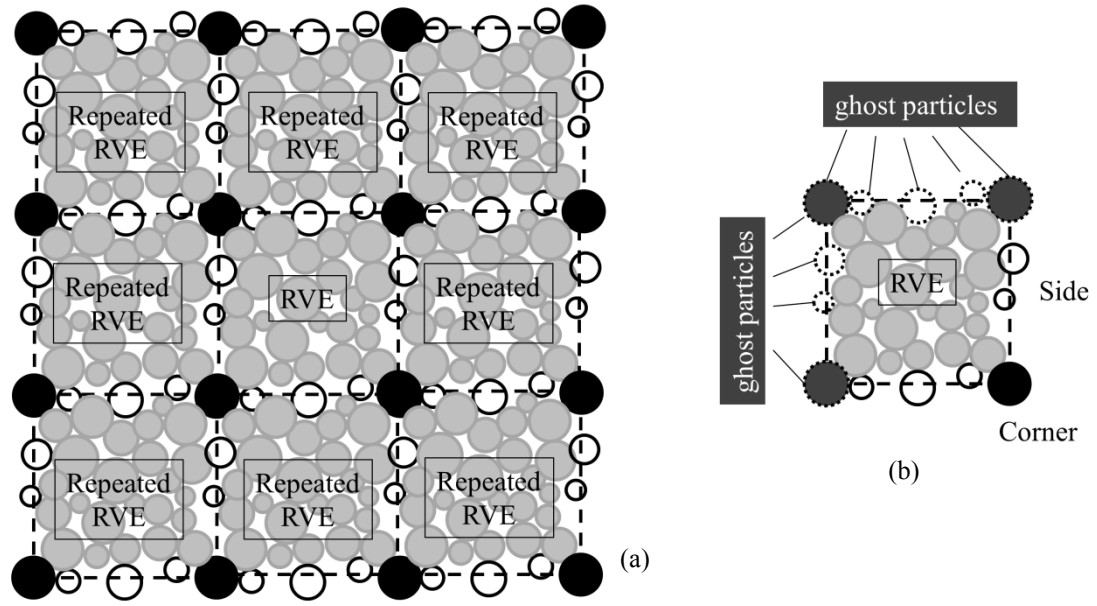



Figure 2.5 Illustration of periodic boundaries: (a) a sample composed of repeated structures; (b) remapping of particles across the periodic boundaries

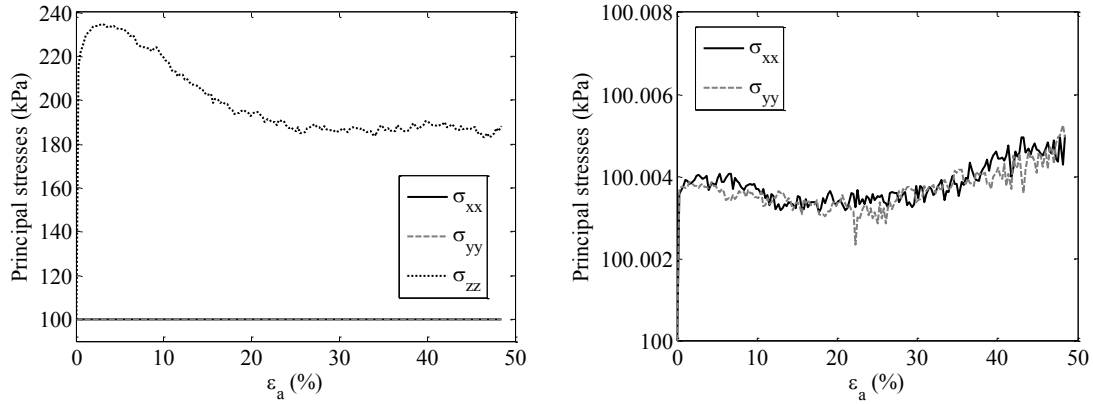



Figure 2.6 Effectiveness of the servo-control algorithm for CDC simulations (Toyoura sand grading, $e_0$=0.533, $\sigma'_3$=100 kPa)

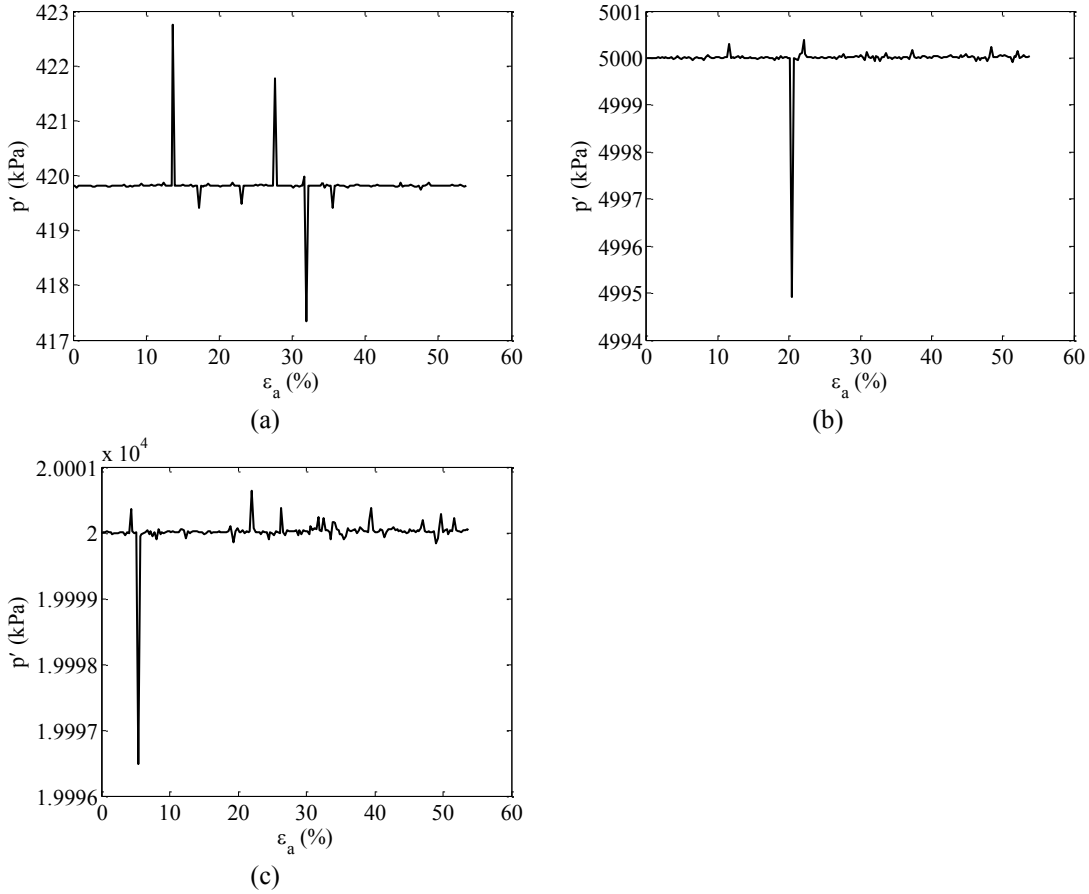



Figure 2.7 Effectiveness of the servo-control algorithm for CP compression simulations (Toyoura sand grading): (a) $p'$=419.8 kPa; (b) $p'$=5000 kPa; (c) $p'$=20 MPa

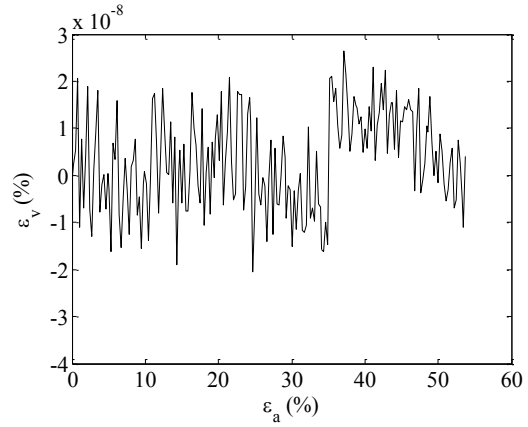



Figure 2.8 Evolution of volumetric strain during a CV simulation (Toyoura sand grading, $e_0$=0.606, $\sigma_{3,0}$=500 kPa)

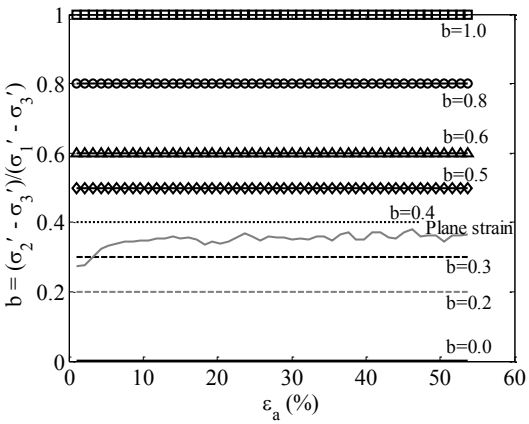



Figure 2.9 Effectiveness of the servo-control algorithm for constant-$\sigma'_3$ true triaxial simulations in controlling the $b$ values. (Toyoura sand grading, $e_0$=0.646, $\sigma'_3$=500 kPa)

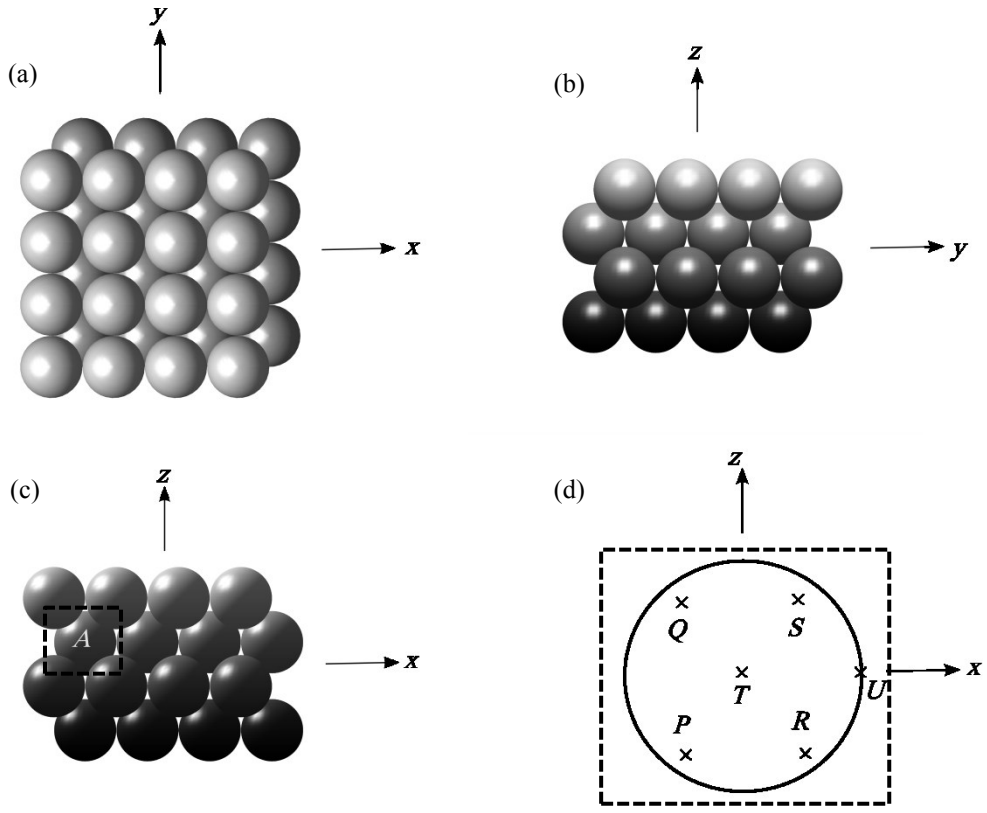
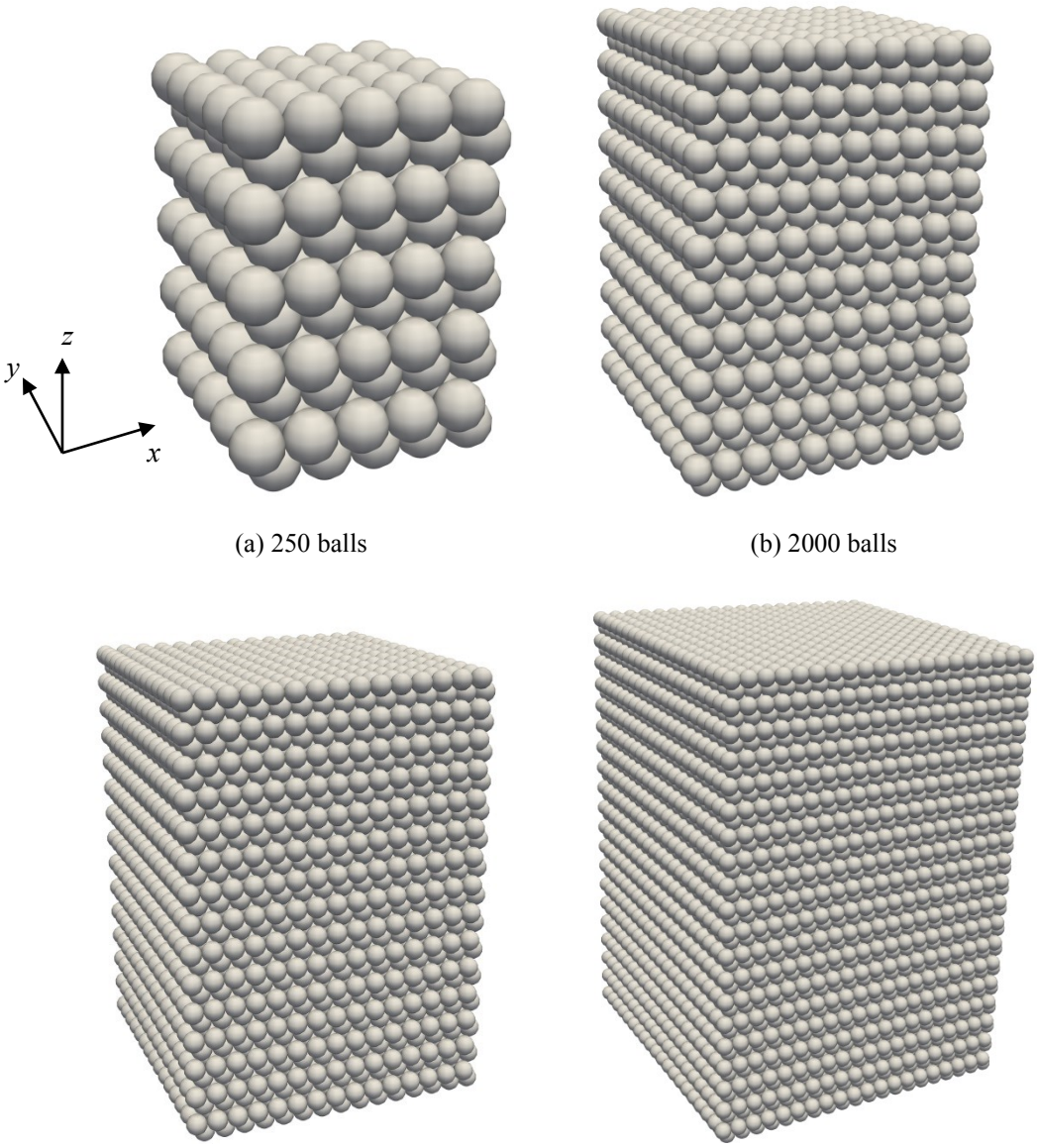


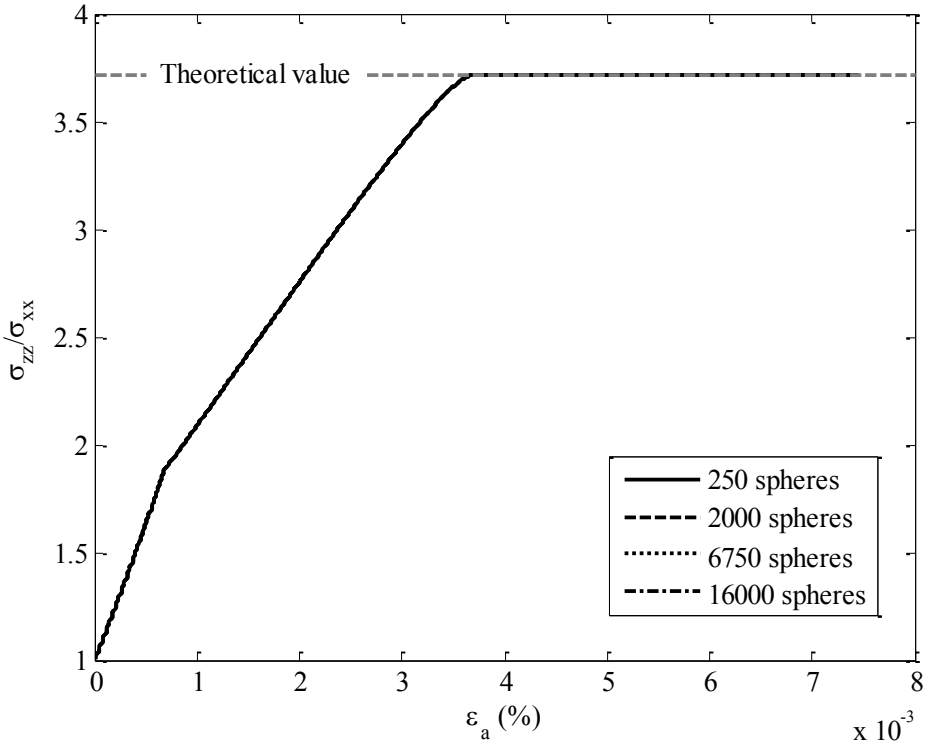

Figure 2.10 Geometry of a FCC assembly: (a) plane view; (b) view from the x axis; (c) view from the y axis; (d) contact distribution for a representative element sphere *A*



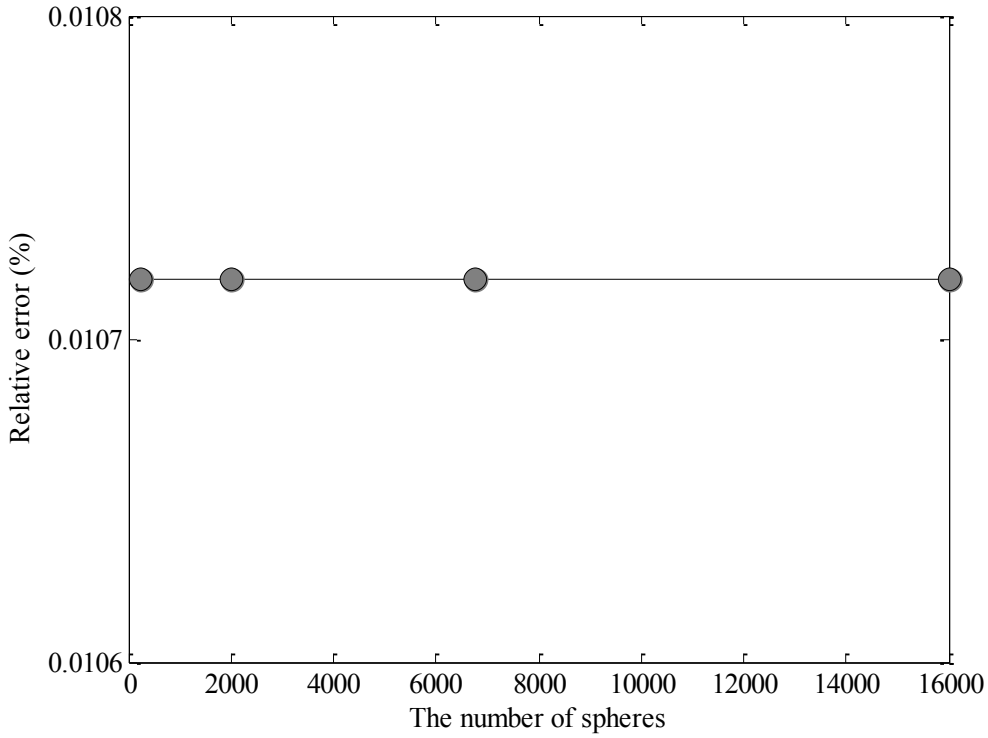

(a) 250 balls (b) 2000 balls

(c) 6750 balls (d) 16000 balls

Figure 2.11 Illustration of FCC samples containing different numbers of particles




(a)




(b)

Figure 2.12 Effect of sample size on the response of FCC assemblies: (a) Evolution of the major principal stress ratio; (b) Effect of sample size on relative error in peak major principal stress ratio

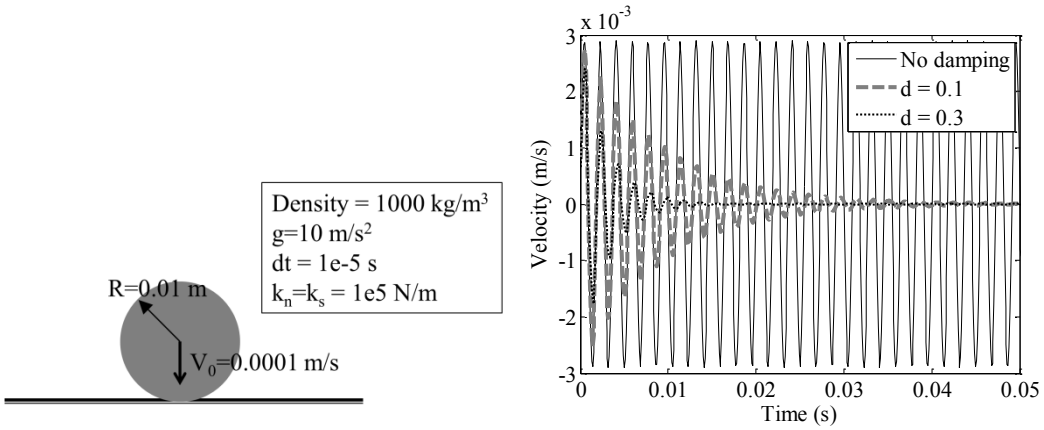



Figure 2.13 Illustration of the effect of local damping considering a single ball bouncing under gravity

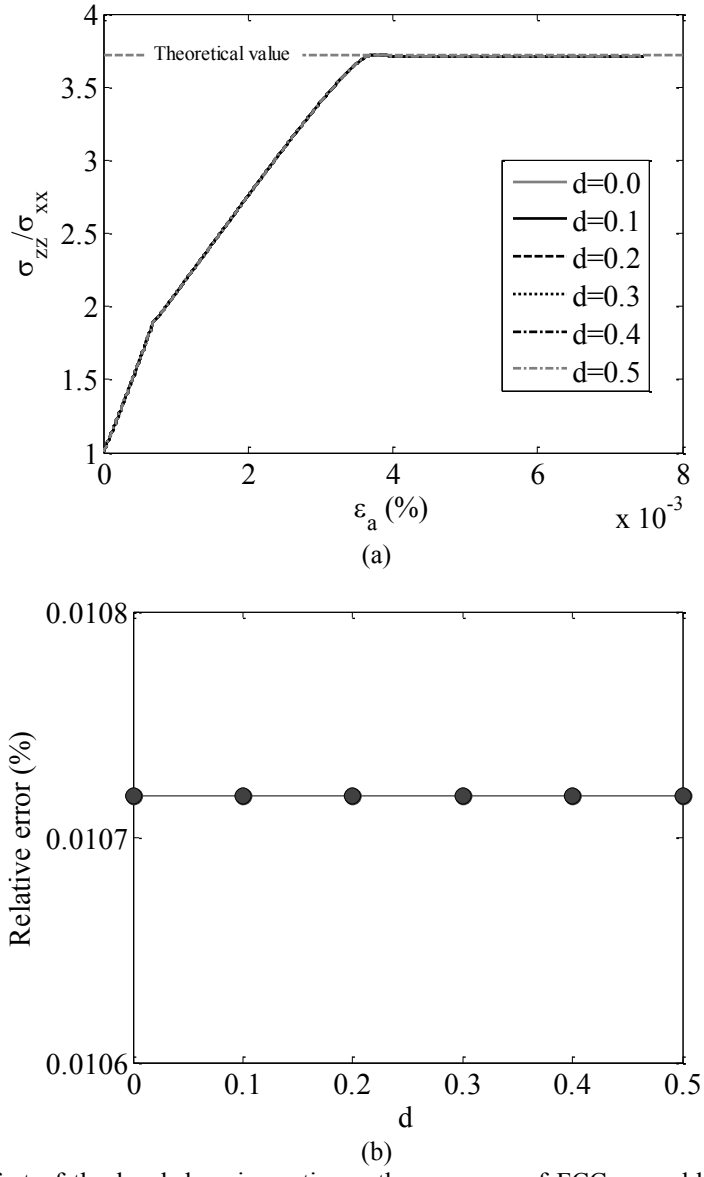
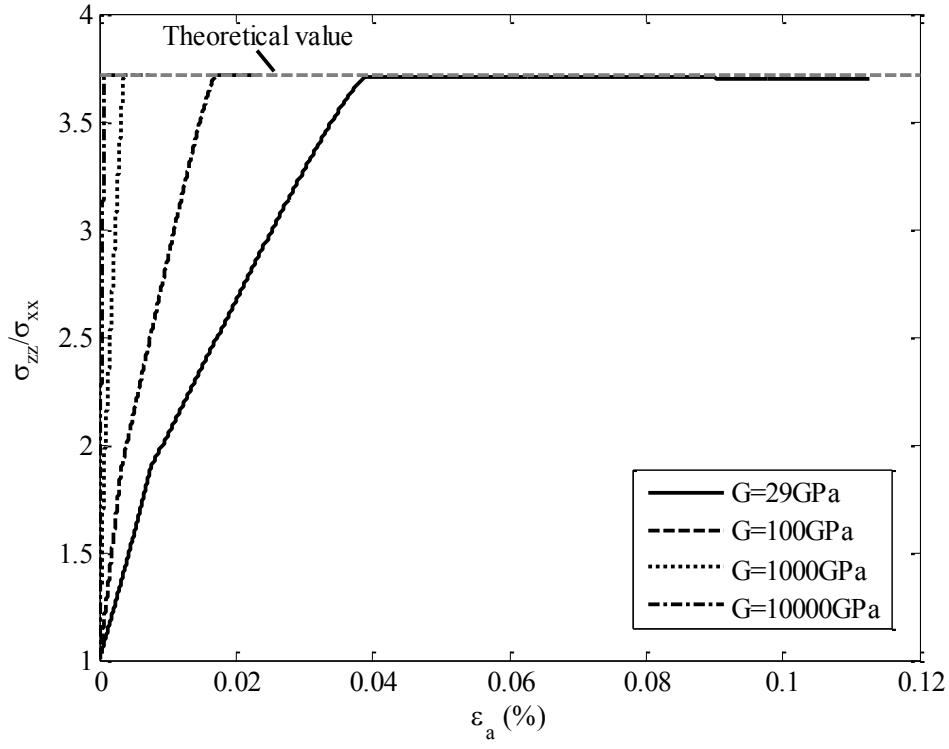
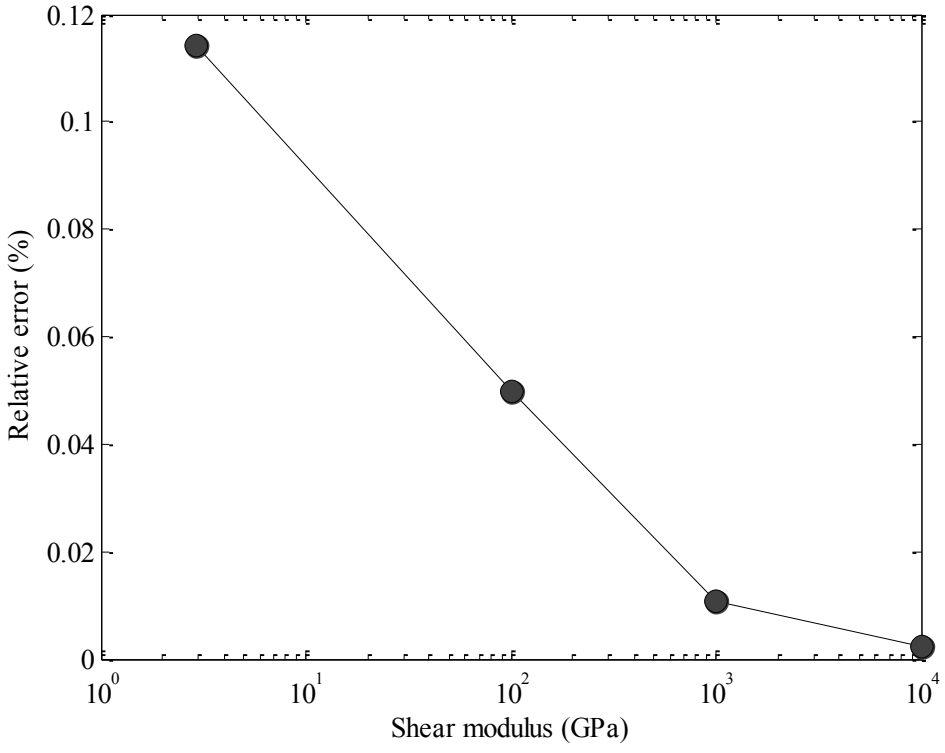



Figure 2.14 Effect of the local damping ratio on the response of FCC assemblies: (a) evolution of major principal stress ratio; (b) Influence of local damping ratio on the relative error in peak major principal stress ratio

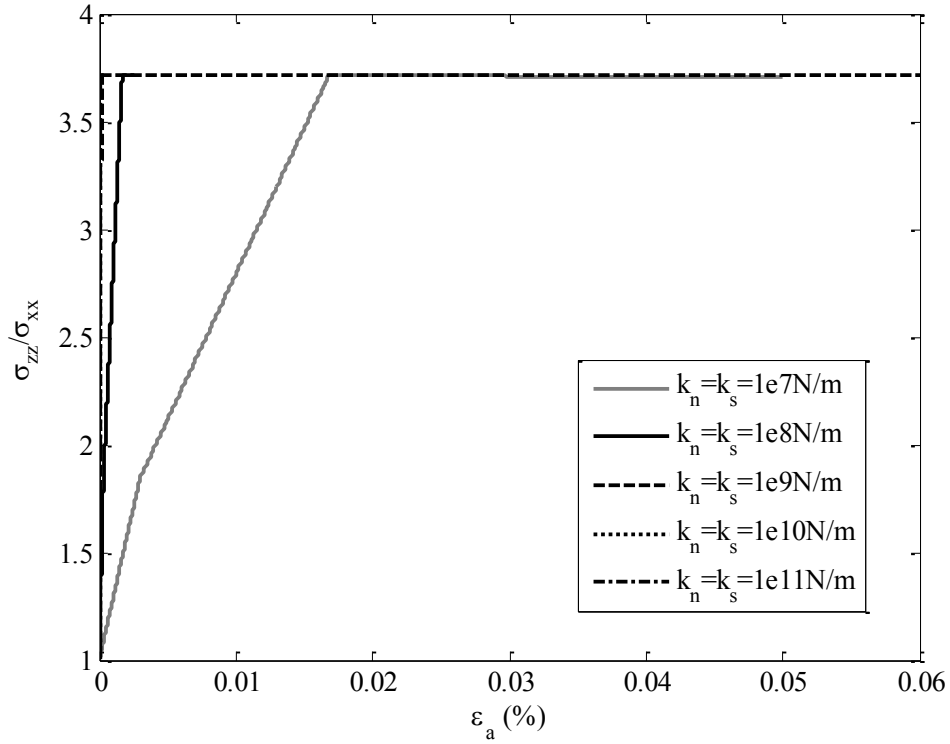



(a)

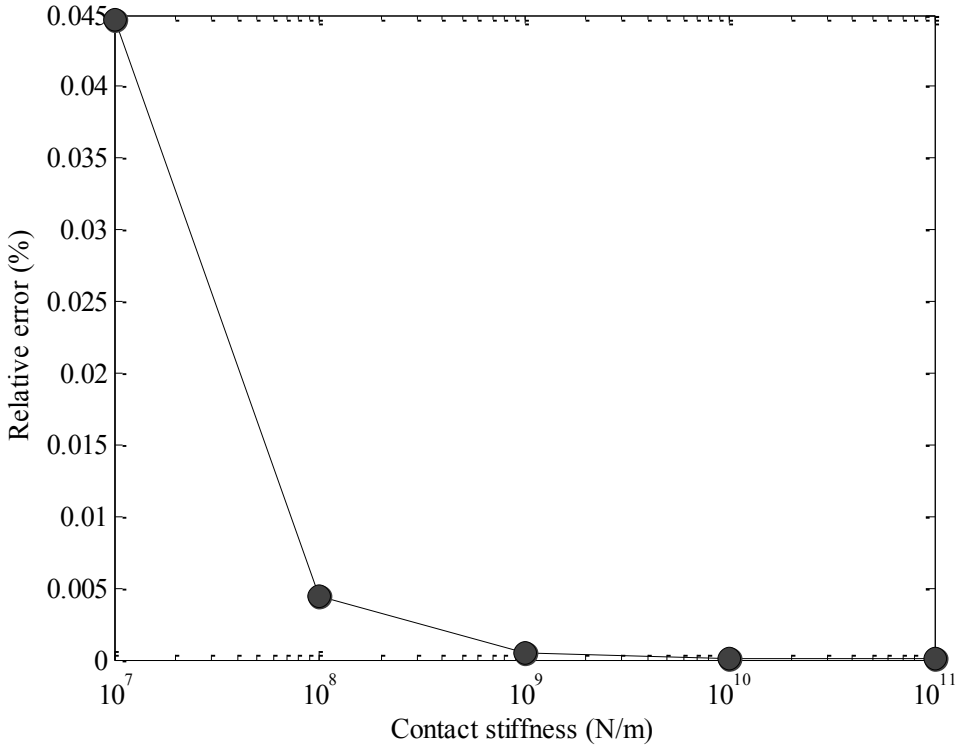



(b)

Figure 2.15 Effect of contact stiffness on the response of FCC assemblies using a simplified Hertz-Mindlin model: (a) evolution of the major principal stress ratio; (b) Effect of shear modulus on the relative error in peak major principal stress ratio




(a)




(b)

Figure 2.16 Effect of contact stiffness on the response of FCC assemblies using a linear elastic model: (a) evolution of the major principal stress ratio; (b) Effect of contact stiffness on the relative error in peak major principal stress ratio

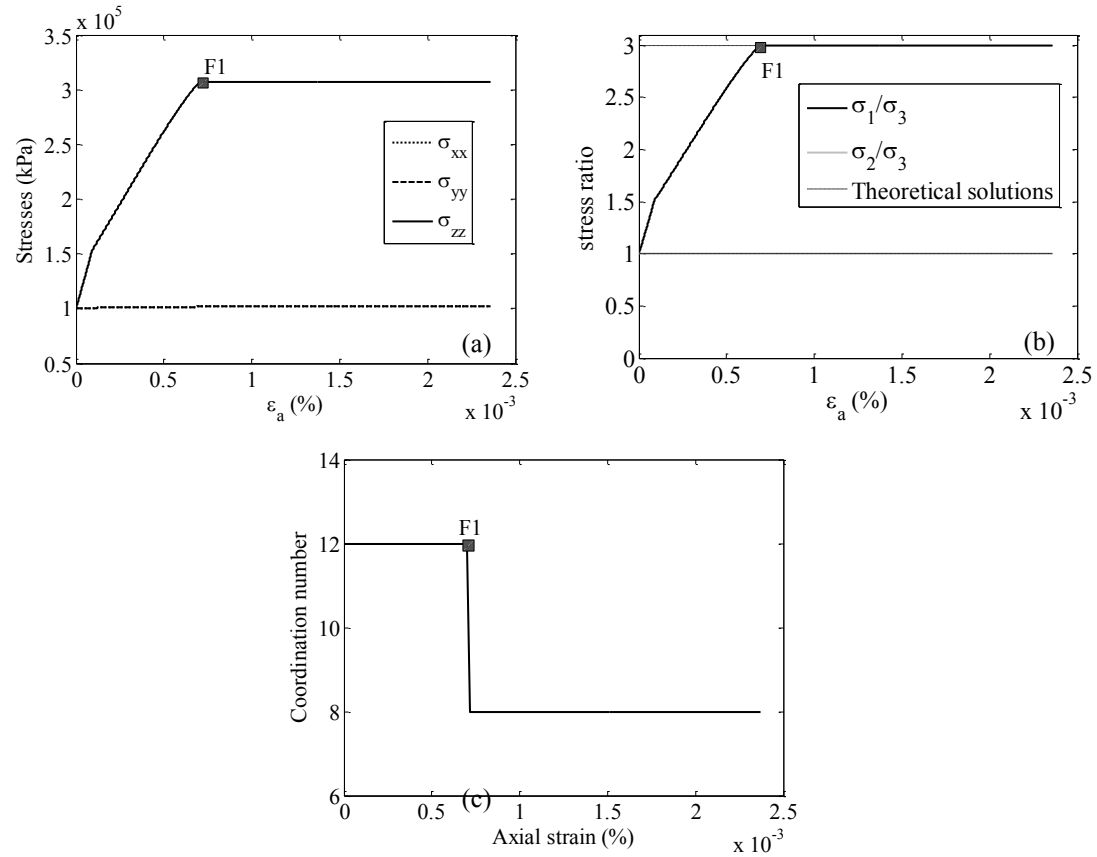



Figure 2.17 Failure mechanisms under axisymmetric triaxial loading conditions ($\mu$=0.2): (a) Principal stresses; (b) Stress ratio; (c) Coordination number

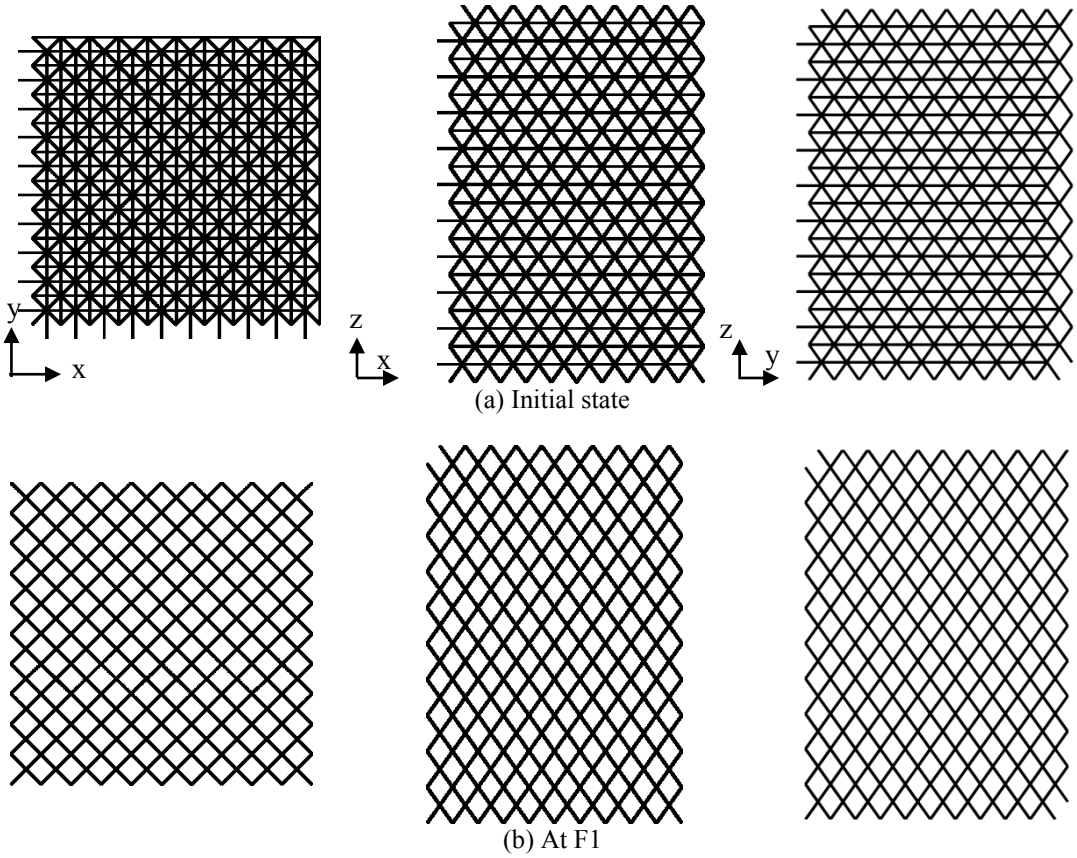



Figure 2.18 Contact force network under axisymmetric triaxial loading conditions ($\mu$=0.2)

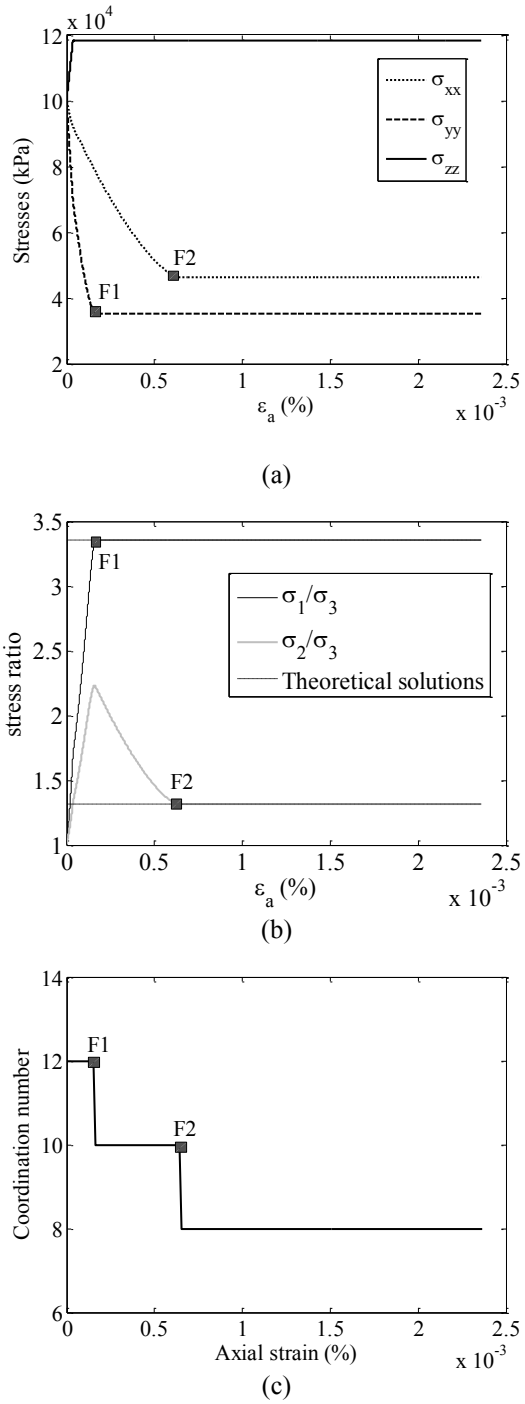



Figure 2.19 Failure mechanisms under true triaxial loading conditions (a=0.2,b=0.8, $\mu$=0.2): (a) Principal stresses; (b) Stress ratio; (c) Coordination number

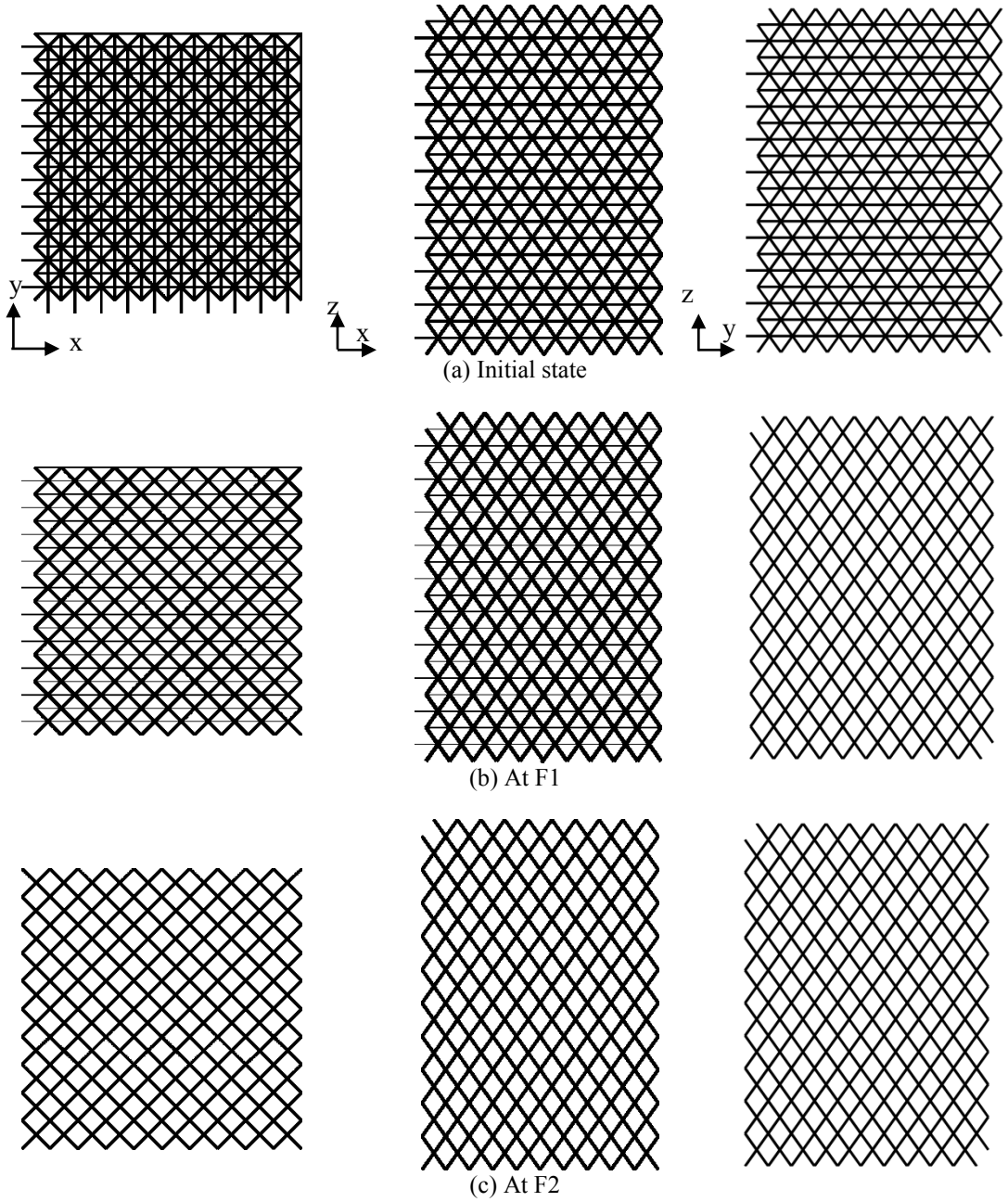



Figure 2.20 Contact force network under true triaxial loading conditions (a=0.2,b=0.8, $\mu$=0.2)

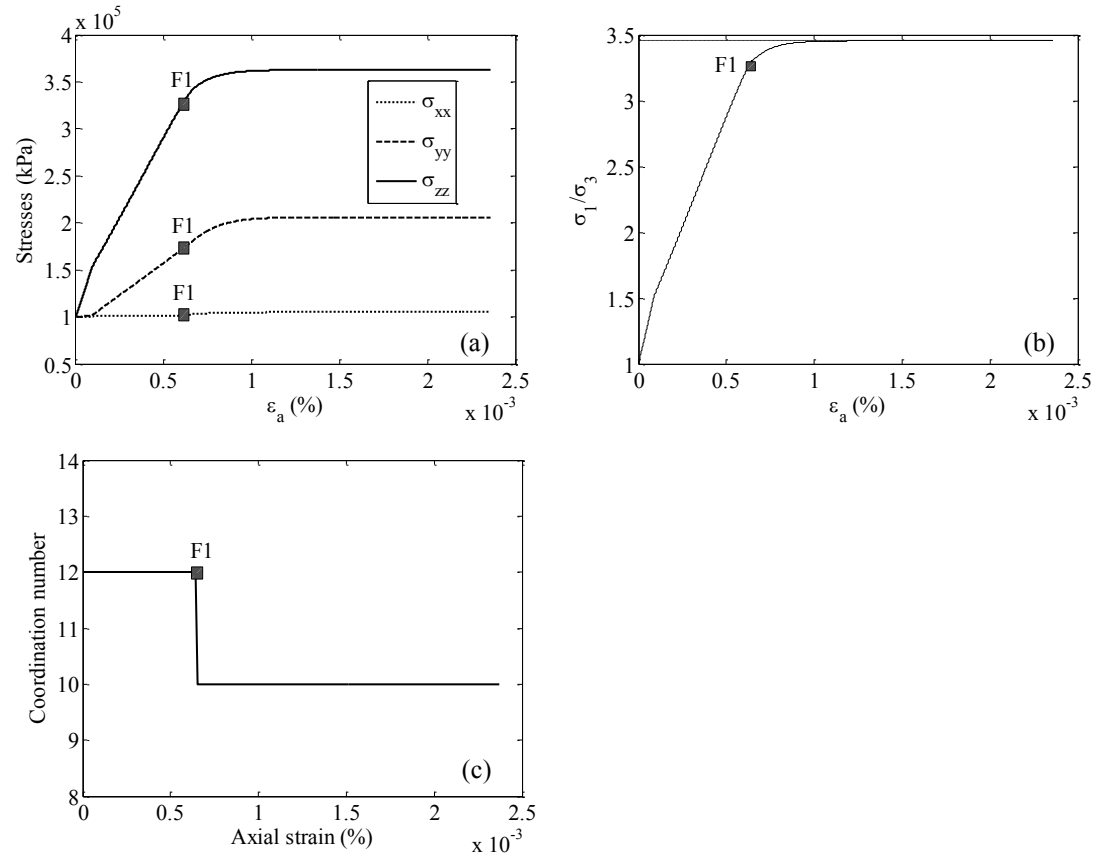
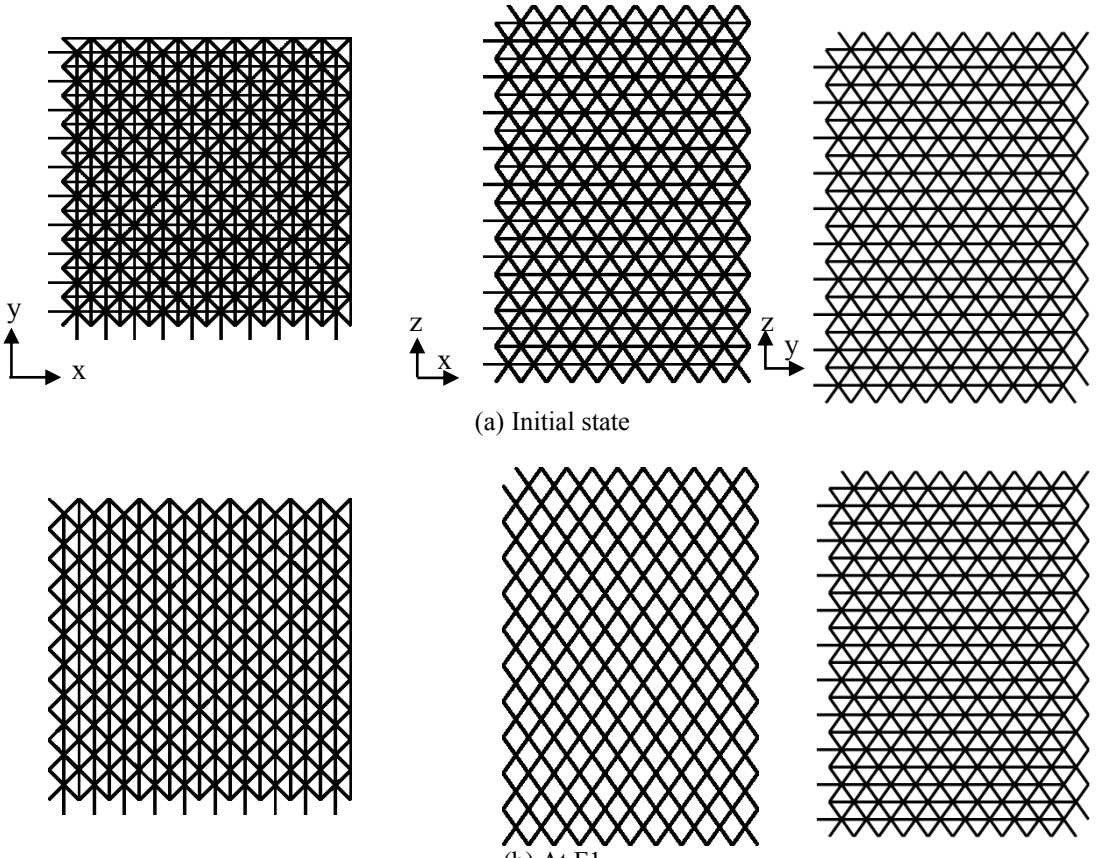



Figure 2.21 Failure mechanisms under plane strain loading conditions ($\mu$=0.2): (a) Principal stresses; (b) Stress ratio; (c) Coordination number




(a) Initial state

(b) At F1

Figure 2.22 Contact force network under plane strain loading conditions ($\mu$=0.2)

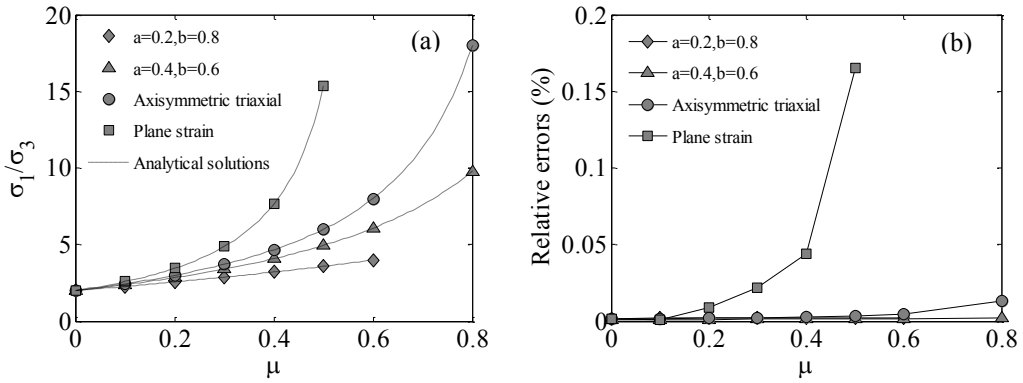



Figure 2.23 Comparing the measured major principal stress ratios with the analytical solutions: (a) Major principal stress ratios vs $\mu$; (b) Relative errors vs $\mu$

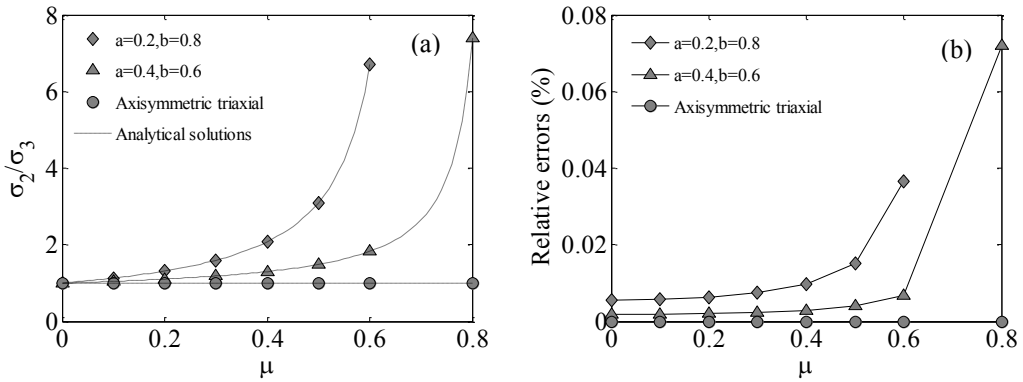



Figure 2.24 Comparing the measured minor principal stress ratios with the analytical solutions: (a) Minor principal stress ratios vs $\mu$; (b) Relative errors vs $\mu$

# Chapter 3 Effects of Sample Size in DEM Simulations

## 3.1 Introduction

DEM has been widely applied to simulate element tests to study fundamental aspects of soil response (e.g., Cui, O'Sullivan & O'Neill, 2007; Kwok & Bolton, 2010;Yan & Dong, 2011). The computational cost limits the number of particles used in these simulations; as documented by O'Sullivan (2011) (Figure 3.1) around 10,000 particles are commonly used in 3D simulations and this number rarely exceeds 100,000. For physical laboratory testing, however, the ratio of sample size to particle size is usually larger than this, e.g., ASTM (2011) suggested that the diameter of a cylindrical sample for triaxial compression tests should not be smaller than 33 mm, which is at least 30 times the characteristic size (i.e., $D_{50}$) of ordinary sands and the specimen diameter shall be larger than six times the largest particle diameter. Head (1994) suggested that the thickness of samples in shear box tests should not be less than 10 times the maximum particle diameter. Adhering to these guidelines when running DEM simulations is difficult, particularly when realistic gradings are used, as many small particles must be simulated for every large particle. The presence of these smaller particles significantly increases the number of degrees of freedom in the system and also necessitates the use of a very small timestep to ensure numerical stability.

## 3.2 Prior studies on sample size effects and boundary effects

A number of prior studies have considered sample size effects in DEM simulations when rigid-wall boundaries were used. O'Sullivan et al. (2002) introduced small perturbations to the DEM sample by varying the particle size distribution (PSD) slightly and noted that the stress-strain response of the smaller samples fluctuated significantly and was more sensitive to the change of PSD than the larger samples as shown in Figure 3.2. Potyondy & Cundall (2004) observed that the bulk properties of bonded materials, e.g., Young's modulus, are sensitive to the size of the sample. Kuhn & Bagi (2009) found that peak compressive strength decreases as sample size is increased. As shown in Figure 3.3, Collop *et al.* (2006) showed that the bulk Young's modulus increases while the Poisson's ratio decreases when the number of particles is increased. It has also been reported that there is a minimum requirement for the number of particles in order to yield consistent behaviour of the numerical assemblies with different sizes as shown in Figure 3.4 (Belheine *et al.*, 2009). However, explanations for these phenomena have not been provided in the literature and

none of these previous studies have examined the effect of sample size on the mechanical behaviour of granular materials using a realistic PSD, which is essential for fair comparison of the numerical simulations and the laboratory tests.

It has been reported that the use of rigid-wall boundaries in DEM simulations results in inhomogeneity regarding the packing density and deformation. For instance, Chan & Ng (1986) observed relatively high porosities in the vicinity of the rigid wall boundaries. It has also been shown by Marketos & Bolton (2010) that under 1D compression, the use of flat rigid boundaries disturbed the grain packing at the boundaries and induced the localisation of porosity, strain and contact force distribution in the area adjacent to the top and bottom boundaries (Figure 3.5). The origin of the inhomogeneity close to the rigid wall boundaries has not yet been well understood. Furthermore, as the external loading is achieved through the interaction between the rigid walls and particles that are close to the rigid boundaries, the observed inhomogeneity within the boundary regions may be related to the size-dependent macro-scale stress-strain response as the relative size of the boundary regions to the overall sample domain decreases with increasing sample size.

In this Chapter, these existing research contributions are extended by considering samples with a realistic PSD. The relationship between the sample size effects and the sample inhomogeneity due to the use of rigid-wall boundaries is discussed. The data are interpreted within the critical state soil mechanics (CSSM) framework.

## 3.3 DEM Samples

Four sample types were considered in this study. Three cylindrical samples enclosed by rigid walls (RW) were created using the PFC3D software (Itasca Consulting Group, 2008) and a fourth sample enclosed by periodic boundaries (PB) was created using a modified version of the open-source LAMMPS code (Plimpton, 1995). As shown in Figure 3.6, the RW samples were created within a cylindrical domain while the PB sample is cuboidal. The smallest rigid-wall sample, RW-S, had 6,783 particles, the medium rigid-wall sample, RW-M, contained 16,073 particles, and the largest rigid-wall sample, RW-L, contained 31,392 particles. The periodically-bounded sample, PB, was composed of 20,164 spherical particles. For all these samples, the PSDs were close to the grading curve of a Toyoura sand (Yang & Sze, 2011) as shown in Figure 3.7. The gradings were generated by discretizing the Toyoura grading into several size classes. The particle diameters were assumed to be uniformly distributed within each of these size classes. Particles with a diameter below 0.1156 mm were ignored because their contribution to the overall volume-based PSD is negligible. Furthermore, the critical timestep in a DEM simulation is proportional to $\sqrt{m}$, where $m$ is the

particle mass. Were these small particles to be included, the computational cost of the simulation would increase substantially.

Prior parametric studies (e.g., Barreto, 2009) showed that when periodic boundaries are used, the mechanical response of DEM assemblies is insensitive to the sample size; thus fewer particles are required. The sensitivity of the mechanical behaviour of PB samples to the sample size is also investigated in this study. Figure 3.8 shows the variation of void ratio after isotropic compression ($e_0$) under a confining pressure of 500 kPa with the inter-particle friction coefficient ($\mu$) for two PB samples containing different numbers of particles. The small PB sample contained 10,624 particles and the large PB sample was comprised of 20,164 particles. For both samples, $e_0$ increased initially with increasing inter-particle friction and was saturated at a value of 0.667 when $\mu$ exceeded 0.8. The attained void ratio for each μ value considered is almost identical. Figure 3.9 compares the stress-strain response of a small PB sample ($e_0$ = 0.529, $\sigma'_3$ =500 kPa) and a large PB sample ($e_0$ = 0.528, $\sigma'_3$ =500 kPa) with similar initial states subjected to drained triaxial simulations. These samples were generated by applying zero friction during isotropic compression, while $\mu$ was increased to 0.5 prior to triaxial shearing. Again the stress and deformation behaviour of these two samples agrees with each other. Figure 3.8 and Figure 3.9 confirm that the mechanical behaviour of PB samples is insensitive to the sample size. For a more convincing statistical particle-scale analysis, the large PB samples composed of 20,164 particles were used throughout this research work.

A simplified Hertz-Mindlin contact model detailed by Itasca Consulting Group (2008) was used. The particle shear modulus ($G$) and Poisson's ratio ($\nu$) were taken to be 29 GPa and 0.12 respectively following the properties of quartz (Simmons & Brace, 1965). Gravity was not simulated and the rigid walls were frictionless. Calculation of the critical timestep considers the smallest particle in the system. The critical time step ($t_{crit}$) is 5.37e-9 s which is 0.1 times the critical time step for the generalised multiple mass-spring system, i.e., $0.1 \cdot \sqrt{m/k}$, in which $m$ is the mass of the smallest particle, $k$ is the equivalent elastic contact stiffness (see Section 2.4.2) assuming 5% overlap between two smallest particles. This value of $t_{crit}$ is even smaller than the value suggested by O'Sullivan & Bray (2004) to ensure the system is stable during shearing. A local damping ratio of 0.1 was adopted in all simulations.

For the rigid-wall simulations, an initial non-contacting cloud of particles at half of their target sizes was randomly generated. The domain considered was confined by a closed, rigid, cylindrical wall in the lateral direction and two rigid, flat walls in the vertical direction. All these rigid walls are frictionless. Large particles were placed within the simulation domain

prior to small ones. The particles were then simultaneously expanded to their final sizes and the sample was cycled to equilibrium. During this procedure, no wall movement was allowed. A servo-control mechanism was then used to adjust both the positions of the flat walls and the radius of the cylindrical wall until an isotropic stress state was attained. Different coefficients of friction ($\mu$) were adopted during the sample preparation stage. For the representative set of simulations which is discussed in Section 3.4, all the samples were compressed to an isotropic stress state of 500 kPa. During this procedure, $\mu$ = 0.07 for RW-S, 0.11 for RW-M, and 0.14 for RW-L were applied to achieve similar void ratios (0.648–0.650) before shearing. For all simulations, $\mu$ was increased to 0.25 prior to shearing. At the onset of shearing, the ratios of sample diameter to the characteristic particle diameter ($D_{50}$) were around 14, 19, and 24 for RW-S, RW-M, and RW-L, respectively.

The periodically-bounded sample, PB, was generated and sheared using a modified version of the DEM code LAMMPS. As documented in Chapter 2, the code used here was successfully validated using the expressions analytically developed by Thornton (1979) for the peak stress ratios in a face-centred cubic assembly of uniform rigid spheres subjected to plane strain and triaxial conditions. To create the sample for this study, a non-contacting 'cloud' of particles was initially generated within a cubical periodic cell using an in-house MATLAB (The MathWorks Inc., 2011) script. Starting from the largest, the radii of the particles were successively determined from the upper and lower limits of each size class assuming a uniform distribution in between. When the accumulated particle volume within a size class approximated the target volume allocated to this size class, the algorithm moved to the next size class. Once all particle radii had been determined, the radii were sorted in descending order. Particles were then sequentially placed within the designated domain. During the placement, particles were allowed to intersect the periodic boundaries but were not permitted to overlap each other. Once all particles had been placed within the simulation domain, the sample was initially compressed to a stable stress state. For the representative PB simulation presented in Section 3.4, a coefficient of friction of 0.28 was used during isotropic compression until an isotropic stress state of 500 kPa was attained. Then the coefficient of friction was set to the final value of 0.25 and the sample was again returned to a stable stress state of 500 kPa. The void ratio after isotropic compression was 0.646. The average ratio of the dimensions of the PB sample to $D_{50}$ was about 25 before shearing.

As presented in Table 3.1, all the samples of the representative set of simulations have quite similar initial states. The coordination number ($Z$) and the deviatoric fabric ($\Phi_d$) were used to characterise the samples at the particle scale. The coordination number is given by $Z = 2N_c/N_p$, where $N_c$ is the number of contacts and $N_p$ is the number of particles. There is a

slight decrease in $Z$ from 4.64 to 4.37 with increasing sample size. The deviatoric fabric, $\Phi_d = \Phi_1 - \Phi_3$, is the difference between the maximum ($\Phi_1$) and minimum ($\Phi_3$) eigenvalues of the fabric tensor of the contact normal as defined by Satake (1982):

$$\Phi_{ij} = \frac{1}{N_c}\sum_{k=1}^{N_c} n_i^k n_j^k \qquad \text{(Eq. 3.1)}$$

where $n_i^k$ denotes the unit contact normal component in the $i$th direction. $\Phi_d$ has been widely used to quantify the structural anisotropy of granular assemblies. The maximum $\Phi_d$ value is 0.011, indicating an almost isotropic packing in all cases. The $\Phi_d$ value for the PB sample was 0.004: lower than the values of all the contrasting rigid-wall samples. The coordination number of the PB sample was 4.37 which was identical to the value for the largest rigid-wall sample, RW-L. The difference in $Z_0$ and $\Phi_{d,0}$ after isotropic compression may also be attributable to the different $\mu$ values used during the sample generation. After isotropic compression, these four samples were subjected to drained triaxial simulations.

The characteristics after isotropic compression for all the RW-S, RW-M and PB samples are detailed in Tables 3.2, 3.3 and 3.4 respectively.

## 3.4 Stress-strain Response

Figure 3.10 (a) illustrates the variation of stress ratio ($q/p$') with axial strain for the representative set of simulations considered. The deviatoric stress $q$ is defined as $\sqrt{\frac{1}{2}((\sigma'_1 - \sigma'_2)^2 + (\sigma'_2 - \sigma'_3)^2 + (\sigma'_3 - \sigma'_1)^2)}$ while the mean effective stress, $p$', is the mean value of the three effective principal stresses ($p' = 1/3(\sigma'_1 + \sigma'_2 + \sigma'_3)$). It is clear that samples behave quite differently from the onset of shear deformation. All the rigid-wall samples are stiffer than the PB sample; however, their stiffness reduces with increasing sample size. The smallest rigid-wall sample, RW-S, mobilized the highest peak stress ratio. In their experimental study of effects of sample size on material behaviour, Jefferies *et al.* (1990) observed that their larger triaxial samples (sample diameters of 15.4 cm and 28.9 cm) showed a significant strain softening behaviour post peak, while the strength of the smaller samples (sample diameters of 3.56 cm and 7.55 cm) they considered decreased more gently as shown in Figure 3.11 (a). Jefferies *et al.* (1990) explained these observed differences by considering the formation of multiple shear bands in large samples. However, shear band formation was not observed in these DEM simulations. This may explain why the difference in the post-peak responses is less marked than in the laboratory tests.

As illustrated in Figure 3.10 (a), all the samples reached an almost identical stress state at large strain levels, suggesting that the ultimate strength at the critical state is a unique property of a material and is insensitive to the sample size and boundary conditions. Though they did not shear their samples to the critical state, Jefferies *et al.* (1990) also expected the shear strengths of differently-sized samples to converge at large strain levels. Considering the volumetric strain response which is illustrated in Figure 3.10 (b), the rigid-wall samples firstly contracted and then dilated until the critical state was attained. This transition from a contractive to a dilative response occurred at a much larger strain level in RW-L than in the smaller rigid-wall samples. The periodically-bounded sample, PB, behaved contractively throughout shearing. The largest rigid-wall sample, RW-L, was significantly less dilative than the smallest rigid-wall sample, RW-S. This sample-size effect on the volumetric response is in agreement with the observation of Jefferies *et al.* (1990) as shown in Figure 3.11 (b). The void ratios at the end of the simulations are 0.676, 0.663, 0.656, and 0.630 for RW-S, RW-M, RW-L, and PB, respectively. Overall, the rigid-wall samples behaved as if they are "dry", or denser than the critical state, while the periodically-bounded sample PB exhibited a "wet" condition, indicative of a sample whose initial state is above the critical state corresponding to the same $p$'.

The critical state data are presented in Figure 3.12. Due to some fluctuations in the stress-strain responses, the values of $e$ , $p'$ and $q$ at the critical state were taken as the corresponding mean values over the last 5% to 10% of axial strain. Figure 3.12 (a) shows the critical-state loci of the DEM samples in the $e$ against $(p'/p'_a)^{\alpha}$ space, where α is a material parameter taken here to be 0.7 (the usual value for Toyoura sand (Li & Wang, 1998) and $p_a$ is atmospheric pressure (taken here to be 101.3 kPa). The CSLs are the best-fit results of the cases shown in Figure 3.10 and some other supplemental simulations detailed in Tables 3.2 to 3.3. The CSL of RW-L is absent as only one simulation was completed due to the high computational cost. Hollow symbols show the initial states, while solid symbols represent the critical states.

All the CSLs are parallel to each other with almost identical slopes of around 0.001. The CSL of the RW-S sample lies above the CSL of the RW-M sample and the CSL of the PB samples is located below all the rigid-wall samples, i.e., the CSL moves downwards as the sample size increases for the rigid-wall samples. The intercepts of the CSLs decrease with increasing sample size, while the slopes seem to be less sensitive to the sample size. The state parameter $\psi$ is defined as the difference between the current void ratio and the void ratio at the critical state corresponding to the same mean effective stress (Been & Jefferies, 1985). Samples with a higher $\psi$ are looser and behave more contractively than samples with

a lower $\psi$. The state parameters for the RW-S and RW-M samples presented in Figure 3.6 are –0.027 and –0.014, respectively. Therefore, when sheared under triaxial loading conditions, the RW-M sample should be more contractive and have lower peak strength than the RW-S sample, which agrees with Figure 3.10.

Figure 3.12(b) shows the stress state at the critical state in terms of $q$ and $p'$. All ($q$, $p'$) points at the critical state can be represented by a single straight line irrespective of the sample size and boundary conditions. The slope ($M$) of this straight line is about 0.696. This corresponds to an angle of shearing resistance of 18.2° at the critical state, calculated from:

$$\phi'_{cv} = \sin^{-1}\left(\frac{3M}{6+M}\right) \quad \text{(Eq. 3.2)}$$

The values of $Z$ and $\Phi_d$ at the critical state for the representative set of simulations are given in Table 3.5. The value of $Z$ decreases with decreasing size for the rigid-wall samples. This concurs with the observation of void ratios above, showing that the sample PB is the densest at the end of the simulation and the void ratio at critical state decreases with increasing sample size. It is interesting to note that while the $\Phi_{d,cv}$ value of the PB sample remains the smallest, the $\Phi_{d,cv}$ values of the rigid-wall samples are almost identical to each other and the difference in the $\Phi_{d,cv}$ values between the rigid-wall samples and the periodically-bounded sample is smaller than at the initial state. The critical-state characteristics of all the simulations are given in Tables 3.6 to 3.8.

## 3.5 Evaluation of Homogeneity

The observed variation of position of CSL in $e$-$(p'/p'_a)^{\alpha}$ space with sample size for the rigid-wall samples seems to violate the principles of classical CSSM which propose that the CSL is a unique characteristic of a given material. Chan & Ng (1986) observed relatively high porosities in the vicinity of rigid wall boundaries. Marketos & Bolton (2010) highlighted that porosity, strain and contact force distributions adjacent to the boundaries differ from those within the bulk material. These prior studies implied that the difference in position of CSL may be attributable to the inhomogeneity of samples due to the use of rigid walls.

To quantify the homogeneity in the vertical direction, the cylindrical rigid-wall samples discussed previously were divided into eight horizontal slices or layers (Figure 3.13(b)). The lateral homogeneity of the rigid-wall samples was studied by looking at 4 cylindrical zones (rings) extending from the bottom rigid wall boundary to the top boundary (Figure 3.13(c)). The sample PB was studied by looking at the corresponding eight isochoric slices whose

thicknesses are larger than twice the maximum particle diameter. Both horizontal and vertical directions were considered (Figure 3.13(d)).

The initial analysis considered the void ratio. As illustrated in Figure 3.13, the solid volume in each slice was accurately considered by introducing the analytical solution of the spherical crown volume (Eq.3.3) and the analytical solution of the volume of intersection between a sphere and a cylinder based on elliptical integrals (Lamarche & Leroy, 1990).

$$V_{inter} = \pi h^2 (r - \frac{h}{3}) \quad \text{(Eq.3.3)}$$

The distributions of void ratio normalized by the overall average void ratio for each sample are shown in Figure 3.14 for the rigid-wall samples, while Figure 3.15 illustrates the distribution of normalized void ratios in the PB sample. Referring to Figure 3.14, it is clear that the void ratios in the boundary regions of the rigid-wall samples are higher than the overall average value while the void ratios of the interior regions are lower than the average value in both the vertical and radial directions. The difference between the boundary void ratio and interior void ratio is more obvious in the radial direction than in the axial direction and decreases when the sample becomes larger. This is in accordance with the experimental observations of Ní Bhreasail (2014) who also observed a higher void ratio in the region adjacent to the cylindrical boundaries than in the interior regions of her oedometer samples after sample preparation. The difference is less obvious for a larger sample (Reigate sand sample with about 55 particles across the sample diameter) (Figure 3.16 (b)) than a smaller sample (cylindrical Leighton Buzzard sand sample with about 15 particles across the sample diameter) (Figure 3.16 (a)). In contrast, Figure 3.15 shows an almost uniform distribution of void ratio in the PB sample. The origin of these differences can be attributed to the geometrical constraints for different types of boundaries as illustrated in Figure 3.17. Considering an idealised 2D case with two identical disks, when rigid boundaries are used, particles cannot extend beyond the boundary and thus the void at the boundary is formed by the peripheral particles and the rigid wall. Two extreme cases can be identified for such a situation: a flat boundary ($R \rightarrow \infty$) and a circular boundary with diameter twice the disc diameter. In the former case, the densest packing is achieved with the void area confined by the two disks and the boundary equalling $(2 - \frac{1}{2}\pi)r^2 \approx 0.429r^2$, in which $r$ is the radius of the disc, while the loosest packing is obtained in the latter case at which the void area equals $\pi r^2$ which is about twice the void area when the flat boundary is applied. This explains the decreasing boundary void ratio with increasing sample size and the lower void ratio close to the flat top and bottom walls than that near the periphery of the cylindrical walls. When the periodic boundary is considered (Figure 3.17 (b)), particles can move across the boundary.

The part of disk *A* that intersects the periodic boundary is considered on the opposite side (disk *A'*), making the contact condition identical to that in the interior region within a periodic cell, leading to a homogeneous distribution of packing density within a PB sample. Figure 3.17 also indicates that increasing sample size helps to reduce the void ratio in the vicinity of the cylindrical boundaries to that around the flat wall boundaries. However, neither of them can reach a state as dense as when periodic boundaries are used.

The calculated unbiased sample variances of void ratio have been used to quantify the degree of homogeneity by Jiang et al. (2003) and are also adopted here. These variances of void ratio are given by:

$$S^2 = \frac{1}{m-1}\sum_{i=1}^{m}(e_i - e_{overall})^2 \qquad \text{(Eq.3.4)}$$

where $m$ is the total number of slices, $e_i$ is the void ratio within zone $i$ and $e_{overall}$ is the overall void ratio. The variances of void ratio of the numerical assemblies used in this study are given in Table 3.9. It is clear that the periodically-bounded sample, PB, has the lowest variances and they are very small in all three Cartesian directions. Moreover, the rigid-wall samples have larger variances in the radial direction than in the vertical direction and the variances decrease with increasing sample size. This may be because the outermost zone in the radial direction contained the entire cylindrical boundary and a fraction of top and bottom boundaries as well, while the outermost zones in the vertical direction contain only the top/bottom rigid wall and a small portion of the cylindrical boundary. With an increase of sample size, there is more space for the placement of particles at the boundaries and the weight of the influence regions of rigid walls to the outmost layers (rings) decreases.

To further investigate the size of the zone of influence of the rigid walls, the RW samples were divided into different numbers of cylindrical rings (7, 8 and 10 rings for RW-S, RW-M and RW-L respectively) in the radial direction with thickness of each ring approximating $D_{50}$. Calculations of void ratios within each ring followed the method described previously. As shown in Figure 3.18, void ratios within the outmost two rings are higher than elsewhere in the RW samples, while the latter are homogeneous. This indicates that the influence of rigid-wall boundaries extends to the area which is about $2 \times D_{50}$ away from rigid-wall boundaries.

At the particle scale, the packing inhomogeneity can be calculated by considering the contact density, i.e., the number of contacts per unit volume. Figures 3.19 and 3.20 present the distribution of initial contact density within the rigid-wall samples and the periodically-bounded sample, respectively. For each sample, the contact densities which are presented were normalised by the overall average contact density within the sample. Although the

samples are quite uniform in the interior regions, there is a considerable reduction in the contact density in the boundary regions of samples generated using rigid boundaries (Figure 3.19), while the contacts are uniformly distributed within the periodically-bounded sample (Figure 3.20). The variances of contact density are given in Table 3.10. As was the case for the void ratio data, the variances of contact density of the periodically-bounded sample are very small in all three directions, while those of the rigid-wall samples are much larger. The variation of contact density in the rigid-wall samples is more obvious in the radial direction than in the vertical direction, in line with the distribution of void ratio. Increasing the sample size reduces the heterogeneity of the sample, as was the case for the void ratio.

The volumetric PSDs for different parts of the rigid-wall samples were determined and their main characteristics are summarized in Table 3.11. In this table, slices 2–7 in the vertical direction are grouped to form the "middle" region, material in rings 1–3 in the radial direction (grouped together) are considered to be the "inner" region, horizontal layers 1 and 8 are the "boundary" regions and ring 4 is the "outer" region. There is indeed a higher proportion of small particles near the boundaries than in the interior regions. However, this difference is not significant and becomes almost unnoticeable in the larger samples, RW-M and RW-L.

Considering the inhomogeneity induced by the rigid walls, the stresses and strains measured at the boundary may not accurately reflect the real material response. Hence, we consider the interior parts of all the samples together to interpret the critical-state behaviour. The average macro stresses of the middle/inner parts of the rigid-wall samples were calculated from average stresses of particles centred within these zones weighted by their volumes (O'Sullivan, 2011).

$$\bar{\sigma}_{ij} = \frac{1}{V}\sum_{p=1}^{N_p} \bar{\sigma}^p{}_{ij}\, V^p \qquad \text{(Eq. 3.5)}$$

where $\bar{\sigma}_{ij}$ is the average stress tensor within the region of interest, i.e., the interior parts of the rigid-wall samples, $V$ is the volume of the domain considered, $N_p$ is the total number of particles and $\bar{\sigma}^p{}_{ij}$ is a representative stress tensor for a single particle of volume $V^p$. The critical states of the interior parts of the rigid-wall samples , i.e., $e_{cv,inter}$, $p'_{cv,inter}$ and $q_{cv,inter}$, are listed in Tables 3.6 and 3.7 and are also shown in Figure 3.21. It is interesting to see that they all approach the CSL of the periodically-bounded samples. This suggests that the critical state behaviour is unique and independent of the sample size given that the stresses and strains are correctly interpreted by eliminating the boundary effect. In this regard, the sample size effect does not violate the basic concepts of CSSM.

## 3.6 Summary

In this Chapter, the sample size effect was investigated within the framework of CSSM. It was observed that the location of the CSL depends on the boundary conditions and the sample size. The CSLs of samples bounded by rigid boundaries locate above the CSL of the periodically-bounded sample, while the slope of the CSL in the $e$–$(p'/p'_a)^{\alpha}$ space seemed to be dependent on neither the sample size nor the boundary conditions. The stress-strain response of the samples differs due to the different relative positions of initial states to the 'apparent' critical states. The ultimate strength of the material is independent of the sample size as well as the boundary conditions. Homogeneity analysis reveals that use of rigid-wall boundaries results in higher void ratio and lower contact density in the region up to $2 \times D_{50}$ from the rigid wall. The origin of the inhomogeneity is attributed to the geometrical constrains imposed by the rigid wall boundaries to the kinematic movements of particles. The critical-state loci of the interior parts excluding the regions of the influence of the rigid walls approach the CSL of the homogeneous periodically-bounded sample with an increase of sample size, indicating that the interior parts of rigid-wall-bounded samples are the most representative of the real material behaviour.

Implications of these findings include:

(1) The application of periodic boundaries may be beneficial as it yields a more homogeneous sample and deformation field than rigid boundaries and thus is more likely to capture the real material responses
(2) When rigid boundaries are used, the sample size should be large enough to reduce the influence of the kinematic boundary constraint which has a major impact on the overall mechanical behaviour of granular materials. Otherwise, the DEM results may not reflect the real material behaviours correctly, e.g., the CSL
(3) In DEM simulations with rigid wall boundaries, the response of an inner region or sub-volume should be compared with the overall material response to demonstrate that the overall response is representative of the material

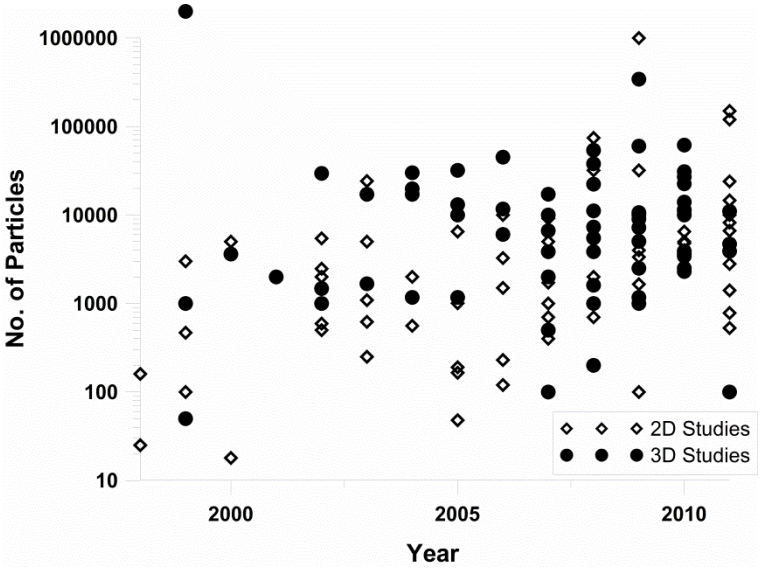
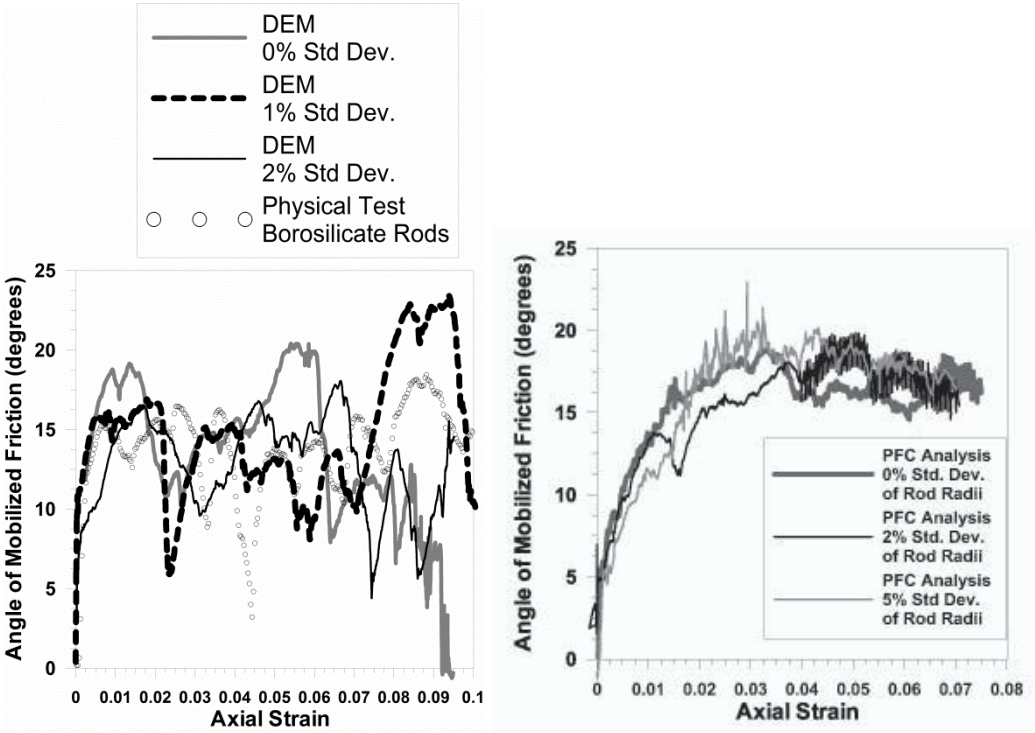



Figure 3.1 Number of particles used in published DEM simulations (O'Sullivan, 2011)




(a) 224 disks (b) 896 disks

Figure 3.2 Sensitivity of the stress-strain response to the small perturbation in PSD (O'Sullivan *et al.*, 2002)

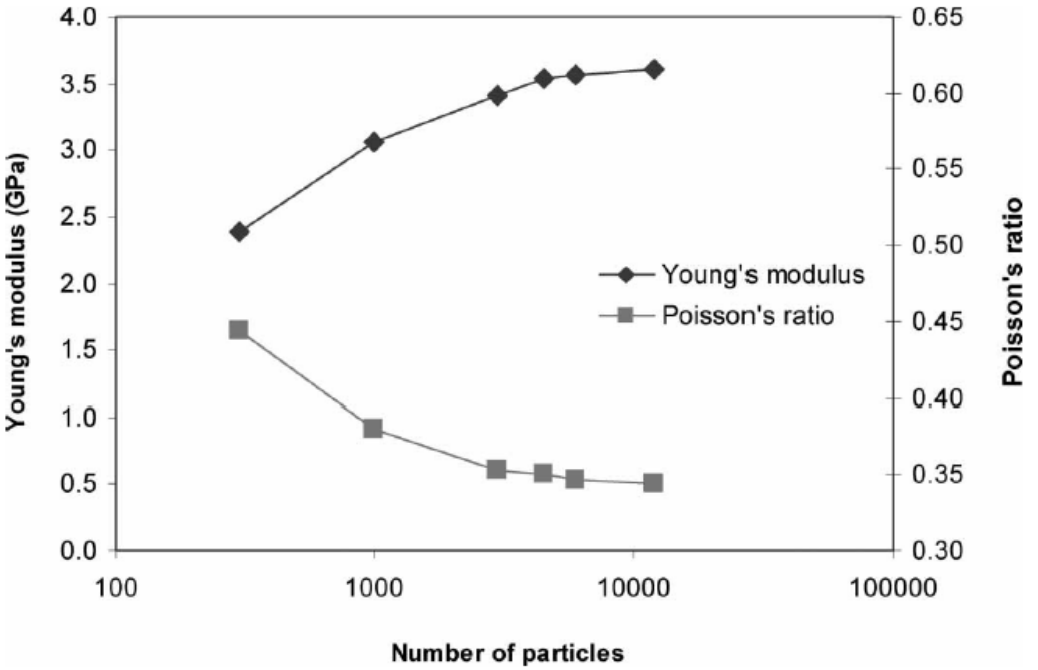



Figure 3.3 Effect of number of particles on the bulk elastic properties (Collop *et al.,* 2006)

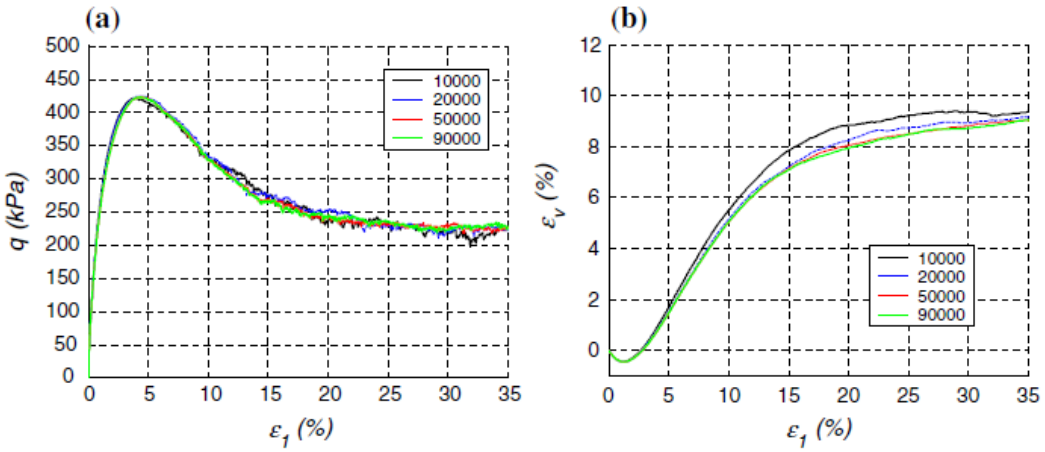



Figure 3.4 Sensitivity of the mechanical behaviour of granular materials to the number of particles under triaxial loading conditions (Belheine *et al.*, 2009): (a) Deviatoric stress; (b) Volumetric strain

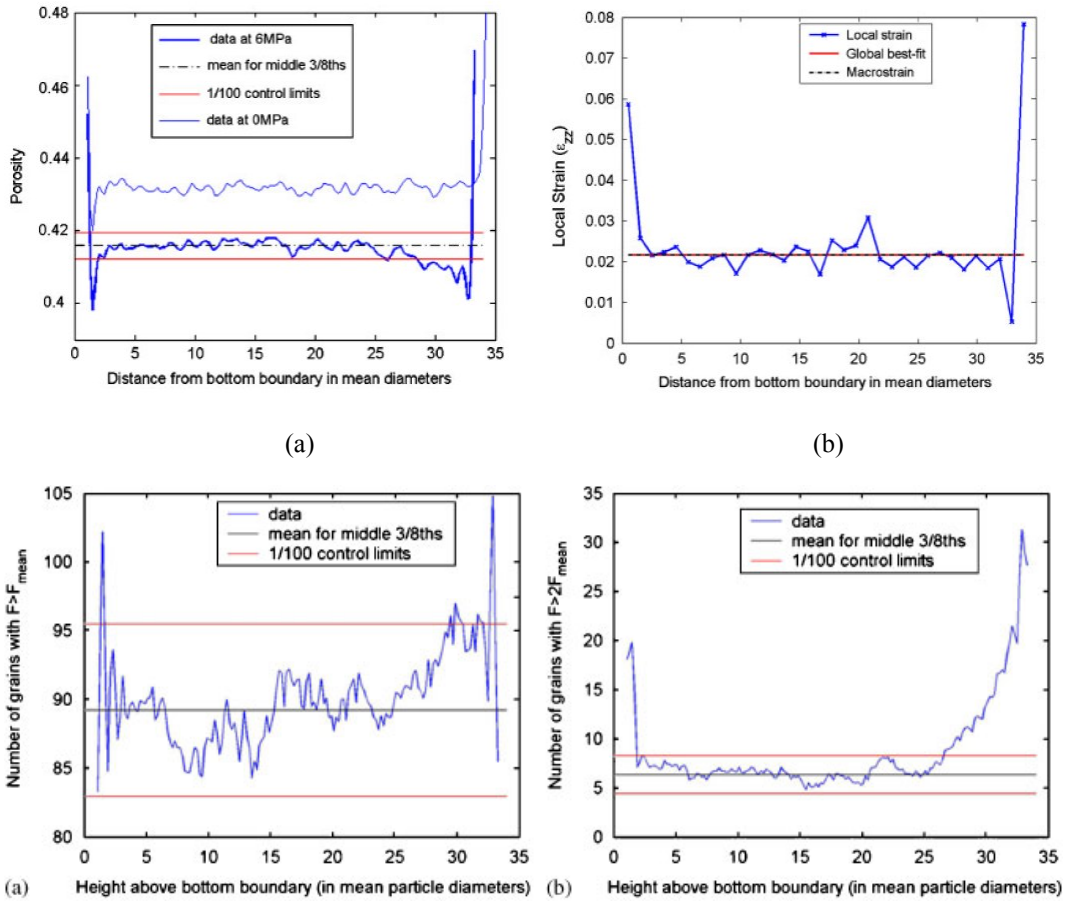



Figure 3.5 Observed localisation phenomena adjacent to the rigid wall boundaries: (a) Porosity; (b) Axial strain; (c) Normal contact force (Marketos & Bolton, 2010)

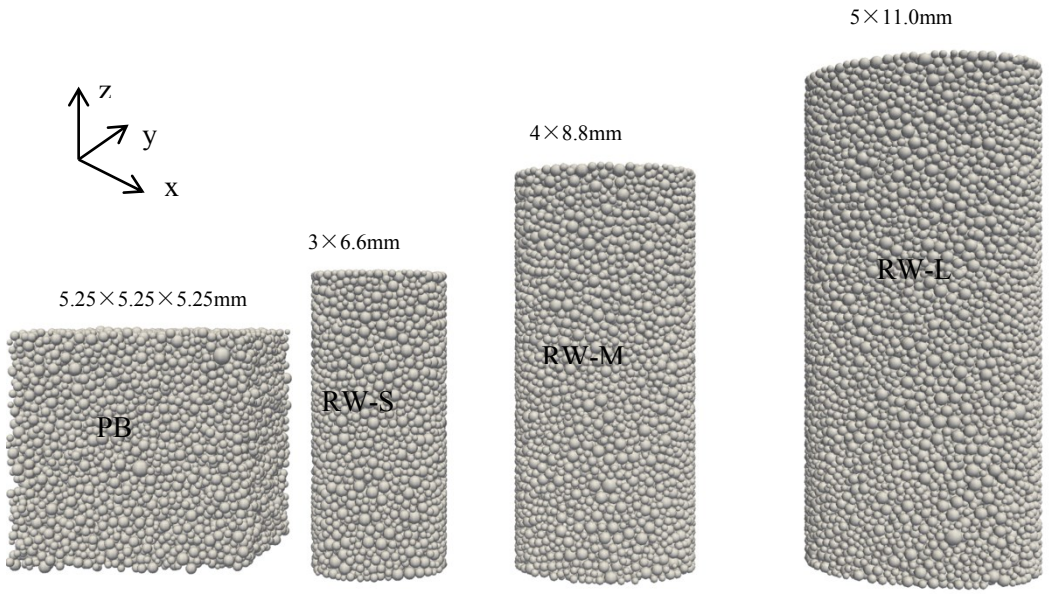



Figure 3.6 Schematic diagrams of the four numerical samples: PB: periodically-bounded sample; RW-S: Small rigid-wall sample; RW-M: Medium rigid-wall sample; RW-L: Large rigid-wall sample

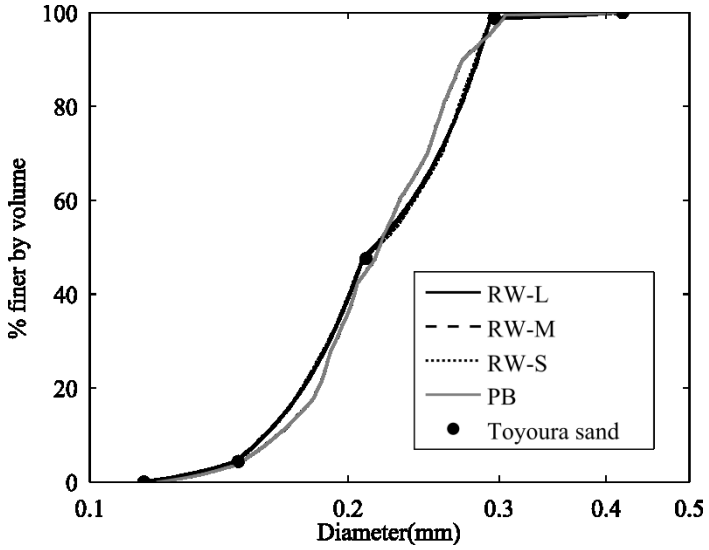



Figure 3.7 Particle size distributions of numerical samples

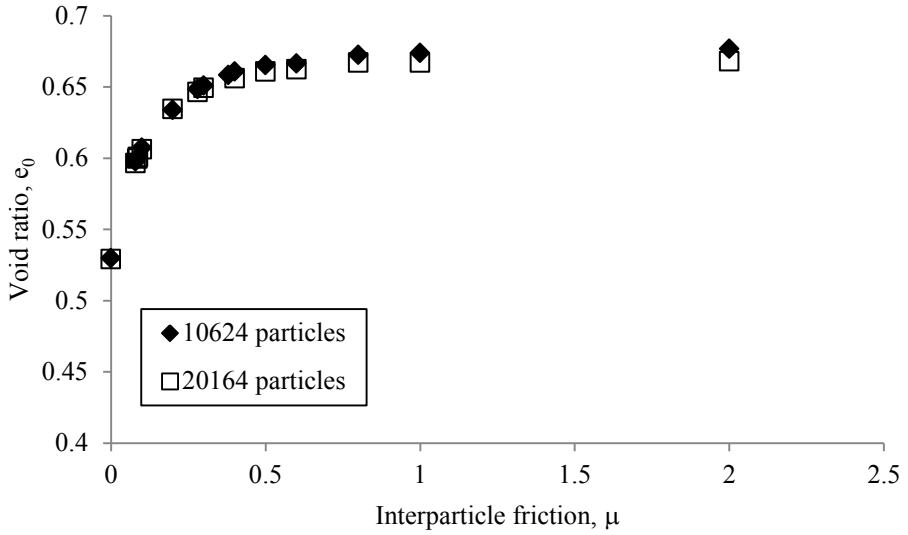



Figure 3.8 Effect of sample size on the void ratio after isotropic compression for the PB samples ($\sigma'_{3,0}$=500 kPa)

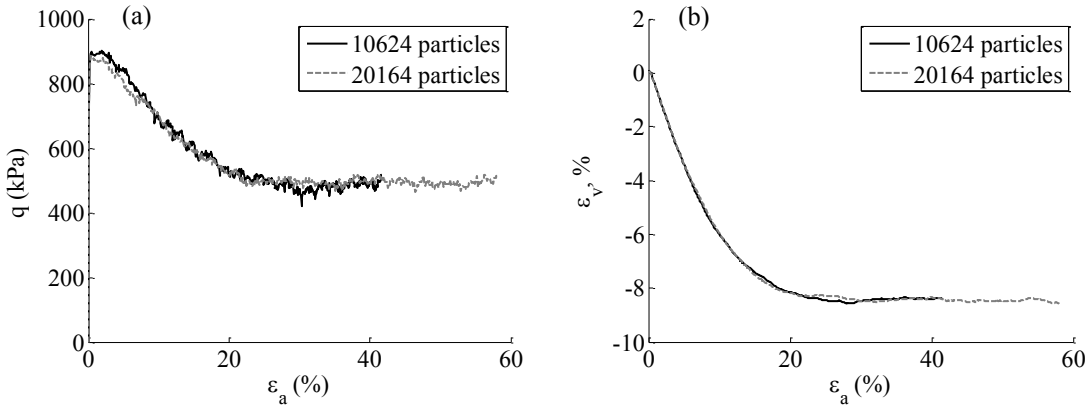
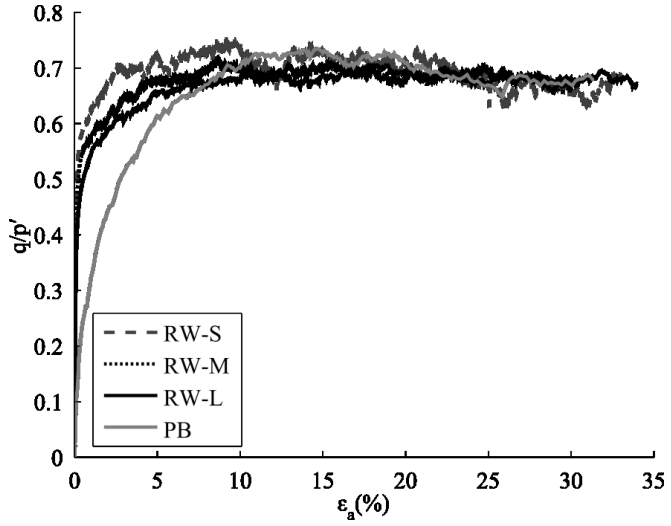
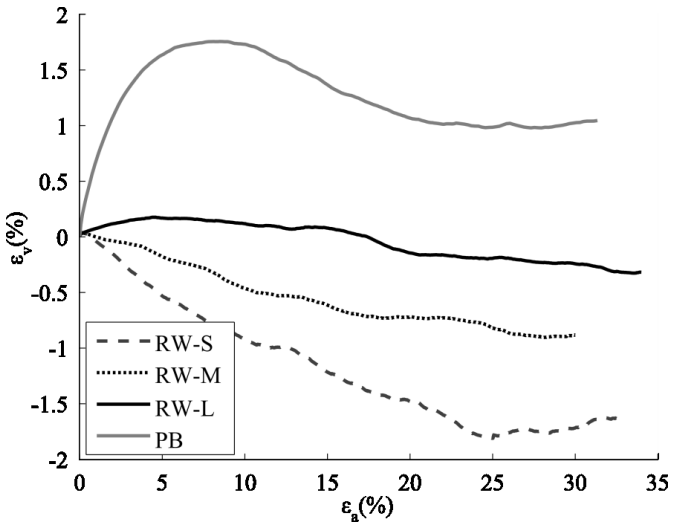



Figure 3.9 Effect of sample size on the stress-strain behaviour for the PB samples: (a) Deviatoric stress; (b) Volumetric strain




(a) Variation of stress ratio with axial strain




(b) Variation of volumetric strain with axial strain

Figure 3.10 Comparing the stress-strain response of samples with different sizes

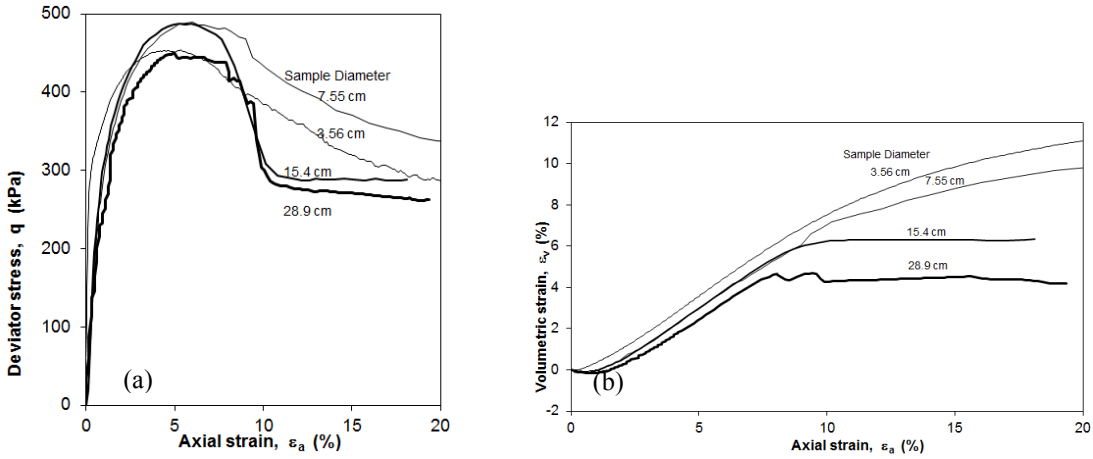
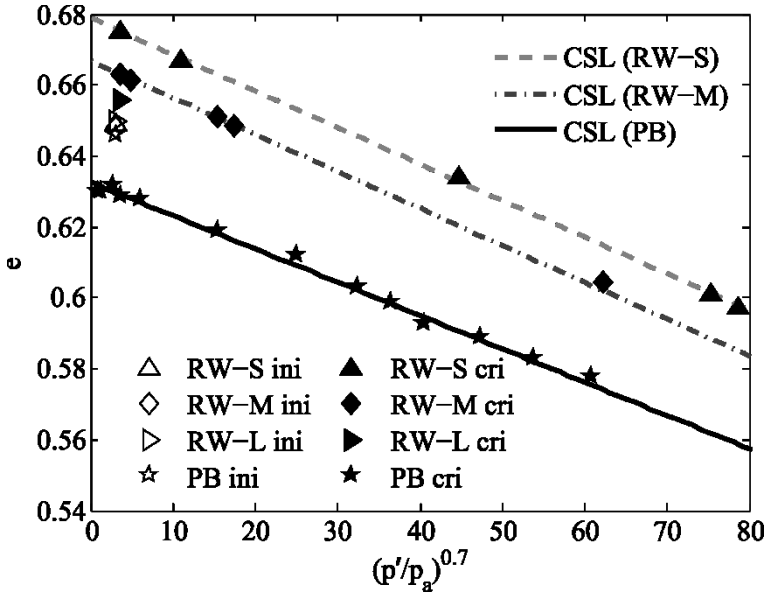
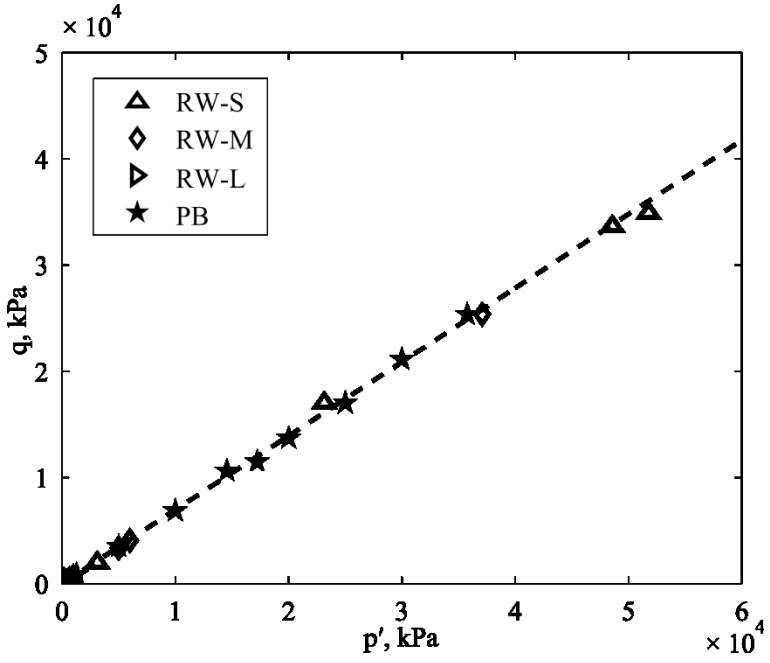



Figure 3.11 Influence of sample size in laboratory tests (Jefferies *et al.* (1990)): (a) Variation of deviatoric stress with axial strain; (b) Variation of volumetric strain with axial strain (dilative strain is positive)




(a) $e$-( $p'/p'_a$)$^{0.7}$




(b) $q$-$p'$

Figure 3.12 Effects of sample size on the critical-state response

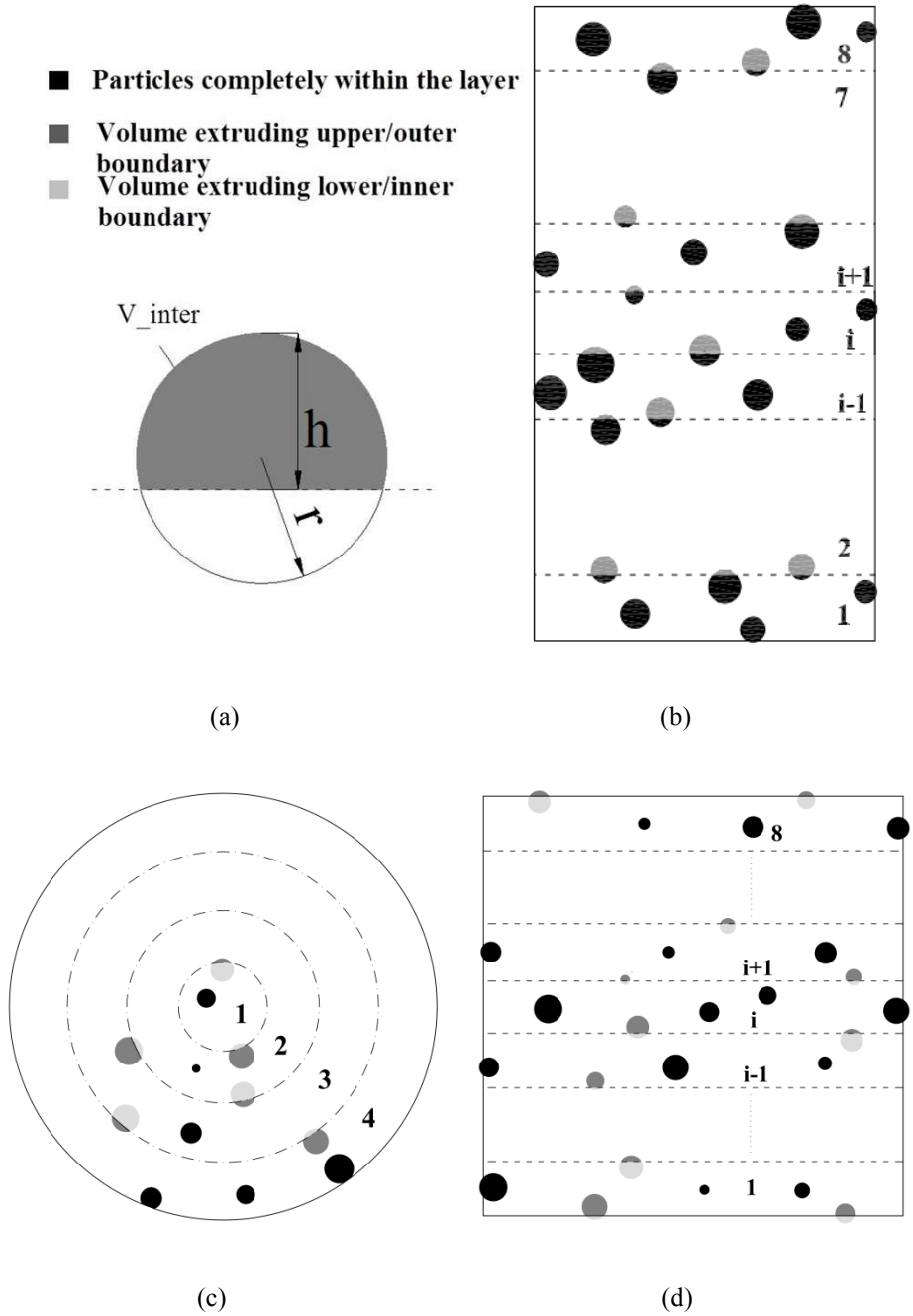



Figure 3.13 The homogeneity of the samples at the initial state: (a) Solid volume within each zones, (b) cylindrical rigid-wall samples at vertical direction, (c) cylindrical zones (rings) extending from bottom rigid wall boundary to top boundary, and (d) sample PB at horizontal and vertical directions.

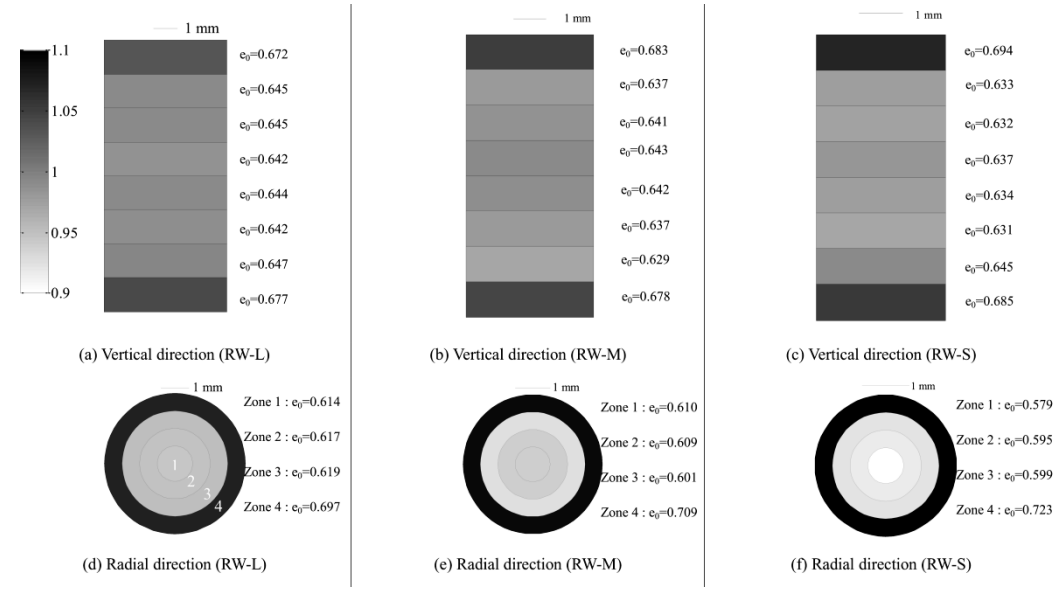



Figure 3.14 Distributions of initial void ratio of rigid-wall samples in which the shading illustrates data values normalized by the mean void ratio ($e_0$ = 0.649) for each sample and the actual void ratio values in each region are given on the right side of each plot.

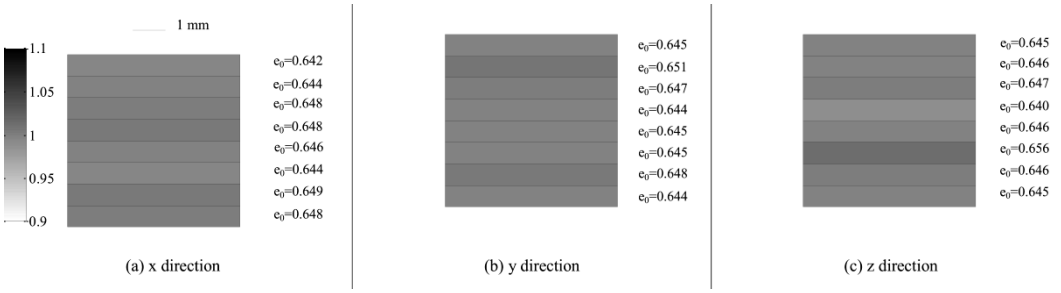



Figure 3.15 Distributions of initial void ratio of the periodically-bounded sample in which the shading indicates void ratios normalized by the mean for the entire sample ($e_0$ = 0.646) and the actual void ratios in each region are given on the right side of each plot.

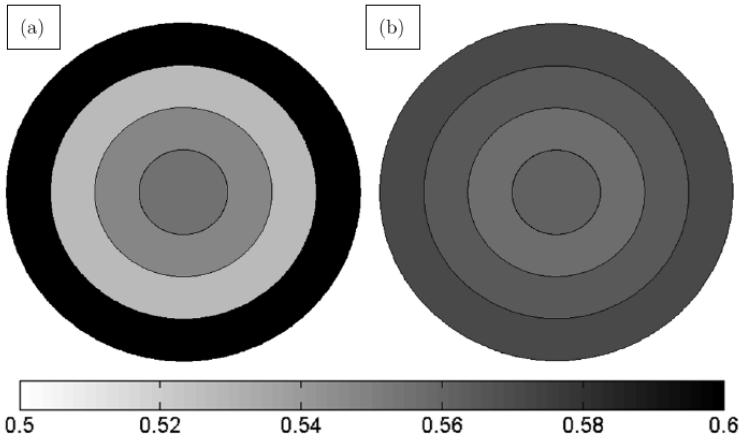
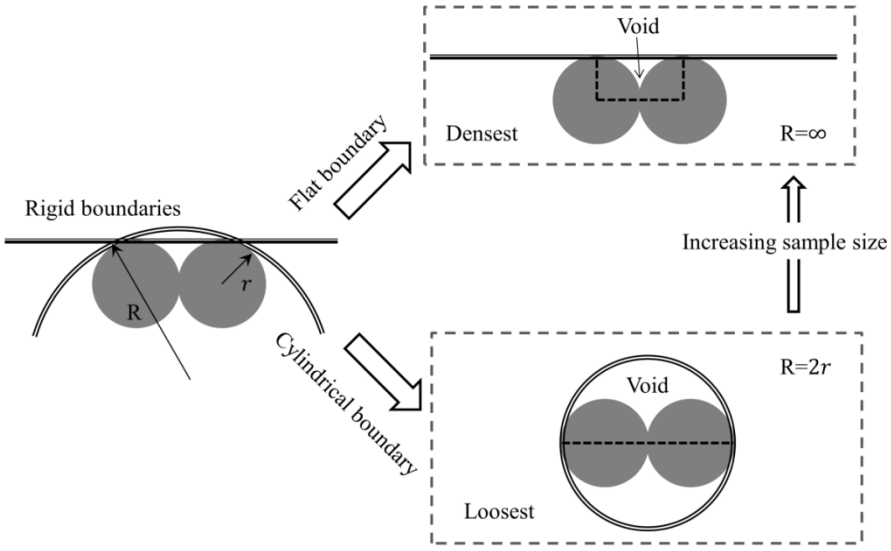
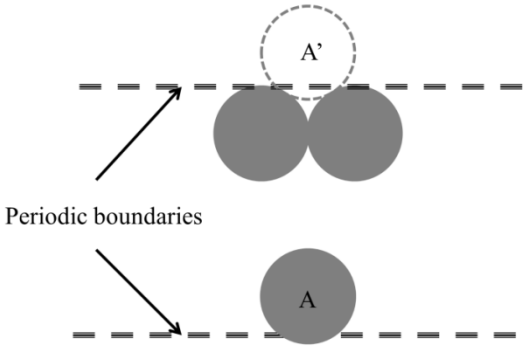



Figure 3.16 Variation in void ratio in the radial direction of a cylindrical child volume: (a) Smaller Leighton Buzzard sand sample; (b) Larger Reigate sand sample (Ní Bhreasail, 2014)




(a)




(b)

Figure 3.17 Illustration of the geometrical constraints at the boundary: (a) Rigid-wall boundaries; (b) Periodic boundaries

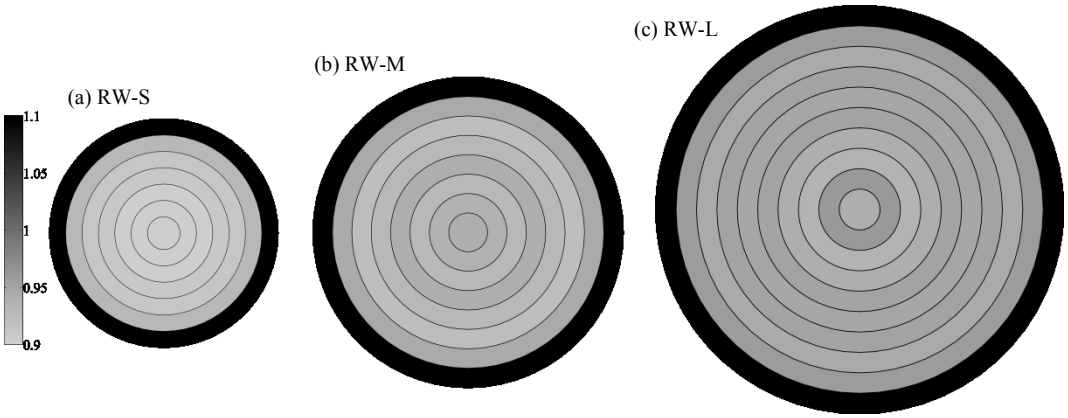



Figure 3.18 Distribution of void ratio within rigid-wall samples along radial direction (Thickness of each ring approximates $D_{50}$.)

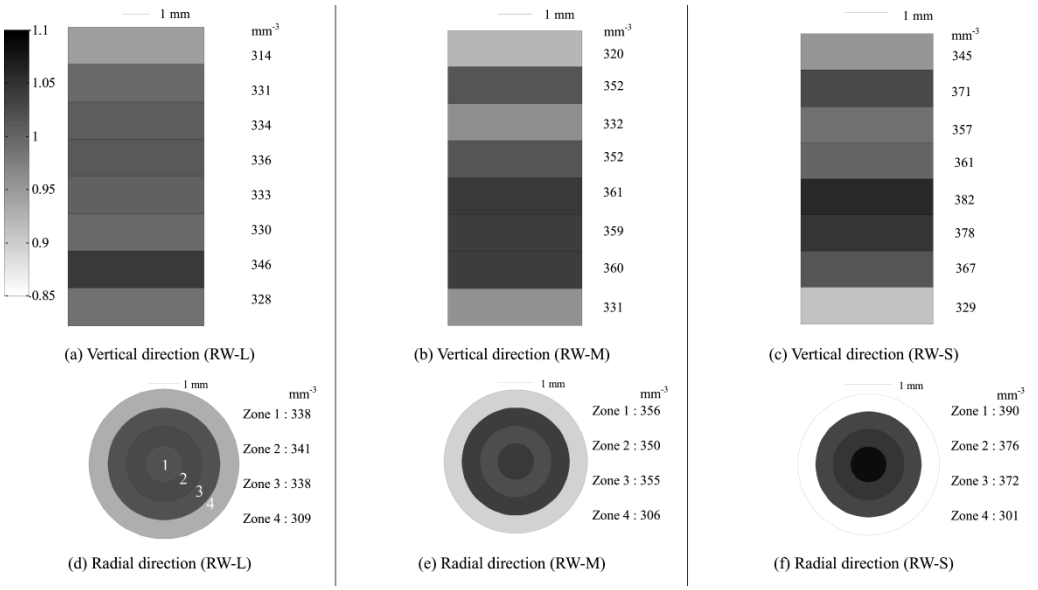



Figure 3.19 Distributions of initial contact density of rigid-wall samples in which the shading illustrates data values normalized by the mean contact density for each sample and the actual contact densities in each region are given on the right side of each plot. (The mean contact densities for RW-L, RW-M, and RW-S are 331, 346, and 361 $mm^{-3}$, respectively.)

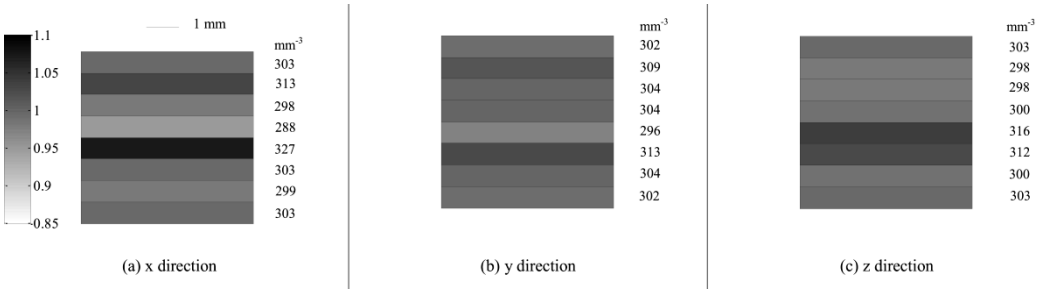



Figure 3.20 Distributions of initial contact density of periodically-bounded sample in which the shading indicates contact densities normalized by the mean contact density for the entire sample and the actual contact densities in each region are given on the right side of each plot. (The mean contact density for PB sample is 301 $mm^{-3}$.)

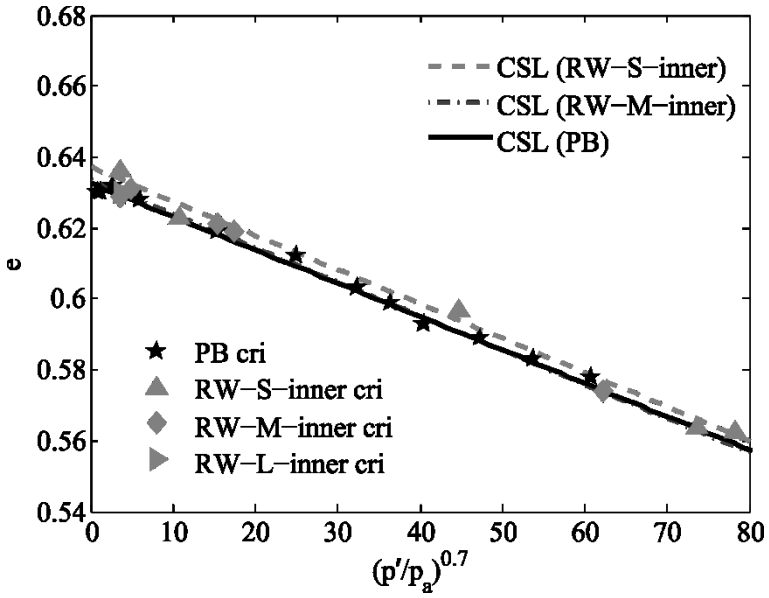



Figure 3.21 The critical state of DEM samples plotted in the $e$ against $(p'/p'_a)^{\alpha}$ space considering homogeneous interior regions only

Table 3.1 Initial characteristics of the prepared virtual samples of the representative set of simulations and a real Toyoura sand for comparison

| Sample | Number of particles | $D_{50}$ (mm) | $C_u$ | $C_c$ | $e_0$ | $Z_0$ | $\Phi_{d,0}$ |
|---|---|---|---|---|---|---|---|
| RW-S | 6,783 | 0.216 | 1.490 | 0.943 | 0.649 | 4.64 | 0.011 |
| RW-M | 16,073 | 0.215 | 1.488 | 0.951 | 0.648 | 4.51 | 0.0091 |
| RW-L | 31,392 | 0.214 | 1.478 | 0.953 | 0.650 | 4.37 | 0.0081 |
| PB | 20,164 | 0.218 | 1.386 | 0.983 | 0.646 | 4.37 | 0.004 |
| Toyoura sand | – | 0.216 | 1.392 | 0.961 | – | – | – |

$C_u$: Coefficient of uniformity; $C_c$: Coefficient of curvature, $e_0$: initial void ratio; $Z$: coordination number; $\Phi_d$: deviatoric fabric

Table 3.2 Initial characteristics of the RW-S samples

| | $\mu$ during isotropic compression | $e_0$ | $\sigma'_{3,0}$ (kPa) | $Z_0$ | $\Phi_{d,0}$ | Loading condition |
|---|---|---|---|---|---|---|
| 0.597-500-CVC | 0.0 | 0.597 | 500 | 5.27 | 0.013 | CVC |
| 0.602-100-CVC | 0.0 | 0.602 | 100 | 5.05 | 0.011 | CVC |
| 0.634-30000-CVC | 0.2 | 0.634 | 30000 | 5.1 | 0.013 | CVC |
| 0.649-500-CDC | 0.07 | 0.649 | 500 | 4.64 | 0.011 | CDC |
| 0.667-1000-CVC | 0.15 | 0.667 | 1000 | 4.28 | 0.006 | CVC |

CVC: Constant volume compression; CDC: Conventional drained compression

Table 3.3 Initial characteristics of the RW-M samples

| | $\mu$ during isotropic compression | $e_0$ | $\sigma'_{3,0}$ (kPa) | $Z_0$ | $\Phi_{d,0}$ | Loading condition |
|---|---|---|---|---|---|---|
| 0.581-5000-CPC | 0.02 | 0.581 | 5000 | 5.70 | 0.006 | CPC |
| 0.596-1000-CPC | 0.02 | 0.596 | 1000 | 5.33 | 0.006 | CPC |
| 0.602-100-CVC | 0.02 | 0.602 | 100 | 5.04 | 0.007 | CVC |
| 0.648-500-CVC | 0.11 | 0.648 | 500 | 4.51 | 0.0091 | CVC |
| 0.648-500-CDC | 0.11 | 0.648 | 500 | 4.51 | 0.0091 | CDC |

Table 3.4 Initial characteristics of the PB samples

| | $\mu$ during isotropic compression | $e_0$ | $\sigma'_{3,0}$ (kPa) | $Z_0$ | $\Phi_{d,0}$ | Loading condition |
|---|---|---|---|---|---|---|
| 0.533-100-CDC | 0.0 | 0.533 | 100 | 5.83 | 0.003 | CDC |
| 0.627-1000-CDC | 0.18 | 0.627 | 1000 | 4.87 | 0.002 | CDC |
| 0.646-500-CDC | 0.28 | 0.646 | 500 | 4.37 | 0.004 | CDC |
| 0.578-1000-CVC | 0.05 | 0.578 | 1000 | 5.59 | 0.003 | CVC |
| 0.599-527-CVC | 0.086 | 0.599 | 527 | 5.29 | 0.002 | CVC |
| 0.603-1000-CVC | 0.1 | 0.603 | 1000 | 5.28 | 0.003 | CVC |
| 0.646-84.49-CPC | 0.25 | 0.646 | 84.49 | 4.23 | 0.003 | CPC |
| 0.643-419.81-CPC | 0.25 | 0.643 | 419.81 | 4.43 | 0.003 | CPC |
| 0.625-5000-CPC | 0.1 | 0.625 | 5000 | 4.96 | 0.003 | CPC |
| 0.612-10000-CPC | 0.25 | 0.612 | 10000 | 5.18 | 0.003 | CPC |
| 0.594-20000-CPC | 0.25 | 0.594 | 20000 | 5.44 | 0.003 | CPC |
| 0.586-25000-CPC | 0.25 | 0.586 | 25000 | 5.54 | 0.003 | CPC |
| 0.579-30000-CPC | 0.25 | 0.579 | 30000 | 5.62 | 0.002 | CPC |

CPC: Constant $p'$ compression

Table 3.5 Micro characteristics of the representative set of simulations at the critical state

| | RW-S | RW-M | RW-L | PB |
|---|---|---|---|---|
| $Z_{cs}$ | 4.14 | 4.18 | 4.22 | 4.39 |
| $\Phi_{d,cs}$ | 0.089 | 0.090 | 0.089 | 0.086 |

Table 3.6 Critical-state characteristics of the RW-S samples

| | $e_{cv}$ | $p'_{cv}$ (kPa) | $q_{cv}$(kPa) | $Z_{cv}$ | $\Phi_{d,cv}$ | $e_{cv,inter}$ | $p'_{cv,inter}$ (kPa) | $q_{cv,inter}$ (kPa) |
|---|---|---|---|---|---|---|---|---|
| 0.597-500-CVC | 0.597 | 51776 | 34980 | 5.31 | 0.068 | 0.562 | 51309 | 35475 |
| 0.602-100-CVC | 0.601 | 48576 | 33740 | 5.27 | 0.072 | 0.564 | 47140 | 32009 |
| 0.634-30000-CVC | 0.634 | 23144 | 17110 | 4.95 | 0.079 | 0.597 | 24438 | 17548 |
| 0.649-500-CDC | 0.675 | 649 | 445 | 4.14 | 0.089 | 0.636 | 646 | 450 |
| 0.667-1000-CVC | 0.667 | 3105 | 2080 | 4.4 | 0.087 | 0.623 | 3190 | 2202 |

Table 3.7 Critical-state characteristics of the RW-M samples

| | $e_{cs}$ | $p'_{cv}$ (kPa) | $q_{cv}$ (kPa) | $Z_{cv}$ | $\Phi_{d,cv}$ | $e_{cv,inter}$ | $p'_{cv,inter}$ (kPa) | $q_{cv,inter}$ (kPa) |
|---|---|---|---|---|---|---|---|---|
| 0.581-5000-CPC | 0.651 | 5000 | 3350 | 4.53 | 0.076 | 0.621 | 4979 | 3383.5 |
| 0.596-1000-CPC | 0.661 | 1000 | 683 | 4.24 | 0.082 | 0.631 | 970.8 | 639.8 |
| 0.602-100-CVC | 0.603 | 37077 | 25360 | 5.22 | 0.068 | 0.574 | 36832 | 25958 |
| 0.648-500-CVC | 0.649 | 5980 | 4060 | 4.57 | 0.076 | 0.619 | 5844.1 | 3892.9 |
| 0.648-500-CDC | 0.663 | 642 | 426 | 4.18 | 0.090 | 0.629 | 644 | 428 |

Table 3.8 Critical-state characteristics of the PB samples

| ID | $e_{cv}$ | $p'_{cv}$ (kPa) | $q_{cv}$ (kPa) | $Z_{cv}$ | $\Phi_{d,cv}$ |
|---|---|---|---|---|---|
| 0.533-100-CDC | 0.630 | 128.75 | 86.22 | 4.25 | 0.089 |
| 0.627-1000-CDC | 0.628 | 1289.7 | 869.1 | 4.48 | 0.083 |
| 0.646-500-CDC | 0.629 | 645.9 | 437.8 | 4.39 | 0.086 |
| 0.578-1000-CVC | 0.578 | 35757 | 25361 | 5.43 | 0.066 |
| 0.599-527-CVC | 0.599 | 17222 | 11571 | 5.18 | 0.07 |
| 0.603-1000-CVC | 0.603 | 15548 | 10625 | 5.11 | 0.072 |
| 0.646-84.49-CPC | 0.63 | 84.49 | 56.52 | 4.22 | 0.091 |
| 0.643-419.81-CPC | 0.632 | 419.81 | 286.17 | 4.35 | 0.088 |
| 0.625-5000-CPC | 0.619 | 5000 | 3513.9 | 4.79 | 0.079 |
| 0.612-10000-CPC | 0.612 | 10000 | 6869.5 | 4.96 | 0.075 |
| 0.594-20000-CPC | 0.593 | 20000 | 13716 | 5.22 | 0.071 |
| 0.586-25000-CPC | 0.589 | 25000 | 17019 | 5.30 | 0.068 |
| 0.579-30000-CPC | 0.583 | 30000 | 21116 | 5.36 | 0.068 |

Table 3.9 Unbiased sample variance of initial void ratio

| | RW-S | | RW-M | | RW-L | | PB | | |
|---|---|---|---|---|---|---|---|---|---|
| | Vertical | Radial | Vertical | Radial | Vertical | Radial | $x$ | $y$ | $z$ |
| $S^2$ | 0.0007 | 0.0054 | 0.0004 | 0.0031 | 0.0002 | 0.0016 | $1.9\times10^{-5}$ | $5.7\times10^{-6}$ | $6.3\times10^{-6}$ |

Table 3.10 Unbiased sample variance of initial contact density

| | RW-S | | RW-M | | RW-L | | PB | | |
|---|---|---|---|---|---|---|---|---|---|
| | Vertical | Radial | Vertical | Radial | Vertical | Radial | $x$ | $y$ | $z$ |
| $S^2$ ($mm^{-6}$) | 706.45 | 4674.86 | 553.57 | 2524.18 | 245.00 | 953.72 | 132.47 | 24.19 | 45.4 |

Table 3.11 Characteristics of PSDs in different parts of the rigid-wall samples

| Sample | $D_{50}$ (mm) | $C_u$ | $C_c$ | $D_{max}$ (mm) |
|---|---|---|---|---|
| RW-S-middle | 0.218 | 1.5 | 0.936 | 0.4117 |
| RW-S-bound | 0.209 | 1.461 | 0.966 | 0.3838 |
| RW-S-inner | 0.217 | 1.50 | 0.942 | 0.4117 |
| RW-S-outer | 0.214 | 1.482 | 0.944 | 0.3319 |
| RW-M-middle | 0.215 | 1.487 | 0.948 | 0.4114 |
| RW-M-bound | 0.216 | 1.497 | 0.956 | 0.4115 |
| RW-M-inner | 0.217 | 1.491 | 0.952 | 0.4115 |
| RW-M-outer | 0.212 | 1.481 | 0.984 | 0.3917 |
| RW-L-middle | 0.214 | 1.478 | 0.951 | 0.4117 |
| RW-L-bound | 0.215 | 1.485 | 0.962 | 0.4118 |
| RW-L-inner | 0.215 | 1.479 | 0.953 | 0.4118 |
| RW-L-outer | 0.213 | 1.485 | 0.949 | 0.4110 |

# Chapter 4 Influence of interparticle friction on critical-state behaviour

## 4.1 Introduction

Sliding, rolling and spinning are the three basic mechanisms of relative movement for contacting particles. As illustrated in Figure 4.1, sliding is the relative translational movement between the two touching particles at contact point, rolling is the relative angular velocity between the two bodies about an axis ***t*** lying in the contact plane, while spinning is the relative angular velocity between the two bodies about the contact normal ***n*** (Duran, 2000; Johnson, 1985). In the past, the conceptual failure model in a granular material has considered sliding along a failure plane. Sliding at the contacts has been thought by many researchers (e.g., Horne, 1969; Rowe, 1962) to be the key failure mechanism of granular materials, while the influence of rolling on the mechanical behaviour of granular materials has been largely ignored. However, the importance of rolling has been identified both experimentally (Oda & Kazama, 1998) and numerically (Iwashita & Oda, 2000). Using DEM (Iwashita & Oda, 1998; Mahmood & Iwashita, 2011) and photoelasticity techniques (Behringer et al., 2008; Drescher & De Josselin De Jong, 1972; Oda et al., 1982), supplemented by analytical work (Tordesillas & Muthuswamy, 2009), supports a hypothesis that failure in a granular material is dominated by buckling failure of discrete, relatively highly loaded force chains that transmit the deviatoric stress through the soil during shear deformation.

It has been widely documented that DEM can qualitatively capture a number of unique mechanical characteristics of granular materials (including soils), e.g., dilatancy, state-dependent strength and stiffness, non-linearity, etc. (e.g., Guo & Zhao, 2013; Thornton, 2000). DEM equips granular-mechanics researchers with the ability to carry out parametric studies to assess how various particle-scale parameters influence the overall response. Here DEM is used in a systematic study that assesses the influence of $\mu$ on the mechanical response in triaxial compression tests. While other researchers (e.g., Thornton, 2000; Yang et al., 2012) have also systematically varied $\mu$, the unique contribution of this work is to look at the influence of $\mu$ on the CSL in both $q$-$p'$ and $e$-log($p'$) spaces.

In this Chapter, the research by giving an overview of key prior publications is contextualised in Section 4.2. Basic information regarding the DEM simulations is provided in Section 4.3. The influence of $\mu$ on the isotropic deformation characteristics of granular

materials is addressed in Section 4.4, followed by an exploration of the influence of $\mu$ on the macro mechanical behaviour of granular materials subjected to triaxial shearing in Section 4.5. A rationale for selecting an appropriate $\mu$ value is discussed within the framework of CSSM. Particle-scale analyses are detailed in Section 4.6 and Section 4.7. The roles of sliding and rolling in determining the failure of granular materials are investigated in Section 4.8 and Section 4.9.

## 4.2 Overview of prior studies

The Mohr-Coulomb equation is widely used to describe the strength of soils. The general expressions of the Mohr-Coulomb equation for cohesionless materials are $tan(\phi) = \tau/\sigma_n$ for shear box tests and $\sigma_1/\sigma_3=tan^2(45°+\phi/2)$ for triaxial tests, in which $\phi$ is the angle of internal friction, $\tau$ and $\sigma_n$ are the horizontal shear stress and the vertical normal stress in a shear box test. The normal stress:shear stress relationship is analogous to the frictional normal force:shear force relationship for sliding on a planar surface. Thus it is intuitive that this overall stress must arise from sliding at the contacts. Between the 1930s and 1970s, a number of analytical expressions relating the macro strength to the particle surface friction were proposed. Caquot (1934) derived the relationship between the ultimate angle of shearing resistance ($\phi'_{cv}$) and the interparticle friction angle ($\phi'_p$) for plane strain tests assuming that at the ultimate state sliding occurs simultaneously on contact faces inclined in all the tangential directions of a spherical surface:

$$tan(\phi'_{cv}) = \frac{1}{2}\pi \cdot tan\phi'_p \qquad \text{(Eq. 4.1)}$$

Assuming that the energy input at the peak state is dissipated by friction, Taylor (1948) derived the peak angle of shearing resistance ($\phi'_{peak}$) for direct shear box tests:

$$tan(\phi'_{peak}) = \frac{\tau_{peak}}{\sigma'} = \mu + (\frac{dy}{dx}) \qquad \text{(Eq. 4.2)}$$

in which $\tau_{peak}$ is the maximum applied horizontal shear stress, $\sigma'$ is the confining normal stress, $\mu$ is the inter-grain friction, while d$y$ and d$x$ are the displacement increments in the vertical and horizontal directions respectively. The strength formula developed by Bishop (1954) for plane strain tests (Eq. 4.3) and for triaxial tests (Eq. 4.4) also considered $\mu$ as the only factor that contributes to $\phi'_{cv}$.

$$\sin(\phi'_{cv}) = \frac{3}{2}\mu \qquad \text{(Eq. 4.3)}$$

$$\sin(\phi'_{cv}) = \frac{15\mu}{10+3\mu} \qquad \text{(Eq. 4.4)}$$

Shear-induced dilatancy is a fundamental feature of granular materials. Newland & Allely (1957) considered the contribution of volume expansion (dilation) to the overall strength. Based on a saw-blade model (Figure 4.2) and assuming an identical inclination of the slippage surface, they proposed that the maximum angle of shearing resistance ($\phi'_{max}$) is related to $\phi'_p$ and a dilation angle ($\theta$) which is defined as the inclination of the slippage surface to the loading direction:

$$\phi'_{max} = \phi'_p + \theta \quad \text{(Eq. 4.5)}$$

This model has been assigned a pedagogical "weight". Schematics similar to Figure 4.2 are routinely included in later contributions (e.g., Bolton, 1986; Rowe, 1962). Rowe's stress-dilatancy theory (Rowe, 1962) which was derived based on regular packings comprised of mono-sized discs implies that the stress ratio at critical state can be expressed by:

$$\frac{\sigma'_1}{\sigma'_3} = tan^2\left(45° + \frac{1}{2}\phi'_p\right) \quad \text{(Eq. 4.6)}$$

Horne (1965a, 1965b) extended Rowe's work to irregular packings composed of mono-sized particles by relating the strain rates to the spatial anisotropy and gave:

$$\frac{\sigma'_1}{\sigma'_3} = \frac{4}{\pi}\frac{m_1}{m_3} tan(45° + \frac{1}{2}\phi'_p) \quad \text{(Eq. 4.7)}$$

in which $m_1$ and $m_3$ are the mean projected solid paths which denotes the mean distance tranversed in the major and minor principal stress directions. In his later work, considering the propagation of sliding groups and the spatial variation of sliding directions, Horne (1969) derived the relationship between the major and minor principal stresses at critical state as:

$$\frac{\sigma'_1}{\sigma'_1-\sigma'_3} = \frac{1}{3} cot\phi'_p \left(\frac{\cos^3\beta_2 - \cos^3\beta_1}{sin\beta_1 - sin\beta_2}\right) + 1 - \frac{1}{3}(\sin^2\beta_1 + sin\beta_1 sin\beta_2 + \sin^2\beta_2) \quad \text{(Eq. 4.8)}$$

where $\beta_1 = 90° - \phi'_p$ is the assumed upper limit of the possible sliding directions with respect to the horizontal plane and $\beta_2$ is the assumed lower bound of the possible sliding directions with respect to the horizontal plane and can be determined from $\beta_1$ by solving $2\beta_1 + sin2\beta_1 + 2cos2\beta_1 = 2\beta_2 + sin2\beta_2 + 2cos2\beta_2$. Bolton (1986) found that if 20% reduction is given to the contribution of dilatancy ($\theta$ in Eq. 4.5), i.e., $\phi' = \phi'_p + 0.8 \cdot \theta$, the global angle of shearing resistance predicted by Eq. 4.5 is closed to that predicted by Eq. 4.6. Note that both Eq. 4.5 and Eq. 4.6 as well as Bolton's formula implies that $\phi'_{cv}$ equals to $\phi'_p$ at critical state.

Experimental assessment of these theoretical contributions is limited mainly because of the difficulties associated with measuring the inter-particle friction. By doing shear box tests on

dry and flooded spherical glass beads, Skinner (1969) observed that both the peak and residual mobilised friction angles were not very sensitive to the inter-particle friction and he attributed this to the dominance of the rolling deformation over the sliding deformation. Oda et al. (1982) showed that while the peak strength of samples composed of flat particles (OVAL Ⅱ) was higher for the high $\mu$ case ($\phi_p' = 52°$) than for the low $\mu$ case ($\phi_p' = 26°$), samples composed of more circular particles (OVAL Ⅰ) were insensitive to the two $\mu$ values considered (Figure 4.3), highlighting the importance of rolling in contributing to the overall strength.

While it is difficult to measure $\mu$ experimentally, DEM allows $\mu$ to be specified and thus provides a virtual experimental environment for assessing the influence of $\mu$ on the overall response. Yang et al. (2012) summarised some published relationships between $\mu$ and the macro angle of shearing resistance observed in DEM simulations superimposed with Skinner's experimental results (Figure 4.4). The database includes drained triaxial simulations using spherical particles (e.g., Thornton, 2000), drained biaxial simulations using polygons (Peña et al., 2008) and drained and constant-volume biaxial simulations using clumps (Yang et al., 2012). All these data indicated nonlinear relationships between $\mu$ and the overall strength. When spherical particles are used, small increases in $\mu$ give measurable increases in $\phi_{mob}$ at small values of $\mu \leq 0.3$; however, at higher $\mu$ values, $\phi_{mob}$ is effectively insensitive to variations in $\mu$. The analytical work of Horne (1969) fails to give an accurate prediction of DEM simulation results. All of the DEM studies presented in Figure 4.4 allowed particles to rotate freely. When particle rotation is restricted, however, the results differ. Morgan (1999) compared the response of freely-rotating 2D discs and non-rotating 2D discs in direct shear tests. Morgan observed a linear increase in the overall strength with increasing $\mu$ when particle rotation is prohibited, while there is a clear limit of sensitivity to $\mu$ when particles are allowed to rotate freely (Figure 4.5 (a)). This observation is confirmed in later 3D triaxial simulations by Suiker & Fleck (2004) (Figure 4.5 (b)). The numerical works of Morgan (1999) and Suiker & Fleck (2004) supported the findings of Oda et al. (1982) and addressed rolling as an indispensable factor that contributes to the overall strength. The dilatancy of granular materials also increases when $\mu$ is increased (Kruyt & Rothenburg, 2006; Yang et al., 2012). By performing true triaxial simulations using periodic boundaries, Barreto & O'Sullivan (2012) showed that increasing $\mu$ increases the peak angle of shearing resistance for granular materials sheared under three-dimensional loading conditions that the size of the yield surface defined by the Lade-Duncan criterion (Lade & Duncan, 1975) is also dependent on $\mu$ (Figure 4.6). Sazzad & Suzuki (2011) observed that

the width of the stress-strain cyclic curve for drained cyclic biaxial simulations increases as $\mu$ increases (Figure 4.8).

DEM also enables analysis of the particle-scale mechanism and allows the micro-scale and macro-scale responses to be reconciled. However, granular materials are complex, statically-indeterminate systems. Measures such as coordination number and fabric tensor are often used to characterise the topology of a granular assembly. Thornton (2000) noted that both the sliding fraction and mechanical coordination number decrease nonlinearly with increasing $\mu$ (Figure 4.8). Similar observations have been made by other researchers, e.g., Suiker & Fleck (2004) and Göncü & Luding (2013). The structure of granular assemblies becomes more anisotropic when $\mu$ is increased (Rothenburg & Kruyt, 2004). Yang et al. (2012) evaluated four types of anisotropies (contact normal anisotropy, contact normal force anisotropy, contact tangential force anisotropy and mobilised friction anisotropy) and found that each of them increased with increasing $\mu$ (Figure 4.9). Barreto & O'Sullivan (2012) observed that the application of a high $\mu$ makes the strong force chains more self-stable and less reliant on the lateral supports provided by weak contacts. Barreto & O'Sullivan also showed that $\mu$ affects the size of failure envelopes defined by the principal values of the fabric tensor similar to the effect of $\mu$ on the stress failure envelopes noted above. Antony & Kruyt (2009) showed that $\mu$ also notably influences on the levels of contribution of contact force components to the overall strength (Figure 4.10). These dependencies of micro-scale measures on $\mu$ must be related to the sensitivity of macro-scale response to $\mu$ as noted above. However, the precise nature of this link has not yet been intensively examined.

The existence of chain-like structures constituting heavily-stressed particles in a granular assembly has been noticed since the 1970s when photo-elasticity techniques were applied to determine the average stress and strain-rate tensors in the interior of a granular assembly (Drescher & De Josselin De Jong, 1972). As shown in Figures 4.11 and 4.12, this observation was confirmed in later experimental contributions using photoelastic materials (e.g., Majmudar & Behringer, 2005; Oda et al., 1982; Oda & Kazama, 1998) and also in both 2D and 3D DEM simulations (Guo & Zhao, 2013; Iwashita & Oda, 1998; Radjai, 1998). Subjected to continuous shearing, these columnar strong force chains evolve and collapse ultimately. In particular, Guo & Zhao showed an evolution of the topology of force network at different stages of loading (Figure 4.12). The term 'buckling' is used to describe such a collapse and buckling of strong force chains has been proposed to be a fundamental mechanism of instabilities and shear band formations for granular materials (Oda & Kazama, 1998; Oda et al., 1982; Rechenmacher, 2006). For example, Oda & Kazama (1998) suggested that strong force chains are formed during the strain-softening stage and start to

buckle around peak state; buckling occurs mostly within the shear bands, leading to high void ratios and the concentration of rotations within a shear band (Figure 4.13 (a)). A similar mechanism was observed by Mahmood & Iwashita (2011) in DEM simulations of biaxial tests using elliptical particles (Figure 4.13(b)). By performing 2D biaxial simulations on a densely-packed granular assembly, Tordesillas (2007) showed that the macro stick-slip behaviour is due to consecutive cycles of jamming-unjamming events which are associated with buckling of strong force chains within the shear band. Tordesillas also showed that buckling of strong force chains accounts for the non-affine deformation within shear bands and the loss of stored potential energy. Using the digital image correlation (DIC) technique, Rechenmacher et al. (2010) presented indirect evidence for the association of force chain build-up and collapse within the shear band with the global stress-strain behaviour by interpreting the kinematics of sand grains along the length of the shear band.

The buckling of strong force chains has also been studied analytically. Tordesillas & Muthuswamy (2009) considered a simple 2D model analogous to a strong force chain as shown in Figure 4.14. The contact between the discs was simulated using linear penalty springs in the normal and tangential directions. Rolling resistance springs were also used. The lateral support from the weak contact network was modelled by a set of elasto-plastic springs acting on the centroids of the middle particles. The buckling force was determined by taking the partial derivatives of the change of potential energy with respect to each degree of freedom (DOF) to be zero. Tordesillas & Muthuswamy showed that their model can qualitatively capture the effect of confining pressure on the strength of granular materials observed in a biaxial test. Hunt et al. (2010) idealised a strong force chain to be a structural system composed of $N$+1 nodes connected by $N$ rigid links (Figure 4.15 (a)). Each node has two DOFs supported by linear springs, one translational and one rotational. The buckling force can be determined by zeroing the partial derivatives of the total potential energy with respective to each DOF. O'Sullivan et al. (2013) extended this model to three-dimensional problems by considering the translational DOF of each node in two lateral directions (Figure 4.15 (b)). The ratio of the spring stiffnesses in different lateral directions is varied to account for the effect of different intermediate stress ratios. It was shown that their model can effectively capture the variation of peak strength with the intermediate stress ratio observed in a series of true triaxial DEM simulations using the exact ratio of stiffnesses obtained in the DEM simulations.

In summary, despite abundant experimental, numerical and theoretical studies, no agreement regarding the fundamental mechanism controlling the failure of granular materials has been made. Mitchell & Soga (2005) pointed out that the basic contributions to soil strength

include the frictional resistance between soil grains in contact and the internal kinematic constraints of soil particles associated with changes in the soil fabric. While obtaining this information in experiments is difficult, DEM enables analyses of particle-scale interactions and thus is very useful to investigate such fundamental issues. Previous research regarding the influence of $\mu$ on the critical-state behaviour only looked at some specific cases, e.g., Thornton (2000), while little attention has been paid to the influence of $\mu$ on the positions of the CSL. Moreover, a wide range of $\mu$ values have been used in prior DEM simulations, some of which are unrealistic. The rationale for selecting an appropriate $\mu$ value requires further discussion.

## 4.3 DEM simulations

The PSD used in most of the samples considered here is the Toyoura sand grading which has been described in Chapter 3. A subset of simulations using the LAMMPS code and periodic boundaries considered an analogue Dunkirk sand. These data were provided by Dr Hanley (personal communication) and are also included in the dataset for completion. The Dunkirk sand grading is included together with the Toyoura sand grading in Figure 4.16. Generation of the Dunkirk sand samples was based on the particle size information from a QicPic apparatus at Imperial College. Particles with diameters smaller than 0.05mm were ignored when generating the Dunkirk sand samples as their contribution to the overall grading is negligible and including these particles in a DEM simulation requires a smaller timestep and thereby increases the computational cost (personal communication with Dr Hanley). The coefficient of uniformity $C_u$ = 1.539 and the coefficient of curvature $C_c$ = 0.977 for the Dunkirk sand grading. Both the PB samples (containing 20,164 particles) and the medium size RW samples (containing around 16,000 particles) were used for the Toyoura sand grading, while the samples for the Dunkirk sand grading contained 43,906 particles. A simplified Hertz-Mindlin (HM) contact model was used for simulations using the Dunkirk sand grading and the particle shear modulus ($G$) and Poisson's ratio ($v$) were taken to be 29.14 GPa and 0.2 respectively. These values are very close to those adopted for simulations using the Toyoura sand grading. The approach used to generate the Dunkirk sand samples is identical to that used to generate the PB Toyoura sand samples as described in Chapter 3.

Three types of loading paths were considered: conventional drained compression (CDC), constant volume compression (CVC) and constant mean effective stress ($p'$) compression (CPC). The variation in initial void ratio was achieved by varying the inter-particle friction coefficients ($\mu$) used during compression. Once the initial state was attained, $\mu$ was changed to take the value used for shearing, i.e., 0.1, 0.25, 0.5, 0.75 or 1.0, and the sample was

allowed to come to a state of equilibrium prior to starting to shear. The range of $\mu$ values during shearing was selected by acknowledging that the recent experimental particle-particle friction tests documented by Senetakis et al. (2013) give $0.12 < \mu < 0.35$ for quartz-based sand grains, and also recognizing that many DEM simulations have used higher values (Table 4.1). Following the approach of Calvetti & Emeriault (1999), for a limited number of PB simulations using the Toyoura sand grading, particle rotations were inhibited; these simulations are denoted as "FR". As summarized in Table 4.2, a total of 51 PB simulations were carried out using the LAMMPS code with periodic boundaries, a Hertz-Mindlin contact model and the Toyoura grading. 12 PFC3D simulations were run using rigid walls and a Hertz-Mindlin contact model, as listed in Table 4.3. Table 4.4 lists a mixture of 12 PFC3D and 15 LAMMPS simulations using a linear contact model. For the 12 PFC3D simulations and nine of the LAMMPS simulations the normal and shear stiffnesses were both equal to $10^5$ N/m. An additional six LAMMPS simulations were carried out with $\mu$=0.5 and normal and shear stiffnesses equal to $10^4$ N/m, to assess the influence of the magnitude of the stiffness on the results. Finally Table 4.5 lists the 34 Dunkirk sand simulations. In line with the finding of Chapter 3, for RW samples, calculation of $e$ and $p$' at the critical state considers only the homogeneous interior part that is $2 \cdot D_{50}$ away from the rigid wall boundaries. This study builds upon the earlier work of Peña et al. (2008) and Yang et al. (2012) by considering a broader range of stress levels, test types, and packing density to facilitate a more comprehensive analysis of the effects of $\mu$ on the critical state line (CSL) in both $q$-$p'$ and $e$-log($p'$) spaces.

## 4.4 Isotropic consolidation

Bagi (2005) categorized the sample genesis methods in DEM into two main groups: the constructive method and the dynamic method. In constructive methods, generation of particles is based on geometric allocation and has no need to calculate the particle motion. Representative examples using the constructive method can refer to Bagi (2005) and Cui & O'Sullivan (2003). In dynamic methods, the particle motion needs to be updated continuously during sample generation. Typical dynamic methods include the radius expansion method, the isotropic compression method, the gravitational deposition method, the multi-layer compaction method and the multi-layer with under-compaction method (Jiang et al., 2003).

When the isotropic compression method is used, DEM samples with different initial void ratios for a given stress level are routinely created by changing $\mu$. The process for achieving a controllable void ratio is rarely clearly stated by DEM analysts. The first stage for such a

method is to compact the cloud of non-contacting particles with a specific $\mu$ value until the target stress level is attained. Then $\mu$ is set to the final value for shearing and the system is again returned to the target stress state.

Figure 4.17 shows the influence of $\mu$ on the void ratio after the first stage of isotropic compression (i.e., before setting $\mu$ to the target interparticle friction ($\mu_{targ}$) for shearing) for two isotropic stress levels, i.e., $p'_0$=500 kPa and $p'_0$=5000 kPa. For both stress levels considered, $e_0$ is nonlinearly related to $\mu$, *i.e.,* $e_0$ increases more rapidly with increasing $\mu$ for $\mu \leq 0.1$ than for $0.1<\mu<0.5$. When $\mu$ exceeds 0.5, the void ratio is no more sensitive to $\mu$. Increasing the stress level reduces the attained void ratio.

Figure 4.18 compares the void ratio before and after setting $\mu$ to a $\mu_{targ}$ value of 0.25 for the case of $p'_0$=500kPa. Note that the void ratio was determined when a state of equilibrium had been reached (i.e., both the void ratio and the stress state remain constant for at least 10 million calculation cycles). As Figure 4.18 shows, when $\mu$ is below $\mu_{targ}$, the void ratio does not change when $\mu$ increases to $\mu_{targ}$; however, when $\mu$ is higher than $\mu_{targ}$, the void ratio drops to between 0.605 and 0.607. To investigate the driving mechanism for such drops in $e$, the entire sample generation procedure for a typical sample with $\mu$ higher than $\mu_{targ}$ is considered in Figure 4.19. The sample was initially istropically compressed from a non-contacting cloud to a stable state with $\mu$ = 1.0 under $p'_0$=500 kPa. $\mu$ was then reduced to $\mu_{targ}$ = 0.25 at 50 million timesteps and the sample was returned to equilibrium again by running another 30 million timesteps. Figure 4.19 (a) shows the evolution of $e$ and $p'$ and Figure 4.19 (b) presents the evolution of $Z$ and the percentage of sliding contacts during the sample generation procedure. As marked by the solid square (Point A) in Figure 4.19 (a), percolation (i.e., the point where $p'$ becomes non-zero) occurred after around five million timesteps, following which $p'$ increased quickly to 500 kPa and was maintained at a constant value until $\mu$ was reduced from 1.0 to 0.25. The void ratio decreased linearly with timestep before percolation due to a constant strain rate and reached a constant value of 0.668 when $p'$ became constant. As shown in Figure 4.19 (b), contacts were formed before percolation as non-zero $Z$ values appeared at point A. A constant Z value of 3.63 was reached and the sliding fraction was almost zero before reducing $\mu$ from 1.0 to 0.25 (Point B). When $\mu$ was reduced from 1.0 to 0.25, $e$ dropped suddenly and $p'$ decreased abruptly to almost 0, indicating an instantaneous collapse of the solid skeleton which sustains the external loading. The particle-scale indications of the structural collapse are the abrupt drop of $Z$ and the spurt of sliding fraction from zero to over 80%. One million timesteps after point B, $p'$ increased again to 500 kPa while $e$ decreased to 0.605. $Z$ also increased to a constant value of 4.13

after one million timesteps, while the sliding fraction still oscillated and dropped to a constant of about 50% five million timesteps after B.

The catastrophic collapse of the previously stable backbone upon reduction of $\mu$ is due to the sudden reduction of shearing resistance at the contacts and the sudden release of strain energy in the shear springs. The fundamental mechanism can be illustrated by a simple spring-block system as shown in Figure 4.19 (b). The contact state at the first stage of isotropic compression is analogous to a block connected to an elastic spring resting on a frictional surface with $\mu = \mu_{targ}$. The tangential force $f_t$ can be decomposed into a frictional force $\mu_{targ}f_n$ and a tractive force $f_t - \mu_{targ}f_n$, in which $f_n$ is analogous to the normal contact force. At this moment, $f_t$ is smaller than $\mu f_n$ but is larger than $\mu_{targ}f_n$. When $\mu$ is reduced to $\mu_{targ}$, a drag force of $f_t - \mu_{targ}f_n$ is imparted to the block as the spring rebounds. The block is pulled back by the spring (compaction) and moves backwards and forwards about the neutral position at which the spring's tensile force equals to $\mu_{targ}f_n$ and finally becomes stationary again at the neutral position with $f_t = \mu_{targ}f_n$. This oscillating response may explain the latter occurrence of a constant sliding fraction than other quantities as indicated in Figure 4.19. From the energy perspective, the sudden reduction of $\mu$ released the strain energy in the shear spring instantaneously. The released strain energy is converted to kinetic energy which drives the rearrangement of particles. The kinetic energy is then dissipated gradually by friction and background damping until a new stable structure is formed (Point C). Figure 4.18 and Figure 4.19 show that generating samples with different packing density by varying inter-particle friction is limited and the loosest packing is reached when $\mu$ is close to $\mu_{targ}$.

Figure 4.20 presents the relationships between both the coordination number ($Z$) and $\mu$, and the mechanical coordination number ($Z_m$) (Thornton, 2000) and $\mu$ for $p'_0$=500 kPa before and after changing $\mu$ values. Before $\mu$ is changed to $\mu_{targ}$ both $Z$ and $Z_m$ follow a power-law decay with $\mu$, i.e., $Z_m = 4.4908\mu^{-0.107}$ and $Z = 3.5892\mu^{-0.159}$. Note that only frictional data are presented in Figure 4.20, while $Z$ and $Z_m$ values for $\mu$ = 0.0 are 5.99 and 6.3 respectively, which are close to the critical value of 6 for frictionless materials under 3D conditions (Gong, 2008). $Z$ and $Z_m$ after $\mu$ is changed to $\mu_{targ}$ follow the same path as that of $Z$ and $Z_m$ before the change of $\mu$ when $\mu$ is smaller than $\mu_{targ}$, but they increase to an almost identical value when $\mu$ exceeds $\mu_{targ}$ mainly because of the similar $e$. The difference between $Z$ and $Z_m$ becomes larger with increasing $\mu$ as the number of rattlers is higher when $\mu$ is higher. The higher number of rattlers indicates a stronger and more stable structure for higher $\mu$ cases.

Figure 4.21 shows the relationship between $Z$ and $e$, and $Z_m$ and $e$ for the first stage of isotropic compression (before setting $\mu$ to $\mu_{targ}$). The data can be represented by a second-order polynomial for both $p'_0$=500 kPa and $p'_0$=5000 kPa cases, but they do not collapse to the same relationship. Higher confining pressure leads to higher $Z$ and $Z_m$. In the regard, $Z$ and $Z_m$ are not uniquely related to $e$ but also depend on $p'$.

An understanding of the data presented in Figures 4.17 to 4.21 is important to enable the control of void ratio required to create samples with differing initial states and hence find the critical state line.

## 4.5 Macro-scale behaviour under triaxial loading conditions

### 4.5.1 Constant-$\sigma'_3$ loading

The stress and deformation responses of a representative subset of the PB simulations of conventional drained triaxial compression tests are illustrated in Figure 4.22. All the simulations in the subset considered the same initial conditions (initial void ratio ($e_0$) of 0.533 and an identical initial isotropic stress ($p_0'$) of 100 kPa). This sample was generated using zero friction to achieve the densest packing at a confining pressure of $\sigma'_3$ = 100 kPa, which was maintained during shearing. The simulations differ in the inter-particle friction coefficients ($\mu$) used during shearing. Referring to Figure 4.22 (a), all of the samples are initially very stiff due to their initially very dense state. The stiffness increases with increasing $\mu$ and the deviatoric stresses of samples with $\mu$ higher than 0.5 go almost vertically to the peak, showing an unrealistically stiff response. As $\mu$ increases, both the peak and critical-state strengths increase. The strength of samples drops more rapidly post-peak for higher $\mu$ values. Figure 4.22 (b) shows that the (dilative) volumetric strain ($\varepsilon_v$) increases with increasing $\mu$, but when $\mu$ exceeds 0.5, the effects of further increases in $\mu$ are negligible. Figure 4.22 (c) illustrates the evolution of dilatancy $-d\varepsilon_v/d\varepsilon_q$ with axial strain ($\varepsilon_a$). Shear strain is defined as, $\varepsilon_q = \frac{2}{3} \cdot (\varepsilon_1 - \varepsilon_3)$ where $\varepsilon_1$ and $\varepsilon_3$ are the major and minor principal strains respectively. Note that the total strain components instead of the plastic strain components are used as the contribution of the elastic components to the dilatancy is negligible. The dilatancy of all the samples increased quickly after loading commenced until a peak value is reached and then gradually decreased to zero at critical state. No obvious difference in peak dilatancy is observed when $\mu$ exceeds 0.5. Taking the peak dilatancy point as the initiation of gross yield, the data show that for lower $\mu$ cases gross yield occurs at a larger strain level than for higher $\mu$ cases. It also appears that there are more fluctuations in the dilatancy when $\mu \geq 0.5$.

Similar observations can be made from a set of simulations on RW samples with the same initial state ($e_0$=0.648, $p'_0$=500 kPa). As shown in Figure 4.23, the strength of the RW samples increases with increasing $\mu$ but the sensitivity of further increases in $\mu$ becomes negligible when $\mu$ exceeds 0.5. For simulations with $\mu \geq 0.25$, samples dilate to the critical state and the dilative response increases with increasing $\mu$, while the sample with $\mu$ equal to 0.1 contracts consistently until the critical state is attained.

Figure 4.24 considers the variation of the angle of shearing resistance $\phi'$ ($= \sin^{-1}\frac{\sigma'_1-\sigma'_3}{\sigma'_1+\sigma'_3}$) for the PB samples at both peak ($\phi'_{peak}$, open squares) and critical states ($\phi'_{cv}$, solid squares) with $\mu$. Both $\phi'_{peak}$ and $\phi'_{cv}$ increase nonlinearly with increasing $\mu$. While $\phi'_{peak}$ increases consistently from 17.99° for $\mu$=0.1 to 32.7° for $\mu$=1.0, the influence of $\mu$ on $\phi'_{cv}$ is less obvious and $\phi'_{cv}$ becomes insensitive to $\mu$ when $\mu$ is higher than 0.5. As shown in Figure 4.25, similar observations can be made for the RW samples. Göncü & Luding (2013) investigated $\mu$ values up to 100 and found that $\phi'_{peak}$ was saturated at $\mu$=0.4. The discrepancy between this study and Göncü & Luding (2013) may be attributable to the difference in PSD and the initial packing density. Note that a dense sample is used in this study, while in the study of Göncü & Luding (2013), dilative volumetric strain only occurred after 8% axial strain, indicating that their samples are at a medium dense state. A more closely-packed sample may have a higher coordination number, which may thereby amplify the effect of the friction coefficient. Note that our observations are similar to Thornton (2000) who also used a dense sample.

### 4.5.2 Constant-*p'* loading

Figure 4.26 illustrates the stress-deformation behaviour of a series of constant-*p'* simulations. Samples were isotropically compressed to a stress state of *p'*=5000 kPa and were then subjected to triaxial loading while *p'* was maintained at 5000 kPa. The same $\mu$ values were used for isotropic compression and shearing, e.g., for $\mu$=1.0 case, $\mu$=1.0 was used during both isotropic compression and shearing. By doing so, samples close to the loosest state under the prescribed stress level for each $\mu$ case can be generated. The void ratios after isotropic compression are 0.589, 0.625, 0.643, 0.647 and 0.649 for $\mu$=0.1, 0.25, 0.5, 0.75 and 1.0 respectively. As can be seen in Figure 4.26 (a), although the initial packing density decreases with increasing $\mu$, $q$ increases with increasing $\mu$, i.e., the effect of $\mu$ surpasses that of void ratio. However, when $\mu$ exceeds 0.5, the influence of $\mu$ on $q$ is negligible. Figure 4.26 (b) compares the void ratio evolution for different $\mu$ cases. Despite an initially looser packing, samples with a higher $\mu$ dilate more than samples with a lower $\mu$. The sample with

$\mu$=1.0 (indicated by the thin black solid line) dilates consistently from $e$=0.649 to $e$=0.678 at critical state, while the sample with $\mu$=0.1 (indicated by the thick gray dot line) contracts consistently from $e$=0.589 to $e$=0.574 at critical state. The behaviour of other samples is intermediate. Considering that $p'$ is identical for each case, the higher void ratio at critical state indicates a higher position of the critical state line (CSL) in $e$-log($p'$) space.

The significant influence of $\mu$ on the volumetric response under drained conditions indicates a considerable impact of $\mu$ on the strength of granular materials under undrained conditions. The response of samples sheared under a constant-volume condition with different $\mu$ and initial void ratios was considered. However, for the HM model adopted here, it was very difficult to select a single $e$ value that can give a reasonable stress-strain response for all the $\mu$ values considered and enable a scientific comparison. If $e$ is high, samples for $\mu$ below 0.5 liquefied immediately after shearing commenced, while if $e$ is low, samples for $\mu$ above 0.5 dilated notably to a very high stress level which induces a significant amount of overlap. Therefore, the influence of $\mu$ on the undrained response is not discussed here. Insights into the influence of $\mu$ on undrained response can be obtained by reference to Yang et al. (2012) who considered a 2D system and a linear elastic contact model.

### 4.5.3 Critical-state characteristics

Figure 4.27 (a) illustrates the location of the CSLs in $q$-$p'$ space for all the Toyoura sand samples where a simplified Hertz-Mindlin contact model was used as listed in Table 4.2 and Table 4.3. For each value of $\mu$ considered, the critical state points in $q$-$p'$ space can be represented by a unique straight line with slope $M$. The value of $M$ tends to increase with increasing $\mu$. When rotation is not restricted, there is little difference between the $M$ values for $\mu \geq 0.5$. Where particle rotations are inhibited, the $M$ values are higher than those for the free rotation cases and increase with $\mu$ even for $\mu \geq 0.5$ in line with the observations of Suiker & Fleck (2004). Figure 4.27 (b) gives the best-fitting angles of shearing resistance at critical state ($\phi'_{cv} = \sin^{-1}\left(\frac{3M}{6+M}\right)$) for all the Toyoura simulations carried out using a HM contact model and periodic boundaries plotted against the inter-particle friction angle, $\phi'_p = \tan^{-1}(\mu)$. In line with the observations of Thornton (2000) and Yang et al. (2012) amongst others and in agreement with Figure 4.24, for the simulations where rotation is not prohibited, the increase in $\phi'_{cv}$ with $\phi'_p$ is nonlinear, i.e., there is a marked increase in $\phi'_{cv}$ with increasing $\phi'_p$ until $\phi'_p \approx 20^o$, i.e., until $\mu \approx 0.36$. When $\phi'_p > 20^o$ the relative influence of increases in $\phi'_p$ (and $\mu$) is less evident. Figure 4.27 (b) includes DEM data from some other

researchers (Thornton, 2000; Peña *et al.*, 2008; Yang et al., 2012) and experimental data from Skinner (1969) as well as the $\phi'_{cv}$ values predicted using the analytical models proposed by Rowe (1962) (Eq. 4.6), Bishop (1954) (Eq. 4.3 for plane strain and Eq. 4.4 for triaxial) and Caquot (1934) (Eq. 4.1 for plane strain).

Figure 4.27 (b) indicates that when rotation is inhibited, the relationship between $\phi'_{cv}$ and $\phi'_p$ is linear for all the $\phi'_p$ values considered here. This coincides with the experimental observation of Oda et al. (1982) that the peak angle of shear resistance of samples composed of flatter particles (that cannot easily rotate) is much more sensitive to inter-particle friction than that of sample composed of rounder, more rotatable particles. All the analytical solutions underestimate $\phi'_{cv}$ for low $\phi'_p$ values but overestimate $\phi'_{cv}$ when $\phi'_p$ is high. This is attributable to the idealised model considering mono-sized particles and neglect of the microscopic constraints. For example, Rowe's equation is based on a regular packing comprised of mono-sized particles. This equation was derived by minimising the internal work in the sliding direction. As noted by Li & Dafalias (2000), this approach simply treated a particulate system as a continuum (i.e., sliding is persistent through the media) and neglected the static and kinematical constraints at the particle contacts, which will be more notable and more important for a polydisperse system as shown in Figure 4.2. Moreover, Rowe's theory also did not consider the evolution of the microstructure and assumed a constant failure direction. These assumptions may possibly lead to the underestimation of the strength when $\phi'_p$ is low. Thornton (2000) attributed this trend to the neglect of rotation in the analytical solutions. However, Figure 4.27 (b) indicates that the analytical solutions fail to predict the shear resistance of granular materials even when rotation is fixed.

The CSLs in *e*-log (*p'*) space for simulations using the Toyoura sand grading are shown in Figure 4.28 and it is clear that the CSL in *e*-log (*p'*) space moves upwards (i.e., at a given *p'*, *e* increases) as $\mu$ increases. For the same $\mu$ values, the CSLs for the simulations where rotation is inhibited are located above the CSLs for the free rotation cases. Where rotation is fixed, *e* does not vary with *p'* for the stress level considered when $\mu = 0.5$; however the results when $\mu = 0.25$ are more reasonable. When $\mu \geq 0.5$, and rotation is free, the effect of $\mu$ on the locus of critical states in *e*-log (*p'*) space is small. The most surprising observation is that, when the particles are allowed to rotate and when $\mu$ is higher than 0.5, initially there is an increase in the value of *e* at the critical state with increasing *p'*, followed by a subsequent decrease. Noting that when rotation is fixed the average particle stress tensors are not symmetric; further discussion is limited to the free rotation simulations. The same trend was observed in additional PB and RW simulations using a linear contact spring (Figure 4.28 (b)) whether the spring stiffness was $10^5$ N/m or $10^4$ N/m. The increase in *e* at the critical state

with $p'$ was also observed in a second series of PB simulations that used a simplified Hertzian contact model and $\mu = 0.5$, but with a PSD close to that of Dunkirk sand (Figure 4.29). The results presented in Figures 4.28 and 4.29 are important as they show that irrespective of the DEM code used (PFC3D or LAMMPS), the contact model adopted (Hertz-Mindlin or linear elastic), or the boundary conditions (periodic or RW) and grading (Toyoura or Dunkirk) used, if a coefficient of friction greater than or equal to 0.5 is used with spherical particles, the critical-state behaviour that emerges in $e$-log ($p'$) space differs markedly from what we would expect for a real, physical material and violates the CSSM framework for soil response. However, if a lower coefficient of friction (0.25) is used, the response in $e$-log ($p'$) space qualitatively agrees with observations of real soil behaviour and the CSSM framework.

Having established the macro-scale response characteristics, the particle-scale DEM data were analysed in detail in an attempt to explain the mechanisms that result in the observed macro-scale sensitivity to $\mu$. The particular areas of interest were the unusual response observed at the critical state in $e$-log ($p'$) space for $\mu \geq 0.5$ and the lack of sensitivity of the response to increases of $\mu$ beyond 0.5.

## 4.6 Micro-structural measures

### 4.6.1 Scalar parameter

Coordination number ($Z$) is a scalar parameter describing the micro structure. A higher coordination number indicates a closer packing and vice versa. Figures 4.30 to 4.32 consider the effect of $\mu$ on $Z$. Figure 4.30 illustrates the evolution of $Z$ with strain for the subset of the samples considered in Figure 4.22. In all cases, $Z$ decreases immediately after loading and attains a constant value at a strain level that is smaller than the onset of a constant-volume critical state (refer to Figure 4.22 (b)). This reflects the fact that all samples dilate through shearing. A similar trend was observed for the mechanical coordination number ($Z_m$) which considers only particles with two or more contacts (Thornton, 2000). Figure 4.31 considers most of the LAMMPS, free-rotation, Hertz-Mindlin dataset (i.e., Table 4.2 data excluding FR simulations and $\mu = 0.75$ simulations) and shows that the values of $Z$ at the critical state increase systematically following a power-law regression with increasing $p'$, *i.e.*, $Z_{cs} = Z_c + \delta(p')^{\xi}$, in which, $Z_c$ is the intercept with the $p'$=0 axis, $\delta$ is a scaling coefficient and $\xi$ is the power. Despite a smaller difference in $\mu$, the spacing between the trend line for $\mu$=0.25 and the trend line for $\mu$=0.5 is larger than that between the trend lines for $\mu$=0.5 and $\mu$=1.0, indicating a nonlinear relationship between $Z$ and $\mu$, at a given $p'$ value. As shown in Figure

4.31 (b), a similar trend was observed for the variation of $Z_m$ with $p'$ at the critical state, *i.e.,* $Z_{m,cs} = Z_{m,c} + \delta_m (p')^{\xi_m}$. Table 4.6 gives the fitting parameters for different $\mu$ cases. The intercepts obtained in the regression, i.e, $Z_c$ and $Z_{m,c}$, decrease with increasing $\mu$ . Referring to Figure 4.32 (a), which again considers the LAMMPS simulations listed in Table 4.2 (excluding FR and $\mu = 0.75$ simulations), the relationship between $e$ and $Z$ at the critical state is complex. For $e$ values < 0.6 the $Z$-$e$ relationship is almost linear; however, when $e > 0.6$, the relationship is nonlinear and depends on $\mu$. Figure 4.32 (b) considers just the subset of data with $e_0$ = 0.533 and $\sigma'_3$ = 100 kPa and shows that during shearing the relationship between $Z$ and $e$ is complex. The data confirm the observation of Barreto & O'Sullivan (2012) that the relationship between $Z$ and $e$ is not a simple one-one function as suggested by Oda (1977) and Hasan & Alshibli (2010) amongst others but also depends on the fabric. $Z$ initially decreases rapidly with increasing $e$ but the trend becomes gentler with increasing $e$ and that there can be a marked variation in $e$ with little change in $Z$ at higher void ratios.

### 4.6.2 Mechanical redundancy

Kruyt & Rothenburg (2009) proposed the index of mechanical redundancy ($I_R$) to quantify the mechanical redundancy of a discrete system, which is defined as the ratio of the total number of governing equilibrium equations (constraints) to the total number of degrees of freedom at the contacts. For a three-dimensional problem, considering constraints on three translational motion directions for elastic contacts ($|f_t| < \mu f_n$) and only one constraint along the normal direction for plastic contacts at which sliding occurs, the total number of governing equilibrium equations becomes $3 \cdot (1 - f) \cdot N_c + f \cdot N_c = (3 - 2f)N_c$ , in which $f$ is the sliding fraction and $N_c$ is the total number of contacts. In total there are $6N_p$ degrees of freedom for a 3D system and thus $I_R$ can be expressed as:

$$I_R = \frac{(3-2f)N_c}{6N_p} \qquad \text{(Eq. 4.9)}$$

If $I_R$ is equal to or higher than unity, the system is mechanically stable; otherwise, the system is mechanically unstable. In line with Kruyt & Rothenburg (2009), the number of particles with zero contacts has been subtracted from $N_p$ considering that these particles are unlikely to participate in the overall force transmission and the corresponding index of mechanical redundancy is denoted $I^{NR}_R$. $I^{NR}_R$ essentially reflects the mechanical redundancy of the solid skeleton. Figure 4.33 (a) shows the evolution of $I^{NR}_R$ with axial strain for the representative set of simulations shown in Figure 4.22. For all the $\mu$ cases considered, $I^{NR}_R$ drops quickly from around 1.54 to close to unity and is maintained constant thereafter. The dependency of $I^{NR}_R$ on $\mu$ is not clear. A $I^{NR}_R$ value close to unity indicates that the solid skeleton topology

approaches the most efficient configuration (i.e., smallest number of contacts) without creating redundant constraints to sustain the external loading regardless of $\mu$. Figure 4.33 (b) considers the mechanical redundancy of the entire system by including all the particles when calculating $N_p$. For each $\mu$ case considered the mechanical redundancy of the entire system decreases initially and reaches a constant value that is below unity at the critical state. Unlike $I^{NR}{}_R$, $I_R$ decreases with increasing $\mu$ which is related to the increasing number of rattlers in the system with increasing $\mu$. The difference between $I^{NR}{}_R$ and $I_R$ reflects the difference between the stability of the force transmission matrix and that of the whole assembly. For uniform materials, the granular assembly may be still in a stable state given that $I^{NR}{}_R$ is higher than unity in spite of a smaller-than-unity $I_R$. However, this may not be true for some materials with a significant size difference between the big and small particles as well as a considerably smaller number of big particles compared to the number of small particles. For these materials, it is highly likely that the strong force network is comprised of only a very small number of big particles connected by some small particles, while the remaining particles are rattlers. This kind of force transmission network is fragile and metastable (Shire, 2014). In such a case, both $I^{NR}{}_R$ and $I_R$ should be evaluated.

The number of rattlers, $N_R$, is an alternative indicator of the mechanical redundancy of an entire particulate system. In this study, rattlers are defined as particles with fewer than two contacts in line with the definition associated with $Z_m$. As would be expected from the decrease in $Z$ and decrease in $I_R$, referring to Figure 4.34 (a), and considering the subset of data with $e_0$ = 0.533 and $\sigma'_3$ = 100 kPa, during shearing the number of rattlers increases rapidly during the initial loading stage and then evolves more gradually until a constant value is attained. Figure 4.34 (b) considers the dataset listed in Table 4.2 (excluding FR simulations and $\mu$ = 0.75 simulations) and indicates that the number of rattlers present at the critical state systematically deceases as $\mu$ decreases and $p'$ increases. The number of rattlers also follows a power-law decay with $p'$, i.e., $N_R = N_{R,c} + \delta_R (p')^{\xi_R}$ and the fitting parameters ($N_{R,c}$, $\delta_R$ and $\xi_R$) are given in Table 4.7. The data presented in Figures 4.32 to 4.34 indicate that fewer particles are needed to maintain a stable force transmission network when $\mu$ is high. At high $\mu$ values, the strong force chains become more self-stable and less dependent on the lateral supports offered by the orthogonal weak contacts, leading to more floating particles. Further analysis (Figure 4.34(c)) shows that the mean size of rattlers increases with increasing $\mu$; strong force chains are usually composed of larger particles and so the data suggest that fewer strong force chains exist in samples with a higher $\mu$.

The rattlers do not contribute to the global force transmission. Therefore, following Thevanayagam & Mohan (2000), these rattlers can be considered as part of the void space and an inter-granular void ratio ($e_s$) can be defined as:

$$e_s = \frac{V_{void}+V_R}{V_s-V_R} \quad \text{(Eq. 4.10)}$$

Where $V_{void}$ is the real void volume, $V_R$ is the volume of rattlers and $V_S$ is the total volume of solids. Figures 4.35 (a) and (b) show the relationships between the inter-granular void ratio and the mean effective stress $p'$ for the Toyoura and Dunkirk gradings respectively. Comparing with Figures 4.28 and 4.29, it is clear that the atypical relationship between $e$ and log ($p'$) is no longer visible and CSLs show a consistent trend with $e_s$ decreasing with $p'$ for all the $\mu$ values investigated. The larger increase of $e_s$ at a lower $p'$ value can be explained by the increased number as well as the increased size of rattlers with decreasing $p'$ as illustrated in Figure 4.34. Moreover, the CSLs with $\mu$ = 0.5 and $\mu$ = 1.0 are clearly distinguishable when rattlers are ignored. A similar observation was made upon detailed analysis of the data with a linear contact model (Table 4.4). This observation does not imply, however, that one should use $e_s$ rather than $e$ when interpreting DEM simulations of shearing; rather it highlights the high number of rattlers present when $\mu$ is ≥0.5 due to the increasing structural stability.

### 4.6.3 Directional fabric

Figure 4.36 (a) and Figure 4.36 (b) illustrate the evolution of deviatoric fabric ($\Phi_d=\Phi_1-\Phi_3$, see Section 3.3) considering all contacts and only strong contacts bearing normal forces that are above the average during shearing, respectively, again for simulations with $e_0$ = 0.533 and $\sigma'_3$ = 100 kPa. The structural anisotropy increases with $\varepsilon_a$ until a peak value is reached; then it starts to decrease and finally attains a constant value. Figure 4.36 (b) also shows that the occurrence of peak structural anisotropy of strong contacts (i.e. those contacts transmitting forces above the mean contact force) coincides with that of peak strength (Figure 4.22 (a)). This supports the hypothesis of Tordesillas & Muthuswamy (2009) that the peak strength corresponds to the initiation of massive strong force chain buckling events which can be characterised by the appearance of a peak followed by an abrupt decrease of structural anisotropy. The peak overall structural anisotropy appears later than the peak strength (Figure 4.36 (a)) due to the lagged response of the weak contacts (i.e., those contacts transmitting forces lower than the mean contact force) as illustrated in Figure 4.36 (c). Note that in Figure 4.36 (c), the difference between the principal fabric of the weak contacts in the major ($\Phi_z$) and minor ($\Phi_x$) principal stress directions rather than $\Phi_1-\Phi_3$ is shown to

illustrate the change of preferential orientation of weak contacts with shearing. $\Phi_z - \Phi_x$ is negative at small strain levels and then becomes positive with shear processing and the influence of $\mu$ on the anisotropy of weak contacts is similar to that of strong contacts. A negative value for weak contacts implies a preferential horizontal orientation for weak contacts. Figure 4.36 also shows that the structural anisotropy increases with $\mu$ but the structural anisotropy is insensitive to increases in $\mu$ when $\mu \geq 0.5$.

Figure 4.37 (a) shows the structural anisotropy of all the contacts, the strong contacts and the weak contacts at critical state as a function of $\mu$. It is indicated that strong contacts are much more anisotropic than the weak contacts and the anisotropy increases nonlinearly with increasing $\mu$. The relative anisotropy between the strong and weak contact network can be evaluated by the ratio of $\Phi_d^s$ to $\Phi_d^w$ in which $\Phi_d^s$ and $\Phi_d^w$ are the deviatoric fabric considering strong and weak contacts respectively. Although both the strong and weak contact force network become more anisotropic, the relative anisotropy ($\Phi_d^s$ / $\Phi_d^w$) decreases from 35 for $\mu$=0.1 to about 7.5 for $\mu$=1. Considering the full Toyoura dataset, Figure 4.37 (c) illustrates the relationship between deviatoric fabric ($\Phi_1 - \Phi_3$) and mean effective stress ($p'$) at the critical state for simulations under different loading paths. As shown in Figure 4.37 (c), the structural anisotropy at the critical state decreases with increasing $p'$ in a way that also follows a power-law regression (indicated by the dash lines), i.e., $\Phi_d = \Phi_{d,c} + \delta_d (p')^{\xi_d}$. The regression parameters $\Phi_{d,c}$, $\delta_d$ and $\xi_d$ are given in Table 4.8. Higher $\mu$ values induce higher degrees of anisotropy; however, when $\mu$ is higher than 0.5 the structural anisotropy does not noticeably vary with $\mu$.

$\Phi_d$ describes the anisotropy of contact normal orientations but gives no information on the spatial distribution of contact forces. Cambou et al. (2004) divided particle-scale anisotropy of granular materials into two categories according to their different origins, namely, the geometrical anisotropy and the mechanical anisotropy. The geometrical anisotropy originates from the local relative positions between two touching particles, while the mechanical anisotropy is mainly due to the direction-dependent distribution of contact forces induced by the external loading. Chantawarangul (1993) and Ouadfel & Rothenburg (2001) performed statistical approximation of the spatial distributions of the contact normal orientation, the branch vector, the normal contact force and the tangential contact force and derived the stress-force-fabric (S-F-F) relationship which relates the fabric anisotropy tensors and the global stress tensor. Four anisotropy sources were considered:

(a) Contact orientation anisotropy ($a_c$)

The fabric tensor can be derived from the spatial distribution of contact normal orientations as shown in Eq. 4.11 (a), in which the probability distribution function $E(\Omega)$ can be approximated by its second-order Fourier expansion as shown in Eq. 4.11 (b). Substituting Eq. 4.11 (b) into Eq. 4.11 (a) and integrating over $\Omega$ give $a_{ij}^c = 15/2\Phi'_{ij}$, where $\Phi'_{ij}$ is the deviatoric part of the fabric tensor. $a_c$ is related to the second invariant of $a_{ij}^c$ as $a_c = \sqrt{3/2 a_{ij}^c a_{ij}^c}$. In fact, $a_c$ equals $15/2\Phi_d$.

$$\Phi_{ij} = \int_{\Omega} E(\Omega) n_i n_j d\Omega = \frac{1}{N_c} \sum_{c \in N_c} n_i n_j \qquad \text{(Eq. 4.11 (a))}$$

$$E(\Omega) = \frac{1}{4\pi}[1 + a_{ij}^c n_i n_j] \qquad \text{(Eq. 4.11 (b))}$$

(b) Branch vector anisotropy ($a_b$)

Similar to $a_c$, $a_b$ is related to the second invariant of $a_{ij}^b$ as $a_b = \sqrt{3/2 a_{ij}^b a_{ij}^b}$ with the average branch vector tensor $d_{ij}$ and the density distribution function $\overline{d}(\Omega)$ given in Eq. 4.12 (a) and Eq. 4.12 (b) respectively. Note that $\overline{d}^0 = d_{ii}$ is the average branch vector length calculated considering all the $\Omega$ and in most cases is different from the mean branch vector length averaged over all contacts.

$$d_{ij} = \frac{1}{4\pi} \int_{\Omega} \overline{d}(\Omega) n_i n_j d\Omega = \frac{1}{N_c} \sum_{c \in N_c} \frac{d^c n_i n_j}{1 + a_{kl}^c n_k n_l} \qquad \text{(Eq. 4.12 (a))}$$

$$\overline{d}(\Omega) = \overline{d}^0 [1 + a_{ij}^b n_i n_j] \qquad \text{(Eq. 4.12 (b))}$$

(c) Normal contact force anisotropy ($a_n$)

The average normal contact force tensor may be expressed by Eq. 4.13 (a) with its probability distribution function approximated by Eq. 4.13 (b) and $a_{ij}^n = \frac{15}{2} \frac{F_{ij}^{'n}}{\overline{f}^0}$. Similar to $\overline{d}^0$, $\overline{f}^0 = F_{ii}$ is the average normal contact force calculated considering the entire $\Omega$ and in most cases is different from the mean normal contact force averaged over all contacts. $a_n$ is related to the second invariant of $a_{ij}^n$ as $a_n = \sqrt{3/2 a_{ij}^n a_{ij}^n}$.

$$F^{n}_{ij} = \frac{1}{4\pi}\int_{\Omega} \overline{f}_n(\Omega) n_i n_j d\Omega = \frac{1}{N_c}\sum_{c\in N_c} \frac{f_n n_i n_j}{1 + a^c_{kl} n_k n_l} \qquad \text{(Eq. 4.13 (a))}$$

$$\overline{f}_n(\Omega) = \overline{f}^0 [1 + a^n_{ij} n_i n_j] \qquad \text{(Eq. 4.13 (b))}$$

(d) Tangential contact force anisotropy ($a_t$)

The average tangential contact force tensor may be expressed by Eq. 4.14 (a) with its probability distribution function approximated by Eq. 4.14 (b) and $a^t_{ij} = \frac{15}{3}\frac{F'^t_{ij}}{\overline{f}^0}$. $a^t$ is related to the second invariant of $a^t_{ij}$ as $a_t = \sqrt{3/2 a^t_{ij} a^t_{ij}}$.

$$F^{t}_{ij} = \frac{1}{4\pi}\int_{\Omega} \overline{f}_t(\Omega) t_i n_j d\Omega = \frac{1}{N_c}\sum_{c\in N_c} \frac{f_t t_i n_j}{1 + a^c_{kl} n_k n_l} \qquad \text{(Eq. 4.14(a))}$$

$$\overline{f}_t(\Omega) = \overline{f}^0 [a^t_{ik} n_k - (a^t_{kl} n_k n_l) n_i] \qquad \text{(Eq. 4.14(b))}$$

$a_c$ and $a_b$ comprise the geometrical anisotropy terms while $a_n$ and $a_t$ describe the mechanical anisotropy. These anisotropy quantities have been used by Guo and Zhao (2013) to illustrate the bimodal characteristics of the evolution of contact networks during triaxial shearing.

The macro stress ratio is related to the anisotropy quantities by Eq. 4.15 (Chantawarangul, 1993):

$$\frac{q}{p'} = \frac{2}{5}(a_c + a_n + \frac{3}{2} a_t) \qquad \text{(Eq. 4.15)}$$

Note that the cross products between the anisotropy tensors were ignored when formulating Eq. 4.15. Guo and Zhao (2013) modified Eq. 4.15 by introducing the contribution from the branch vector (i.e., $a_b$) to give:

$$\frac{q}{p'} = \frac{2}{5}(a_c + a_b + a_n + \frac{3}{2} a_t) \qquad \text{(Eq. 4.16)}$$

The effectiveness of the S-F-F relationship to represent the overall strength of granular assemblies has been confirmed by a number of researchers (e.g., Gu et al., 2013; Guo & Zhao, 2013;Ouadfel & Rothenburg, 2001). A good agreement between the stress ratio obtained from the stress components and that calculated by the S-F-F relation is also evident in Figure 4.38. Note that in Figure 4.38, Eq. 4.16 is adopted and the difference between Eq.

4.15 and Eq. 4.16 is small due to the dominance of $a_n$ and $a_c$ over $a_b$ and $a_t$ which will be shown below. Also note that only cases with $\mu$=0.1, 0.25 and 1.0 are presented for clarity; the $\mu$=0.5 and 0.75 cases show a similar trend. The small deviation between the measured stress ratio and the stress ratio from the S-F-F relationship is attributable to the neglect of the cross product between the anisotropy tensors.

The influence of $\mu$ on the variation of each anisotropy measure is illustrated in Figure 4.39. Variations of $a_c$ with axial strain coincide with those of $\Phi_d$, while $a_b$ increases initially with axial strain followed by a decreasing trend and becomes constant at critical state. Both $a_n$ and $a_t$ increase abruptly to a peak value and decrease until the critical state is attained. Variation of $a_b$ is possibly related to the volumetric response (Figure 4.22 (b)) as a looser state indicates a more opened structure and thus a longer branch vector length, while variation of $a_n$ and $a_t$ possibly depends on the evolution of contact forces which is related to the macro stresses (e.g., Figure 4.22 (a)). Generally, both the geometrical anisotropies and the mechanical anisotropies increase with increasing $\mu$. Figure 4.40 considers the contribution of each anisotropy quantity to the global stress ratio. As shown in Figures 4.40 (a) and (b), the influence of $\mu$ on contributions of the geometric anisotropies ($a_c$ and $a_b$) to the overall strength is limited, i.e., contributions of $a_c$ and $a_b$ to the overall strength only increase slightly with increasing $\mu$. The influence of $\mu$ on the contribution of mechanical anisotropies is more notable. The contribution of $a_n$ decreases with $\mu$ while the contribution of $a_t$ increases with $\mu$. This is due to the increase of the tangential force magnitude relative to the normal contact force with increasing $\mu$. Moreover, from Figure 4.39 and Figure 4.40, we can see that for each $\mu$ case, regarding the contribution to the overall strength, $a_c$ and $a_n$ are dominant while $a_t$ and $a_b$ are comparatively tiny. This agrees with the observations of Guo and Zhao (2013).

Figure 4.41 illustrates the contact rose diagrams of strong and weak contacts at the critical state for the subset of simulations with $e_0$ = 0.533, $\sigma'_3$ = 100 kPa and $\mu$ = 1.0, 0.5 and 0.1. In Figure 4.41, the projection of contact orientations onto the vertical plane is considered and $10^o$ angular increments are used. The radial length of each bin indicates the number of contacts oriented within the angles defining the bin, while the colour of each bin is proportional to the sum of normal contact forces for the contacts orientated in that bin. Figure 4.41 shows clearly that the strong contacts have a preferential vertical orientation (i.e., they are preferentially aligned with the major principal stress direction), while the weak contacts are more isotropic, indicating that weak contacts make little contribution to the global deviatoric stress (Radjai et al., 1996). Figure 4.41 also shows that although there are fewer strong contacts than weak contacts, they transmit markedly higher contact forces. As $\mu$

increases, the proportion of horizontally-orientated strong contacts decreases, providing further evidence that as $\mu$ increases fewer strong contacts are mobilised to support the force chains transmitting the deviatoric load. Figure 4.41 also indicates that as the number of contacts decreases with increasing $\mu$, the stress concentration in the vertical direction becomes more notable, suggesting that although the number of strong force chains decreases, the magnitudes of the forces they transmit increase with increasing $\mu$.

## 4.7 Contact force characteristics

The previous Section illustrates the preferential rearrangement of particles upon shearing; it is also of importance to understand how external loading is transmitted within granular assemblies, which is addressed in this Section.

### 4.7.1 Configuration of the contact forces

Figure 4.42 (a) shows the variation of the proportion of weak contacts during shearing. For the representative set of simulations considered, upon shearing the weak contact fraction increases quickly to a peak value and decreases thereafter to a constant value beyond 10% axial strain. Referring to Figure 4.22 (a), the axial strain at which the weak contact fraction attains a maximum is close to but does not coincide with the appearance of the peak strength. The weak contact proportion for the $\mu$ = 0.1 case is lowest while the weak contact proportions are similar for other cases prior to the attainment of a constant value but all the curves merge to a constant value around 60.5% at critical state regardless of $\mu$. The insensitivity of the configuration of contact forces to $\mu$ at the critical state can be further manifested by the probability density function (PDF) of the normal contact force. Figure 4.42 (b) plots the probability density ($P$) as a function of the normalised normal contact force ($f_n/\langle f_n \rangle$) at critical state for the representative set of simulations. The PDF is consistent for all the $\mu$ values considered. A peak $P$ value around 0.7 is reached for all the cases and $P$ follows an exponential decay with $f_n/\langle f_n \rangle$ for $f_n$ that is above the mean value $\langle f_n \rangle$. Figure 4.42 indicates that $\mu$ has little influence on the configuration of contact forces. Though the configuration of contact forces is insensitive to $\mu$, the difference in their spatial distributions for different $\mu$ cases as noted in previous section may affect the constitution of the overall strength by the contact forces which is analysed below.

### 4.7.2 Influence of $\mu$ on the bimodal force transmission character

The bimodal theory (Radjai et al., 1998) proposed that the force network within a granular assembly subjected to shearing can be decomposed into two subnetworks with distinct roles,

i.e., a strong force network comprised of contacts carrying higher-than-mean contact force transfers the whole deviatoric stress and a weak force network composed of contacts carrying lower-than-mean contact force acts as lateral props to prevent the buckling of strong force chains.

The average stress within a granular assembly can be calculated directly from the contact forces (Bagi, 1996).

$$\sigma_{ij} = \frac{1}{V}\sum_1^{N_c} f_i l_j \qquad \text{(Eq. 4.17)}$$

in which $V$ is the volume of domain considered, $f_i$ is the $i$th component of the contact force vector, $l_j$ is the $j$th component of the branch vector, $N_c$ is the number of contacts. The branch vector joins the centroids of two touching particles, e.g., particle $A$ and particle $B$, and gives the relative location of them. The branch vector is given by $\boldsymbol{l} = \boldsymbol{x^A} - \boldsymbol{x^B}$ where $\boldsymbol{x^A}$ and $\boldsymbol{x^B}$ are the coordinates of particle $A$ and particle $B$ respectively. For spherical particles, the branch vector direction coincides with the contact normal, i.e., $\boldsymbol{l} = l\mathbf{n}$, in which $l$ is the branch vector length and $\mathbf{n}$ is the unit vector of the contact normal. Evaluation of the importance of strong and weak contact force networks on the macro strength can be achieved by decomposing the ensemble average stress tensor ($\sigma'_{ij}$) into the contribution from the strong contacts ($\frac{1}{V}\sum_1^{N_c^s} f_i^s l_j^s$) and that from the weak contacts ($\frac{1}{V}\sum_1^{N_c^w} f_i^w l_j^w$), i.e., $\sigma'_{ij} = \frac{1}{V}\sum_1^{N_c^s} f_i^s l_j^s + \frac{1}{V}\sum_1^{N_c^w} f_i^w l_j^w$ , in which $f_i^s$ and $f_i^w$ are the $i$th component of the strong and weak contacts, $l_j^s$ and $l_j^w$ are the $j$th components of the branch vector of the strong and weak contacts, and $N_c^s$ and $N_c^w$ are the numbers of strong and weak contacts respectively. As shown in Figure 4.43 (a), the strong contact contribution to the overall stress ratio ($q/p'$) decreases gradually with increasing axial strain which is possibly due to the decrease of anisotropy as shown in Figure 4.36 (b), while the opposite is true for the weak contact contribution. Both the contributions from strong and weak contacts attain an almost constant value at the critical state. The dominance of strong contacts in deviatoric stress transmission resides in the more anisotropic structure and higher contact force magnitude compared to the weak contact network as shown in Figure 4.41. The decreasing trend of the contribution of strong contacts and the increasing trend of the contributions of weak contacts to the overall strength with $\mu$ is attributable to the decrease of relative anisotropy between the strong and weak contacts with $\mu$ as noted in Figure 4.37(b) and Section 4.6.3. Although the contribution of strong contacts is dominant (>92%), the contribution of weak contacts is not negligible and increases with increasing $\mu$. The noticeable contribution of weak contacts to the stress ratio also suggests that some of the weak contacts also participate in global force transmission rather than solely

acting as lateral props to the strong force chains, indicating that the previous partition criterion based on $f_n/\langle f_n \rangle = 1$ proposed by Radjai et al. (1998) is not robust.

Minh et al. (2014) observed in their 1D compression simulations that the characteristic normalised normal contact force ($f^*$) which marks the transition from negative to positive contribution of the contact forces to the overall deviatoric stress lies between 1.2 to 1.4 rather than unity. Following the approach of Radjai et al. (1998) and Minh et al. (2014), Figure 4.44 presents the cumulative contribution of contact forces to the overall deviatoric stress as a function of $f_n/\langle f_n \rangle$ for the representative set of simulations at the critical state (30% axial strain). An enlarged view for the range $0 < f_n/\langle f_n \rangle < 1$ is superimposed on the figure to gain a closer examination of the transition from negative to positive contributions to the overall strength. As Figure 4.44 shows, $f^*$ at the critical state is smaller than unity for all the $\mu$ values considered and varies with $\mu$ ($f^*$ are 0.71, 0.416, 0.206, 0.169, 0.27 for $\mu$ = 0.1, 0.25, 0.5, 0.75 and 1.0 respectively.). Figure 4.45 (b) illustrates the cumulative contribution curves at three characteristic states for an undrained simulation (Stress-stain curve is given in Figure 4.45 (a)), i.e., the instability state (IS), the phase transformation state (PT) and the critical state (CS). The cumulative contribution curve differs for different loading stages and $f^*$ are 1.32, 0.8, 0.61 for IS, PT and CS respectively, showing a decreasing trend with the increasing axial strain. Hence, the previous partition rule based on $f_n/\langle f_n \rangle = 1$ is scientifically not robust though convenient.

### 4.7.3 Influence of $\mu$ on the contributions of contact forces in the normal and tangential directions

Calculation of the ensemble average stress tensor ($\sigma'_{ij}$) can also be decomposed into a normal contact force term ($\frac{1}{V}\sum_1^{N_c} f_n^i l_j$) and a tangential contact force term ($\frac{1}{V}\sum_1^{N_c} f_t^i l_j$), i.e., $\sigma'_{ij} = \frac{1}{V}\sum_1^{N_c} f_n^i l_j + \frac{1}{V}\sum_1^{N_c} f_t^i l_j$ , in which $\boldsymbol{f_n}$ is the normal contact force, $\boldsymbol{f_t}$ is the tangential contact force and $N_c$ is the total number of contacts (Thornton & Antony, 2000). As shown by Thornton & Antony (2000), the tangential contact force is purely deviatoric and makes no contribution to $p'$ due to the orthogonality between the tangential contact force and the contact normal (i.e., $f_t^i l_i$ =0). Prior studies (e.g., Thornton, 2000) showed that the contribution of tangential contact force to the deviatoric stress is small compared to that of the normal contact force. This may possibly be due to the relatively small magnitude of $\boldsymbol{f_t}$ with respect to $\boldsymbol{f_n}$. Since $\mu$ determines the limiting shear force that can be mobilized at a contact, it is of interest to investigate the influence of $\mu$ on the contribution of tangential contact forces.

Figure 4.46 compares the contribution of the normal and tangential contact forces to the macro stress ratio. The contribution of the normal contact forces to the macro stress ratio increases initially with axial strain and remains at an approximately constant value that depends on $\mu$ at critical state, while the contribution of tangential contact forces to the macro stress ratio decreases initially and becomes approximately constant and depends on $\mu$ at critical state. The contribution of tangential contact forces to the macro stress ratio increases with $\mu$, while the opposite is true for the contribution of normal contact forces. The normal contact force contribution dominates for all the $\mu$ values considered. Even for the $\mu$=1.0 case where the normal force contribution is the smallest, the normal contact force contribution of 85% greatly exceeds the tangential contact force contribution (≈15%). The influence of $\mu$ on the relative values of the two contributions is also nonlinear and becomes less noticeable when $\mu$ exceeds 0.5.

### 4.7.4 Tangential force characteristics

While it has been largely ignored previously, Figure 4.46 shows that the role of tangential forces in force transmission is not negligible and increases when $\mu$ is increased. The extent to which the friction is mobilised in a particulate system can be quantified using the friction mobilisation index $I_{mf} = \frac{|f_t|}{\mu f_n}$ (Azéma & Radjaï, 2012; Majmudar & Behringer, 2005). The variable $I_{mf}$ ranges between 0 and 1 and informs how far the contact is away from the Coulomb criterion. If $f_t$ is at the Coulomb failure limit, $I_{mf}$=1.

Figure 4.47 considers the probability density distribution of $I_{mf}$ for different $\mu$ cases at critical state. To plot the probability density distribution, $I_{mf}$ is considered at intervals of 0.02 between 0.0 and 1.0 for each case. Figure 4.47 (a) considers the whole range of $I_{mf}$, while the data points for $I_{mf}$ = 1.0 are neglected in Figure 4.47 (b) for clarity. For cases with $\mu$ above 0.5, a local maximum and a global maximum are obvious. For the cases with $\mu$=0.1 and $\mu$=0.25, only one maximum point occurs. For cases with $\mu \geq 0.5$, the probability density ($P$) increases initially to a local peak value, then decreases before rapidly increasing to the global maximum at the sliding limit, i.e., $I_{mf}$=1.0, while for the $\mu = 0.1$ case, $I_{mf}$ increases consistently with increasing $\mu$ and increases more rapidly when it is close to the sliding limit. For the case with $\mu$=0.25, $I_{mf}$ increases initially to a plateau and then starts to increase again. $P$ at the global maximum is the highest for $\mu$=0.1 and decreases with increasing $\mu$. The value of $I_{mf}$ which corresponds to the local maximum probability density decreases with increasing $\mu$. Simulations with higher $\mu$ tend to have a higher $P$ at small $I_{mf}$ regime (away from sliding) and a lower $P$ at large $I_{mf}$ regime (approaching sliding) than simulations with lower $\mu$.

Figure 4.48 shows the cumulative contribution of single contact evaluated by $I_{mf}$. As Figure 4.48 shows, the majority of the deviatoric stress is transmitted by contacts with shear force further away from the sliding limit for high $\mu$ cases than for low $\mu$ cases. For example, the value of $I_{mf}$ at which 80% of the deviatoric stress is attained is around 0.3 for the $\mu$=1.0 case while this value is close to unity for the $\mu$=0.1 case. Moreover, the deviatoric stress is less likely to be transmitted by contacts with shear forces close to the sliding limit in high $\mu$ cases than in low $\mu$ cases. Figure 4.49 shows the spatial distribution of $I_{mf}$ for the $\mu$=0.1, 0.25 and 1.0 cases. The colour in each bin is proportional to the average $I_{mf}$ within that bin. As Figure 4.49 indicates, the friction is less mobilised in high $\mu$ cases than in low $\mu$ cases. Contacts aligning horizontally tend to be closer to the sliding limit than contacts aligning vertically. The shear forces of weak contacts are closer to the sliding limit than that of strong contacts; however, the difference between the strong and weak contacts becomes less noticeable as $\mu$ decreases.

$I_{mf}$ provides general information on the shear force values relative to the sliding limit. It is also useful to investigate the absolute shear force magnitude relative to the normal contact force. Figure 4.50 considers the probability density distribution of the shear force ratio ($|f_t|/f_n$). Similar to $I_{mf}$, the probability density distribution of the shear force ratio for simulations with $\mu \geq 0.5$ are also marked by a local maximum and a global maximum, while the probability density distributions for simulations with $\mu < 0.5$ only has one global maximum at the sliding limit. More interestingly, the peak $P$ corresponds to a $|f_t|/f_n$ of about 0.2 for all $\mu \geq 0.5$ cases. A $|f_t|/f_n$ of 0.2 also marks the point at which $P$ starts to increase more rapidly to the global maximum for $\mu$=0.25. As shown in Figures 4.51 and 4.52 this is also true for the RW samples. Further investigation shows that provided the same $\mu$, the probability density distributions of $|f_t|/f_n$ and $I_{mf}$ are unique and do not depend on the packing density and loading conditions (Figure 4.53), the boundary conditions (Figure 4.54) and the contact models (Figure 4.55). Note that in Figure 4.54, for conciseness only three representative $\mu$ values are presented, i.e., $\mu$=0.1, 0.25 and 1.0, and for clarity the tail is ignored for the $\mu$=0.1 and 0.25 cases. No prior publication noting this phenomenon could be found and the data using Dunkirk sand grading also supported such observations (personal communication with Dr Hanley).

Figure 4.56 and Figure 4.57 show the rose diagrams of contacts which are divided into two sub-networks based on the shear force ratio at the critical state for the $\mu$=0.25 case and the $\mu$=1.0 case respectively. In both cases, the contact force data are decomposed to consider the cases where $|f_t|/f_n \leq 0.2$ and $|f_t|/f_n > 0.2$. The colour of each bin is proportional to the ratio of

the mean normal contact force in that bin to the overall mean normal contact force. As Figure 4.56 and Figure 4.57 show, the sub-network composed of contacts with $|f_t|/f_n \leq 0.2$ is more anisotropic than the overall network and the sub-network that composed of contacts with $|f_t|/f_n > 0.2$ is more isotropic than the overall network. This can be further confirmed considering the deviatoric fabric separately for each sub-network as shown in Figure 4.58. Moreover, Figure 4.56 and Figure 4.57 also show that while prior partition of force network only considered the normal contact force, it may be possible to further dividing the strong and weak contact networks into a more isotropic sub-network and a more anisotropic sub-network based on the shear force characteristics. This again indicates that dividing the contact force network into two sub-networks according to the mean normal contact force is not robust.

## 4.8 Sliding and rolling

Contact sliding represents a yielding in the direction orthogonal to the contact normal and is a significant source of energy dissipation. Rolling denotes a relative angular movement between two particles in contact and has been considered to account for the formation of shear bands (Iwashita & Oda, 1998; Oda & Kazama, 1998; Proubet & Bardet, 1991). Rolling is related to the tangential force. Thus it is intuitive that sliding and rolling are not isolated. The interplay between them is addressed in this section.

### 4.8.1 Analysis of sliding fraction

As presented in Figure 4.59 (a), for each $\mu$ considered, the sliding fraction increases abruptly from zero to a peak value and decreases slightly until a constant state is attained. The initial rapid increase in sliding fraction indicates a dramatic rearrangement of particles and the associated sharp shift from isotropic to anisotropic fabric due to the deviatoric loading as illustrated in Figure 4.36. A higher $\mu$ value yields a smaller proportion of sliding contacts. Figure 4.59 (b) shows the relationship between the sliding fraction at the critical state and $\mu$ for the representative set of simulations considered in previous discussions. In line with Thornton (2000) the sliding fraction decreases with increasing $\mu$. Note that the relationship between $\mu$ and sliding fraction is nonlinear; the sliding fraction drops rapidly from around 37% to only 7% when $\mu$ increases from 0.1 to 0.5 but then reduces only slightly to about 3% when $\mu$ is further increased to 1. This indicates that $\mu$ alone does not govern the sliding behaviour. The importance of rolling to friction mobilisation will be addressed in Section 4.8.3. A cumulative distribution plot of sliding contacts at the critical state as a function of $f_n/\langle f_n \rangle$ is given in Figure 4.59 (c). It also shows that the proportion of sliding strong contacts (i.e.,

contacts with $f_n/\langle f_n \rangle$ larger than 1) decreases with increasing $\mu$, suggesting that a strong contact force chain is more stable when $\mu$ is higher. Radjai et al. (1998) proposed that sliding takes place only at contacts carrying below-mean contact force; however, Figure 4.59 (c) reveals that while this is true for simulations with $\mu > 0.5$, when $\mu$ is smaller, a considerable number of strong contacts also slide.

### 4.8.2 Influence of $\mu$ on the rotational behaviour

Figure 4.60 (a) considers the variation in the mean resultant particle rotational velocity ($\omega_r = \sqrt{\omega_x^2 + \omega_y^2 + \omega_z^2}$) at $\varepsilon_a$ = 50 % with $\mu$ (for the case of $e_0$ = 0.533, $\sigma'_3$ = 100 kPa) while Figure 4.60 (b) considers the cumulative distribution of the mean particle rotational velocities at the same state for the same subset of the data. There is a marked difference in the rotational velocities when $\mu \geq 0.5$ compared with the lower $\mu$ values. For the cases with $\mu \geq 0.5$, the rotational velocities are significantly higher than the cases with $\mu < 0.5$ indicating that rolling type behaviour is much more likely at these high $\mu$ values. The increasing tangential force and the decreasing coordination number as $\mu$ increases may account for the more significant rotational behaviour in higher $\mu$ cases shown in Figure 4.60.

### 4.8.3 Interplay between sliding and rolling

To understand the interplay between rolling and sliding, a simple model considered by Ke & Bray (1995) is revisited in this study, i.e., a ball, subject to gravitational loading, moving along on plane inclined at an angle $\beta$ (Figure 4.61 (a)). Following the basic algorithm of DEM, the shear force increment ($\Delta \boldsymbol{f_t}$) corresponding to an incremental displacement in the tangential direction ($\Delta \boldsymbol{s}$) can be expressed by:

$$\Delta \boldsymbol{f_t} = -k_s \Delta \boldsymbol{s} = -k_s(\boldsymbol{V^t} - \boldsymbol{\omega} \times (\boldsymbol{x} - \boldsymbol{x^c}))\Delta t \qquad \text{(Eq. 4.18)}$$

in which $k_s$ is the tangential contact stiffness, $\boldsymbol{V^t}$ is the translational velocity vector, $\boldsymbol{\omega}$ is the angular velocity vector and $\boldsymbol{x}$ and $\boldsymbol{x^c}$ are the coordinates of the particle and the contact point respectively. The kinematics of the ball in Figure 4.61 (a) are:

$$\begin{cases} ma = mg \cdot sin\beta - f_t \\ I\ddot{\theta} = f_t R \\ f_n = mg \cdot cos\beta \end{cases} \qquad \text{(Eq. 4.19)}$$

where $a$ is the acceleration of the ball along the inclined plane, $I$ (=2/5$mR^2$) is the moment of inertia, $R$ is the radius of the ball and $\ddot{\theta}$ is the angular acceleration. A constant $\boldsymbol{f_t}$ indicates $\Delta \boldsymbol{f_t} = 0$, which leads to $a = \ddot{\theta}(R - U_n) \approx \ddot{\theta}R$, where $U_n$ is the contact overlap. This leads

to a critical tangential force $f_t^L = \frac{2}{7}mgsin\beta$ at which the particle moves along the inclined plane with a constant tangential force. $f_t^L$ corresponds to a transition friction coefficient:

$$\mu_{transition} = f_t^L / f_n = \frac{2}{7} \cdot tan\beta \quad \text{(Eq. 4.20)}$$

When $\mu$ is below this value, the frictional limit ($\mu f_n$) will be fully mobilised in the tangential direction, i.e., sliding takes place, otherwise, $f_t^L$ is the maximum shear force that can be attained, i.e., the contact is a rolling contact. Two occasions can thereby be identified for the kinematics of the ball:

(1) Sliding ($\mu \leq \mu_{transition}$)

$$\begin{cases} a = g(sin\beta - \mu gcos\beta) \\ \ddot{\theta} = \frac{5\mu gcos\beta}{2R} \end{cases} \quad \text{(Eq. 4.21)}$$

(2) Rolling ($\mu > \mu_{transition}$)

$$\begin{cases} a = \frac{5}{7}gsin\beta \\ \ddot{\theta} = \frac{5gsin\beta}{7R} \end{cases} \quad \text{(Eq. 4.22)}$$

To verify Eq. 4.21 and Eq. 4.22, the simple case in Figure 4.61 (a) was considered following the approach of Ke & Bray (1995). When resting the ball on the inclined plane under gravity, a vertical rigid wall was set in front of the ball to prevent it from moving downwards. A damping ratio of 0.2 was adopted at this stage to facilitate the resting of the ball. After the ball has become stationary, the vertical wall was removed, the damping ratio was reduced to zero and the ball was allowed to move along the inclined plane. Its angular velocity around the out-of-plane axis was recorded. The same set of input parameters used by Ke & Bray was adopted (i.e., $R$ = 1m; particle density=1000$kg/m^3$; $k_n$=$10^{10}$N/m; $k_s$=0.1$k_n$; $\Delta t$=0.01s; $\beta$=45°). The theoretical accumulated rotation can be obtained by integrating Eq. 4.21 and Eq. 4.22 over the period considered. Note that a large $\Delta t$ was used to ensure that either a sliding state (Eq. 4.21) or a rolling state (Eq. 4.22) can be reached at the first timestep of integration when the ball starts to move. Figure 4.61 (b) compares the accumulated rotations after 0.2 s obtained from DEM simulations using PFC3D and those predicted by integrations using Eq. 4.21 and Eq. 4.22. It can be seen that these two agree with each other.

Figure 4.62 illustrates the variation of $\mu_{transition}$ with $\beta$ according to Eq. 4.20. For a given $\beta$, if $\mu$ is smaller than $\mu_{transition}$, sliding will occur; otherwise the particle will roll down the plane with a shear force that is below the sliding limit. Thus Figure 4.62 indicates that simulations

with higher $\mu$ are more likely to be in the rolling zone than in the sliding zone, i.e., the sliding limit is less likely to be attained for higher $\mu$ cases than for lower $\mu$ cases. Figures 4.37 and 4.41 confirm that at larger $\mu$ values there is indeed a strong preferential vertical contact orientation that is parallel to the major principal stress direction. Taking the inclined plane to be analogous to a particle-particle contact, small $\beta$ values represent the particles in a strong force chain where the contact normals are almost vertical and in these cases rolling will initiate at small $\mu$ values. Thus the simple analysis presented in Figure 4.62 suggests that rolling at the contacts in the strong force chains is highly likely in the simulations with higher $\mu$ values and this is confirmed by the higher rotational velocities observed (Figure 4.60). However, when $\mu$ is low, e.g., $\mu$ = 0.1, quite a number of contacts tend to align horizontally, i.e., orthogonal to the major principal stress direction. These horizontally-oriented contacts correspond to higher $\beta$ values, where rolling will only occur at a high $\mu$ value, and so sliding will dominate. A clear distinction between rolling-dominated and sliding-dominated behaviour at the contacts when rolling resistance is introduced was reported by Estrada et al. (2008). Furthermore, Eq. 4.18 also indicates that when rotation is inhibited, the shear displacement will eventually reach the sliding limit for a given contact. This may account for the more sensitive response of the strength to $\mu$ when particles are not allowed to rotate than that when particles can rotate freely as observed by Morgan (1999) and Suiker & Fleck (2004).

## 4.9 A simple conceptual model of strong force chain buckling

As reviewed in Section 4.2, it is evident that force transmission within a granular assembly is through some highly-loaded columnar structures composed of particles aligning parallel to the major principal stress direction. Buckling of these columnar structures has been related to the global stress-strain response and localisation phenomena, i.e., shear band formation (Mahmood & Iwashita, 2011; Rechenmacher, 2006). Theoretically, buckling is caused by a bifurcation in the solution to the equations of static equilibrium (Wikipedia). O'Sullivan et al. (2013) took the first non-trivial bifurcation point in the solution to the equations of equilibrium as the occurrence of buckling.

An analogue unconfined force chain can be created using a particle column comprised of several mono-sized particles. In a real granular material, force chains comprising perfectly vertical columns are never seen and so perturbations were added to create a more realistic analogue model. Two types of perturbation were considered: in the first case, the force chain was inclined (Figure 4.63 (a)) and in the second case, a small deflection was imposed in the middle of a straight column (Figure 4.63 (b)). In both cases the bottom particle is fixed and

loading is applied by moving the top ball at a constant downward vertical velocity of 0.0001 m/s. During the simulation, the contact force between the bottom ball and its neighbouring ball is recorded and taken as the axial load. A typical evolution of the bottom contact force with timestep is illustrated in Figure 4.64. In line with Hunt et al. (2010) and O'Sullivan et al. (2013), these force chains were considered to fail in buckling and the first peak ($P_{crit}$) in the axial load versus displacement curve is taken as the critical buckling force. Referring to Figures 4.63 (a) and 4.63 (b), for both scenarios $P_{crit}$ is not linearly related to $\mu$. Following an initial increase with increasing $\mu$, $P_{crit}$ becomes constant when $\mu$ exceeds a value which depends on the inclination of the particle column. The smaller the perturbation ($\beta$) is, the less sensitive $P_{crit}$ is to $\mu$ and $P_{crit}$ decreases with increasing $\beta$. These simple analyses provide an explanation for the non-linear relationship between $\phi'_{cv}$ and $\phi'_{p}$ presented in Figure 4.27 (b). Initial increases in $\mu$ lead to an increase in the critical buckling load for a given forces chain and thus $\phi'_{cv}$ increases. Beyond a limiting $\mu$ value, no further increase in the critical buckling load is achieved and so $\phi'_{cv}$ does not increase. Note also that at high $\mu$ values, the reduction in support from the lateral contacts means that this relationship between $\mu$ and the critical buckling load becomes more important.

## 4.10 Summary

In this Chapter, the effect of inter-particle friction on the stress-strain behaviour of granular materials is investigated by discussing the results of DEM triaxial test simulations using five different $\mu$ values. In particular, the effect of inter-particle friction on the critical state characteristics was discussed. The variation of the particle-scale measures with $\mu$ and its correlations with macro-scale stress-strain response has been explored. The failure mechanism of granular materials subject to shearing was discussed considering the inter-relationship between sliding and rolling behaviour and a buckling-type conceptual model.

When the macro-scale data are considered, it is clear that, despite the inherent simplifications of the DEM model, for all the $\mu$ values considered, a locus of critical points emerges that closely resembles the classical response one would expect to see in sand. The parametric study indicates that the inter-particle friction coefficient, $\mu$, influences the critical-state parameters, $M$, and the position of the CSL in $e$-log ($p'$) space, but the sensitivity of the critical-state response to $\mu$ decreases with increasing $\mu$. In particular, increasing $\mu$ beyond 0.5 seems to have little influence on the system response.

A very important finding was that, for values of $\mu \geq 0.5$, the critical-state void ratio initially increases with increasing $p'$ at low $p'$ regime. This is counter-intuitive and not what one

would expect for a real sand. The extent of this deviation from a critical-state-type response becomes more evident with increasing $\mu$. The stress level below which this odd response occurs increases with increasing $\mu$ and increasing contact stiffnesses. This observation is in conflict with experimental observations and was made using two different DEM codes, with two different contact models, two different boundary conditions and two different particle size distributions. Extensive analysis of the particle-scale data, supplemented by analysis of simple analogue models, has revealed that at high values of $\mu$ (i.e., $\geq 0.5$) the strong force chains that are orientated in the direction of the major principal stress become more self-stable and the lateral force network that is necessary for stability when $\mu$ is low may not form. At these high $\mu$ values there is more rolling than sliding at the contact points, which likely further enhances their stability. The particle-scale data revealed that the increase in strong force chain stability attained with increasing $\mu$ corresponded to a decrease in the number of force transmitting particles and an increase in the number of rattlers (particles with fewer than two contacts that do not transmit load) especially at low stress levels. This possibly accounts for the odd trend of CSL at low stress regime.

DEM simulations using spheres tend to yield lower angles of shearing resistance ($\phi'_{cv}$ values) when realistic friction values are used because of the omission of interlocking between irregular real sand grains. It has been highlighted via the literature review summary in Table 4.1 that there is a strong likelihood that DEM analysts will adopt $\mu = 0.5$. The data presented here indicate that for the normal stiffness parameters used in the literature, the micro-structure and particle-scale kinematics induced through use of $\mu \geq 0.5$ results in a volumetric response that differs both qualitatively and quantitatively from that of a real sand at low stresses. An additional limitation on the use of $\mu \geq 0.5$ is the unrealistically stiff response observed in the initial section of the stress-strain curve. We therefore conclude that artificially increasing $\mu$ is not a good way to compensate for the ideal geometry of DEM spheres. In fact, rather than adding to rotational resistance, this approach will induce more rolling and such rolling would be inhibited by a non-spherical geometry.

Particle-scale measures like $Z$ and anisotropy parameters vary nonlinearly with $\mu$. $\mu$ has little influence on the contact force configuration as manifested by the weak contact proportion and the probability density distribution of normalised normal contact force. However, $\mu$ has a remarkable influence on the contributions of the contact force partitions to the overall strength due to the dependency of structural anisotropies on $\mu$. The contribution of weak contacts to the overall strength increases with increasing $\mu$, while the opposite is true for that of strong contacts due to the decreasing relative anisotropy between strong and weak

contacts; Increasing $\mu$ also enhances the contribution of tangential contact forces to the overall strength by increasing the sliding limit. The S-S-F relationship shows that while the contribution of the geometrical anisotropy to the overall strength is not very sensitive to $\mu$, the contribution of the mechanical anisotropy is affected by $\mu$. The contribution of tangential force anisotropy increases while the contribution of normal force anisotropy decreases with increasing $\mu$.

The characteristic normalised normal contact force ($f^*$) which marks the transition from negative contribution to positive contribution of contact forces to the overall deviatoric stress is not a constant but depends on $\mu$ and varies during shearing. This reveals that, though practically convenient, the previously widely-used partition criterion for the contact force network based on the mean normal contact force as proposed by Radjai et al. (1998) is scientifically not rigorous.

A very interesting finding arises when considering the probability density distribution of the ratio of the shear force to the normal force. For $\mu \geq 0.25$, the first local maximum of the probability density distribution of the shear force ratio ($|f_t|/f_n$) always occurs at $|f_t|/f_n = 0.2$ regardless of the packing density, loading conditions, boundary conditions and contact models. The strong and weak contact force networks can be further divided into a more-anisotropic-than-overall subnetwork ($|f_t|/f_n \leq 0.2$) and a more-isotropic-than-overall subnetwork ($|f_t|/f_n > 0.2$). This finding may be useful to enhance understanding of the force transmission mechanism within a granular assembly.

Some analytical solutions relating the overall strength to $\mu$ were revisited. These analysts assumed contact sliding to be the basic failure mechanism. However, as shown in Figure 4.27(b), in the low $\mu$ region, where contact sliding is indeed likely, they underestimated the shearing resistance by ignoring the contribution from the lateral contacts supporting the strong force chains, while they overestimate the shearing resistance for high $\mu$ values because these expressions do not consider the transition from sliding to rolling at contacts. Where rotation is inhibited, the relationship between $\phi'_p$ and $\phi'_{cv}$ differs from the case where the particles can rotate, further confirming the significance of the interplay between rolling and sliding at the contacts. A further explanation of the non-linear relationship between $\mu$ and $\phi'_{cv}$ was found by subjecting isolated force chains to a buckling-type analysis. These analyses showed that the critical buckling load has a nonlinear relationship with $\mu$, and there is a limiting $\mu$ value beyond which increases in $\mu$ do not increase buckling resistance, explaining why $\phi'_{cv}$ does not increase with $\mu$ at higher $\mu$ values.

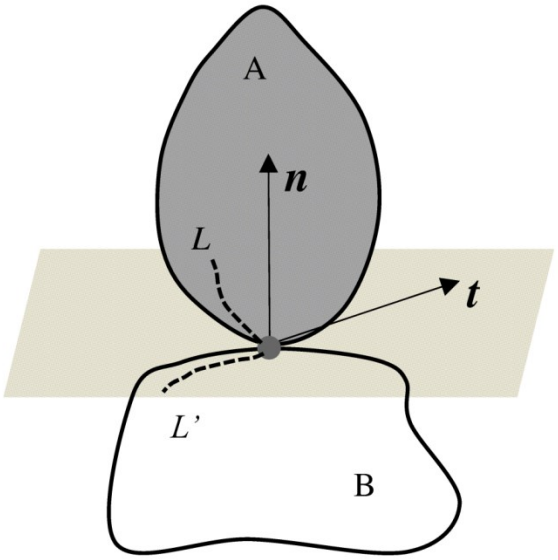



Figure 4.1 Geometry of two particles (A and B) in contact: **n** is the contact normal; **t** represents a direction on the contact plane; *L* and *L'* are the traces of contact points when A and B move against each other (After Duran, 2000)

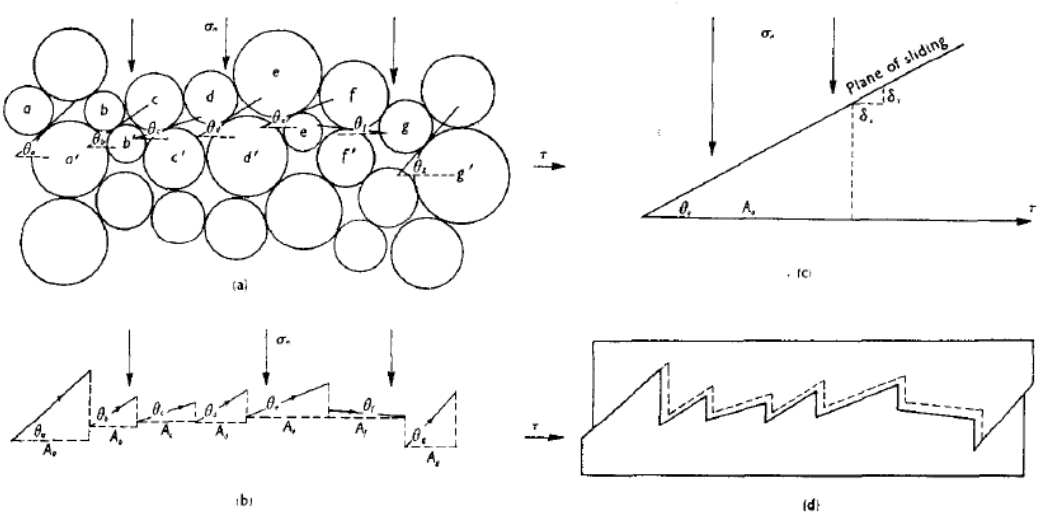
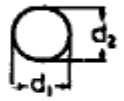



Figure 4.2 The saw-blade model of dilatancy (Newland & Allely, 1957)

| CROSS SECTION | AXIAL RATIO $d_1/d_2$ | DIAMETERS $d_1/d_2$ (mm) | |
|---|---|---|---|
| OVAL I | 1.1 | LARGE : 14.8 / 13.4<br>MEDIUM : 9.9 / 8.9<br>SMALL : 6.3 / 5.7 |  |
| OVAL II | 1.4 | LARGE : 16.0 / 11.3<br>MEDIUM : 10.7 / 7.4<br>SMALL : 7.1 / 4.9 |  |

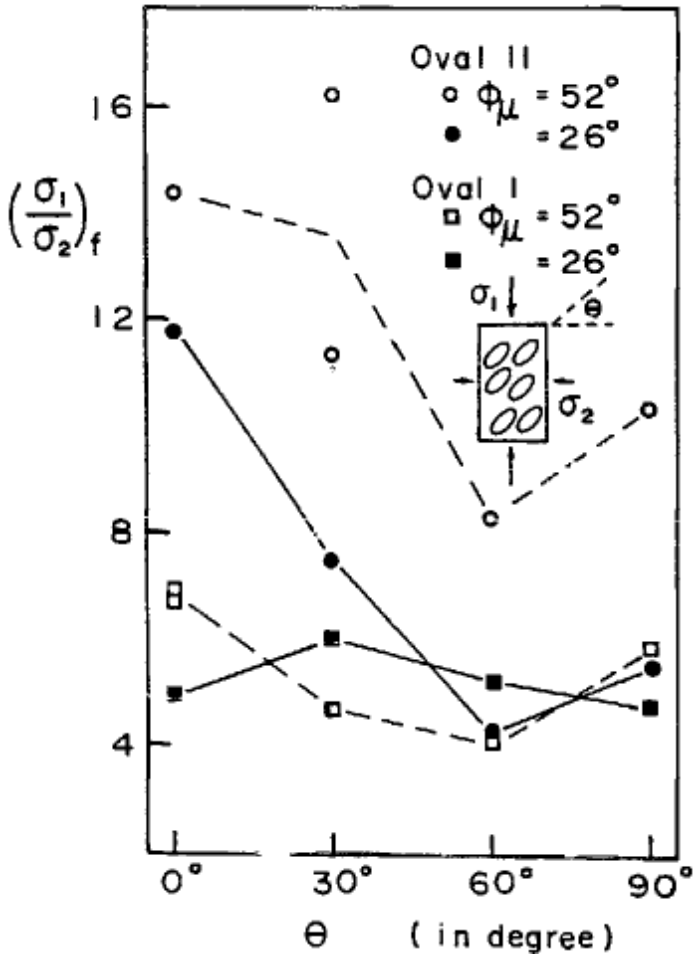



Figure 4.3 Variation of stress ratios with the tilt angle (Oda et al., 1982)

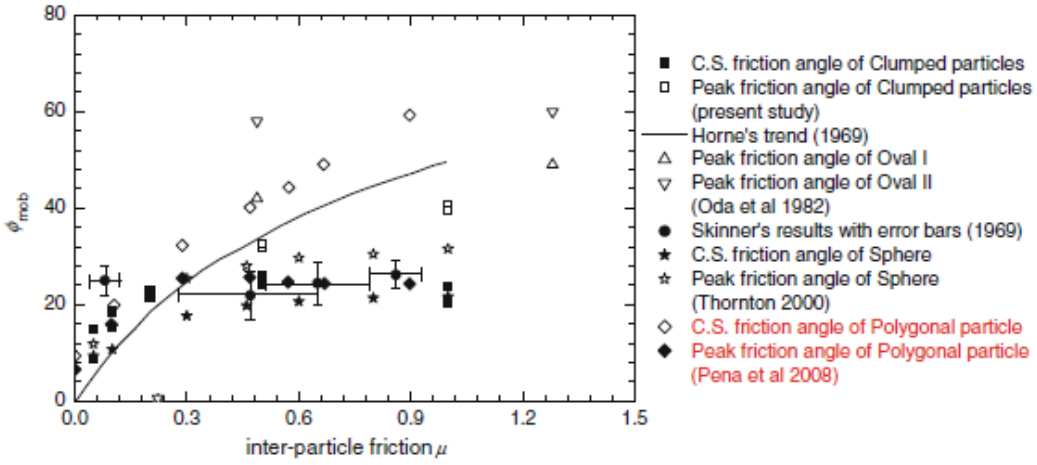
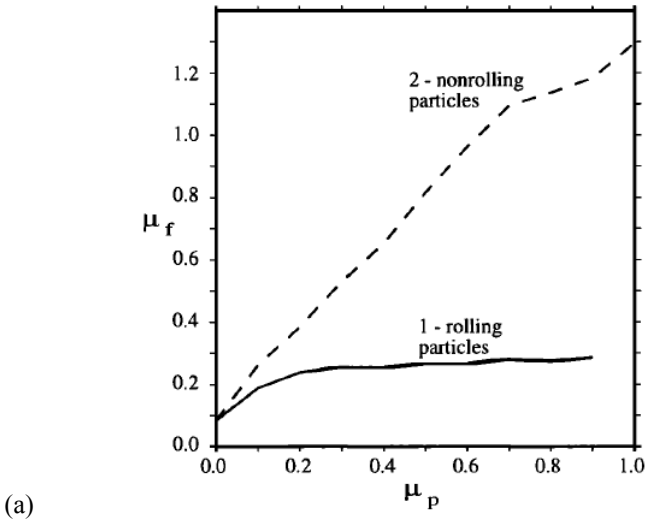
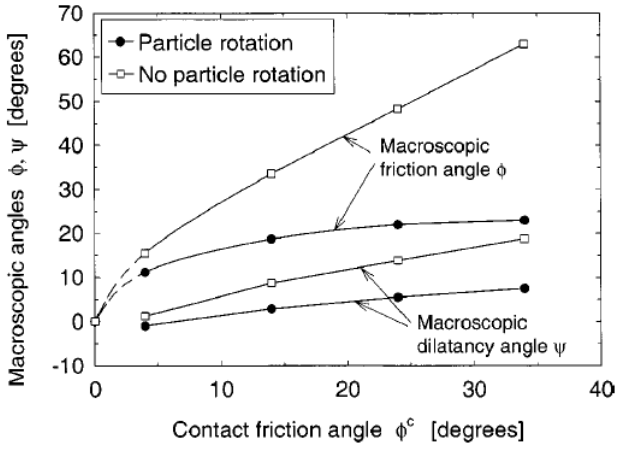



Figure 4.4 Observed effect of interparticle friction on the strength of granular materials when particles are free to rotate (Yang et al., 2012)




(a)




(b)

Figure 4.5 Observed effect of interparticle friction on the strength of granular materials when particle rotation is not allowed: (a) 2D results ($\mu_f$: global friction at failure; $\mu_p$: inter-particle friction) (Morgan, 1999); (b) 3D results (Suiker & Fleck, 2004)

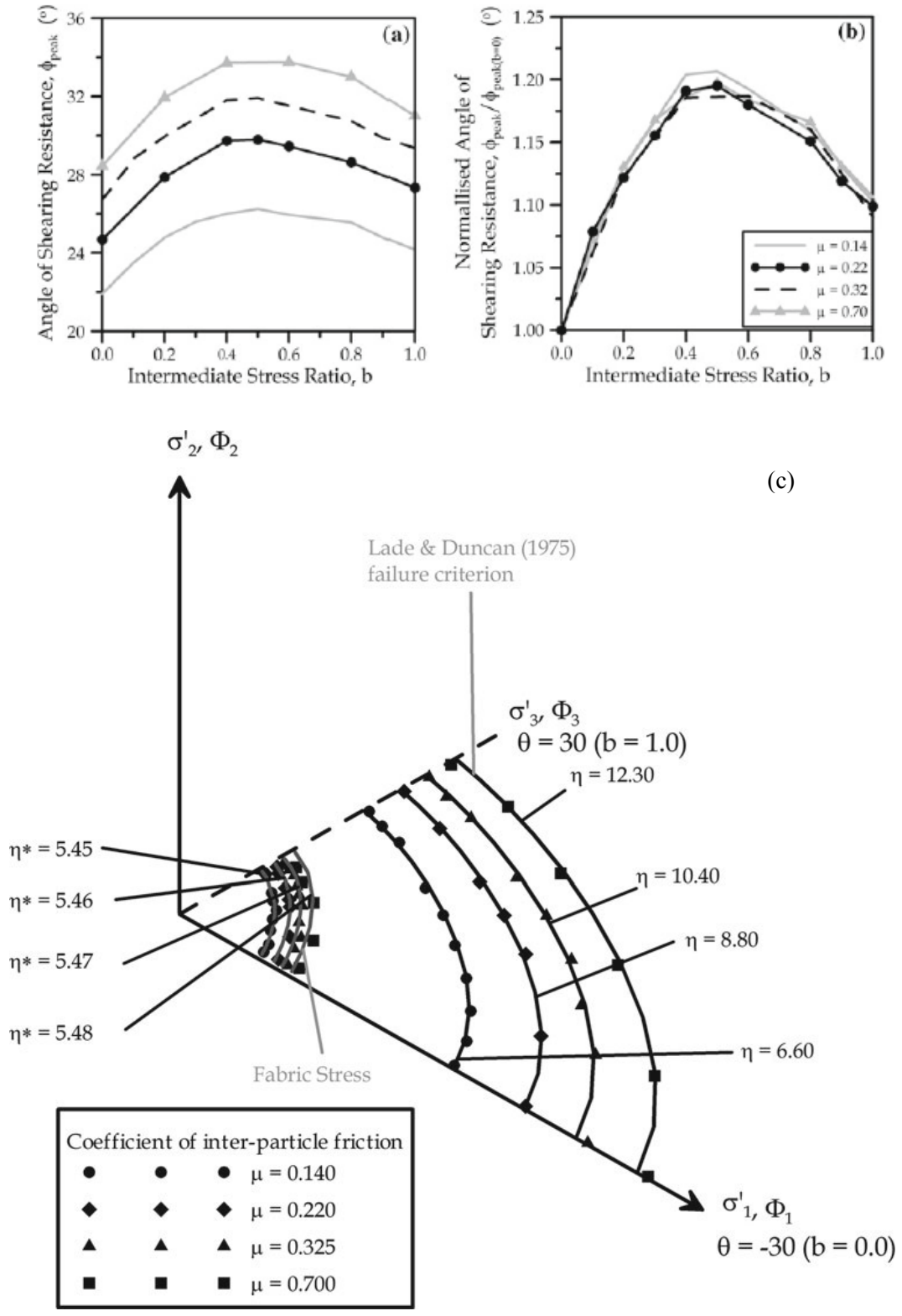



Figure 4.6 Influence of $\mu$ on the peak strength of granular materials under true triaxial conditions: (a) Peak angle of shearing resistance; (b) Normalised peak angle of shearing resistance (c) Influence of μ on the peak stress and fabric states for true triaxial compression in the generalised stress plane (Barreto & O'Sullivan, 2012)

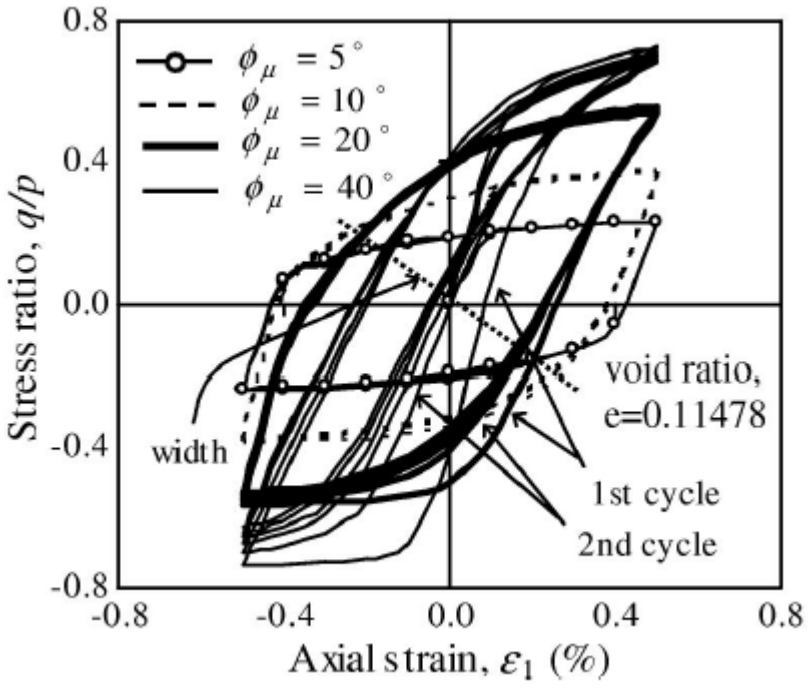



Figure 4.7 Influence of μ on the cyclic stress-strain behaviour (Sazzad & Suzuki, 2011)

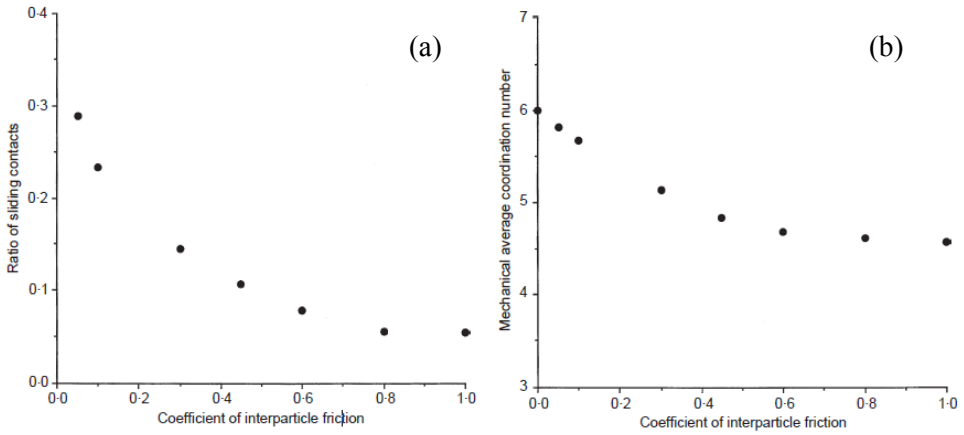



Figure 4.8 Influence of μ on the micro-scale characteristics: (a) Ratio of sliding contacts; (b) Mechanical coordination number (Thornton, 2000)

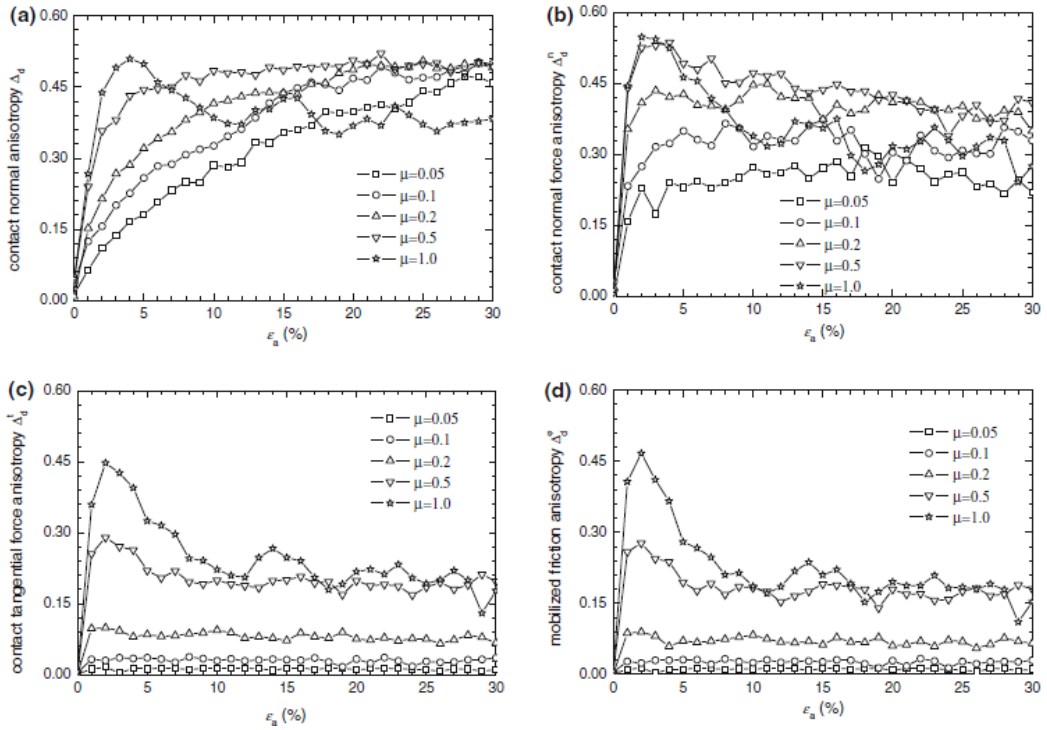



Figure 4.9 Evolution of contact parameters' anisotropy with various inter-particle frictions for drained tests: (a) Contact normal anisotropy; (b) Contact normal force anisotropy; (c) Contact tangential force anisotropy; (d) Mobilised friction anisotropy (Yang et al., 2012)

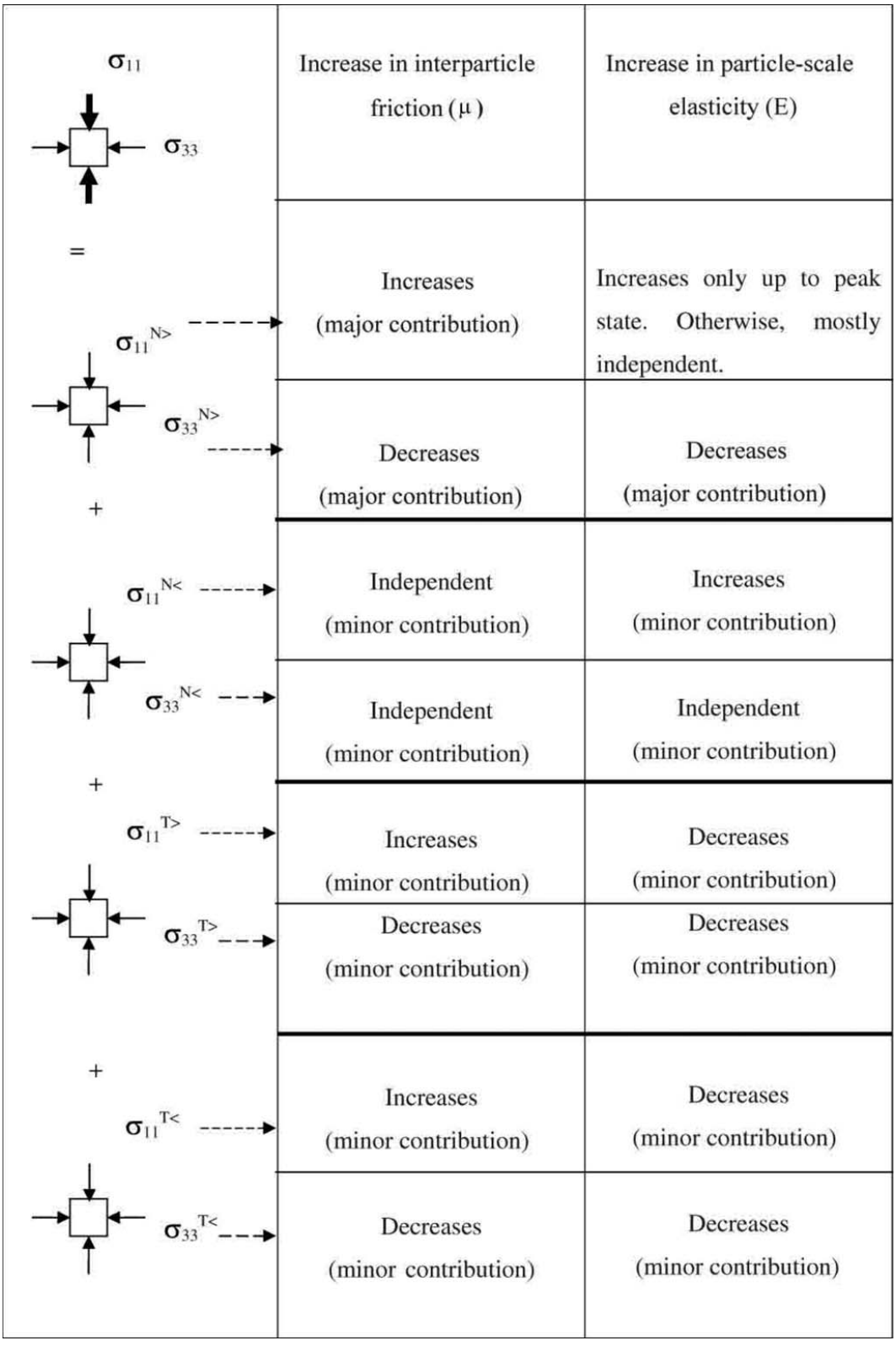
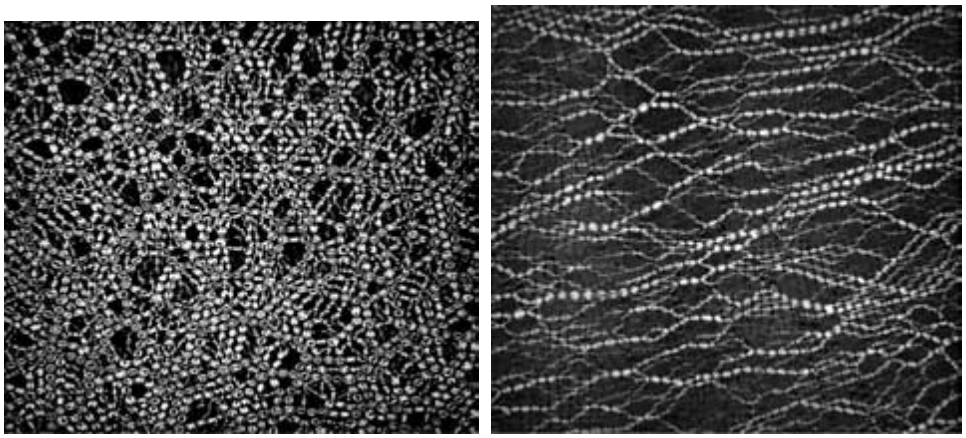



Figure 4.10 Influence of μ on the contribution of contact force components to macro stress components (Antony & Kruyt, 2009)



(a) (b)

Figure 4.11 Force transmission within a photoelastic assembly : (a) isotropic state; (b) during pure shear (Majmudar & Behringer, 2005)

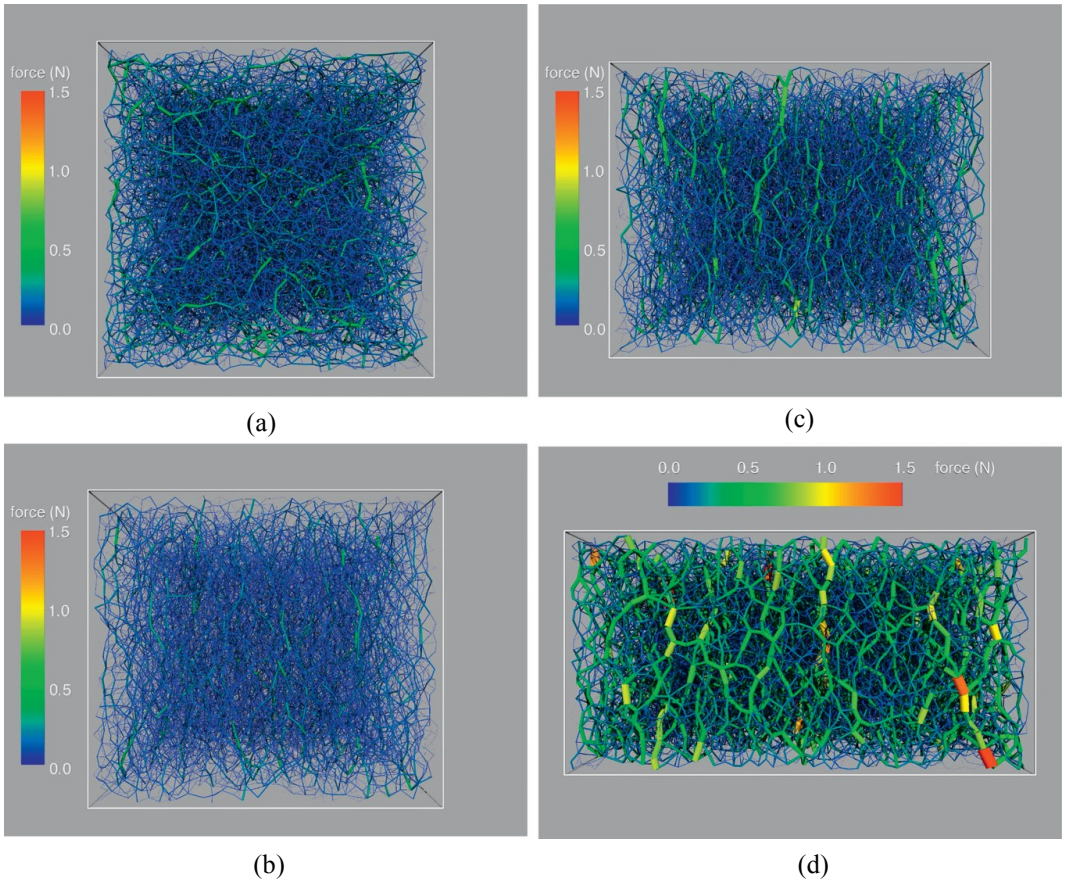
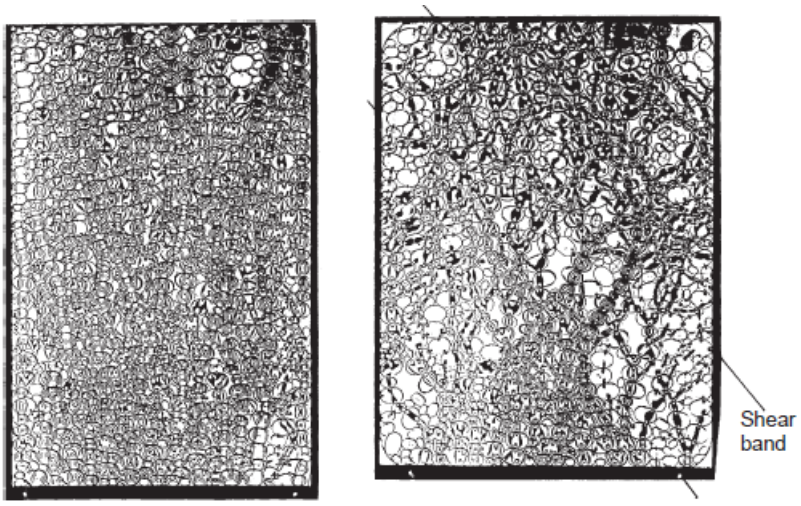
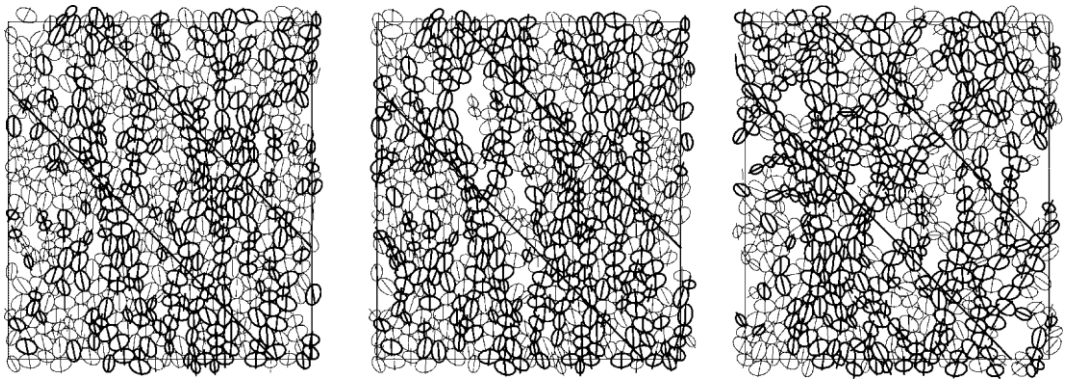



Figure 4.12 Evolution of contact force network within a granular assembly subjected to constant-volume triaxial shearing: (a) Initial state; (b) Phase transformation state (c) 16.75% axial strain; (d) Critical state. (Guo & Zhao, 2013)




(a)



(b)

Figure 4.13 Strong force chain buckling and shear band formations: (a) Experimental observation (Oda & Kazama, 1998) ; (b) DEM observation ( Mahmood & Iwashita, 2011)

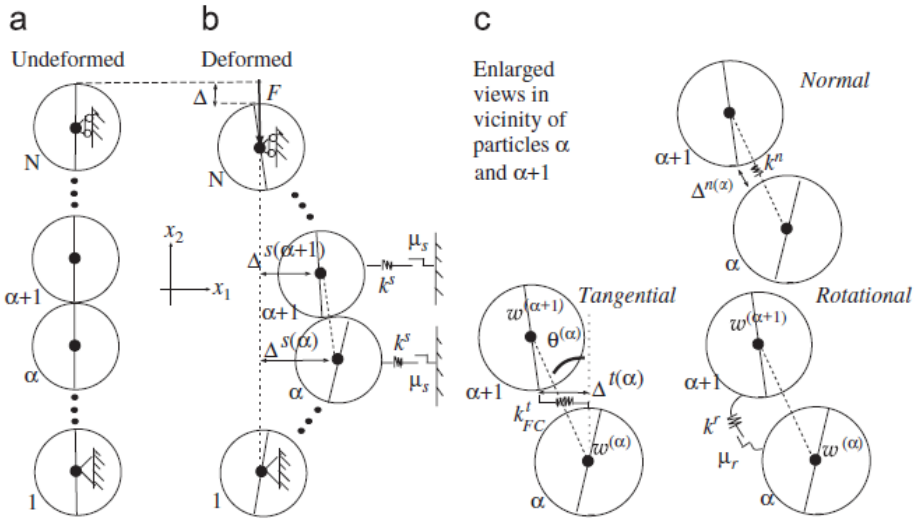
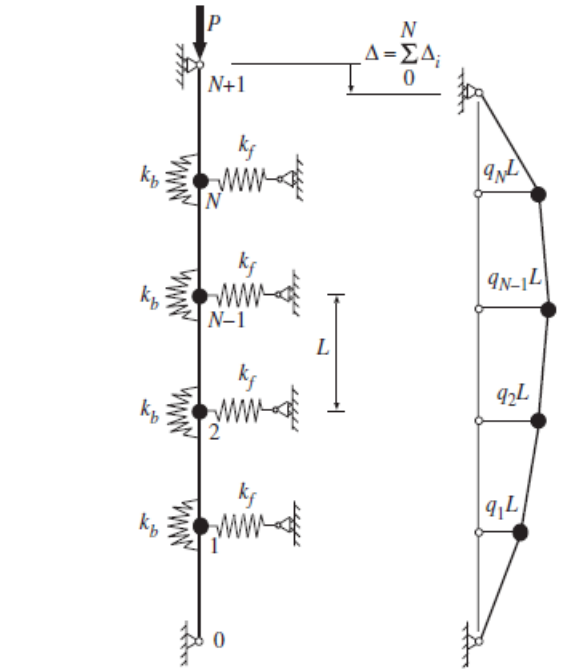
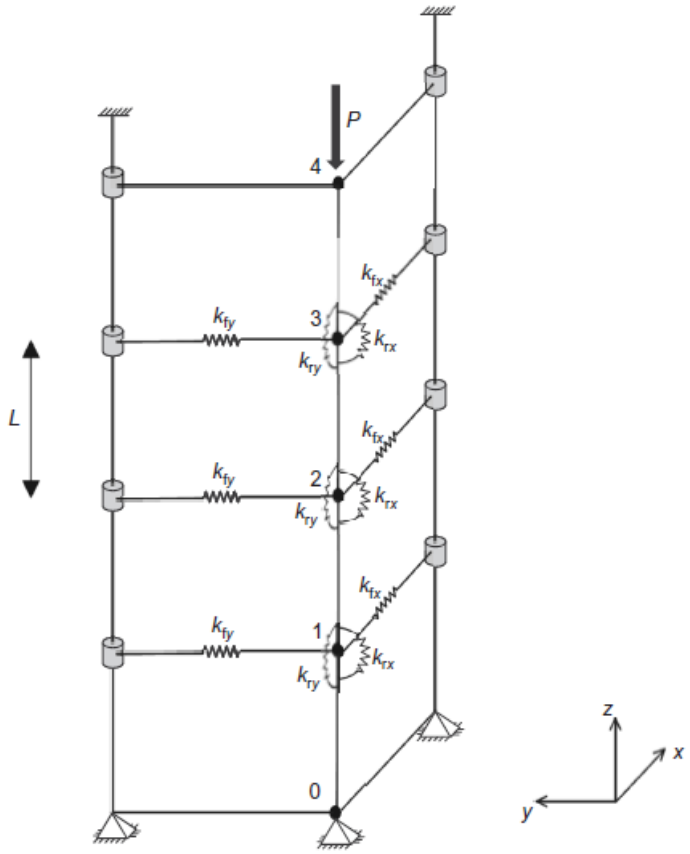



Figure 4.14 Boundary conditions, degrees of freedom, and contact models for an N-particle force chain:(a) prior to buckling; (b) after buckling;(c) enlarged views of (b). (Tordesillas & Muthuswamy, 2009)




(a)




(b)

Figure 4.15 Spring and link models analogous to strong force chain buckling: (a) 2D (Hunt et al., 2010) (b) 3D (O'Sullivan et al., 2013)

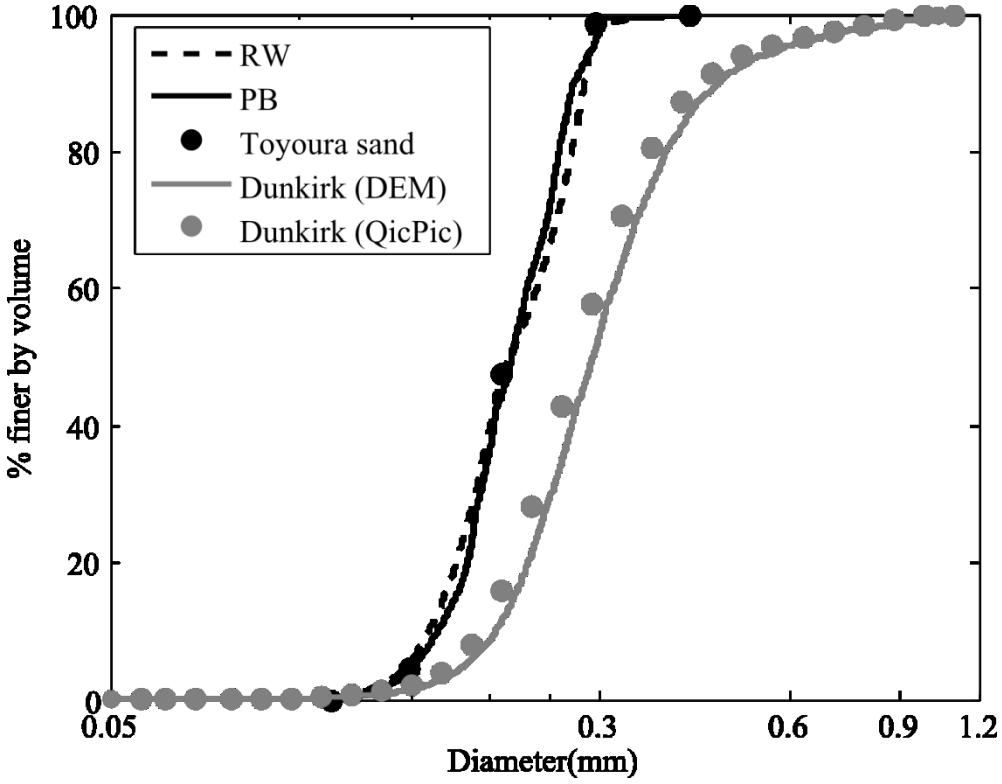



Figure 4.16 Comparing the numerical grading curves and the experimental grading curves (RW: rigid-wall samples using the Toyoura sand grading; PB: periodically-bounded samples using the Toyoura sand grading)

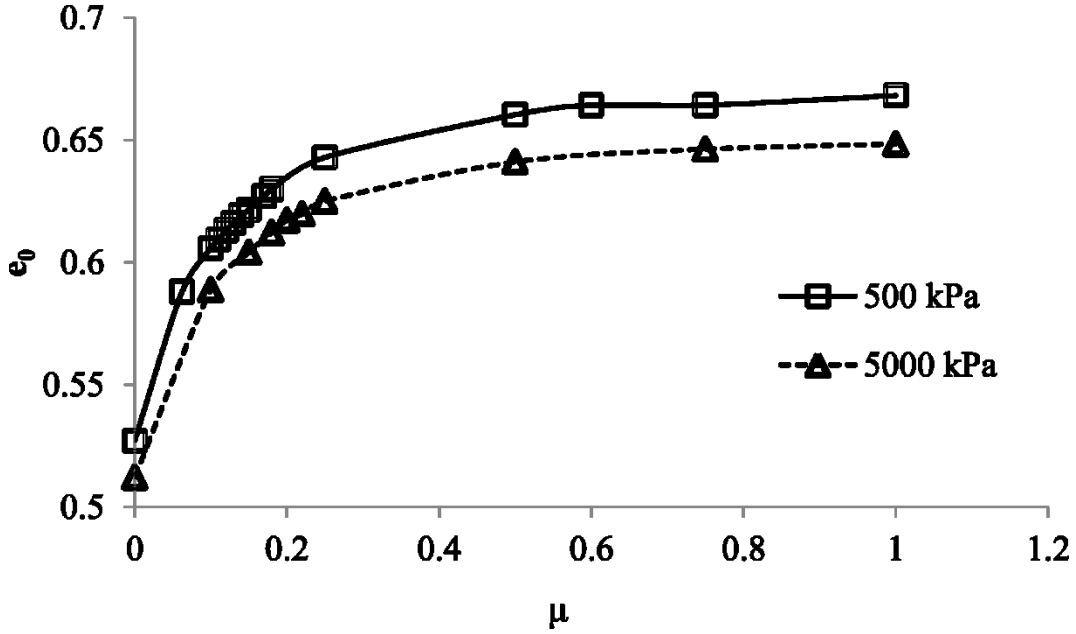



Figure 4.17 Variation of the initial void ratio after isotropic compression with $\mu$

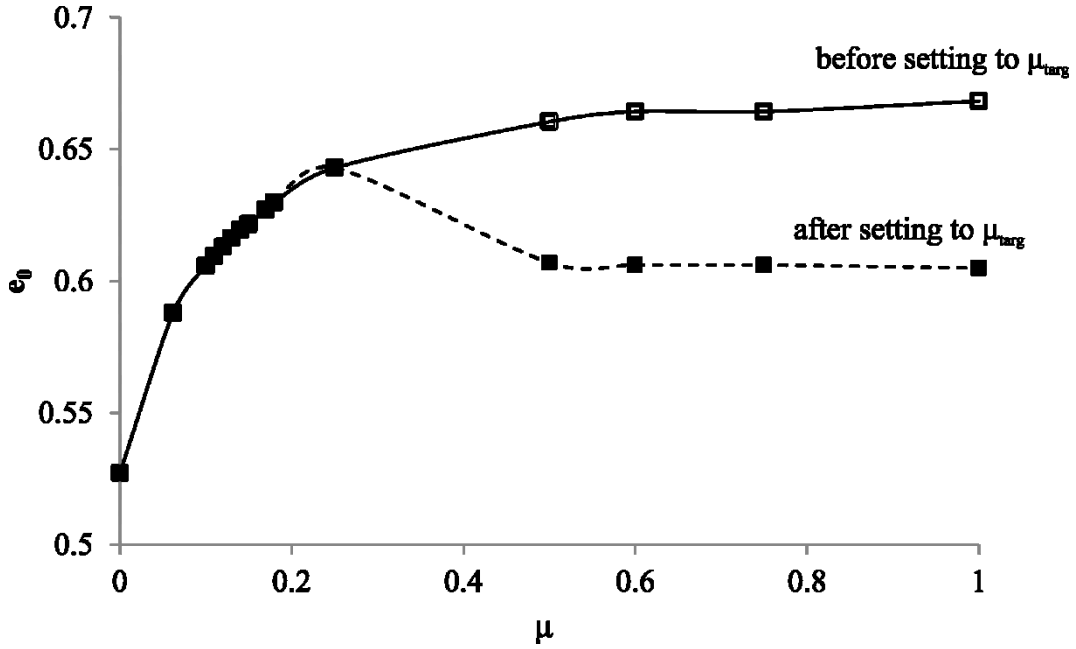
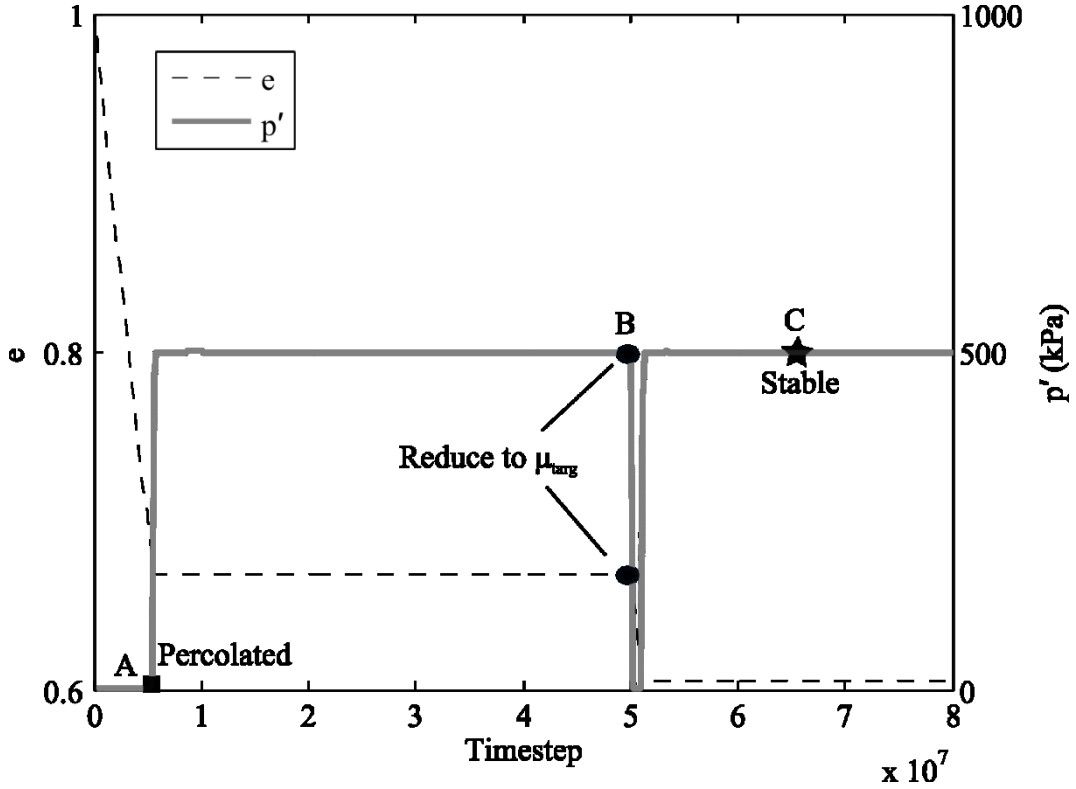
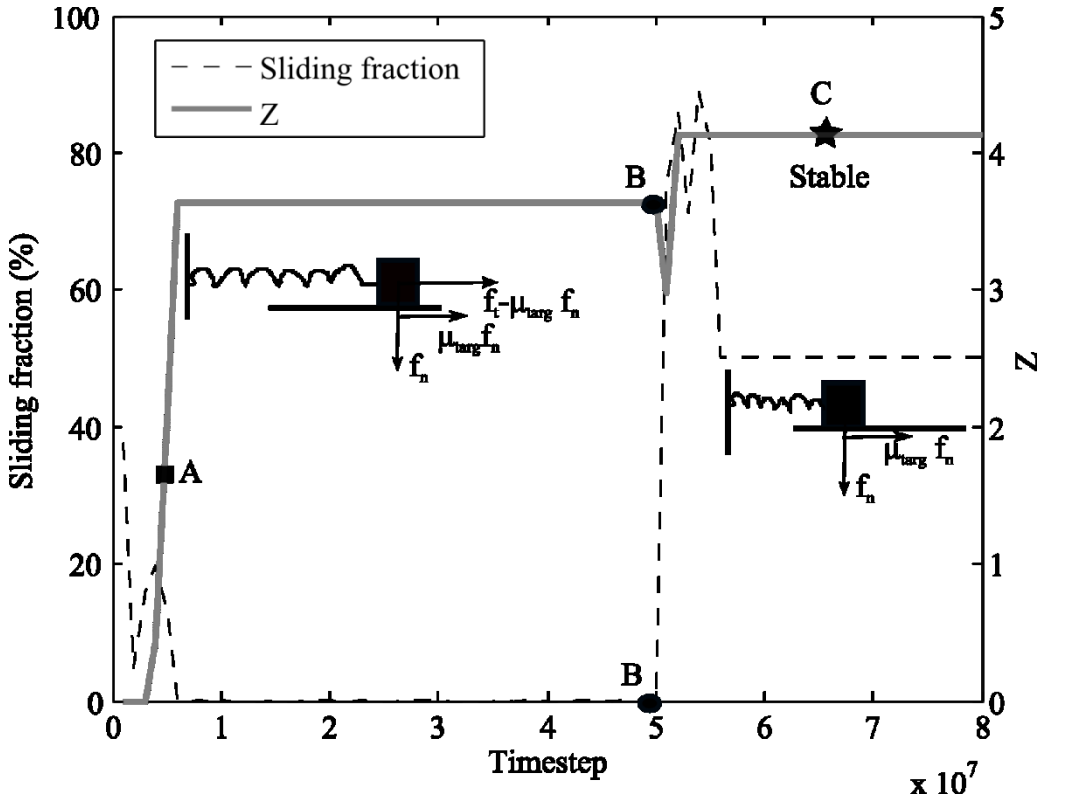



Figure 4.18 Comparing the void ratio before and after set $\mu$ to $\mu_{targ}$ ($\mu_{targ}$ = 0.25 and $p'_0$=500kPa)




(a) Void ratio and mean effective stress




(b) Sliding fraction and coordination number

Figure 4.19 Structural change due to the reduce of $\mu$ during isotropic compression ($\mu$ = 1.0, $\mu_{targ}$ = 0.25 and p'$_0$=500 kPa)

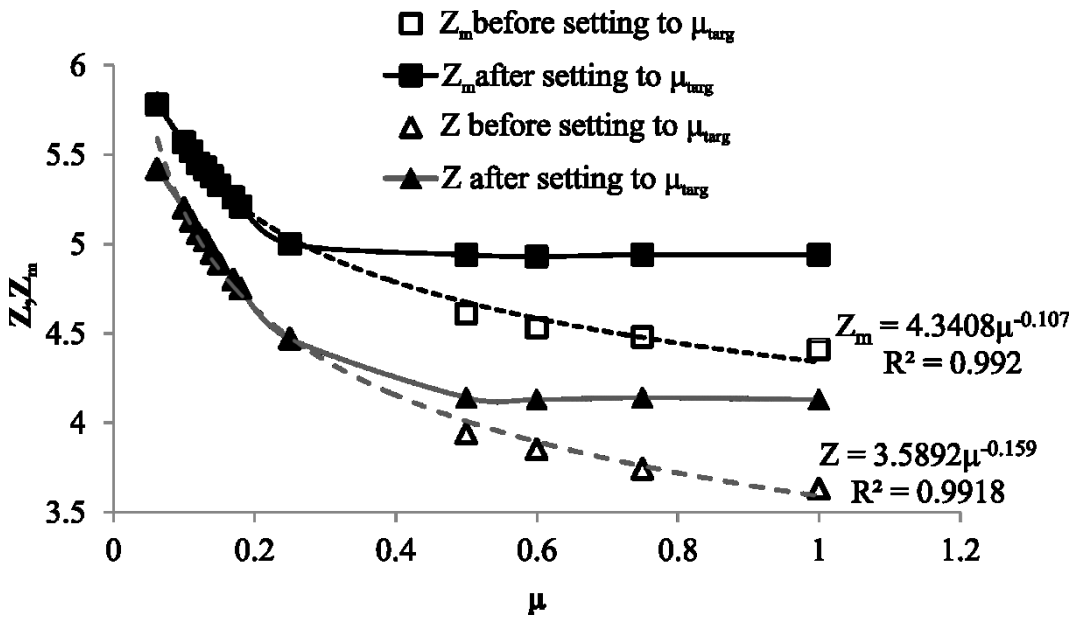



Figure 4.20 Variation of the coordination number (Z) and mechanical coordination number ($Z_m$) with $\mu$ after isotropic compression ($p'_0$=500 kPa)

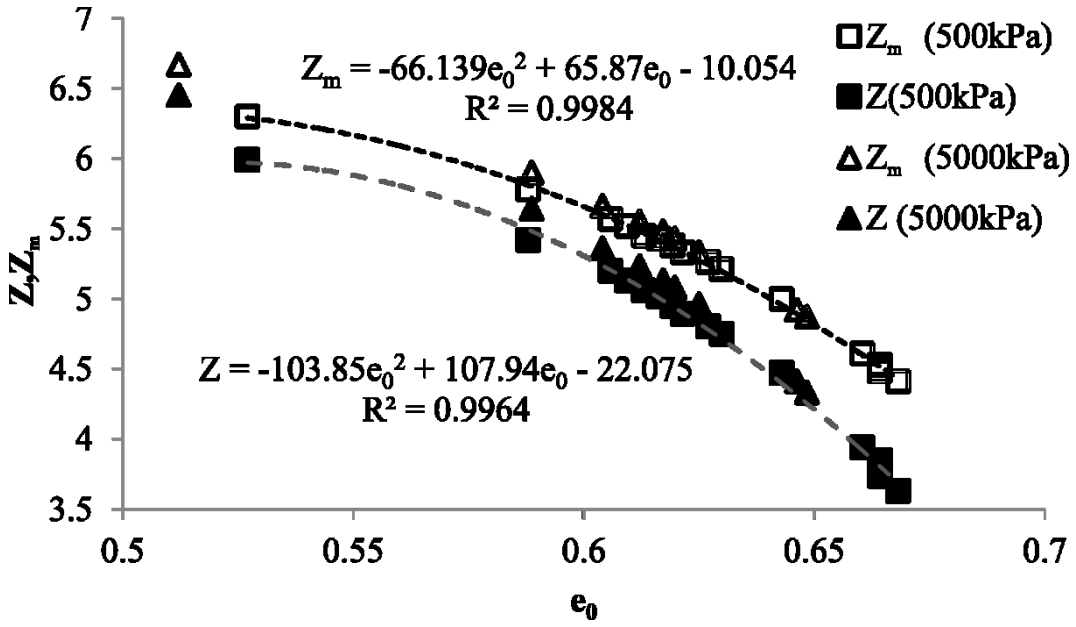
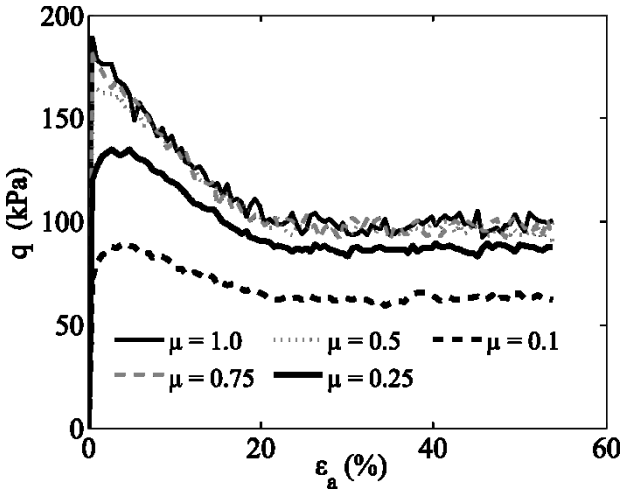
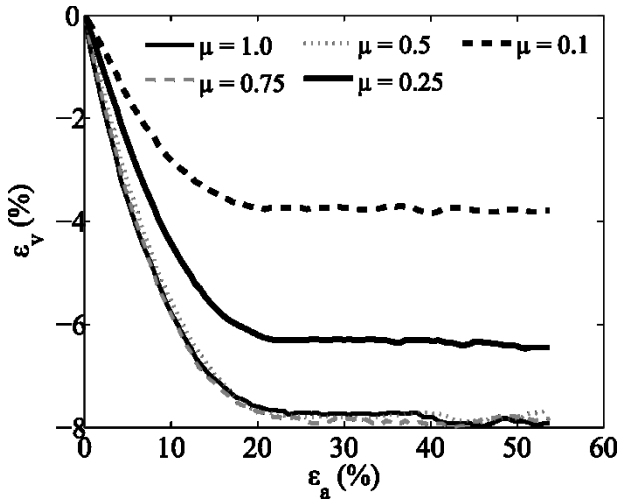


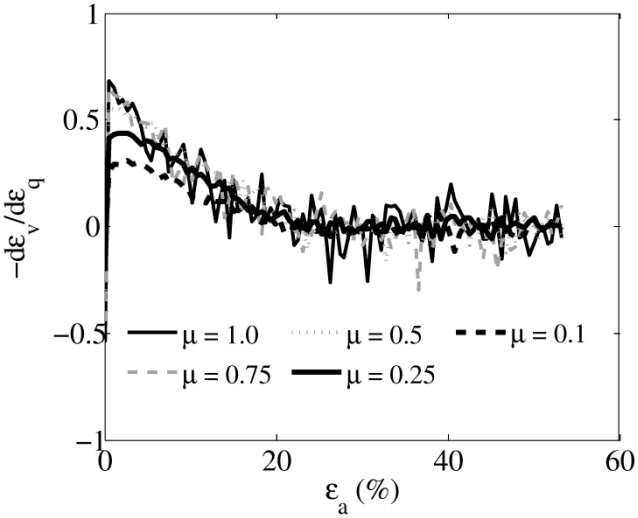

Figure 4.21 Correlations between $Z$ and $e$ and $Z_m$ and $e$ after isotropic compression before changing $\mu$ to $\mu_{targ}$




(a) Deviatoric stress

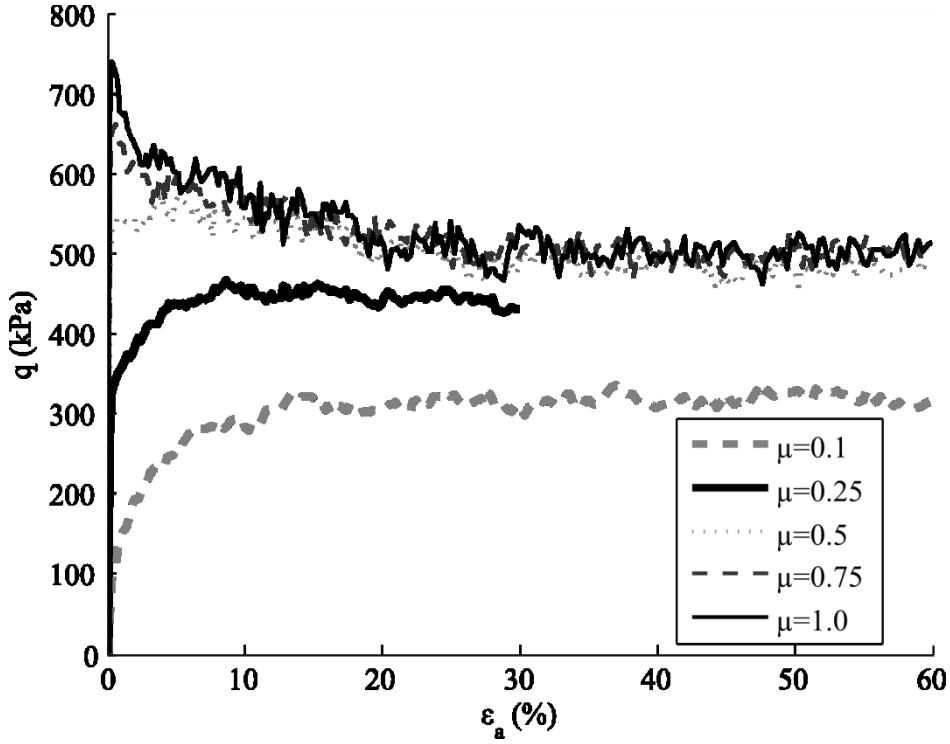



(b) Volumetric strain

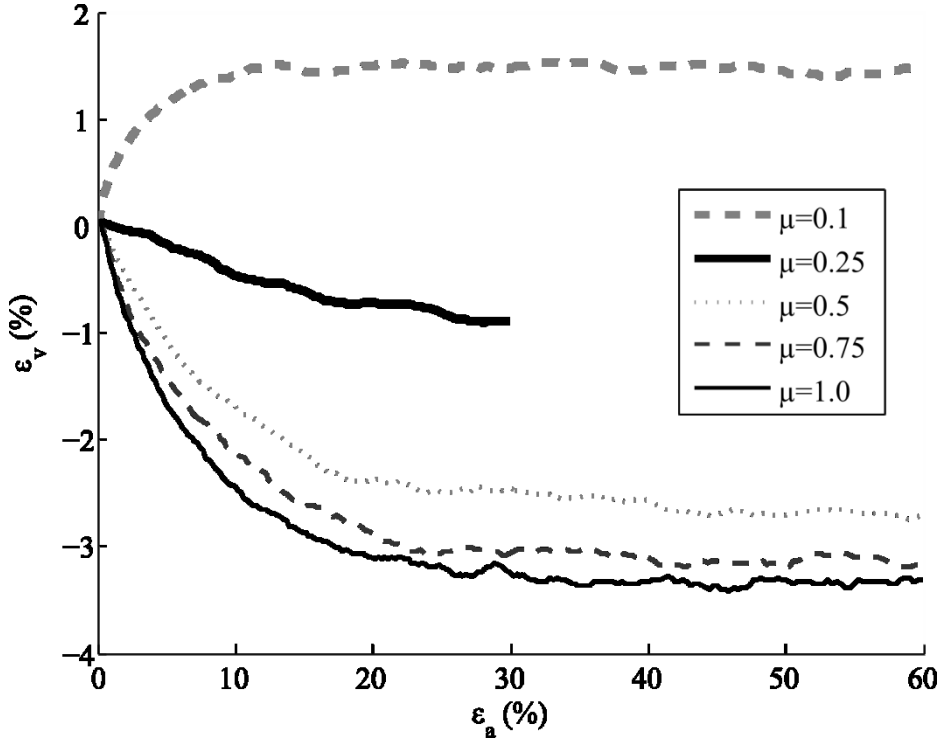



(c) Dilatancy

Figure 4.22 Effect of $\mu$ on the macromechanical response for PB simulations under conventional drained condition (Toyoura PSD, $e_0$ = 0.533 and $\sigma'_3$ = 100 kPa)




(a) Deviatoric stress




(b) Volumetric strain

Figure 4.23 Effect of interparticle friction on the macromechanical response for RW simulations under conventional drained condition (Toyoura PSD, $e_0 = 0.648$ and $\sigma'_3 = 500$ kPa)

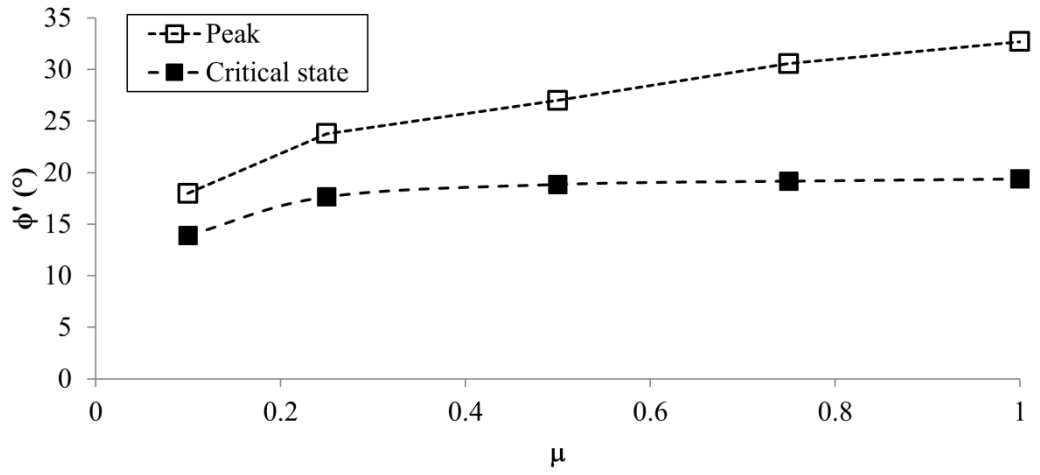



Figure 4.24 Variation of angle of shearing resistance of PB samples with $\mu$ (Toyoura PSD, $e_0$ = 0.533 and $\sigma'_3$ = 100 kPa)

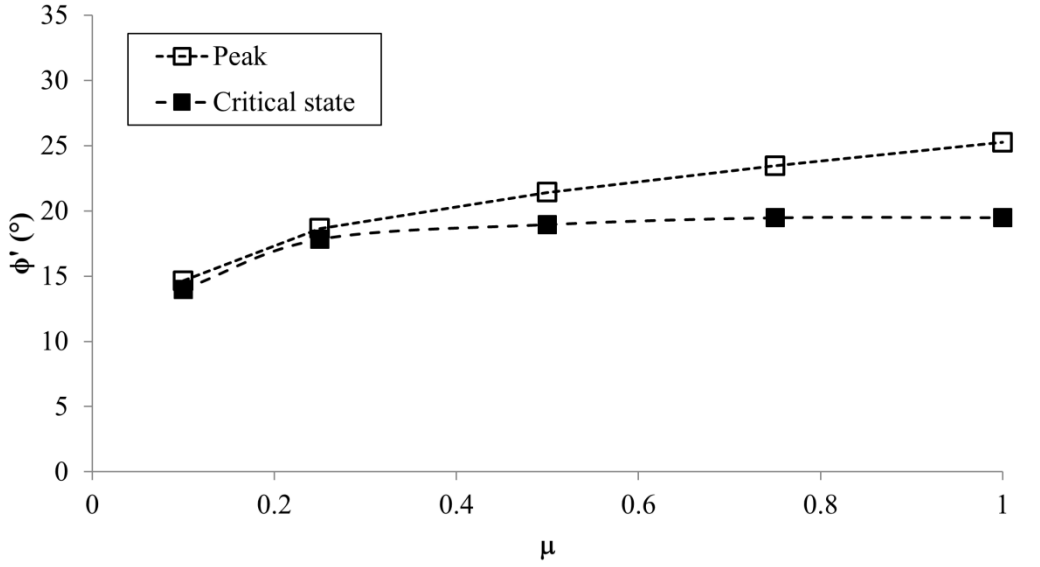
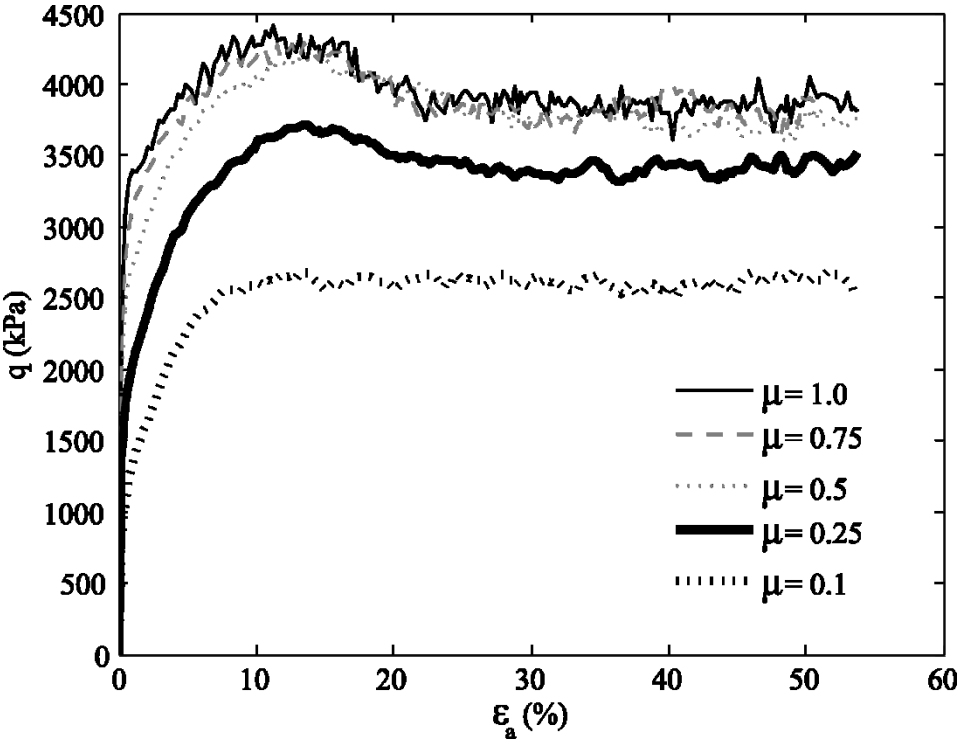
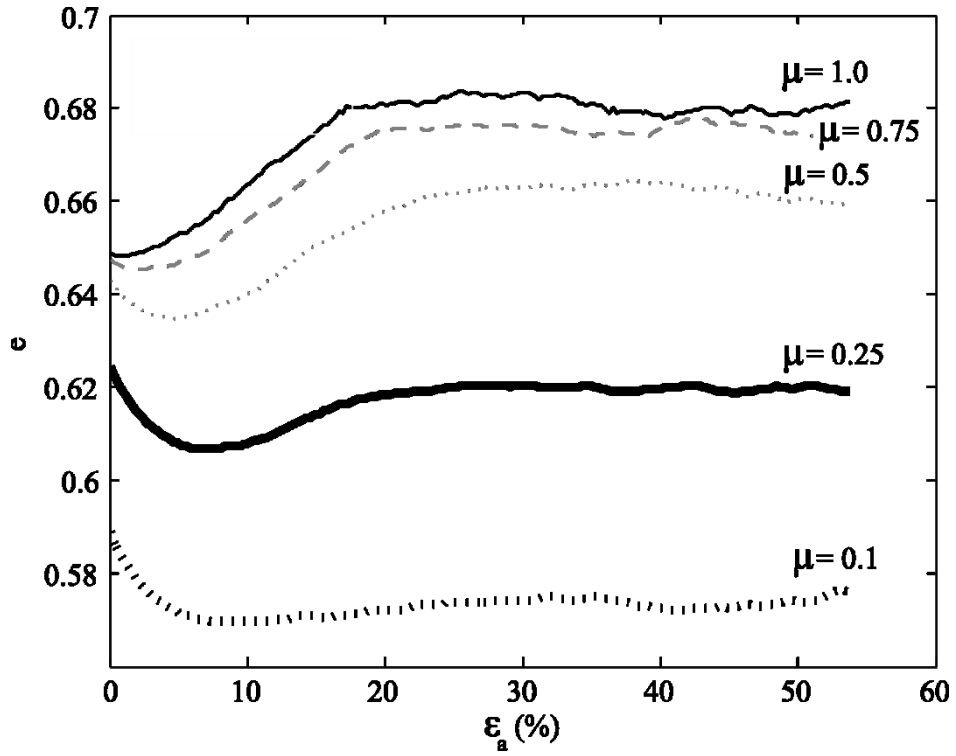



Figure 4.25 Variation of angle of shearing resistance of RW samples with $\mu$ (Toyoura PSD, $e_0$ = 0.648 and $\sigma'_3$ = 500 kPa)

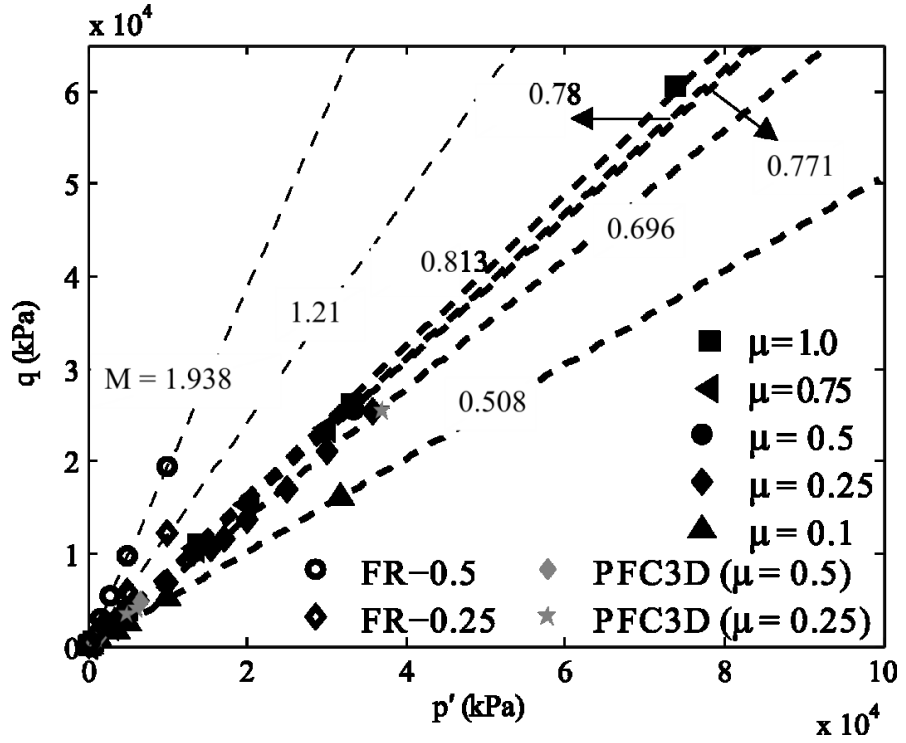



(a) Deviatoric stress

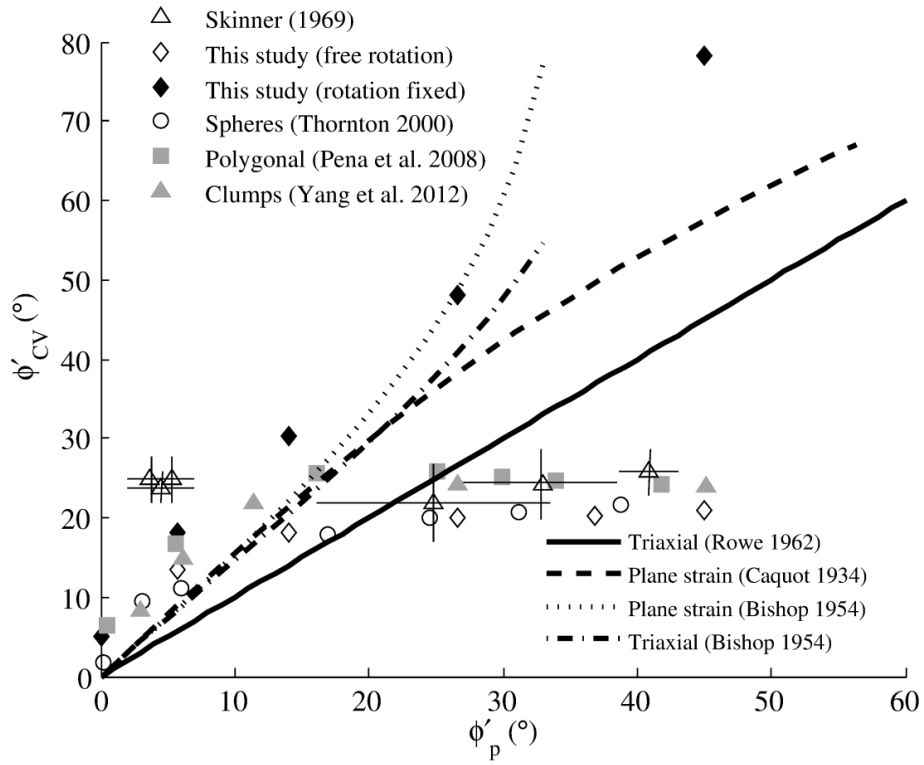



(b) Void ratio

Figure 4.26 Effect of interparticle friction on the macromechanical response for PB simulations under constant-*p'* condition (Toyoura PSD, *p'* = 5000 kPa)

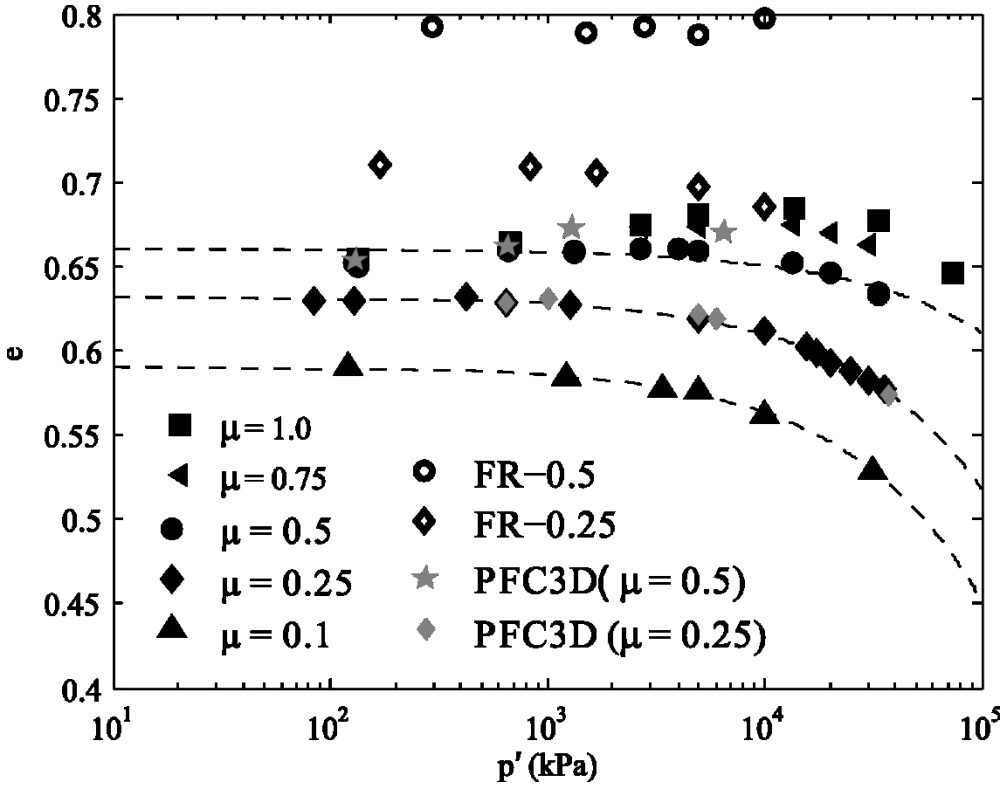



(a) Stress paths on *q-p'* plane

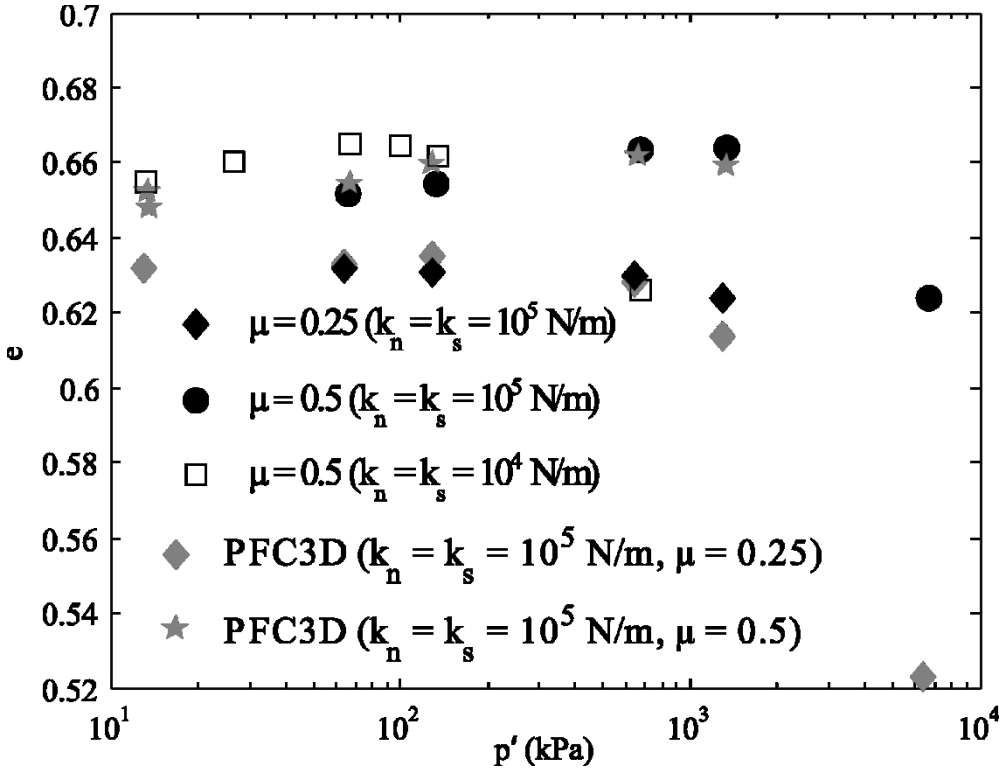



(b) Critical-state angle of shearing resistance

Figure 4.27 Effects of $\mu$ and rotation on the shear resistance at critical state: FR=rotation fixed; simulations not denoted as PFC3D used periodic boundaries PB and Toyoura PSD




(a)




(b)

Figure 4.28 Effect of $\mu$ and rotation on the CSL in $e$-log $p'$ space; FR=rotation fixed; simulations not denoted as PFC3D used periodic boundaries: (a) Toyoura PSD with HM contact model (b) Toyoura PSD with linear contact model

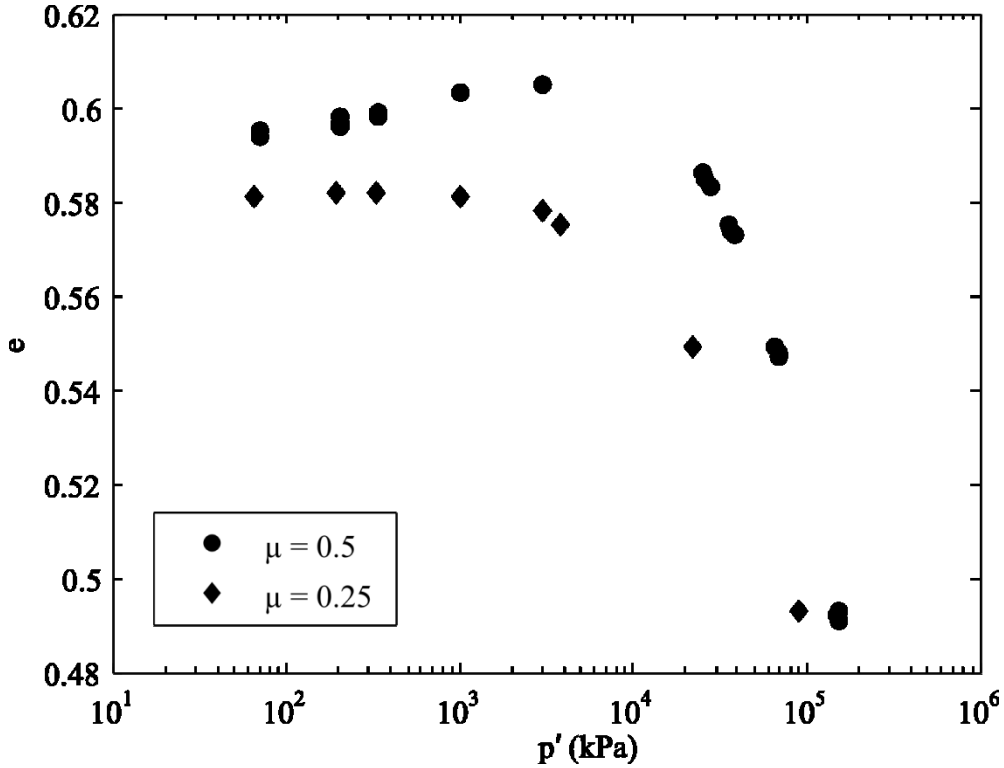



Figure 4.29 CSL in e-log(*p'*) space for samples using Dunkirk PSD and a HM contact model

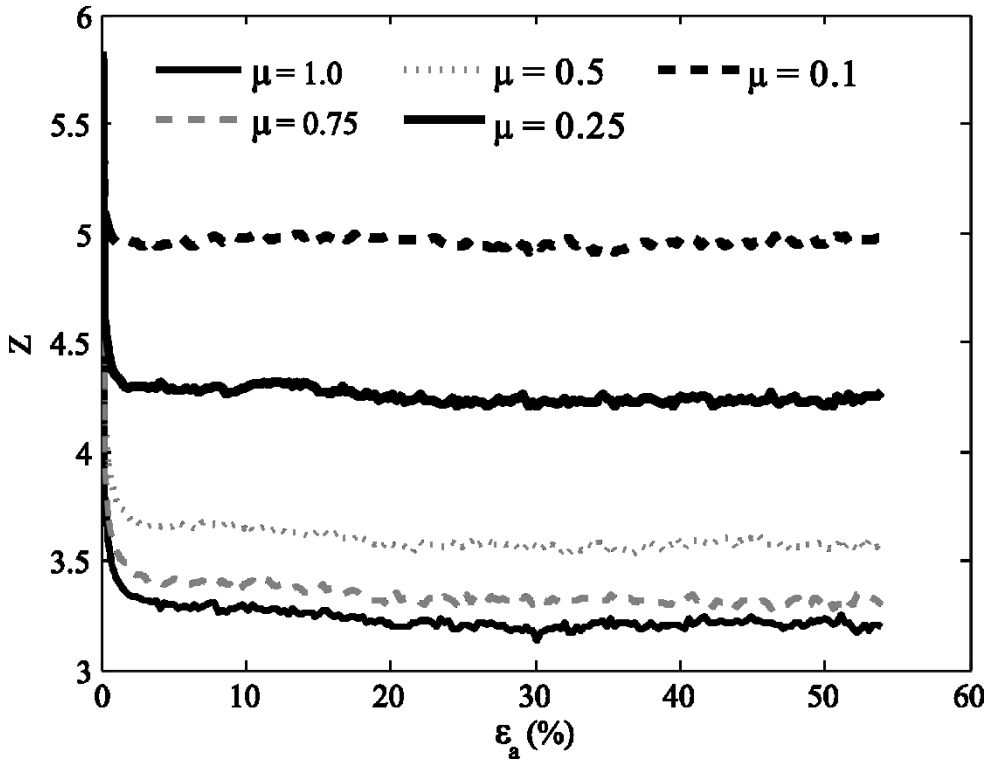
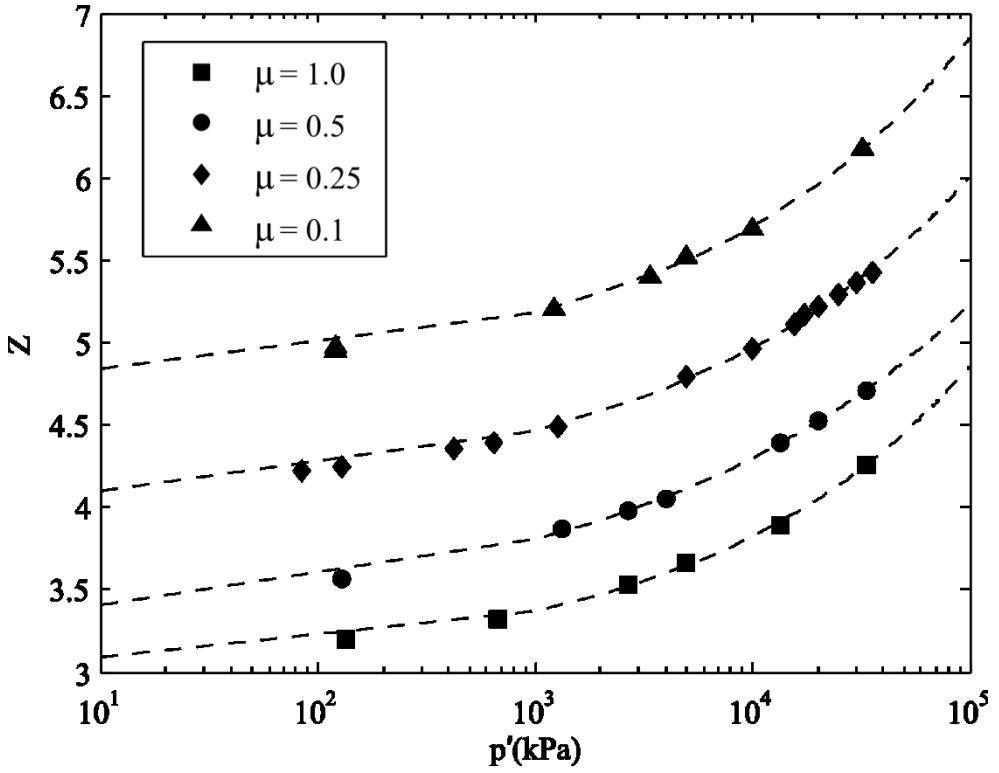
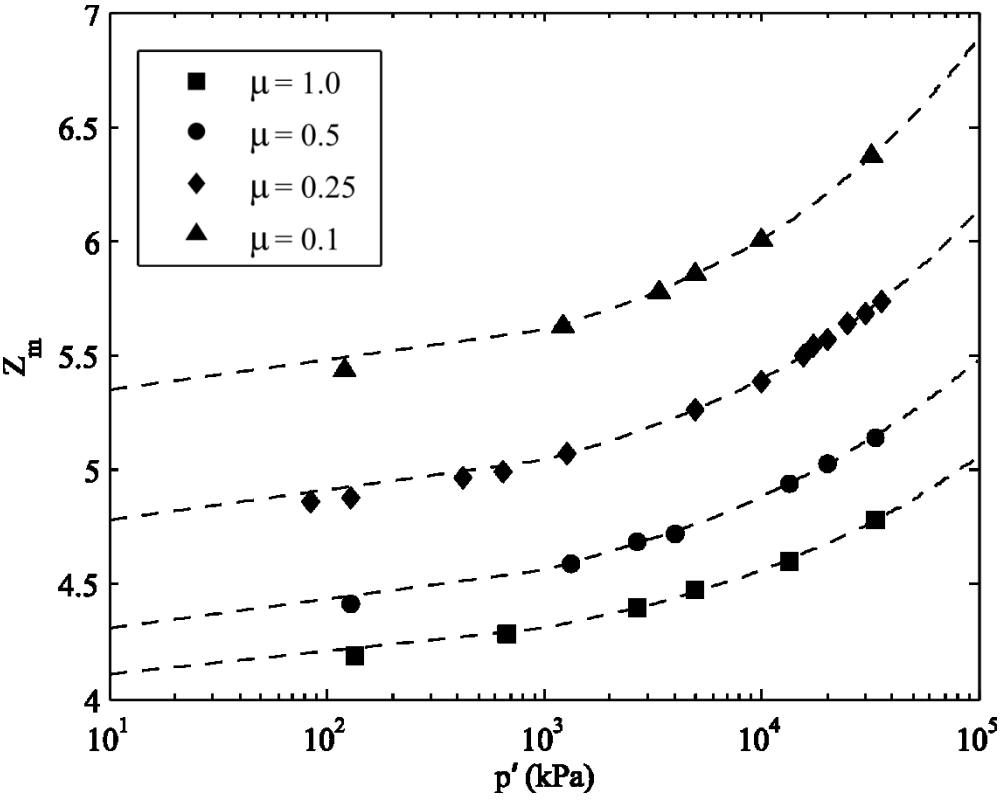



Figure 4.30 Influence of $\mu$ on the variation in $Z$ with axial strain ($e_0$ = 0.533, $\sigma'_3$ = 100 kPa)

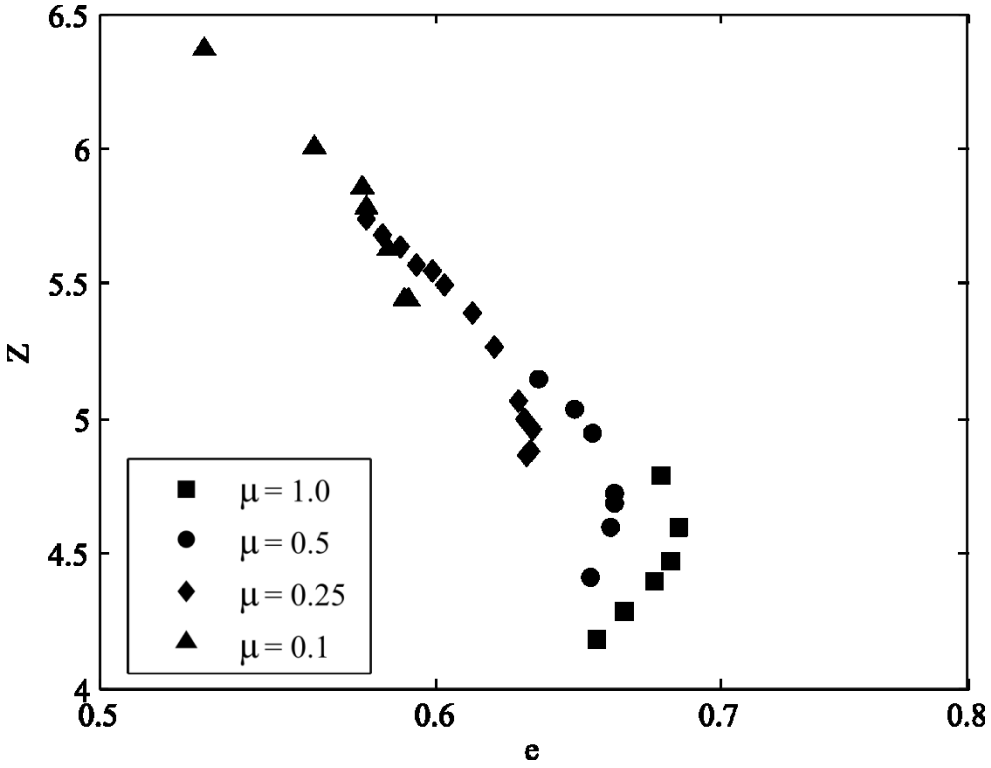



(a)

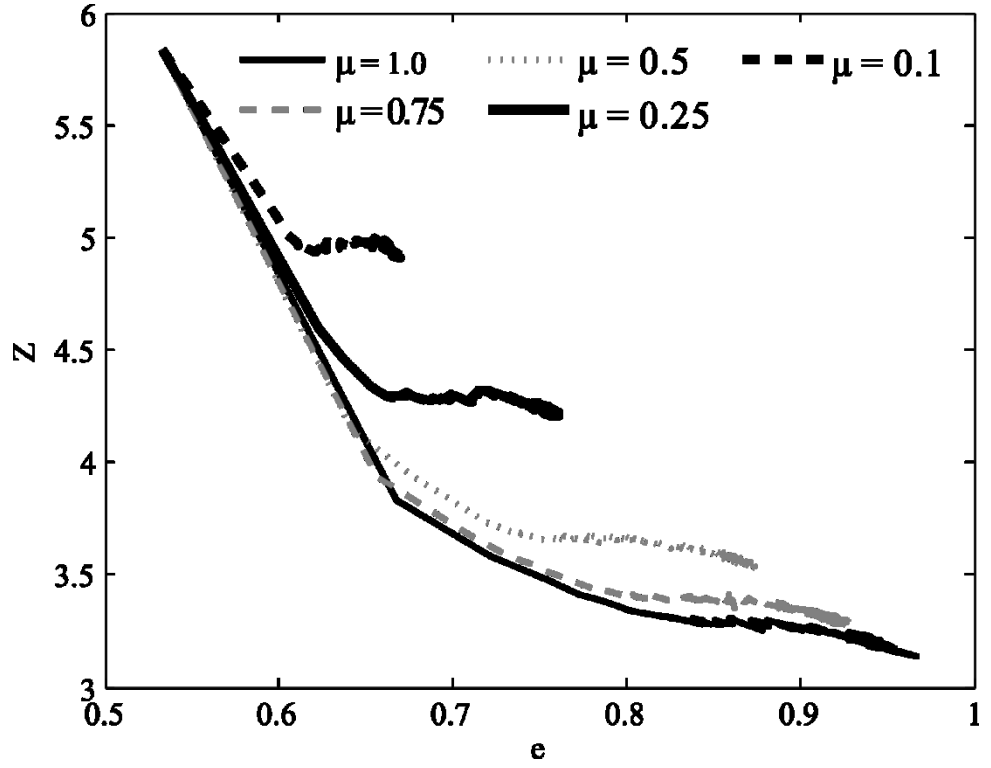



(b)

Figure 4.31 The effect of $\mu$ on the coordination number $Z$ at critical state for LAMMPS simulations with Toyoura PSD, HM contact model: (a) Variation in $Z$ with $p'$; (b) Variation in $Z_m$ with $p'$

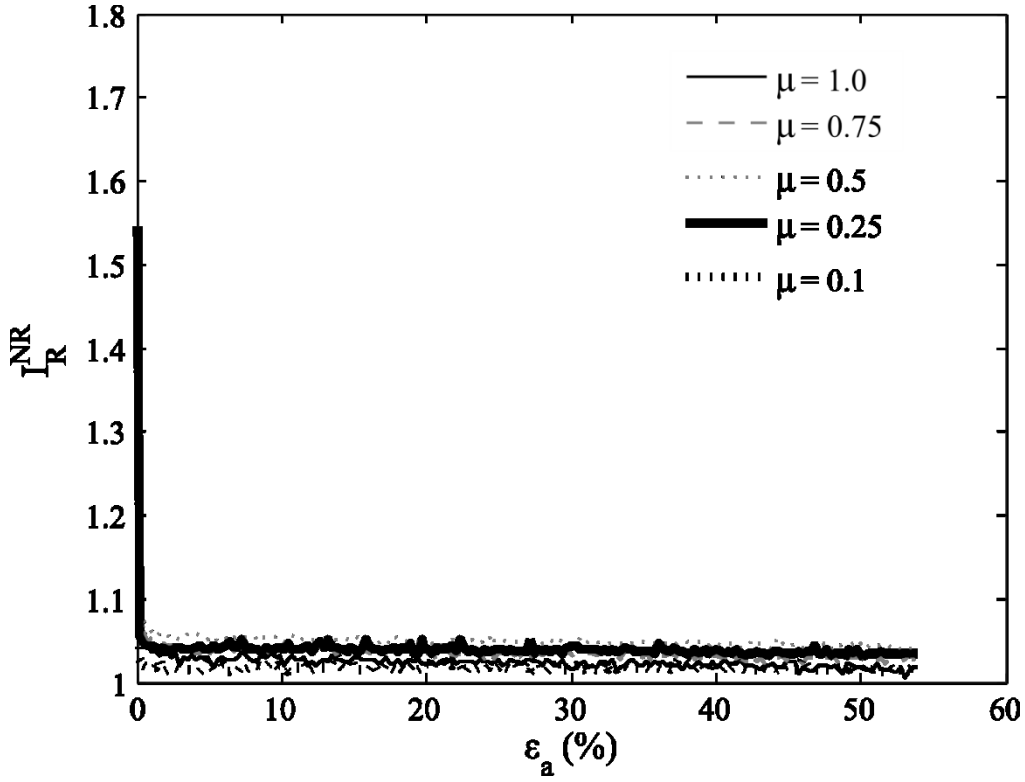



(a)

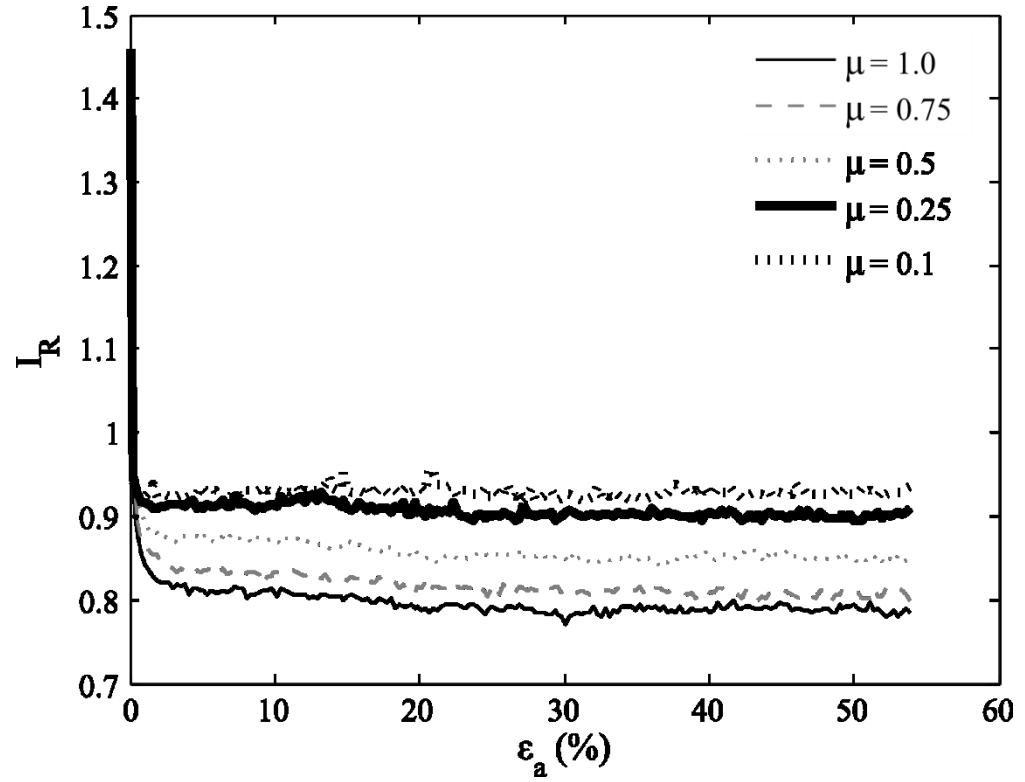



(b)

Figure 4.32 The effect of $\mu$ on the relationship between Z and $e$ for LAMMPS simulations with Toyoura PSD, HM contact model: (a) Variation in $Z$ with $e$ at critical state ; (b) Variation in $Z$ with void ratio ($e_0$ = 0.533, $\sigma'_3$ = 100 kPa)

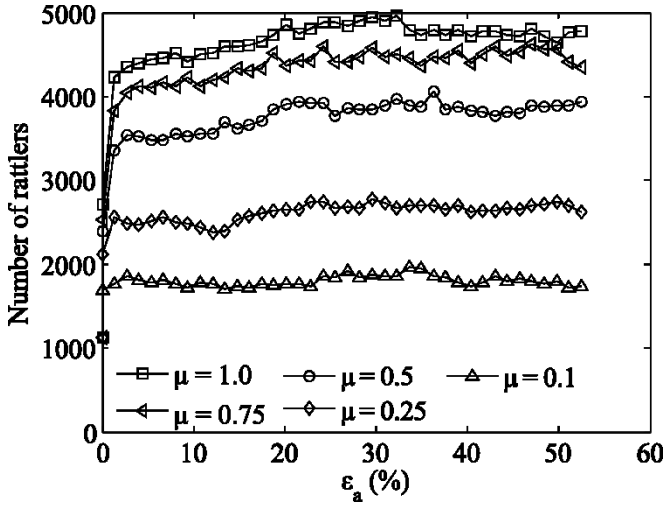



(a)

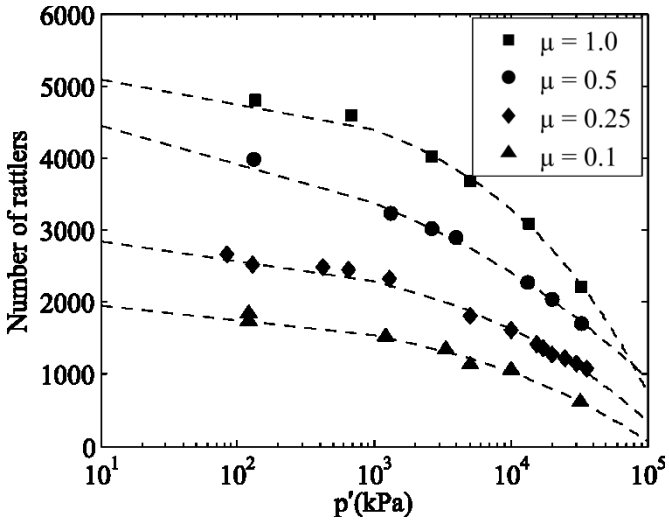



(b)

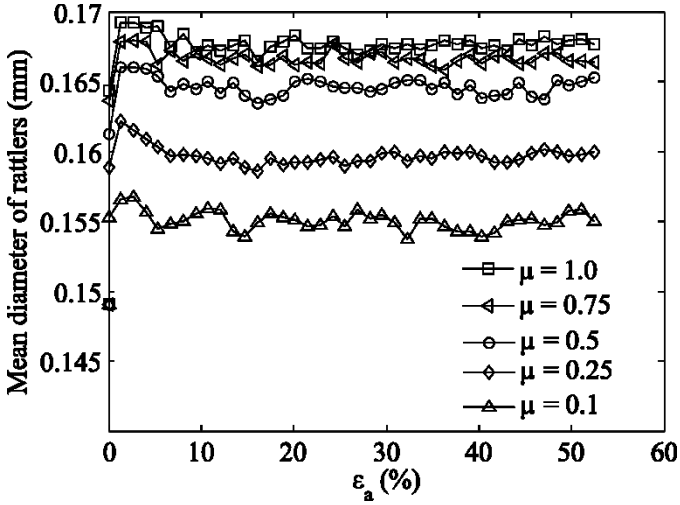
Figure 4.33 Index of mechanical redundancy: (a) excluding particles with zero contacts (b) including all particles ($e_0$ = 0.533, $\sigma'_3$ = 100 kPa)




(a) Number of rattlers against axial strain ($e_0$ = 0.533, $\sigma'_3$ = 100 kPa)

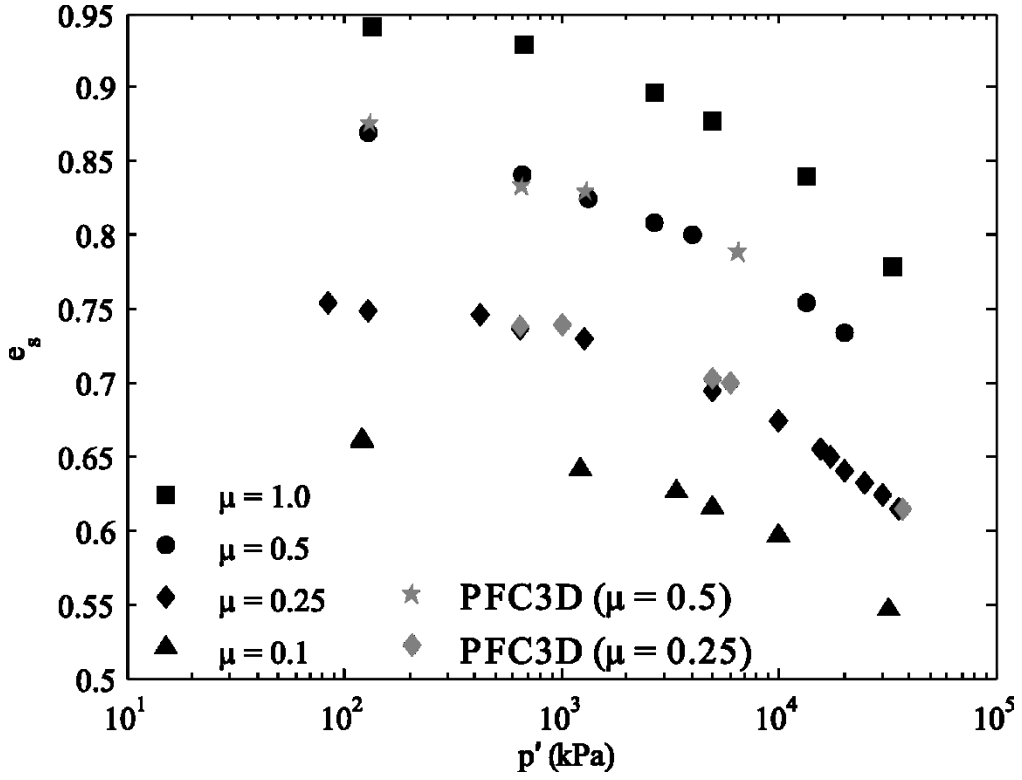



(b) Number of rattlers at critical state

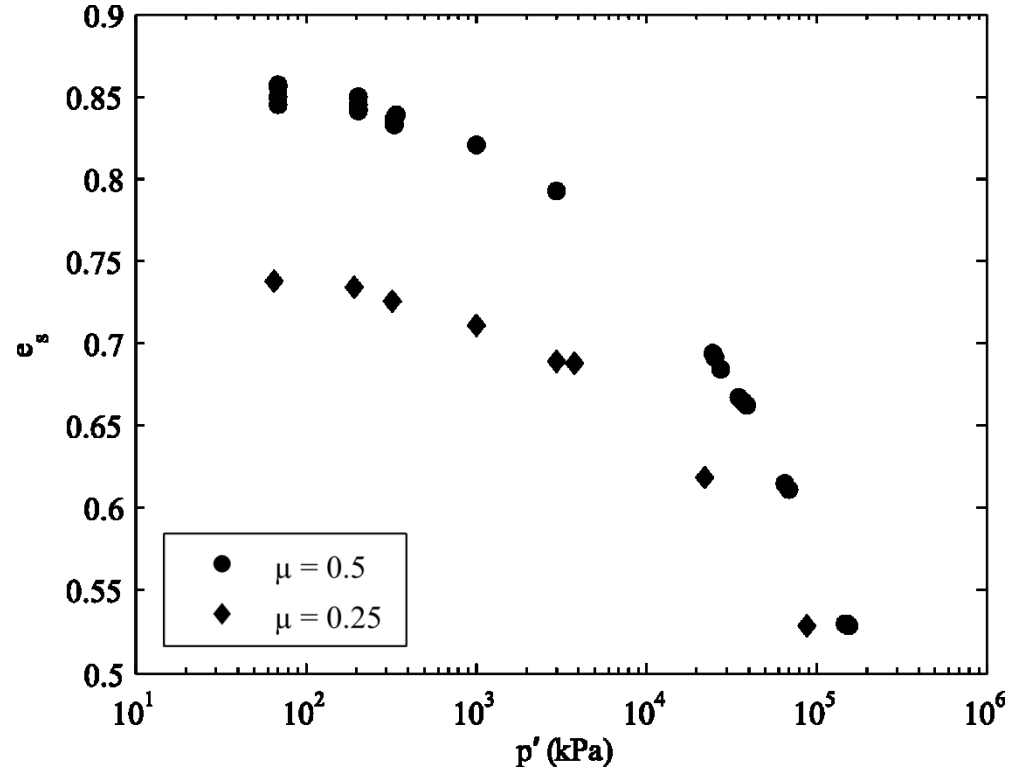



(c) Mean diameter of rattlers

Figure 4.34 Effect of $\mu$ on the number of rattlers for LAMMPS simulations using the Toyoura PSD

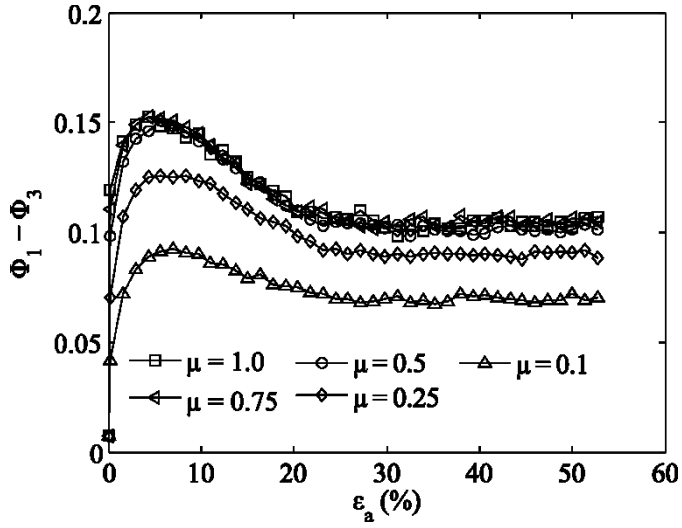



(a)

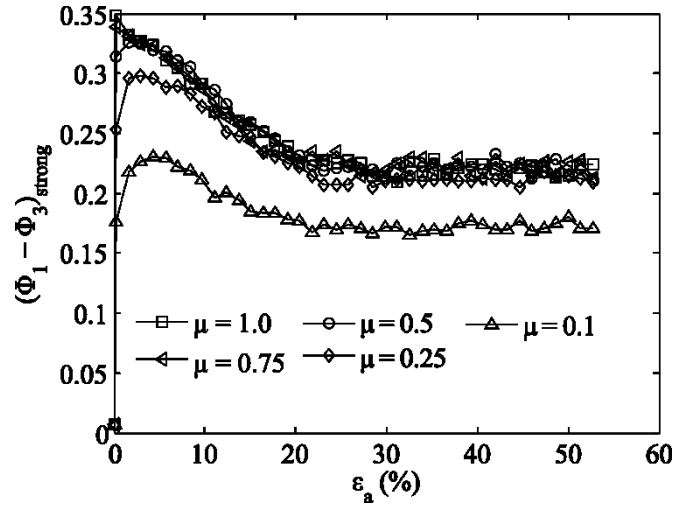



(b)

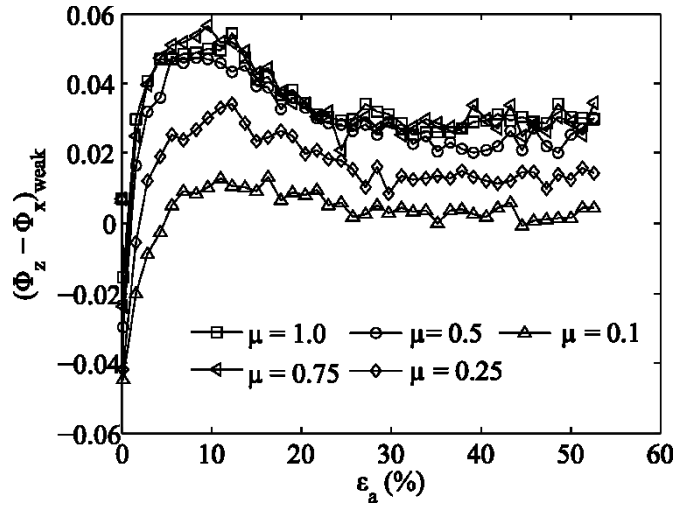
Figure 4.35 CSL in e-log(p') space excluding rattlers: (a) Simulations using the Toyoura PSD (b) Simulations using the Dunkirk PSD




(a) All contacts

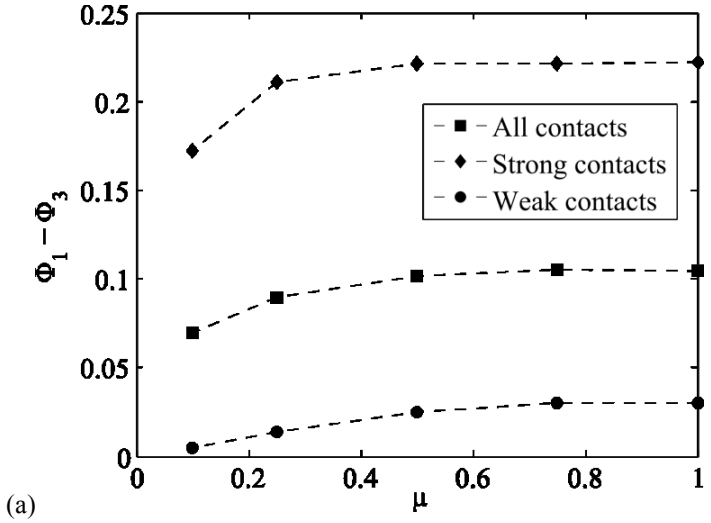



(b) Strong contacts

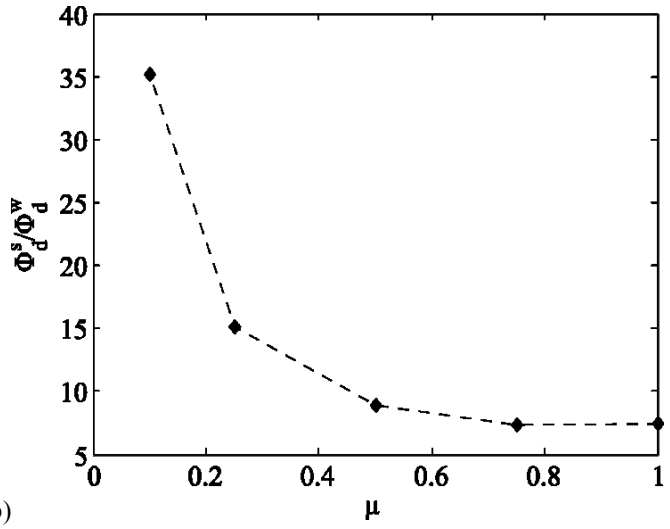



(c) Weak contacts

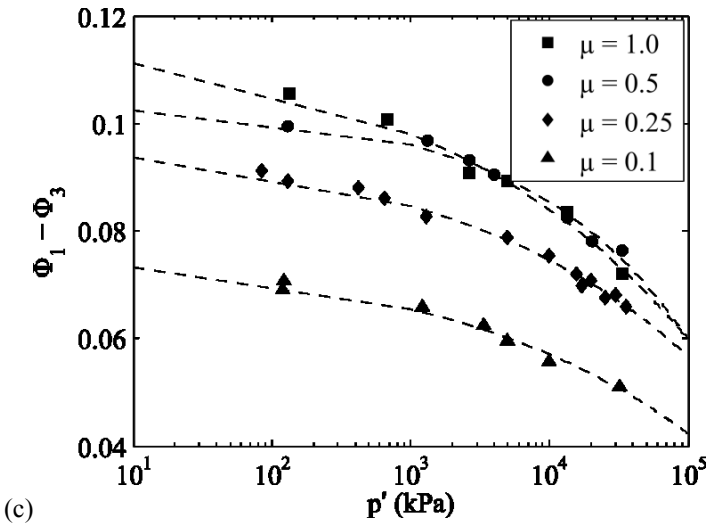
Figure 4.36 Evolution of deviatoric fabric for LAMMPS simulations, Toyoura PSD ($e_0$ = 0.533, $\sigma'_3$ = 100 kPa)




(a)




(b)




(c)

Figure 4.37 Influence of $\mu$ on the deviatoric fabric at critical state (Toyoura PSD, HM model): (a) Variation of deviatoric fabric with $\mu$ at critical state ($e_0$ = 0.533, $\sigma'_3$ = 100 kPa); (b) Relative anisotropy between the strong and weak contact network at critical state ($e_0$ = 0.533, $\sigma'_3$ = 100 kPa); (c) Relationship between the deviatoric fabric and mean effective stress

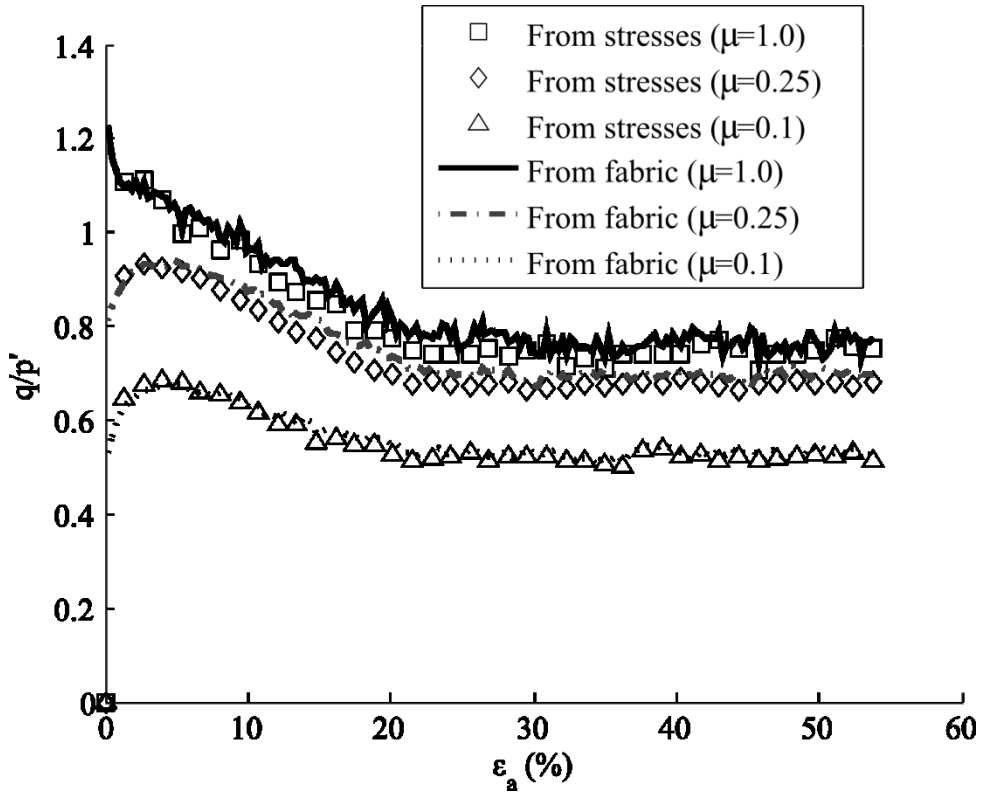
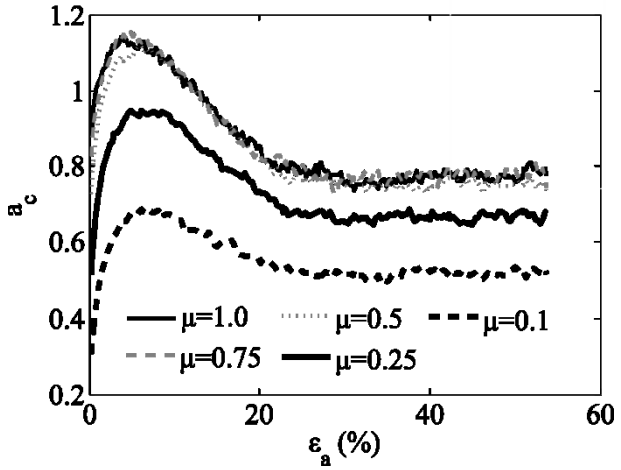
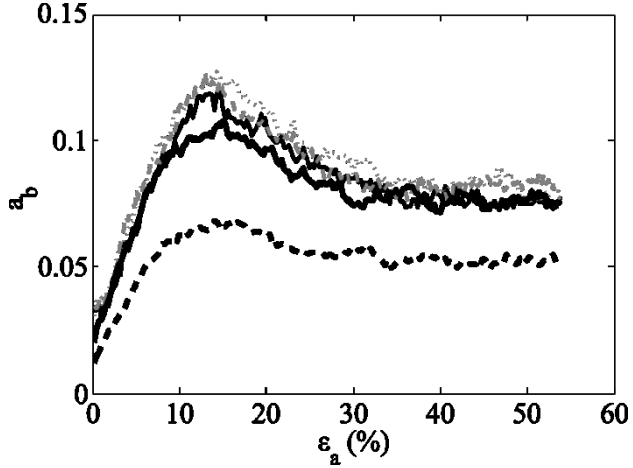


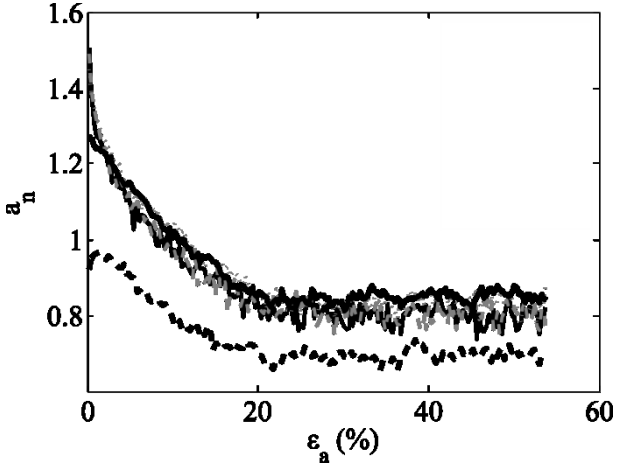

Figure 4.38 Comparing the stress ratio calculated from stress components and the stress ratio calculated from the stress-force-fabric relationship



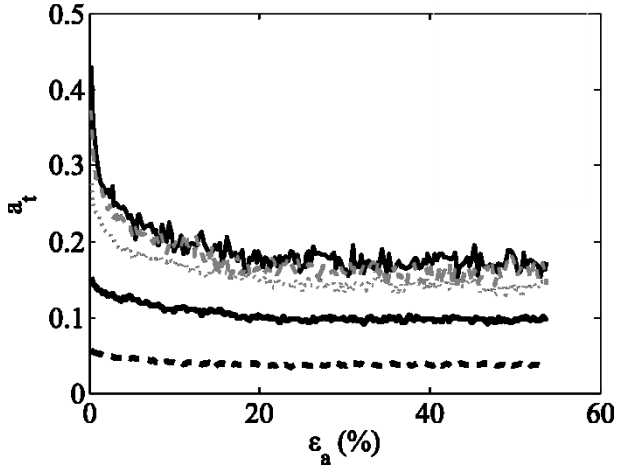

(a) $a_c$




(b) $a_b$

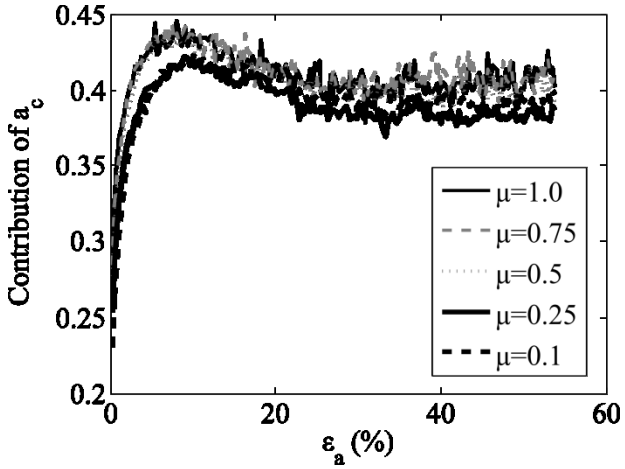



(c) $a_n$

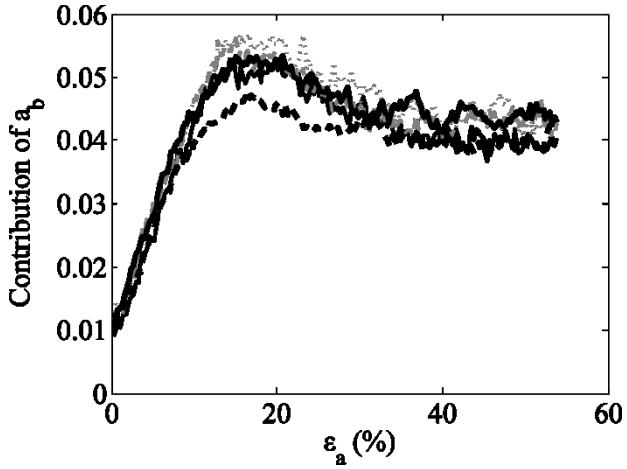



(d) $a_t$

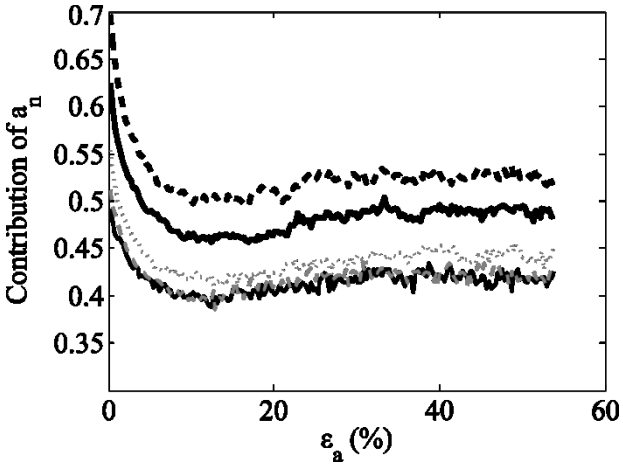
Figure 4.39 Influence of $\mu$ on the variation of the structural anisotropy quantities with axial strain



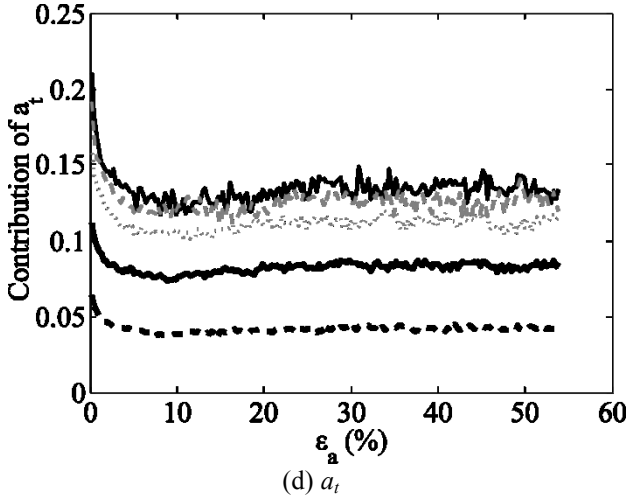

(a) $a_c$




(b) $a_b$

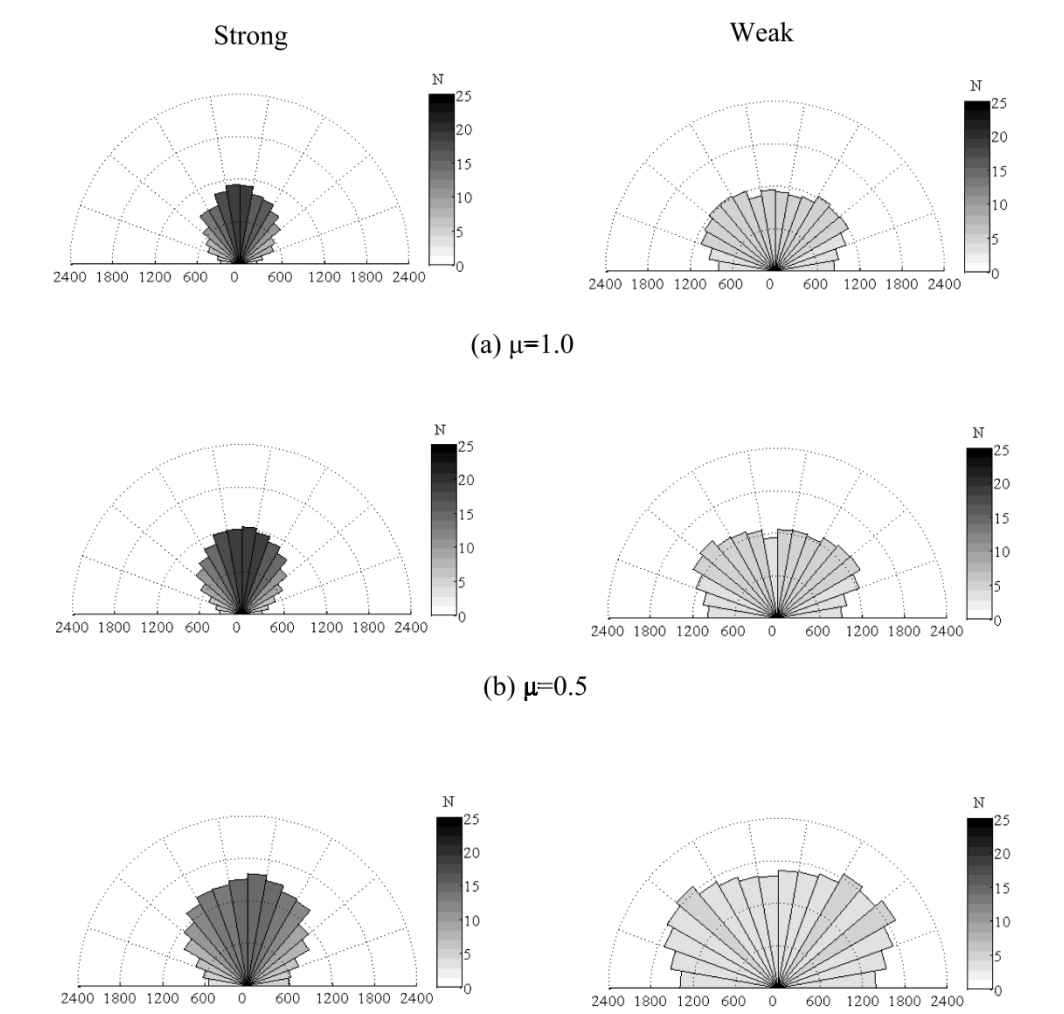



(c) $a_n$




(d) $a_t$

Figure 4.40 Influence of $\mu$ on the contribution of the structural anisotropy quantities to the stress ratio

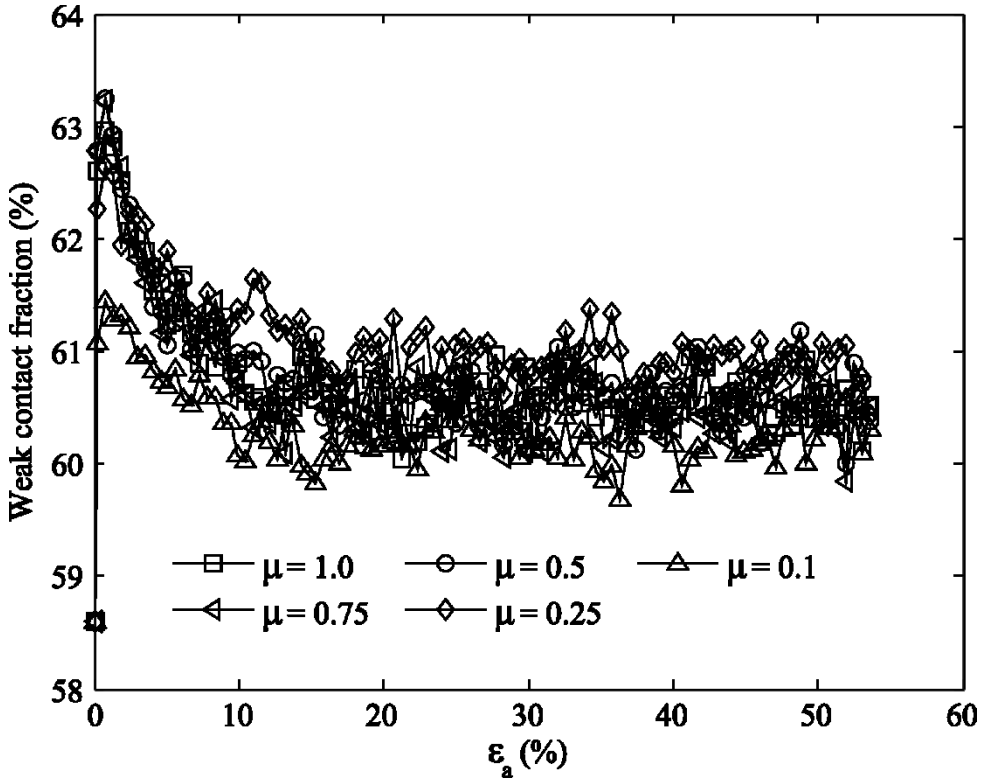



(a) μ=1.0

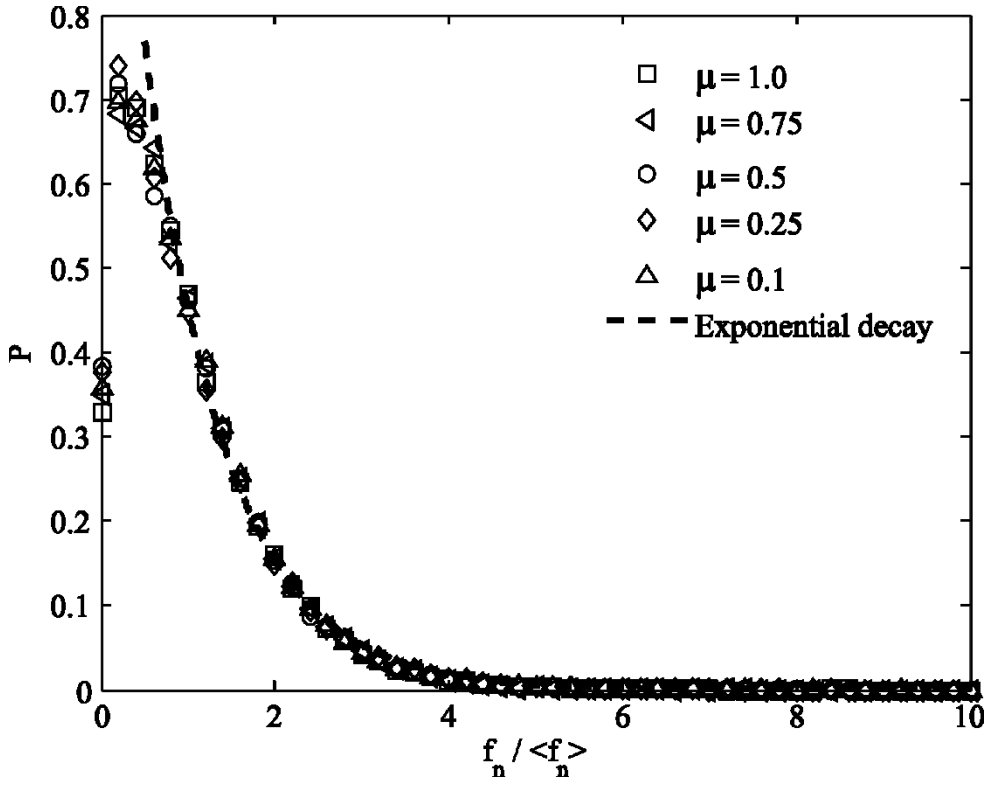
(b) μ=0.5

(c) μ=0.1

Figure 4.41 Contact rose diagram at critical states for LAMMPS simulations, Toyoura PSD ($e_0$ = 0.533, $\sigma'_3$ = 100 kPa)

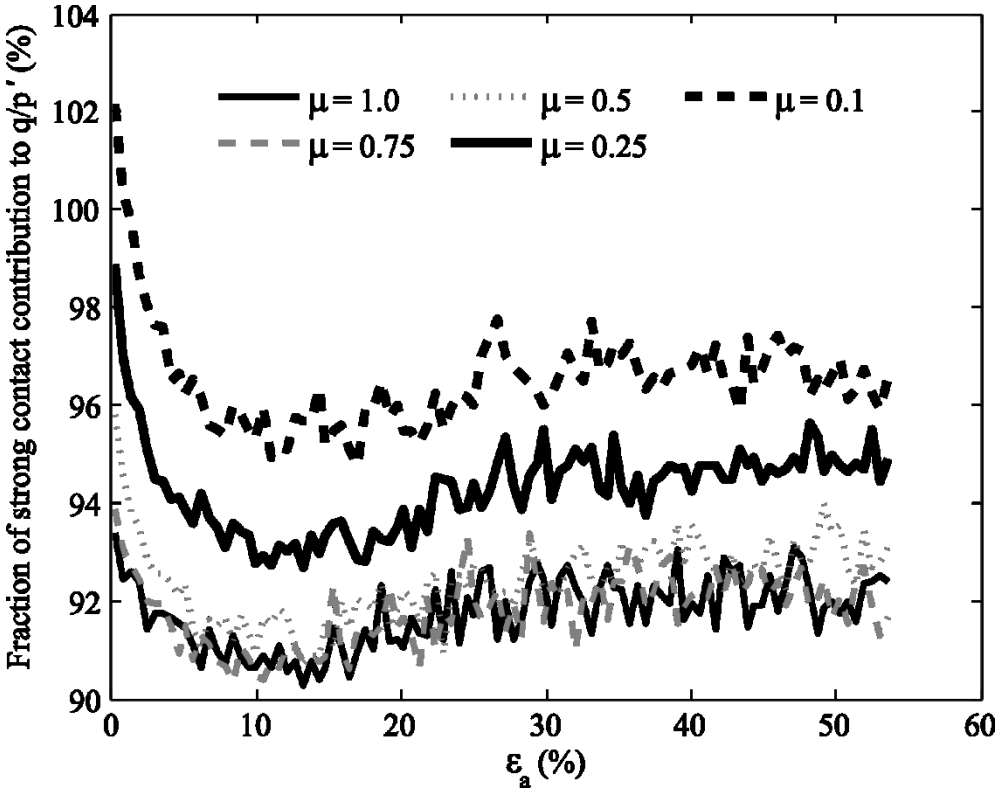



(a) Proportion of weak contacts

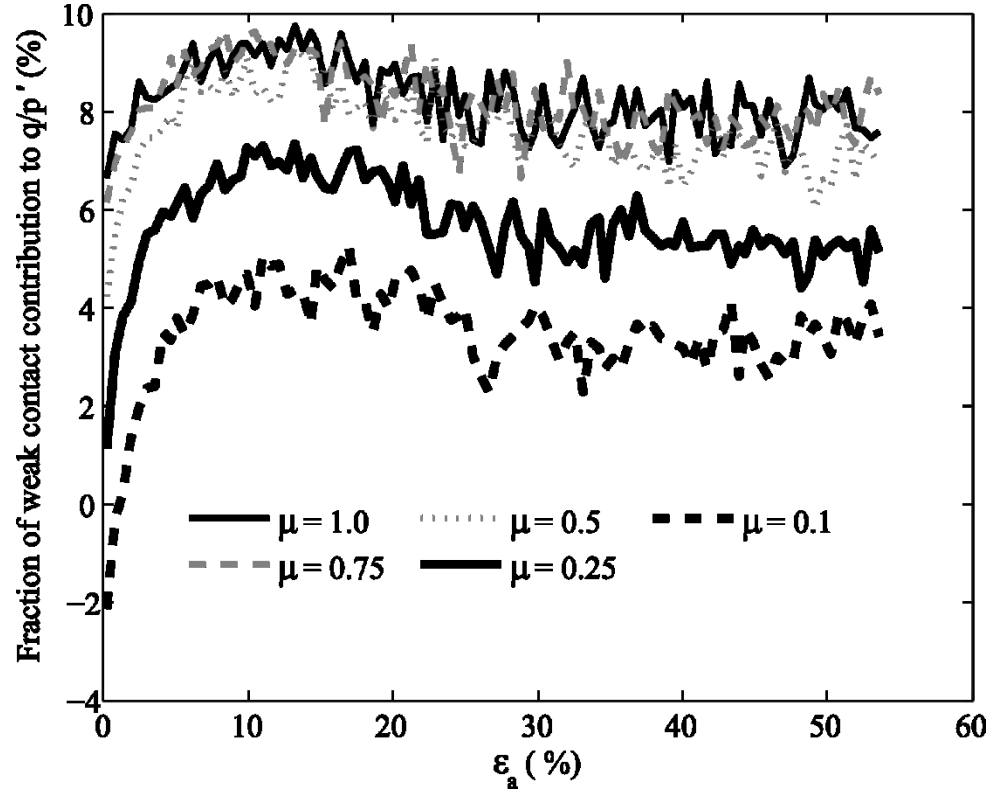



(b) PDF of the normal contact force at critical state

Figure 4.42 The effect of $\mu$ on the contact force configuration ($e_0$ = 0.533, $\sigma'_3$ = 100 kPa)




(a) Strong contact contribution




(b) Weak contact contribution

Figure 4.43 Bimodal force transmission for a representative set of simulations ($e_0$ = 0.533, $\sigma'_3$ = 100 kPa)

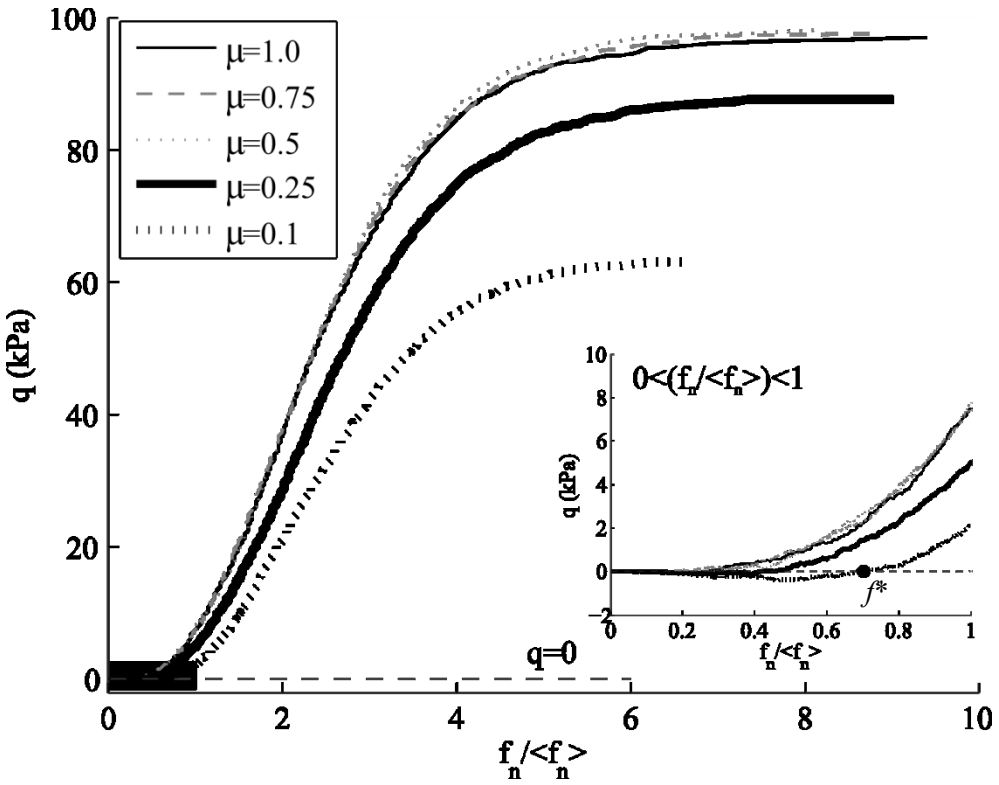
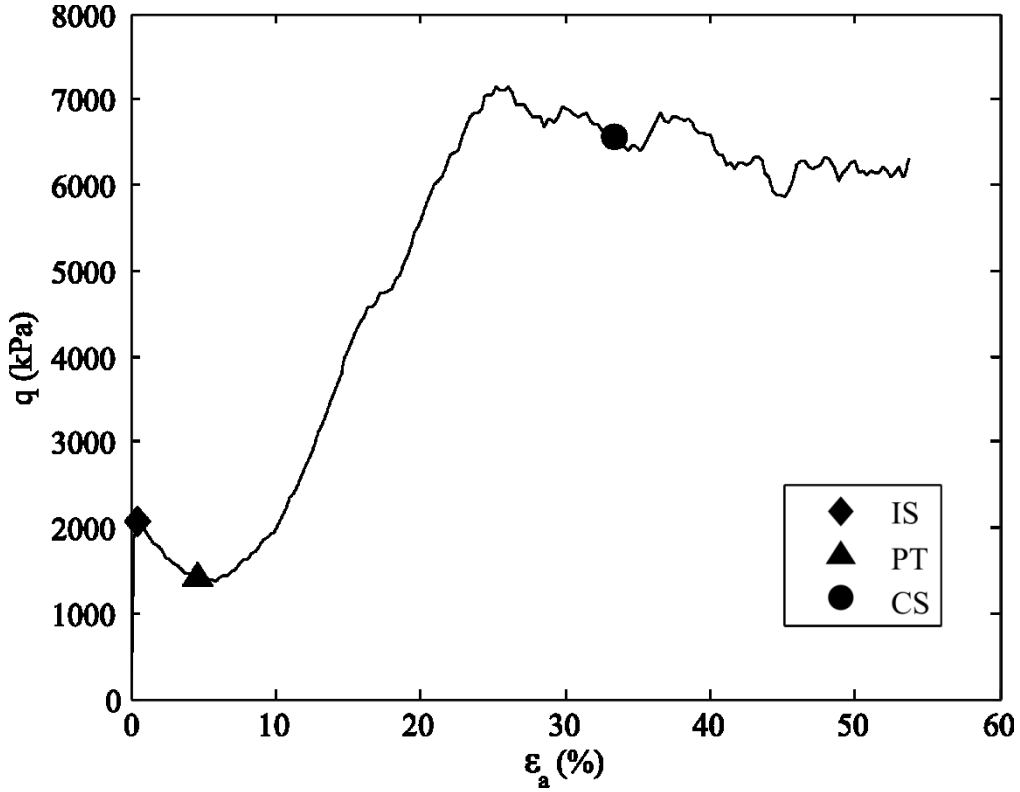
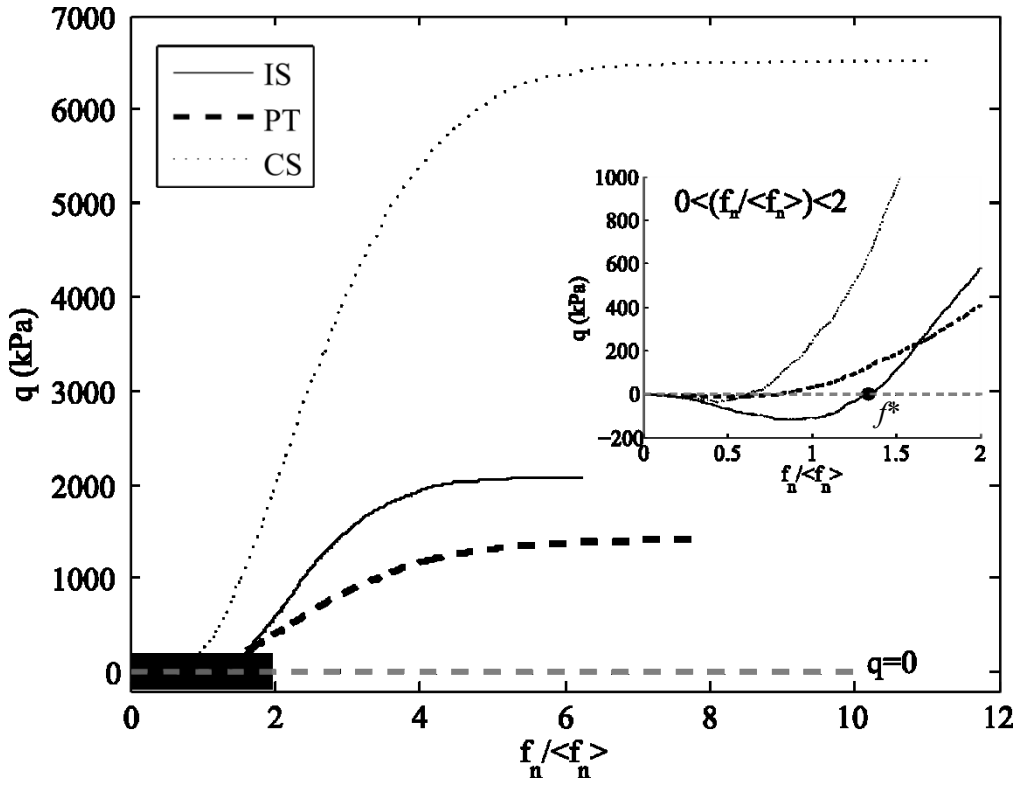



Figure 4.44 Cumulative contribution of contact forces to the deviatoric stress ($e_0$ = 0.533, $\sigma'_3$ = 100 kPa)

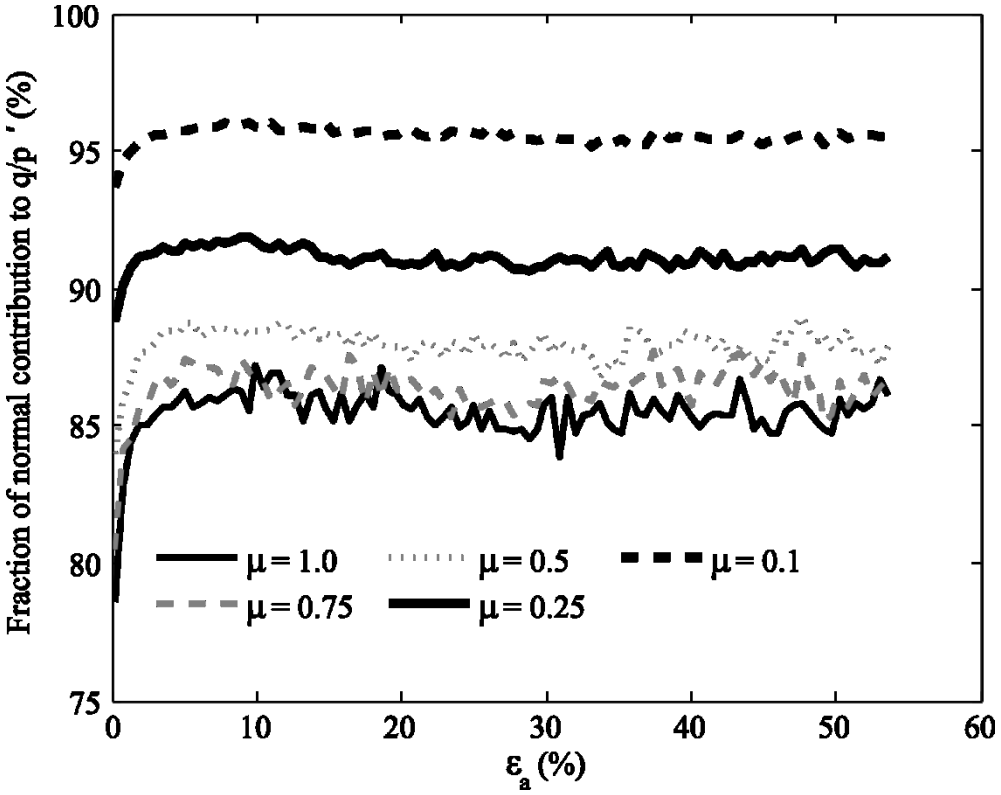



(a)

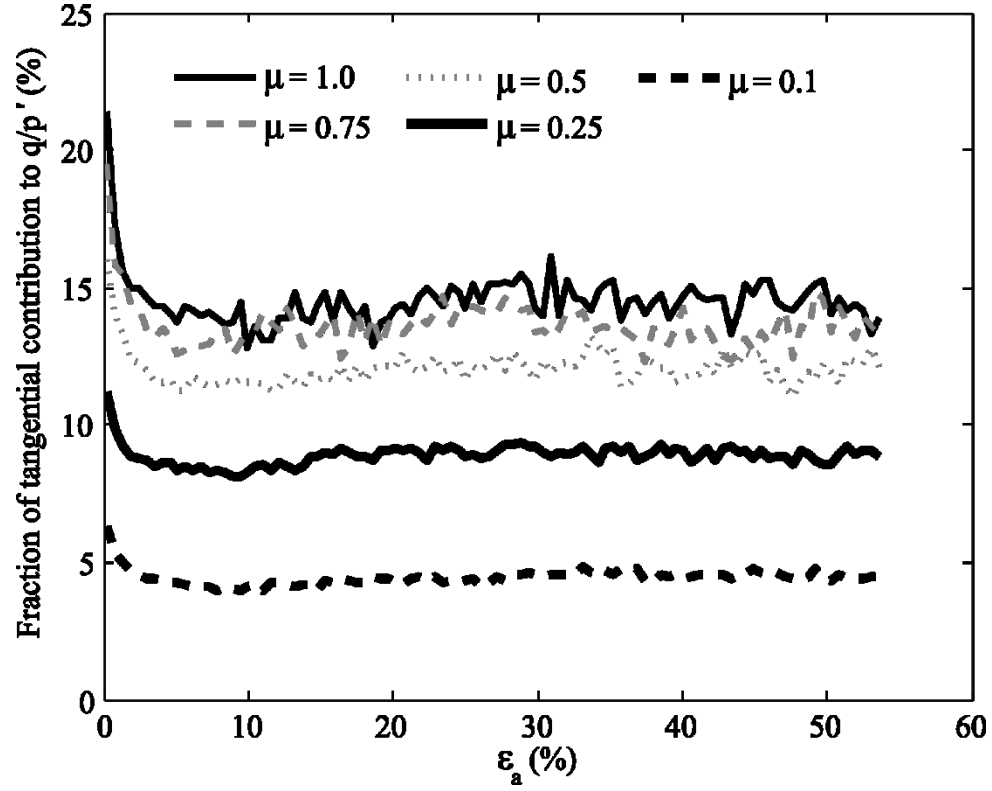



(b)

Figure 4.45 Variation of $f^*$ with shearing for an undrained simulation ($e_0$=0.612, $\sigma'_{3,0}$ =5000 kPa): (a) stress-strain curve; (b) cumulative contribution curves at three characteristic states

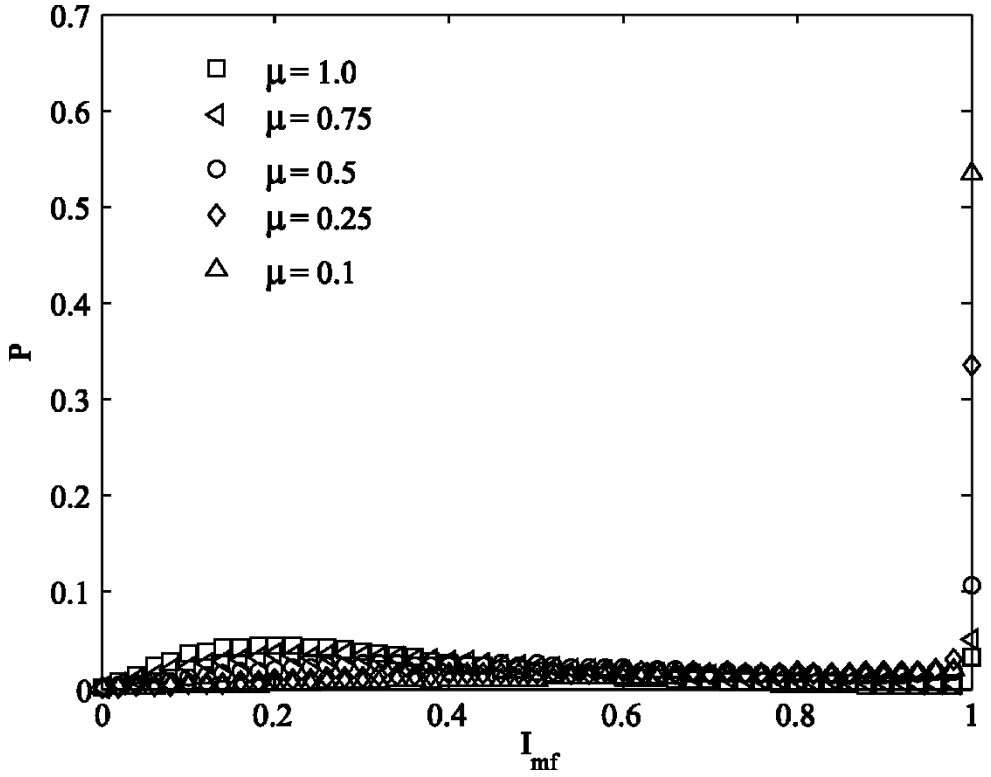



(a) Normal contact force

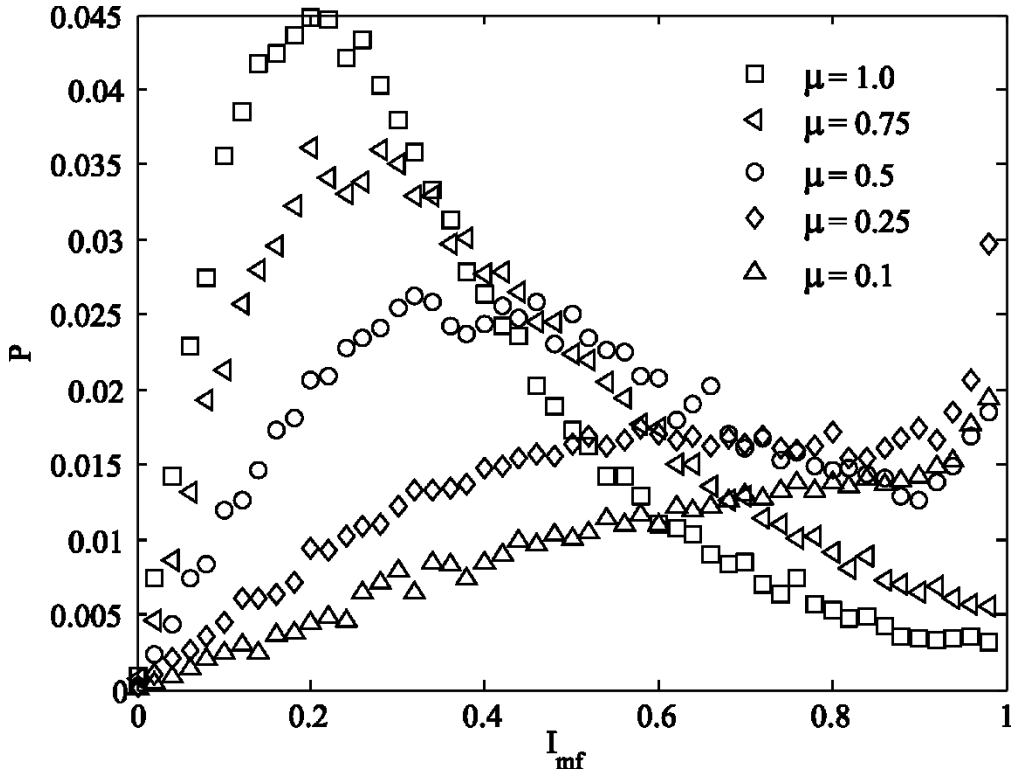



(b) Tangential contact force

Figure 4.46 Evolution of contact force contributions to the stress ratio




(a) $0 \leq I_{mf} \leq 1$




(b) $0 \leq I_{mf} < 1$

Figure 4.47 Probability density distribution of the mobilised friction index for PB samples (Toyoura PSD, $e_0$=0.533 and $\sigma'_3$=100 kPa)

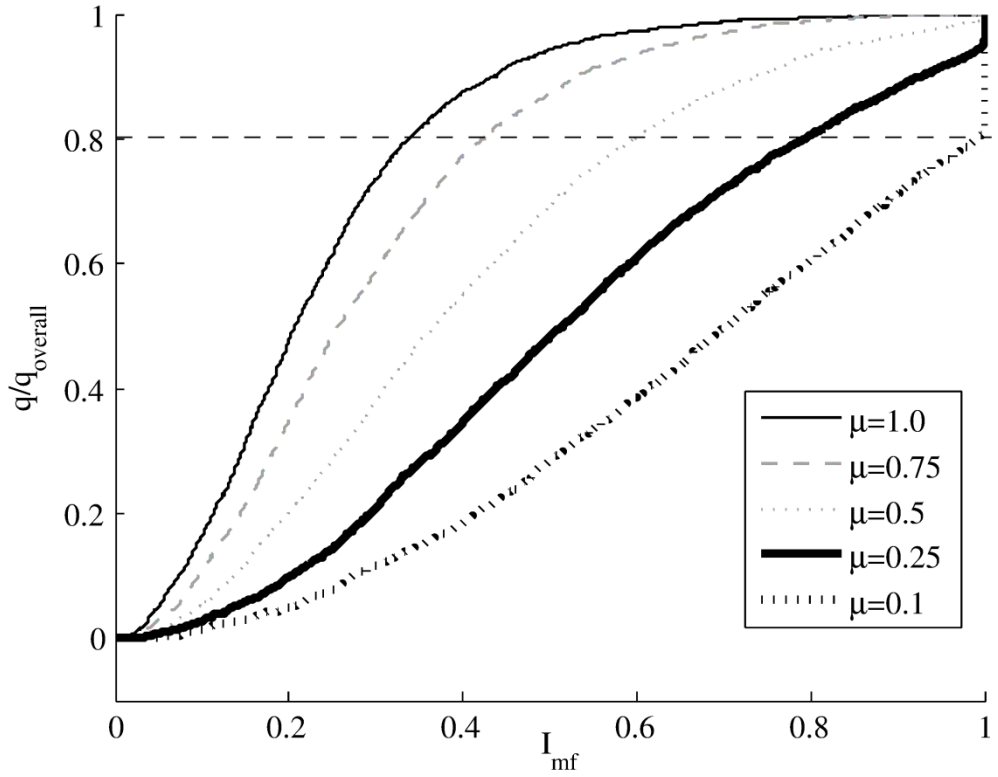



Figure 4.48 Cumulative contribution of single contact to $q$ evaluated by $I_{mf}$

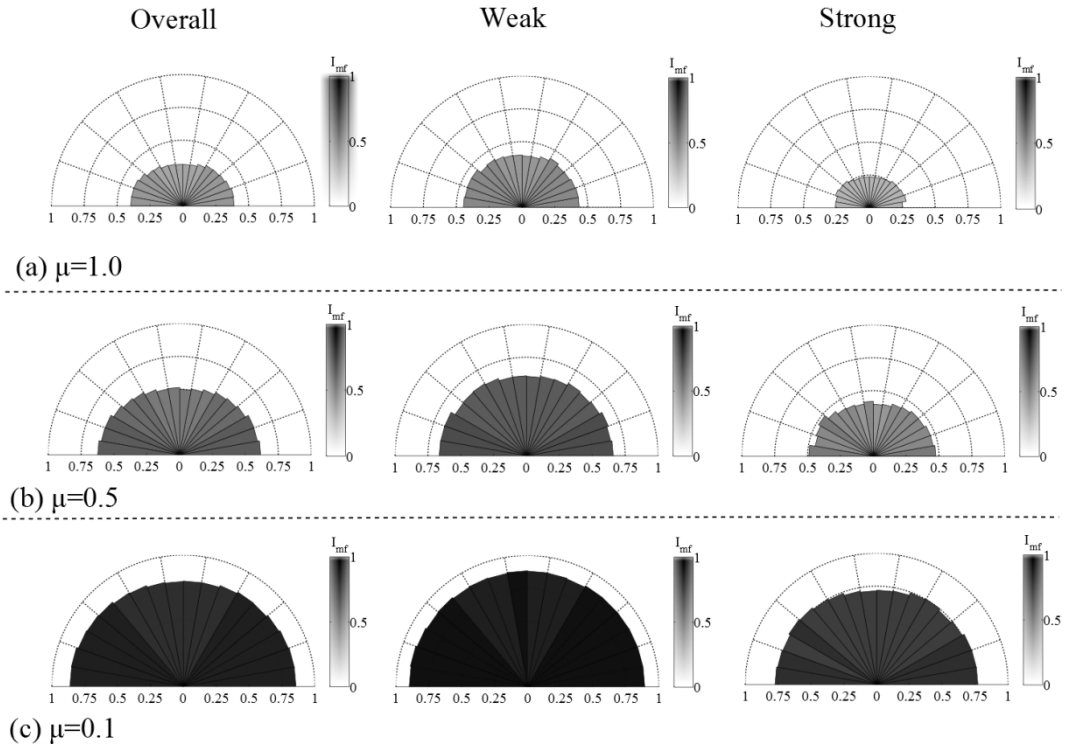
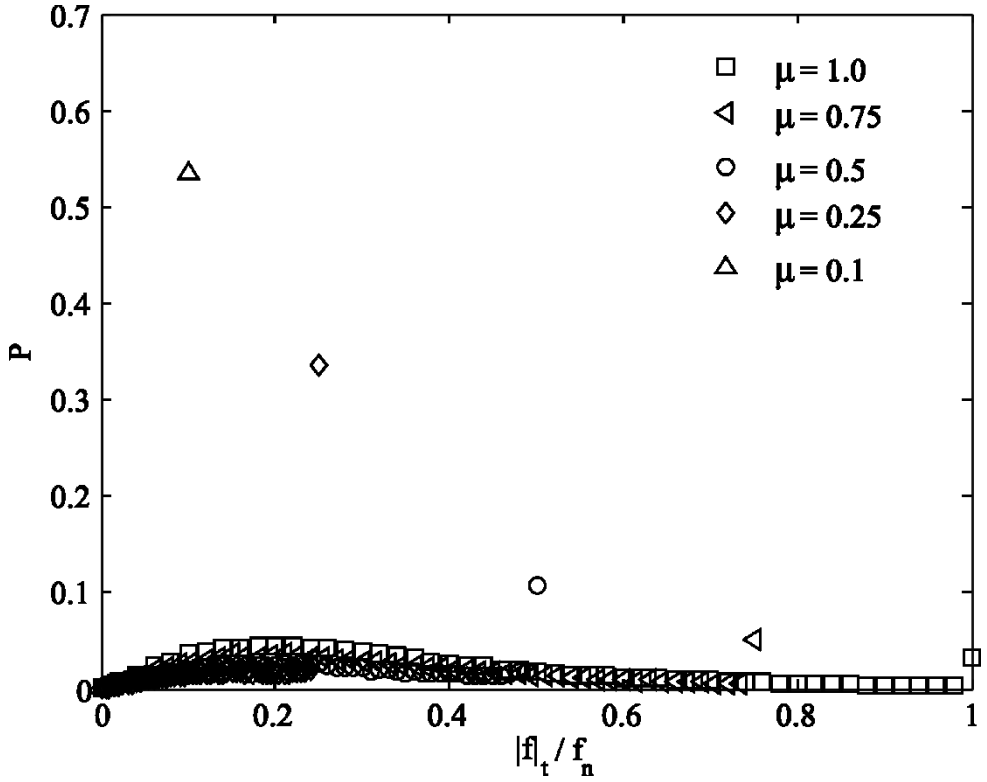
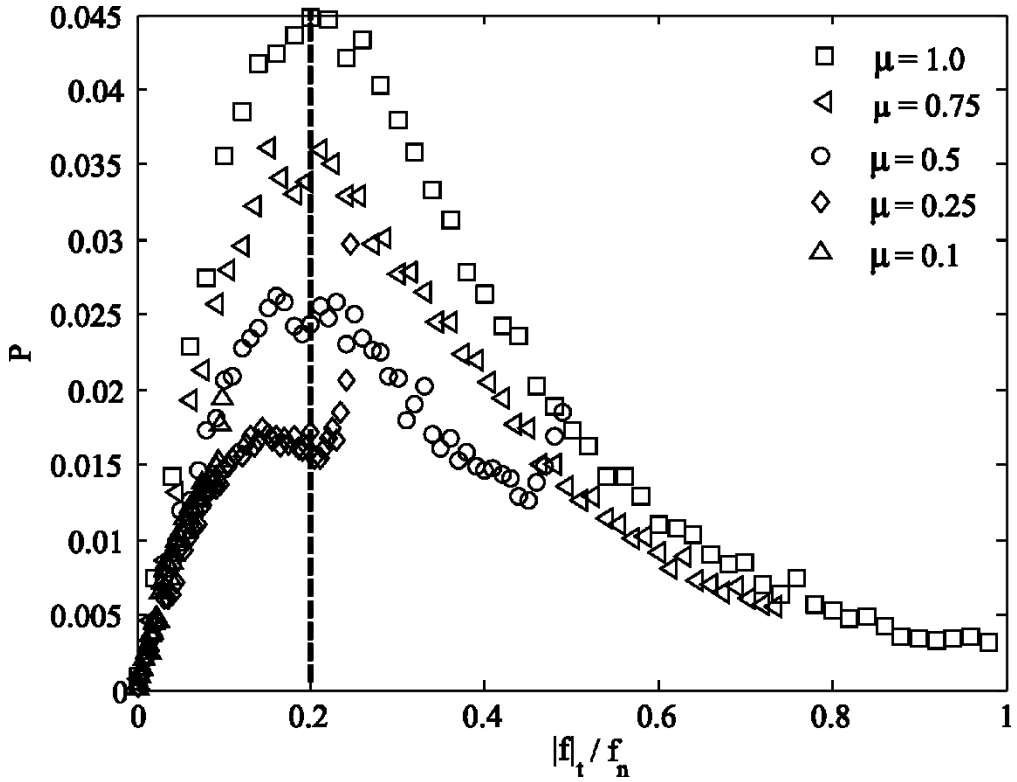



Figure 4.49 Spatial distribution of $I_{mf}$ (Toyoura PSD, $e_0$=0.533 and $\sigma'_3$=100 kPa)

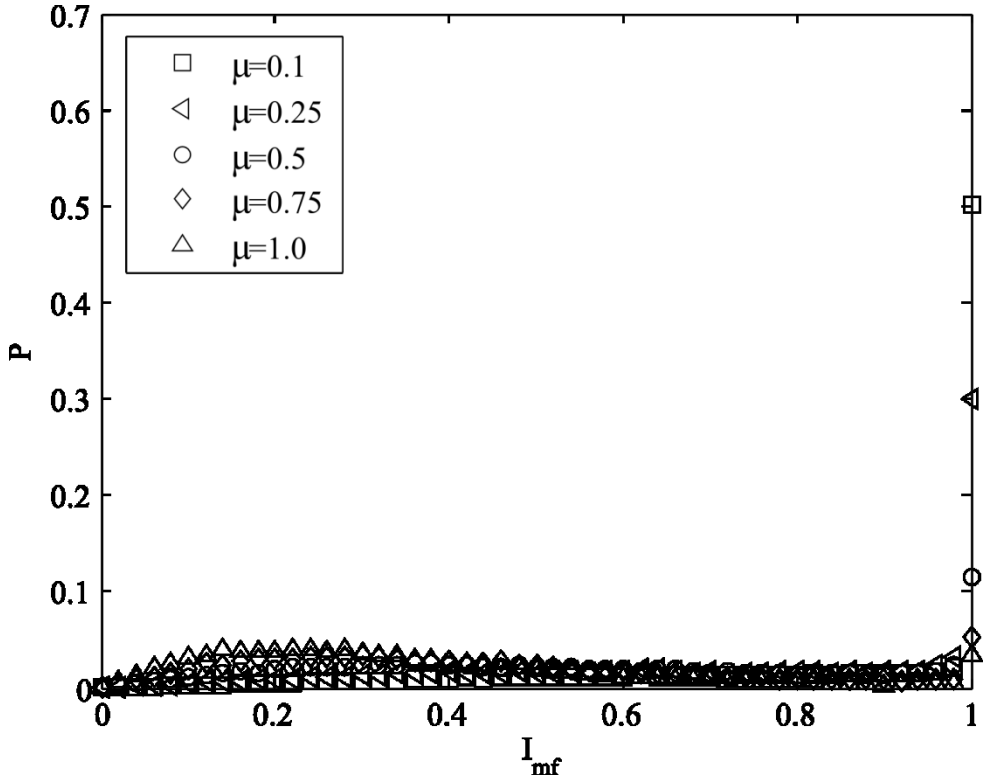



(a) With the tail

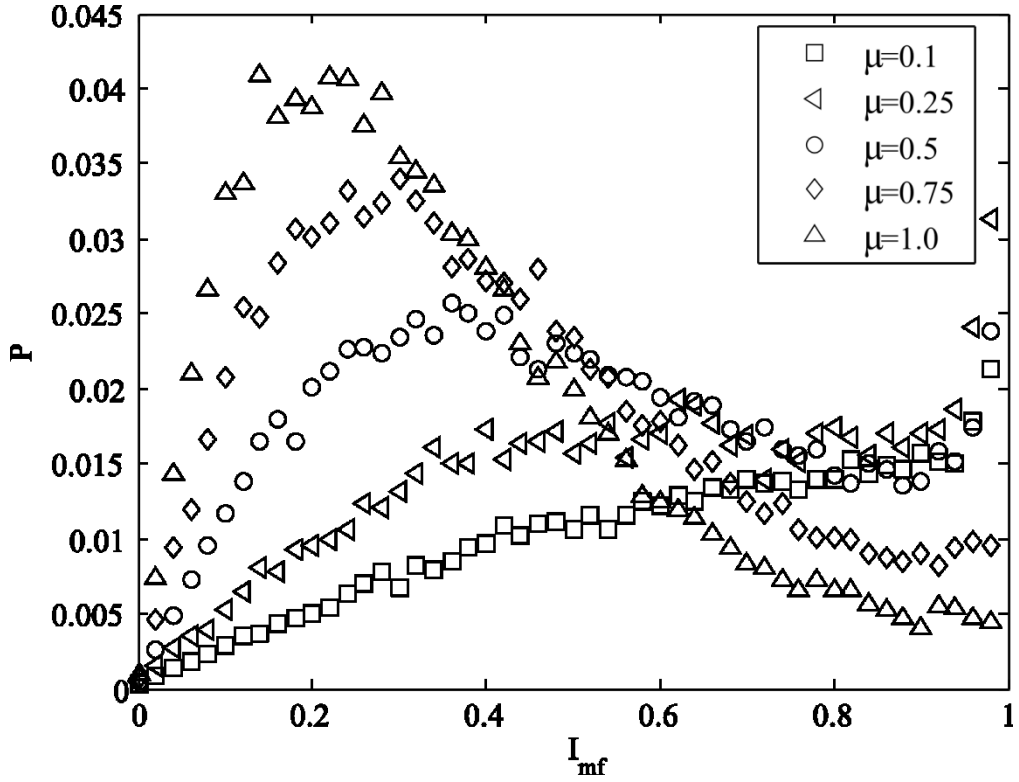



(b) Without the tail

Figure 4.50 Probability density distribution of the shear force ratio for PB samples (Toyoura PSD, $e_0$=0.533 and $\sigma'_3$=100 kPa)

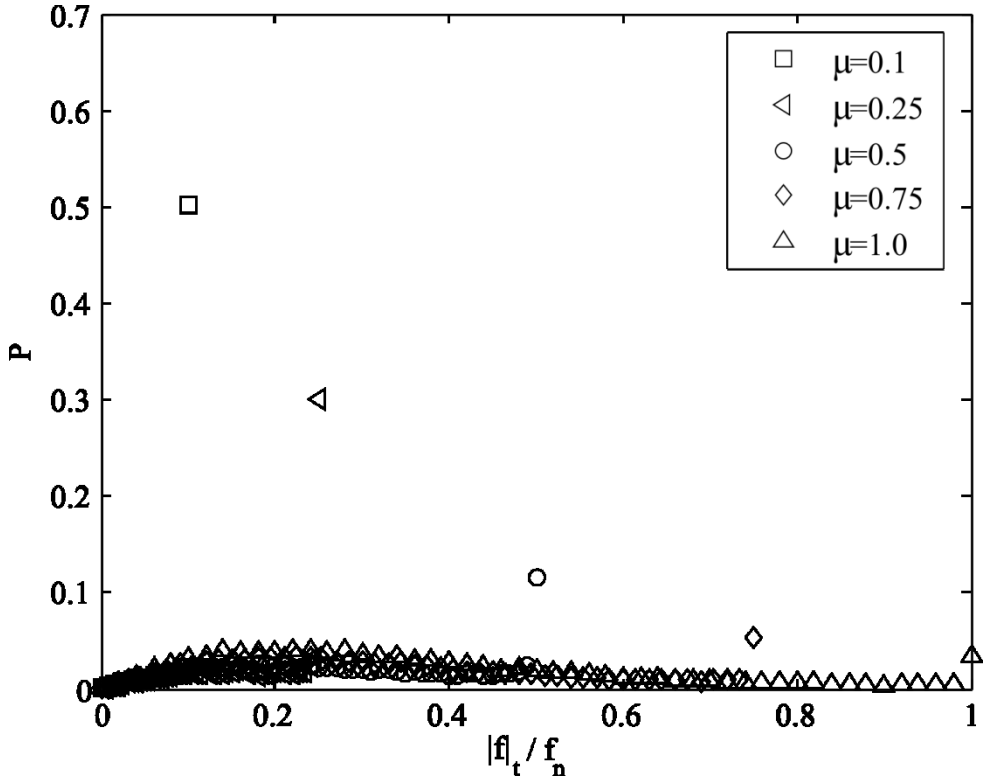



(a) With the tail

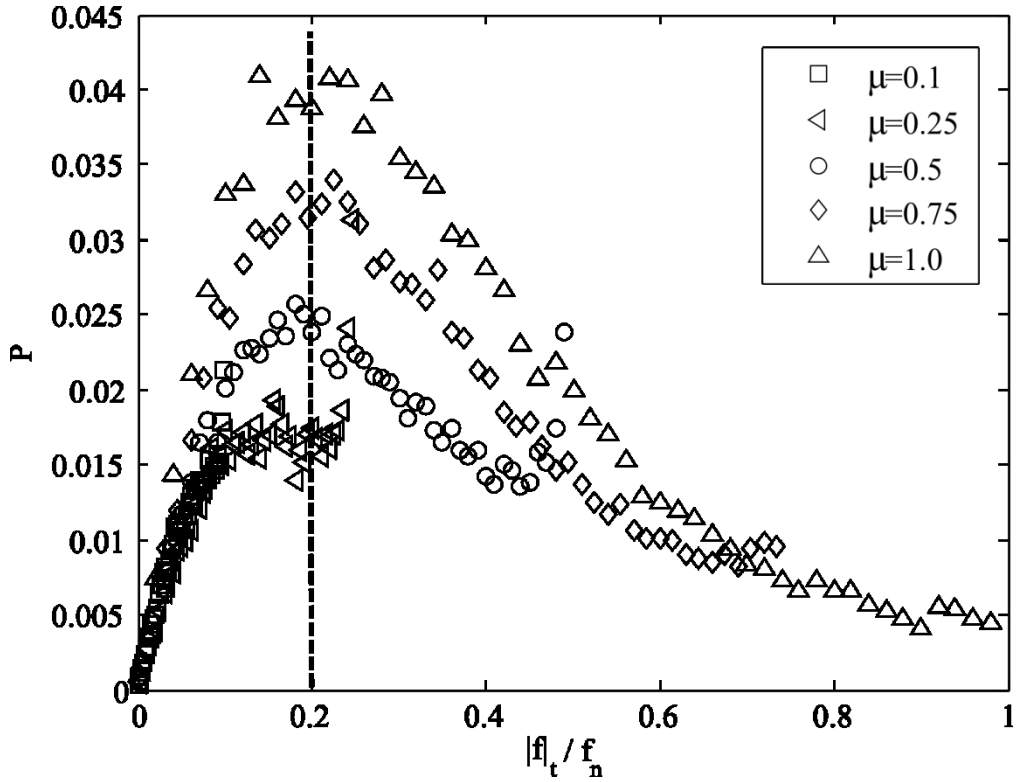



(b) Without the tail

Figure 4.51 Probability density distribution of the mobilised friction index for RW samples ($e_0$=0.648,$\sigma'_3$=500 kPa)

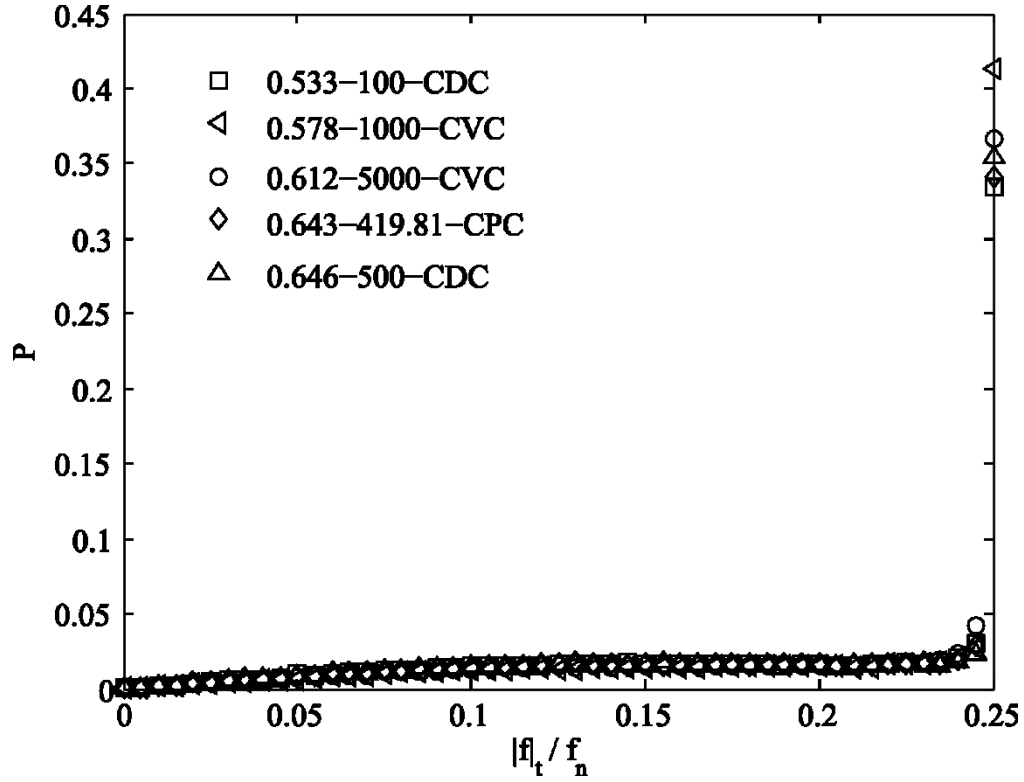



(a) With the tail

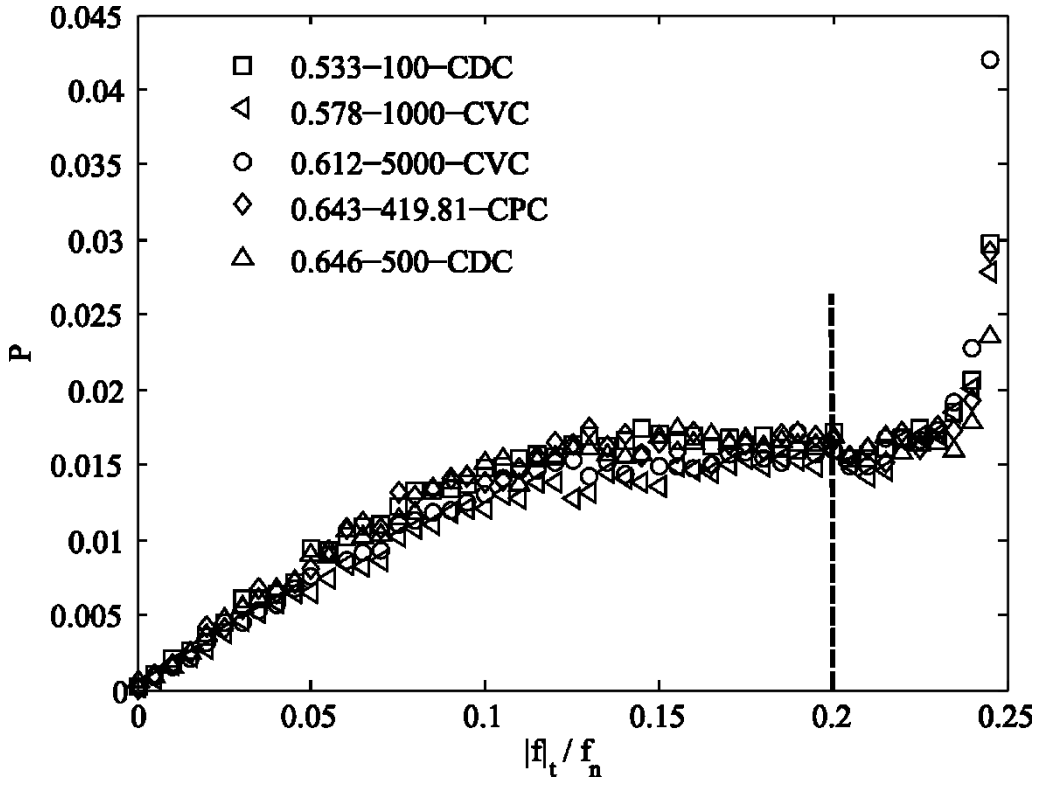



(b) Without the tail

Figure 4.52 Probability density distribution of shear force ratio for RW samples ($e_0$=0.648,$\sigma'_3$=500 kPa)

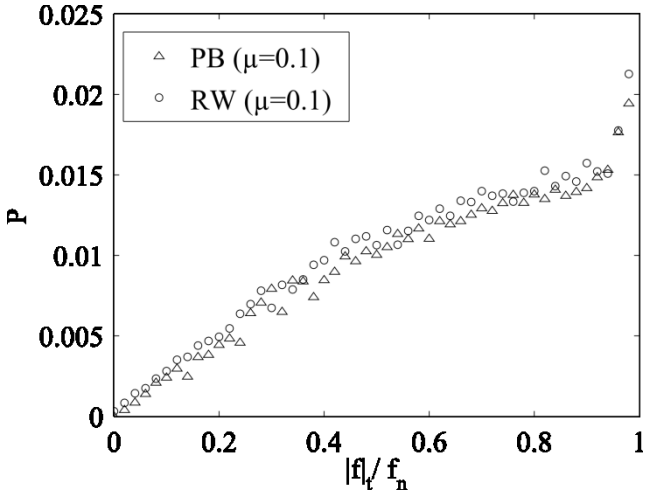



(a) With the tail

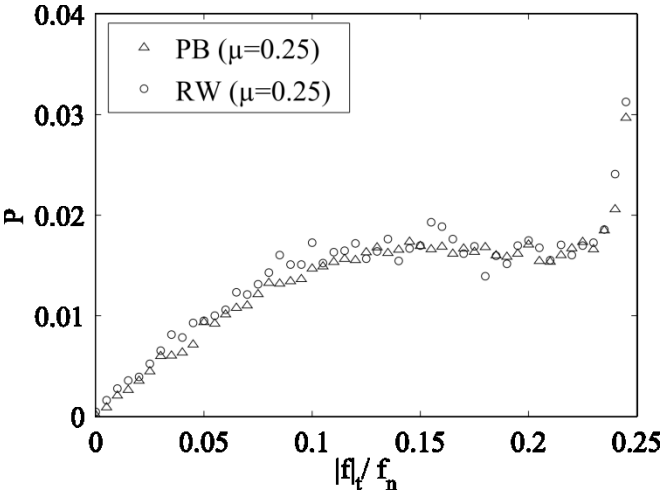



(b) Without the tail

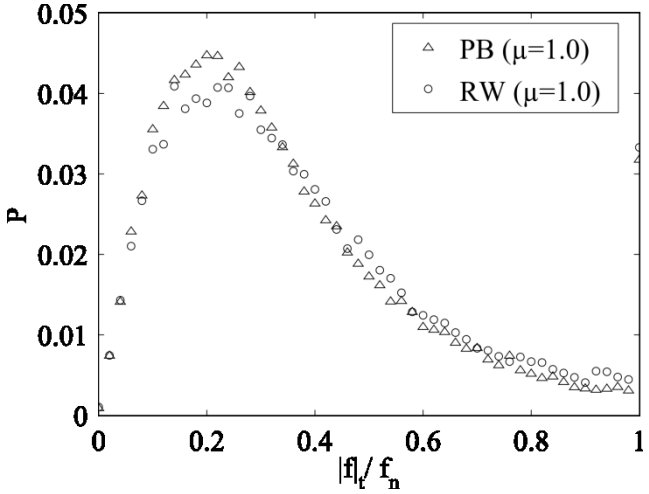
Figure 4.53 Influence of loading conditions and initial packing density on the probability density distribution of shear force ratio for PB samples ($\mu$=0.25)




(a) $\mu$=0.1




(b) $\mu$=0.25




(c) $\mu$=1.0

Figure 4.54 Comparing the probability density distribution of shear force ratio of RW and PB samples

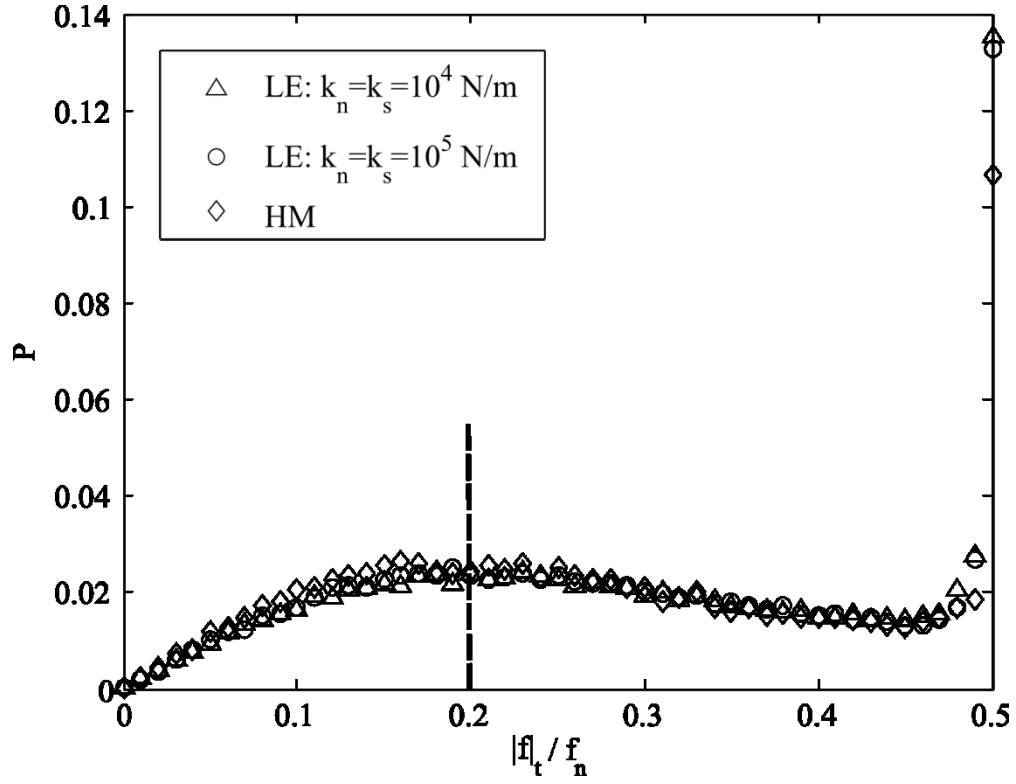



Figure 4.55 Comparing the probability density distribution of shear force ratio of PB samples with different contact models: LE: linear elastic; HM: Hertz-Mindlin (Toyoura grading, $\mu = 0.5$)

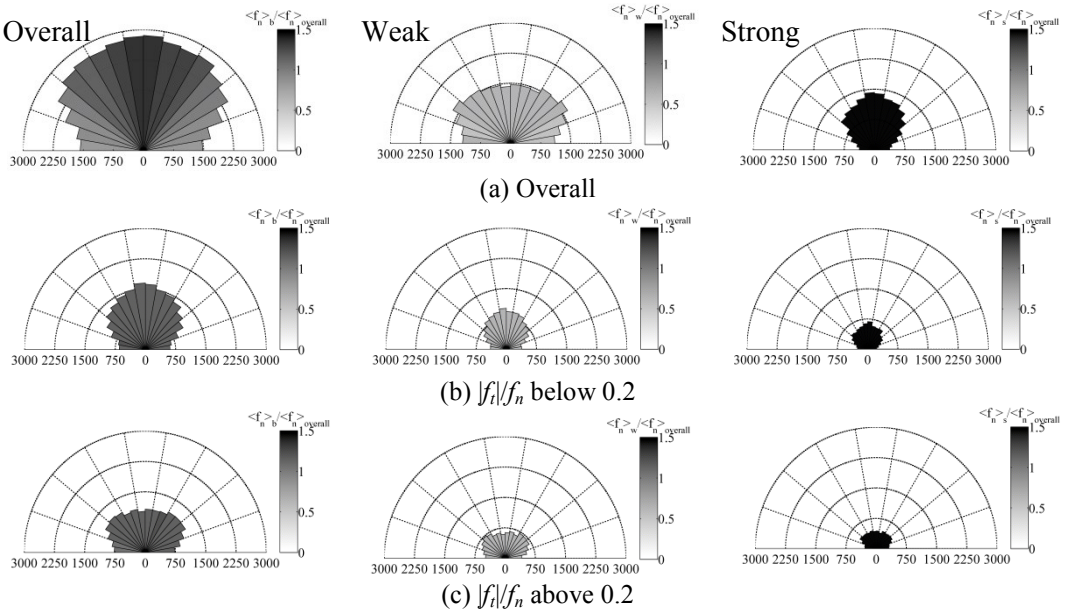



Figure 4.56 Rose diagram on the x-z plane of the isolated contact force network with different shear force ratios (μ=0.25)

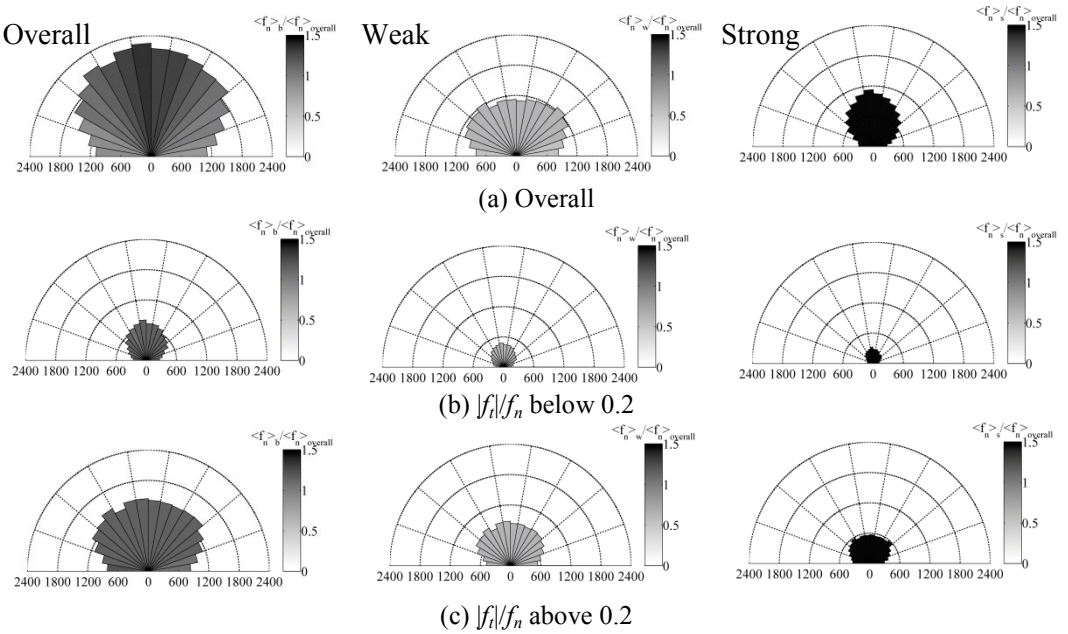
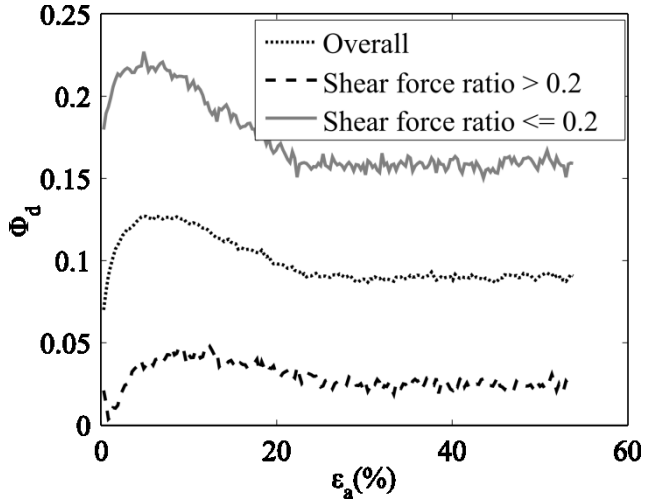
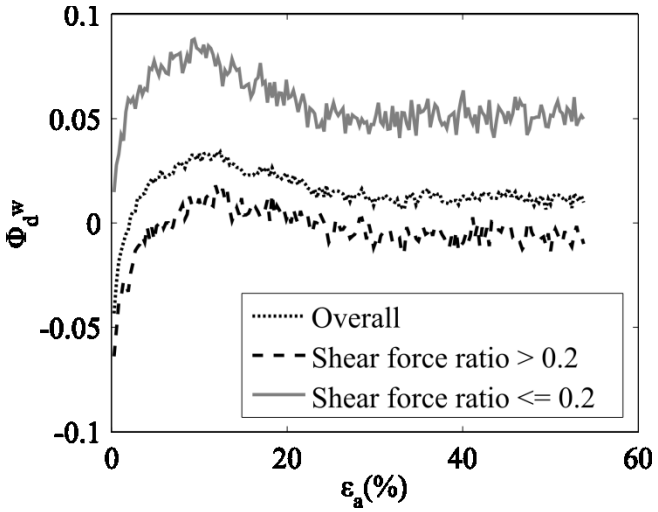


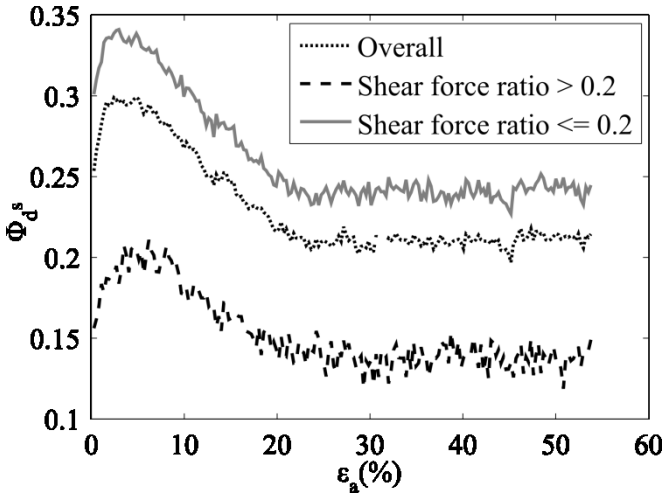

Figure 4.57 Rose diagram on the x-z plane of the isolated contact force network with different shear force ratios ($\mu$=1.0)




(a)

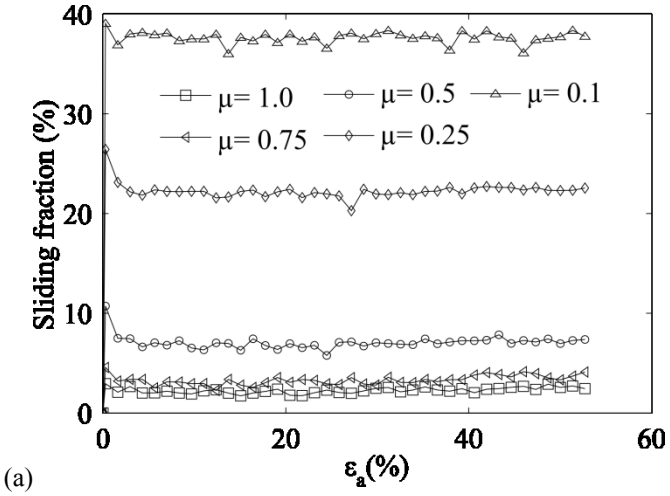



(b)

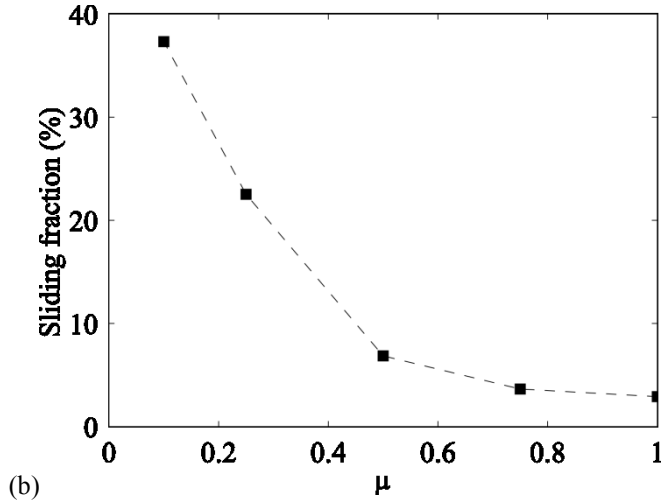



(c)

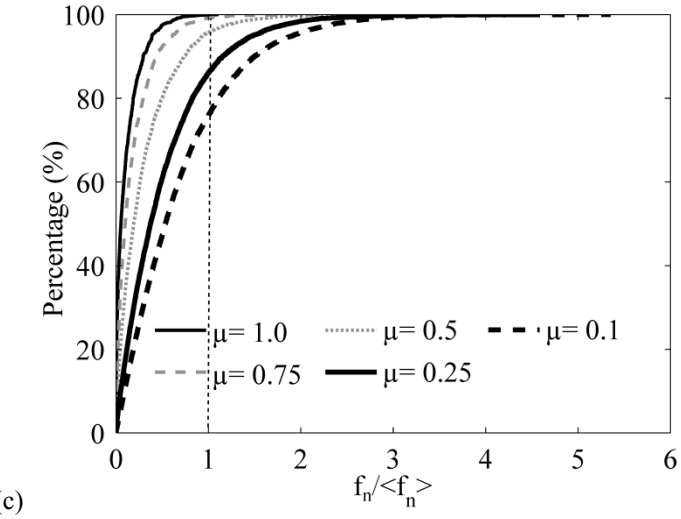
Figure 4.58 Structural anisotropy of two sub-networks with different shear force ratios considering all contacts (PB, Toyoura PSD, $e_0$=0.533,$\sigma'_3$=100 kPa and μ=0.25): (a) Overall; (b) Strong; (c) Weak




(a)

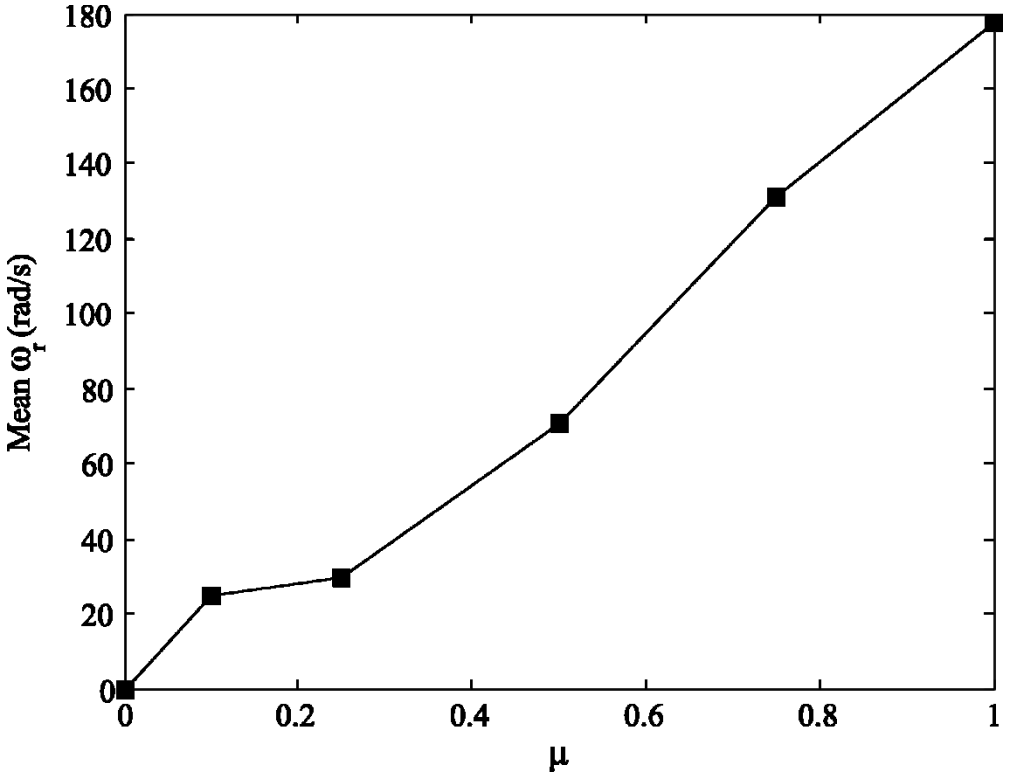



(b)

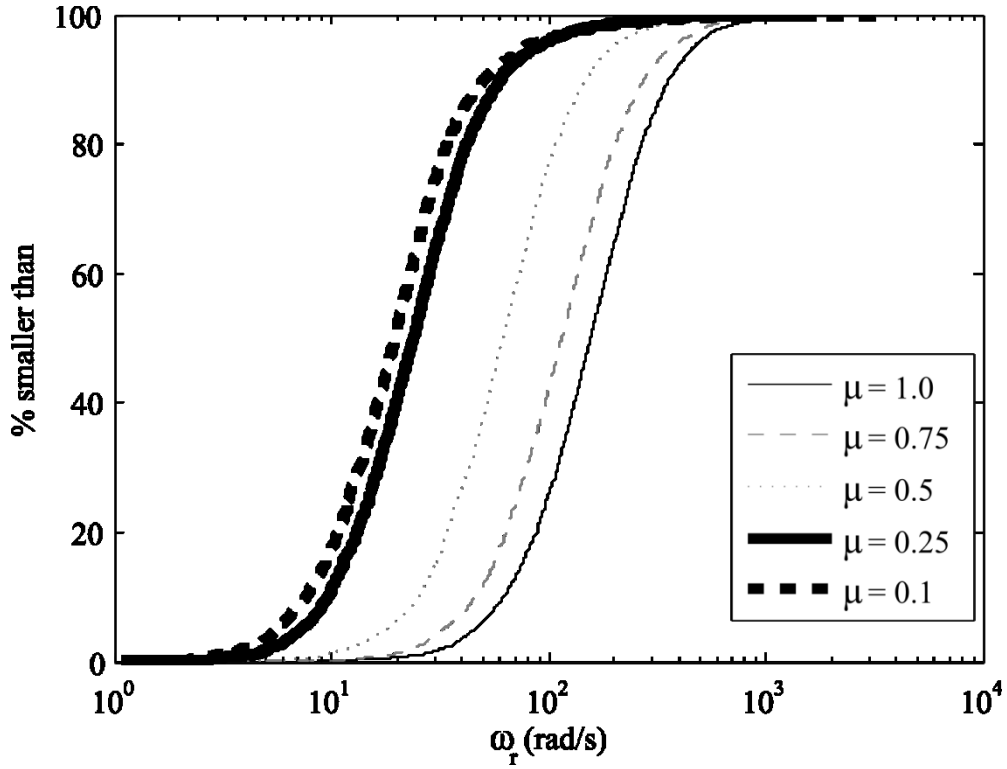



(c)

Figure 4.59 Influence of $\mu$ on the sliding behaviour (PB samples, Toyoura PSD, $e_0$=0.533 and $\sigma'_3$=100 kPa): (a) Evolution of sliding fraction ; (b) Sliding fraction at critical state; (c) Configuration of sliding contact at critical state

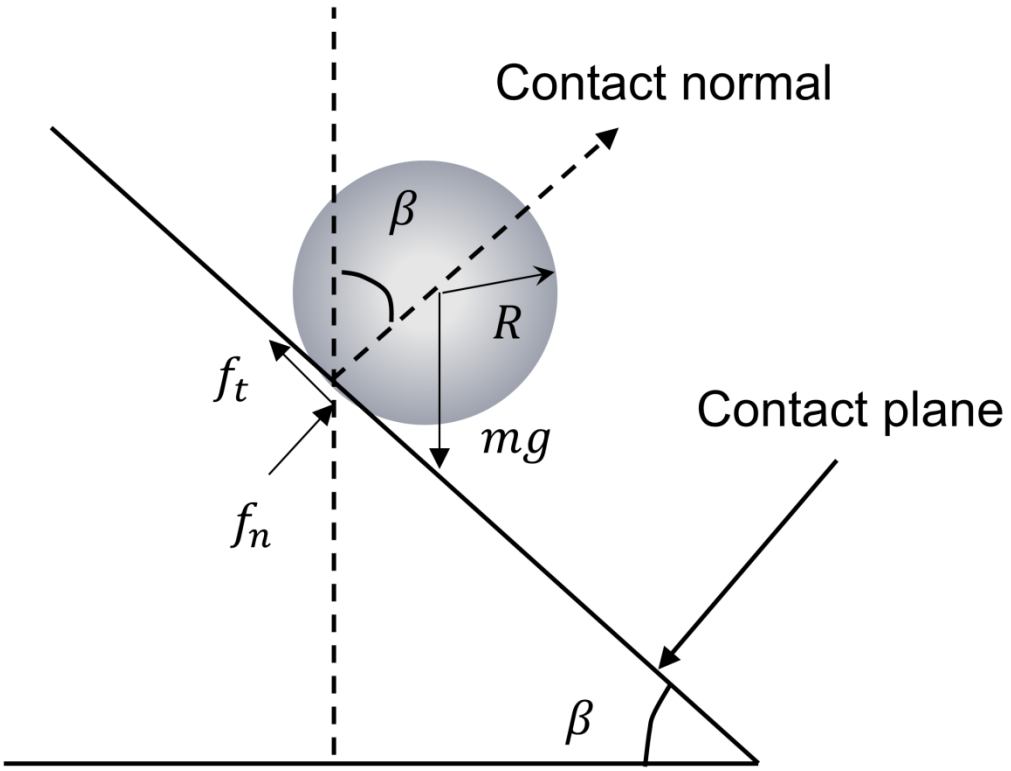



(a)

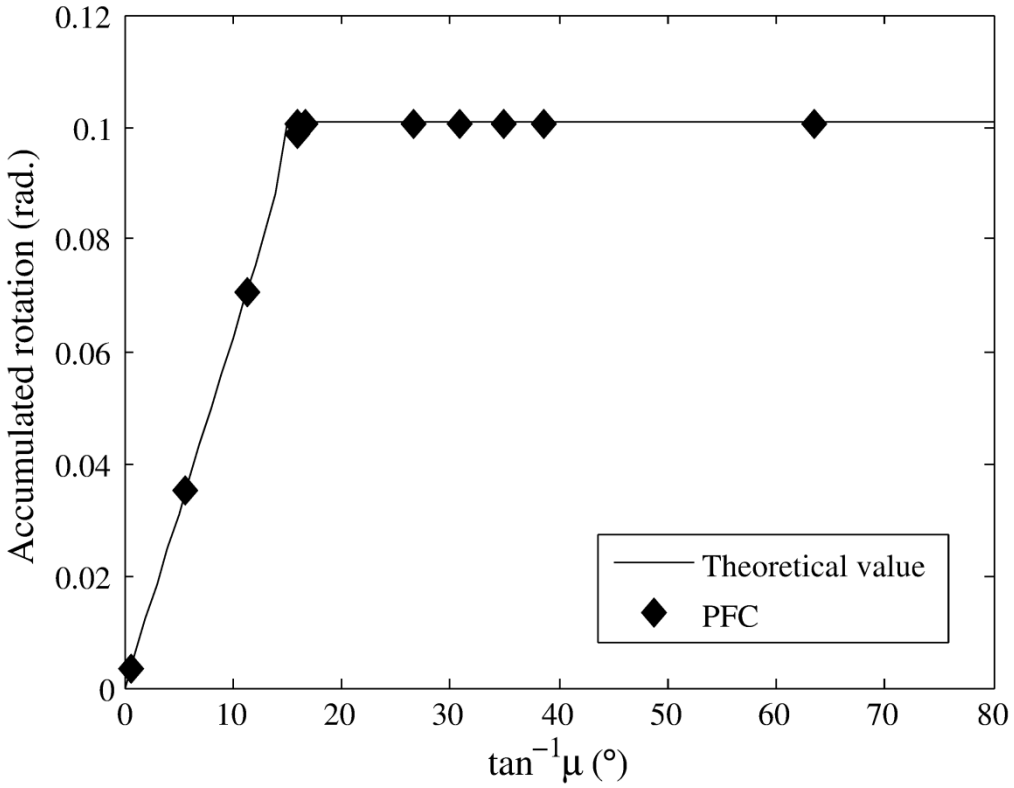



(b)

Figure 4.60 Effect of μ on the angular velocity for LAMMPS simulations, Toyoura PSD ($e_0$ = 0.533 and $\sigma'_3$ = 100 kPa): (a) variation in mean resultant angular velocity with μ at $\varepsilon_a$ = 50% and (b) cumulative distribution of resultant angular velocities at $\varepsilon_a$ = 50%.




(a) Sketch of the simple model




(b) Accumulated rotation after 0.2 s

Figure 4.61 Study the sliding and rolling states of a simple model

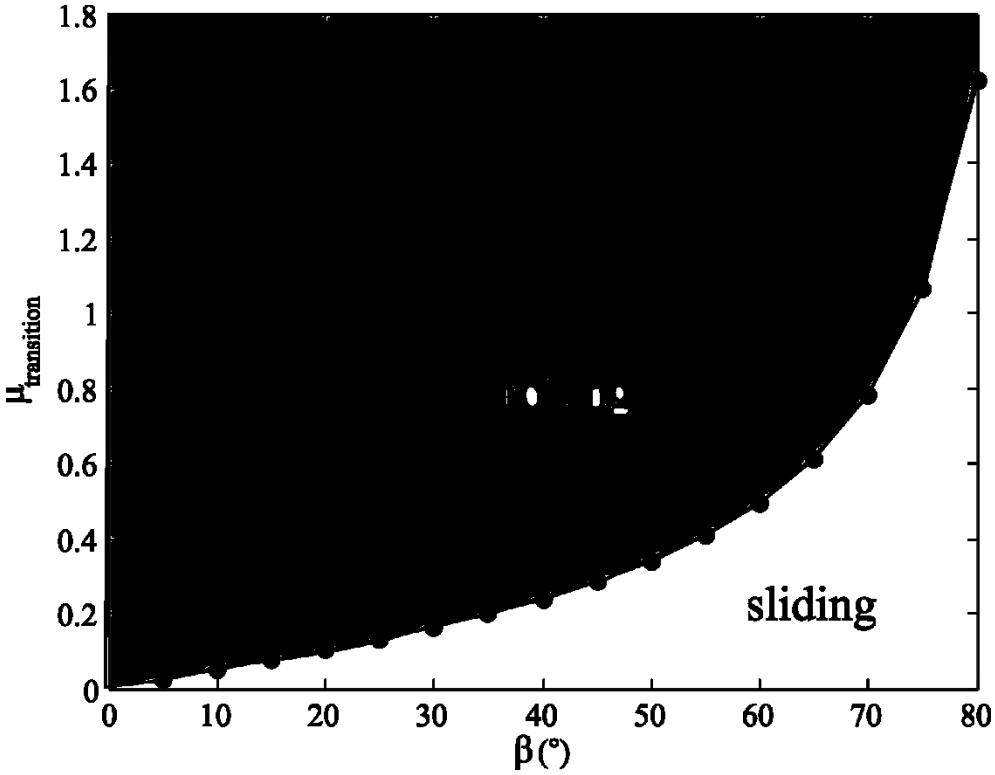
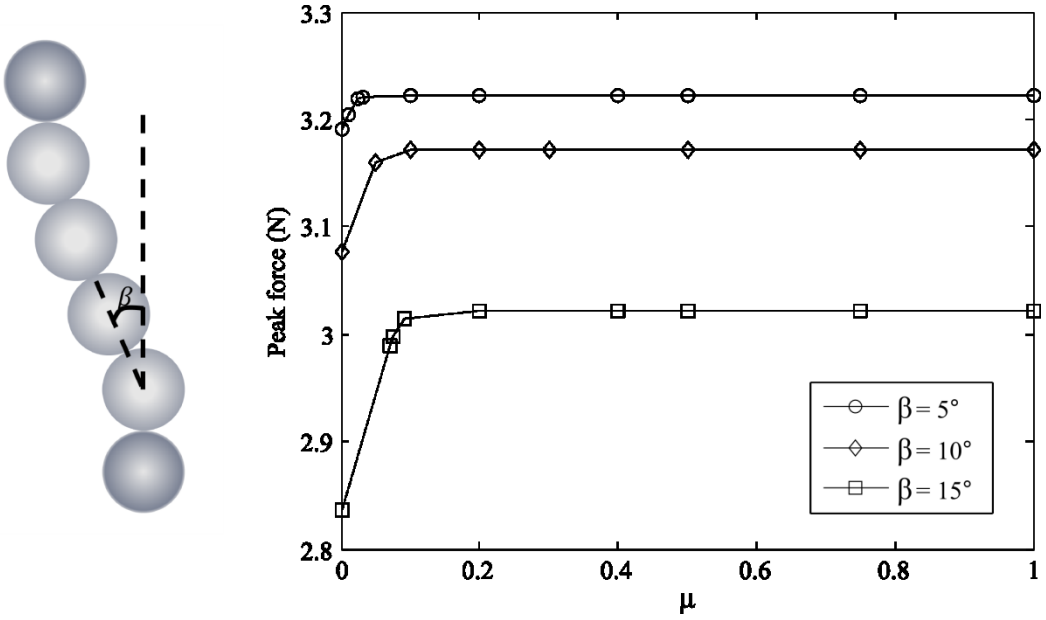
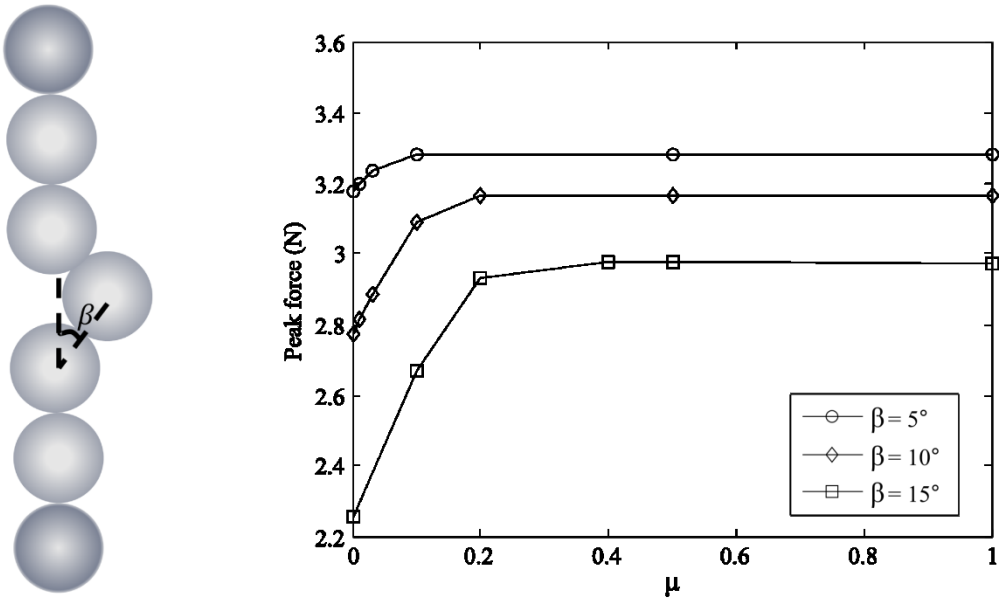



Figure 4.62 Transition between sliding dominant and rolling dominant behaviour




(a) Inclined column




(b) Straight column with a middle perturbation

Figure 4.63 Influence of $\mu$ on the peak force of a single column

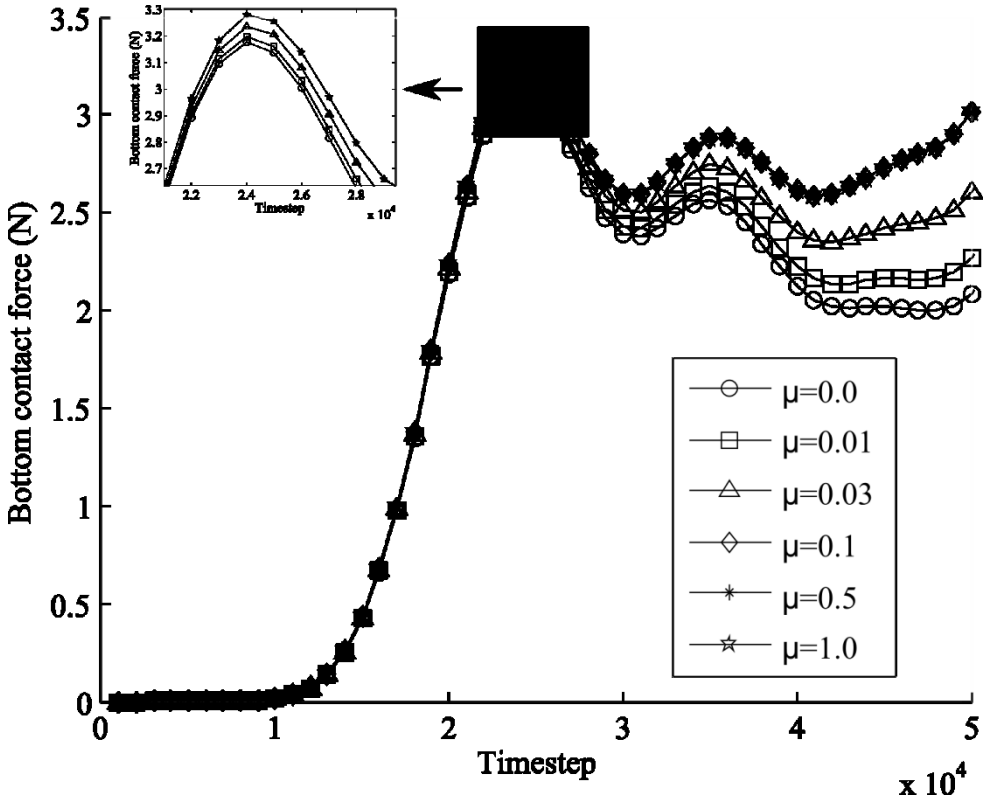



Figure 4.64 A typical force evolution during the simulation of strong force chain buckling (A straight column with a middle deflection, $\beta$=15°)

Table 4.1 Examples of prior research using spherical or elliptical particles and $\mu \geq 0.5$

| | Dimension | Contact models | Boundary conditions | $\mu$ | Number of particles | Particle shape |
|---|---|---|---|---|---|---|
| Pena et al. (2008) | 2D | linear ($k_n$ = 1.6e8 N/m, $k_s/k_n$ = 0.33) | rigid | 0.5 | 900 | polygonal |
| Sitharam (2008) | 3D | linear ( estimate overlap ratio 0.5% to 3%, $G$ = 30 GPa,$v$ = 0.3) | periodic | 0.5 | 1,000 | spherical |
| Ng (2009a) | 3D | HM ($G$ = 29 GPa, $v$ = 0.15) | rigid | 0.5 | 1,170-3,000 | elliptical |
| Fu and Dafalias (2011) | 2D | linear | rigid | 0.7 | ≈ 8,000 | elliptical |
| Yan & Dong (2011) | 3D | linear varying with $r$ ($k_n/r = k_s/r$ = 1/1.2e3 kPa) | rigid | 0.5 | 4,500 - 11,000 | spherical |
| Yimsiri & Soga (2011) | 3D | HM ($G$ = 29 GPa,$v$ = 0.2) | rigid | 1.0 | 3,500-3,900 | spherical |
| Yan & Zhang (2013) | 2D | linear ($k_n = k_s$ = 6 e7 N/m) | rigid | 0.5 | 3,000*3 | clump |
| Guo & Zhao (2013) | 3D | linear varying with $r$ ($k_n/r = k_s/r$ = 100 MPa) | rigid | 0.5 | ≈ 32,000 | spherical |

Table 4.2 Summary of LAMMPS simulations with a simplified Hertz-Mindlin contact model, Toyoura PSD and periodic boundaries

| Simulation ID | $\mu$ | $e_0$ | $\sigma'_3$ (kPa) | Test type | $e_{cs}$ | $\boldsymbol{e^s_{cs}}$ | $p'_{cs}$ (kPa) | $Z_{cs}$ | $Z_{m(cs)}$ | $(\Phi_1 - \Phi_3)_{overall,CS}$ | $(\Phi_1 - \Phi_3)_{strong,CS}$ |
|---|---|---|---|---|---|---|---|---|---|---|---|
| 0.533-100-CDC-1.0 | 1.0 | 0.533 | 100 | CDC | 0.654 | 0.941 | 133.5 | 3.211 | 4.189 | 0.106 | 0.222 |
| 0.591-33216-CPC-1.0 | 1.0 | 0.591 | 33216 | CPC | 0.677 | 0.778 | 33200 | 4.261 | 4.787 | 0.072 | 0.206 |
| 0.628-10000-CDC-1.0 | 1.0 | 0.628 | 10000 | CDC | 0.684 | 0.84 | 13565 | 3.896 | 4.599 | 0.084 | 0.217 |
| 0.649-5000-CPC-1.0 | 1.0 | 0.649 | 5000 | CPC | 0.681 | 0.878 | 5000 | 3.663 | 4.473 | 0.089 | 0.219 |
| 0.658-2000-CDC-1.0 | 1.0 | 0.658 | 2000 | CDC | 0.675 | 0.896 | 2666 | 3.526 | 4.398 | 0.091 | 0.217 |
| 0.667-500-CDC-1.0 | 1.0 | 0.667 | 500 | CDC | 0.664 | 0.929 | 672 | 3.319 | 4.286 | 0.101 | 0.221 |
| 0.533-100-CDC-0.75 | 0.75 | 0.533 | 100 | CDC | 0.653 | - | 130.15 | 3.311 | 4.254 | 0.100 | 0.222 |
| 0.599-30000-CPC-0.75 | 0.75 | 0.599 | 30000 | CPC | 0.663 | - | 30000 | - | - | - | - |
| 0.615-20000-CPC-0.75 | 0.75 | 0.615 | 20000 | CPC | 0.670 | - | 20000 | - | - | - | - |
| 0.628-10000-CDC-0.75 | 0.75 | 0.628 | 10000 | CDC | 0.675 | - | 13542 | - | - | - | - |
| 0.647-5000-CPC-0.75 | 0.75 | 0.647 | 5000 | CPC | 0.674 | - | 5000 | - | - | - | - |
| 0.658-2000-CDC-0.75 | 0.75 | 0.658 | 2000 | CDC | 0.674 | - | 2689 | - | - | - | - |
| 0.667-500-CDC-0.75 | 0.75 | 0.667 | 500 | CDC | 0.663 | - | 670 | - | - | - | - |
| 0.533-100-CDC-0.5 | 0.5 | 0.533 | 100 | CDC | 0.650 | 0.869 | 133.3 | 3.577 | 4.414 | 0.101 | 0.221 |
| 0.618-15000-CDC-0.5 | 0.5 | 0.618 | 15000 | CDC | 0.647 | 0.734 | 20100 | 4.52 | 5.03 | 0.08 | 0.22 |
| 0.621-3000-CDC-0.5 | 0.5 | 0.621 | 3000 | CDC | 0.661 | 0.8 | 3992.1 | 4.05 | 4.72 | 0.091 | 0.217 |
| 0.627-2000-CDC-0.5 | 0.5 | 0.627 | 2000 | CDC | 0.661 | 0.809 | 2666.1 | 3.98 | 4.69 | 0.093 | 0.225 |
| 0.628-10000-CDC-0.5 | 0.5 | 0.628 | 10000 | CDC | 0.653 | 0.754 | 13366 | 4.392 | 4.944 | 0.083 | 0.217 |
| 0.635-500-CVC-0.5 | 0.5 | 0.635 | 500 | CVC | 0.635 | 0.703 | 33216 | 4.71 | 5.14 | 0.076 | 0.22 |
| 0.643-5000-CPC-0.5 | 0.5 | 0.643 | 5000 | CPC | 0.660 | 0.783 | 5000 | 4.143 | 4.761 | 0.089 | 0.224 |
| 0.646-500-CDC-0.5 | 0.5 | 0.646 | 500 | CDC | 0.659 | 0.841 | 663.3 | 3.74 | 4.53 | 0.094 | 0.221 |
| 0.662-1000-CDC-0.5-0.5 | 0.5 | 0.662 | 1000 | CDC | 0.660 | 0.825 | 1331.8 | 3.86 | 4.59 | 0.097 | 0.229 |
| FR-0.724-100-CDC-0.5 | 0.5 | 0.724 | 100 | CDC | 0.792 | - | 294 | - | - | - | - |
| FR-0.718-500-CDC-0.5 | 0.5 | 0.718 | 500 | CDC | 0.789 | - | 1498 | - | - | - | - |
| FR-0.713-1000-CDC-0.5 | 0.5 | 0.713 | 1000 | CDC | 0.792 | - | 2819 | - | - | - | - |
| FR-0.692-5000-CPC-0.5 | 0.5 | 0.692 | 5000 | CPC | 0.788 | - | 5000 | - | - | - | - |
| FR-0.676-10000-CPC | 0.5 | 0.676 | 10000 | CPC | 0.797 | - | 10000 | - | - | - | - |
| 0.533-100-CDC-0.25 | 0.25 | 0.533 | 100 | CDC | 0.630 | 0.755 | 129 | 4.236 | 4.879 | 0.089 | 0.211 |
| 0.578-1000-CVC-0.25 | 0.25 | 0.578 | 1000 | CVC | 0.578 | 0.615 | 35757 | 5.43 | 5.74 | 0.066 | 0.218 |
| 0.579-30000-CPC-0.25 | 0.25 | 0.579 | 30000 | CPC | 0.583 | 0.623 | 30000 | 5.36 | 5.68 | 0.068 | 0.218 |
| 0.586-25000-CPC-0.25 | 0.25 | 0.586 | 25000 | CPC | 0.589 | 0.633 | 25000 | 5.30 | 5.64 | 0.068 | 0.207 |
| 0.594-20000-CPC-0.25 | 0.25 | 0.594 | 20000 | CPC | 0.593 | 0.641 | 20000 | 5.22 | 5.57 | 0.071 | 0.210 |
| 0.599-527-CVC-0.25 | 0.25 | 0.599 | 527 | CVC | 0.599 | 0.650 | 17222 | 5.18 | 5.55 | 0.070 | 0.207 |
| 0.603-1000-CVC-0.25 | 0.25 | 0.603 | 1000 | CVC | 0.603 | 0.656 | 15548 | 5.11 | 5.50 | 0.072 | 0.209 |
| 0.612-10000-CPC-0.25 | 0.25 | 0.612 | 10000 | CPC | 0.612 | 0.674 | 10000 | 4.96 | 5.39 | 0.076 | 0.211 |

Table 4.2 Summary of LAMMPS simulations with a simplified Hertz-Mindlin contact model, Toyoura PSD and periodic boundaries (continued)

| Simulation ID | $\mu$ | $e_0$ | $\sigma'_3$ (kPa) | Test type | $e_{cs}$ | $\boldsymbol{e^s_{cs}}$ | $p'_{cs}$ (kPa) | $Z_{cs}$ | $Z_{m(cs)}$ | $(\Phi_1 - \Phi_3)_{\text{overall,CS}}$ | $(\Phi_1 - \Phi_3)_{\text{strong,CS}}$ |
|---|---|---|---|---|---|---|---|---|---|---|---|
| 0.625-5000-CPC-0.25 | 0.25 | 0.625 | 5000 | CPC | 0.619 | 0.694 | 5000 | 4.79 | 5.27 | 0.079 | 0.215 |
| 0.627-1000-CDC-0.25 | 0.25 | 0.627 | 1000 | CDC | 0.628 | 0.730 | 1290 | 4.48 | 5.07 | 0.083 | 0.206 |
| 0.643-419.81-CPC-0.25 | 0.25 | 0.643 | 419.81 | CPC | 0.632 | 0.746 | 420 | 4.35 | 4.96 | 0.088 | 0.208 |
| 0.646-500-CDC-0.25 | 0.25 | 0.646 | 500 | CDC | 0.629 | 0.737 | 646 | 4.39 | 5.50 | 0.086 | 0.208 |
| 0.646-84.49-CPC-0.25 | 0.25 | 0.646 | 84.49 | CPC | 0.630 | 0.755 | 84 | 4.22 | 4.86 | 0.091 | 0.208 |
| FR-0.694-100-CDC-0.25 | 0.25 | 0.694 | 100 | CDC | 0.71 | - | 171.1 | - | - | - | - |
| FR-0.691-500-CDC-0.25 | 0.25 | 0.691 | 500 | CDC | 0.709 | - | 843.2 | - | - | - | - |
| FR-0.687-1000-CDC-0.25 | 0.25 | 0.687 | 1000 | CDC | 0.706 | - | 1697.6 | - | - | - | - |
| FR-0.669-5000-CPC-0.25 | 0.25 | 0.669 | 5000 | CPC | 0.697 | - | 5000 | - | - | - | - |
| FR-0.654-10000-CPC-0.25 | 0.25 | 0.654 | 10000 | CPC | 0.685 | - | 10000 | - | - | - | - |
| 0.529-500-CVC-0.1 | 0.1 | 0.529 | 500 | CVC | 0.529 | 0.547 | 31743 | 6.18 | 6.37 | 0.051 | 0.172 |
| 0.533-100-CDC-0.1 | 0.1 | 0.533 | 100 | CDC | 0.590 | 0.661 | 121 | 4.962 | 5.442 | 0.069 | 0.173 |
| 0.577-10000-CPC-0.1 | 0.1 | 0.577 | 10000 | CPC | 0.562 | 0.597 | 10000 | 5.70 | 6.01 | 0.056 | 0.173 |
| 0.578-1000-CVC-0.1 | 0.1 | 0.578 | 1000 | CVC | 0.578 | 0.627 | 3366 | 5.40 | 5.78 | 0.062 | 0.174 |
| 0.578-1000-CDC-0.1 | 0.1 | 0.578 | 1000 | CDC | 0.584 | 0.642 | 1214 | 5.21 | 5.63 | 0.066 | 0.174 |
| 0.598-5000-CPC-0.1 | 0.1 | 0.598 | 5000 | CPC | 0.576 | 0.616 | 5000 | 5.53 | 5.86 | 0.060 | 0.170 |

Table 4.3 Summary of PFC3D simulations with a simplified Hertz-Mindlin contact model, Toyoura PSD and rigid boundaries (RW=rigid wall boundaries using PFC3D code)

| Simulation ID | $\mu$ | $e_0$ | $\sigma'_3$ (kPa) | Test type | $e_{cs}$ | $\boldsymbol{e^s_{cs}}$ | $p'_{cs}$ (kPa) | $Z_{cs}$ | $Z_{m(cs)}$ | $(\Phi_1 - \Phi_3)_{overall}$ | $(\Phi_1 - \Phi_3)_{strong}$ |
|---|---|---|---|---|---|---|---|---|---|---|---|
| RW-0.648-500-CDC-1.0 | 1.0 | 0.648 | 500 | CDC | 0.675 | 0.935 | 662 | 3.2447 | 4.1729 | 0.091 | 0.215 |
| RW-0.648-500-CDC-0.75 | 0.75 | 0.648 | 500 | CDC | 0.673 | 0.914 | 670 | 3.3543 | 4.2445 | 0.092 | 0.221 |
| RW-0.651-100-CDC-0.5 | 0.5 | 0.651 | 100 | CDC | 0.653 | 0.875 | 132.3 | 3.4325 | 4.2853 | 0.091 | 0.214 |
| RW-0.648-500-CDC-0.5 | 0.5 | 0.648 | 500 | CDC | 0.662 | 0.833 | 660 | 3.634 | 4.4056 | 0.088 | 0.220 |
| RW-0.692-1000-CDC-0.5 | 0.5 | 0.692 | 1000 | CDC | 0.672 | 0.843 | 1311 | 3.7224 | 4.4609 | 0.084 | 0.218 |
| RW-0.627-5000-CDC-0.5 | 0.5 | 0.627 | 5000 | CDC | 0.67 | 0.788 | 6580 | 4.0375 | 4.6698 | 0.077 | 0.211 |
| RW-0.648-500-CDC-0.25 | 0.25 | 0.648 | 500 | CDC | 0.629 | 0.738 | 664 | 4.1769 | 4.809 | 0.078 | 0.204 |
| RW-0.648-500-CVC-0.25 | 0.25 | 0.648 | 500 | CVC | 0.649 | 0.7 | 5988 | 4.5685 | 5.0934 | 0.066 | 0.201 |
| RW-0.601-100-CVC-0.25 | 0.25 | 0.601 | 100 | CVC | 0.604 | 0.614 | 36832 | 5.2203 | 5.5419 | 0.058 | 0.202 |
| RW-0.596-1000-CPC-0.25 | 0.25 | 0.596 | 1000 | CPC | 0.631 | 0.739 | 1000 | 4.2406 | 4.8528 | 0.074 | 0.208 |
| RW-0.581-5000-CPC-0.25 | 0.25 | 0.581 | 5000 | CPC | 0.621 | 0.703 | 5000 | 4.5371 | 5.0731 | 0.069 | 0.200 |
| RW-0.648-500-CDC-0.1 | 0.1 | 0.648 | 500 | CDC | 0.597 | 0.670 | 609 | 4.8071 | 5.2997 | 0.021 | 0.167 |

Table 4.4 Summary of simulations with the LE contact model and Toyoura PSD (RW=rigid wall boundaries using PFC3D code)

| Simulation ID | $k_n$=$k_s$(N/m) | $\mu$ | $e_0$ | $\sigma'_3$ (kPa) | Test type | $e_{cs}$ | $\boldsymbol{e^s_{cs}}$ | $p'_{cs}$ (kPa) | $Z_{cs}$ | $Z_{m(cs)}$ | $(\Phi_1 - \Phi_3)_{overall}$ | $(\Phi_1 - \Phi_3)_{strong}$ |
|---|---|---|---|---|---|---|---|---|---|---|---|---|
| 0.662-50-CDC-0.5 | $10^5$ | 0.5 | 0.662 | 50 | CDC | 0.652 | 0.864 | 66.13 | 3.520 | 4.355 | 0.105 | 0.228 |
| 0.666-100-CDC-0.5 | $10^5$ | 0.5 | 0.666 | 100 | CDC | 0.654 | 0.860 | 132.22 | 3.576 | 4.396 | 0.104 | 0.222 |
| 0.659-500-CDC-0.5 | $10^5$ | 0.5 | 0.659 | 500 | CDC | 0.664 | 0.830 | 669.22 | 3.856 | 4.601 | 0.095 | 0.230 |
| 0.651-1000-CDC-0.5 | $10^5$ | 0.5 | 0.651 | 1000 | CDC | 0.664 | 0.798 | 1336.1 | 4.060 | 4.715 | 0.089 | 0.225 |
| 0.603-5000-CDC-0.5 | $10^5$ | 0.5 | 0.603 | 5000 | CDC | 0.624 | 0.680 | 6712.4 | 4.849 | 5.224 | 0.075 | 0.227 |
| 0.663-10-CDC-0.5 | $10^4$ | 0.5 | 0.663 | 10 | CDC | 0.655 | 0.869 | 13.26 | 3.527 | 4.375 | 0.102 | 0.220 |
| 0.667-20-CDC-0.5 | $10^4$ | 0.5 | 0.667 | 20 | CDC | 0.660 | 0.842 | 26.49 | 3.699 | 4.464 | 0.101 | 0.231 |
| 0.662-50-CDC-0.5 | $10^4$ | 0.5 | 0.662 | 50 | CDC | 0.665 | 0.819 | 66.47 | 3.908 | 4.604 | 0.094 | 0.230 |
| 0.658-75-CDC-0.5 | $10^4$ | 0.5 | 0.658 | 75 | CDC | 0.665 | 0.803 | 99.82 | 4.006 | 4.653 | 0.092 | 0.228 |
| 0.654-100-CDC-0.5 | $10^4$ | 0.5 | 0.654 | 100 | CDC | 0.662 | 0.796 | 134.09 | 4.080 | 4.711 | 0.090 | 0.220 |
| 0.605-500-CDC-0.5 | $10^4$ | 0.5 | 0.605 | 500 | CDC | 0.626 | 0.682 | 675.63 | 4.864 | 5.228 | 0.073 | 0.220 |
| 0.647-50-CDC-0.25 | $10^5$ | 0.25 | 0.647 | 50 | CDC | 0.632 | 0.759 | 64.3 | 4.178 | 4.833 | 0.092 | 0.215 |
| 0.646-100-CDC-0.25 | $10^5$ | 0.25 | 0.646 | 100 | CDC | 0.631 | 0.753 | 129.0 | 4.228 | 4.868 | 0.091 | 0.210 |
| 0.640-500-CDC-0.25 | $10^5$ | 0.25 | 0.640 | 500 | CDC | 0.630 | 0.724 | 646.0 | 4.523 | 5.060 | 0.083 | 0.213 |
| 0.633-1000-CDC-0.25 | $10^5$ | 0.25 | 0.633 | 1000 | CDC | 0.624 | 0.703 | 1302.4 | 4.725 | 5.212 | 0.083 | 0.214 |
| RW-0.651-10-CDC-0.5 | $10^5$ | 0.5 | 0.651 | 10 | CDC | 0.648 | 0.898 | 13.69 | 3.257 | 4.187 | 0.108 | 0.215 |
| RW-0.721-10-CDC-0.5 | $10^5$ | 0.5 | 0.721 | 10 | CDC | 0.652 | 0.911 | 13.78 | 3.265 | 4.181 | 0.097 | 0.227 |
| RW-0.651-50-CDC-0.5 | $10^5$ | 0.5 | 0.651 | 50 | CDC | 0.655 | 0.870 | 67.33 | 3.389 | 4.289 | 0.092 | 0.214 |
| RW-0.650-100-CDC-0.5 | $10^5$ | 0.5 | 0.650 | 100 | CDC | 0.660 | 0.868 | 129.3 | 3.521 | 4.359 | 0.091 | 0.217 |
| RW-0.636-500-CDC-0.5 | $10^5$ | 0.5 | 0.636 | 500 | CDC | 0.662 | 0.806 | 666.6 | 3.888 | 4.587 | 0.083 | 0.219 |
| RW-0.621-1000-CDC-0.5 | $10^5$ | 0.5 | 0.621 | 1000 | CDC | 0.659 | 0.776 | 1326 | 4.130 | 4.746 | 0.078 | 0.224 |
| RW-0.664-10-CDC-0.25 | $10^5$ | 0.25 | 0.664 | 10 | CDC | 0.632 | 0.777 | 13.10 | 3.895 | 4.606 | 0.083 | 0.201 |
| RW-0.671-50-CDC-0.25 | $10^5$ | 0.25 | 0.671 | 50 | CDC | 0.633 | 0.768 | 65.12 | 4.007 | 4.712 | 0.079 | 0.201 |
| RW-0.672-100-CDC-0.25 | $10^5$ | 0.25 | 0.672 | 100 | CDC | 0.635 | 0.759 | 129.45 | 4.086 | 4.769 | 0.078 | 0.204 |
| RW-0.672-500-CDC-0.25 | $10^5$ | 0.25 | 0.672 | 500 | CDC | 0.628 | 0.720 | 647.79 | 4.443 | 5.026 | 0.071 | 0.212 |
| RW-0.668-1000-CDC-0.25 | $10^5$ | 0.25 | 0.668 | 1000 | CDC | 0.614 | 0.683 | 1296.69 | 4.708 | 5.197 | 0.068 | 0.209 |
| RW-0.598-5000-CDC-0.25 | $10^5$ | 0.25 | 0.598 | 5000 | CDC | 0.523 | 0.545 | 6470.03 | 5.704 | 5.912 | 0.051 | 0.216 |

Table 4.5 Summary of LAMMPS simulations with the simplified Hertz-Mindlin contact model, Dunkirk PSD, and periodic boundaries

| Simulation ID | $\mu$ | $e_0$ | $\sigma'_3$ (kPa) | Test type | $e_{cs}$ | $\boldsymbol{e^s_{cs}}$ | $p'_{cs}$ (kPa) | $Z_{cs}$ | $Z_{m(cs)}$ | $(\Phi_1 - \Phi_3)_{overall}$ | $(\Phi_1 - \Phi_3)_{strong}$ |
|---|---|---|---|---|---|---|---|---|---|---|---|
| 0.493-50- CDC-0.5 | 0.5 | 0.493 | 50 | CDC | 0.595 | 0.857 | 70.26 | 2.814 | 4.359 | 0.098 | 0.218 |
| 0.492-150- CDC-0.5 | 0.5 | 0.492 | 150 | CDC | 0.597 | 0.850 | 202.25 | 2.896 | 4.437 | 0.096 | 0.218 |
| 0.491-250- CDC-0.5 | 0.5 | 0.491 | 250 | CDC | 0.599 | 0.833 | 337.61 | 2.965 | 4.474 | 0.096 | 0.222 |
| 0.549-50- CDC-0.5 | 0.5 | 0.549 | 50 | CDC | 0.595 | 0.856 | 70.07 | 2.823 | 4.364 | 0.096 | 0.210 |
| 0.548-150- CDC-0.5 | 0.5 | 0.548 | 150 | CDC | 0.598 | 0.845 | 202.25 | 2.895 | 4.426 | 0.096 | 0.221 |
| 0.547-250- CDC-0.5 | 0.5 | 0.547 | 250 | CDC | 0.599 | 0.833 | 337.80 | 2.958 | 4.471 | 0.095 | 0.219 |
| 0.575-50- CDC-0.5 | 0.5 | 0.575 | 50 | CDC | 0.594 | 0.850 | 70.03 | 2.843 | 4.373 | 0.097 | 0.214 |
| 0.574-150- CDC-0.5 | 0.5 | 0.574 | 150 | CDC | 0.597 | 0.841 | 202.55 | 2.910 | 4.427 | 0.095 | 0.215 |
| 0.573-250- CDC-0.5 | 0.5 | 0.573 | 250 | CDC | 0.598 | 0.836 | 338.00 | 2.957 | 4.465 | 0.095 | 0.217 |
| 0.583-50- CDC-0.5 | 0.5 | 0.583 | 50 | CDC | 0.594 | 0.845 | 70.14 | 2.852 | 4.376 | 0.099 | 0.221 |
| 0.586-150- CDC-0.5 | 0.5 | 0.586 | 150 | CDC | 0.596 | 0.842 | 202.55 | 2.912 | 4.432 | 0.099 | 0.225 |
| 0.585-250- CDC-0.5 | 0.5 | 0.585 | 250 | CDC | 0.599 | 0.838 | 338.82 | 2.948 | 4.460 | 0.094 | 0.212 |
| 0.493-50- CVC-0.5 | 0.5 | 0.493 | 50 | CVC | 0.493 | 0.530 | 152817.46 | 4.970 | 5.829 | 0.057 | 0.228 |
| 0.492-150- CVC-0.5 | 0.5 | 0.492 | 150 | CVC | 0.492 | 0.530 | 149069.57 | 5.008 | 5.887 | 0.055 | 0.219 |
| 0.491-250- CVC-0.5 | 0.5 | 0.491 | 250 | CVC | 0.491 | 0.529 | 154582.58 | 4.981 | 5.860 | 0.056 | 0.226 |
| 0.549-50- CVC-0.5 | 0.5 | 0.549 | 50 | CVC | 0.549 | 0.615 | 65722.51 | 4.402 | 5.434 | 0.066 | 0.229 |
| 0.548-150- CVC-0.5 | 0.5 | 0.548 | 150 | CVC | 0.548 | 0.611 | 69179.61 | 4.438 | 5.460 | 0.066 | 0.221 |
| 0.547-250- CVC-0.5 | 0.5 | 0.547 | 250 | CVC | 0.547 | 0.611 | 69276.52 | 4.457 | 5.484 | 0.066 | 0.220 |
| 0.575-50- CVC-0.5 | 0.5 | 0.575 | 50 | CVC | 0.575 | 0.667 | 35411.63 | 4.067 | 5.226 | 0.072 | 0.226 |
| 0.574-150- CVC-0.5 | 0.5 | 0.574 | 150 | CVC | 0.574 | 0.665 | 36917.82 | 4.075 | 5.236 | 0.073 | 0.226 |
| 0.573-250- CVC-0.5 | 0.5 | 0.573 | 250 | CVC | 0.573 | 0.662 | 38871.36 | 4.098 | 5.242 | 0.072 | 0.227 |
| 0.583-50- CVC-0.5 | 0.5 | 0.583 | 50 | CVC | 0.583 | 0.684 | 27783.95 | 3.967 | 5.149 | 0.074 | 0.224 |
| 0.586-150- CVC-0.5 | 0.5 | 0.586 | 150 | CVC | 0.586 | 0.694 | 24911.19 | 3.885 | 5.107 | 0.075 | 0.224 |
| 0.585-250- CVC-0.5 | 0.5 | 0.585 | 250 | CVC | 0.585 | 0.691 | 25779.07 | 3.899 | 5.111 | 0.075 | 0.223 |
| 0.487-1000- CPC-0.5 | 0.5 | 0.487 | 1000 | CPC | 0.603 | 0.820 | 1000.00 | 3.050 | 4.543 | 0.093 | 0.223 |
| 0.480-3000- CPC-0.5 | 0.5 | 0.480 | 3000 | CPC | 0.605 | 0.792 | 3000.00 | 3.274 | 4.701 | 0.087 | 0.219 |
| 0.493-50- CDC-0.25 | 0.25 | 0.493 | 50 | CDC | 0.581 | 0.738 | 65.20 | 3.462 | 4.819 | 0.085 | 0.204 |
| 0.492-150- CDC-0.25 | 0.25 | 0.492 | 150 | CDC | 0.582 | 0.734 | 196.46 | 3.540 | 4.875 | 0.083 | 0.199 |
| 0.491-250- CDC-0.25 | 0.25 | 0.491 | 250 | CDC | 0.582 | 0.725 | 327.26 | 3.601 | 4.916 | 0.083 | 0.205 |
| 0.493-50- CVC-0.25 | 0.25 | 0.493 | 50 | CVC | 0.493 | 0.528 | 89499.20 | 5.176 | 6.046 | 0.053 | 0.202 |
| 0.549-50- CVC-0.25 | 0.25 | 0.549 | 50 | CVC | 0.549 | 0.619 | 22009.43 | 4.485 | 5.558 | 0.066 | 0.200 |
| 0.575-50- CVC-0.25 | 0.25 | 0.575 | 50 | CVC | 0.575 | 0.688 | 3848.24 | 3.931 | 5.169 | 0.074 | 0.201 |
| 0.487-1000- CPC-0.25 | 0.25 | 0.487 | 1000 | CPC | 0.581 | 0.711 | 1000.00 | 3.730 | 5.007 | 0.081 | 0.204 |
| 0.480-3000- CPC-0.25 | 0.25 | 0.480 | 3000 | CPC | 0.578 | 0.689 | 3000.01 | 3.918 | 5.146 | 0.074 | 0.199 |

Table 4.6 Fitting parameters for the power-law relationships between $Z$ and $p'$ and $Z_m$ and $p'$ at critical state

| μ | Z | | | $Z_m$ | | |
|---|---|---|---|---|---|---|
| | $Z_c$ | δ | ξ | $Z_{m,c}$ | $\delta_m$ | $\xi_m$ |
| 0.1 | 4.75 | 0.041 | 0.342 | 5.29 | 0.0299 | 0.346 |
| 0.25 | 3.99 | 0.0546 | 0.313 | 4.70 | 0.0386 | 0.314 |
| 0.5 | 3.25 | 0.0838 | 0.275 | 4.21 | 0.0535 | 0.275 |
| 1.0 | 3.03 | 0.0281 | 0.362 | 4.03 | 0.0371 | 0.288 |

Table 4.7 Fitting parameters for the power-law relationships between $N_R$ and $p'$ at critical state

| μ | $N_{R,c}$ | $\delta_R$ | $\xi_R$ |
|---|---|---|---|
| 0.1 | 2120 | -89.31 | 0.272 |
| 0.25 | 3043 | -109.9 | 0.278 |
| 0.5 | 5245 | -529.1 | 0.182 |
| 1.0 | 5242 | -69.34 | 0.363 |

Table 4.8 Fitting parameters for the power-law relationships between $\Phi_d$ and $p'$ at critical state

| $\mu$ | $\Phi_{d,c}$ | $\delta_d$ | $\xi_d$ |
|---|---|---|---|
| 0.1 | 2120 | -89.31 | 0.272 |
| 0.25 | 3043 | -109.9 | 0.278 |
| 0.5 | 5245 | -529.1 | 0.182 |
| 1.0 | 5242 | -69.34 | 0.363 |

Table 4.9 Input parameters for the single column test

| Density (kg/m3) | $R$(m) | $k_n$ (N/m) | $k_s$ (N/m) | Timestep (s) |
|---|---|---|---|---|
| 1000 | 1 | $10^5$ | $10^5$ | $10^{-4}$ |

# Chapter 5 Critical state behaviour of granular materials

## 5.1 Introduction

The behaviour of granular materials (including soils) is state-dependent, i.e., dependent on the initial packing density, the stress state and affected by the loading path. Consequently, prediction of soil response is not easy. The critical state soil mechanics framework (CSSM) to describe soil behaviour has been under development since the 1950s and 1960s (Roscoe et al., 1958; Schofield & Wroth, 1968). A key assumption of CSSM is the uniqueness of the critical state lines in both $q$-$p'$ and $e$-log($p'$) spaces. The state parameter which denotes the proximity between the current state and the critical state line (CSL) in $e$-log($p'$) space has been shown to effectively describe the state-dependent dilatancy and strength of sands (Been & Jefferies, 1985). This state parameter is important when using the CSSM framework to develop constitutive models for soils.

Early experimental investigations of CSSM used standard triaxial tests which apply a radial confining pressure to cylindrical samples. However, this kind of axisymmetric stress condition is rarely encountered in reality. A more general three-dimensional stress state with differing values of the intermediate and minor principal stresses can be attained in a true triaxial apparatus (Ko & Scott, 1967; Green & Bishop, 1969). The loading path in a true triaxial apparatus is typically controlled by the dimensionless intermediate stress ratio, $b = (\sigma'_2 - \sigma'_3)/(\sigma'_1 - \sigma'_3)$, where $\sigma'_1$, $\sigma'_2$ and $\sigma'_3$ are the major, intermediate, and minor principal stresses, respectively. Standard triaxial compression corresponds to $b = 0.0$ when $\sigma'_2 = \sigma'_3$, while triaxial extension is equivalent to $b = 1.0$ when $\sigma'_1 = \sigma'_2$.

The major objective of this Chapter is to investigate some key controversial issues regarding the response of soils under generalised three-dimensional loading conditions using DEM. In particular, the uniqueness of the CSL in $e$-log($p'$) space and the influence of $b$ on the material strength are explored. An overview of prior studies regarding these issues is given in Section 5.2. Following a description of the simulation approach in Section 5.3, the influence of different factors, e.g., initial conditions and the intermediate stress ratio, on the mechanical behaviour of granular materials is demonstrated in Section 5.4. The uniqueness of the CSL is discussed in Section 5.5 from both macro-scale and micro-scale perspectives. In Section 5.6, the capacity of a DEM model to capture the sensitivity of the material response to the state parameter ($\psi$) that one would expect for a real sand is discussed.

Finally, the potential of using DEM to advance critical state-based constitutive models for sand is explored in Section 5.7.

## 5.2 Literature review

The term "critical void ratio" has been used since the pioneer work of Casagrande (1936) to describe a particular state for sands at which prevention of volume change leads to no strength. Two alternative definitions were proposed by Taylor (1948), namely, the constant-$\sigma'_3$ critical void ratio and the constant-volume critical void ratio. The former originates from drained triaxial tests and differs from Casagrande's definition of critical void ratio in that the void ratio after rather than before consolidation is taken as the initial void ratio, while the latter corresponds to the observations from undrained tests. These two definitions were unified by Roscoe et al. (1958) to form the concept of a unique critical void ratio line (C.V.R line) in ($p'$,$e$,$q$) space considering the behaviour of Weald Clay. This key concept acts as the cornerstone for the framework of critical state soil mechanics (CSSM) (Schofield & Wroth, 1968). The original CSSM framework described the critical state by two unique relationships (Figure 5.1):

$$q = Mp' \qquad \text{(Eq. 5.1)}$$

$$\Gamma = v + \lambda \ln p' \qquad \text{(Eq. 5.2)}$$

in which $M$ is a material constant characterising the intrinsic frictional coefficient between grain surfaces, $\Gamma$ is the intercept of the critical state line (CSL) in $v$-ln$p'$ space with $p'$=1kPa axis, $v$(=1+$e$) is the specific volume and $\lambda$ is the slope of the CSL in $v$-ln$p'$ space. Soils with initial state above the CSL defined by Eq. 5.2 in $v$-ln$p$' space are in a 'wet' (loose) state and contract to the CSL, while soils with initial state below the CSL are in a 'dry' (dense) state and dilate to the CSL.

While it is accepted that the CSSM framework effectively captures the mechanical behaviour of clays, its application to sands is less successful. One of the most important reasons is the inconsistent observations regarding the uniqueness of the CSL in $e$-log($p'$) space.

### 5.2.1 Experimental investigations on critical state behaviour of sands

Despite a considerable number of experimental studies, debates continue around whether the locus of the CSL in $e$-log($p'$) space depends on the initial state, the initial anisotropy, the loading conditions or the loading modes. Most researchers tend to agree that the position of the CSL in $e$-log($p'$) space is independent of the initial state and the loading conditions provided that the same loading mode is applied (e.g., triaxial compression). By performing

triaxial tests on Erksak sand, Been et al. (1991) showed that the CSL in *e*-log(*p'*) space is unique and independent of the initial states, the loading conditions and the initial anisotropy (Figure 5.2). Verdugo & Ishihara (1996) showed that both drained and undrained tests yield the same CSL for Toyoura sand (Figure 5.3 (a)). The concept of a unique CSL in *e*-log(*p'*) space has also been shown to be applicable to silty sands (Figure 5.3 (b)) (Murthy *et al.,* 2007) and mixtures of clean sands and differently-shaped fine particles (Figure 5.3 (c)) (Yang & Wei, 2012). Conversely, by interpreting the volumetric behaviour within the shear bands for plane strain tests using the digital image correlation (DIC) techniques, Finno & Rechenmacher (2003) suggested that the position of the CSL depends on the consolidation history and initial packing density (Figure 5.4). However, the approach used by Finno & Rechenmacher (2003) is not ideal as they neglected that the stress state within the shear band may also be different from the global measured one by using the global *p'* when plotting the CSL in *e*-log(*p'*) space.

While the experimental results of Vasquez & Dobry showed a clear effect of the sample preparation method (initial anisotropy) on the position of the CSL (Figure 5.5 (a)) (Verdugo, 1992), most of available experimental evidence indicates that the initial anisotropy induced by different sample preparation methods is erased at large strain levels, resulting in a unique CSL (Been et al., 1991; Carrera et al., 2011; Ishihara, 1993; Murthy et al., 2007) (See Figure 5.2(d), Figure 5.3(b) and Figures 5.5(b) and (c)).

Experimental data reporting observations of critical state behaviour under true triaxial conditions is rarely reported, mainly due to the loss of homogeneity in deformation at large strain levels in this type of test. Prior studies have considered the influence of *b* mainly by comparing the behaviour of sands under triaxial compression (*b*=0.0) and triaxial extension loading conditions (*b*=1.0). While Been et al. (1991) reported that the CSL obtained from triaxial compression tests and that determined from triaxial extension tests are identical (Figure 5.2 (c)), a general consensus has been formed among other researchers that the CSL for triaxial extension lies below that for triaxial compression as shown in Figure 5.5 (c) (Carrera et al., 2011) and Figure 5.6 (Riemer & Seed, 1997; Vaid et al., 1990). They attributed this to the bedding effect (i.e., the orientation of the loading direction with respect to the sedimentation direction) which leads to a stiffer fabric parallel to the deposition direction than that orthogonal to the deposition direction. On the other hand, the work of Finno *et al.* (1996) and Wanatowski & Chu (2007) showed that sands subjected to plane strain loading collapsed to a CSL that locates above (to the right of) the CSL obtained under triaxial compression loading conditions in *e*-log(*p'*) space (Figure 5.7). Since plane strain is in fact a special case of true triaxial loading conditions with *b* evolving rather than being

constant, plane strain test data cannot really be used to draw quantitative conclusions on the effect of $b$ on the position of the CSL.

Sayão and Vaid (1996) summarised six types of relationship that have been reported in the literature to describe the influence of $b$ on the angle of shearing resistance $\phi'$ (Figure 5.8):

- *Type-a*: $b$ has no influence on $\phi'$
- *Type-b*: $\phi'$ increases nonlinearly with increasing $b$
- *Type-c*: $\phi'$ initially increases with increasing $b$ and attains a constant value at a certain $b$ value
- *Type-d*: $\phi'$ initially increases with increasing $b$ followed by a decrease in $\phi'$ with $b$ beyond a certain $b$ value. $\phi'$ for triaxial extension ($b$=1.0) is higher than $\phi'$ for triaxial compression ($b$=0.0)
- *Type-e*: $\phi'$ initially increases with increasing $b$ to a maximum and then decreases with further increasing in $b$. $\phi'$ for triaxial extension ($b$=1.0) equals $\phi'$ for triaxial compression ($b$=0.0)
- *Type-f*: $\phi'$ again initially increases with increasing $b$ to a maximum and then it decreases such that $\phi'$ for triaxial extension ($b$=1.0) is lower than $\phi'$ for triaxial compression ($b$=0.0)

A number of factors may explain the lack of consensus amongst published experimental data (Carrera et al., 2011; Sayão & Vaid, 1996): (1) the accuracy of the measurements; (2) different degrees of initial anisotropy; (3) the difference in the loading direction relative to the deposition direction (i.e., inherent anisotropy direction); (4) inhomogeneous deformation and localisation phenomena (e.g., necking).

### 5.2.2 DEM studies on the mechanical behaviour of granular materials under generalised loading conditions

The difficulties associated with experimental studies of critical state behaviour under a true triaxial loading state can be overcome by employing DEM. Using DEM an idealised virtual experimental environment can be created in which the loading conditions and simulation parameters can be precisely controlled and the stress-strain responses can be exactly measured. DEM simulations have been carried out to study the critical-state behaviour of granular materials using both 2D disk systems (e.g., Maeda *et al.*, 2010) and 3D sphere systems (Gu et al., 2014; Guo & Zhao, 2013; Ng, 2009a; Sitharam & Vinod, 2009; Yan & Dong, 2011). As illustrated in Figure 5.9, most prior DEM analysts have confirmed that under triaxial compression loading condition ($b$ = 0) the CSL is unique and is independent of

the initial states and loading conditions. One notable exception is the work of Zhao & Evans (2011) who showed that the position of CSL in *e*-log(*p'*) space varied with initial void ratio. However, their conclusions were based on observations up to 10% axial strain, while the true critical-state response (which is normally attained at strains exceeding 10% axial strain) remained unclear.

Prior DEM studies have investigated the effects of *b* on the load-deformation response (Barreto & O'Sullivan, 2012; Ng, 2004b; Sazzad & Suzuki, 2013; Thornton, 2000). Prior studies simulating true-triaxial element tests (Barreto & O'Sullivan, 2012; Thornton, 2000; Thornton & Zhang, 2010; Zhao & Guo, 2013) have shown that DEM can replicate the failure envelope proposed by Lade & Duncan (1975) for real sands. Ng (2004b) considered four failure criteria at the peak stress levels. Most of these studies have focused only on small strain levels and peak states, while the effects of *b* on the critical-state response have seldom been discussed. A type-*d* relationship between *b* and $\phi'$ was evident in DEM simulations by Ng (2004b) and Sazzad & Suzuki (2013). Zhao & Guo (2013) considered five *b* values and reported that the critical states in *e-log*(*p'*) space collapse to a unique power-law relationship which is independent of *b* (Figure 5.10 (c)). However, close examination of their data does reveal some differences in the position of the CSL in *e*-log(*p'*) space, with the data for the case with *b*=1.0 lying above the data with *b*=0. Furthermore, the observations of Zhao & Guo are not in complete agreement with data reported by other DEM analysts. For example, Li (2006) considered triaxial tests on spherical particles and observed that triaxial extension simulations yield a CSL that is above the CSL obtained from triaxial compression simulations (Figure 5.10 (a)). A similar conclusion was made by Ng (2009b) using elliptical particles (Figure 5.10 (b)). Note that in both cases, the samples were generated by a gravity deposition method which yields an initially anisotropic structure as is the case in physical experiments. Thornton & Antony (2000) considered isotropic samples and also noticed a higher strength for constant-volume triaxial extension simulations than for constant-volume triaxial compression simulations and a more dilative response for constant-*p'* triaxial extension simulations than that for constant-*p'* triaxial compression simulations. While they did not present data to give the full locus of a CSL, Thornton and his colleagues also observed a systematic increase in the dilative volumetric strain at critical state with increasing *b* (Thornton & Zhang, 2010; Thornton, 2000). Similar observations can also be found in Sazzad & Suzuki (2013). These studies indicate that rigorous scrutiny of the uniqueness of the CSL at varying *b* values is required to further develop the work of Zhao and Guo (2013). This will be addressed in Section 5.5 below.

### 5.2.3 Parameters to describe the state-dependent nature of sands

Been and Jefferies (1985) defined the state parameter ($\psi$) to be the difference between the current void ratio and the void ratio at the critical state ($e_{cs}$) at the same $p'$ to describe the state-dependent nature of soil response (Figure 5.11). A positive value of $\psi$ represents a loose state while a negative $\psi$ value indicates a dense state. Triaxial compression test data show a convincing link between $\psi$ and the mechanical response of soils, most notably, strength and dilatancy (e.g., Been & Jefferies, 1985). Yang (2002) found that the stress ratio of undrained tests at instability state follows a power-law relationship with the state parameter. A number of recently-developed constitutive models for soil have explicitly considered $\psi$ in their formulation, e.g., NorSand (Jefferies, 1993; Jefferies & Shuttle, 2002), Wood et al. (1994), Severn–Trent sand (Gajo & Wood, 1999) and the model proposed by Li and Dafalias (Li & Dafalias, 2000; Li, 2002; Li et al., 2002).

Alternative parameters have been proposed to describe the state-dependent behaviour of soils. For example, Wang et al., (2002) proposed using the ratio of $p'$ at the current state to $p'$ at the critical state corresponding to the current void ratio. Wang's parameter is limited as it is inapplicable to very loose sands which will experience total liquefaction ($p'$=0) when subjected to undrained shearing. Bolton (1986) proposed a relative dilatancy index, $I_R$=$I_D$($Q$-ln$p'$)-$R$, in which $I_D$ is the relative packing density and $Q$ and $R$ are material constants. $I_R$ aims to describe the dependence of peak strength and peak dilatancy on both packing density and stress state. The $I_R$ parameter is dependent on $I_D$ which is difficult to obtain in DEM simulations.

A recent extension of CSSM is the Anisotropic Critical State Theory (ACST)(Li & Dafalias, 2012) which was inspired by the finding of DEM analysts that a critical-state fabric exists which is anisotropic and whose principal orientation is coincident with the loading direction at the critical state. The ACST acknowledges the influence of fabric anisotropy on soil behaviour and considers the intensity of fabric development and evolution of fabric orientations relative to the loading direction by introducing a scalar-valued fabric anisotropy variable $A$=$\boldsymbol{F}$:$\boldsymbol{n}$, where $\boldsymbol{F}$ is a deviatoric fabric tensor normalised by its form at the critical state and $\boldsymbol{n}$ is the unit-norm deviatoric tensor-valued loading direction. $A$ evolves as shearing progresses and eventually $A$=1 at the critical state. Therefore, apart from the assumption of unique CSL in both $p'$-$q$ and $e$-log($p'$) space, the ACST requires the fabric direction and the loading direction to be coincident, i.e.:

$$\eta = \frac{q}{p'} = M,\ e = e_c = \hat{e}_c(p'),\ A = A_c = 1 \qquad \text{(Eq. 5.3)}$$

Li and Dafalias (2012) defined a Dilatancy State Line (DSL) in *e-p'* space relating the dilatancy void ratio ($e_d$) to *A* (Figure 5.12):

$$e_d = \hat{e}_c(p') + \hat{e}_A(e, p')(A - 1) \qquad \text{(Eq. 5.4)}$$

in which $e_d$ is the void ratio on the DSL for the current $p'$ and $\hat{e}_A$ corresponds to the downward translation of the DSL from the CSL at the current state ($e$,$p'$). The DSL coincides with the CSL when $A$=1. The role of state parameter in describing the contractive or dilative state of soil is replaced by the dilatancy state parameter $\zeta$ ($=e - e_d$) which is defined as the difference between the current void ratio and the void ratio on the DSL corresponding to the same $p'$. This idea has been incorporated into a soil constitutive model that considers the evolution of fabric by Gao *et al.* (2013).

In summary, although considerable experimental as well as numerical efforts have been made to investigate the critical state behaviour of granular materials under generalised 3D loading conditions, no consensus has been reached regarding the uniqueness of the CSL. The failure mechanism for soils under 3D loading conditions remains poorly understood. Since the true effect of the loading mode may be concealed by other factors, e.g., the initial anisotropy, this study isolates the effects of loading mode by considering samples that are initially isotropic. Furthermore, the effectiveness of the state parameter to describe the stress-strain behaviour under generalised 3D loading conditions is examined in detail in this Chapter.

## 5.3 DEM simulations of three-dimensional loading conditions

Figure 5.13 (a) shows a typical cuboidal sample considered in this study. The major principal stress $\sigma'_1$ is parallel to the $z$ axis, while the intermediate ($\sigma'_2$) and minor ($\sigma'_3$) principal stresses coincide with the $y$ and $x$ axes respectively. The possible total stress loading paths for true triaxial loading modified from Atkinson (2007) are illustrated in Figure 5.13 (b), in which the traditional definitions of deviatoric stress $q$= $\sigma_z$-$\sigma_x$ and mean stress $p$=($\sigma_x$+ $\sigma_y$+ $\sigma_z$) /3 in terms of total stresses for asymmetric triaxial loading conditions are adopted. In Figure 5.13 (b), $\sigma_z$ is equivalent to the axial load, $\sigma_a$, and $\sigma_x$ corresponds to the radial confining pressure, $\sigma_r$. The loading stress paths can be categorised into four types: loading compression (LC), unloading compression (UC), loading extension (LE) and unloading extension (UE). Loading refers to an increase in $p$, while unloading indicates a decrease in $p$. In compression the vertical load is higher than the lateral load, while in extension the opposite is true. The gradient of each stress path is determined by the ratio between the deviatoric stress increment ($dq$) and the mean stress increment ($dp$) which can be expressed by:

$$\frac{dq}{dp} = \frac{d\sigma_1 - d\sigma_3}{\frac{1}{3}[(1+b)d\sigma_1 + (2-b)d\sigma_3]} \quad \text{(Eq. 5.5)}$$

For simulations with a constant confining pressure ($d\sigma_3 = 0$), Eq. 5.5 reduces to d$q$/d$p$=3 for $b$=0.0 and d$q$/d$p$=3/2 for $b$=1.0, while the gradients for other $b$ values lie in between. All these four paths were considered in this study.

True triaxial simulations were performed using samples with a grading similar to Toyoura sand, while in some cases triaxial compression simulation results using samples with a grading that is close to Dunkirk sand are presented for comparison. For convenience, simulations using the Toyoura sand grading are denoted as 'ST', while simulations using the Dunkirk sand grading are named as 'SD'. Initially isotropic samples were generated following the approach detailed in Sections 4.3 and 4.4. 102 ST simulations were performed under true triaxial loading conditions and the data for the eight triaxial compression simulations ($b$=0) carried out on 'SD' samples are from Dr Hanley (Personal communication). True triaxial simulations were carried out under constant-$b$ and constant-$\sigma'_3$ conditions using the ST samples. Eight different $b$ values were investigated, i.e., $b$ = 0.0, 0.2, 0.3, 0.4, 0.5, 0.6, 0.8 and 1.0, varying from triaxial compression ($b$=0.0) to triaxial extension ($b$=1.0) conditions. A set of plane strain simulations (PS) were also conducted by fixing the positions of the periodic boundaries orthogonal to the $y$ axis. Some additional constant-volume and constant-$p'$ simulations were performed under triaxial compression and triaxial extension conditions. The constant-volume simulations approximate the undrained condition for fully-saturated sands and have been used in a number of DEM studies of undrained sand behaviour (e.g., Gu et al., 2014; Guo and Zhao, 2013). The interparticle friction coefficient ($\mu$) during shearing for most of the simulations was 0.25, while $\mu$ = 0.1 was applied to nine triaxial compression ST simulations to investigate the effect of particle surface friction. Those samples are denoted as ST-b0.0-$\mu$0.1. Unless it is otherwise specified, the simulations presented in this Chapter have $\mu$ = 0.25 in line with the findings of Chapter 4.

## 5.4 Mechanical response under three-dimensional loading conditions

### 5.4.1 Mechanical response under triaxial loading conditions

*A. Constant-$\sigma'_3$ drained loading*

Figure 5.14 includes the load-deformation response for three triaxial drained simulations each with a confining pressure ($\sigma_3'$) of 500 kPa but different initial void ratios ($e_0$). The initial void ratios ($e_0$) are 0.588, 0.606 and 0.646 for the dense, medium and loose samples respectively. As would be expected, the densest sample with the lowest $e_0$ exhibited the

highest peak strength and dilated throughout shearing, while the loosest sample with the highest $e_0$ had the lowest peak strength, initially contracted prior to dilating and had an overall contractive response. The medium dense sample with a value of $e_0$ = 0.606 had a response that was intermediate between these two scenarios. For all three samples, the stress ratio obtained by the S-F-F relationship (Eq. 4.16) agrees with that calculated from the stress tensor. As Figure 5.14 (c) shows eventually all three samples had the same void ratio and $p'$, indicative of an identical critical state which is independent of the initial packing density.

Figure 5.15 shows the evolution of $Z$ and $Z_m$ during shearing for the simulations presented in Figure 5.14. For both the medium dense and the dense samples, $Z_m$ and $Z$ decreased consistently to a critical-state value. For the loose sample $Z$ increased initially and then decreased slightly to a constant value at the critical state, while $Z_m$ increased consistently to a critical-state value. Comparing Figure 5.14 (b) and Figures 5.15 (a) and (b) reveals that constant $Z$ and $Z_m$ values were attained at a much lower strain level than that at which the volumetric strain became constant. $Z$ and $Z_m$ at the critical state are identical for all three samples considered, in line with Thornton (2000) amongst others. It is useful to understand the possible factors governing the evolution of $Z$. As discussed in Section 4.6.2, when subjected to deviatoric shearing, the initially highly-jammed state of isotropically-consolidated samples would be distorted, redundant contacts are released while the remaining contacts would rearrange themselves to form the most efficient contact orientations and contact force magnitude configuration to sustain the external loading. This is manifested by the rapid drop of the index of mechanical redundancy ($I^{NR}_R$) as shown in Figure 5.16. The release of redundant contacts upon shearing can also be reflected by the variation of the probability density distribution of connectivity (the number of contacts for individual particles) at different stages of loading as presented in Figure 5.17. It is evident in Figure 5.17 that the probability of connectivity that is higher than 4 is the highest at the initial state of loading and decreases when shearing is commenced. The difference of the probability density distribution of the connectivity between different stages of loading decreases with decreasing packing density.

On the other hand, unless extremely dense, granular assemblies usually experience an initial contraction when subjected to drained shearing which may in turn increase the number of contacts within the system. The evolution of $Z$ and $Z_m$ at early stage of loading is in fact the competing result between the release of redundant contacts and the gain of new contacts due to contraction. If the former surpasses the latter, $Z$ and $Z_m$ decrease, otherwise, $Z$ and $Z_{\mathrm{m}}$ increases. As Figure 5.16 shows, the release of redundant contacts is completed at a very early stage of loading, after which the evolution of coordination number is dominated by the

volume change. Hence, a decrease in $Z$ may be observed when samples shift from contraction to dilation as reported by Zhao and Guo (2013).

Figure 5.18 illustrates the evolution of four fabric anisotropy descriptors, i.e., $a_c$, $a_b$, $a_n$ and $a_t$ as defined in Section 4.6. All the four anisotropy descriptors increased upon shearing and evolved during the course of shearing. For all the samples, the geometric anisotropy descriptors $a_c$ and $a_b$ increased initially to a peak value and then decreased until the critical state was reached. For the dense and medium dense samples, the mechanical anisotropies $a_n$ and $a_t$ increased abruptly to a peak value upon shearing and dropped thereafter to a constant value at the critical state, while for the loose sample, $a_n$ and $a_t$ increased consistently to the critical-state value, which is in agreement with the evolution of stress ratio (Figure 5.14 (a)). For different samples, all four anisotropy descriptors converged at the critical state, indicative of a critical-state fabric which is independent of the initial packing density.

*B. Constant-volume loading*

The stress-strain responses for three representative constant-volume simulations with $\sigma_{3,0}$ = 500 kPa, and $e_0$ values of 0.606 (Dense), 0.613 (Medium) and 0.616 (Loose) are presented in Figure 5.19. Referring to Figure 5.19 (a), the medium and loose samples exhibited the typical three stages of loose to medium dense sand behaviour under undrained loading conditions (Murthy et al, 2007), i.e., an undrained instability state (IS), a phase transformation state (PT) and a critical state (CS), while the dense sample dilated consistently to the critical state. The quasi-steady state (QS) is not obvious in Figure 5.19 and may be taken as being coincident with the PT state. It is also evident in Figure 5.19 (a) that $q$ at the IS state, $q$ at the PT state, and $q$ at the CS state all decreased with increasing $e_0$. Considering the stress paths in $q$-$p'$ space in Figure 5.19 (b), it is clear that for all samples, $p'$ initially decreased to the PT state and increased thereafter until a nearly constant value was reached at the CS state. The maximum reduction in $p'$ ($p'$ at the PT state) increased with increasing $e_0$; this is in line with the experimental observation of Wanatowski (2007). The instability lines, or flow liquefaction lines (FLL), which connect the origin and instability point in $q$-$p'$ space (Lade, 1993) are overlaid on Figure 5.19 (b). The slope of the FLL quantifies the highest undrained strength that a sand can experience at small strain levels and thus is critical for practical design. As shown in Figure 5.19 (b), the FLL is not unique but varies with $e_0$. The slope of the FLL decreases with increasing $e_0$, suggesting a reduction in liquefaction resistance with increasing $e_0$ as would be expected. The correlation between the IS strength and the state parameter will be addressed in Section 5.6.

Figure 5.20 presents the evolution of $Z$ and $Z_m$ during constant-volume shearing for the simulations considered in Figure 5.19. For all three samples, both $Z$ and $Z_m$ decreased initially to a minimum value and increased thereafter until a constant critical-state value was attained. The $Z$ and $Z_m$ at the PT state are close to the minimum values, in agreement with Guo and Zhao (2013). Figures 5.20 (a), (b) and (c) also show that the 'valley' of the evolution curve of $Z$ and $Z_m$ is not a unique feature of the PT state as the dense sample also exhibits such a 'valley'. This can again be explained by the competing between the release of redundant contacts and the gain of new contacts due to the increase of $p'$ induced by dilation. At the initial stage of loading, since no volume change occurs, the evolution of $Z$ and $Z_m$ was dominated by the release of redundant contacts which can be interpreted from the rapid drop of $I^{NR}_R$ (Figure 5.21). For all the three samples, $I^{NR}_R$ dropped rapidly upon shearing to a minimum value and increased thereafter slightly due to the increasing $p'$. The oscillation evident with the $I^{NR}_R$ data may be associated with the constant-volume servo-control algorithm. Meanwhile, for the medium and loose samples, $p'$ decreased initially due to contraction while for the dense sample, $p'$ increased initially due to dilation. The decreases in $p'$ for the medium and loose samples exacerbated the decreasing trend of $Z$ and $Z_m$, while the increase in $p'$ for the dense sample compensated partially for the release of redundant contacts. Therefore, the reduction in $Z$ and $Z_m$ was less significant for the dense sample than that for the loose and medium samples and $Z$ and $Z_m$ started to increase at the earliest stage of loading for the dense sample. For the medium and loose samples, $Z$ and $Z_m$ also began to increase after the PT state, at which $p'$ started to increase due to dilation. The competition between the release of redundant contacts and gain/loss of contacts due to dilative/contractive behaviour can be revealed by comparing the probability density distributions of the connectivity at different stages of loading as shown in Figure 5.22. The probability of having a connectivity that is higher than 4 initially decreased upon shearing and reached minimum at the 'valley'/PT state and then increased until the critical state is reached. $Z$ and $Z_m$ at critical state increased with increasing packing density due to a higher $p'$ for the denser sample.

Figure 5.23 illustrates the evolution of the four anisotropy descriptors. $a_c$ and $a_b$ initially increased to a peak value and decreased thereafter to the critical state value, showing an opposite trend to that of $Z$ and $Z_m$ (Figure 5.20). The evolution of mechanical anisotropies ($a_c$ and $a_t$) is similar to that of $q$ (Figure 5.19 (a)). Both $a_c$ and $a_t$ increased rapidly upon shearing to a peak value, followed by a decreasing trend prior to increasing again until the critical state was reached. Generally, the geometrical anisotropies decreased with increasing packing density, while the mechanical anisotropies increased with increasing packing density. The

lower geometrical anisotropies were compensated by the higher mechanical anisotropies, leading to an identical critical-state stress ratio.

### 5.4.2 Triaxial Compression (TC) vs Triaxial Extension (TE)

*A. Drained simulations with different loading paths*

Four types of loading path illustrated in Figure 5.13 was investigated by considering samples with the same initial state ($\sigma'_{3,0}$ = 500 kPa and $e_0$ = 0.646). The conventional triaxial drained loading condition (LC) was applied to the first sample with loading proceeding in the $z$ direction while the horizontal stresses ($\sigma'_3=\sigma'_x=\sigma'_y$) were kept constant; for the second sample, the dimension in the $x$ direction was extended while the confining pressures in both $y$ and $z$ directions were maintained constant, i.e., a UC loading condition was applied. A LE loading condition was imposed on the third sample by squeezing it in the $x$ direction and concurrently maintaining the confining pressures in the $y$ and $z$ directions ($\sigma'_3=\sigma'_y=\sigma'_z$); the fourth sample was subjected to a UE loading condition with the sample expanding in the $z$ direction while the horizontal stresses were kept constant.

Figure 5.24 compares the stress-strain behaviour of these samples. The axial strain ($\varepsilon_a$) is taken as the strain along the loading/unloading direction, i.e., $\varepsilon_a$ is horizontal for UC and LE and vertical for LC and UE, and $q$ equals to $\sigma'_z - \sigma'_x$ following the traditional soil-mechanics convention. $q$ for 'compression' samples LC and UC were positive, while $q$ for 'extension' samples LE and UE were negative. If the absolute value of $q$ is used in calculating the stress ratio, the stress ratios for LC and LE converged and so did the stress ratios for UC and UE. Moreover, the volumetric strain for the LE sample followed that of the LC sample while the volumetric strain for the UE sample was similar to that of the UC sample. In these regards, the traditional definition of compression and extension according to whether the vertical stress is higher or lower than the horizontal stress fails to unify the mechanical behaviour of samples sheared under 'compression' or that of samples sheared under 'extension'. The compression and extension loading conditions can also be distinguished based on the intermediate stress ratio ($b$), i.e., $b$ = 0 for triaxial compression and $b$ = 1.0 for triaxial extension. Under this scheme, both LC and LE correspond to triaxial compression ($b$ = 0.0), while UC and UE refer to triaxial extension ($b$ = 1.0). The difference between LC and LE and also between UC and UE essentially corresponds to the difference in loading directions. Therefore, Figure 5.24 confirms that isotropic samples sheared in the same loading mode defined by $b$ values effectively yield the same behaviour regardless of loading directions. The samples considered here are close to isotropic ($\Phi_d$ = 0.004) and so the small differences

observed between the UC and UE samples, and also between the LC and LE samples, are a consequence of the finite sample size.

*B. Constant-volume simulations*

Constant-volume triaxial compression (*CVC*) and constant-volume triaxial extension (*CVE*) simulations were performed on samples with the same initial state. The sample volume was maintained constant by continuously adjusting the positions of the lateral boundaries of the periodic cell. Figure 5.25 presents the stress-strain response of two constant volume simulations with the same initial state ($\sigma'_{3,0}$ = 500 kPa and $e_0$ = 0.619): one compressive ($\varepsilon_a > 0$) and the other extensive ($\varepsilon_a < 0$). For a straightforward comparison, the magnitudes of the axial strain and the deviatoric stress, i.e., $|\varepsilon_a|$ and $|q|$, are considered in Figure 5.25 (a).

Figure 5.25(a) shows that both samples exhibited the typical behaviour expected for loose to medium dense sand under undrained loading conditions. In both cases the instability state was attained at about 0.2% axial strain. The CVC sample began to dilate at 4.4% axial strain while the PT state for the CVE sample occurred at about 5.2% axial strain. The CVE sample has a slightly smaller IS strength ($q$=202.1 kPa) than the CVC sample ($q$=218.5 kPa), which is in line with experimental observations (Vaid & Thomas, 1995; Carrera, et al., 2011). However, $q$ for the CVE sample started to exceed that for the CVC sample at about 0.5% axial strain and the critical-state strength for CVE sample is much higher in triaxial extension than in triaxial compression. In this sense, these DEM results do not agree with the common experimental observations. The different response under triaxial compression and triaxial extension loading conditions and the discrepancy between the DEM simulation data and the experimental observations can be explained within the framework of ACST (Li and Dafalias, 2012).

Li and Dafalias (2012) attributed the more contractive response under TE than under TC to the greater deviation of the fabric direction (initially the sedimentation direction) from the loading direction in TE than in TC. Consequently, the DSL is further below the CSL for TE than for TC (Figure 5.12 (b)). Therefore, given the same initial state, the sample is 'looser' in TE than in TC with reference to its DSL. The extent of the coaxiality between the fabric direction and the loading direction cannot be measured in laboratory tests (i.e., the $A$ parameter in ASCT). However, the deviation of the fabric direction from the loading direction can be calculated using the data available in DEM simulations. Zhao and Guo (2013) proposed an $A'$ parameter to evaluate the coaxiality between the fabric direction and the loading direction:

$$A' = n_{ij}^F n_{ij}^s \quad \text{(Eq. 5.6)}$$

where $n_{ij}^F$ is the deviatoric fabric direction in terms of contact orientations and $n_{ij}^s$ is the deviatoric stress direction. *A'* is close to unity when the deviatoric fabric direction coincides with the deviatoric stress direction. As noted by Zhao & Guo, *A'* is a normalised form of the *A* parameter proposed by Li and Dafalias (2012). The variation of *A'* during shearing for the CVC and CVE samples is given in Figure 5.26 (a). For the isotropic samples considered, *A'* increased quickly to be almost unity in both the CVC and CVE cases, i.e., the fabric direction and the loading direction became coaxial shortly after loading commenced. While it is not clear from Figure 5.26 (a), the initial preferential contact orientation for the DEM sample is slightly biased to the vertical direction as indicated by a small non-zero value of deviatoric fabric $\Phi_{d,0}$ ($\Phi_{z,0}$ -$\Phi_{x,0}$ =0.003). This small bias vanished immediately upon shearing and may be responsible for the lower strength of the CVE sample than that of the CVC sample at very early stage of loading ($\varepsilon_a$<0.484%). After the fabric direction became coincident with the loading direction, the DSL and CSL converged. The more dilative response for the CVE sample thereafter originated from the higher position of the CSL in *e*-log(*p'*) space, indicating a 'denser' state for the CVE sample than for the CVC sample. This issue will be further discussed in Section 5.5. In contrast, as indicated by the constitutive modelling results of Li and Dafalias (2012) (Figure 5.26 (b)), in laboratory tests the fabric direction deviates from the loading direction quite significantly and only converges to the loading direction at the very end of loading. This probably accounts for the more obvious difference between TC strength and TE strength as well as a longer period of more contractive (lower strength) response observed in the laboratory tests for TE than for TC. Therefore, the true difference between TC and TE after the coaxiality between the fabric direction and the loading direction may still remain unclear in the laboratory tests. Furthermore, the reliability of experimental data at large strain levels may be compromised as the strength and deformation at large strain levels in extension are governed by significant localisation and inhomogeneous deformation, e.g., necking, which makes it impossible to identify an accurate critical state in experiments. It is worth noting that Li (2006) and Thornton & Antony (2000) also observed an obviously higher strength for CVE simulations, in comparison to CVC simulations.

*C. Constant-p' simulations*

Figure 5.27 compares the stress-strain responses of three samples with the same initial state ($\sigma'_{3,0}$ = 20 MPa and $e_0$ = 0.594) but sheared under constant-*p'* vertical triaxial compression

(V-CPC), vertical triaxial extension (V-CPE) and horizontal triaxial extension (H-CPE) conditions. As Figure 5.27 (a) shows, the magnitude of stress ratio of the sample subjected to triaxial compression is higher than that under triaxial extension loading conditions which is in agreement with the observation for the drained constant-$\sigma'_3$ simulations. Figure 5.27(b) shows that the volumetric strain for the V-CPC sample was slightly contractive at the critical state whereas the volumetric strains of the V-CPE and H-CPE samples were dilative, i.e., samples are more dilative in extension than in compression at the critical state. The volumetric response at the small axial strain level differs to that at large strain levels as shown in a sub figure superimposed in Figure 5.27 (b). The V-CPE and H-CPE samples were more contractive than the V-CPC sample at initial stage of loading ($\varepsilon_a$< 1.83%), similar to the constant-volume observations (Figure 5.25). As presented in Figure 5.28, the fabric direction deviates more from the loading direction for the CPE simulations than for the V-CPC simulation at the initial stage of loading. This does not agree with the ACST framework which predicts a smaller deviation of the fabric direction from the loading direction for the CPE simulations than for the V-CPC simulations. This may be attributable to the use of a different definition of structural anisotropy in the current study. Note that the original ACST framework used the anisotropy of void space to represent the anisotropy of the whole assembly. Despite deviating slightly from the V-CPE simulation during shearing, the volumetric response of the H-CPE simulation converged to that of the V-CPE simulation at the critical state. The small differences observed between the H-CPE and V-CPE samples are a consequence of the finite sample size. In reality, sand grains may be crushed under such a high stress level. No such mechanism is simulated in the current study, i.e., the PSD remains unchanged. Thus the observed different responses between CPC and CPE can be solely attributed to the effects of loading mode.

### 5.4.3 Influence of the intermediate stress ratio

*Overall stress-strain behaviour*

The different responses of granular materials subjected to two extreme loading modes has been identified in the previous Section, i.e., TC ($b$ = 0.0) and TE ($b$ = 1.0). In this Section, the influence of loading mode on the mechanical behaviour of granular materials is further illustrated by a series of constant-$\sigma'_3$ drained simulations considering eight $b$ values ranging from 0 to 1. A plane-strain simulation was also carried out at each stress level. Eight initial states were considered:

(i) $\sigma'_{3,0}$ = 100 kPa, $e_0$ = 0.533, (ii) $\sigma'_{3,0}$ = 200 kPa, $e_0$ = 0.568, (iii) $\sigma'_{3,0}$ = 300 kPa, $e_0$ = 0.549, (iv) $\sigma'_{3,0}$ = 500 kPa, $e_0$ = 0.588, (v) $\sigma'_{3,0}$ = 500 kPa, $e_0$ = 0.646, (vi) $\sigma'_{3,0}$ = 1000 kPa, $e_0$ = 0.627, (vii) $\sigma'_{3,0}$ = 2000 kPa, $e_0$ = 0.625, and (viii) $\sigma'_{3,0}$ = 5000 kPa, $e_0$ = 0.612.

Details of these simulations are summarised in Table 5.1. Figures 5.29 and 5.30 illustrate the typical responses observed by considering a representative set of simulations with initial state (v) (i.e., $\sigma'_{3,0}$ = 500 kPa, $e_0$ = 0.646).

In Figure 5.29 (a), the deviatoric stress is defined as $q = \sqrt{3 \cdot J_2}$, where $J_2$ is the second invariant of the stress deviatoric tensor $s'_{ij} = \sigma'_{ij} - p' \cdot \delta_{ij}$ ($\delta_{ij}$ is the Kronecker parameter). Using this definition, $q$ becomes equivalent to the traditional definition of the deviatoric stress ($q = \sigma'_1 - \sigma'_3$) used in soil mechanics for triaxial compression ($b$ = 0.0) and triaxial extension ($b$ = 1.0). The data in Figure 5.29 (a) indicate that the mobilised stress ratios ($q/p'$) were initially independent of $b$. The responses started to diverge at about 2% axial strain; beyond this point there is a clear dependence on $b$, with both the peak and critical-state stress ratios decreasing with increasing $b$. It is useful to examine the individual principal stress components to understand how they contribute to this variation. Referring to Figure 5.29 (b), the peak and critical-state values of $\sigma'_1$ increased with increasing $b$ until $b$≈0.5 and subsequently decreased as $b$ increased. The peak and critical-state values of $\sigma'_1$ under triaxial extension conditions ($b$ = 1.0) were slightly higher than those under triaxial compression conditions ($b$ = 0.0). As would be expected both the peak and critical state values of $\sigma'_2$ increased consistently with increasing $b$ thus explaining the different shapes of the responses illustrated in Figure 5.29.

As shown in Figure 5.30 (a), the observed intermediate principal strain ($\varepsilon_2$) becomes progressively more compressive as $b$ increases. When $b$ is smaller than 0.3, the response is extensive following a slight initial compression; however it becomes compressive throughout shearing when $b$ exceeds 0.4. All the simulations show an extensive response along the $\sigma'_3$ direction as shown in Figure 5.30 (b), and the magnitude of $\varepsilon_3$ increases with $b$. The evolution of volumetric strain ($\varepsilon_v$) is illustrated in Figure 5.30 (c). All the samples initially contract; this is followed by a period of dilation until an approximately constant volumetric strain is reached at the critical state. The axial strain at which the contraction-dilation phase transformation occurs decreases with increasing $b$. When $\varepsilon_a$ < 4% the volumetric strain is more contractive with increasing $b$ but the volumetric strain at the critical state decreases with increasing $b$. This can also be explained within the framework of ACST, i.e., the rapid convergence of the fabric direction and the loading direction (Figure 5.31 (a)) and a higher location of CSL in $e$-log($p'$) space as $b$ is increased which will be

shown in Section 5.5. Figure 5.31 (b) shows that although *A'* at critical state is close to unity (> 0.99) for all the *b* values considered, it seems to vary with *b* values; while *A'* initially decreases with increasing *b* until *b* reaches 0.5, it increases thereafter and attains almost unity at *b* = 1. The plane strain case is overlaid on Figure 5.31 (b), taking the average *b* values for the last 10 % of axial strain which leads to *b* = 0.36 and it follows the general trend of the true triaxial simulations.

Under true triaxial loading conditions, the stress paths are related to a constant Lode angle ( $\theta = \tan^{-1}(\sqrt{3}(\sigma_2' - \sigma_3')/(2\sigma_1' - \sigma_2' - \sigma_3'))$ ), which defines the angle between the projection of the stress vector $(\sigma_1', \sigma_2', \sigma_3')$ and the projection of the $\sigma_1'$ direction in the deviatoric plane. Similarly, the direction of the strain increment vector $(d\varepsilon_1, d\varepsilon_2, d\varepsilon_3)$ in the deviatoric plane in terms of $d\varepsilon_1$, $d\varepsilon_2$ and $d\varepsilon_3$ can be calculated by $\theta_{d\varepsilon} = \tan^{-1}(\sqrt{3}(d\varepsilon_2 - d\varepsilon_3)/(2d\varepsilon_1 - d\varepsilon_2 - d\varepsilon_3))$. As shown in Figure 5.32 (a), $\theta_{d\varepsilon}$ increases with increasing *b* and, for *b* values above 0, $\theta_{d\varepsilon}$ tends to approach the triaxial extension condition ($\theta_{d\varepsilon} \approx 60°$) with increasing axial strain. When *b* = 0, $\theta_{d\varepsilon}$ remains close to 0 for the duration of shearing. As shown in Figure 5.32 (b), Sazzad & Suzuki (2013) also made similar observations. There was a large initial negative value of $\theta_{d\varepsilon}$ for the plane-strain simulation due to an adjustment imposed by the servo control scheme to enable restriction of the deformation in the intermediate stress direction. Figure 5.32(c) shows the deviation between the direction of the stress vector and the direction of the strain increment vector in the deviatoric plane ($\theta - \theta_{d\varepsilon}$); this deviation is termed deviatoric non-coaxiality and is a measure of the coaxiality of the material response in the deviatoric plane (Gutierrez & Ishihara, 2000). $\theta$ and $\theta_{d\varepsilon}$ are initially equal but start to differ once shearing starts. The extent of the deviation varies with *b* value. At any given axial strain level $\varepsilon_a$ (>0), $\theta - \theta_{d\varepsilon}$ increases from around 0 at *b* = 0 to attain a maximum at *b* = 0.3; when b>0.3, $\theta - \theta_{d\varepsilon}$ decreases with increasing *b* to attain a value of 0 at *b* = 1. Coaxiality in the deviatoric plane occurs only under triaxial compression (*b* = 0.0) and triaxial extension (*b* = 1.0) loading conditions. This agrees with the experimental observations of Suzuki & Yanagisawa (2006) (Figure 5.32 (d)).

The DEM sample response at the critical state can be compared with established three-dimensional empirical failure criteria that were developed using experimental data for real soils. These criteria are isotropic in nature and are most suitable for the DEM simulations considered in this study. The four criteria considered are as follows:

Ogawa model (Ogawa et al., 1974):

$$\frac{\sigma'_1\sigma'_2+\sigma'_1\sigma'_3+\sigma'_2\sigma'_3}{(\sigma'_1+\sigma'_2+\sigma'_3)^2}+n\left[\frac{3\sigma'_1\sigma'_2\sigma'_3-(\sigma'_1\sigma'_2+\sigma'_1\sigma'_3+\sigma'_2\sigma'_3)(\sigma'_1+\sigma'_2+\sigma'_3)}{3(\sigma'_1+\sigma'_2+\sigma'_3)^3}\right]=\eta \quad \text{(Eq. 5.7)}$$

Satake model (Satake, 1975):

$$\left(\frac{\sigma'_1-\sigma'_3}{\sigma'_1+\sigma'_3}\right)^2+\left(\frac{\sigma'_1-\sigma'_2}{\sigma'_1+\sigma'_2}\right)^2+\left(\frac{\sigma'_2-\sigma'_3}{\sigma'_2+\sigma'_3}\right)^2=\eta \quad \text{(Eq. 5.8)}$$

Lade model (Lade & Duncan, 1975):

$$\frac{(\sigma'_1+\sigma'_2+\sigma'_3)^3}{\sigma'_1\sigma'_2\sigma'_3}-27=\eta \quad \text{(Eq. 5.9)}$$

Matsuoka-Nakai model (Matsuoka & Nakai, 1974):

$$\frac{(\sigma'_1-\sigma'_3)^2}{\sigma'_1\sigma'_3}+\frac{(\sigma'_1-\sigma'_2)^2}{\sigma'_1\sigma'_2}+\frac{(\sigma'_2-\sigma'_3)^2}{\sigma'_2\sigma'_3}=\eta \quad \text{(Eq. 5.10)}$$

An overview of these four criteria can be found in Ng (2004b).

Figure 5.33 (a) compares the variation of the angle of shearing resistance at peak state ($\phi'_{peak}$) for simulations with $\sigma'_{3,0}$ = 500 kPa and $e_0$ = 0.646, while Figure 5.33 (c) shows the variation of the critical-state angle of shearing resistance ($\phi'_{cv}$) with $b$ for five of the constant-$\sigma'_3$, true triaxial simulations covering the loosest samples ($e_0$=0.646, $\sigma'_{3,0}$=500 kPa) and the densest samples ($e_0$=0.533, $\sigma'_{3,0}$=100 kPa). The $\phi'_{peak}$ and $\phi'_{cv}$ values predicted by the four failure criteria are also given on Figures 5.33 (a) and (c). The $\phi'_{peak}$ values depend on $\sigma'_3$ and $e_0$ so only one representative set of data is presented. Thus for $\phi'_{peak}$, the parameters for each failure criterion were obtained from least-squares regression using the true triaxial simulation data with $\sigma'_{3,0}$ = 500 kPa and $e_0$ = 0.646 and are given in Table 5.2. For $\phi'_{cv}$ the failure criteria parameters were obtained using all the constant-$\sigma'_3$, true triaxial simulations and corresponding fitting parameters are listed in Table 5.3. The *type-d* relationship (Sayão and Vaid, 1996) between the angle of shearing resistance and $b$ is evident. Both $\phi'_{peak}$ and $\phi'_{cv}$ initially increase with increasing $b$ and reach maximum values at $b$ = 0.5. When $b$ > 0.5, both $\phi'_{peak}$ and $\phi'_{cv}$ decrease with increasing $b$. According to the DEM data, $\phi'_{peak}$ at $b$ = 1.0 is slightly higher than $\phi'_{peak}$ at $b$ = 0.0, and the same observation is true for $\phi'_{cv}$.

Figures 5.33 (b) and (d) directly compare the measured $\phi'_{peak}$ and $\phi'_{cv}$ values with those obtained using the failure criteria. All four failure criteria approximate the DEM data quite well. For both $\phi'_{peak}$ and $\phi'_{cv}$, the Ogawa model gives the best fit. Both the Satake and the Matsuoka models give almost identical predictions that do not match the DEM data as closely as the Ogawa and Lade models. The Lade and Ogawa models capture the observed higher strength for triaxial extension ($b$ = 1.0) in comparison with triaxial compression ($b$ = 0.0), while the Satake and Matsuoka models predict the same strength under triaxial compression and extension. Similar observations have been reported by Ng (Ng, 2004b) who considered only $\phi'_{peak}$ and who reported a higher peak strength in extension than in compression as well. Comparing Figures 5.33 (b) and (d), it is worth noting that all the failure criteria fit the DEM data better for $\phi'_{cv}$ than for $\phi'_{peak}$ ; the predicted values and the DEM data for $\phi'_{cv}$ differ by less than 3% for all failure criteria, while for some simulations the differences are as large as 5% for $\phi'_{peak}$. This may be because the angle of shearing resistance at peak strongly depends on the initial state and thus is more variable while the angle of shearing resistance at the critical state is almost unaffected by the initial state.

*Particle-Scale Analyses*

Additional insight into the influence of the intermediate stress ratio on the material response can be gained by considering the particle-scale response. The evolution of coordination number, $Z$, during drained shearing for simulations with $\sigma'_{3,0}$=500 kPa and $e_0$ = 0.646 but differing $b$ values is shown in Figure 5.34. For all the simulations, $Z$ initially increases and then decreases with increasing $\varepsilon_a$; this qualitatively mirrors the volumetric strain response (Figure 5.30 (c)). However, while $\varepsilon_{vol}$ varies with systematically with $b$ at a given $\varepsilon_a$ value, $Z$ is independent of $b$.

The principal values of the fabric tensor ($\Phi_1$, $\Phi_2$ and $\Phi_3$) quantify the extent to which contacts cluster in the principal fabric directions. Considering the drained simulations with $\sigma'_{3,0}$=500 kPa and $e_0$ = 0.646, the evolution of $\Phi_1$, $\Phi_2$ and $\Phi_3$ is presented in Figures 5.35 (a) to (c). As shown in Figure 5.35 (a), the degree of clustering in the $\Phi_1$ direction increases with axial strain for all $b$ cases and then decreases slightly after the peak to attain a constant value at large strain levels. This means that upon shearing, particles tend to align along the major principal stress direction to sustain axial loading. The degree of clustering along the $\Phi_1$ direction decreases with increasing $b$. Referring to Figure 5.35 (b), for simulations with $b$ below the plane strain condition (i.e., when $b$ < 0.36), the degree of clustering in the $\Phi_2$ direction decreases with axial strain while the opposite is true when $b$ > 0.36. This correlates with the variation of $\varepsilon_2$ in Figure 5.30 (a) which shows an extensive response when $b$ is

lower than the plane strain condition. A comparison of Figures 5.35 (a) and (b) indicates that the difference between $\Phi_1$ and $\Phi_2$ becomes smaller with increasing $b$, suggesting that the role of contacts in the $\Phi_2$ direction shifts from one of offering lateral support to becoming significant force transmitting elements. For all the simulations, the degree of clustering along the $\Phi_3$ direction decreases with increasing axial strain and $\Phi_3$ decreases with increasing $b$, i.e., contact loss occurring along the $\Phi_3$ direction increases with increasing $b$. This agrees with Figure 5.30 (b) which shows that $\varepsilon_3$ is extensive for all $b$ values and the extensive strain increases as $b$ increases. This difference in the stress-deformation response along the minor and intermediate stress directions indicates the directional contact rearrangement during shearing, i.e., as $b$ increases contacts tend to be lost in the minor principal stress direction which is extensive but contacts tend to be formed in the intermediate principal stress direction which changes from extensive to compressive with increasing $b$.

As $b$ increases beyond the plane strain condition, the contact network becomes aligned along the major and intermediate principal stress directions. The contact intensity at the critical state can be appreciated by reference to the equal-angle stereo projections of contact orientations in Figure 5.36. The basic idea of the equal-angle stereo projection is that the 3D space can be envisaged as a unit sphere $\boldsymbol{R}$. Each contact normal can be described as a unit vector originating from the centre of $\boldsymbol{R}$ and intersecting $\boldsymbol{R}$. For any point $P$ on $\boldsymbol{R}$, there is a unique line that connects $P$ and the north pole of $\boldsymbol{R}$. The intersection point ($P'$) of this line and the equator describes the spatial orientation of the contact normal with respect to the vertical axis. The stereographic projection defined in Figure 5.36 (a) sends the "south pole" (0, 0, −1) to (0, 0), the equator to the unit circle, the southern (lower) hemisphere to the region inside the circle, and the northern (upper) hemisphere to the region outside the circle. Considering the symmetry about the equatorial plane, the spatial distribution of contact normal orientations with respect to the vertical axis can be reflected by the equal-angle projections of the south (lower) hemisphere which are illustrated in Figure 5.36 (b) to (f) for selected $b$ values. The centre of the equatorial plane ($O$) corresponds to the intersection point of contact normal exactly along the vertical axis, while the edge point of the equator (e.g., $Q'$) is a collective of the projection points of contact normals perpendicular to the vertical axis. The closer the intersection point is to the centre of the equatorial circle, the closer the contact orientation is to the vertical axis.

Figure 5.36 (b) indicates a clear clustering of contacts along the $\sigma'_1$ direction at the critical state when $b$ = 0. Figures 5.36 (c) – (e) illustrate a gradual transition to the scenario evident in Figure 5.36 (f) which indicates a clustering in $\sigma'_1$-$\sigma'_2$ plane. Following the ideas of Barreto & O'Sullivan (2012) and O'Sullivan et al. (2013) among others, failure is associated

with buckling of the strong force chains. When buckling occurs there is a displacement of the strong force chains orthogonal to the strong force chain axes. As argued by Barreto and O'Sullivan, resistance to buckling is provided by friction at the contacts and the weak force network which is orthogonal to the strong force network. The intensity of the weak force network is described by the minor principal fabric, $\Phi_3$. When $b$ = 0, the weak force network is axi-symmetric and there is a limited kinematic constraint such that the initial displacement associated with the buckling failure can have any direction in the $\Phi_2$-$\Phi_3$ plane which is indicated by the radiate decreasing of contact density from the centre to the periphery of the equatorial plane for the $b$=0.0 and $b$=0.2 cases (Figures 5.36 (b) and (c)). As $b$ increases, $\sigma'_2$ increases with $b$ for a given $\sigma'_3$ and the support provided by weak force network in the $\sigma'_2$, $\Phi_2$ direction increases. This imposes an increasingly strong kinematic constraint on the initial buckling displacement so that it becomes restricted to be oriented in the $\sigma'_3$, i.e., $\Phi_3$ direction. For $b$ values exceeding the plane strain case, the buckling strong force chains are oriented to be coplanar with the $\sigma'_1$-$\sigma'_2$ axes, with $\sigma'_3$ acting as orthogonal confinement. This is illustrated by the fact that $\Phi_2 > \Phi_3$ and the development of a clear band structure in the stereographs (Figures 5.36 (d) to (f)). The alignment of the force network in this way means that an analogy can be drawn with a flat plate axially loaded in two orthogonal directions, as schematically illustrated in Figure 5.37. In that case, elastic buckling theory relates the buckling stress in the $\sigma'_1$ direction to $\sigma'_2$ as $\sigma'_1 = -C_1\sigma'_2 + C_2$, where $C_1$ and $C_2$ are positive constants that depend on the plate geometry and material properties (Bulson, 1970). This analogy thus provides a plausible explanation as to why $\sigma'_1$ reduces with $b$ when $b$ exceeds 0.5.

## 5.5 Uniqueness of the critical state

### 5.5.1 Critical state line in *e*-log(*p'*) and *q*-*p'* space

The observed responses at the critical state for all the true triaxial simulations are plotted in Figure 5.38. Triaxial compression simulations loaded along the $z$ direction are denoted as VC, while triaxial extension simulations sheared in the $z$ and $x$ direction are denoted as VE and HE respectively. Data for the PFC3D simulations of triaxial compression (RW-C) and triaxial extension (RW-E) are also included in Figure 5.38. Calculations of void ratio ($e$) and stress state for the RW-C and RW-E simulations considered only the homogeneous interior regions, i.e., particles which are at least two times the mean particle size ($D_{50}$) away from the rigid boundaries according to the findings of Chapter 3. The critical-state ($e$,$p'$) data were fitted to the power-law relationship ($e_{cs} = \Gamma - \lambda \left(\frac{p'}{p_a}\right)^{\alpha}$) proposed by Li and Wang (1998)

with α equalling 0.7. For clarity only regression lines for $b$=0.0 and $b$=1.0 are given in Figure 5.38 (a) for all $b$ values considered. The fitting parameters (the slope $\lambda$ and the intercept $\Gamma$ of the CSL with the $e$ axis) are given in Table 5.4. There were some fluctuations in the stress-strain responses and so the data presented in Figures 5.38 (a) and (c) are taken as the mean values of $e$ , $p'$ and $q$ over the last 5% to 10% of axial strain.

Referring to Figure 5.38 (a), the data for all the triaxial compression simulations ($b$ = 0.0) collapse to the same CSL regardless of the loading conditions. The data for triaxial extension simulations ($b$ = 1.0) also collapse to a single CSL that differs from the triaxial compression CSL. For intermediate $b$ values ($0<b<1$), the CSLs show an obvious dependency on $b$; they move upwards in $e$-$log(p')$ space as $b$ increases, with the compression and extension CSLs acting as lower and upper bounds on the full data set. As $p'$ increases, the difference between different $b$ cases becomes less notable in $e$-$log(p')$ space. The RW simulation data (i.e., the PFC3D data) for triaxial compression and extension agree with the PB simulations, showing that the findings are not a function of the DEM code and boundary conditions adopted. On initial examination it appears that these data contradict the findings of Zhao and Guo (2013) (Figure 5.10 (c)) who proposed that a single line could describe the locus of points at the critical-state in $e$-$log(p')$ space, independent of $b$. However close examination of Zhao and Guo's data reveals that the results for $b$=0 and $b$=1.0 do act as upper and lower bounds respectively to their critical state data in $e$-$log(p')$ space although the variation in $e$ with $b$ at a given $p$' value is less marked than in the current dataset. The difference in sensitivity to $b$ may arise either because Zhao and Guo used an interparticle friction value of 0.5 or because of their lower values of contact stiffness (their linear normal and tangential stiffnesses ranged from $2 \times 10^4\ N/m$ to $6 \times 10^4\ N/m$). Note that although the equivalent contact stiffnesses evolve in simulations presented in this study, they reached almost constant values at critical state which are between $10^5$ and $10^6$ N/m. The higher value of coefficient of friction used by Zhao and Guo should produce a stronger and more stable force network while the lower stiffness results in higher coordination number (Antony & Kruyt, 2009). Both factors may contribute to the lower sensitivity of the critical state $e$ to $b$ observed in the study of Zhao and Guo. Also note that both Li (2006) (Figure 5.10 (a)) and Ng (2009b) (Figure 5.10 (b)) observed a higher position of CSL for extension than for compression in $e$-log($p'$) space.

Figure 5.38 (b) shows the variation of $\lambda$ and $\Gamma$ with $b$. The intercept $\Gamma$ increases consistently with increasing $b$ in an almost linear manner. There is also apparently a correlation between $\lambda$ and $b$: $\lambda$ initially decreases and then increases with increasing $b$. Data from the plane strain simulations are also included in Figure 5.38 (b) in which the $b$ value is the mean value over

the last 10% axial strain and are found to match the general trend of true triaxial simulation results. Figure 5.38 (c) shows the critical-state stresses in *q-p'* space and it is clear that the loci of the stress states for each *b* value follow a unique linear relationship. As shown in Figure 5.38 (d) and also in Table 5.4, the slopes of these linear plots (*M*) decrease consistently with increasing *b*.

### 5.5.2 Critical state from the particle-scale perspective

Figure 5.39 (a) illustrates the relationship between both *Z* and *p'* and $Z_m$ and *p'* at the critical state for the full dataset. The dashed and solid lines are the best-fit power-law regressions to *Z* and $Z_m$, respectively. In contrast to the data relating *e* and *p'* (Figures 5.38 (a)) the CSLs in *Z*-log(*p'*) and $Z_m$-log(*p'*) space are both independent of *b* (*Z* for *b*=1.0 seems to be slightly smaller than *Z* for *b*=0.0 but the difference is minute and $Z_m$ are indeed identical for both cases.). Both *Z* and $Z_m$ increase with increasing *p'*, reflecting the decrease in *e* (Figures 5.38 (a)). As *p'* increases, the number of rattlers (particles with fewer than two contacts) decreases, and so the difference between *Z* and $Z_m$ also decreases. There are obviously power-law relationships between *Z* and $e_{cs}$ and $Z_m$ and $e_{cs}$; the data presented in Figure 5.39 (b) indicate that these relationships are nonlinear and depend on *b*. The dependency on *b* is more obvious at higher *e* values or lower *Z* values, where it is apparent that for the same *e*, *Z* and $Z_m$ both increase with increasing *b*. The triaxial compression and extension cases again act as lower and upper bounds, respectively, on the data.

As discussed in Section 5.4.3, the extent of contact clustering is related to the deformation characteristics along different principal stress directions. Therefore, correlations between the fabric tensor and the overall stress-deformation response may provide useful information to the development of constitutive models that account for evolution of the micro-structure. Here the deviatoric fabric is taken as $\Phi_d = \sqrt{3 \cdot J_2^F}$ where $J_2^F$ is the second invariant of the fabric deviatoric tensor $F_{ij} = \Phi_{ij} - 1/3 \cdot \delta_{ij}$ ($\delta_{ij}$ is the Kronecker parameter). This definition of $\Phi_d$ is 2/15 of the $F_c$ parameter defined by Zhao and Guo (2013) which is identical to $a_c$ as defined in Section 4.6.3. Zhao and Guo proposed a power-law correlation between the deviator fabric and the normalised mean effective stress $p'/p_a$. When the approach of Zhao and Guo was applied to this dataset a better correlation was obtained when an offset term $\varepsilon_F$ was introduced:

$$\Phi_d = m_F \left(\frac{p\prime}{p_a}\right)^{\zeta} + \varepsilon_F \qquad \text{(Eq. 5.11)}$$

The efficacy of this correlation is illustrated in Figure 5.40 and the fitting parameters ($m_F$, $\zeta$ and $\varepsilon_F$) are summarised in Table 5.5. While the triaxial compression and extension data clearly bound the dataset, a simple correlation between the locus of critical states in $\Phi_d$-$p'/p_a$ and $b$ was not evident for 0.0< $b$ <1.0 when the data is viewed from this perspective. Generally, the critical-state $\Phi_d$ increases with increasing $b$, i.e., anisotropy increases with $b$. Comparing Figure 5.31 and Figure 5.35 shows that the fabric still evolves even after its direction coincides with the loading direction. Therefore, apart from the coaxiality condition ($A'$ = 1), a fabric condition, $\Phi_d = \widehat{\Phi}_{d,c}(p')$ , needs to be included in Eq. 5.3 to describe the critical state, where $\Phi_d$ represents a family of fabric descriptors. This should be addressed in the constitutive modelling of soils considering fabric anisotropy.

To explore the relationship between $e_{cs}$ and $b$, a semi-log plot of the variation in dilatancy with $\Phi_d$ during shearing is illustrated in Figure 5.41 for three representative sets of drained true triaxial simulations (i.e., loose ($\sigma'_{3,0}$ = 500 kPa, $e_0$ = 0.646), medium ($\sigma'_{3,0}$ = 1000 kPa, $e_0$ = 0.627) and dense ($\sigma'_{3,0}$ = 100 kPa, $e_0$ = 0.533)). Data below 0.25% axial strain were taken to be purely elastic and thus ignored. Both the dilatancy and the deviatoric fabric are higher for the dense samples than for the loose samples. For each case considered, the dilatancy increased with increasing deviatoric fabric and the variation was independent of $b$ at larger strains. Considering Figures 5.40 and 5.41 together, a higher $b$ gives a higher $\Phi_d$ ; dilatancy increases with $\Phi_d$ and this may explain the increase in $e_{cs}$ with $b$.

An additional particle-scale explanation for the dependence of $e_{cs}$ on $b$ can be found by reference to Figure 5.42. Figures 5.42 (a), (b) and (c) illustrate the spatial distribution of the branch vectors projected in $x(\sigma'_3)$-$y(\sigma'_2)$, $x(\sigma'_3)$-$z(\sigma'_1)$ and $y(\sigma'_2)$-$z(\sigma'_1)$ planes respectively. The branch vectors are the vectors joining the centroids of contacting particles. Three loading conditions are presented ($b$ = 0.0, plane strain, and $b$ = 1.0) for the representative series of drained simulations ($\sigma'_{3,0}$ = 500 kPa, $e_0$ = 0.646) at the critical state. An angular increment of 10° is used. The radial length of each bin indicates the number of branch vectors oriented within the angles defining the bin. The colour of each bin is proportional to the mean branch vector length ($L_{br}$) for that bin. The data presented in Figure 5.42 indicate that the longer branch vectors tend to align towards the higher principal stress directions (i.e., $\sigma'_1$ and $\sigma'_2$). For example, in the plane-strain case, the branch vectors oriented in the $\sigma'_1$ direction are on average the longest, the branch vectors in the $\sigma'_3$ direction are on average the shortest and the average branch vectors in the $\sigma'_2$ direction are intermediate between the maximum and minimum values. When $b$=0 these longer branch vectors form only in the $\sigma'_1$ direction, while when $b$=1.0 these longer branch vectors form in both the $\sigma'_1$ and $\sigma'_2$ directions. Figure 5.43 illustrates the contact force network at around 30% axial strain

viewed from the *x* axis. Each cylinder in Figure 5.43 connects the centroids of two touching particles and thus represents a contact. The thickness and the colour of each cylinder are proportional to the corresponding normal contact force normalised by the mean value. Strong contacts tend to rotate from being vertical to have an approximately 45 degree inclination with respect to the *z* axis when *b* increases from 0 to 1. This is in accordance with the spatial distribution of the branch vector length as stronger contacts are mainly formed between bigger particles which results in a longer branch vector length. Thus there is a systematic self-organization of the topology of the contact force network that manifests as a dependency of $e_{cs}$ upon *b* at the macro-scale.

As Figure 5.38 (c) and Figure 5.40 indicate neither the stress ratio nor the deviatoric fabric at critical state have a unique relationship that is independent of *b* with *p'*. Noting that the failure envelope of fabric is in an inverted shape of the stress failure envelope in the deviatoric plane, Zhao and Guo (2013) proposed using the first joint invariant of the deviatoric stress tensor and the deviatoric fabric tensor ($K_c = s'_{ij}F'_{ij}$) to describe the fabric anisotropy and suggested a power-law relationship between $K_c$ and *p'* at critical state which is independent of the *b* values (Figure 5.44 (a)).

$$K_c = \alpha {p'}^{\zeta_{K_c}} \qquad \text{(Eq. 5.12)}$$

where $\alpha$ and $\zeta_{K_c}$ are the fitting parameters. Reforming the expression for $K_c$ by separating $s_{ij}$ and $F_{ij}$ into a module and a unit tensor leads to:

$$K_c = \sqrt{s_{ij}s_{ij}} \cdot n_{ij}^{s} \sqrt{F_{ij}F_{ij}} \cdot n_{ij}^{F} = \sqrt{s_{ij}s_{ij}} \cdot \sqrt{F_{ij}F_{ij}} \cdot A' = \frac{2}{3} q F_c A' \qquad \text{(Eq. 5.13)}$$

Considering that the fabric direction and loading direction are effectively coaxial at critical state as shown in Figure 5.31, $A' \approx 1.0$ at the critical state. Therefore, $K_c \approx \frac{2}{3} q F_c$. This is evident in Figure 5.44 (b) which shows that the relationship between $K_c$ and *p'* at critical state is approximately two-thirds of the product of Eq. 5.11 and *M(b)p'* indicated by the dash lines (*M(b)* is given in Table 5.4). The fitting coefficients for Eq. 5.12 can be estimated from Eq. 5.11 and $q = M(b)p'$: $\alpha = \frac{2}{3} M(b) m_F / (p_a)^{\zeta}$ and $\zeta_{K_c} = 1 + \zeta$. The latter is evident from Zhao and Guo's data in which the fitting $\zeta_{K_c} = 0.894$ is very close to $1 + \zeta$ with $\zeta$ values ranging between -0.14 and -0.09. Eq. 5.13 indicates that $K_c$ is not an independent fabric descriptor but depends on *q* and $F_c$.

## 5.6 DEM analysis of the state parameter

Been and Jefferies (1985) defined the state parameter ($\psi$) to describe the proximity between the current state and the critical state. Triaxial test data show a clear link between $\psi$ and the strength and dilatancy of sand (e.g., Been & Jefferies, 1985; Yang, 2002). $\psi$ has also been incorporated in many recently-developed constitutive models for soil, e.g., NorSand (Jefferies, 1993; Jefferies & Shuttle, 2002), Wood et al. (1994), Severn–Trent sand (Gajo & Wood, 1999) and the model proposed by Li and Dafalias (2000). Calibration of these models is complicated by the development of post-peak strain localizations in laboratory tests. There is also a scarcity of large-strain laboratory test data for 3D general loading conditions; this limits the ability to develop and to apply these models to field applications where the stress state is not axisymmetric. Prior studies simulating true-triaxial element tests (Barreto & O'Sullivan, 2012; Ng, 2004; Thornton, 2000; Zhao & Guo, 2013) have shown that DEM can replicate the failure envelopes proposed for real sands. Thus, if a DEM model can be shown to capture the sensitivity of the material response to $\psi$ that one would expect for a real sand, there is then potential to use DEM to advance critical state-based constitutive models for sand. This challenge is addressed here.

### 5.6.1 Correlations between the state parameter and strengths

To quantitatively assess the similarity of the state-dependent response of a DEM model with the general response of real sand reported by Been and Jefferies (1985), the peak angle of shearing resistance ($\phi'_{peak}$) for drained simulations under both constant $\sigma'_3$ and constant $p'$ conditions is plotted against the initial state parameter ($\psi_0$) in Figure 5.45. As before, simulations using the Toyoura sand grading are denoted as ST, while simulations using the Dunkirk sand grading are marked as SD. The experimental data for real sands documented in Jefferies & Been (2006) (available at the Golder Associates website) are also included in Figure 5.45. It is clear that the general trend in both cases is a decrease of $\phi'_{peak}$ with increasing $\psi_0$. The $\phi'_{peak}$ values for the DEM simulations are consistently below the experimental $\phi'_{peak}$ values; this can be attributed to the use of spherical particles which cannot capture the interlocking effects observed in irregular real sand particles. As noted by Cho et al. (2006) amongst others, sand strength decreases with increasing particle roundness. The initial isotropic fabric in the DEM simulations may also contribute to the difference between the experimental and DEM data. For the DEM simulations with $\mu = 0.25$, the cases with intermediate principal stress ratios of $b = 0.0$ and $b = 0.5$ give lower and upper bounds respectively to the $\phi'_{peak}$ values. This is in accordance with the variation of peak strength with intermediate stress ratio discussed in Section 5.4.3. The DEM simulations with $\mu = 0.1$

give $\phi'_{peak}$ values that are lower than those observed for $\mu$ = 0.25; the dependency of this relationship on the interparticle friction may indicate a dependency on mineralogy in physical tests. The trend is observed for both DEM sample types SD triaxial simulations give responses that are close to those observed for the ST simulations with $b$ = 0.

Taylor (1948) proposed that soil strength can be decomposed into a dilational component and an intrinsic component, leading to the development of the stress-dilatancy theory (Rowe, 1962). Following the approach of Been and Jefferies (1985), the dilational component of the strength at peak for the DEM simulations, i.e., $\phi'_{peak}$ - $\phi'_{cv}$, is plotted against $\psi_0$ in Figure 5.46. The experimental data reported by Jefferies and Been (2006) are also included in Figure 5.46. It is clear that the responses observed in the DEM simulations lie within the bounds of the reported experimental data. This indicates that the relationship between $\phi'_{peak}$ - $\phi'_{cv}$ and $\psi_0$ is not shape-dependent; the DEM parametric study also reveals a lack of dependence upon $b$ and perhaps $\mu$ as well. The experimental data exhibit more scatter around the general trend than the DEM data. This may be attributable to the differences in initial fabric due to the use of different sample preparation methods. All the DEM samples start from an isotropic state, so any fabric dependency will not be evident from the simulation results. An exponential function of the form $\phi'_{peak} - \phi'_{cv} = \alpha e^{-\beta\psi_0}$ gives a good fit to the DEM-derived data in Figure 5.46 ($R^2$=0.972), with α=1.1874 and β=17.86. The resultant correlation between $\phi'_{peak}$ and $\phi'_{cv}$ is thus given by

$$\phi'_{peak} = \phi'_{cv} + \alpha e^{-\beta\psi_0} \qquad \text{(Eq. 5.14)}$$

Eq. 5.14 expresses the same idea as given in the empirical formulation proposed by Bolton (1986), i.e., the dilational contribution to the overall strength depends on both packing density and stress state. Note that Eq. 5.14 is independent of $b$.

Yang (2002) proposed an exponential correlation between the stress ratio at instability state ($\eta_{IS} = q_{IS}/p'_{IS}$) and $\psi_0$ to illustrate the state-dependent undrained strength of sands:

$$\eta_{IS} = \frac{M}{B} \mathrm{e}^{A\psi_0} \qquad \text{(Eq. 5.15)}$$

where $M$ is the critical-state stress ratio and $A$ and $B$ are fitting parameters. For undrained triaxial compression simulations listed in Table 5.6 (i.e., b=0), $A \approx$ -19.77 and $B \approx$ 1.72 with $M$ = 0.696; the best-fit line and data are illustrated in Figure 5.47 .

### 5.6.2 Correlations between the state parameter and dilatancy

Bolton (1986) clearly links the difference between the mobilized angle of shearing resistance and $\phi'_{cv}$ to dilatancy and Been and Jefferies (1985) proposed that the dilation rate ($D^p = -d\varepsilon_v^p / d\varepsilon_q^p$) at the peak stress ratio ($D^p_{max}$) is linked to $\psi_0$. Figure 5.48 plots $D^p_{max}$ against $\psi_0$ for the DEM dataset and also includes the experimental data presented in Jefferies and Been (2006). Note that $D^p$ was calculated using total strains, rather than the plastic strain components assuming that the elastic strain components are negligible at this point. The work conjugate shear strain ($\varepsilon_q$) proposed by Jefferies & Shuttle (2002) is used to ensure that the work done by the stress invariants ($q$ and $p'$) equals that calculated considering the principal stresses and strains.

$$\varepsilon_q = \frac{s_1\varepsilon_1 + s_2\varepsilon_2 + s_3\varepsilon_3}{q} \qquad \text{(Eq. 5.16)}$$

where $s_1 = (2\sigma'_1 - \sigma'_2 - \sigma'_3)/3$ , $s_2 = (2\sigma'_2 - \sigma'_3 - \sigma'_1)/3$ and $s_3 = (2\sigma'_3 - \sigma'_1 - \sigma'_2)/3$. Eq. 5.16 reduces to the traditional definition of deviatoric strain, i.e., $\varepsilon_q = \frac{2}{3}(\varepsilon_1 - \varepsilon_3)$, under triaxial conditions. Just as was the case when $\phi'_{peak}$-$\phi'_{cv}$ was plotted against $\psi_0$, plotting $D^p_{max}$ against $\psi_0$ for the DEM data indicates a unique relationship that does not depend on $b$ and the DEM data lie within the range defined by the experimental data.

It is also interesting to consider the state parameter when the peak stress is mobilised, $\psi_p$ , i.e., the difference between the void ratio at the peak and $e_{cs}$ at the same $p'$ value. Following Jefferies & Shuttle (2002), $D^p_{max}$ and $\psi_p$ can be represented by following relationship considering $D^p_{max} = 0$ at the critical state ($\psi_p = 0$):

$$D^p_{max} = -\chi \cdot \psi_p \qquad \text{(Eq. 5.17)}$$

As shown in Figure 5.49 (a), this linear correlation is also evident for the DEM simulations. As shown in Figure 5.49 (b), $\chi$ varies linearly with $b$ and the DEM simulation results for the two PSDs considered do not noticeably differ.

Figures 5.50 (a) and (b) plot the peak strength against the dilatancy at peak ($D^p_{max}$) of DEM data in terms of angle of shearing resistance ($\phi'_p$) and stress ratio ($\eta_p$), respectively. The resultant linear correlation between $\phi'_p$ and $D^p$ corresponds with what we would expect for a real sand (e.g., Vaid & Sasitharan, 1991). Considering the ST simulations with $\mu = 0.25$, the slope and position of the best-fit lines appear to be dependent on $b$, in line with the dependency of strength on $b$. The best-fit lines for the ST simulations with $\mu = 0.1$ are

located below those for $\mu = 0.25$. The SD DEM data collapse to give effectively the same trend that was observed for the ST data with $\mu = 0.25$ and $b = 0$.

According to stress-dilatancy theory, the critical state strength can be estimated from the strength - dilatancy relationship shown in Figure 5.50 by considering the critical state as $D^p = 0$, i.e., the intercept of the linear best-fit function. Building on the idea proposed by Bishop (1971), Vaid and Sasitharan (1991) suggested this might be a valid method to estimate the critical-state strength from the peak strength, noting that it is not always easy to achieve the large strains associated with the critical state. Figure 5.51 (a) and (b) support this idea as the critical-state strengths predicted in this way are in good agreement with the measured critical-state strengths. The small difference between the measured and predicted values may be attributable to the use of total strains instead of plastic strains when calculating the dilatancy.

### 5.6.3 Micro-scaled equivalent of the state parameter

DEM allows the link between the state-dependent material behaviour and the internal topology, or fabric, of the material to be established. The coordination number, $Z$, is a measure of the packing density of a granular assembly. As showed in Section 5.5.2 the critical states for the true triaxial tests presented here can be described by a relationship in $Z$-log ($p'$) space that is independent of the intermediate stress ratio and loading conditions, indicating that $Z$ is a micro-scale measure of 'state'. A micro-scale state parameter ($Z$-$Z_{cv}$) is proposed here to be the difference between the current $Z$ value and the value of $Z$ at the critical state corresponding to the same $p'$, similar to the definition of traditional state parameter. $Z_0$ is the initial coordination number and Figure 5.52 (a) shows that there is a correlation between $Z_0$-$Z_{cv}$ and $D^p_{max}$ that appears to be independent of loading path. The data for ST-b0.0-μ0.1 and SD-b0.0 tend to align in the same trend as that of ST-μ0.25, in line with the relationship between $\psi_0$ and $D^p_{max}$. There is also a good correlation between $Z_0$-$Z_{cv}$ and peak strength. While Barreto & O'Sullivan (2012) observed that there is no simple functional relationship between either $Z$ and $e$ or $Z$ and $p'$ during shearing, Figure 5.52 (b) reveals a clear linear correlation between $Z_0$-$Z_{cv}$ and $\psi_0$ for drained simulations, which may possibly account for the good correlations between $Z_0$-$Z_{cv}$ and both strength and dilatancy. Considering that the same isotropic compression method was used and particles were spherical, whether these observations are also applicable to samples generated by other methods which may possibly yield an initially preferential fabric direction and thereby a different $Z_0$ for the same $e_0$ and $\sigma'_{3,0}$ combination (e.g, Ng, 2004a) requires further exploration.

While the material considered here is initially isotropic, the stress conditions during shearing will induce an anisotropic fabric and the structural anisotropy can be quantified by the fabric tensor (Satake, 1982). As shown in Figure 5.53, when the deviatoric fabric $\Phi_d$ is calculated considering all the contacts, $\Phi_d$ at the point where peak strength is mobilized decreases with increasing $\psi_0$. The data for the simulations using $\mu$ = 0.1 are generally located below the data for simulations with $\mu$ = 0.25. For simulations using $\mu$ = 0.25, the relationship between $\Phi_d$ and $\psi_0$ for different loading paths tends to converge for $\psi_0 \leq$ -0.1, more scatter is evident for $\psi_0 >$ -0.1. In their DEM simulations, Sazzad & Suzuki (2013) noted a linear relationship between the stress ratio ($q/p'$) and a strong deviatoric fabric $\Phi_d^s$ which is calculated by considering only strong contacts (i.e., contacts transmitting above-mean contact forces). Figure 5.54 (a) shows the variation of $\Phi_d^s$ at peak strength ($\Phi_{d,peak}^s$) with $\psi_0$. It is evident that the locations of ($\Phi_{d,peak}^s$,$\psi_0$) drift systematically downwards with increasing $b$. The value of $\Phi_{d,peak}^s$ for $\mu$ = 0.1 is smaller than that for $\mu$ = 0.25 at the same $b$. This agrees with the variation of critical stress ratio with $b$ and $\mu$ as listed in Table 5.4. Just as the case of the relationship between $\phi'_{\text{peak}} - \phi'_{cv}$ and $\psi_0$, when the structural anisotropy at the critical state is removed from the anisotropy at peak strength, the difference between the different loading paths and different $\mu$ cases becomes less noticeable as illustrated in Figure 5.54 (b). These observations are not surprising as the strong contacts transmit most of the forces so there is a strong link between $\Phi^s_{ij}$ and $\sigma_{ij}$. Therefore the correlations with $\Phi^s_d$ presented in Figure 5.54 may arise from the existence of the correlations with ϕ' presented in Figures 5.45 and 5.46.

## 5.7 Application of NorSand to model the DEM data

A number of constitutive models for sands have been proposed based on critical state soil mechanics (CSSM) and explicitly consider the state parameter (e.g., Gajo & Wood, 1999; Jefferies, 1993; Li & Dafalias, 2000; Manzari & Dafalias, 1997). Development and calibration of these models is hindered by the lack of available data on critical state behaviour under 3D generalised stress states. The data presented here include a number of non-axisymmetric stress simulations and to illustrate the potential for such a dataset to aid in the development of constitutive models, the NorSand model (Jefferies, 1993; Jefferies & Shuttle, 2002) is calibrated against this dataset.

### 5.7.1 NorSand Overview

The NorSand model was presented in Jefferies (1993) and Jefferies & Shuttle (2002). Perhaps the most detailed description of NorSand can be found in Jefferies & Been (2006). The key idea of NorSand is the concept of the image state at which $\dot{\varepsilon}_v = 0$ but where $\ddot{\varepsilon}_v$ may

not be zero. The image state coincides with the critical state when $\ddot{\varepsilon}_v = 0$. The image state is always on the yield surface, while the CSL only intersects the yield surface at the critical state (Figure 5.55).

*Basic formulations*

The yield surface ($F$) for NorSand is derived from the stress-dilatancy relationship ($D^p = M\text{-}\eta$) and the normality condition based on the image state ($p' = p'_i, \eta = M_i$).

$$F = \eta - M_i[1 - \ln(p'/p_i)] = 0 \qquad \text{(Eq. 5.18)}$$

in which $p'_i$ is the mean effective stress at the image state and $M_i$ is the stress ratio at the image state.

The hardening law is given by:

$$\frac{dp_i'}{p'} = H\frac{M}{M_{tc}}\exp\left(1 - \frac{\eta}{M_{tc}}\right)\left[\left(\frac{dp_i'}{p'}\right)_{max} - \frac{dp_i'}{p'}\right]d\varepsilon_q \qquad \text{(Eq. 5.19)}$$

in which the maximum hardness $\left(\frac{dp_i'}{p'}\right)_{max} = \exp(-\chi(\theta)\psi_i/M(\theta))$ and $\psi_i = e - e_{c,i}$ is the state parameter at image state, $e_{c,i}$ is the critical void ratio at $p'_i$ and the deviatoric strain increment $d\varepsilon_q$ is in accordance with Eq. 5.16.

The work-conjugate deviatoric strain defined in Eq. 5.16 is adopted. Its linear nature allows the usual elastic-plastic decomposition (Jefferies and Shuttle, 2002). Thus the dilatancy can be related to the Lode angle θ by,

$$D^p = \frac{3(1+z_2+z_3)}{(sin\theta+\sqrt{3}cos\theta)-2\sin(\theta)z_2+(sin\theta-\sqrt{3}cos\theta)z_3} \qquad \text{(Eq. 5.20)}$$

in which $z_2 = d\varepsilon_2^p/d\varepsilon_1^p$ and $z_3 = d\varepsilon_3^p/d\varepsilon_1^p$.

*Implementation of NorSand*

One common way to implement a constitutive model is to decompose the strain increments into an elastic part and a plastic part, i.e., $d\varepsilon_i = d\varepsilon_i^e + d\varepsilon_i^p (i = 1,2,3)$. Modelling is advanced by imposing a plastic strain increment and computing the individual plastic strain increments and stress increments from the model formulations. The elastic strain increments are obtained following Hooke's law. The overall stresses and strains are updated by accumulating their increments. For the true-triaxial simulations considered in this study, integration proceeds by imposing an plastic axial strain increment $d\varepsilon_1$. Following Jefferies and Shuttle (2002), a trigonometric interpolation is used to account for the variation of the

ratio of the minor to major principal strains with $\theta$, i.e., $z_3 = z_{3,tc} - (z_{3,tc} - z_{3,te})\cos(\frac{3\theta+90}{2})$ , in which $z_{3,tc} = (2D_{tc}^p - 3)/(6 + 2D_{tc}^p)$ and $z_{3,te} = (2D_{te}^p - 6)/(3 + 2D_{te}^p)$ are the strain rate ratios of the minor principal strain to the major principal strain for triaxial compression and triaxial extension loading conditions. Substituting $z_3$ into Eq. 5.20 yields $z_2 = \frac{(sin\theta+\sqrt{3}cos\theta)D^p+((sin\theta-\sqrt{3}cos\theta)D^p-3)z_3-3}{2sin\theta D^p+3}$. Therefore, the intermediate and minor principal strain increments can be obtained directly from $d\varepsilon_2^p = z_2 d\varepsilon_1^p$ and $d\varepsilon_3^p = z_3 d\varepsilon_1^p$. Following this approach, differentiation of the potential surface is no longer required.

The stress component increments can be obtained from the consistency condition d$F$ = 0 under the d$\sigma'_3$=0 condition. Eq. 5.21 (a) and Eq. 5.21 (b) give the major principal stress increments from the consistency condition for plane strain and true triaxial loading conditions respectively.

$$d\sigma'_1 = p'\left(\frac{\eta\frac{dM_i}{M_i} + M_i\frac{dp'_i}{p'} + \frac{Ed\varepsilon_2^p}{p'}\left(\frac{D^p}{3} + \frac{\partial q}{\partial \sigma'_2}\right)}{\frac{\partial q}{\partial \sigma'_1} + v\frac{\partial q}{\partial \sigma'_2} + \frac{1+v}{3}D^p}\right) \qquad \text{(Eq. 5.21 (a))}$$

$$d\sigma'_1 = p'\left(\frac{\eta\frac{dM_i}{M_i} + M_i\frac{dp'_i}{p'}}{\frac{\partial q}{\partial \sigma'_1} + b\frac{\partial q}{\partial \sigma'_2} + \frac{1+b}{3}D^p}\right) \qquad \text{(Eq. 5.21 (b))}$$

The intermediate principal stress increment $d\sigma'_2 = vd\sigma'_1 - Ed\varepsilon_2^p$ for plane strain can be obtained from Hooke's law noting that $d\varepsilon_2^e = -d\varepsilon_2^p$, while $d\sigma'_2 = b\sigma'_1$ can be directly derived from the definition of $b$ for true triaxial loading in the case of d$\sigma'_3$=0. The overall stress components ($\sigma'_1$ and $\sigma'_2$) can thereby be updated by adding up corresponding increments d$\sigma'_1$ and d$\sigma'_2$. The elastic strain increments ($d\varepsilon_1^e, d\varepsilon_2^e, d\varepsilon_3^e, d\varepsilon_v^e$ and $d\varepsilon_q^e$) can be determined according to Hooke's law.

NorSand is essentially an isotropic elasto-plastic model and thus is suited to modelling the DEM simulations presented here which start from isotropic states. The implementation of 3D NorSand in this study is the modified version of the NorSand modelling Excel spreadsheet originally downloaded from the website of the geotechnical group of the University of British Columbia (Jefferies & Shuttle, 2005). Modifications include:

(a) The substitution of the CSL expression in terms of $e$ and log ($p'$) with the power-law relationship proposed by Li & Wang (1998).

(b) The complete formulation of NorSand as introduced in Jefferies & Been (2006) was implemented.

(c) The state parameter at the image state rather than at the current state was used to calculate $M_i$, $dp'_i/p'$ and $(dp'_i/p')_{max}$, where $p'_i$ is the mean effective stress at the image state at which $D^p = 0$ but $\dot{D}^p \neq 0$.

(d) The interpolated variation of the critical-state stress ratio with Lode angle $\theta$ used is that proposed by Jefferies & Shuttle (2011) as it agrees well with the DEM data as shown in Figure 5.56.

$$M_\theta = M_{tc} - \frac{M_{tc}^2}{3+M_{tc}}\cos(\frac{3\theta}{2}+\frac{\pi}{4}) \qquad \text{(Eq. 5.22)}$$

in which $M_{tc}$ is the critical stress ratio for triaxial compression.

(e) 3D NorSand was implemented for true triaxial tests under constant-$b$ and constant-$\sigma'_3$ conditions.

### 5.7.2 Calibration of NorSand

NorSand uses the critical-state parameters $\Gamma$, $\lambda$ and $M$. The plasticity parameters considered are $H$, the hardening modulus, $\chi$, which reflects the variation of $D^p_{max}$ with $\psi_i$, and $N$ which controls the relative distance between the isotropic normal consolidation line (NCL) and the CSL measured by the corresponding mean stress ratio. The elastic parameters are the elastic rigidity, $I_r = G/p'$, and Poisson's ratio, $\upsilon$. Many of the NorSand model parameters can be determined from the data presented above: $\Gamma$, $\lambda$ and $M$ are listed in Table 5.4 (note that the power-law interpretation of the CSL is adopted). At the peak state, d$q$=0, provided that the normality condition is true, $d\varepsilon_v^p = d\varepsilon_v^e = 0$ at peak. Therefore, the image state at peak coincides with the real state, i.e., $\psi_i = \psi$, therefore $\chi$ can be determined from the $D^p_{max}$-$\psi_p$ relationships presented in Figure 5.49. $N$ equals to 1- $k$, where $k$ is the slope of the linear relationship shown in Figure 5.50 (b) and $N$ increases linearly with increasing $b$ (Figure 5.57). A Poisson's ratio of 0.2 is reasonable as $\upsilon$ does not vary greatly between different types of granular materials. The tangent shear modulus ($G$) was determined considering the elastic range of stress-strain behaviour and was found to be related to $e$ and $p'$ following Eq.

5.23 by Zheng (2014) (Msc project in progress at Imperial College, Personal communication):

$$G = \frac{139967.7042 \times (1.1666 - e)^2}{1+e} (p')^{0.36554} \quad \text{(Eq. 5.23)}$$

Parametric study shows that the stress-strain behaviour in NorSand under the drained loading conditions is not very sensitive to the input $G$ values mainly because of the dominance of plastic strain. The corresponding $I_r$ values can be determined, thereby leaving $H$ as the only parameter to calibrate. Calibration of $H$ was achieved by minimising the squared deviations between the DEM data for deviatoric stress ($q$) versus axial strain ($\varepsilon_a$) and the corresponding NorSand response considering the full axial strain range.

### 5.7.3 Performance of NorSand under 3D general loading conditions

Figures 5.58 and 5.59 compare the stress-strain behaviour modelled using NorSand with the measured stress-strain behaviour in DEM simulations for a dense sample ($e_0$ = 0.549, $\sigma'_3$ = 300 kPa) and a loose sample ($e_0$ = 0.646, $\sigma'_3$ = 500 kPa) respectively. For clarity, only data for simulations of triaxial compression ($b$ = 0.0), plane strain (PS) and true triaxial compression with $b$ = 0.8 are presented. The $H$ and $I_r$ values vary with the initial state but are found to be independent of the intermediate stress ratio as listed in Table 5.7.

Referring to Figure 5.58 (a), the deviatoric stress of the dense sample initially increases sharply to the peak followed by an obvious softening response and becomes constant at the critical state. Although the modelled behaviour slightly over-estimates the peak strength of the DEM simulation results for all the stress conditions considered, there is in general a good agreement with the DEM data. As illustrated in Figure 5.58 (b), the measured and modelled volumetric behaviour is also very close, showing an initially contractive followed by a dilative response. Good agreement was achieved between the model and the simulated data for the loose sample, as illustrated in Figure 5.59.

Similarly, effective calibration was achieved for other DEM simulations. The large number of simulations allowed the factors which determine the modelling hardening modulus ($H$) to be established. Referring to Figure 5.60, the linear relationship between $H$ and $\psi_0$ proposed by Jefferies & Been (2006) considering experimental data is also evident considering the calibration against the DEM data. The slope of the $H$-$\psi_0$ relationship is higher for the DEM data than for the experimental data considered by Jefferies & Been (2006). This can possibly be attributed to the lower location of the CSL in $e$-log ($p'$) space of the DEM data in comparison to the experimental data. Given the same $\psi_0$, the void ratio of DEM data is

actually much smaller than the experimental data, which results in a stiffer response. This void ratio difference also explains the higher $H$ value for the SD simulations in comparison with the ST simulations.

## 5.8 Discussions and Conclusions

The influence of the intermediate principal stress ratio, $b$, on the critical state characteristics of cohesionless soil was explored using DEM simulations of four test types: constant-$b$ drained, constant-volume, constant-$p'$ and plane strain loading conditions. While most of the simulations were carried out using a periodic cell and the LAMMPS code, selected simulations were completed using PFC3D and rigid boundaries to demonstrate the lack of dependence on either code or boundary conditions. The constraints imposed by the narrow range of attainable void ratios in DEM simulations using spheres were overcome by performing contrasting simulations under three types of loading condition.

Considering firstly $q$-$p'$ space, the critical state can be represented by a straight line for each $b$ case. The slope of these lines decreases consistently with increasing $b$. This dependency on $b$ relates to the dependency of $\phi'_{cv}$ on $b$ and is in line with what would be expected from empirical three-dimensional failure criteria. Both the Ogawa and Lade criteria gave good fits to the data; in particular they captured the observed higher strength in extension than in compression.

Perhaps the most significant finding of current study is that the CSL in $e$-$log(p')$ space moves upwards as $b$ increases. To examine the potential for correlations in our data, data for each $b$ value were fitted by power-law regression separately. When the CSL is plotted in terms of $e$ and $(p'/p_a)^{\alpha}$ for each $b$-value individually, the intercepts with the $e$-axis of the resulting straight lines ($\Gamma$) increase almost linearly with $b$. The slopes of the lines ($\lambda$) also show a slight sensitivity to $b$. This suggests constitutive models should include CSLs that vary with $b$. The final void ratio values reflect the fact that, as observed from the stress-strain data, while samples tended to be more contractive with increasing $b$ at low strain levels, they became dilative at the critical state as $b$ increased. This was explained within the framework of ACST, i.e., the rapid convergence of the fabric direction and the loading direction and a higher position of CSL in $e$-log($p'$) space for a higher $b$ value.

The observed dependency of the CSL in $e$-log($p'$) space on $b$ is inconsistent with the recent study by Zhao and Guo (2013) who suggested that the CSL in $e$-log($p'$) space is unique. However, a careful examination of their data revealed a less obvious systematic variation of

their $e$ values at critical state ($e_{cs}$) with $b$ at a given $p'$. The discrepancy between this earlier study and the current study may be attributable to the different input parameters.

At the particle scale, one notable finding was that the relationship between $Z$ and $p'$ or $Z_m$ and $p'$ at critical state does not depend on $b$, despite the differences in the relationship between $e$ and $p'$ at the critical state. In fact, it appears that for a given critical-state $e$, $Z$ and $Z_m$ increase with increasing $b$, reflecting the fact that $e$ depends on both $Z$ and $\Phi_d$. No unique fabric-$p'$ relationships were found and $\Phi_d$ varies with $b$. The $K_c$ parameter proposed by Zhao and Guo reflects the coaxiality of the fabric direction and the loading direction and is 2/3 of the product of the deviatoric stress and the deviatoric fabric. The principal fabric values can be taken as an indication of the intensity of contacts in a given direction and a clear dependency on $b$ is shown. There is a correlation with strain; a decrease in contact clustering (decrease in principal fabric value) corresponds to an extensive response while an increase in contact clustering corresponds to a compressive response. When $b$ exceeds the plane strain condition, the clustering of contacts along the $\sigma'_1$-$\sigma'_2$ plane may explain the decrease in $\phi'$ with increasing $b$, as the buckling of this planar network of contacts is analogous to the bucking of a biaxially-loaded plate.

At a given stress ratio, the dilatancy was observed to increase with $b$. The deviatoric fabric at the critical state increased with $b$, and dilatancy increased with deviatoric fabric. These dependencies of the volumetric response on $b$ are closely related to the variation in $e_{cs}$ with $b$. A detailed examination of the contact force network topologies revealed that there is a systematic variation in the length of branch vectors with $b$, with the longer branch vectors being oriented in the direction of the major principal stress. This again is in agreement with the variation in $e_{cs}$ with $b$ as $\sigma'_1=\sigma'_2$ when $b$=1.

This study has also explored the state-dependent mechanical behaviour of granular materials using DEM simulations of true triaxial tests. A particular emphasis is placed on examining the link between the state parameter and the mechanical behaviour that had previously been established by Jefferies and his colleagues.

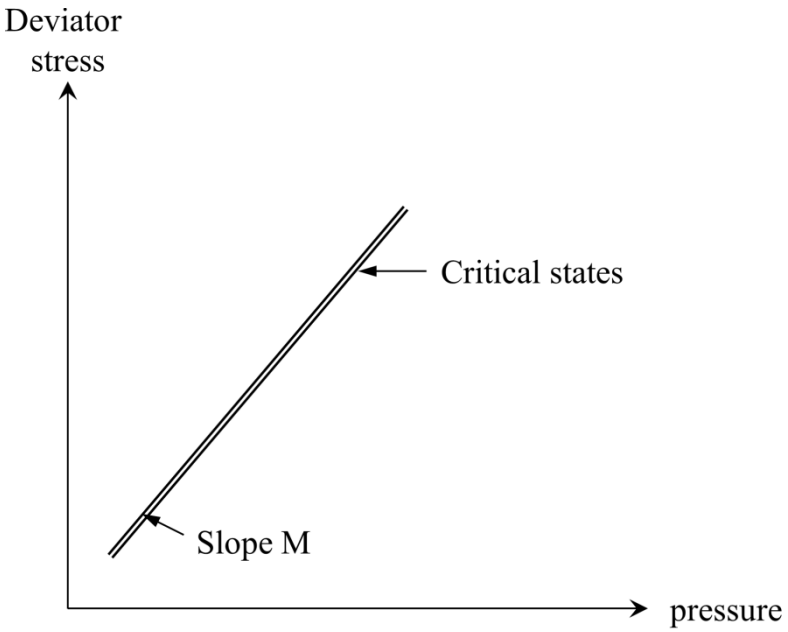
The relationships observed in the DEM simulations between the state parameter, $\psi_0$, and both the dilational component of strength ($\phi'_{peak} - \phi'_{cv}$) and the dilatancy at peak ($D^p_{max}$) quantitatively agree with the empirical data presented by Jefferies and Been (2006). This observation strengthens the case for the use of DEM in fundamental studies of soil behaviour. An exponential function incorporating $\psi_0$ was proposed to account for the influence of initial state on the dilational contribution to the overall strength. This relationship was shown to be unique and independent of the loading path, $\mu$ and PSD considered in this study. However,

all the simulations present in this study were performed on initially isotropic samples composed of spherical particles. Whether these observations are also true for initially anisotropic materials and how the particle shape could affect the results require further exploration.

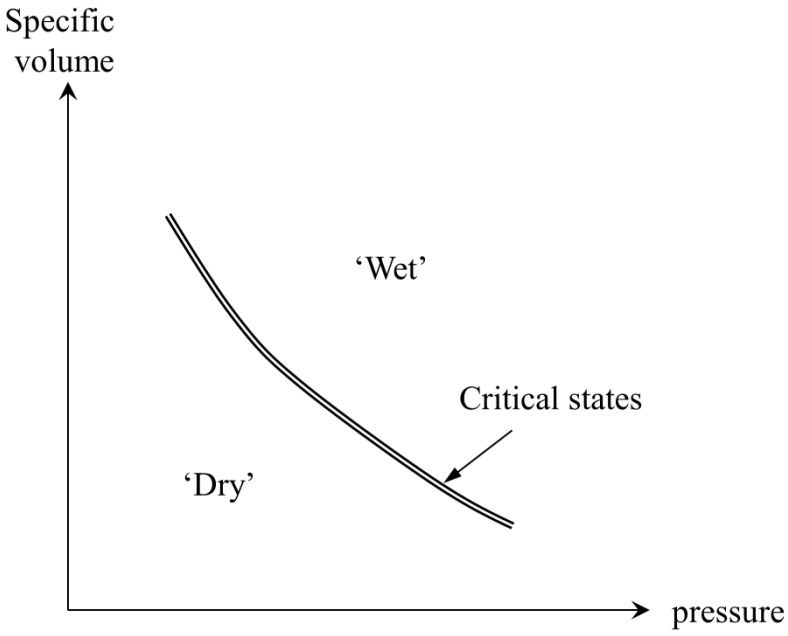
In drained triaxial loading conditions, the peak strength ($\phi'_{peak}$) was observed to decrease systematically with increasing initial state parameter ($\psi_0$), giving a trend that is qualitatively in agreement with the empirical data reported in Jefferies and Been (2006). Many prior studies have shown either experimentally (e.g., Cho et al., 2006) or using DEM (e.g., Maeda et al., 2009) that the critical state strength depends on particle geometry, and so it is not surprising that the DEM data, obtained using spherical particles, lie below the experimental data that were obtained using real, non-spherical grains. Thus, this qualitative agreement also strengthens the case for DEM's ability to capture the type of response we would expect within the CSSM framework. The DEM data showed that the relationship between peak strength and $\psi_0$ depends on the intermediate stress ratio. For DEM simulations of constant volume triaxial tests, the strength was observed to systematically increase with decreasing $\psi_0$, in line with Yang (2002).

The good agreement between the DEM simulation results and the available experimental data indicates the potential for DEM to be used in the development of continuum constitutive models. In particular, DEM models can develop data for generalised stress states at large strains, approaching a critical state; such data cannot easily be obtained in laboratory tests. To demonstrate this point, NorSand, an isotropic critical state-based constitutive model originated from the laboratory-testing data, was shown to be able to effectively model the DEM data, following the same calibration procedure one would apply to an experimental data set. The applicability of other constitutive models, e.g., Li & Dafalias (2000), to DEM data under axisymmetric loading conditions has also been shown by Yan and Dong (2011).

Good correlations were observed between the micro-scale state parameter ($Z_0$-$Z_{cv}$) and both strength and dilatancy. This can be attributed to the linear relationship between $Z_0$-$Z_{cv}$ and $\psi_0$. DEM simulations generate the data necessary to quantitatively link the granular material fabric to the overall mechanical response. Here, the deviatoric fabric for the strong contacts, i.e., the above-mean contacts, was seen to agree with the variation of the macro-strength with $\psi_0$. This is perhaps unsurprising as the strong contacts are known to play a dominant role in stress transmission (see Section 4.7.2); however, no such correlation could be observed when considering the structural anisotropy of all contacts.

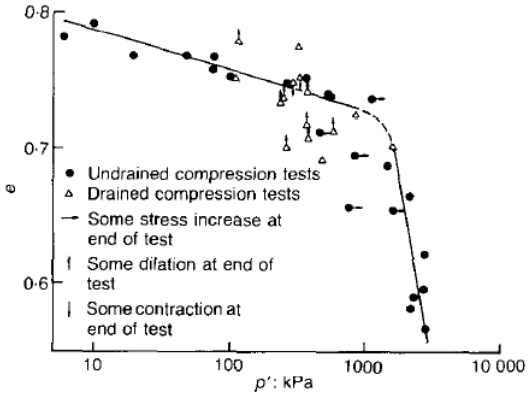



(a) *q-p'* space

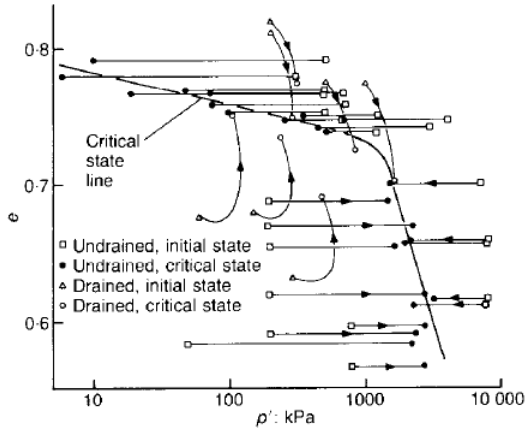



(b) *v*-ln*p'* space

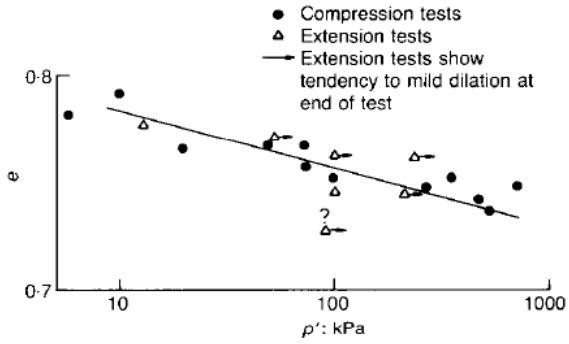
Figure 5.1 Definitions of the CSL (After Schofield & Wroth, 1968)



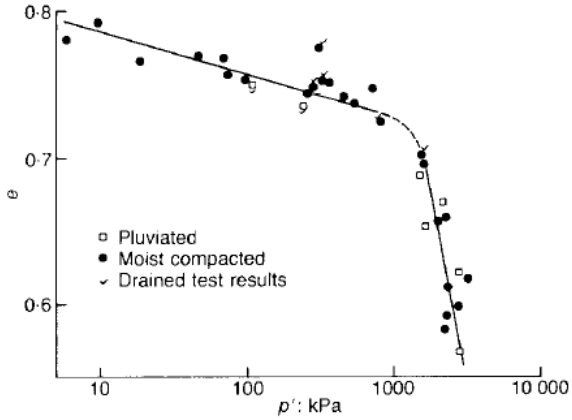

(a) Drained VS Undrained




(b) Different initial states

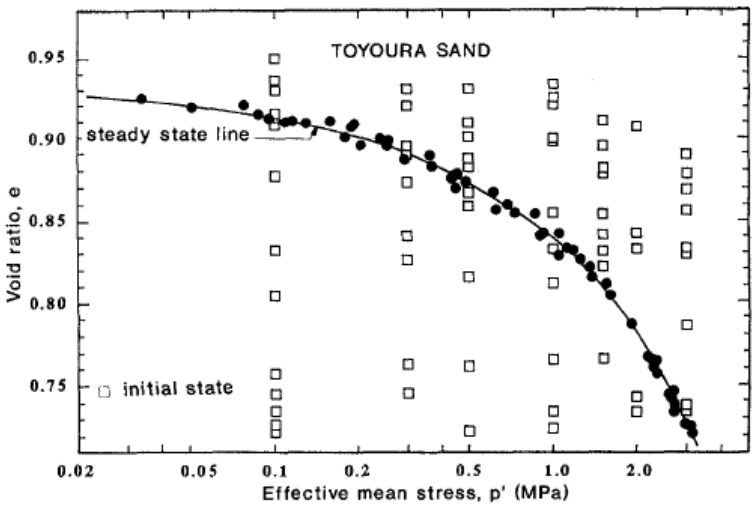



(c) Compression VS Extension

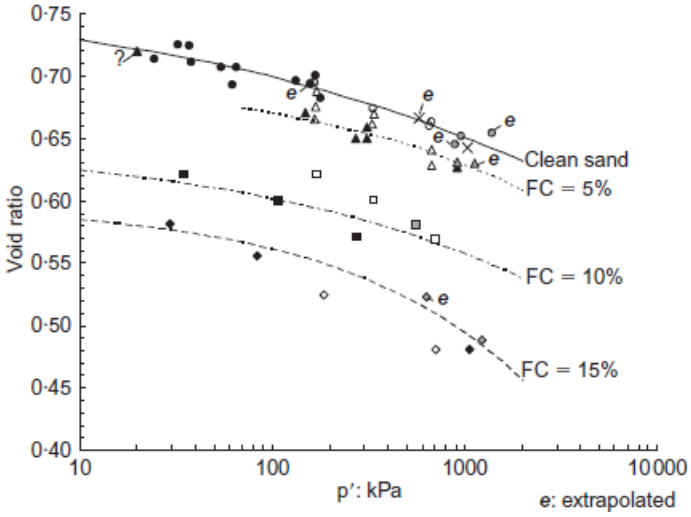



(d) Inherent anisotropy

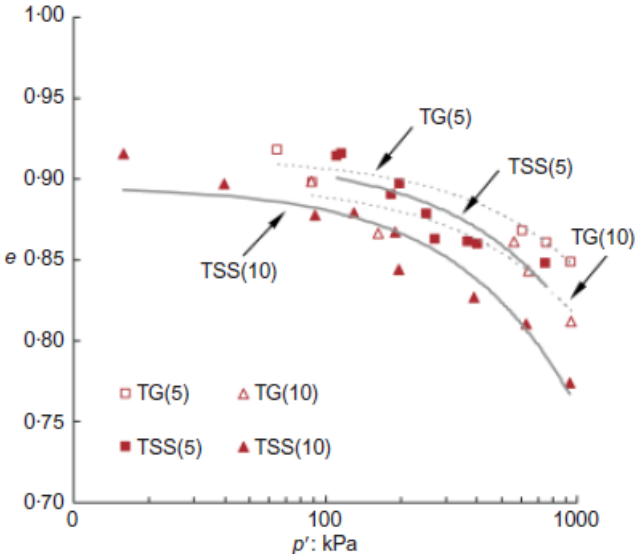
Figure 5.2 Evaluating the uniqueness of the CSL in *e*-log(*p'*) space (Been et al., 1991)




(a) Toyoura sand (Verdugo & Ishihara, 1996)




(b) Silty sand (Murthy et al., 2007)




(c) Mixture of clean sands with fine particles of different shapes: TG indicates Toyoura sand mixed with glass bead, TSS denotes Toyoura sand mixed with crushed silica, the number within parentheses indicates the fines content (Yang & Wei, 2012)

Figure 5.3 Positive evidence regarding the uniqueness of CSL in e-log(p') space

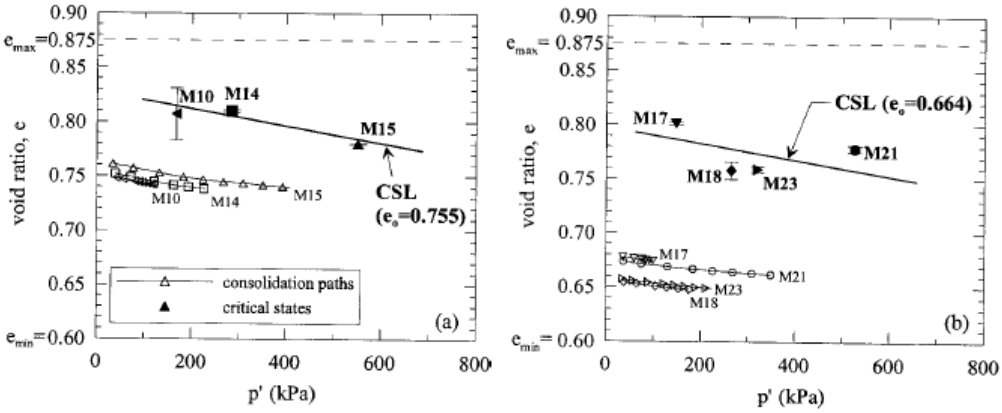
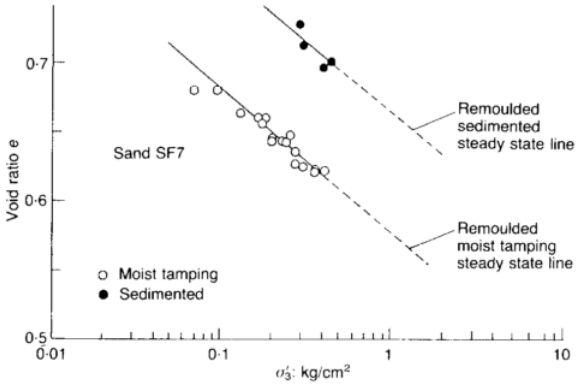
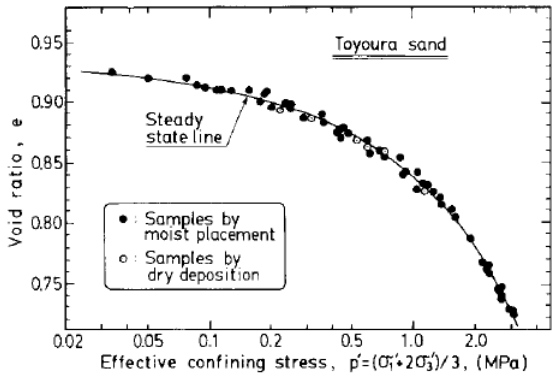


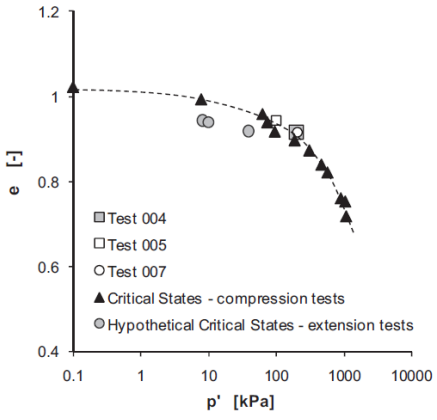

Figure 5.4 Dependency of the position of the CSL on initial void ratio (Finno & Rechenmacher, 2003)




(a) Verdugo (1992)

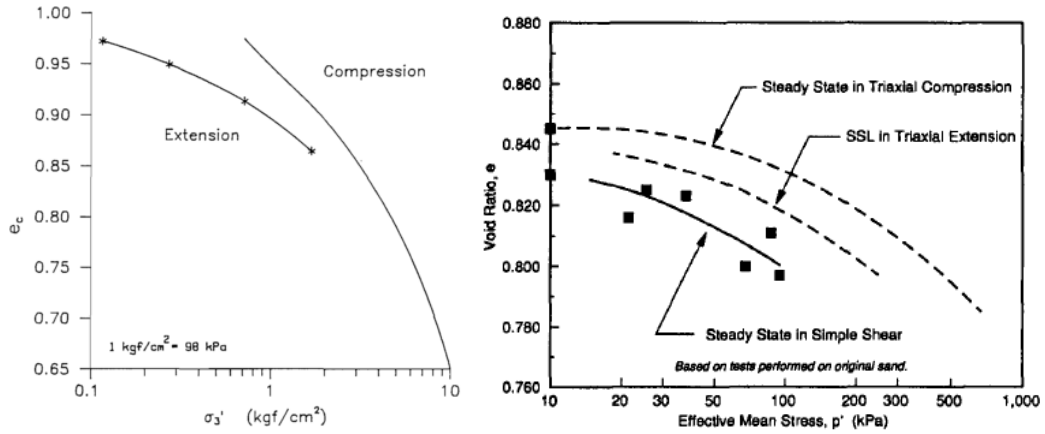



(b) Ishihara (1993)



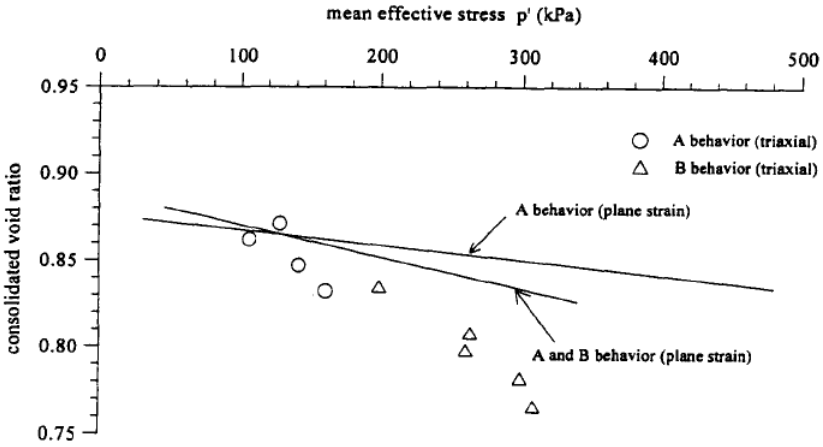

(c) Carrera et al. (2011)

Figure 5.5 Dependency of the CSL on the initial anisotropy: (a) indicates dependency ; (b)-(c) show no dependency

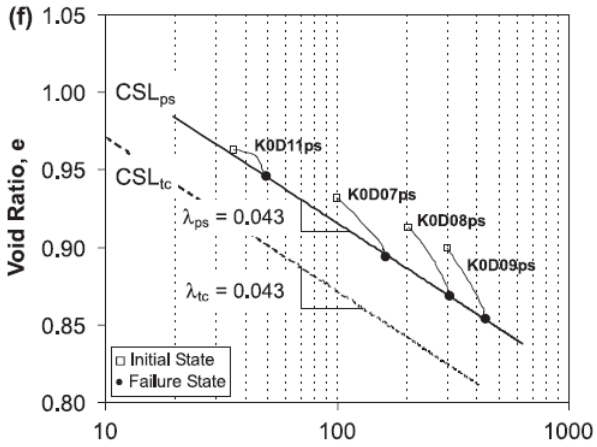



(a) Vaid et al. (1990) (b) Riemer & Seed (1997)

Figure 5.6 Comparing the CSLs obtained from triaxial compression and triaxial extension tests

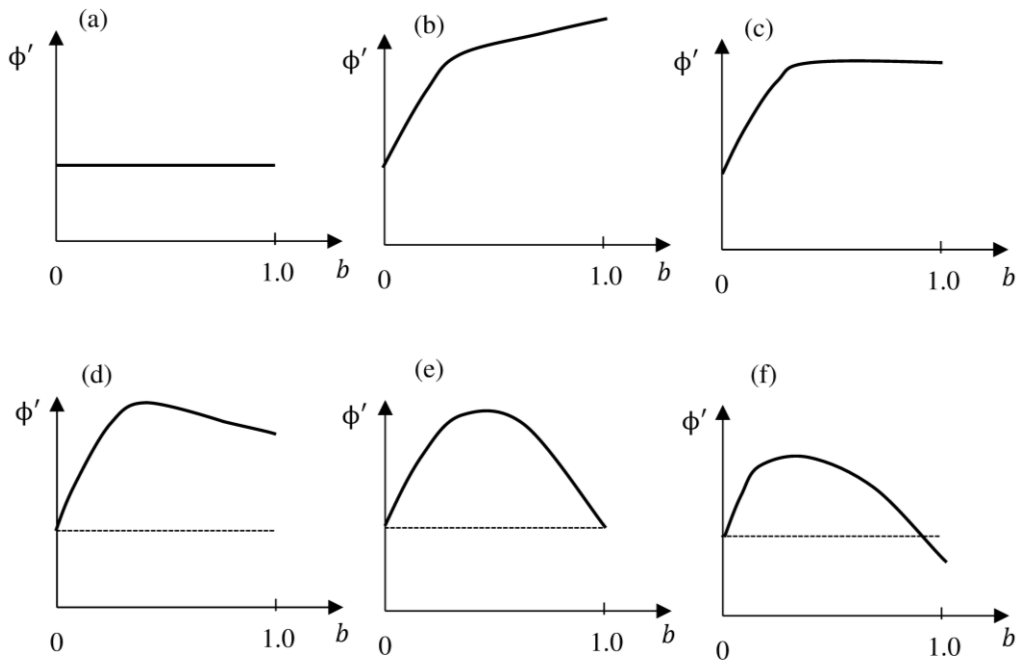



(a) Finno *et al.* (1996)



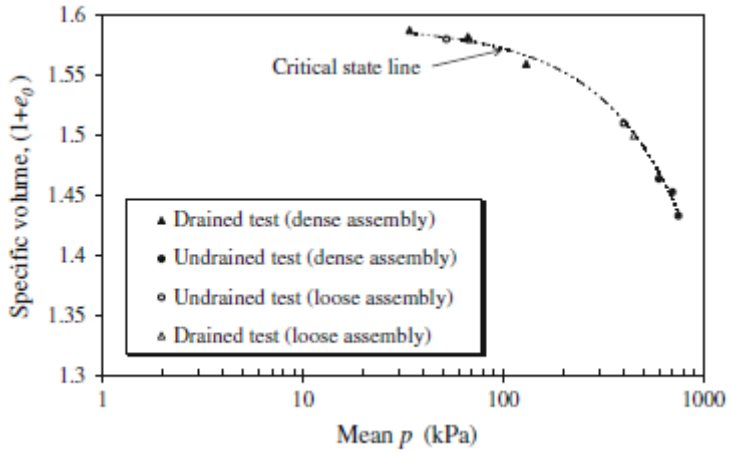

(b) Wanatowski & Chu (2007)

Figure 5.7 A higher position of the CSL in *e*-log(*p'*) for plane strain tests than for triaxial tests

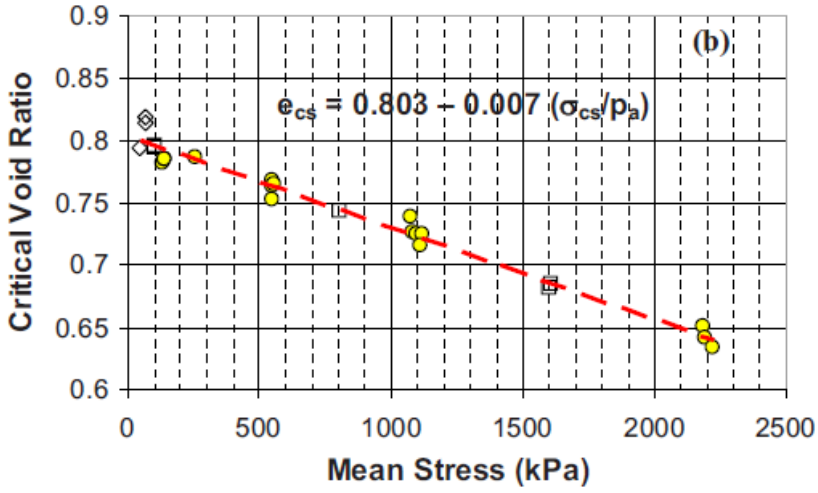



| CURVE | REFERENCE | RELATIVE DENSITY |
|---|---|---|
| (a) | Bishop (1966) | Loose |
| (b) | Lade & Duncan (1973)<br>Reades & Green (1976) | Loose<br>Loose to Dense |
| (c) | Green (1971)<br>Lade & Duncan (1973) | Loose to Dense<br>Dense |
| (d) | Ergun (1981)<br>Haruyama (1981) | Dense<br>Loose |
| (e) | Sutherland & Mesdary (1969)<br>Ramamurthy & Rowat (1973) | Loose to Dense<br>Dense |
| (f) | Shankariah & Ramamurthy (1980) | Medium to Dense |

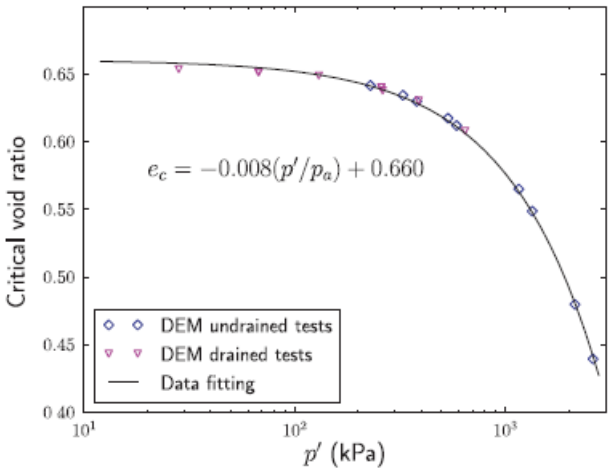
Figure 5.8 Reported variation of angle of shearing resistance with *b* in sands (After Sayão & Vaid, 1996)




(a) Sitharam & Vinod (2009)

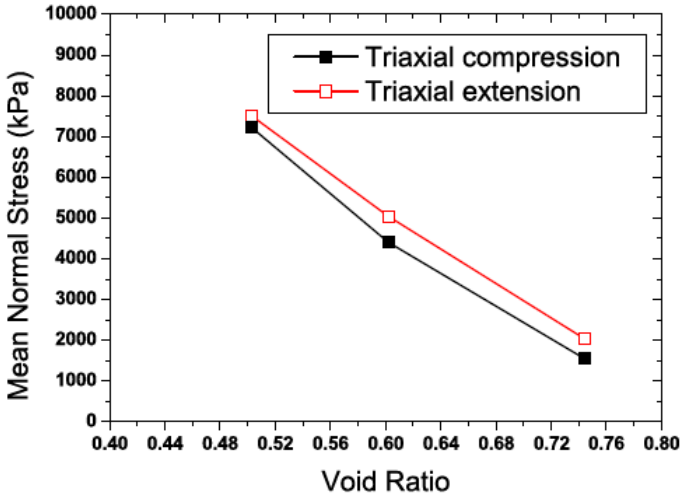



(b) Ng (2009a)

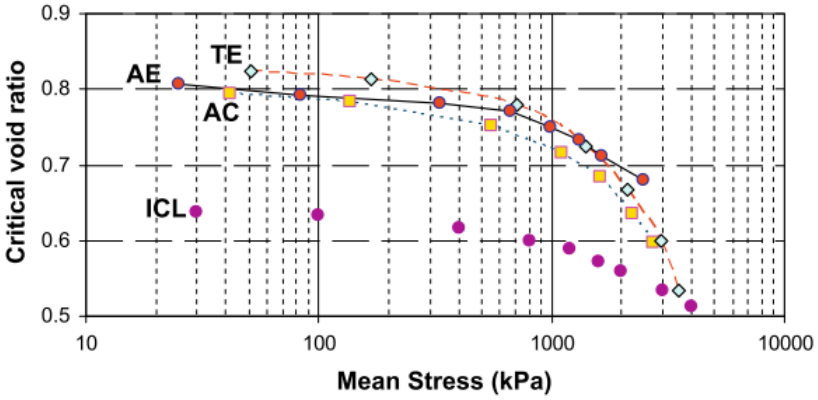



(c) Guo & Zhao (2013)

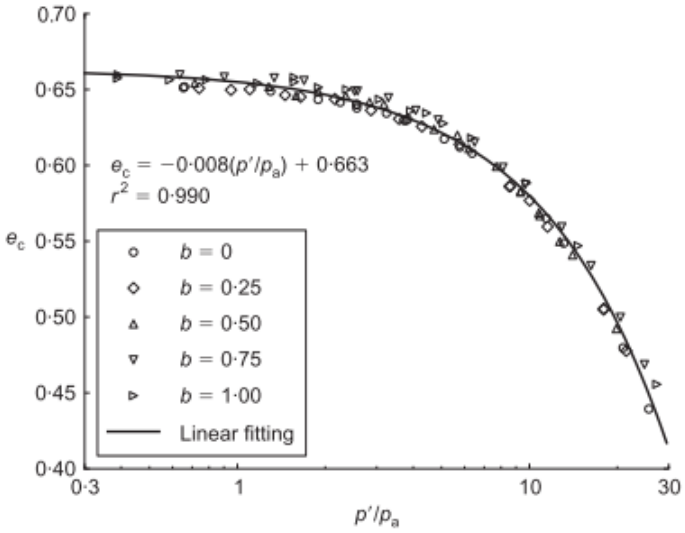
Figure 5.9 DEM studies of the uniqueness of CSL in *e*-log(*p'*) space under conventional triaxial loading conditions (b = 0.0)




(a) Li (2006)




(b) Ng (2009b): TE: triaxial extension; AE: Axial extension; AC: Axial compression; ICL: Isotropic compression line




(c) Zhao and Guo (2013)

Figure 5.10 DEM studies on the influence of loading mode on the position of the CSL

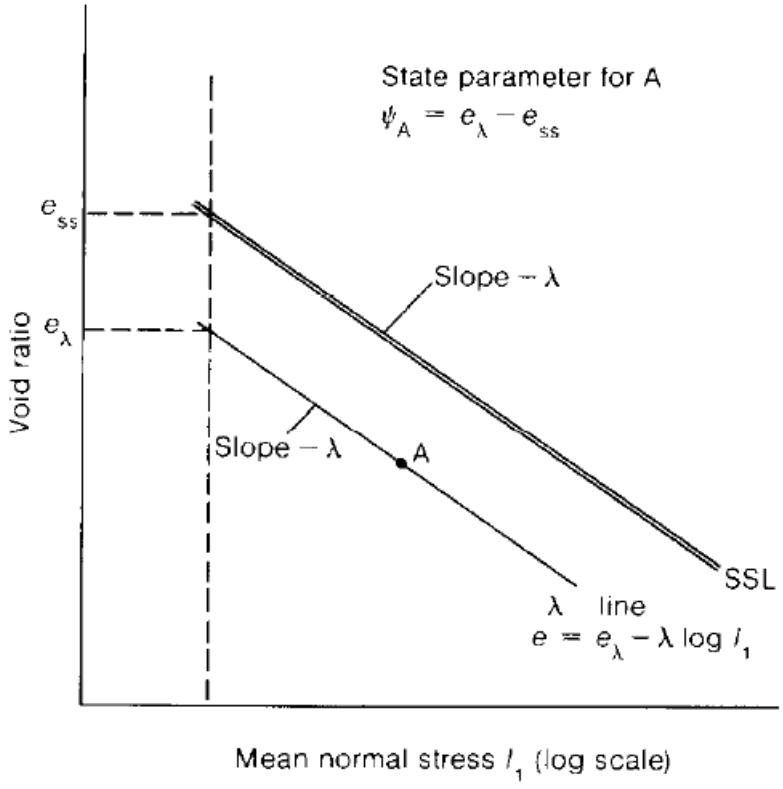



Figure 5.11 Definition of the state parameter (Been & Jefferies, 1985)

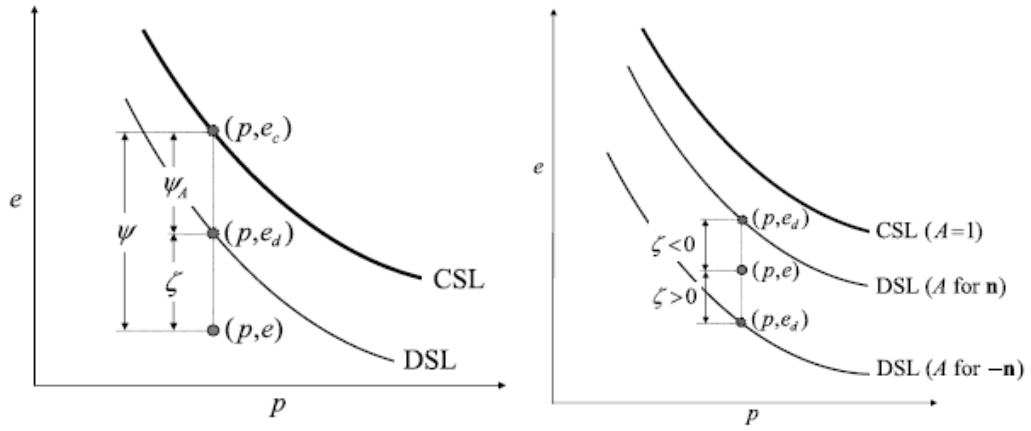
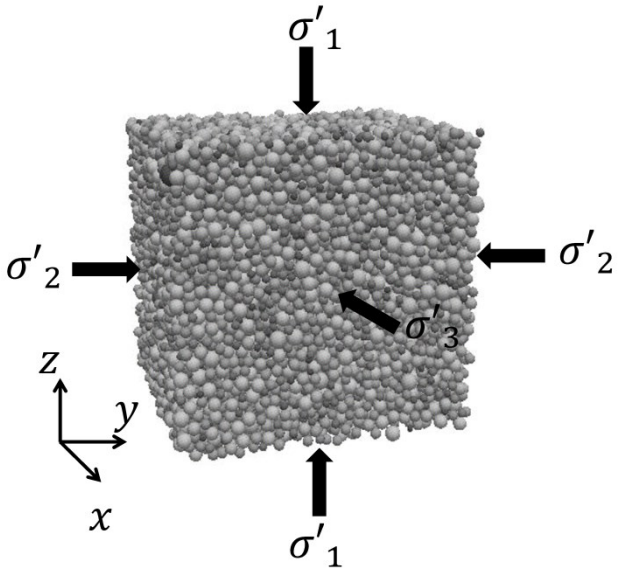
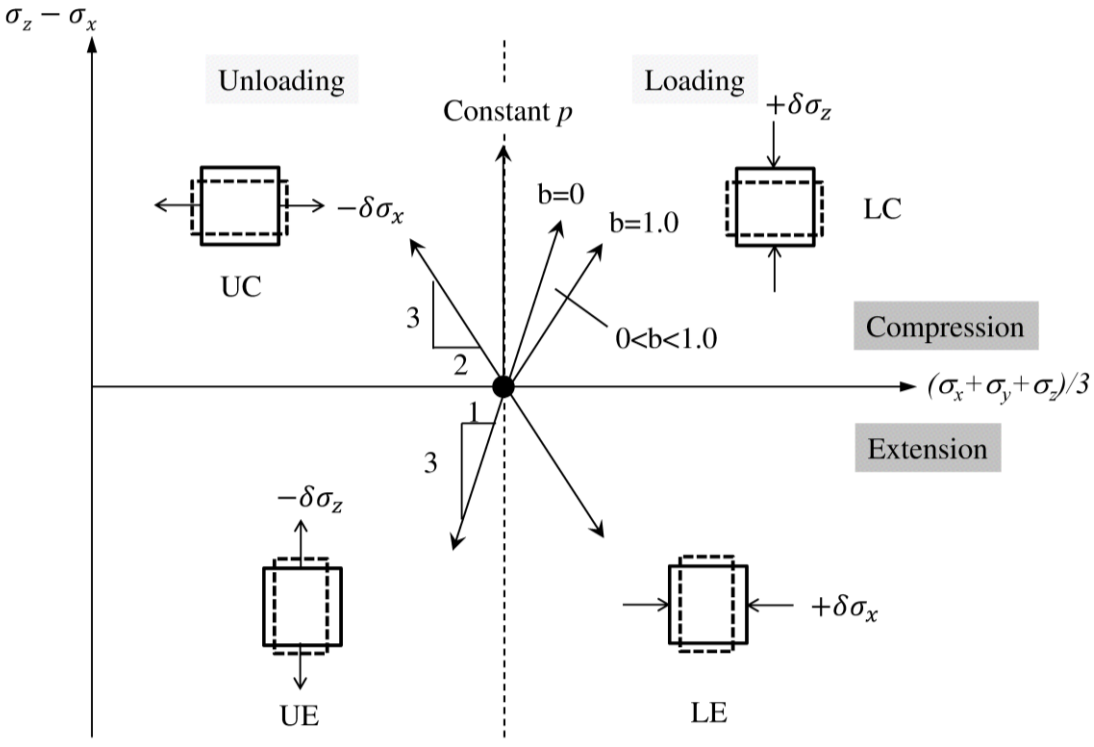



Figure 5.12 Illustration of the dilatancy state line (DSL) and associated parameters in the Anisotropy Crtical State Theory (ACST) (Li & Dafalias, 2012)

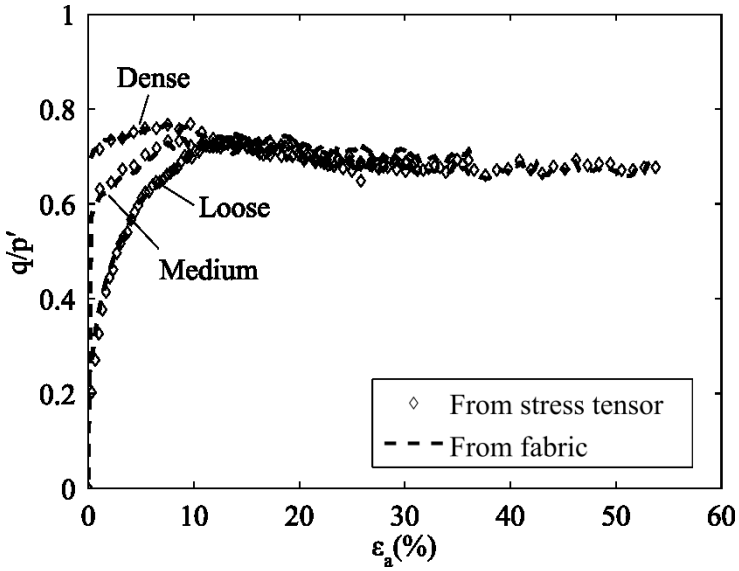



(a)

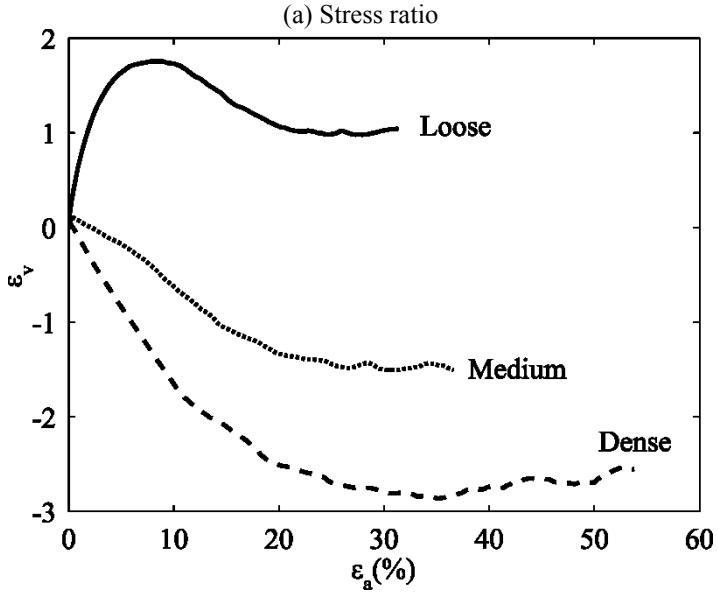



(b)

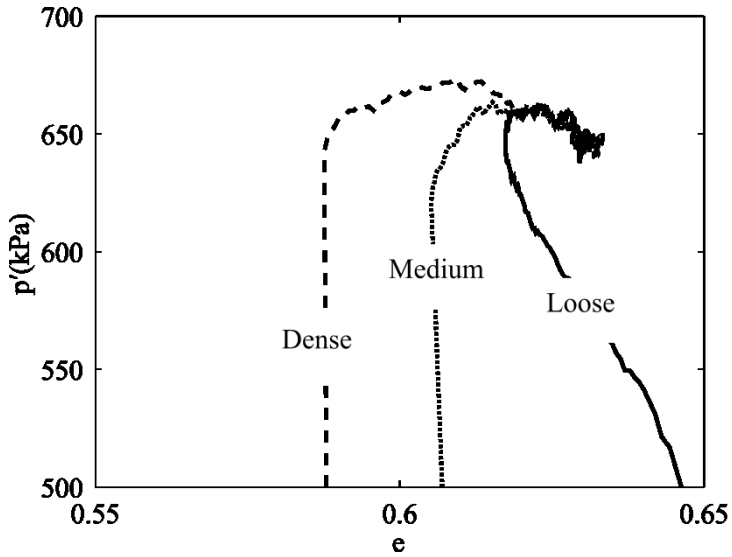
Figure 5.13 Illustration of the three-dimensional loading conditions: (a) A DEM sample subjected to three-dimensional loading; (b) Total stress paths considered in this study




(a) Stress ratio

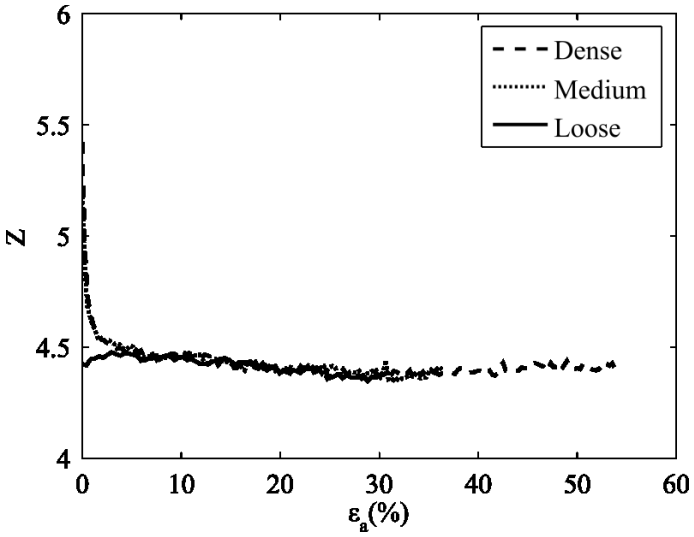



(b) Volumetric strain

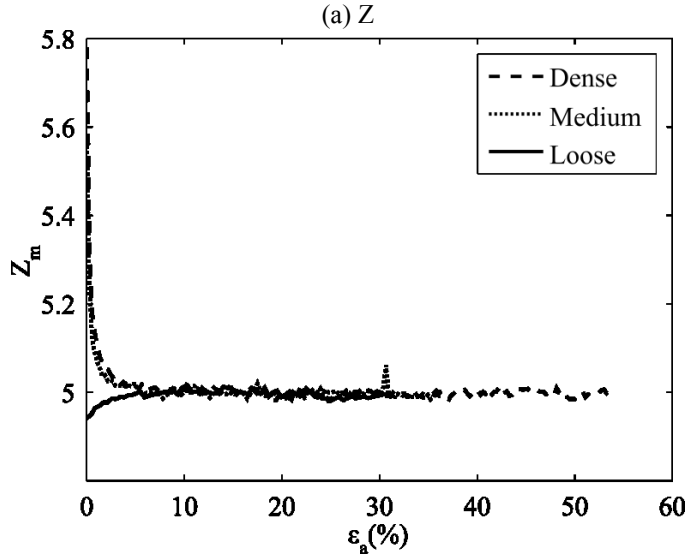



(c) Mean effective stress against void ratio

Figure 5.14 Stress-deformation response under triaxial drained loading conditions ($\sigma_3' = 500\ kPa$)



(a) Z



(b) $Z_m$

Figure 5.15 Evolution of coordination number and mechanical coordination number under triaxial drained loading conditions ($\sigma_3' = 500\ kPa$)

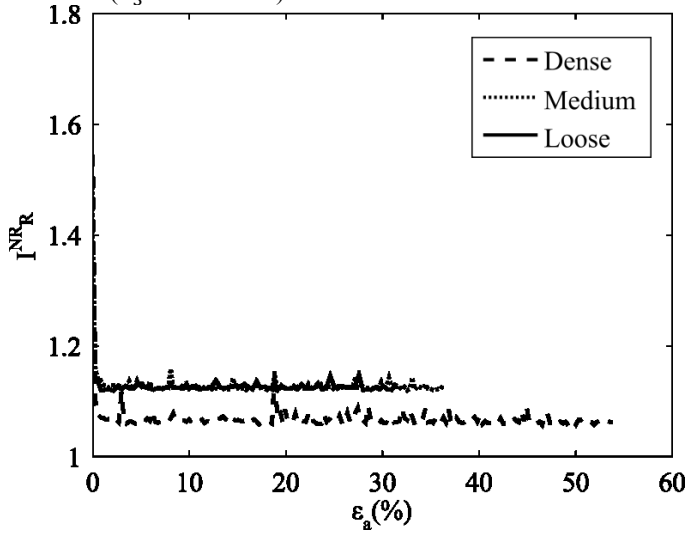



Figure 5.16 Evolution of the index of mechanical redundancy under triaxial drained loading conditions ($\sigma_3' = 500\ kPa$)

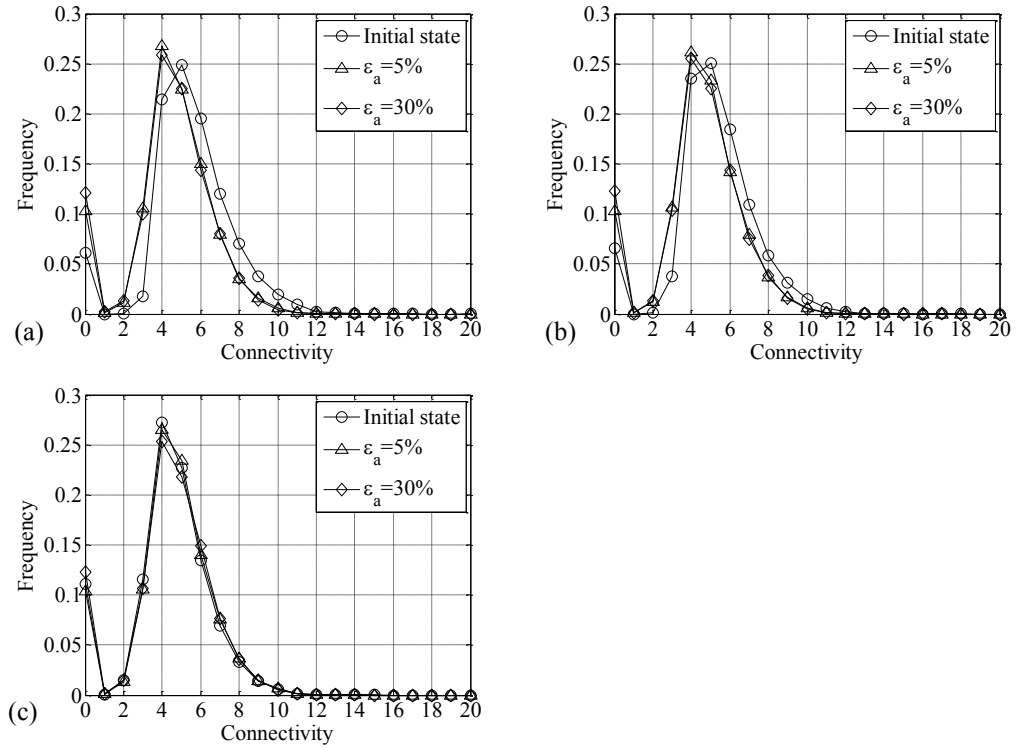



Figure 5.17 Probability density distribution of the coordination number under drained triaxial loading conditions ($\sigma_3' = 500\ kPa$): (a) Dense; (b) Medium dense; (c) Loose

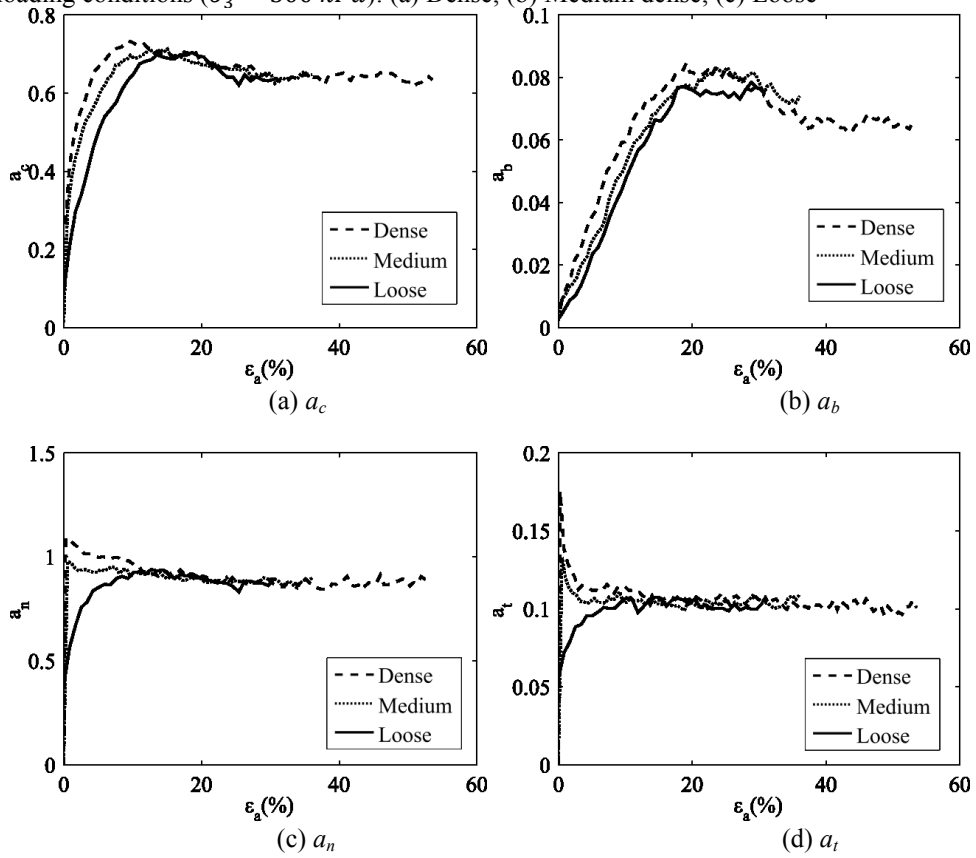
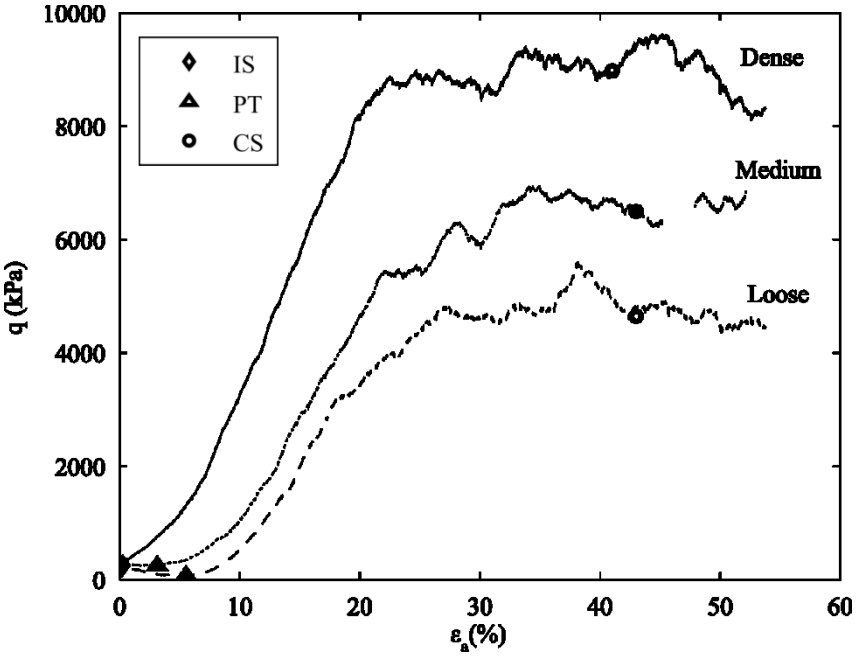
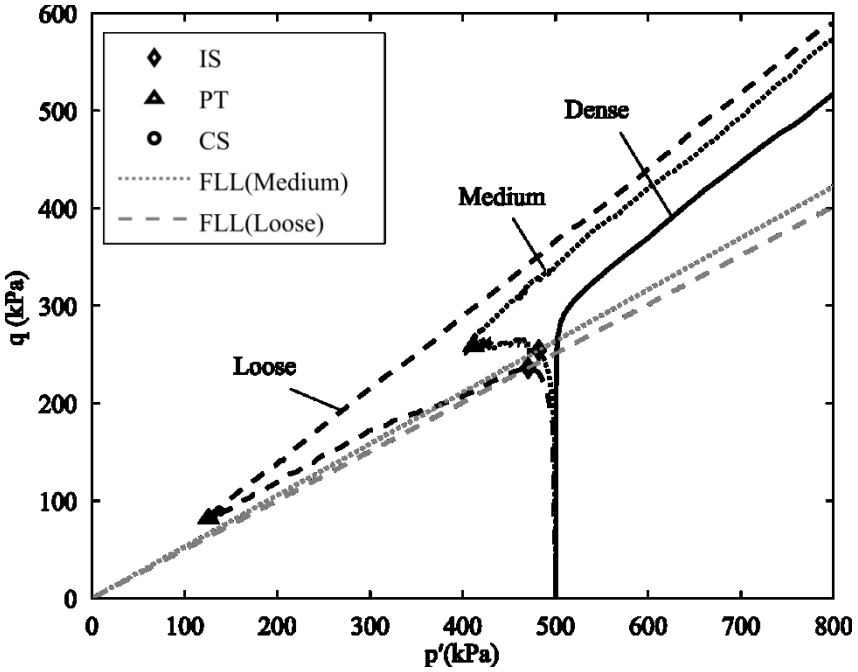



Figure 5.18 Evolution of anisotropy parameters under triaxial drained loading conditions ($\sigma_3' = 500\ kPa$)

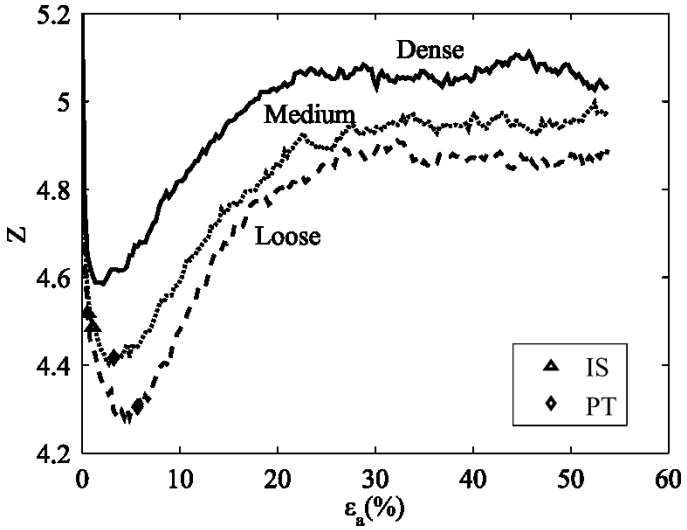



(a) Deviatoric stress

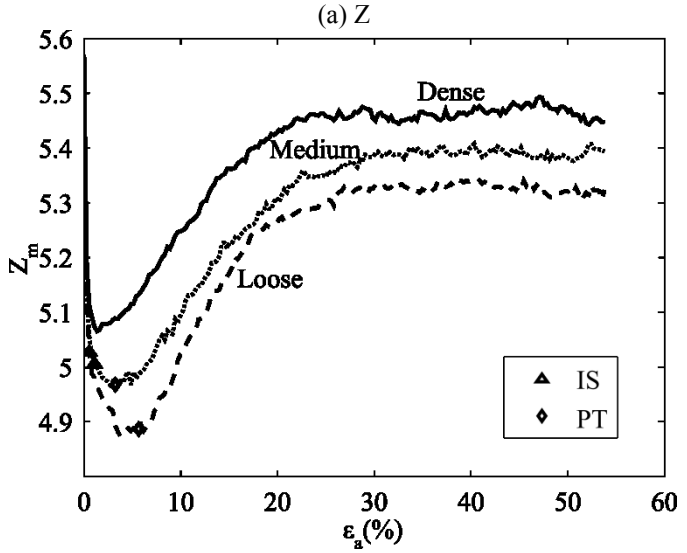



(b) Stress path

Figure 5.19 Stress-strain behaviour under constant-volume triaxial loading conditions ($\sigma_{3,0} = 500\ kPa$)




(a) Z




(b) $Z_m$

Figure 5.20 Evolution of the coordination number (Z) and mechanical coordination number ($Z_m$) under constant-volume triaxial loading conditions ($\sigma_{3,0} = 500\ kPa$)

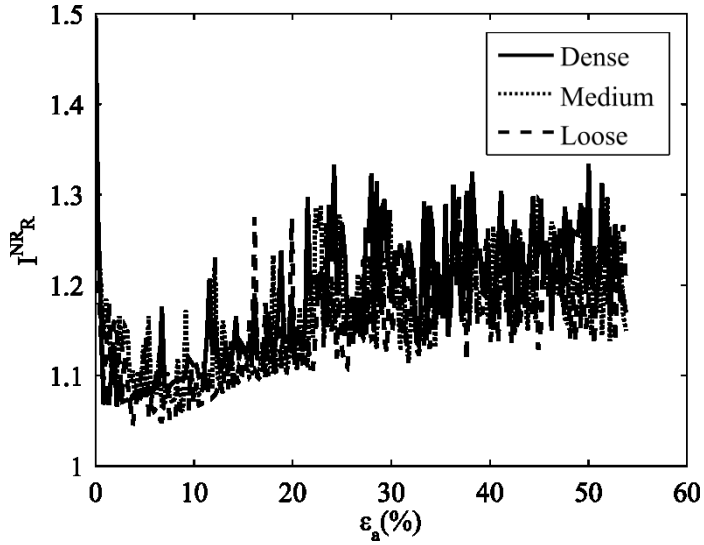



Figure 5.21 Evolution of the index of mechanical redundancy under constant-volume triaxial loading conditions ($\sigma_{3,0} = 500\ kPa$)

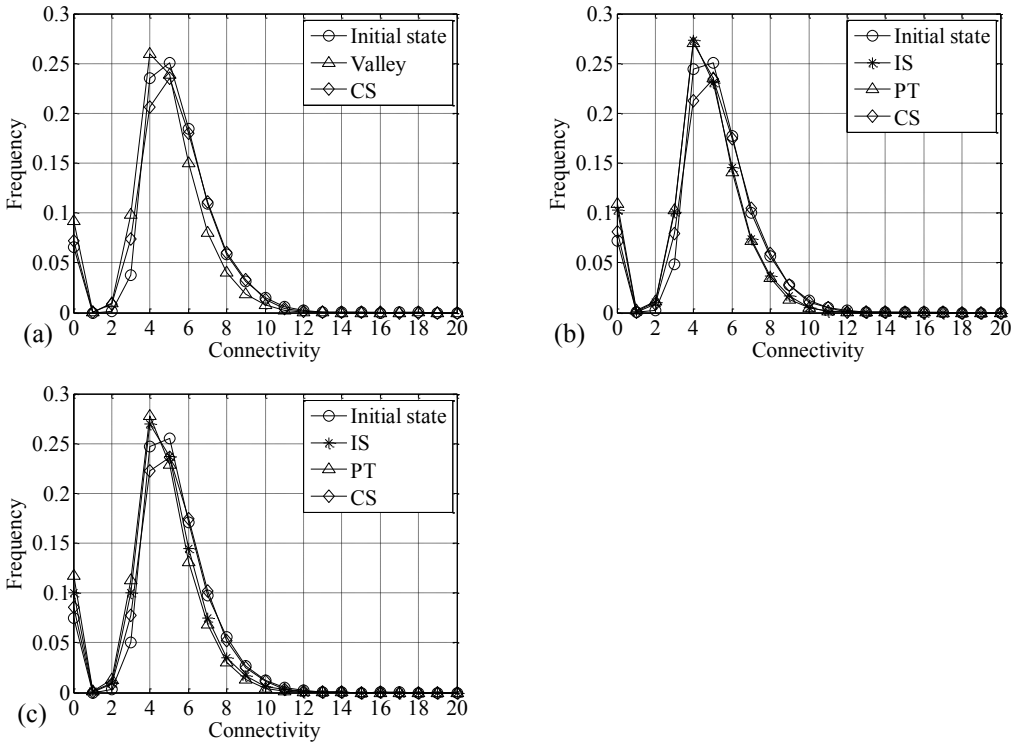
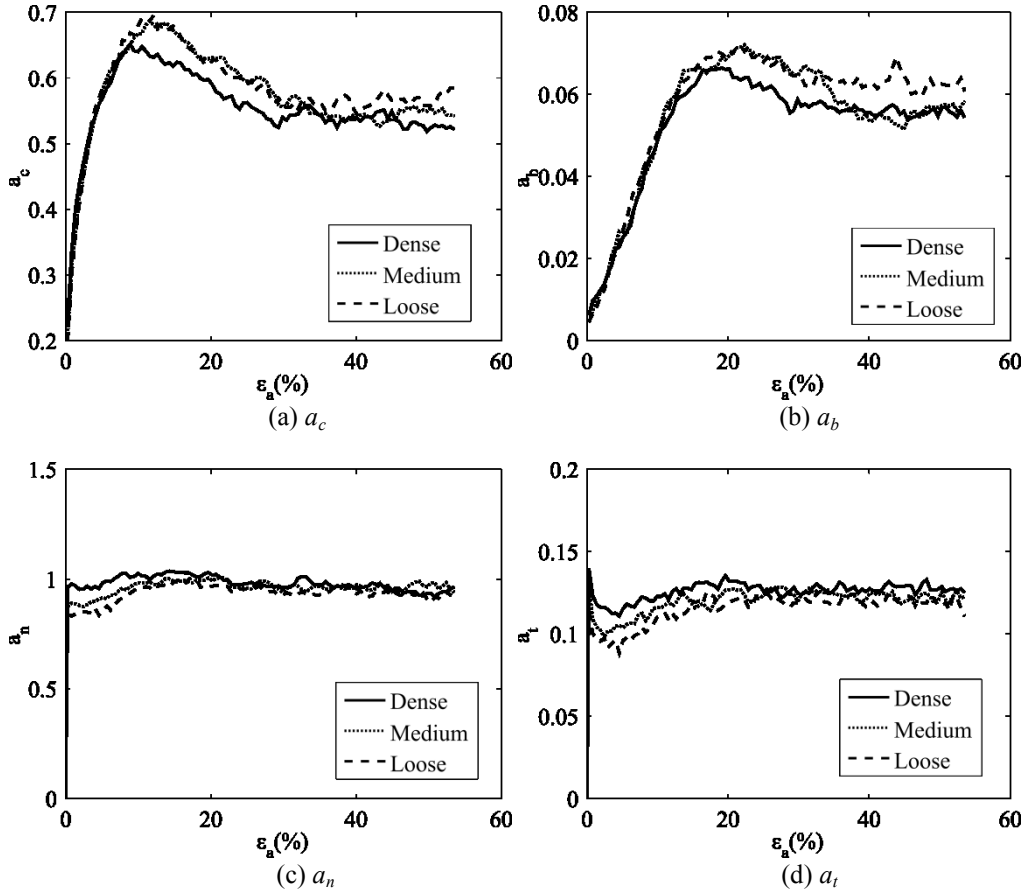


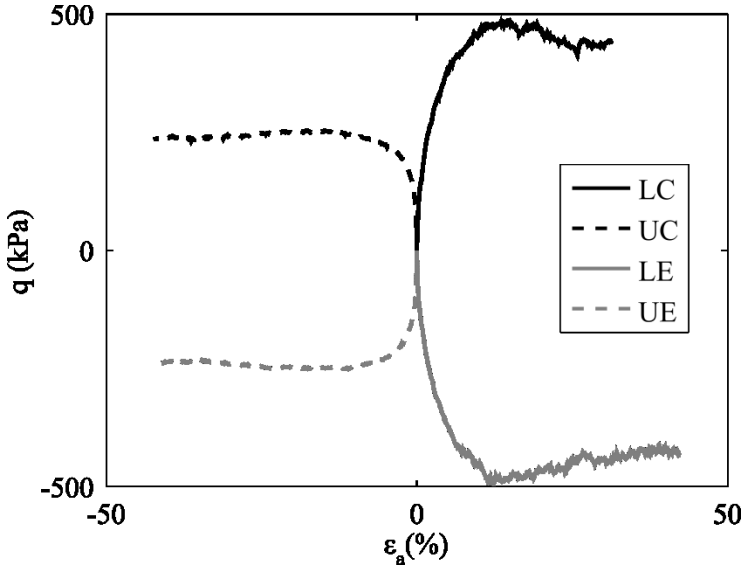

Figure 5.22 Probability density distribution of the coordination number under constant-volume triaxial loading conditions ($\sigma_3' = 500\ kPa$): (a) Dense; (b) Medium dense; (c) Loose



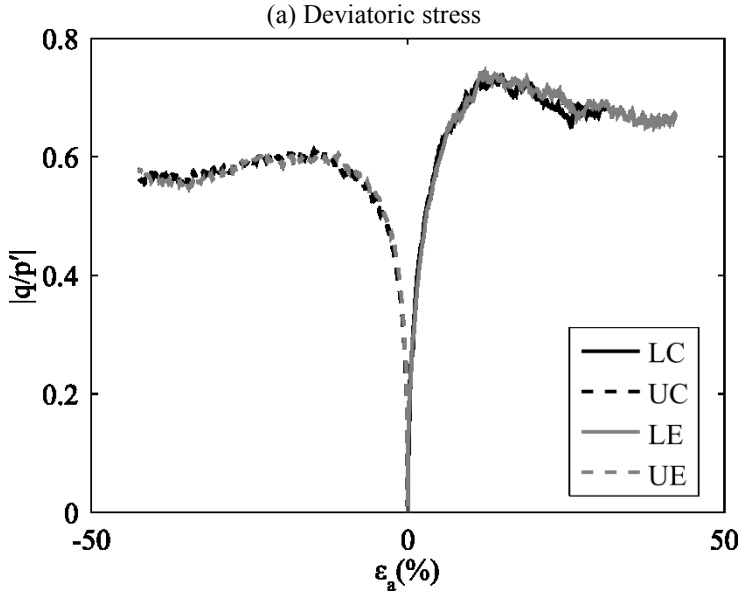

(a) $a_c$ (b) $a_b$

(c) $a_n$ (d) $a_t$

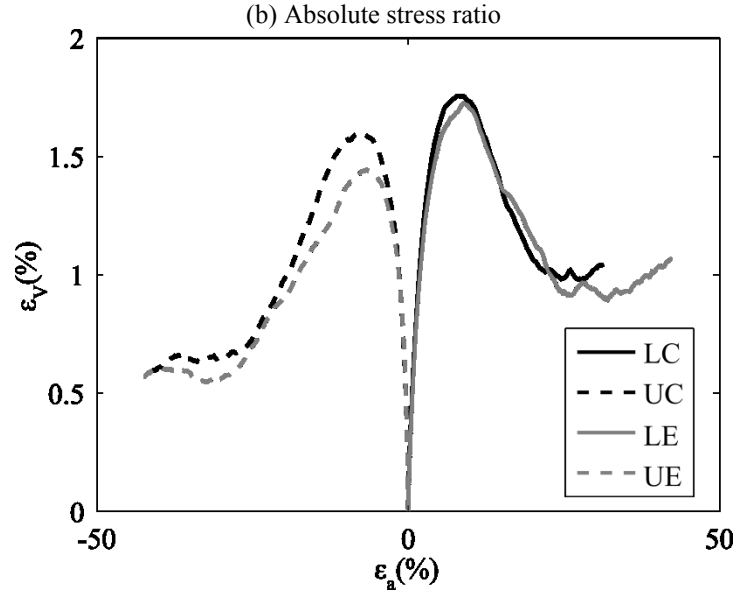
Figure 5.23 Evolution of anisotropy quantities under constant-volume triaxial loading conditions ($\sigma_{3,0} = 500\ kPa$)




(a) Deviatoric stress

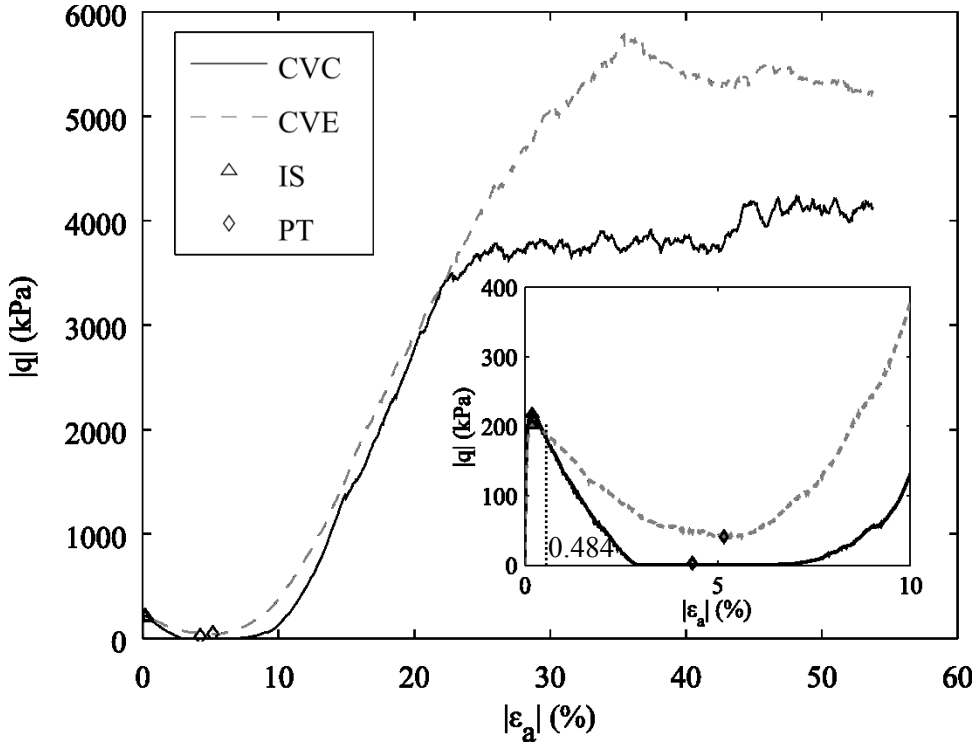



(b) Absolute stress ratio

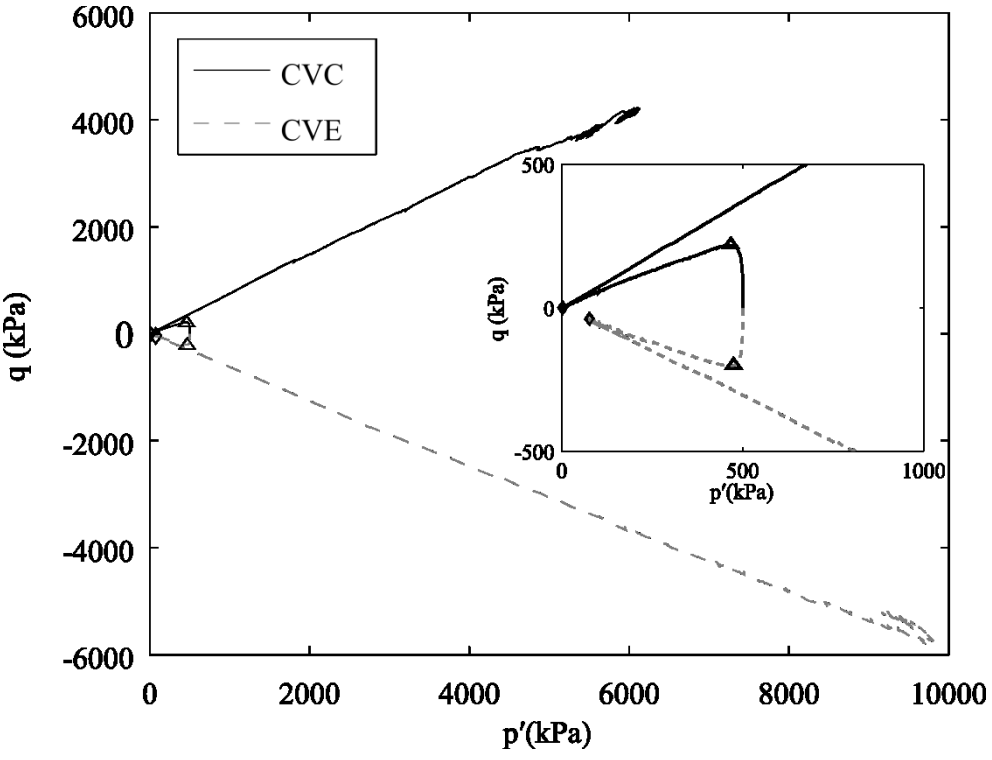



(c) Volumetric strain

Figure 5.24 Stress-strain behaviour of a DEM sample sheared under different loading paths ($e_0$=0.646,$\sigma'_3$=500 kPa)

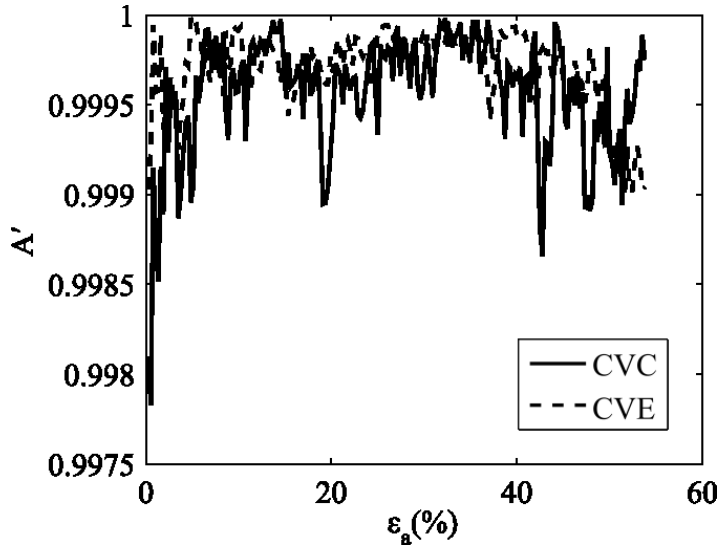



(a)

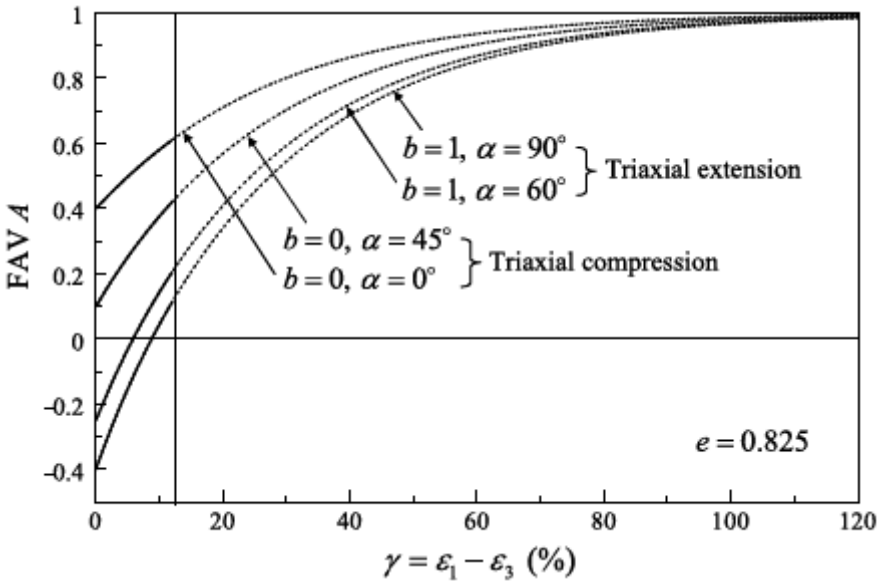



(b)

Figure 5.25 Comparing the stress-strain response of granular materials subjected to constant-volume compression (CVC) and constant-volume extension (CVE) ($e_0$=0.619, $\sigma_3$=500 kPa): (a) |q|; (b) stress path

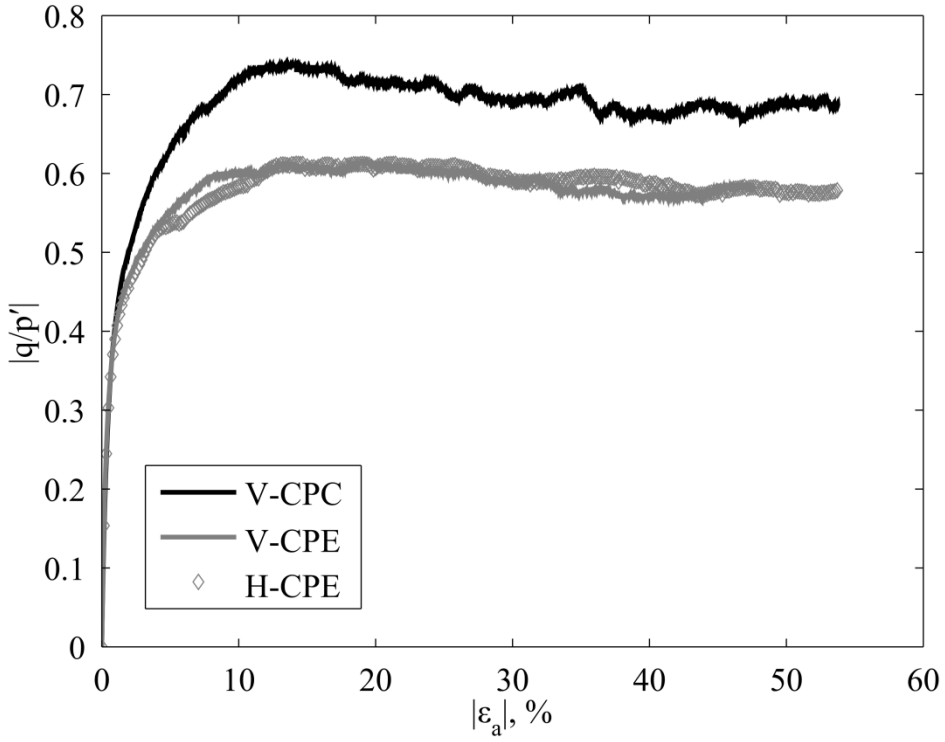



(a)

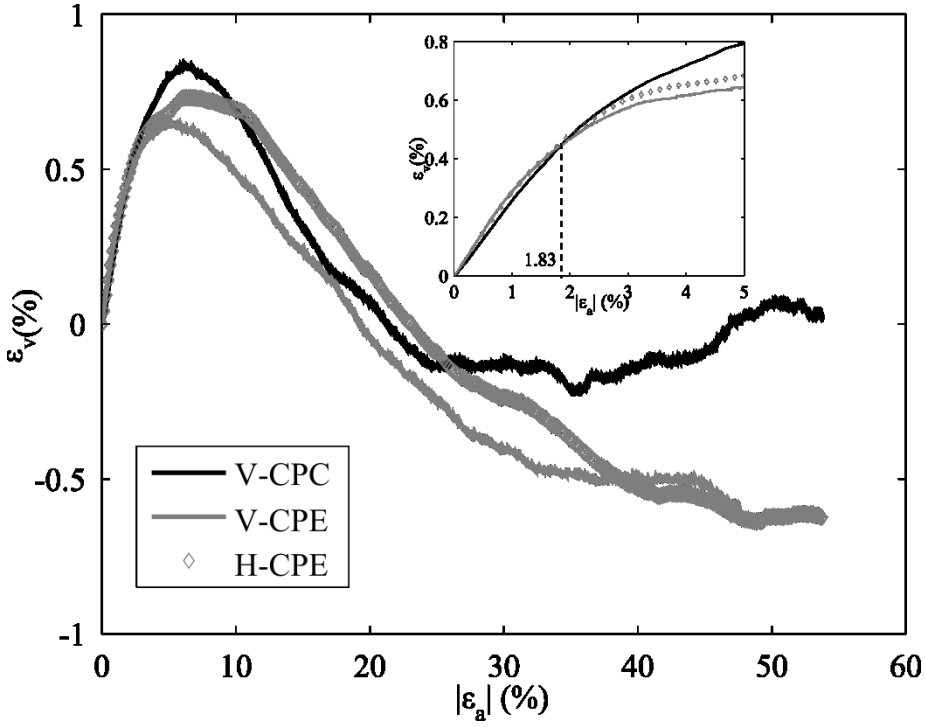



(b)

Figure 5.26 Coaxiality between the fabric direction and the loading direction: (a) Evolution of *A'* for DEM simulations; (b) Modelling values of FAV A for the experimental data of Yoshimine et al. (1998) (Li and Dafalias, 2012)




(a)




(b)

Figure 5.27 Comparing the stress-strain response of granular materials subjected to constant-p' compression (CPC) and constant-p' extension (CPE) ($e_0$=0.594, $\sigma'_3$=20 MPa): (a) q/p'; (b) $\varepsilon_v$

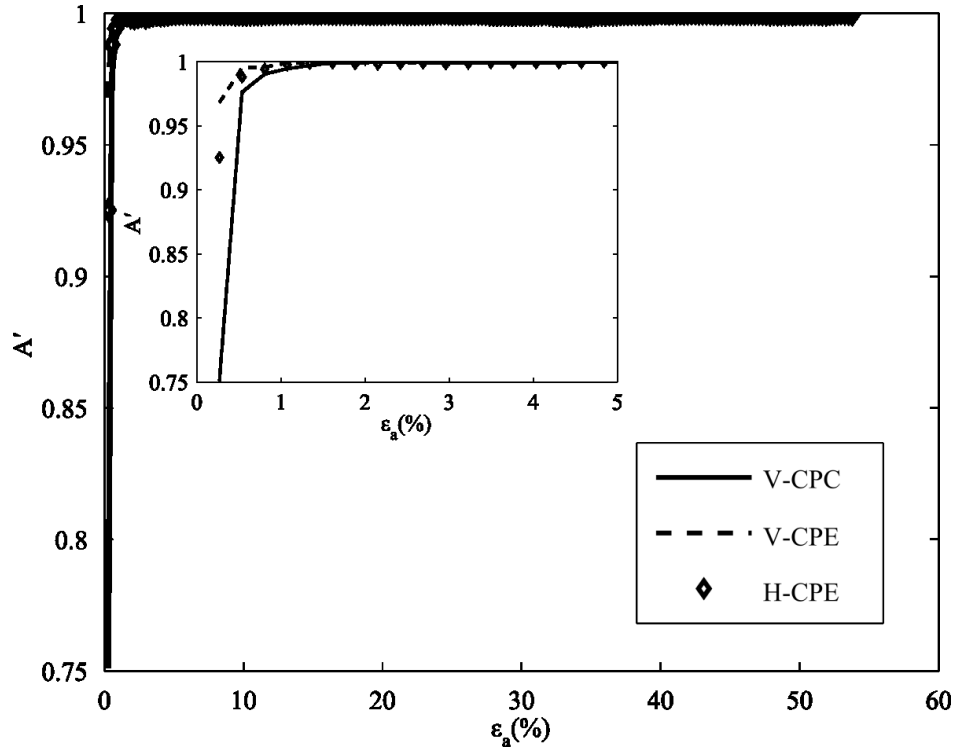
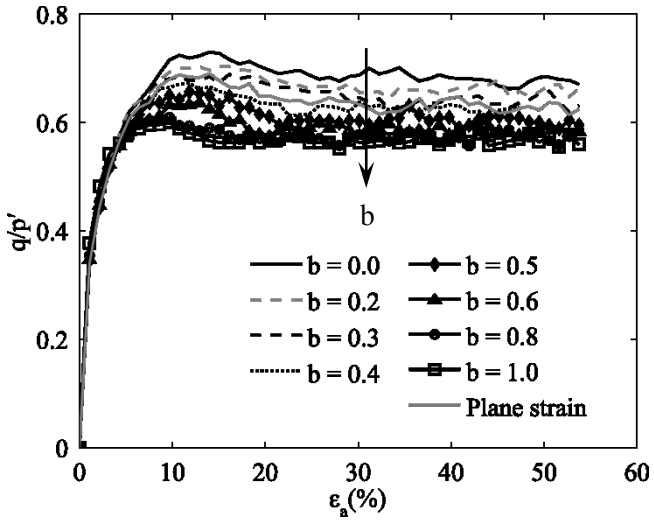
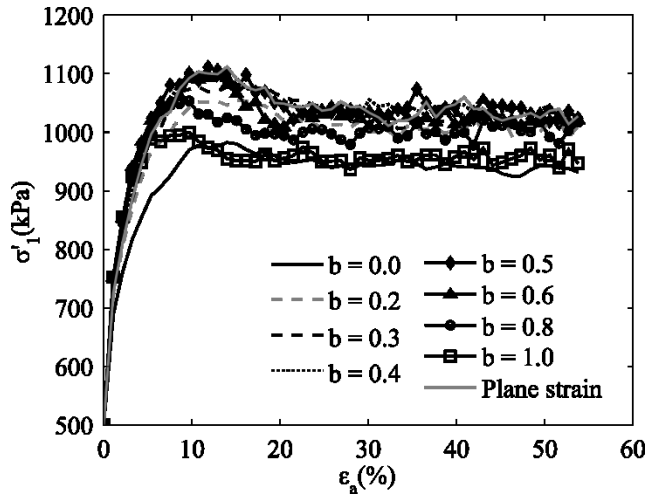


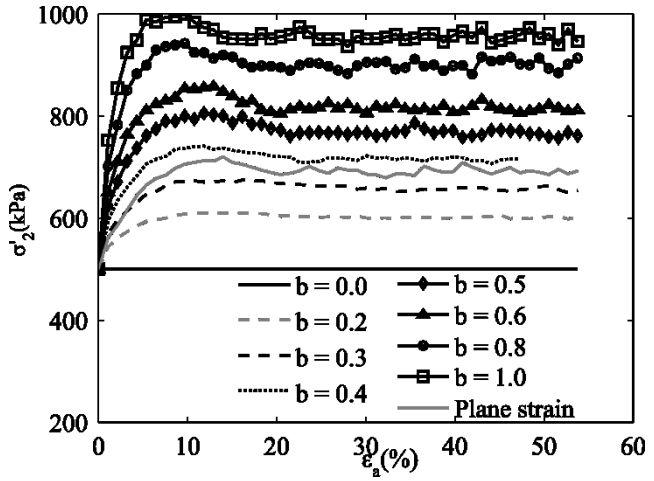

Figure 5.28 Evolution of *A'* for constant-*p'* simulations ($e_0$=0.594, $\sigma'_3$=20 MPa)




(a)

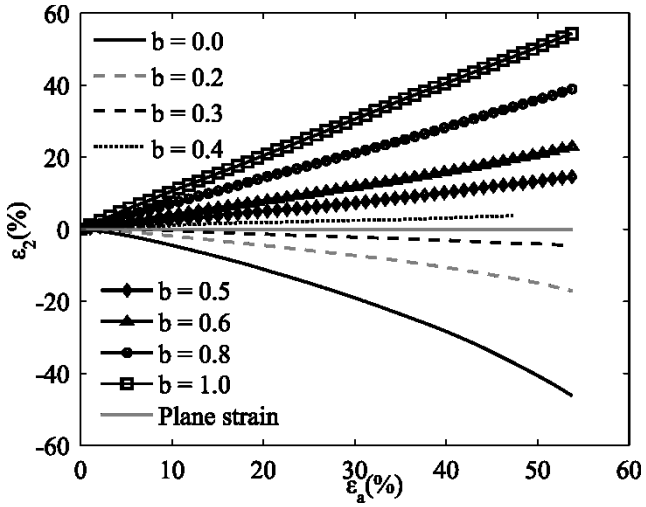



(b)

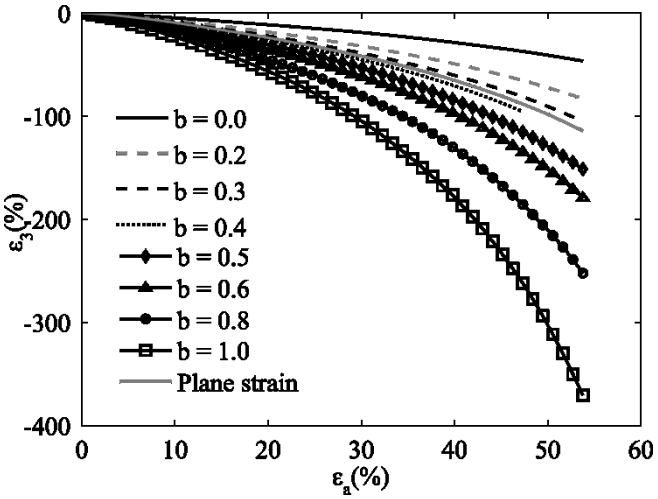



(c)

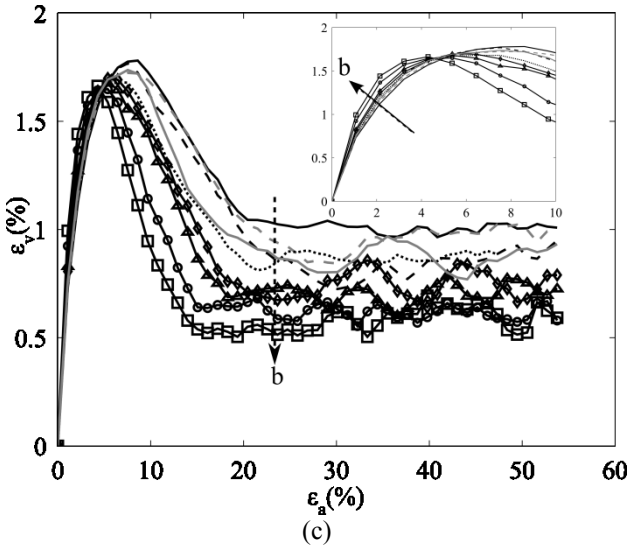
Figure 5.29 Variation of stresses with $b$ during "drained" shearing ($\sigma'_{3,0}$ = 500 kPa, $e_0$ = 0.646): (a) Stress ratio $q/p'$; (b) Major principal stress $\sigma'_1$; (c) Intermediate stress $\sigma'_2$




(a)

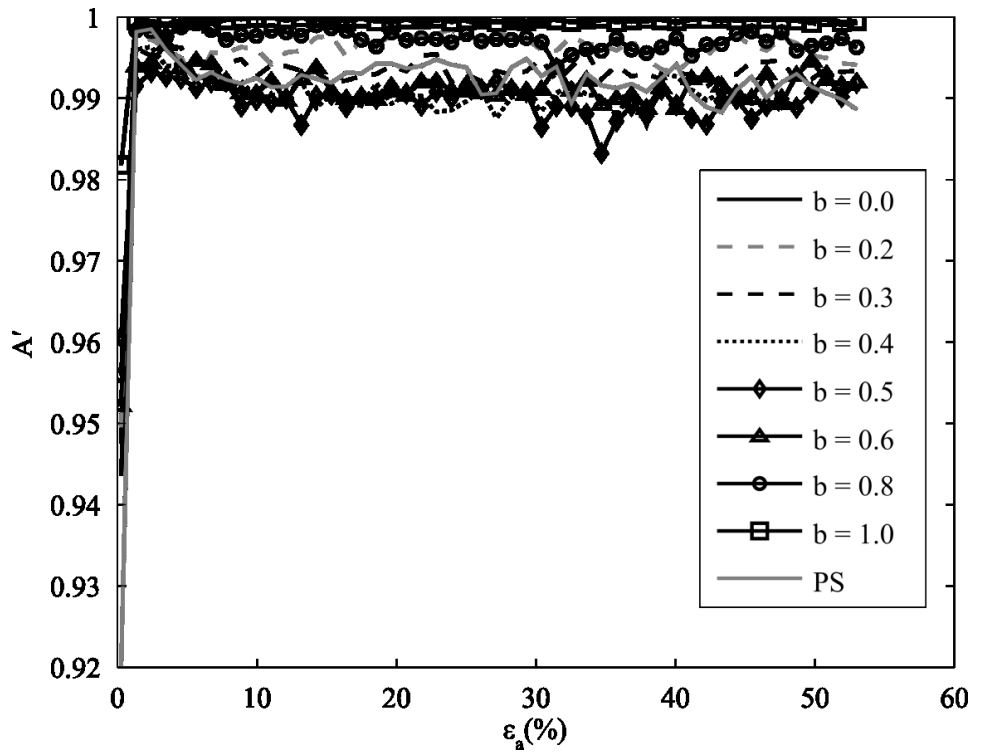



(b)

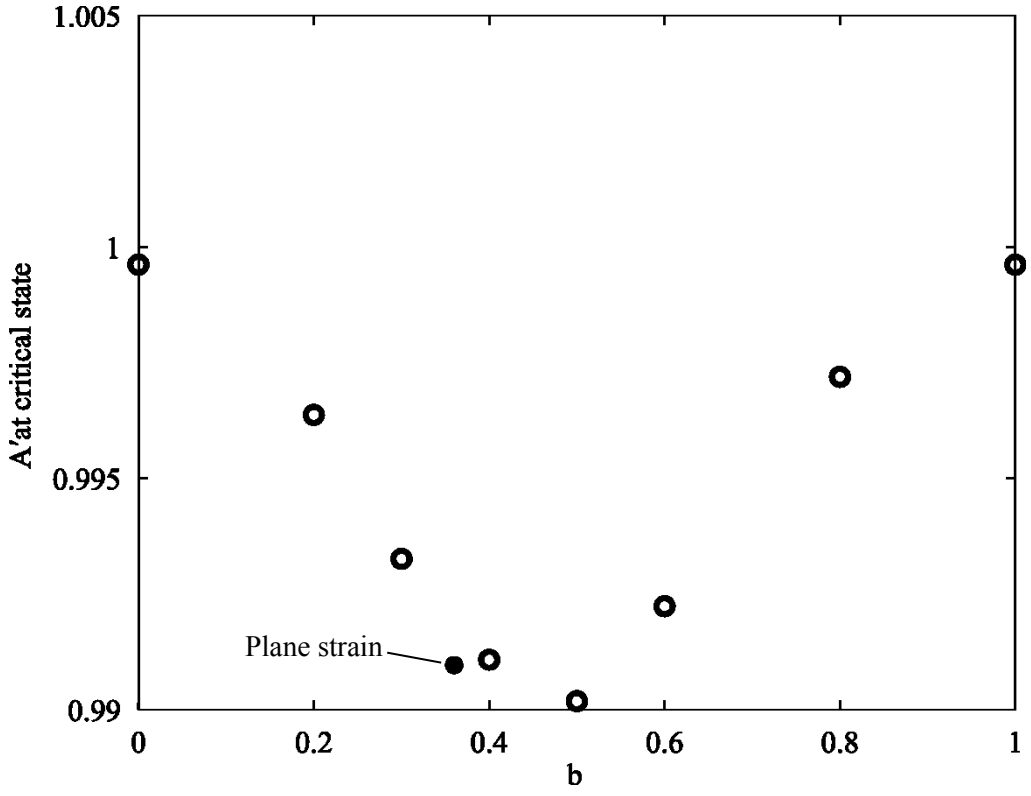



(c)

Figure 5.30 Variation of strains with $b$ during "drained" shearing ($\sigma'_{3,0}$ = 500 kPa, $e_0$ = 0.646): (a) Intermediate principal strain; (b) Minor principal strain; (c) Volumetric strain




(a)




(b)

Figure 5.31 Coaxiality between the fabric direction and the loading direction at various $b$ values (($\sigma'_{3,0}$ = 500 kPa, $e_0$ = 0.646): (a) Evolution of $A'$ during the course of shearing; (b) Variation of $A'$ at critical state with $b$

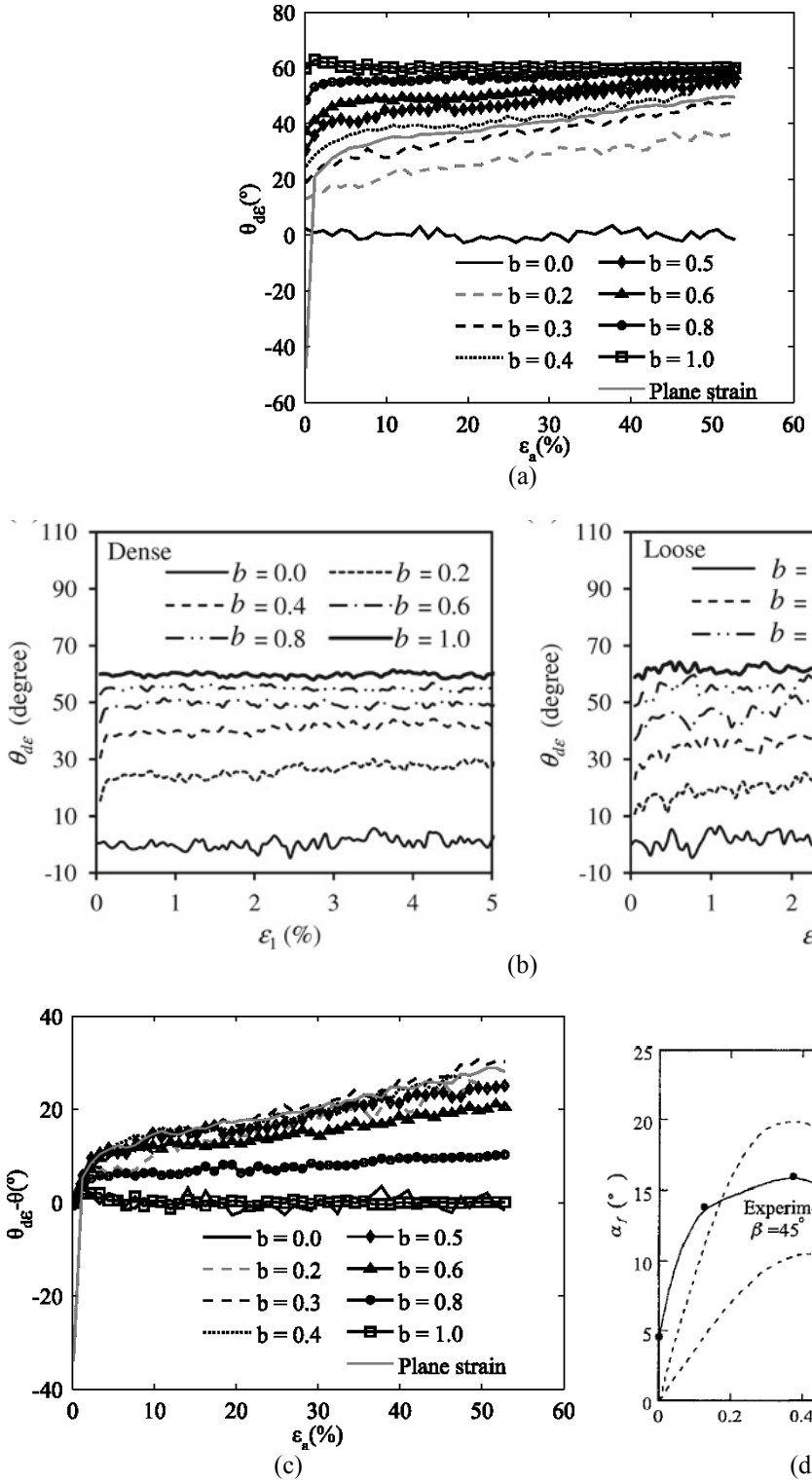
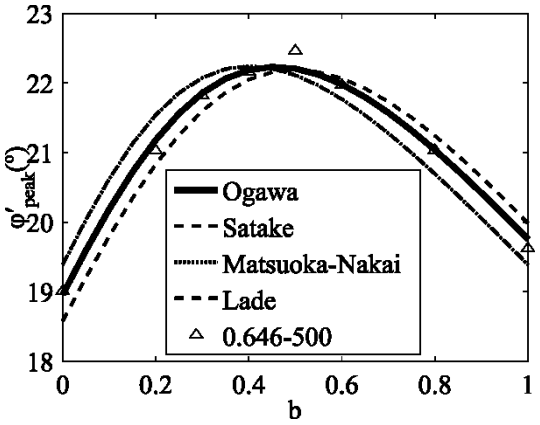
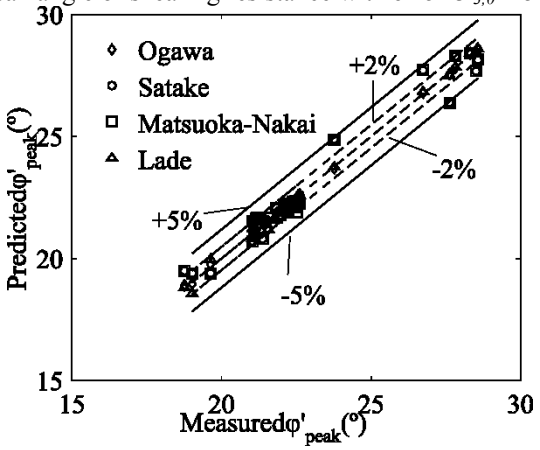


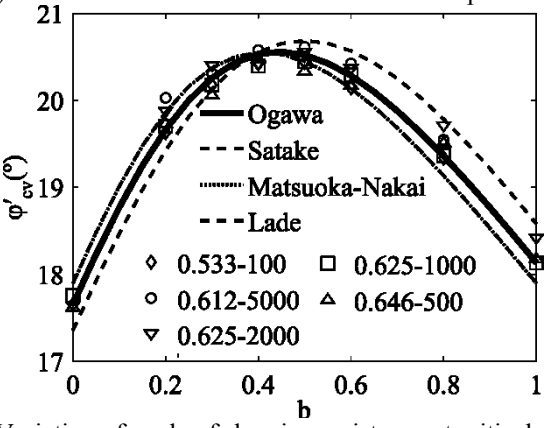

Figure 5.32 Deviation between the direction of the stress vector and that of the strain increment vector under true triaxial loading conditions ($\sigma'_{3,0}$ = 500 kPa, $e_0$ = 0.646): (a) Orientation of the strain increment vector (This study) ; (b) Orientation of the strain increment vector (Sazzad & Suzuki, 2013); (c) Angle of deviation between the direction of the strain increment vector and the direction of the stress vector (This study); (d) Experimental observation of the angle of deviation between the direction of the strain increment vector and the direction of the stress vector at failure: $\beta$ is the angle between the major principal stress direction and the deposition direction and $\kappa$ is the Lade-Duncan strength parameter (Suzuki & Yanagisawa, 2006)



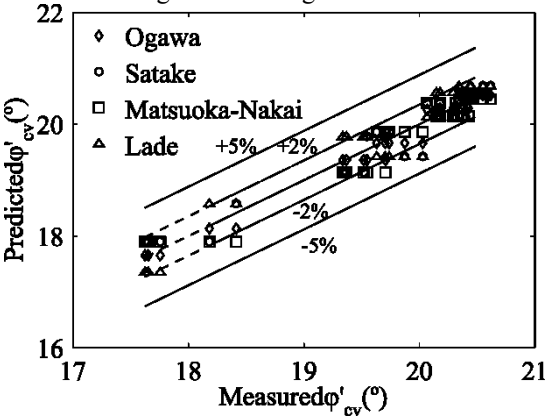

(a) Variation of peak angle of shearing resistance with $b$ for $\sigma'_{3,0}$ = 500 kPa, $e_0$ = 0.646




(b) Performance of different failure criteria at peak state




(c) Variation of angle of shearing resistance at critical state




(d) Performance of different failure criteria at critical state

Figure 5.33 Evaluation of different failure criteria

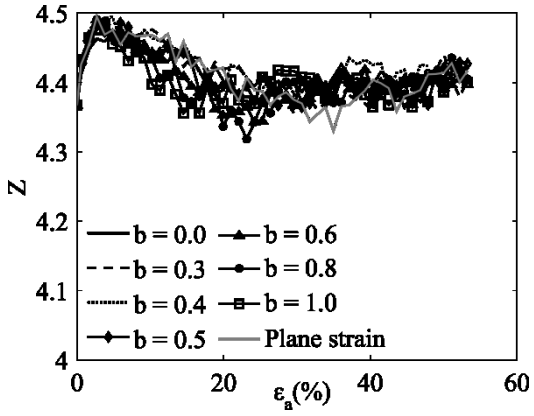
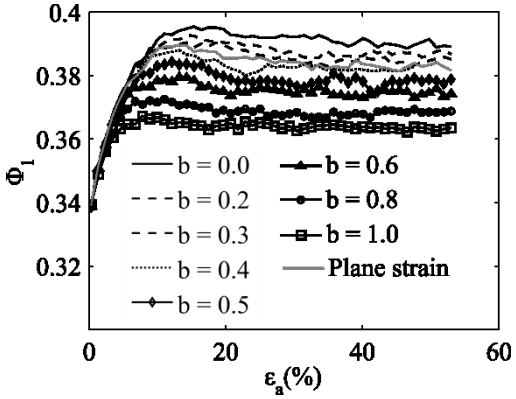
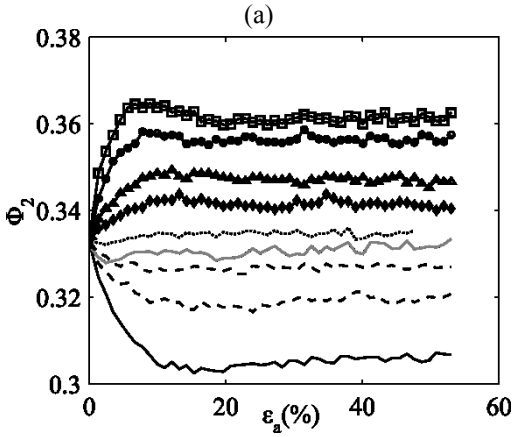


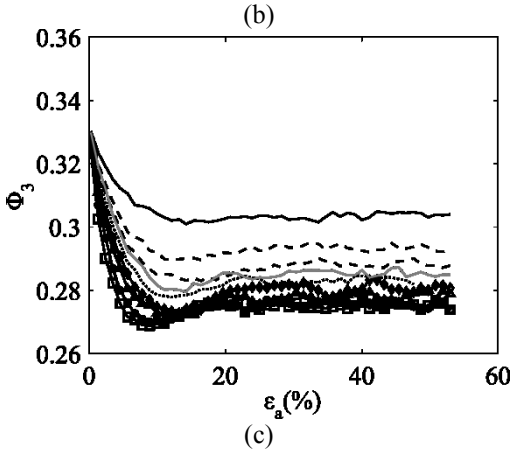

Figure 5.34 Evolution of Z with axial strain for drained shearing ($\sigma'_{3,0}$ = 500 kPa and $e_0$ = 0.646)




(a)

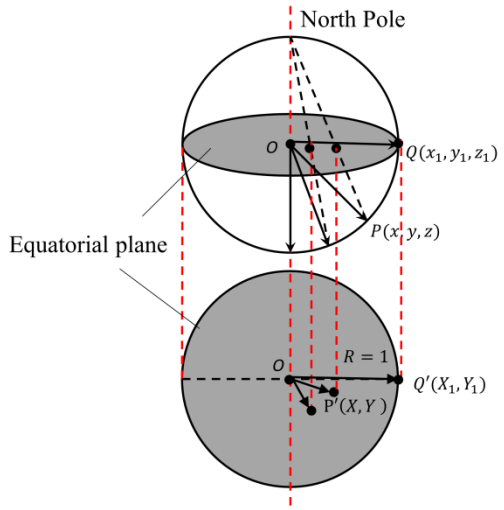



(b)

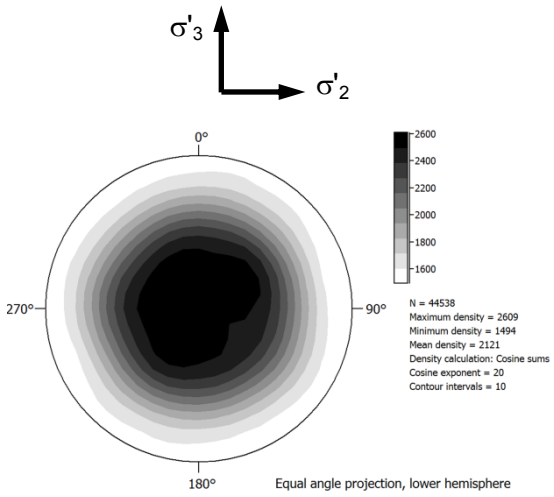



(c)

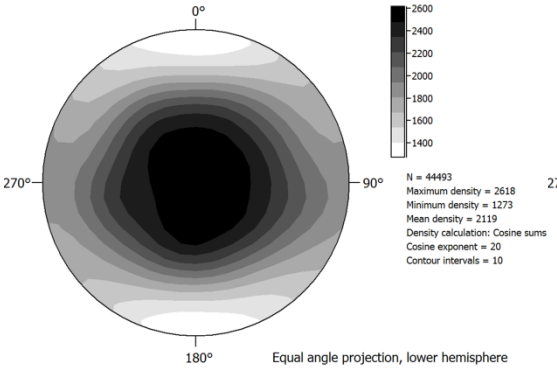
Figure 5.35 Clustering of contacts along the principal stress directions ($\sigma'_{3,0}$ = 500 kPa and $e_0$ = 0.646): (a) $\Phi_1$; (b) $\Phi_2$; (c) $\Phi_3$



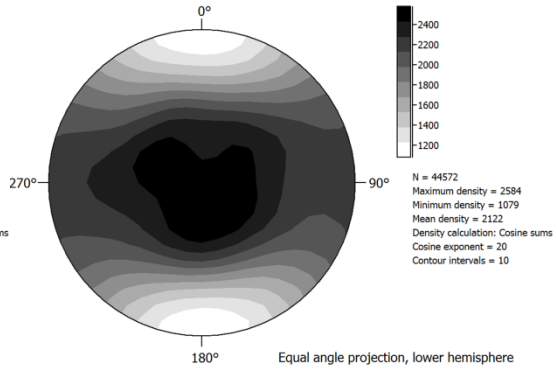

(a) Schematic of the equal-angle stereo projection



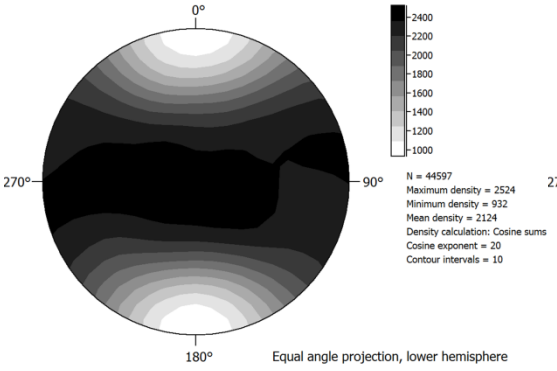

(b) $b = 0.0$



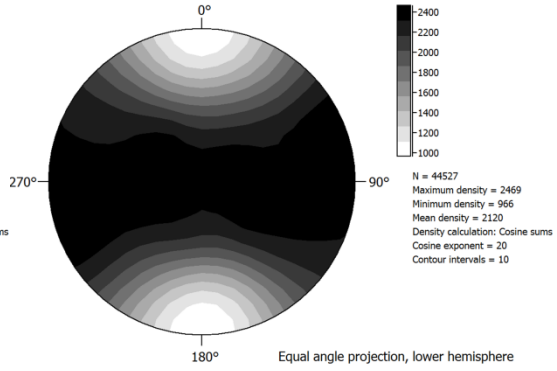

(c) $b = 0.2$




(d) $b = 0.5$




(e) $b = 0.8$




(f) $b = 1.0$

Figure 5.36 Spatial contact density distributions at the critical state

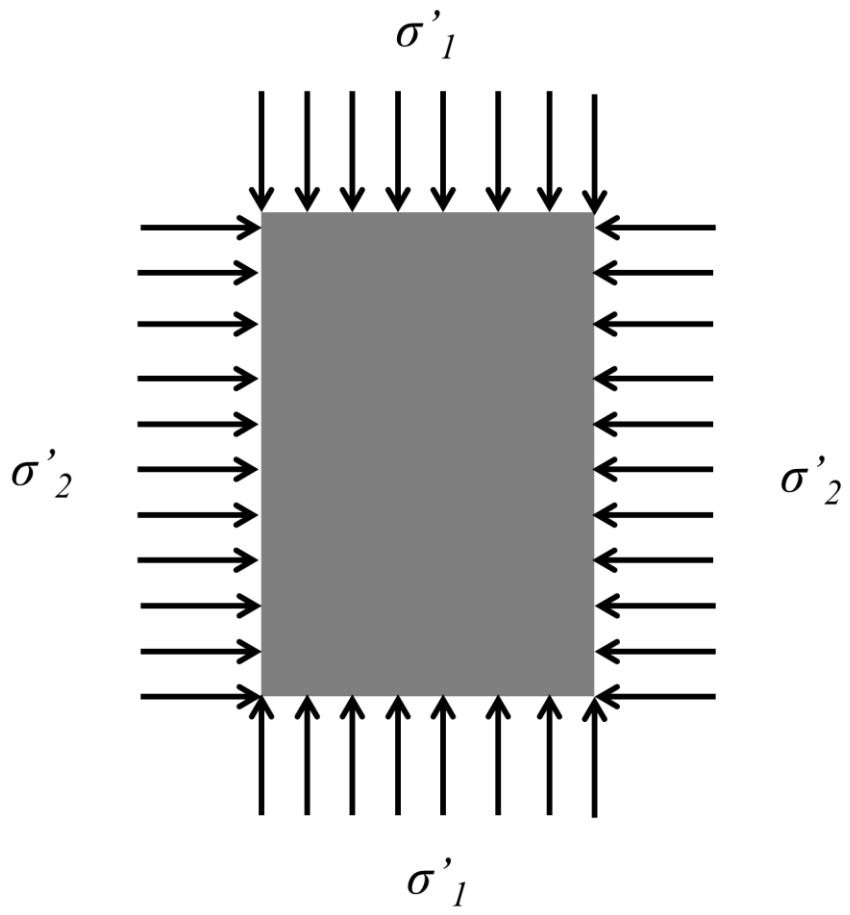
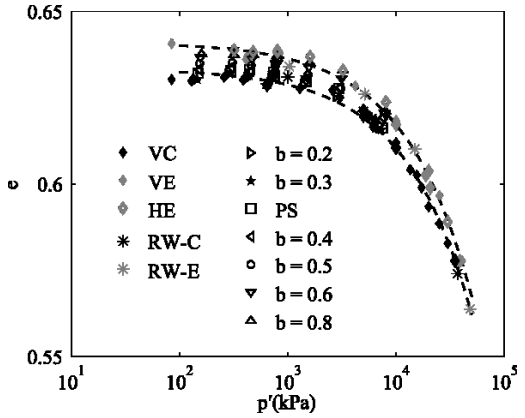
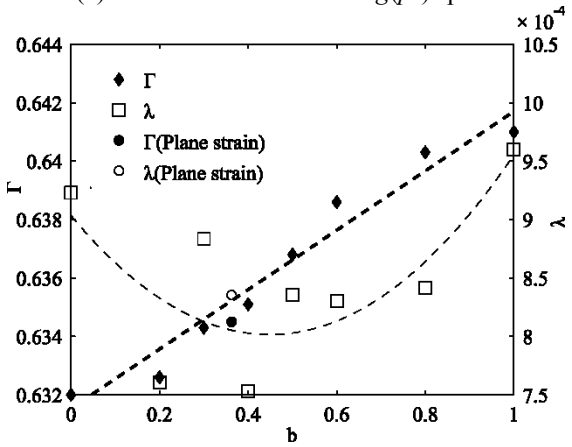


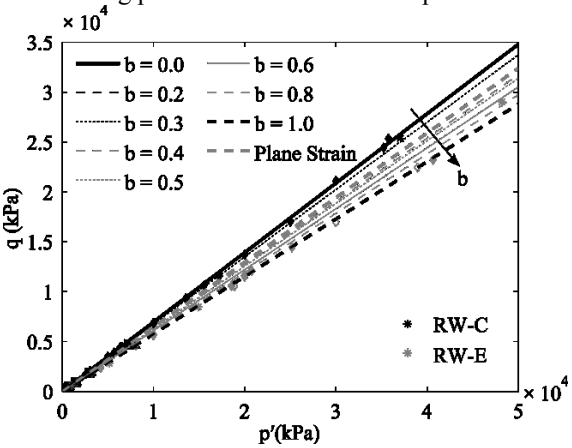

Figure 5.37 Biaxially loaded plate



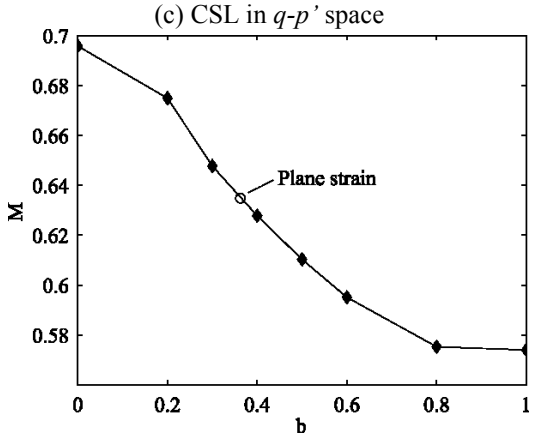

(a) Critical state loci in *e-log(p')* space




(b) Variation of the fitting parameters of the linear expression for the CSL with *b*

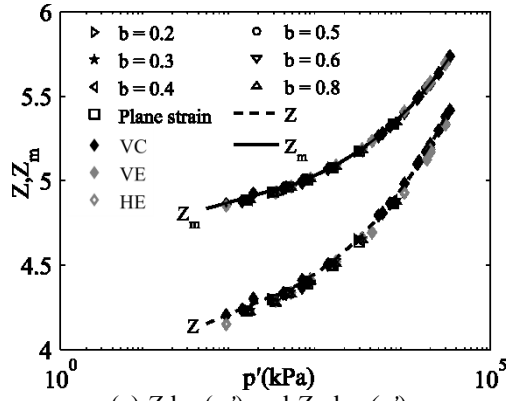



(c) CSL in *q-p'* space

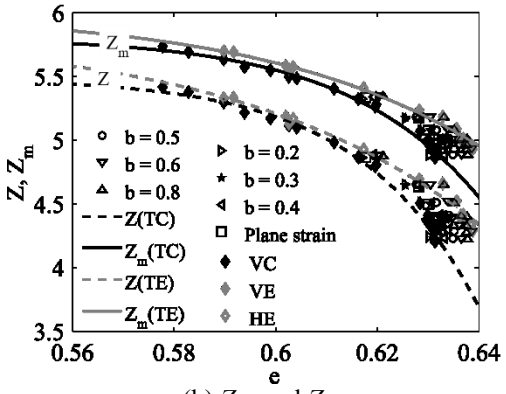



(d) Critical-state stress ratio at various b values

Figure 5.38 Critical state characteristics

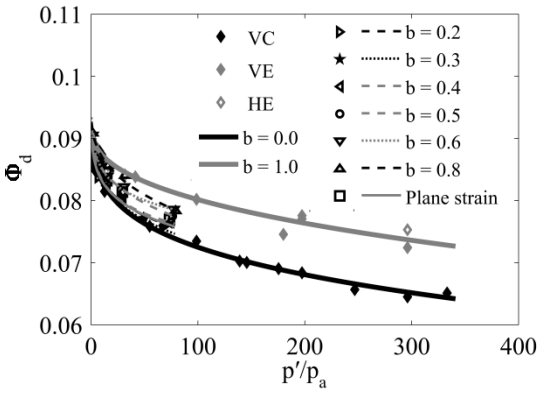



(a) $Z$-log($p'$) and $Z_m$-log($p'$)

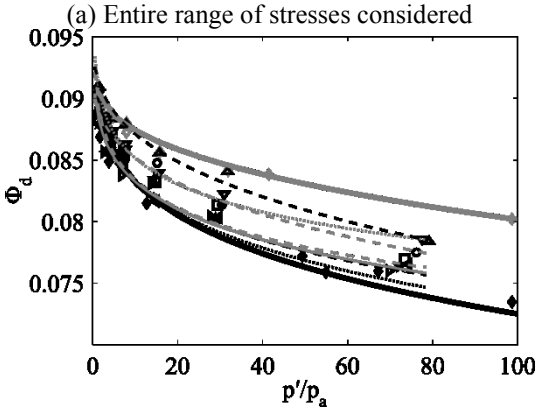



(b) $Z$-$e$ and $Z_m$-$e$

Figure 5.39 Variation of $Z$ and $Z_m$ at the critical state with $b$




(a) Entire range of stresses considered




(b) Small stress regime

Figure 5.40 Correlation between the deviatoric fabric and mean effective stress at the critical state

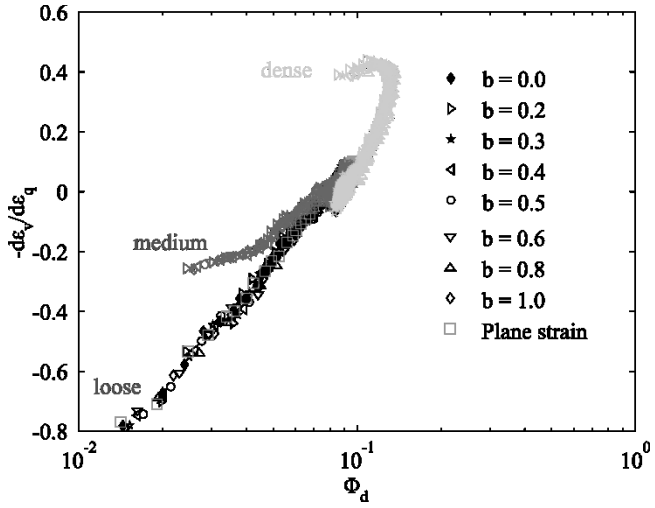
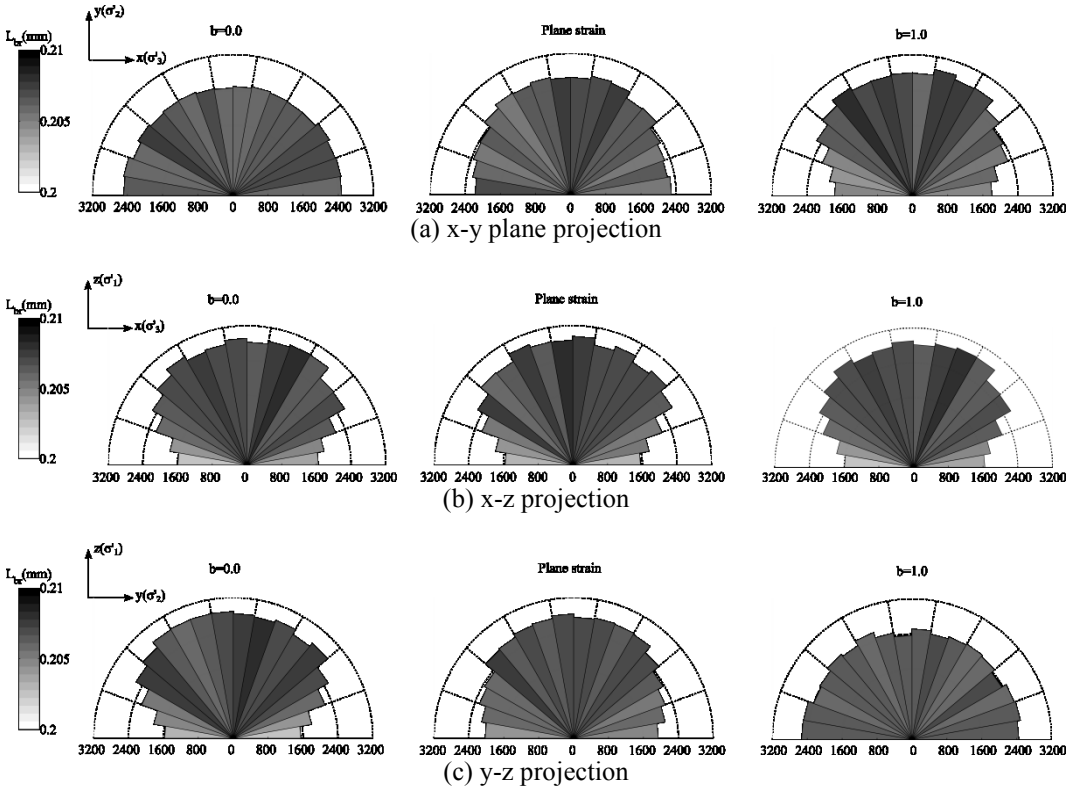



Figure 5.41 Correlation between the dilatancy and the deviatoric fabric for three representative sets of simulations: loose ($\sigma'_{3,0}$ = 500 kPa, $e_0$ = 0.646); medium ($\sigma'_{3,0}$ = 1000 kPa, $e_0$ = 0.627); dense ($\sigma'_{3,0}$ = 100 kPa, $e_0$ = 0.533))

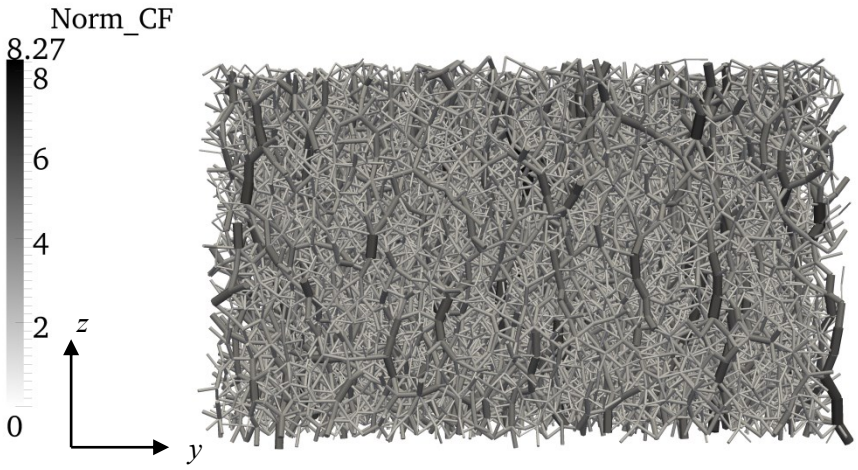



(a) x-y plane projection

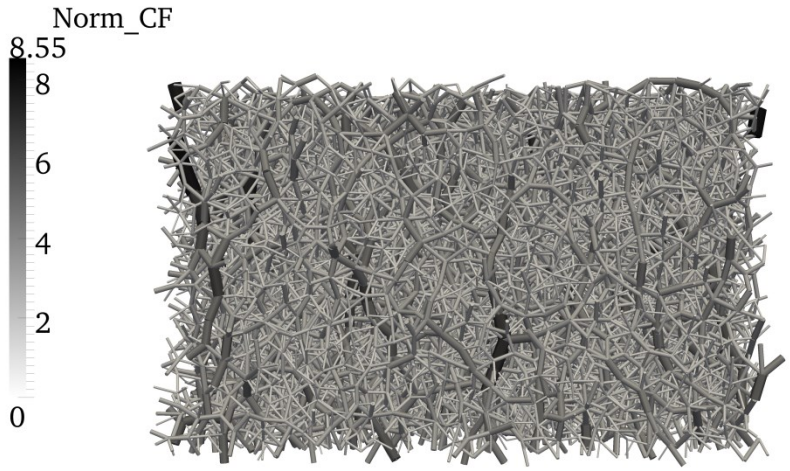
(b) x-z projection

(c) y-z projection

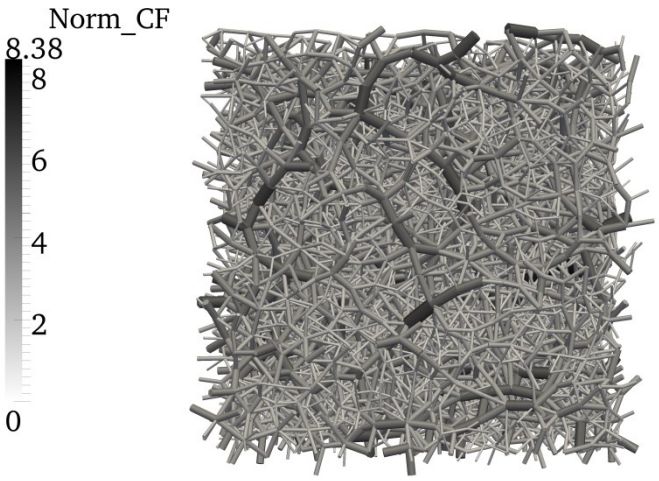
Figure 5.42 Rose diagram of the branch vector ($\sigma'_{3,0}$ = 500 kPa, $e_0$ = 0.646)




(a)

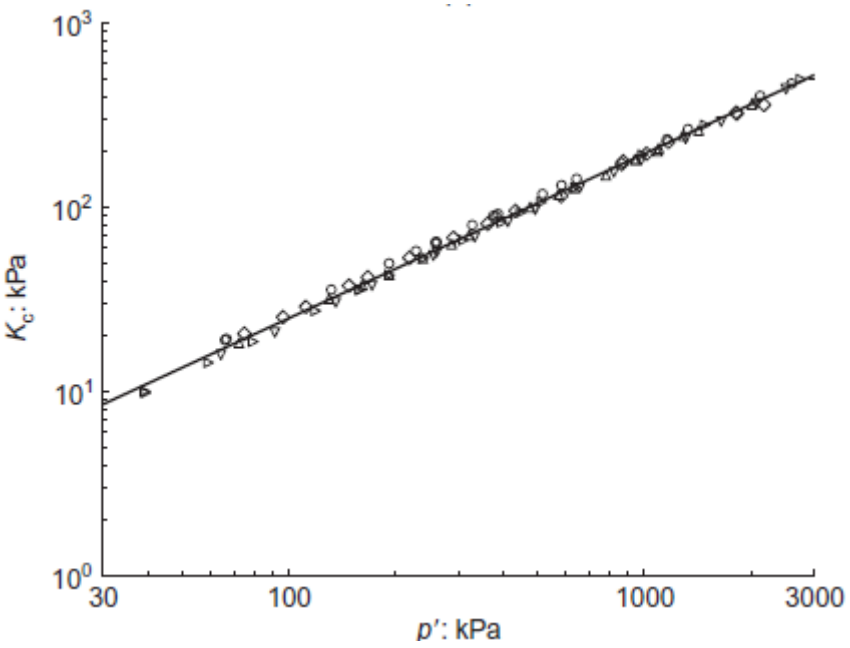



(b)

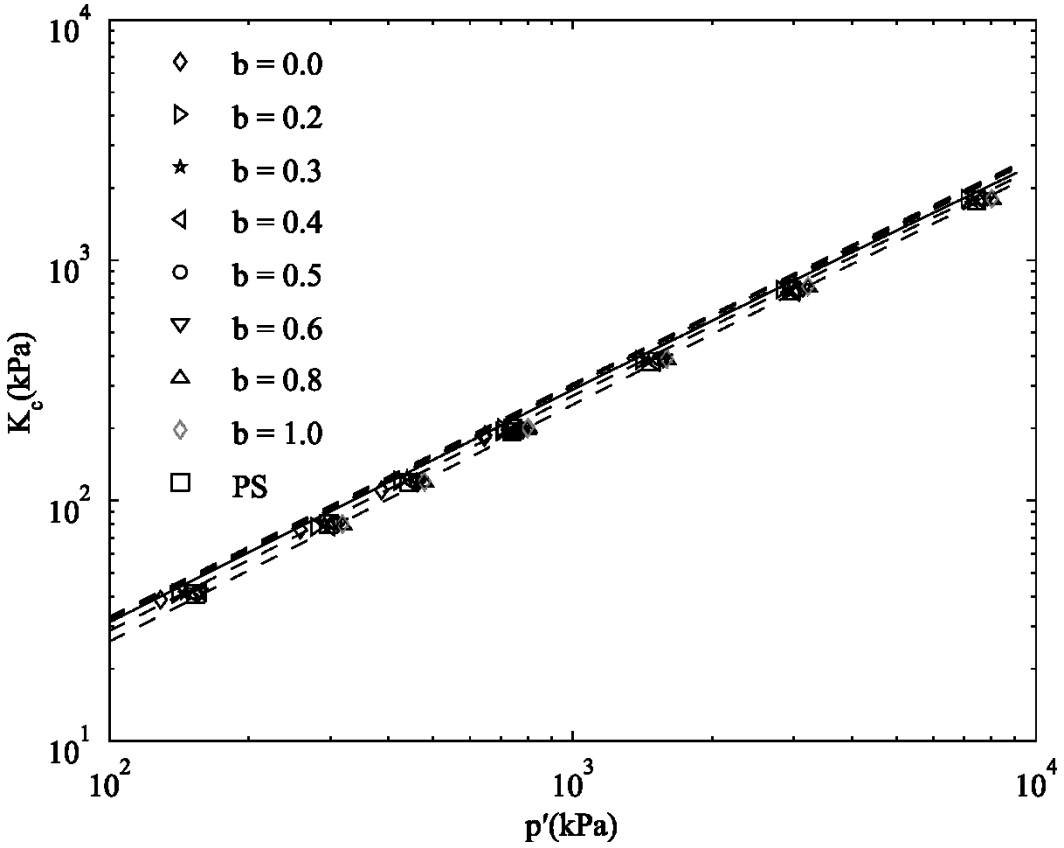



(c)

Figure 5.43 Contact force network at critical state ($\sigma'_{3,0}$ = 500 kPa, $e_0$ = 0.646): (a) b=0.0; (b) Plane strain; (c) b=1.0




(a)




(b)

Figure 5.44 Correlations between $K_c$ and $p'$ at critical state: (a) Zhao and Guo (2013); (b) This study (dashed lines indicate the product of the $\Phi_d$-$p'$ relationship and M($b$)$p'$ for various b values)

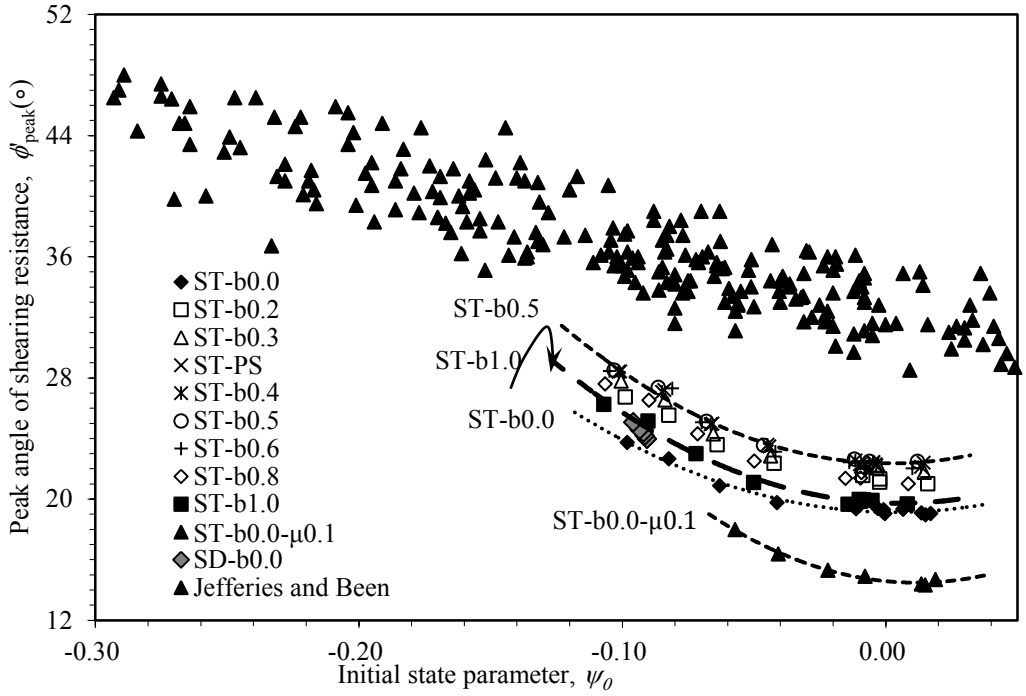



Figure 5.45 Initial state parameter ($\psi_0$) and peak angle of shearing resistance ($\phi'_{peak}$), DEM simulation results presented along with the experimental data reported in Jefferies and Been (2006)

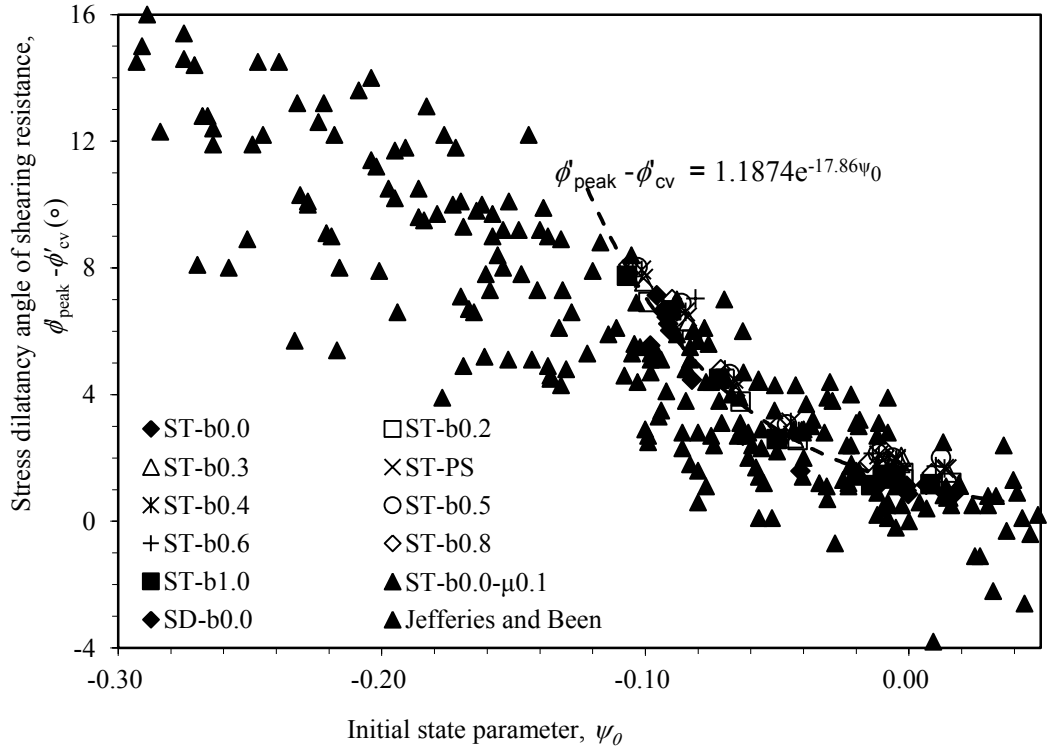



Figure 5.46 Initial state parameter ($\psi_0$) and stress dilatancy angle of shearing resistance ($\phi'_{peak}$- $\phi'_{cv}$), DEM simulation results presented along with the experimental data reported in Jefferies and Been (2006)

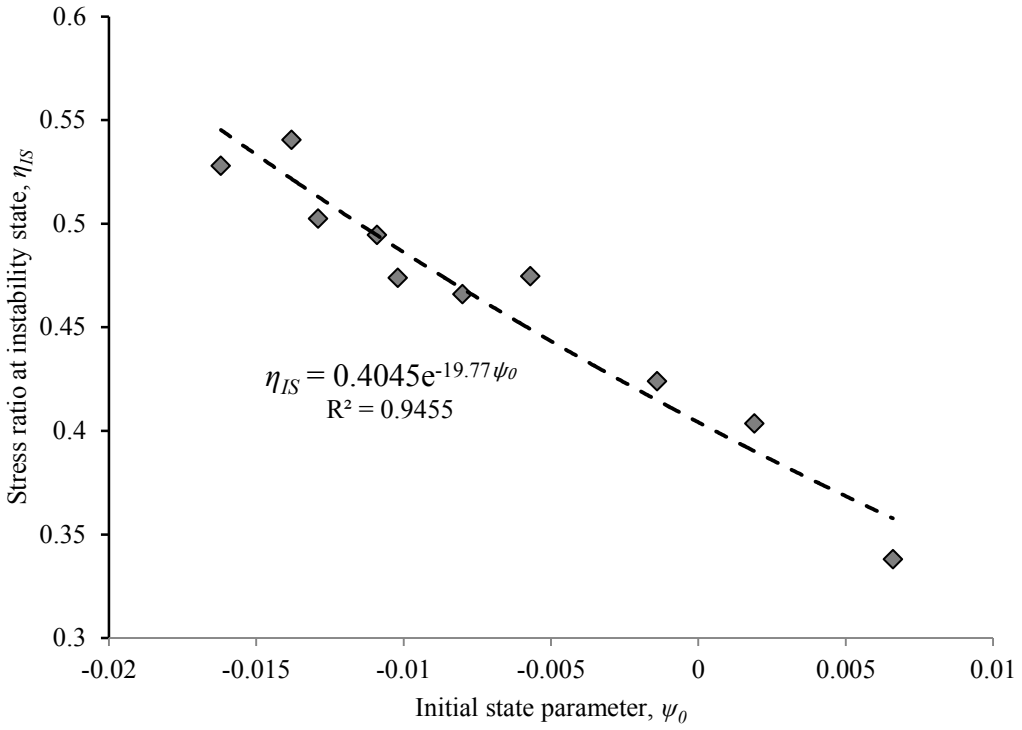



Figure 5.47 Relationship between the stress ratio at instability state ($\eta_{IS}$) and initial state parameter ($\psi_0$) for undrained triaxial compression simulations ($b$=0)

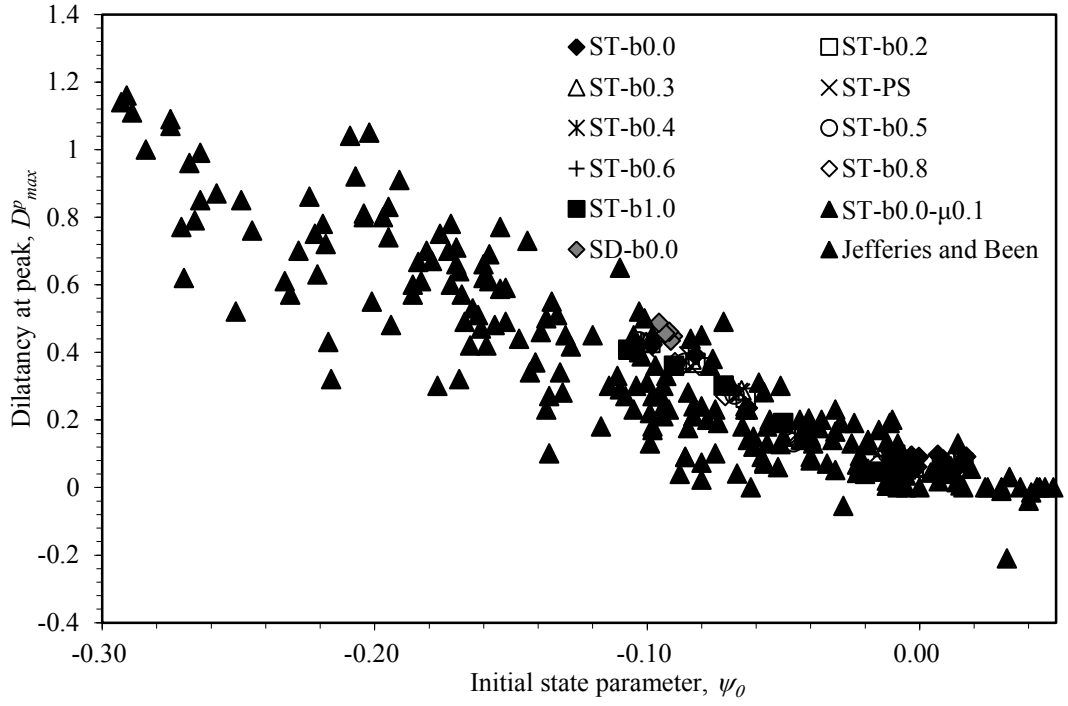
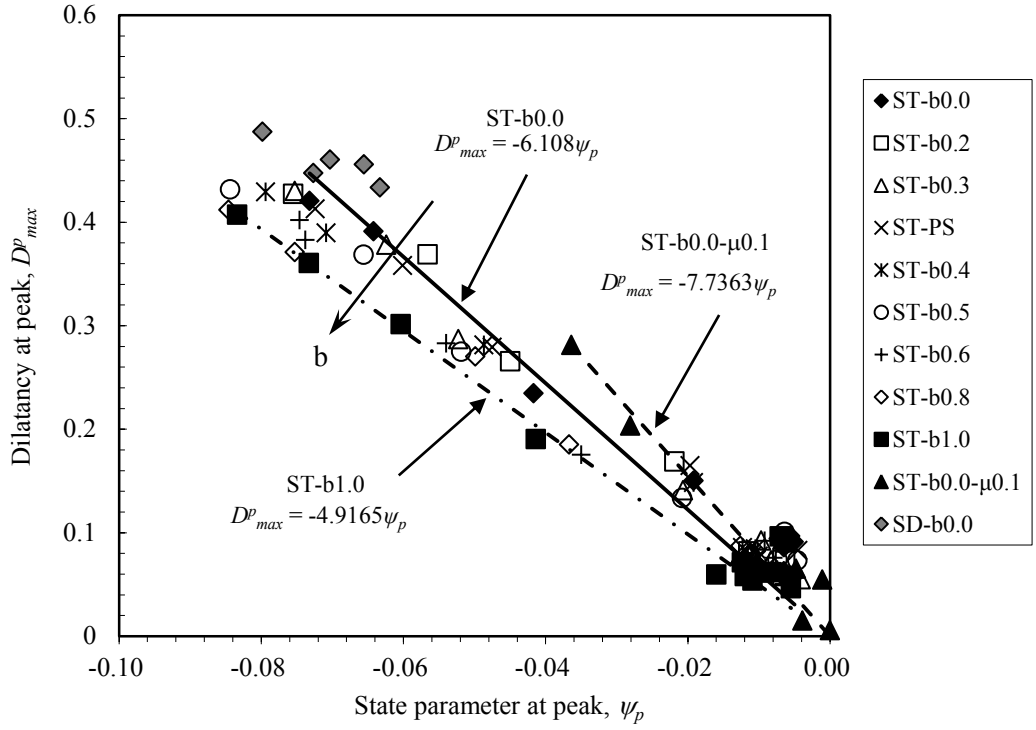
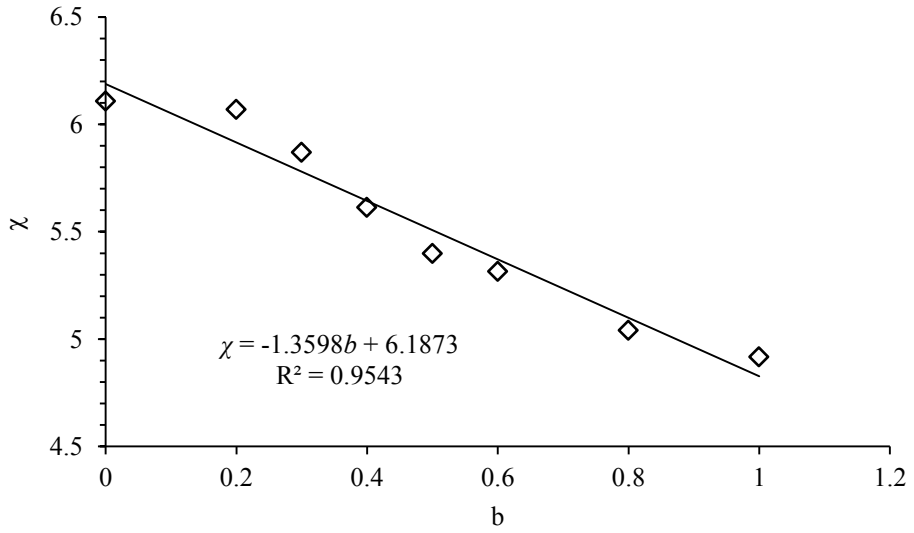



Figure 5.48 Relationship between the peak dilatancy ($D^p_{max}$) and the initial state parameter ($\psi_0$), DEM simulation results presented along with the experimental data reported in Jefferies and Been (2006)

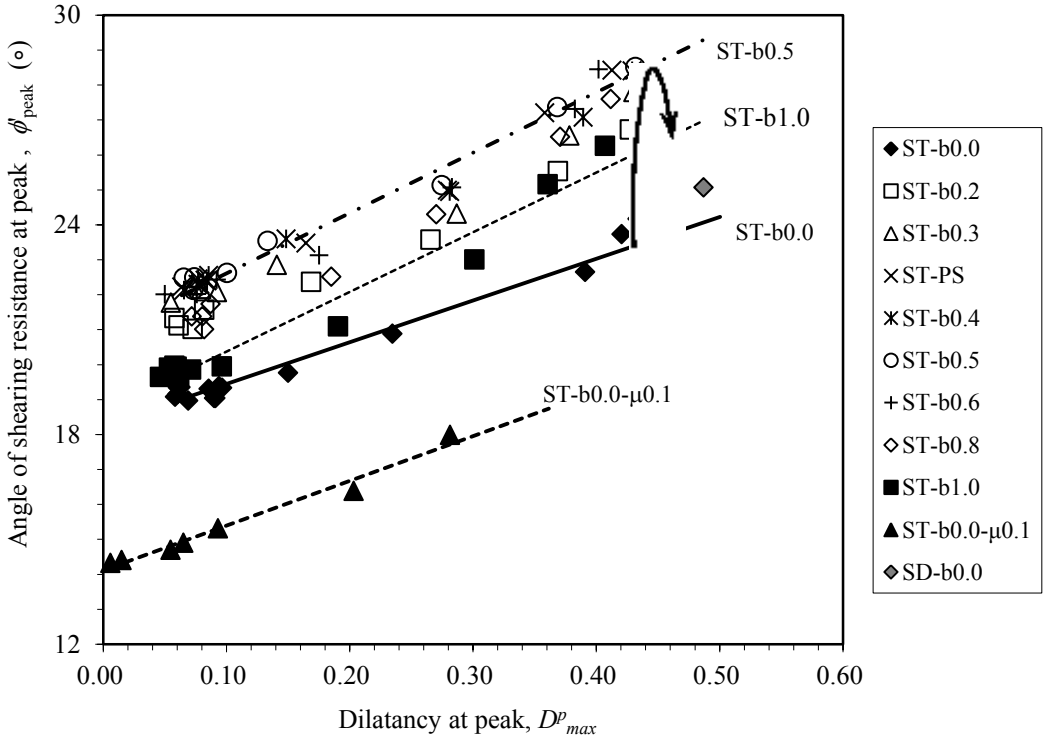



(a) $D^p_{max}$ versus $\psi_p$

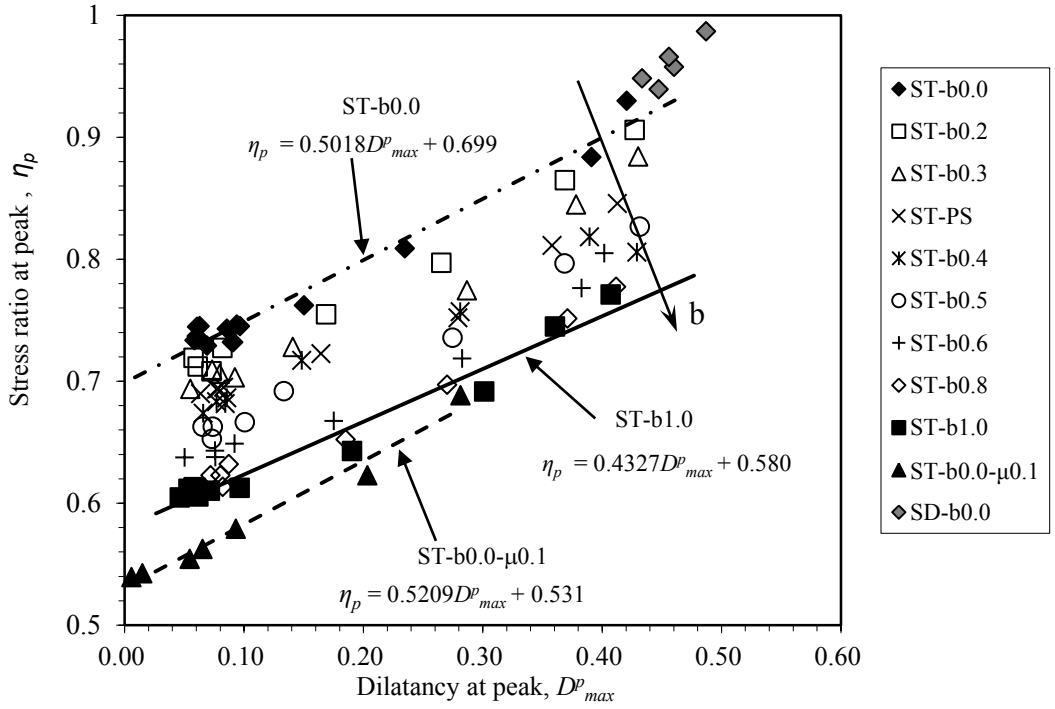



(b) Variation of χ with intermediate stress ratio ($b$)

Figure 5.49 Relationships between the dilatancy at peak ($D^p_{max}$) and the state parameter at peak ($\psi_p$)

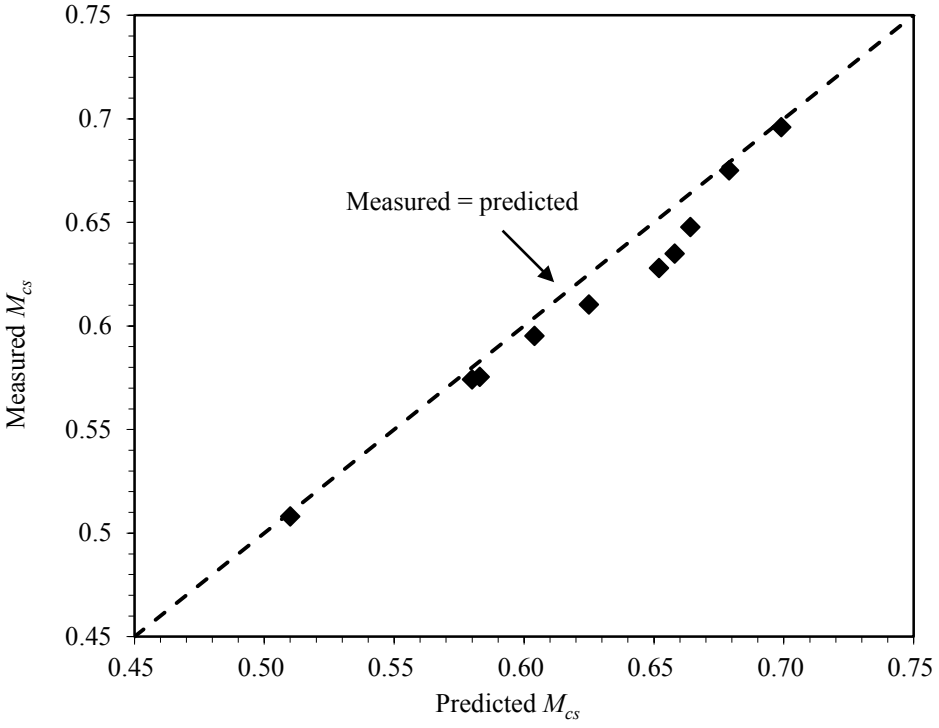



(a) Dilatancy at peak against peak angle of shearing resistance

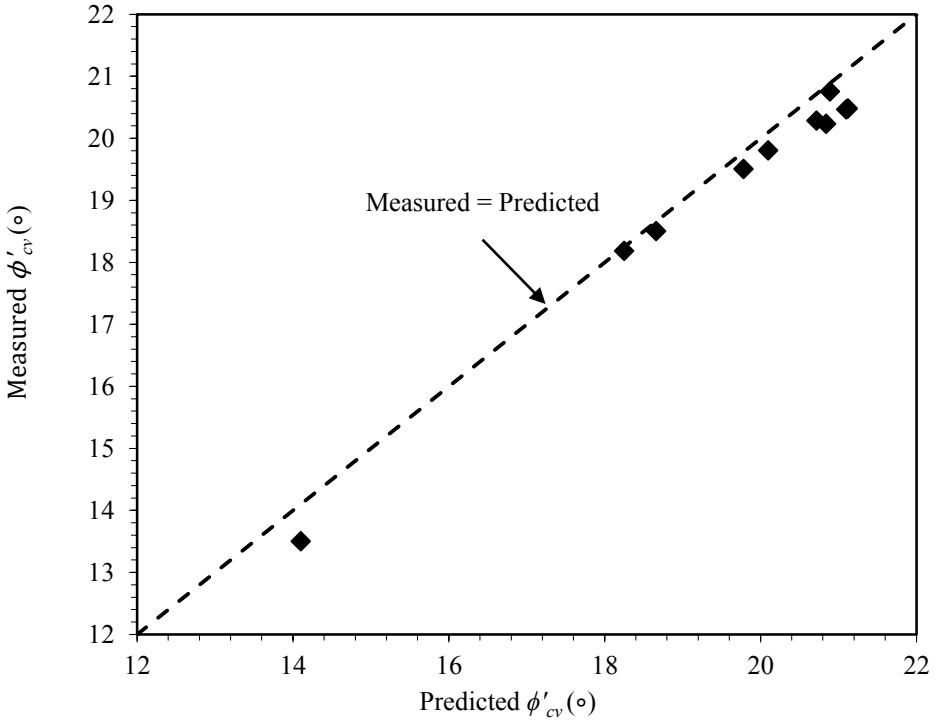



(b) Dilatancy at peak against peak stress ratio

Figure 5.50 Relationship between the peak strength and dilatancy at peak

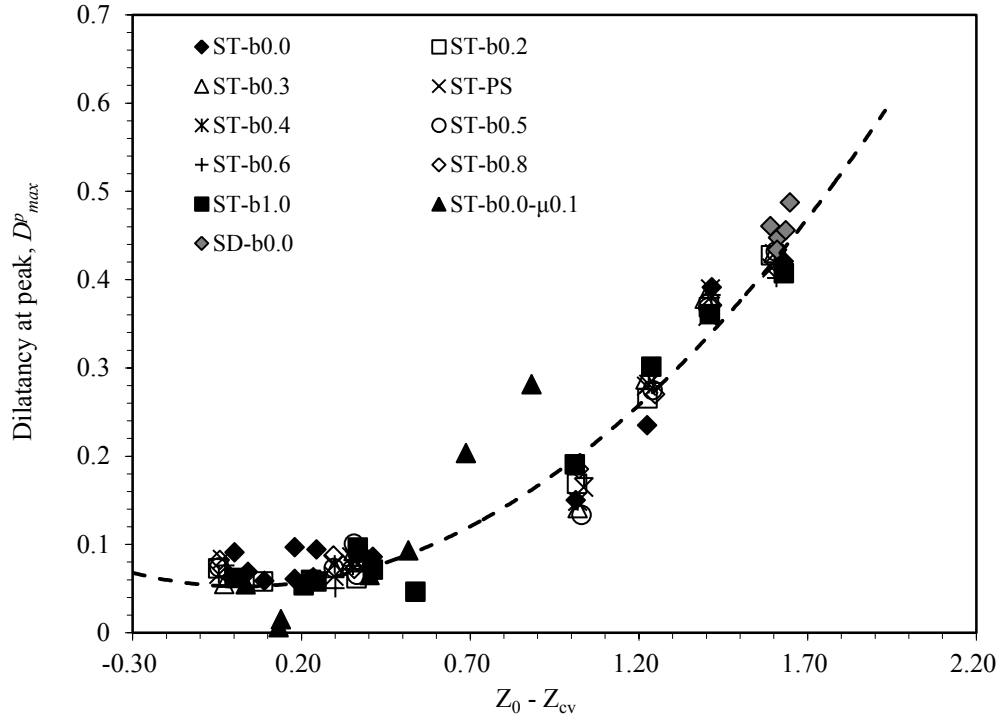



(a) Stress ratio

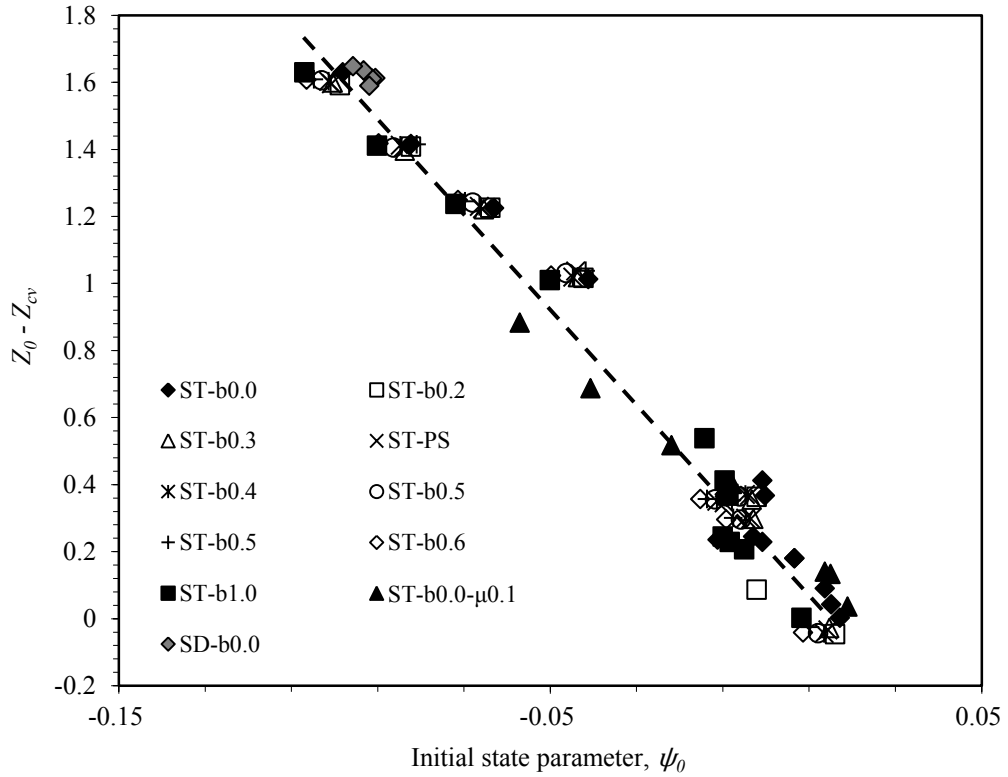



(b) Angle of shearing resistance

Figure 5.51 Comparison between the measured critical state strength and the critical state strength predicted from the strength and dilatancy relationship




(a) $Z_0 - Z_{cv}$ and $D^p_{max}$




(b) $Z_0 - Z_{cv}$ and $\psi_0$

Figure 5.52 Relationships between micro-scale state measurement and macro-scale state measurement

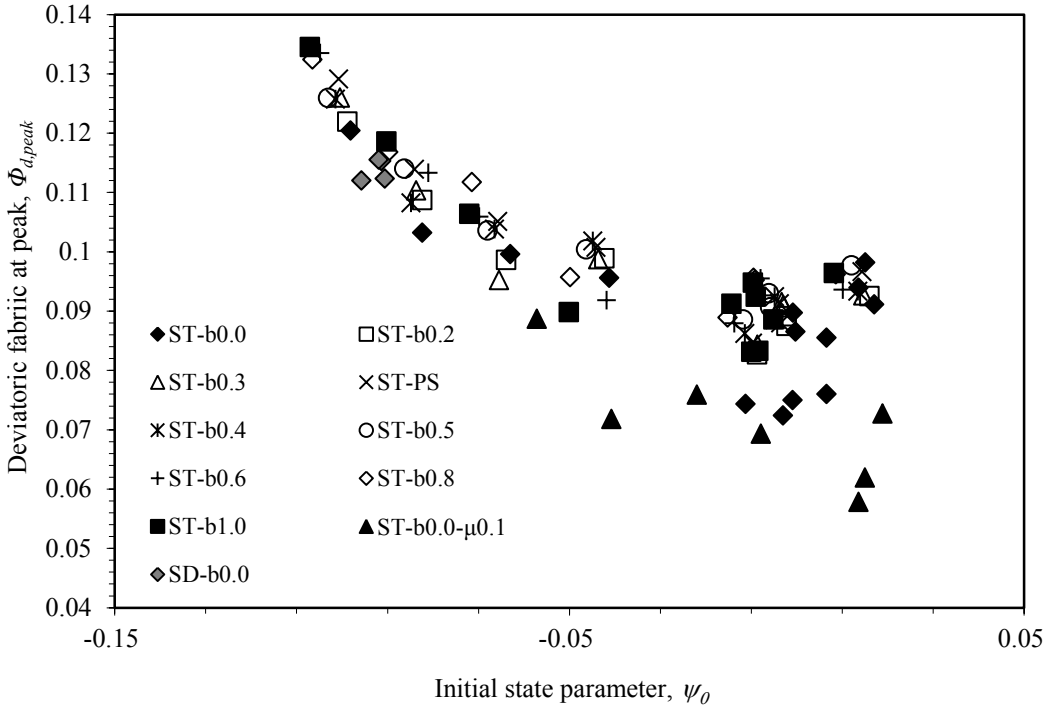
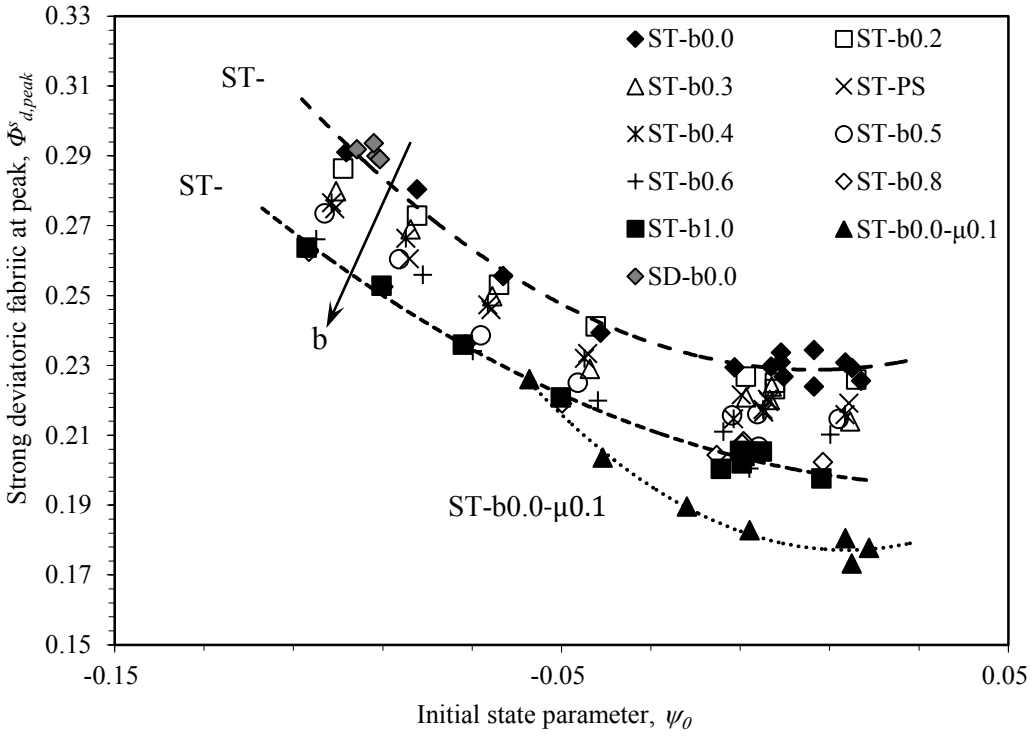
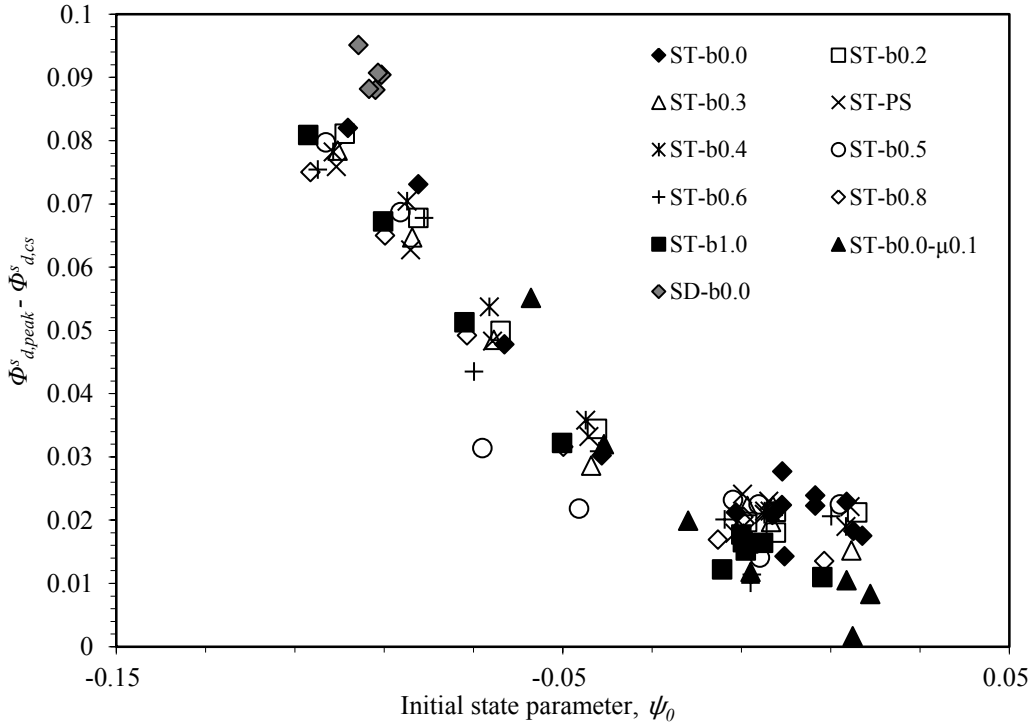



Figure 5.53 Relationships between the deviatoric fabric at peak and initial state parameter




(a) Strong deviatoric fabric at peak




(b) Difference between the strong deviatoric fabric at peak and at critical state

Figure 5.54 Correlations between the strong deviatoric fabric and initial state parameter

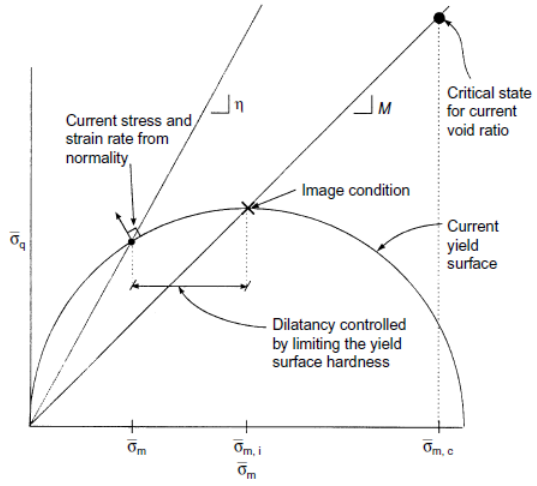



Figure 5.55 Definition of image condition on yield surface (Jefferies and Shuttle, 2002)

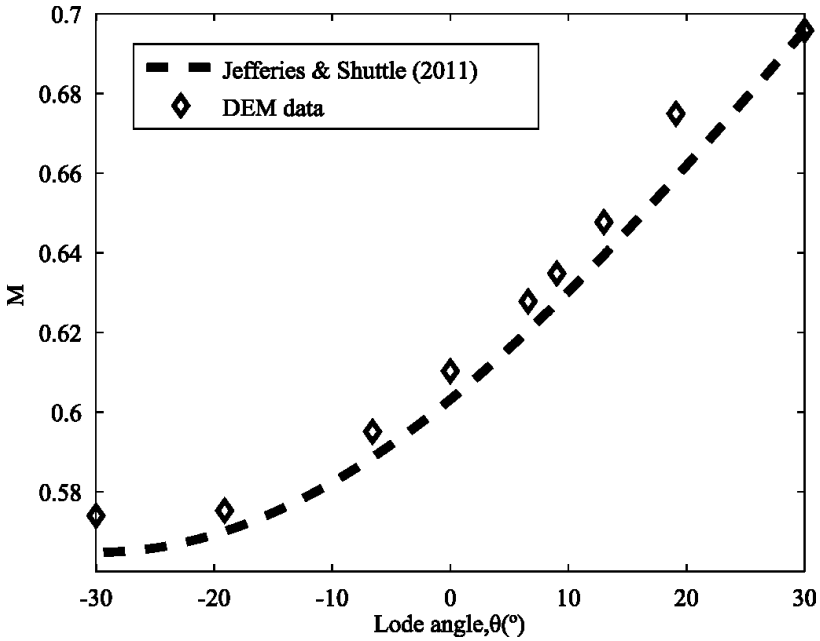



Figure 5.56 Variation of critical state stress ratio ($M_{cs}$) with Lode angle ($\theta$)

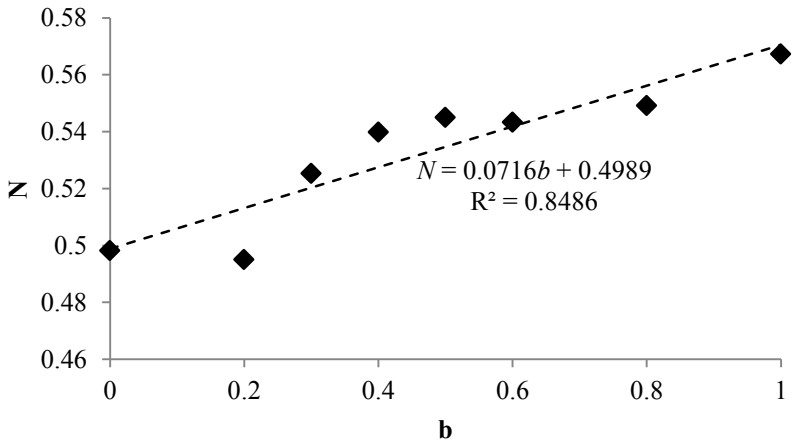
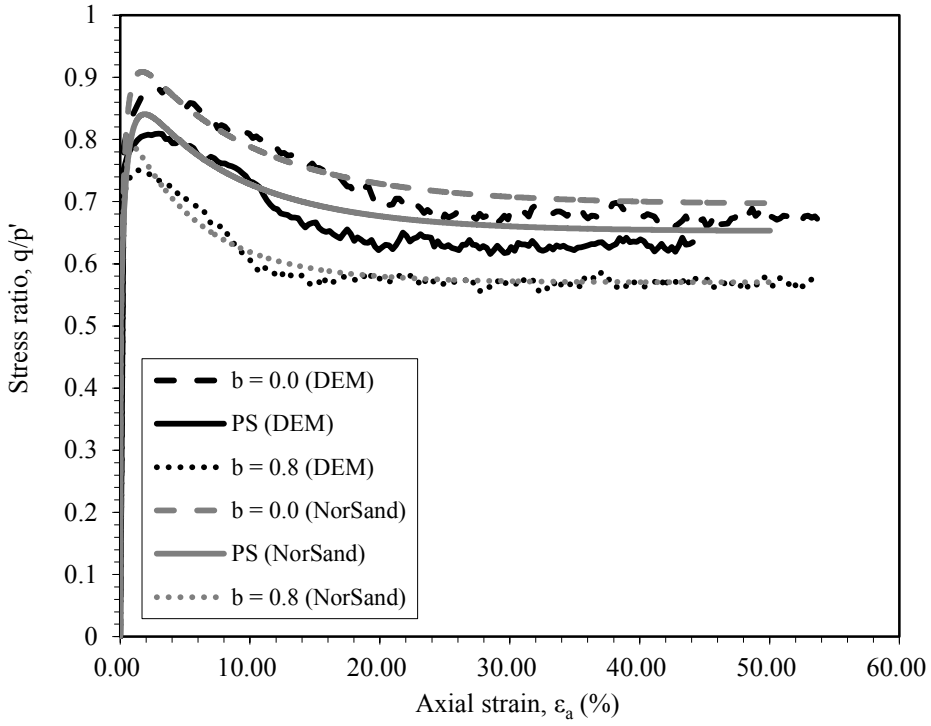
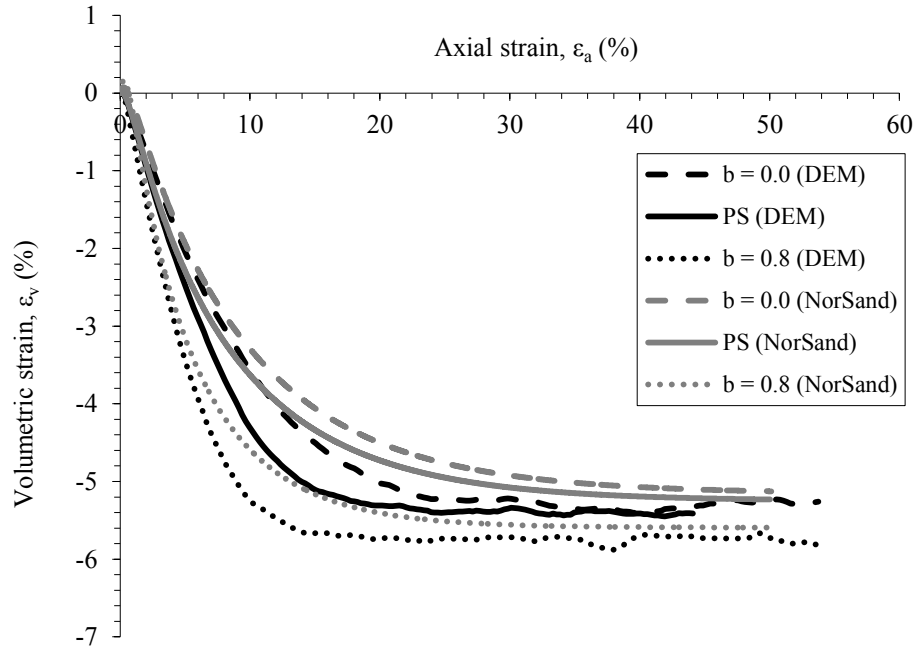



Figure 5.57 Variation of N with b

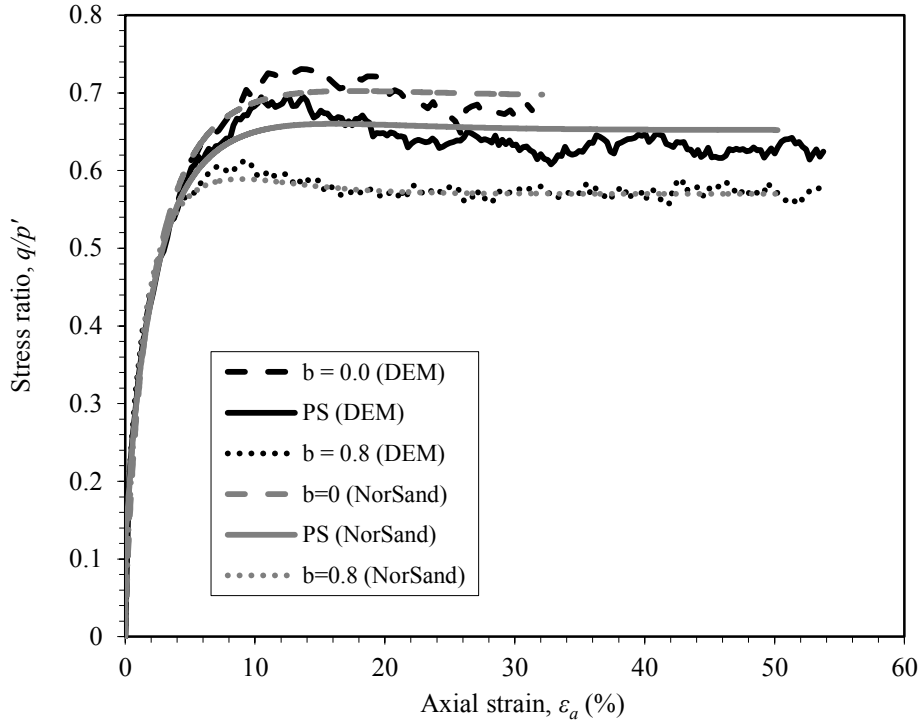



(a) Stress ratio

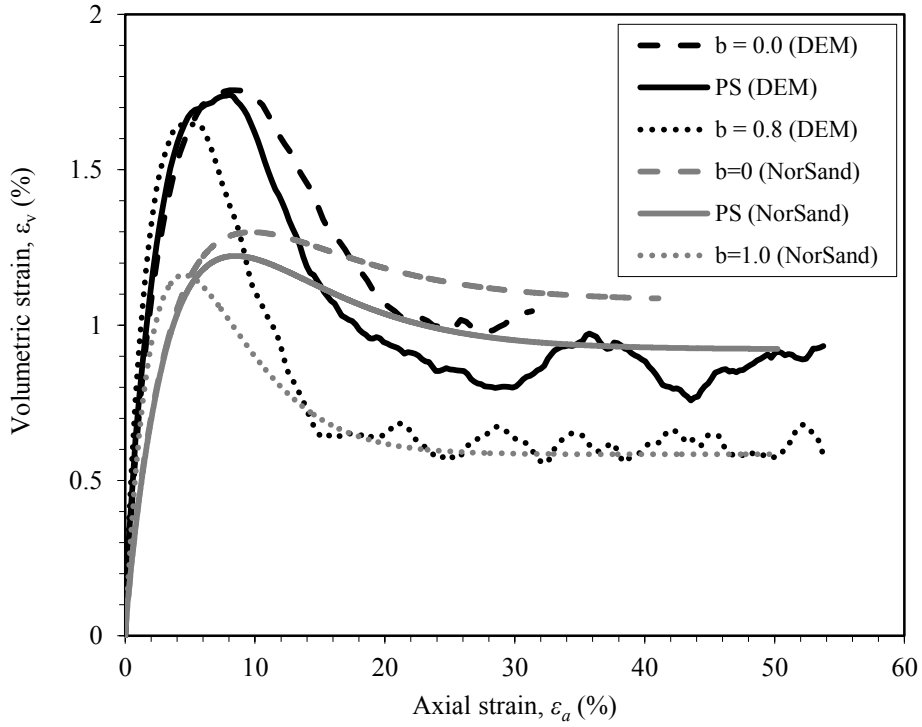



(b) Volumetric strain

Figure 5.58 Comparison between the NorSand modelling results and the DEM data for a dense sample ($e_0$ = 0.549, $\sigma'_3$ = 300 kPa)




(a) Stress ratio




(b) Volumetric strain

Figure 5.59 Comparison between the NorSand modelling results and the DEM data for a loose sample ($e_0$ = 0.646, $\sigma'_3$ = 500 kPa)

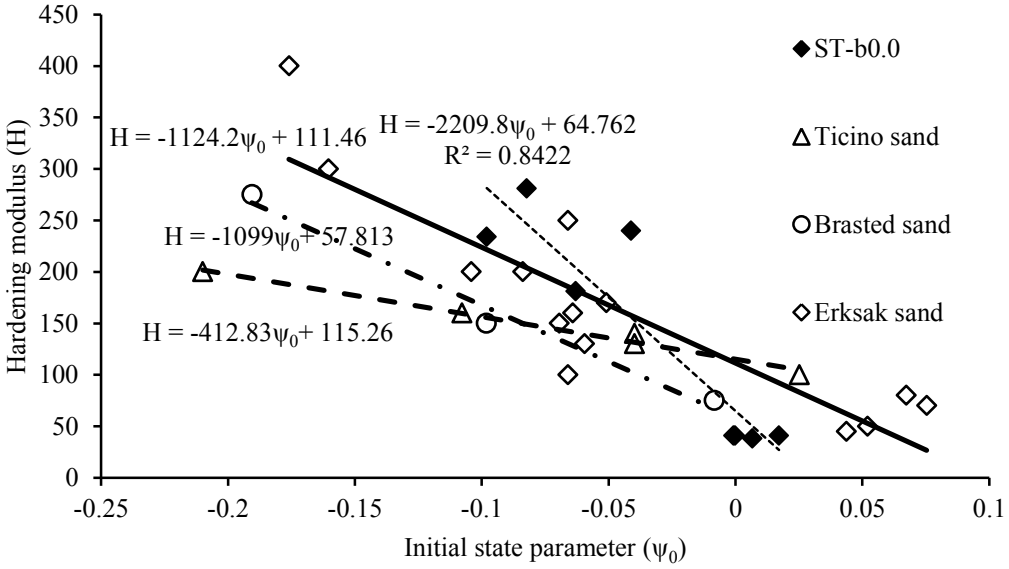



Figure 5.60 Variation of hardening modulus ($H$) with initial state parameter ($\psi_0$)

Table 5.1 Summary of the true triaxial simulations

| b | ID | $\sigma'_{3,0}$ (kPa) | $e_0$ | $Z_0$ | $\Phi_{d,0}$ | $e_{cs}$ | $p'_{cs}$ (kPa) | $q_{cs}$(kPa) | $Z_{cs}$ | $\Phi_{d,cs}$ |
|---|---|---|---|---|---|---|---|---|---|---|
| 0.0 | 0.533-100 | 100 | 0.533 | 5.83 | 0.003 | 0.630 | 129.0 | 86.2 | 4.24 | 0.089 |
| | 0.568-200 | 200 | 0.568 | 5.53 | 0.002 | 0.631 | 258.2 | 174.6 | 4.30 | 0.087 |
| | 0.549-300 | 300 | 0.549 | 5.75 | 0.002 | 0.630 | 386.8 | 259.0 | 4.33 | 0.085 |
| | 0.588-500 | 500 | 0.588 | 5.42 | 0.002 | 0.629 | 646.6 | 437.5 | 4.41 | 0.085 |
| | 0.646-500 | 500 | 0.646 | 4.37 | 0.004 | 0.629 | 645.0 | 437.8 | 4.37 | 0.085 |
| | 0.627-1000 | 1000 | 0.627 | 4.87 | 0.002 | 0.628 | 1228.4 | 869.1 | 4.50 | 0.082 |
| | 0.625-2000 | 2000 | 0.625 | 4.9489 | 0.0018 | 0.627 | 2587.4 | 1762.0 | 4.62 | 0.082 |
| 0.2 | 0.533-100 | 100 | 0.533 | 5.83 | 0.003 | 0.630 | 140.5 | 92.7 | 4.24 | 0.089 |
| | 0.568-200 | 200 | 0.568 | 5.53 | 0.002 | 0.632 | 279.7 | 182.5 | 4.3 | 0.086 |
| | 0.549-300 | 300 | 0.549 | 5.75 | 0.002 | 0.631 | 423.1 | 282.1 | 4.34 | 0.086 |
| | 0.588-500 | 500 | 0.588 | 5.42 | 0.002 | 0.630 | 706.3 | 472.6 | 4.41 | 0.086 |
| | 0.646-500 | 500 | 0.646 | 4.37 | 0.004 | 0.630 | 703.1 | 465.4 | 4.41 | 0.084 |
| | 0.627-1000 | 1000 | 0.627 | 4.87 | 0.002 | 0.629 | 1407.1 | 932.5 | 4.51 | 0.083 |
| | 0.625-2000 | 2000 | 0.625 | 4.9489 | 0.0018 | 0.626 | 2823.6 | 1886.6 | 4.65 | 0.080 |
| | 0.612-5000 | 5000 | 0.612 | 5.23 | 0.0014 | 0.617 | 7084.1 | 4774.3 | 4.86 | 0.076 |
| 0.3 | 0.533-100 | 100 | 0.533 | 5.83 | 0.003 | 0.630 | 145.6 | 93.6 | 4.23 | 0.088 |
| | 0.568-200 | 200 | 0.568 | 5.53 | 0.002 | 0.632 | 291.3 | 187.1 | 4.29 | 0.087 |
| | 0.549-300 | 300 | 0.549 | 5.75 | 0.002 | 0.631 | 439 | 285 | 4.34 | 0.087 |
| | 0.588-500 | 500 | 0.588 | 5.42 | 0.002 | 0.631 | 727.5 | 466.5 | 4.40 | 0.086 |
| | 0.646-500 | 500 | 0.646 | 4.37 | 0.004 | 0.632 | 726.4 | 464.3 | 4.39 | 0.086 |
| | 0.627-1000 | 1000 | 0.627 | 4.87 | 0.002 | 0.630 | 1456.5 | 936.2 | 4.50 | 0.084 |
| | 0.625-2000 | 2000 | 0.625 | 4.9489 | 0.0018 | 0.625 | 2927.5 | 1902 | 4.65 | 0.080 |
| | 0.612-5000 | 5000 | 0.612 | 5.23 | 0.0014 | 0.616 | 7305 | 4726.7 | 4.87 | 0.076 |
| 0.4 | 0.533-100 | 100 | 0.533 | 5.83 | 0.003 | 0.633 | 150.1 | 93.5 | 4.23 | 0.089 |
| | 0.568-200 | 200 | 0.568 | 5.53 | 0.002 | 0.634 | 298.6 | 184.1 | 4.30 | 0.086 |
| | 0.549-300 | 300 | 0.549 | 5.75 | 0.002 | 0.633 | 448.6 | 277.6 | 4.33 | 0.086 |
| | 0.588-500 | 500 | 0.588 | 5.42 | 0.002 | 0.633 | 748.6 | 464.3 | 4.41 | 0.084 |
| | 0.646-500 | 500 | 0.646 | 4.37 | 0.004 | 0.632 | 751.3 | 469.3 | 4.41 | 0.085 |
| | 0.627-1000 | 1000 | 0.627 | 4.87 | 0.002 | 0.631 | 1499.5 | 932.9 | 4.50 | 0.082 |
| | 0.625-2000 | 2000 | 0.625 | 4.9489 | 0.0018 | 0.628 | 2999.6 | 1866.9 | 4.65 | 0.080 |
| | 0.612-5000 | 5000 | 0.612 | 5.23 | 0.0014 | 0.619 | 7530 | 4725.3 | 4.89 | 0.077 |
| 0.5 | 0.533-100 | 100 | 0.533 | 5.83 | 0.003 | 0.635 | 153.7 | 92.9 | 4.23 | 0.089 |
| | 0.568-200 | 200 | 0.568 | 5.53 | 0.002 | 0.635 | 307.1 | 185.5 | 4.29 | 0.089 |
| | 0.549-300 | 300 | 0.549 | 5.75 | 0.002 | 0.634 | 458.6 | 274.6 | 4.34 | 0.087 |
| | 0.588-500 | 500 | 0.588 | 5.42 | 0.002 | 0.635 | 770.5 | 468.5 | 4.39 | 0.085 |
| | 0.646-500 | 500 | 0.646 | 4.37 | 0.004 | 0.634 | 766.5 | 461.5 | 4.41 | 0.085 |
| | 0.627-1000 | 1000 | 0.627 | 4.87 | 0.002 | 0.632 | 1537 | 930 | 4.51 | 0.085 |
| | 0.625-2000 | 2000 | 0.625 | 4.9489 | 0.0018 | 0.628 | 3081.9 | 1873.5 | 4.65 | 0.081 |
| | 0.612-5000 | 5000 | 0.612 | 5.23 | 0.0014 | 0.619 | 7717.9 | 4706.5 | 4.88 | 0.078 |

Table 5.1 Summary of the true triaxial simulations (continued)

| b | | $\sigma'_{3,0}$ (kPa) | $e_0$ | $Z_0$ | $\Phi_{d,0}$ | $e_{cs}$ | $p'_{cs}$ (kPa) | $q_{cs}$(kPa) | $Z_{cs}$ | $\Phi_{d,cs}$ |
|---|---|---|---|---|---|---|---|---|---|---|
| 0.6 | 0.533-100 | 100 | 0.533 | 5.83 | 0.003 | 0.637 | 156.1 | 91.6 | 4.23 | 0.091 |
| | 0.568-200 | 200 | 0.568 | 5.53 | 0.002 | 0.639 | 312 | 183.1 | 4.28 | 0.088 |
| | 0.549-300 | 300 | 0.549 | 5.75 | 0.002 | 0.636 | 456.7 | 270.9 | 4.33 | 0.087 |
| | 0.588-500 | 500 | 0.588 | 5.42 | 0.002 | 0.634 | 781.5 | 460.0 | 4.39 | 0.086 |
| | 0.646-500 | 500 | 0.646 | 4.37 | 0.004 | 0.635 | 781 | 459.2 | 4.39 | 0.086 |
| | 0.627-1000 | 1000 | 0.627 | 4.87 | 0.002 | 0.634 | 1566.5 | 925.8 | 4.52 | 0.084 |
| | 0.625-2000 | 2000 | 0.625 | 4.9489 | 0.0018 | 0.630 | 3138.5 | 1860.6 | 4.65 | 0.082 |
| | 0.612-5000 | 5000 | 0.612 | 5.23 | 0.0014 | 0.620 | 7859.8 | 4673.6 | 4.88 | 0.079 |
| 0.8 | 0.533-100 | 100 | 0.533 | 5.83 | 0.003 | 0.638 | 159.4 | 90.8 | 4.23 | 0.091 |
| | 0.568-200 | 200 | 0.568 | 5.53 | 0.002 | 0.638 | 318.5 | 180.9 | 4.28 | 0.088 |
| | 0.549-300 | 300 | 0.549 | 5.75 | 0.002 | 0.638 | 478.3 | 272.3 | 4.33 | 0.088 |
| | 0.588-500 | 500 | 0.588 | 5.42 | 0.002 | 0.637 | 800.4 | 458.8 | 4.40 | 0.088 |
| | 0.646-500 | 500 | 0.646 | 4.37 | 0.004 | 0.637 | 801.1 | 459.9 | 4.41 | 0.088 |
| | 0.627-1000 | 1000 | 0.627 | 4.87 | 0.002 | 0.635 | 1595.6 | 909.6 | 4.51 | 0.086 |
| | 0.625-2000 | 2000 | 0.625 | 4.9489 | 0.0018 | 0.633 | 3221.1 | 2034.8 | 4.65 | 0.084 |
| | 0.612-5000 | 5000 | 0.612 | 5.23 | 0.0014 | 0.621 | 8017.9 | 4608.8 | 4.88 | 0.078 |
| 1.0 | 0.568-200 | 200 | 0.568 | 5.53 | 0.002 | 0.639 | 319 | 178.5 | 4.29 | 0.089 |
| | 0.549-300 | 300 | 0.549 | 5.75 | 0.002 | 0.638 | 478.4 | 267.6 | 4.34 | 0.089 |
| | 0.588-500 | 500 | 0.588 | 5.42 | 0.002 | 0.639 | 801.3 | 451.9 | 4.40 | 0.087 |
| | 0.646-500 | 500 | 0.646 | 4.37 | 0.004 | 0.638 | 801.5 | 452.2 | 4.41 | 0.088 |
| | 0.627-1000 | 1000 | 0.627 | 4.87 | 0.002 | 0.636 | 1602.5 | 903.5 | 4.52 | 0.086 |
| | 0.625-2000 | 2000 | 0.625 | 4.9489 | 0.0018 | 0.633 | 3227.9 | 1841.4 | 4.66 | 0.084 |
| PS | 0.533-100 | 100 | 0.533 | 5.83 | 0.003 | 0.632 | 148.2 | 93.7 | 4.23 | 0.088 |
| | 0.568-200 | 200 | 0.568 | 5.53 | 0.002 | 0.633 | 297.5 | 186.8 | 4.29 | 0.087 |
| | 0.549-300 | 300 | 0.549 | 5.75 | 0.002 | 0.633 | 443.9 | 280.7 | 4.34 | 0.087 |
| | 0.588-500 | 500 | 0.588 | 5.42 | 0.002 | 0.631 | 744.7 | 472.5 | 4.39 | 0.086 |
| | 0.646-500 | 500 | 0.646 | 4.37 | 0.004 | 0.632 | 740.3 | 463.8 | 4.39 | 0.086 |
| | 0.627-1000 | 1000 | 0.627 | 4.87 | 0.002 | 0.630 | 1477.5 | 934.1 | 4.50 | 0.083 |
| | 0.625-2000 | 2000 | 0.625 | 4.9489 | 0.0018 | 0.628 | 2963.1 | 1878.6 | 4.64 | 0.081 |
| | 0.612-5000 | 5000 | 0.612 | 5.23 | 0.0014 | 0.616 | 7445.9 | 4724.3 | 4.87 | 0.077 |

Table 5.2 Fitting parameters for different failure criteria at peak state ($e_0$=0.646, $\sigma'_3$=500 kPa)

| Ogawa | Satake | Lade | Matsuoka & Nakai |
|---|---|---|---|
| n=3.97, η =0.024 | η = 0.217 | η =31.47 | η = 0.948 |

Table 5.3 Fitting parameters for different failure criteria at critical state

| Ogawa | Satake | Lade | Matsuoka & Nakai |
|---|---|---|---|
| n=3.64, η =0.05 | η = 0.190 | η =30.82 | η = 0.838 |

Table 5.4 Summary of the critical-state parameters

| | b=0 | b=0.2 | b=0.3 | PS | b=0.4 | b=0.5 | b=0.6 | b=0.8 | b=1.0 | $\mu$ = 0.1 | Dunkirk |
|---|---|---|---|---|---|---|---|---|---|---|---|
| $\Gamma$ | 0.632 | 0.633 | 0.634 | 0.635 | 0.635 | 0.637 | 0.639 | 0.640 | 0.641 | 0.508 | 0.702 |
| $\lambda$ | 0.00092 | 0.00076 | 0.00088 | 0.00084 | 0.00075 | 0.00084 | 0.00083 | 0.00084 | 0.00096 | 0.0011 | 0.0008 |
| $M$ | 0.696 | 0.673 | 0.647 | 0.634 | 0.627 | 0.609 | 0.594 | 0.575 | 0.573 | 0.508 | 0.702 |
| $\phi'_{cv}$ (°) | 18.2 | 19.8 | 20.2 | 20.8 | 20.5 | 20.5 | 20.3 | 19.5 | 18.5 | 13.5 | 18.3 |

Table 5.5 Summary of fitting parameters for the $\Phi_d$–$p'$ relationship at critical state

| | b=0 | b=0.2 | b=0.3 | PS | b=0.4 | b=0.5 | b=0.6 | b=0.8 | b=1.0 |
|---|---|---|---|---|---|---|---|---|---|
| $m_F$ | -0.009916 | -0.01279 | -0.009473 | -0.01248 | -0.03996 | -0.003653 | -0.0412 | -0.003895 | -0.002027 |
| $\zeta$ | 0.2181 | 0.1673 | 0.213 | 0.1655 | 0.06869 | 0.333 | 0.06319 | 0.3392 | 0.3902 |
| $\varepsilon_F$ | 0.09957 | 0.1022 | 0.09864 | 0.1015 | 0.1302 | 0.09305 | 0.1328 | 0.09562 | 0.09238 |

Table 5.6 Initial state parameter ($\psi_0$) and stress ratio at instability state ($\eta_{IS}$) for undrained simulations

| ID | $e_0$ | $\sigma'^{0}_{3}$ | $\psi_0$ | $\eta_{IS}$ |
|---|---|---|---|---|
| 0.613-500 | 0.613 | 500 | -0.0162 | 0.528 |
| 0.6163-500 | 0.6163 | 500 | -0.0129 | 0.502 |
| 0.619-500 | 0.619 | 500 | -0.0102 | 0.474 |
| 0.6165-1000 | 0.6165 | 1000 | -0.0109 | 0.495 |
| 0.6166-2000 | 0.6166 | 2000 | -0.008 | 0.466 |
| 0.6165-5000 | 0.6165 | 5000 | -0.0014 | 0.424 |
| 0.604-5000 | 0.604 | 5000 | -0.0138 | 0.540 |
| 0.6122-5000 | 0.6122 | 5000 | -0.0057 | 0.475 |
| 0.6198-5000 | 0.6198 | 5000 | 0.0019 | 0.403 |
| 0.6245-5000 | 0.6245 | 5000 | 0.0066 | 0.338 |

Table 5.7 Input modelling parameters for NorSand

| | Plasticity | | | | | | | | | Elasticity | | | | | |
|---|---|---|---|---|---|---|---|---|---|---|---|---|---|---|---|
| | $H$ | | | $\chi$ | | | $N$ | | | $I_r$ | | | $\upsilon$ | | |
| | b = 0.0 | PS | b = 0.8 | b = 0.0 | PS | b = 0.8 | b = 0.0 | PS | b = 0.8 | b = 0.0 | PS | b = 0.8 | b = 0.0 | PS | b = 0.8 |
| $e_0$ = 0.549, $\sigma'_3$ = 300 kPa | 281 | 281 | 281 | 6.108 | 5.9556 | 5.0411 | 0.4982 | 0.582 | 0.5134 | 924.18 | 924.18 | 924.18 | 0.2 | 0.2 | 0.2 |
| $e_0$ = 0.646, $\sigma'_3$ = 500 kPa | 41 | 41 | 41 | 6.108 | 5.9556 | 5.0411 | 0.4982 | 0.582 | 0.5134 | 446.91 | 446.91 | 446.91 | 0.2 | 0.2 | 0.2 |

# Chapter 6 Using rotational resistance to study the effect of particle geometry

## 6.1 Introduction

Soil grains have distinct shape characteristics, e.g., sphericity, roundness and roughness, that depend upon their production, transportation and deposition histories as well as their mineralogical composition. Different degrees of shape irregularity result in different degrees of interlocking between soil grains. The significance of particle shape on soil behaviour has been considered in many experimental studies (e.g., Cho et al., 2006; Shin & Santamarina, 2013; Yang & Wei, 2012). Cho et al. (2006) analysed a large dataset from physical experiments and they showed that particle shape affects the packing density, the small strain stiffness, the volumetric response and the strength. In particular, Cho et al. (2006) showed that the critical state parameters depend on particle shape (Figure 6.1).

As already discussed in Chapter 4, the strength obtained in a DEM simulation using spherical particles is much lower than that of real sand despite the similarity in grading. This was attributed to the neglect of interlocking between particles as the influence of interparticle friction coefficient was found to be limited. Considering the non-spherical nature of soil grains in DEM simulations is recognised to be a challenging issue. In general, there are two prevailing approaches. The first approach is to create particles with non-spherical shapes. This can be achieved by using regularly-shaped particles, e.g., ellipses in 2D (Fu & Dafalias, 2011), ellipsoids in 3D (Ng, 2009b) (Figure 6.2 (a)), polygons in 2D (Peña et al., 2008) (Figure 6.2 (b)) and polyhedrons in 3D (Langston et al., 2013) (Figure 6.2 (c)). Alternatively, small particles can be 'glued' together to create clusters/clumps with different topological features (e.g., Ferellec & McDowell, 2010; Kozicki et al., 2012; Yang et al., 2012) (Figure 6.2 (d)). All of these methods can only reproduce very simple topologies rather than the real geometrical characteristics of soil grains. Attempts have also been made to generate particles with accurate shape characteristics (e.g., Mollon & Zhao, 2012, 2014). The concept of 'potential particles' proposed by Houlsby (2009) describes the periphery of a particle by different mathematical functions ($f(x,y)$ in 2D and $f(x,y,z)$ in 3D) with respect to a local coordinate system (Figure 6.3 (a)) and enables a variety of convex particles to be created by adopting a combination of different $f$ functions to represent the periphery (Figure 6.3 (b)). Despite these efforts, whichever of these methods is used, there is an increase in the computational cost due to the increased complexity of contact detection and contact force

calculation. The resulting increased simulation times largely compromise the scale of the problems that can be investigated.

An alternative approach is to introduce additional rotational resistance at the interparticle contacts between discs or spheres, i.e., to use a rotational resistance model. The idea arises from the fact that for nonspherical particles, the branch vector direction ($\overrightarrow{O_A O_B}$) is no longer coincident with the contact normal direction $\vec{f_n}$ (Figure 6.4 (a)). Under such circumstances, the contact normal does not pass through the particle centroid and thus imposes a moment on the particle. In addition, as shown in Figure 6.4 (b), when non-convex particles roll over each other the bias between the normal contact force ($f_n$) at the 'teeth' and the particle centroid induces a moment that is opposite to the relative rolling direction for both particles in contact. The resistance to the relative angular motion depends on the penetration of the 'teeth' (asperities) which is associated with $f_n$. A larger $f_n$ should lead to deeper penetration of the two particles which thereby increases the rotational resistance. This is the origin of the interlocking effect. When the rotational resistance model is adopted for spherical particles, the equation of angular momentum for individual spherical particles becomes:

$$\boldsymbol{I}\frac{\partial \boldsymbol{\omega}}{\partial t} = \sum_1^{N_c}(\boldsymbol{M^k} + \boldsymbol{M_r^k}) \qquad \text{(Eq. 6.1)}$$

where $\boldsymbol{I}$ is the moment of inertia of a sphere, $\boldsymbol{\omega}$ is the angular velocity, $N_c$ is the number of contacts that the particle owns, $\boldsymbol{M^k}$ is the torque resulting from the tangential force at the $k^{\text{th}}$ contact and $\boldsymbol{M_r^k}$ is the rotational resistance at the $k^{\text{th}}$ contact. The rotational resistance simulates the restriction on the relative angular motion between touching particles resulting from interlocking between real non-spherical soil grains. This approach is computationally more efficient than the attempts to model non-spherical particles described above as the contact detection scheme and the contact force calculation scheme remain the same as those for spherical particles. Rotational resistance models have been shown to be able to replicate the influence of particle shape on stress-deformation characteristics and localisation phenomena, e.g., shear banding, in a number of studies including Iwashita & Oda, (1998), Jiang et al. (2005), Mohamed & Gutierrez (2010) and Zhao & Guo (2014) amongst others.

This Chapter investigates the effect of particle shape on the critical-state behaviour by introducing a new rotational resistance model which attempts to capture as closely as possible the physical origin of interlocking between irregularly-shaped soil grains described above. The model is introduced and the effect of rotational resistance on the overall behaviour is explored. The Chapter is organised in the following manner: an overview of rolling resistance models that have been considered in the literature is given in Section 6.2;

the formulation and implementation of the new rotational resistance model is detailed in Section 6.3; the influence of the rotational resistance on the mechanical response of granular materials is discussed in Section 6.4.

## 6.2 Overview of prior rotational resistance models

Since the pioneering 2D work of Iwashita & Oda (1998), a number of rolling resistance models have been proposed and applied in DEM simulations. In general, these models can be categorised into four groups according to whether the rotational resistance is related to the magnitude of normal contact force $f_n$ and how the relative angular motion is defined in the formulation of the rolling resistance, $\boldsymbol{M_r}$. This classification is based on whether the physical origin of the rolling resistance model as introduced in Section 6.1 is considered, i.e., whether the rotational resistance is related to the normal contact force $f_n$ and thus the classification proposed here is different from that suggested by Ai et al. (2011).

*Type A:*

$\boldsymbol{M_r}$ is proportional to the magnitude of $f_n$ and acts in a direction that is opposite to the direction of relative angular velocity. The general form of this type of model is given by Eq. 6.2:

$$\boldsymbol{M_{r,i}} = -\boldsymbol{M_{r,j}} = -\mu_r f_n \frac{\boldsymbol{\omega_{rel}}}{|\boldsymbol{\omega_{rel}}|} \qquad \text{(Eq. 6.2)}$$

in which $\boldsymbol{M_{r,i}}$ and $\boldsymbol{M_{r,j}}$ are the rolling resistances imposed on particle $i$ and particle $j$ respectively, $\mu_r$ is the rolling friction and $\boldsymbol{\omega_{rel}} = \boldsymbol{\omega_i} - \boldsymbol{\omega_j}$ is the relative angular velocity between the two particles. In this model, $\boldsymbol{M_r}$ is constant when there is no change in $f_n$. A representative Type-A model is the model proposed by Zhou et al. (1999). As noted by Ai et al. (2011), this type of model is numerically unfavourable as $\boldsymbol{M_r}$ oscillates when $\boldsymbol{\omega_{rel}}$ approaches zero.

*Type B:*

$\boldsymbol{M_r}$ is related to both $f_n$ and the magnitude of the rotational component of the relative tangential velocity ($\boldsymbol{V_{rel}} = \left|\boldsymbol{\omega_i} \times \boldsymbol{R_i} - \boldsymbol{\omega_j} \times \boldsymbol{R_j}\right|$). The rotational resistance is given by

$$\boldsymbol{M_{r,i}} = -\boldsymbol{M_{r,j}} = -\mu_r f_n \boldsymbol{V_{rel}} \frac{\boldsymbol{\omega_{rel}}}{|\boldsymbol{\omega_{rel}}|} \qquad \text{(Eq. 6.3)}$$

In this model, rolling resistance decreases with decreasing relative rotational velocity. This type of model has been adopted by Brilliantov et al. (1996), Luding (2008) and Zhou et al. (1999) .

*Type C:*

$\boldsymbol{M_r}$ is related to both $f_n$ and relative rotation $\boldsymbol{\theta_r} = \boldsymbol{U_r}/R_r$, in which $\boldsymbol{U_r}$ is the relative displacement at the contact purely due to rolling while $R_r$ is the rolling radius. The general formulation of this Type-C models is:

$$\boldsymbol{M_{r,i}} = -\boldsymbol{M_{r,j}} = -k_r\boldsymbol{\theta_r} \quad \text{(Eq. 6.4)}$$

where the rolling stiffness $k_r$ is a function of $f_n$. The value of $k_r$ for this type of model usually follows the expression proposed by Bardet & Huang (1993) for cylinders, i.e., $k_r = 2J_n f_n R_r$ where $J_n$ is a parameter that depends on the particle roundness (Ai et al., 2011; Gao & Wang, 2013; Li, 2006; Mohamed & Gutierrez, 2010). Jiang et al. (2005) derived a different form of $k_r$ considering the uneven distribution of normal contact force over a finite contact area based on a 2D case.

*Type D:*

The calculation of $\boldsymbol{M_r}$ for this type of model is similar in form to Eq. 6.4. The difference between Type-C models and Type-D models resides in the definition of $k_r$. In a Type-D model $k_r$ is either considered as an individual input parameter (e.g., Tordesillas & Walsh, 2002) or it is related to the tangential contact stiffness assuming the rotational resistance is of the same order of magnitude as the moment induced by the tangential force (Belheine et al., 2009; Iwashita & Oda , 1998, 2000; Plassiard et al., 2009; Zhao & Guo, 2014). Although the number of input parameters can be reduced, obtaining $k_r$ using this approach is not physically rigorous as $f_n$ is excluded in the formulation of the rotational stiffness.

*The limit of the rotational resistance and interlocking*

A typical rotational resistance model is elasto-plastic and, just as with the Coulomb friction law, $\boldsymbol{M_r}$ is bounded by a limit value, $M_r^m$, which is normally in the following form:

$$M_r^m = \mu_r f_n l \quad \text{(Eq. 6.5)}$$

in which the rolling friction $\mu_r$ captures the particle irregularity and $l$ is a characteristic length. Different definitions of $l$ have been proposed: for example, $l$ has been defined as the radius of the smaller particle of a contacting pair (Li, 2006), the rolling radius (Ai et al., 2011; Mohamed & Gutierrez, 2010), the approach of two touching particles (Estrada et al., 2008) or the bias of the resultant normal contact force direction from the centroid of the contact area (Zhao & Guo, 2014). Use of Eq. 6.5 implies that the rotational resistance model is

'frictional' in nature. However, treating the rotational resistance in this way deviates from the real interlocking mechanism. Again considering the case illustrated in Figure 6.4 (b), when rolling over each other, the asperities of particle A are pushed against the asperities of particle B at the contact which induces an moment that is opposite to the angular motion of each particle. The angular velocities ($\omega_A$ and $\omega_B$) of these two particles are thereby reduced and the kinetic energy is gradually transformed into strain energy which is stored in the overlap between asperities of the two particles. The interlocking effect is reduced when the asperities are damaged and the contact is smoothed. As a consequence, the strain energy stored in the deformed asperities is released instantaneously and some energy is also dissipated in plastic yield of asperities. Prior to this, everything is elastic and no frictional mechanism is involved in the entire procedure. In this sense, rotational resistance should be treated as a source of strain energy and the release of strain energy when the strength of asperities is reached should be considered, i.e., a limit must exist.

Despite the variety of existing rolling resistance models, for most of them, determination of the model parameters such as the rolling stiffness ($k_r$) is not predicated on physically reasonable assumptions. The mechanism underlying the role of rolling resistance also lacks extensive discussion. These issues will be addressed in the following Sections.

## 6.3 Description and formulation of the new model

### 6.3.1 Basic assumptions and formulation

*Basic assumptions*

The rotational resistance model proposed herein is derived based on the following assumptions:

- Interaction between two touching particles occurs over a finite circular area
- The contact is idealised to be composed of uniformly-distributed elastic springs in both the normal and tangential directions as shown in Figure 6.5. The mean contact stiffnesses ($\bar{k}_n$ and $\bar{k}_s$) of the equivalent springs distributed over the contact area can be derived by equating the integrated contact forces ($f_n$ and $f_t$) over the entire contact area to that calculated from a single spring system ($k_n$ and $k_s$) by:

$$f_n = k_n U_n = \int_0^{2\pi} \int_0^B (\bar{k}_n \cdot U_n) \cdot (r \cdot dr \cdot d\varphi) = \bar{k}_n \cdot U_n \cdot \pi B^2 \qquad \text{(Eq. 6.6 (a))}$$

$$\Delta f_t = k_s \Delta s = \int_0^{2\pi} \int_0^B (\bar{k}_s \cdot \Delta s) \cdot (r \cdot dr \cdot d\varphi) = \bar{k}_s \cdot \Delta s \cdot \pi B^2 \qquad \text{(Eq. 6.6 (b))}$$

where $U_n$ is the contact overlap, $\Delta f_t$ is the tangential force increment, $\Delta s$ is the tangential displacement increment and $B$ is the radius of the contact plane. Therefore $\bar{k}_n = k_n/A$ and $\bar{k}_s = k_s/A$, where $A = \pi B^2$ is the area of the circular contact plane. Note that local equilibrium is preserved in Eq. 6.6.

*Derivation of the rolling resistance model*

Rolling is the relative angular velocity between the two bodies about an axis ($x$ or $y$ axis) lying in the contact plane. For the idealised model illustrated in Figure 6.5, when two touching particles have the tendency to roll against each other about an axis in the contact plane (either the $x$ or the $y$ axis), the normal contact springs towards the front of the contact area in the relative rotation direction will be extended while the contact springs towards the rear of the contact area will be compressed (Figures 6.6 (a) and (b)). Therefore, $M_r^i$ $(i = x, y)$, which acts to oppose the relative rotation, results from the uneven redistribution of the normal contact force and can be determined by:

$$M_r^i = \int_0^{2\pi}\int_0^B (r \cdot sin\varphi) \cdot (\bar{k}_n \cdot r \cdot \theta_r^i \cdot dr \cdot d\varphi) = \bar{k}_n \frac{\pi}{4} B^4 \theta_r^i = \bar{k}_n I_i \theta_r^i \ (i = x, y) \quad \text{(Eq. 6.7)}$$

in which $I_i = \frac{\pi}{4} B^4$ is the area moment of inertia of a circular area with respect to the $i^{\text{th}}$ axis in the contact plane and $\theta_r^i$ is the relative rotation angle around the $i^{\text{th}}$ axis. Eq. 6.7 indicates that the rolling stiffness $k_r = \bar{k}_n I_i$. The contact opens when the relative angular displacement exceeds a limit value $\theta_r^m = \tan^{-1}(\frac{U_n}{B})$ as shown in Figure 6.6 (c).

According to Oda et al. (1982), there are three mechanisms of the relative displacement between two touching particles: pure rolling, pure sliding and rolling-sliding. The pure rolling and pure sliding motions in the absence of relative rigid-body rotation are illustrated in Figure 6.7. In the pure rolling case, the incremental trace of contact point on the two particle surfaces are the same in magnitude but opposite in direction ($\widehat{cc_1} = -\widehat{cc_2}$), while $\widehat{cc_1} = \widehat{cc_2}$ for pure sliding. When rolling and sliding occur concurrently, $|\widehat{cc_1}| \neq |\widehat{cc_2}|$. Calculation of the relative rotation $\theta_r^i$ here followed Jiang et al. (2005). Figure 6.8 shows the kinematics of two touching particles projected in the local $x(y)$-$z$ coordinate system from time step $t$-$\Delta t$ to time step $t$, where $z$ is parallel to the contact normal at the time step $t$. The incremental trace of the contact point on particle $i$ and particle $j$ can be given by:

$$\begin{cases} da = \widehat{c'c'_1} = r_1(d\theta_1 - d\alpha) \\ db = \widehat{c'c'_2} = r_2(d\theta_2 - d\alpha) \end{cases} \quad \text{(Eq. 6.8)}$$

where $r_1$ and $r_2$ are the radii of particle $i$ and particle $j$ respectively, $d\theta_1$ and $d\theta_2$ are the incremental angles between $O_1O_2$ and $O'_1c'_1$ and between $O_1O_2$ and $O'_2c'_2$ and $d\alpha$ is the incremental change of the contact direction (i.e., the increment of rigid-body rotation) with reference to the local coordinate system, taking counter-clockwise rotation as positive. Assuming that the sliding component of the relative displacement increment $dU_s$ and the rolling component of the relative displacement increment $dU_r$ contribute unequally to *da* and *db,* i.e.,

$$\begin{cases} da = m_1 dU_s + m_2 dU_r \\ db = m_3 dU_s + m_4 dU_r \end{cases} \quad \text{(Eq. 6.9)}$$

in which $m_1$ and $m_3$ denote the fractions of sliding component of relative displacement to *da* and *db* respectively, while $m_2$ and $m_4$ quantify the fractions of rolling component of relative displacement to *da* and *db* respectively. Considering the pure rolling condition (Eq. 6.10) and the pure sliding condition Eq. 6.11, $dU_r$ and $dU_s$ can be expressed by Eq. 6.12.

$$\begin{cases} d\alpha = 0,\ d\theta_1 = -\frac{r_2}{r_1} d\theta_2, da = -db \neq 0 \\ dU_s = 0, dU_r = da = r_1\theta_1 \end{cases} \quad \text{(Eq. 6.10)}$$

$$\begin{cases} d\theta_1 = d\theta_2 = 0, da = \frac{r_1}{r_2} db \\ dU_r = 0, dU_s = da + db \end{cases} \quad \text{(Eq. 6.11)}$$

$$\begin{cases} dU_r = \frac{r_2 da - r_1 db}{r_1 + r_2} \\ dU_s = da + db \end{cases} \quad \text{(Eq. 6.12)}$$

Therefore, the relative rotation increment can be found by Eq. 6.13,

$$d\theta_{ri} = d\theta_{1i} - d\theta_{2i} = \frac{dU_{ri}}{r_1} - \frac{-dU_{ri}}{r_2} = \frac{dU_{ri}}{\frac{r_1 r_2}{r_1 + r_2}},\ i = x, y \quad \text{(Eq. 6.13)}$$

which naturally gives the rolling radius $R_r = \frac{r_1 r_2}{r_1 + r_2}$.

*Derivation of the twisting resistance model*

Spinning/twisting is the other type of relative angular motion between touching bodies that needs to be considered for three-dimensional problems. The axis of spinning is aligned with the contact normal ***n*** (Duran, 2000; Johnson, 1985). The current twisting resistance model is also built up on the spring system illustrated in Figure 6.5. With a finite relative spinning movement $\theta_t$, the annularly-distributed springs will deform accordingly, thereby inducing annularly-shaped shear stress flows on the contact plane (Figure 6.9 (a)). The magnitude of the shear stress ($\tau = \overline{k}_s \cdot r \cdot \theta_t$) is proportional to the distance ($r$) between the tangential spring at that point and the centre of the contact plane. This distance increases linearly in the

radial direction. The annular shear stress results in a torque that acts to oppose the spinning motion which can be expressed by:

$$M_t = \int_0^{2\pi} \int_0^B r \cdot (\bar{k}_s \cdot r \cdot \theta_t \cdot r \cdot d\varphi \cdot dr) = \bar{k}_s \cdot \frac{\pi}{2} B^4 d\theta_z = \bar{k}_s \cdot J_z \cdot \theta_t \quad \text{(Eq. 6.14)}$$

in which $J_z = \frac{\pi}{2} B^4$ is the polar area moment of inertia with respect to the $z$ axis. Note that due to axisymmetry, the annular shear stress flow does not induce additional tangential force.

Note that derivation of Equations 6.7-6.14 is based on the local coordinate system ($x$-$y$-$z$) with the $z$ axis coinciding with the contact normal. Since the directional quantities in LAMMPS are stored in the global coordinate frame (X-Y-Z) and the integration of the governing equations and the contact force calculation are also based on the global coordinate system, a transformation between the two systems are necessary. At the beginning of each timestep, for individual contacts, the calculated global relative angular motion increments ($d\theta_I = \omega_I \Delta t, I = X, Y, Z$) are transformed to get the relative angular motion increments ($d\theta_i, i = x, y, z$) in the local coordinate system to calculate the local rolling and twisting resistance increments ($dM_i, i = x, y, z$) which are then transformed to the global equivalents ($dM_I, I = X, Y, Z$). Coordinate transformations are performed using quaternions in the current study as the corresponding intrinsic function is available in LAMMPS.

*Quaternion and coordinate transformation*

In mechanical problems, the rotation of the coordinate system is encountered quite frequently, e.g., calculation of the principal stresses. Usually this is achieved by introducing a rotation matrix. However, when a rotation matrix is used, the axes may be no longer orthogonal due to accumulated round-off errors, which may induce quite significant errors when performing coordinate transformation. This can be avoided by using unit quaternions. A quaternion ($\boldsymbol{q} = b + a_x \boldsymbol{i} + a_y \boldsymbol{j} + a_z \boldsymbol{k}$) can be conveniently envisioned as either, a) a vector with four components; b) a scalar plus a vector with three components; or c) a complex number with three different "imaginary" parts.

- Quaternions and spatial rotation

A rotation with an angle $\theta$ around the axis defined by a unit vector $\boldsymbol{u} = u_x \boldsymbol{i} + u_y \boldsymbol{j} + u_z \boldsymbol{k}$ is represented by a quaternion**:**

$$\boldsymbol{q} = cos\left(\frac{1}{2}\theta\right) + \left(u_x \boldsymbol{i} + u_y \boldsymbol{j} + u_z \boldsymbol{k}\right) sin\left(\frac{1}{2}\theta\right) \quad \text{(Eq. 6.15)}$$

where $\theta$ is the rotation angle which takes counter-clockwise rotation as positive.

As shown in Figure 6.10 (a), an ordinary vector $\boldsymbol{p}$ can be treated as a special quaternion with zero real part, i.e., $\boldsymbol{p} = p_x\boldsymbol{i} + p_y\boldsymbol{j} + p_z\boldsymbol{k}$. The new position ($\boldsymbol{p'}$) of $\boldsymbol{p}$ after rotating around a vector $\boldsymbol{u} = u_x\boldsymbol{i} + u_y\boldsymbol{j} + u_z\boldsymbol{k}$ by $\theta$ can be obtained by the conjugation of $\boldsymbol{p}$ by $\boldsymbol{q}$:

$$\boldsymbol{p'} = \boldsymbol{qpq^{-1}} \quad \text{(Eq. 6.16)}$$

where

$$\boldsymbol{q^{-1}} = cos\left(\frac{1}{2}\theta\right) - \left(u_x\boldsymbol{i} + u_y\boldsymbol{j} + u_z\boldsymbol{k}\right)sin(\frac{1}{2}\theta) \quad \text{(Eq. 6.17)}$$

Unit quaternions, also known as versors, provide a convenient mathematical notation for representing orientations and rotations of objects in three dimensions. Compared to Euler angles, they are simpler to compose and can avoid the problem of gimbal lock, which occurs when the axes of two of the three gimbals are driven into a parallel configuration, "locking" the system into rotation in a degenerate two-dimensional space (Wikipedia).

The basic form of a unit quaternion can be described as:

$$\begin{cases} \boldsymbol{q} = q_0 + q_1\boldsymbol{i} + q_2\boldsymbol{j} + q_3\boldsymbol{k} \\ q_0^2 + q_1^2 + q_2^2 + q_3^2 = 1 \end{cases} \quad \text{(Eq. 6.18)}$$

If there are several rotation events followed by one another, the new position of $\boldsymbol{p}$ after rotation can be described by:

$$\boldsymbol{p'} = \boldsymbol{q_n} \cdots \boldsymbol{q_1 p q_1^{-1}} \cdots \boldsymbol{q_n^{-1}} \quad \text{(Eq. 6.19)}$$

where $\boldsymbol{q_1}$ to $\boldsymbol{q_n}$ are unit quaternions for the $1^{st}$ to the $n^{th}$ rotations. Thus, we have the equivalent quaternion to combine arbitrary numbers of rotation to be a single rotation using the equivalent quaternion $\boldsymbol{q'} = \boldsymbol{q_n} \cdots \boldsymbol{q_1}$.

- Quaternion and rotation matrix

The use of unit quaternions to account for one time rotation of *Z* axis as shown in Figure 6.10 (b) is described below.

The old axes can be described in quaternion form as $\boldsymbol{OX} = 1\boldsymbol{i} + 0\boldsymbol{j} + 0\boldsymbol{k}$, $\boldsymbol{OY} = 0\boldsymbol{i} + 1\boldsymbol{j} + 0\boldsymbol{k}$ and $\boldsymbol{OZ} = 0\boldsymbol{i} + 0\boldsymbol{j} + 1\boldsymbol{k}$. The right-hand rule is used. Therefore, the rotation angle between the old and new *Z* axes is obtained by:

$$\theta = arcsin(\frac{|\boldsymbol{OZ} \times \boldsymbol{Oz}|}{|\boldsymbol{OZ}| \cdot |\boldsymbol{Oz}|}) \quad \text{(Eq. 6.20)}$$

while the rotation axis is the cross product of the old and new Z axes:

$$\boldsymbol{u} = \boldsymbol{OZ} \times \boldsymbol{Oz} \tag{Eq. 6.21}$$

The unit vector of the rotation axis is given by $\boldsymbol{u} = u_X\boldsymbol{i} + u_Y\boldsymbol{j} + u_Z\boldsymbol{k}$. Hence, the corresponding unit quaternion accounting for such a rotation is:

$$\boldsymbol{q} = q_0 + q_1\boldsymbol{i} + q_2\boldsymbol{j} + q_3\boldsymbol{k} \tag{Eq. 6.22}$$

where $q_0 = cos(\frac{1}{2}\theta)$, $q_1 = sin\left(\frac{1}{2}\theta\right)u_X$, $q_2 = sin\left(\frac{1}{2}\theta\right)u_Y$ and $q_3 = sin\left(\frac{1}{2}\theta\right)u_Z$.

So, the position of the new Cartesian axes (*x*-*y*-*z*) after rotation with respect to the old coordinate system can be obtained by:

$$\begin{cases} \boldsymbol{Ox} = \boldsymbol{qOXq^{-1}} \\ \boldsymbol{Oy} = \boldsymbol{qOYq^{-1}} \\ \boldsymbol{Oz} = \boldsymbol{qOZq^{-1}} \end{cases} \tag{Eq. 6.23}$$

which yields:

$$\begin{bmatrix} \boldsymbol{Ox} \\ \boldsymbol{Oy} \\ \boldsymbol{Oz} \end{bmatrix} = T \begin{bmatrix} \boldsymbol{OX} \\ \boldsymbol{OY} \\ \boldsymbol{OZ} \end{bmatrix} \tag{Eq. 6.24}$$

where,

$$T = \begin{bmatrix} q_0^2 + q_1^2 - q_2^2 - q_3^2 & 2(q_1q_2 - q_0q_3) & 2(q_1q_3 + q_0q_2) \\ 2(q_1q_2 + q_0q_3) & q_0^2 - q_1^2 + q_2^2 - q_3^2 & 2(q_2q_3 - q_0q_1) \\ 2(q_1q_3 - q_0q_2) & 2(q_2q_3 + q_0q_1) & q_0^2 - q_1^2 - q_2^2 + q_3^2 \end{bmatrix} \tag{Eq. 6.25}$$

and $T^{-1} = T^T$. In fact, $T$ is the rotation matrix in terms of quaternions. For multiple rotations, the rotation matrix can be determined by substituting $\boldsymbol{q}$ by the equivalent quaternion $\boldsymbol{q'}$.

- Application in the rotational resistance model

Since only spherical particles are considered, the directions of the body-frame coordinate system with the origin locating in the particle centroid always coincide with that of the space-frame (global) system. Taking the $\overrightarrow{Oz}$ axis in Figure 6.10 (b) as the contact normal and $\overrightarrow{OZ}$ as the global *z* axis direction, the unit vector of the contact normal at the current time step can be expressed by:

$$\overrightarrow{Oz} = n_X\boldsymbol{i} + n_Y\boldsymbol{j} + n_Z\boldsymbol{k} \tag{Eq. 6.26}$$

in which $n_X = \frac{X_2 - X_1}{\sqrt{(X_2-X_1)^2+(Y_2-Y_1)^2+(Z_2-Z_1)^2}}, n_Y = \frac{Y_2 - Y_1}{\sqrt{(X_2-X_1)^2+(Y_2-Y_1)^2+(Z_2-Z_1)^2}}$ and $n_Z = \frac{Z_2 - Z_1}{\sqrt{(X_2-X_1)^2+(Y_2-Y_1)^2+(Z_2-Z_1)^2}}$ and $(X_1,Y_1,Z_1)$ and $(X_2,Y_2,Z_2)$ are the coordinates of the two touching particles in the global coordinate system.

Therefore, the vector that is orthogonal to both $\overrightarrow{OZ}$ and $\overrightarrow{Oz}$ can be determined by:

$$\boldsymbol{c} = \overrightarrow{OZ} \times \overrightarrow{Oz} = -n_Y \boldsymbol{i} + n_X \boldsymbol{j} \quad \text{(Eq. 6.27)}$$

and the rotation angle from $\overrightarrow{OZ}$ to $\overrightarrow{Oz}$ around $\boldsymbol{c}$ can be calculated by:

$$cos\theta = \frac{Z_2 - Z_1}{\sqrt{(X_2-X_1)^2+(Y_2-Y_1)^2+(Z_2-Z_1)^2}} \quad \text{(Eq. 6.28)}$$

Therefore the unit quaternion accounting for this rotation becomes,

$$q = \cos\left(\frac{1}{2}\theta\right) + \left(-\frac{n_Y}{\sqrt{n_X^2+n_Y^2}}\boldsymbol{i} + \frac{n_X}{\sqrt{n_X^2+n_Y^2}}\boldsymbol{j}\right)\sin(\tfrac{1}{2}\theta) \quad \text{(Eq. 6.29)}$$

This gives,

$$\begin{cases} q_0 = cos(\frac{1}{2}\theta) \\ q_1 = -sin\left(\frac{1}{2}\theta\right)\frac{n_Y}{\sqrt{n_X^2+n_Y^2}} \\ q_2 = sin\left(\frac{1}{2}\theta\right)\frac{n_X}{\sqrt{n_X^2+n_Y^2}} \\ q_3 = 0 \end{cases} \quad \text{(Eq. 6.30)}$$

Substituting Eq. 6.30 into Eq. 6.25, the rotation matrix T is obtained. Note that due to orthogonality, the X and Y axes after rotation, $\overrightarrow{Ox}$ and $\overrightarrow{Oy}$**,** are located in the contact plane. The transformation from global rotation to rotation around local axes from the previous time step to the current time step can thus be obtained by:

$$\begin{bmatrix} d\theta_x \\ d\theta_y \\ d\theta_z \end{bmatrix}_{t-\Delta t \to t} = T \begin{bmatrix} d\theta_X \\ d\theta_Y \\ d\theta_Z \end{bmatrix}_{t-\Delta t \to t} \quad \text{(Eq. 6.31)}$$

where $d\theta_x$ and $d\theta_y$ account for the relative rotation around the two orthogonal axes ($\overrightarrow{Ox}$ and $\overrightarrow{Oy}$) in the contact plane and $d\theta_z$ reflects twisting around the contact normal, $\overrightarrow{Oz}$. The inverse procedure is applied to perform the transformation from the local $dM_i$ to the global $dM_I$:

$$\begin{bmatrix} dM_X \\ dM_Y \\ dM_Z \end{bmatrix}_{t-\Delta t \to t} = T^{-1} \begin{bmatrix} dM_x \\ dM_y \\ dM_z \end{bmatrix}_{t-\Delta t \to t} \quad \text{(Eq. 6.32)}$$

The obtained global $dM_I$ are cumulatively added into the governing equation of angular motion (Eq. 6.1). Considering that the real particle surface is rough rather than smooth, the contact radius $B$ is multiplied by a roughness index $\delta$ to give a corrected contact area, i.e., $\bar{k}_n = k_n/[\pi(\delta B)^2], \bar{k}_s = k_s/[\pi(\delta B)^2]$, $I = \frac{\pi}{4}(\delta B)^4$ and $J_z = \frac{\pi}{2}(\delta B)^4$. It is reasonable to restrict the corrected width to be smaller than the particle radius. Under this circumstance, $\delta$ should be in a range of 1 to 10 assuming a maximum 5% allowable overlap.

*Limiting values for rotational resistance*

The asperities are not rigid, thus the rotational resistance cannot increase infinitely. A limiting value $M_r^m = \kappa f_n R_r$ ($R_r = \frac{r_1 r_2}{r_1 + r_2}$ is the rolling radius) is assigned to the rolling-induced contact moment $M_r$ in which $\kappa$ is a strength index which relates the strength of the asperities to the normal contact force. Recognising that the tangential shear flow $\tau$ is limited to $\mu \bar{f}_n$, where $\bar{f}_n$ is the normal contact force at the corresponding point, it is reasonable to assume the limiting value for the torque resistance to be the product of $\mu$ and $M_r^m$, i.e., $M_t \leq \mu\kappa f_n R_r$. The formulation for the resulting rotational resistance model is summarised in Eq. 6.33.

$$\begin{cases} M_{r,i} = \overline{k_n} I_i \theta_{r,i} \,\&\, M_{r,i} \leq \kappa f_n R_r \;\; (i = x, y) \\ M_{t,i} = \overline{k_s} J \theta_{t,i} \,\&\, M_{t,i} \leq \mu\kappa f_n R_r \;\; (i = z) \end{cases} \quad \text{(Eq. 6.33)}$$

As suggested by Jiang et al. (2005), there are two options after the limiting value for the rolling resistance has been reached:

- Option 1: The rolling resistance is maintained at the limit, i.e., $M_r = \kappa f_n R_r$
- Option 2: The rolling resistance drops to zero, i.e., $M_r = 0$

The first option assumes that the asperity is perfectly elasto-plastic, plastic deformation develops once the limit is reached and the interlocking effect is maintained at the highest degree. The second option which is brittle elasto-plastic assumes the asperities are damaged instantaneously after the strength is attained and so the interlocking effect is removed accordingly. From an energy perspective, the first option is frictional and can effectively dissipate the energy, while the energy is dissipated due to the breakage of asperities when the second option is used. Only the first option is considered for the twisting resistance due to its

frictional nature. Comparison of these two options for the rolling resistance will be given in Section 6.3.3.

The derived new model has a reasonable physical basis. When compared with traditional DEM only two additional model parameters have been introduced, $\delta$ and $\kappa$, both of which have clear physical meanings: $\delta$ is related to the surface roughness while $\kappa$ reflects the strength of the material. The model can be classified as an elasto-plastic model which yields the most numerical stable and realistic results (Ai et al., 2011).

### 6.3.2 The critical timestep

The numerical solution for the integration of the equations of motion of DEM follows an explicit Verlet time integration scheme. It is conditionally stable and requires the integration timestep to be below a critical value ($\Delta t_{crit}$). For a linear, undamped system, $\Delta t_{crit}$ can be determined by Eq. 6.34 (Belytschko, 1983):

$$\Delta t_{crit} = \frac{2}{\omega_{max}} \qquad \text{(Eq. 6.34)}$$

in which $\omega_{max} = \sqrt{\lambda_{max}}$ is the maximum natural frequency of the discrete system and $\lambda_{max}$ is the maximum eigenvalue of the $[M^{-1}][K]$ matrix ($[M]$ is the mass matrix and $[K]$ is the stiffness matrix of the entire system). Considering that $\lambda_{max} \leq \lambda^{e}{}_{max}$, where $\lambda^{e}{}_{max}$ is the maximum eigenvalue of the $[M]^{e-1}[K]^{e}$ matrix ($\boldsymbol{e}$ denotes a single element and the same notation is used in the sequel) for individual elements, Eq. 6.34 can be expressed as:

$$\Delta t_{crit} = \frac{2}{\sqrt{\lambda^{e}{}_{max}}} \qquad \text{(Eq. 6.35)}$$

The importance of selecting a reasonable timestep in DEM simulations was discussed by O'Sullivan & Bray (2004). They showed that a smaller timestep is required when the rotational degrees of freedom are taken into account. Since both the rolling and twisting resistances affect the angular motion, it is necessary to examine whether $\Delta t_{crit}$ should be more or less restrictive in the presence of the rolling and twisting resistances. This issue has been neglected in prior published rotational resistance models.

Following the approach of O'Sullivan & Bray (2004) and also PFC3D (Itasca Consulting Group, 2007), the particles and contacts of a discrete element system are considered to be analogous to the nodes and elements of a finite element mesh respectively (Figure 6.11). The assembly of the stiffness matrix can be achieved using the force-displacement law at the contacts. As indicated by Eq. 6.35, assuming that the translational and rotational degrees of

freedom are uncoupled, $\Delta t_{crit}$ can be selected as the smallest critical timestep of individual elements (contacts) considering all degrees of freedom.

Considering the simplest case comprising only two particles (Figure 6.12), two sets of reference frames need to be established: the global coordinate system (X,Y,Z) and the local coordinate system ($x$,$y$,$z$) at the contact with the $z$ axis being coincident with the contact normal direction. The force-displacement law gives,

$$[F]^e = \left[K\right]^e [\mathrm{d}]^e = [\mathrm{T}]^{eT} [\mathrm{K}_L]^e [\mathrm{T}]^e [\mathrm{d}]^e \qquad \text{(Eq. 6.36)}$$

$[K]^e$ is the global stiffness matrix for the contact. $[T]^{\mathrm{e}}$, given by Eq. 6.37, is the global-to-local transformation matrix in which $n_{Ij}$ denotes the direction cosine between the global coordinate axis and the local coordinate axis.

$$[T]^{\mathrm{e}} = \begin{bmatrix} n_{Xx} & n_{Yx} & n_{Zx} & 0 & 0 & 0 \\ n_{Xy} & n_{Yy} & n_{Zy} & 0 & 0 & 0 \\ n_{Xz} & n_{Yz} & n_{Zz} & 0 & 0 & 0 \\ 0 & 0 & 0 & n_{Xx} & n_{Yx} & n_{Zx} \\ 0 & 0 & 0 & n_{Xy} & n_{Yy} & n_{Zy} \\ 0 & 0 & 0 & n_{Xz} & n_{Yz} & n_{Zz} \end{bmatrix} \qquad \text{(Eq. 6.37)}$$

$[\mathrm{K}_L]^e$ is the local contact stiffness matrix which is diagonally symmetric. For spherical particles, $[\mathrm{K}_L]^e$ can be expressed as Eq. 6.38 in which $k_{\theta,n}$ is the twisting resistance stiffness and the global displacement vector $[d]^e$ is given in Eq. 6.39.

$$[\mathrm{K}]_L^e = \begin{bmatrix} k_t & 0 & 0 & 0 & k_t r_A & 0 & -k_t & 0 & 0 & 0 & k_t r_B & 0 \\ 0 & k_t & 0 & k_t r_A & 0 & 0 & 0 & -k_t & 0 & k_t r_B & 0 & 0 \\ 0 & 0 & k_n & 0 & 0 & 0 & 0 & 0 & -k_n & 0 & 0 & 0 \\ 0 & k_t r_A & 0 & k_t r_A^2 - k_r & 0 & 0 & 0 & -k_t r_A & 0 & k_t r_A r_B + k_r & 0 & 0 \\ k_t r_A & 0 & 0 & 0 & k_t r_A^2 - k_r & 0 & -k_t r_A & 0 & 0 & 0 & k_t r_A r_B + k_r & 0 \\ 0 & 0 & 0 & 0 & 0 & -k_{\theta,n} & 0 & 0 & 0 & 0 & 0 & k_{\theta,n} \\ -k_t & 0 & 0 & 0 & -k_t r_A & 0 & k_t & 0 & 0 & 0 & -k_t r_B & 0 \\ 0 & -k_t & 0 & -k_t r_A & 0 & 0 & 0 & k_t & 0 & -k_t r_B & 0 & 0 \\ 0 & 0 & -k_n & 0 & 0 & 0 & 0 & 0 & k_n & 0 & 0 & 0 \\ 0 & k_t r_B & 0 & k_t r_A r_B + k_r & 0 & 0 & 0 & -k_t r_B & 0 & k_t r_B^2 - k_r & 0 & 0 \\ k_t r_B & 0 & 0 & 0 & k_t r_A r_B + k_r & 0 & -k_t r_B & 0 & 0 & 0 & k_t r_B^2 - k_r & 0 \\ 0 & 0 & 0 & 0 & 0 & k_{\theta,n} & 0 & 0 & 0 & 0 & 0 & -k_{\theta,n} \end{bmatrix} \qquad \text{(Eq. 6.38)}$$

$$[d]^e = \begin{bmatrix} u_A & v_A & w_A & \theta_{x,A} & \theta_{y,A} & \theta_{z,A} & u_B & v_B & w_B & \theta_{x,B} & \theta_{y,B} & \theta_{z,B} \end{bmatrix}^T \quad \text{(Eq. 6.39)}$$

Assuming the nodal (particle) mass is equally distributed to the elements (contacts) that it participates in, the mass matrix for the contact linking particle *A* and particle *B* as illustrated in Figure 6.12 can be expressed by Eq. 6.40, in which $n_A^c$ and $n_B^c$ are the numbers of contacts involving particles A and B respectively.

$$[M]_L^e = \begin{bmatrix}
\frac{m_A}{n_A^c} & 0 & 0 & 0 & 0 & 0 & 0 & 0 & 0 & 0 & 0 & 0 \\
0 & \frac{m_A}{n_A^c} & 0 & 0 & 0 & 0 & 0 & 0 & 0 & 0 & 0 & 0 \\
0 & 0 & \frac{m_A}{n_A^c} & 0 & 0 & 0 & 0 & 0 & 0 & 0 & 0 & 0 \\
0 & 0 & 0 & \frac{I^x{}_A}{n_A^c} & 0 & 0 & 0 & 0 & 0 & 0 & 0 & 0 \\
0 & 0 & 0 & 0 & \frac{I^y{}_A}{n_A^c} & 0 & 0 & 0 & 0 & 0 & 0 & 0 \\
0 & 0 & 0 & 0 & 0 & \frac{I^z{}_A}{n_A^c} & 0 & 0 & 0 & 0 & 0 & 0 \\
0 & 0 & 0 & 0 & 0 & 0 & \frac{m_B}{n_B^c} & 0 & 0 & 0 & 0 & 0 \\
0 & 0 & 0 & 0 & 0 & 0 & 0 & \frac{m_B}{n_B^c} & 0 & 0 & 0 & 0 \\
0 & 0 & 0 & 0 & 0 & 0 & 0 & 0 & \frac{m_B}{n_B^c} & 0 & 0 & 0 \\
0 & 0 & 0 & 0 & 0 & 0 & 0 & 0 & 0 & \frac{I^x{}_B}{n_B^c} & 0 & 0 \\
0 & 0 & 0 & 0 & 0 & 0 & 0 & 0 & 0 & 0 & \frac{I^y{}_B}{n_B^c} & 0 \\
0 & 0 & 0 & 0 & 0 & 0 & 0 & 0 & 0 & 0 & 0 & \frac{I^z{}_B}{n_B^c}
\end{bmatrix}$$

(Eq. 6.40)

Calculating the eigenvalues of $[M]^{e^{-1}}[T]^T[K]_L^e[T]$ is equivalent to the calculation of the eigenvalues of $[M]^{e^{-1}}[K]_L^e$ (Golub & Van Loan, 1983) as noted by O'Sullivan and Bray (2004). The global mass matrix $[M]^e$ is identical to the local mass matrix $[M]_L^e$ due to the axisymmetric nature of spherical particles. Thus, $\Delta t_{crit}$ can be determined using Eq. 6.38

and Eq. 6.40. Considering the extreme case, i.e., two smallest particles with identical mass of $m$, moment of inertia of $I$ and the same number of neighbouring particles, $n_c$, (i.e., $m_A$=$m_B$= $m$, $I_A$=$I_B$=$I$ and $n_A^c = n_B^c = n_c$) , and ignoring the identical eigenvalues, $\lambda^e{}_{max} = \max\left(\frac{2k_t \cdot m \cdot n_c \cdot r^2 + 2I \cdot k_t \cdot n_c}{I \cdot m}, \frac{2k_n n_c}{m}, \frac{2k_r n_c}{I}, \frac{2k_{\theta,n}}{I}\right) = \max\left(\frac{7k_t n_c}{m}, \frac{2k_n n_c}{m}, \frac{2k_r n_c}{I}, \frac{2k_{\theta,n}}{I}\right)$ . $\Delta t_{crit}$ is not a constant but varies during the simulation with the changing number of contacts. The contact width is far smaller than the particle radius, which gives $k_{\theta,t} = k_t {r_A}^2 - k_r = k_t {r_A}^2 - k_n \frac{(\delta B)^2}{4} \approx k_t {r_A}^2$ , $k_r = k_n \frac{(\delta B)^2}{4} << k_n {r_A}^2$ and $\left|k_{\theta,n}\right| = k_t \frac{(\delta B)^2}{2} << k_t {r_A}^2$. For the simplified Hertz-Mindlin model used in the current study, the ratio of the equivalent stiffnesses $\frac{k_t}{k_n} = \frac{2(1-\nu)}{2-\nu} \approx 0.94$, and thus $\lambda^e{}_{max} = \frac{7k_t n_c}{m}$. It is reasonable to assign an $n_c$ value of 4 (the minimum number of contacts required to maintain the mechanical stability of individual particles in a frictional system) as the smallest particles are unlikely to participate in force transmission. This leads to $\Delta t_{crit}$ =0.378$\sqrt{\frac{m}{k_t}}$, which is larger than the critical timestep used for simulations where rotational resistance is absent, i.e., $\Delta t_{crit} = 0.1\sqrt{\frac{m_{min}}{k_n}}$. For consistency, the same critical timestep is adopted in simulations where rotational resistance is present .

### 6.3.3 Model verification and preliminary testing

To verify the implementation of the developed model, some simple scenarios with available analytical solutions are considered.

*A single ball spinning on a flat plane*

The first case considered is the motion of a single ball on a frictionless plane ($\mu$=0) (Figure 6.13). Gravity was applied to the ball along with a local damping ratio value of 0.5. DEM calculation cycles were performed until the ball came to rest. Then an initial rotational velocity ($\omega_{x,0}$=-10 rad/s) was applied around the $x$-axis which passes through the centroid of the ball and lies in the plane. The main input parameters are given in Figure 6.13. The equation of angular motion for such a case can be expressed by:

$$I_x \ddot{\theta}_x = -k_r \theta_x \qquad \text{(Eq. 6.41)}$$

Solving Eq. 6.41, the angular velocity $\omega_x$ follows a harmonic pattern of motion:

$$\omega_x = \omega_{x,0} \cos(\sqrt{k_r / I_x}\, t) \qquad \text{(Eq. 6.42)}$$

in which $k_r$ is the rolling stiffness and $I_x$ is the moment of inertia about the $x$ axis. If the limiting value ($M_r^m = \kappa f_n r$) set for the rolling resistance is higher than the accumulated rolling resistance at the point when the angular velocity approaches zero, i.e., $M_r^m \geq (M_r)_{\omega_x=0} = \omega_{x,0}\sqrt{Ik_r} \approx 6.99e-5\ Nm$, the ball will rotate around the $x$ axis exactly following Eq. 6.42. In this case, the system response is elastic and there is no energy dissipation. This is verified in Figure 6.14 which shows that when there is no limit set for the rolling resistance, the angular motion obtained in the LAMMPS simulation matches that predicted by Eq. 6.42 with an amplitude of $\omega_{x,0}$. The timestep used in this simulation is $1 \times 10^{-6}\ s$ which is slightly smaller than the calculated $\Delta t_{crit} = min\left(\sqrt{\frac{2m}{k_n}}, \sqrt{\frac{2I}{k_r}}\right) \approx 5.3 \times 10^{-6}\ s$ according to Eq. 6.38 and Eq. 6.40. Figure 6.14 (c) compares the measured $\omega_x$ at the peaks and the valleys with the corresponding theoretical values ($10\ rad/s$ and $-10\ rad/s$). Although there are some differences between the measured value and the theoretical value, the error does not grow, indicating that the simulation is stable. As further shown in Figure 6.15, when the timestep is reduced by three orders of magnitude to $\Delta t = 1 \times 10^{-9}\ s$, the error is reduced almost by the same orders of magnitude.

If the rolling resistance is restricted to take a value that is lower than $(M_r)_{\omega_x=0}$, the motion of the ball will be rather complex. In such a case, three stages of motion can be identified (Figure 6.16):

- Stage-I ($0<t\leq t1$): the ball moves following the harmonic motion as defined by Eq. 6.42 until the accumulated rolling resistance reaches $M_r^m$
- Stage-II ($t1<t\leq t2$): the torque acting on the ball is constant and thus the angular velocity approaches zero linearly with time
- Stage-III ($t2<t\leq t3$): when the angular velocity approaches zero, driven by $M_r^m$ the ball starts to rotate in the direction opposite to $\omega_{x,0}$, i.e., back rolling takes place. Under such circumstance, the direction of the rolling resistance increment shifts and the ball's motion follows:

$$I_x\ddot{\theta}_x = -k_r(\theta_x - (\theta_x)_{\omega=0}) + M_r^m \qquad \text{(Eq. 6.43)}$$

The angular velocity for the aforementioned three stages of motion can be expressed by Eq. 6.44.

$$\omega_x = \begin{cases} \omega_{x,0}\cos(\sqrt{I/\mathrm{k}_r}\,\mathrm{t}), & \mathrm{t} \le \mathrm{t}1 \;\; StageI \\ \dfrac{\omega_{x,0}}{|\omega_{x,0}|} M_r^m \cdot (t - t1)/I + \omega_{x,0}\cos(\sqrt{I/\mathrm{k}_r}\,\mathrm{t}1), & t1 < \mathrm{t} \le t2 \;\; StageII \\ -\dfrac{\omega_{x,0}}{|\omega_{x,0}|} M_r^m \cdot \sqrt{I/\mathrm{k}_r} \cdot \sin(\sqrt{I/\mathrm{k}_r}(t - t2))/I, & \mathrm{t} > \mathrm{t}2 \;\; StageIII \end{cases} \quad \text{(Eq. 6.44)}$$

in which $t1 = \sin^{-1}(M_r^m / \omega_{x,0} / \sqrt{Ik_r}) \cdot \sqrt{I/\mathrm{k}_r}$ marks the transition instant from Stage I to Stage II, $t2 = t1 + I\omega_{x,0}\cos(\sqrt{I/\mathrm{k}_r}\,\mathrm{t}1)/M_r^m$ defines the transition point from Stage II to Stage III and $M_r^m = \kappa f_n r$ is the limited value for the rolling resistance. Energy dissipation only takes place during Stage II, while Stage I and Stage III are purely elastic. Eq. 6.44 reflects two distinct roles of $\kappa$ and $\delta$ for the current model: $\kappa$ defines $M_r^m$ and thus controls the energy dissipation rate while $\delta$ determines the frequency of the harmonic motion and thus quantifies the transformation rate between the kinetic energy and strain energy stored in the rolling springs. Figure 6.16 illustrates the three-stage motion defined by Eq. 6.44 for the case of $\kappa$=0.5. The input parameters are the same as indicated in Figure 6.13. The two filled circles in Figure 6.16 represent the two transition points (*t1* and *t2*). Again, the LAMMPS simulation results are in good agreement with the theoretical values.

Despite the good agreement between the simulation results and the theoretical values, the harmonic pattern of motion (back-rolling) does not favour the local stability in a granular assembly as the angular velocity oscillates. As shown in Figure 6.17, the frequency of the oscillation increases as $\delta$ increases. This may induce some fluctuations in the stress-strain curve which will be shown in Section 6.4. Ai et al. (2011) suggested using a viscous damping at the contact in conjunction with the rolling spring. However, this increases the number of input parameters and it would be difficult to relate the damping parameter to a physical property. In the current model, no viscous damping is introduced, rather the local damping mechanism described in Chapter 2 is adopted for convenience.

Figure 6.18 illustrates the influence of $\kappa$ on the angular motion of the ball. It can be observed that the amplitude of angular velocity at Stage III decreases as $\kappa$ decreases, indicating the total energy dissipation at Stage II increases. The other thing worth noticing is that when $\kappa$ is reduced, the slope of the $\omega$-$t$ curve at Stage II decreases which indicates that the energy dissipation rate during Stage II decreases.

As introduced in Section 6.3.1, there are two options after the rolling resistance limit is reached. From an energy perspective, Option 1 dissipates energy gradually through friction

while using Option 2 the energy is released instantaneously due to the damage of asperities. As reflected in Figure 6.19, given the same input conditions, Option 1 can dissipate more energy than Option 2 indicated by a smaller peak value of rotational velocity. However, the oscillation in motion is obvious when Option 1 is adopted, while the angular motion can be maintained constant using Option 2. Moreover, as shown in Figure 6.20, provided that $\kappa$ is large enough, Option 2 can also effectively dissipate the kinetic energy. Particularly for the case considered in Figure 6.20, when $\kappa$=1 is used, the angular velocity reduces to almost zero.

The twisting characteristics (spinning around the contact normal ($z$ axis)) are similar to those described above and therefore are not discussed here.

*A single ball moves along a flat plane*

For the first two examples, the horizontal plane was assumed to be frictionless. To investigate the interaction between the frictional force and the rolling resistance moment, the scenario shown in Figure 6.21 (a) is considered. In this scenario, instead of giving an initial angular velocity, the ball is assigned an initial translational velocity of 0.01 m/s in the $x$ direction after completing the settling process discussed above. The translational movement of the ball generates a shear force that is opposite to the direction of the movement. This shear force induces angular motion around the $y$ axis. The input parameters are identical to the previous section, however, the friction coefficients were set to be 0.25 for both the ball and the flat wall. The initial translational velocity and the friction coefficients were chosen so that the sliding limit was reached in the first integration time step so that the motion of the ball can be determined analytically. Figure 6.21 (b) shows the evolution of the translational velocity with time while the evolution of angular velocity is presented in Figure 6.21 (c). For both motions, two distinct stages can be identified:

- Stage I: The shear force ($f_s$) is constant and equals to the limiting value $\mu f_n$. Therefore the translational velocity ($V_x$) decreases linearly with time, while the angular velocity initially follows the harmonic pattern defined by Eq. 6.45. As shown in Figure 6.21 (c), the measured angular motion at Stage I coincides with the predicted motion defined by Eq. 6.45.

$$\omega_y = \frac{f_s R}{k_r}\sqrt{\frac{k_r}{I}}\sin\left(\sqrt{\frac{k_r}{I}}t\right) \qquad \text{(Eq. 6.45)}$$

- Stage II: After $V_x$ reaches zero, $f_s$ starts to decrease and the equation of the angular motion becomes:

$$I\ddot{\theta} = (\mu f_n - k_t(\theta - \theta_{t1})r + k_t s(\theta)) - k_r(\theta - \theta_{t1}) \qquad \text{(Eq. 6.46)}$$

in which $s(\theta)$ is the relative displacement at the contact due to the translational movement that is also a function of $\theta$ as the shear force is related to $\theta$. Since no closed-form solution can be found for Eq. 6.46, no direct comparison can be made between the simulation data and the theoretical values.

## 6.4 Influence of rotational resistance on the mechanical behaviour

This section describes the system response observed when the rotational resistance model was applied to a representative selection of simulations.

### 6.4.1 Packing density after isotropic compression

The sample generation procedure described in Section 4.4 was used to generate initially isotropic samples. The samples were isotropically compressed under a confining pressure of 100 kPa. Six $\kappa$ (0.01, 0.05, 0.1, 0.3, 0.5 and 1) values were applied, while $\delta$=1 and $\mu$=0.25 for all the samples. Figure 6.22 shows the influence of the strength index ($\kappa$) on the void ratio after isotropic compression. The filled diamonds in Figure 6.22 represent data for the six finite $\kappa$ values considered while the dashed line indicates the void ratio obtained in a single simulation performed without setting a limit for the rolling resistance. As indicated in Figure 6.22, $\kappa$ has a significant effect on the packing density when it is below 0.3; however, when $\kappa$ exceeds 0.3, the effect of $\kappa$ is less marked and the void ratio obtained is very close to that in the simulation without the rotational resistance limit. As described in Section 6.3.1, $\kappa$ can represent the strength of asperities. The decreasing sensitivity of packing density to $\kappa$ can represent the smaller amount of asperity damage due to increasing strength, i.e., less significant change in particle topology. For the $\kappa$ values considered, the fraction of contacts at which the accumulated rolling resistance exceeds the limit defined by Eq. 6.33 is almost zero while the fraction of contacts at which the twisting resistance limit decreases with increasing $\kappa$ as indicated by the open triangles in Figure 6.22. When $\kappa$ is below 0.3, the twisting resistance limit is reached at a measurable number of contacts. Kinetic energy is dissipated at these contacts through rotational friction and according to Eq. 6.44 the rate of energy dissipation increases as $\kappa$ increases. Therefore, the sample becomes stiffer when $\kappa$ is increased. On the other hand, when $\kappa$ exceeds 0.3, the number of contacts for which both the rolling and twisting resistances reach the corresponding limit reduces to almost zero. In such a case, the overall response depends on the $\delta$ value which quantifies the transformation rate between the kinetic energy and the strain energy. Thus the response varies little with $\kappa$ when the same $\delta$ value is used and $\kappa$ exceeds 0.3.

Figure 6.23 illustrates the influence of $\delta$ on the packing density. Two stress levels were considered ($\sigma'_3$ = 100 kPa and $\sigma'_3$ = 500 kPa) and different $\delta$ values were applied during isotropic compression. No limit was set for the rolling resistance so as to isolate the effect of $\delta$ from the effect of $\kappa$ and $\mu$=0.25. The influence of $\delta$ on the packing density is notable. For both stress levels considered, the void ratio after isotropic compression increases consistently with increasing $\delta$ and this is related to the transformation rate between the kinetic energy and the strain energy stored in the rolling spring. A $\delta$ value of 10 is considered to be the cut-off for $\delta$ in the current study as it corresponds to a modified radius ($\delta B$) of the contact plane that is equal to the radius of the smaller particle of a touching pair for the extreme case when the largest allowable overlap ratio (5%) is reached. The decreasing packing density with increasing $\delta$ is analogous to the decreasing packing density due to the increasing particle irregularity.

Figure 6.24 compares the variation of packing density after isotropic compression to a stress level of 100 kPa with $\delta$ considering the two post-yield options, i.e., Option 1: $M_r = M_r^m$ post yield; Option 2: $M_r$ = 0 post yield. The value of $\kappa$ is equal to 0.5 for all the simulations. As shown in Figure 6.24, when $\delta$<3, the obtained void ratios are almost identical for both options; however, when $\delta \geq 3$, Option 1 yields higher void ratios than Option 2 and this difference increases with increasing $\delta$ values. This is because, when $\delta$ is small, the rotational limits are less likely to be reached and the relative motion at the contacts follows a similar manner for both options; therefore the difference between the two options is small. In contrast, when $\delta$ is high, the rotational limits at the contacts are more likely to be attained, i.e., more asperity damage events occur. In such a case, the dissipated energy is limited for Option 2 in comparison with Option 1 as indicated by Figure 6.19. Therefore, the difference in the packing density between the two options becomes more obvious as $\delta$ increases. The nonlinear effect of the rotational resistance on the packing density reflected in Figures 6.22-6.24 does not agree with Cho et al. (2006) (Figure 6.25) which proposed that the packing density increases linearly with increasing shape irregularity.

Figure 6.26 presents the correlations between the void ratio and the coordination number ($Z$) and between the void ratio and the mechanical coordination number ($Z_m$) for the two stress levels considered in Figure 6.23. The data without rolling resistance (NRR) are overlaid in Figure 6.26. For both stress levels considered, the $Z$-$e$ and $Z_m$-$e$ relationships for simulations considering the rotational resistance (RR) collapse to the same trend as for simulations when the rotational resistance is absent. The inclusion of rotational resistance extends the data to a broader range of $e$ values. While the $Z_m$-$e$ relationship generally follows a linear relationship, the $Z$-$e$ relationship 'bends' downwards and the difference between $Z$ and $Z_m$ at the same

void ratio becomes more obvious as the void ratio increases, indicative of a higher number of rattlers when rotational resistance is considered.

### 6.4.2 Stress-strain behaviour during shearing

*(a) Effect of κ*

Figure 6.27 shows the influence of $\kappa$ on the stress-deformation behaviour of a numerical assembly during triaxial shearing. The sample was isotropically compressed to a stress level of 100 kPa. During this procedure, the rotational resistance model was switched off. The sample was then subjected to drained triaxial shearing. An interparticle friction of 0.25 was used during both isotropic compression and triaxial shearing while the remaining input parameters are the same as those used in Chapter 4 and Chapter 5. Four $\kappa$ values were investigated and one additional simulation was performed without setting a limiting value for the rolling or twisting resistance. Only the Option 1 post yielding behaviour was considered, i.e., the rotational resistance was held constant once the limiting value has been attained. As can be seen in Figure 6.27 (a), from the onset of shearing the deviatoric stress is much higher when rotational resistance is considered (the RR samples) than when it is ignored (the NRR sample). The angle of shearing resistance ($\phi'$) at the critical state approaches that of the real Toyoura sand (31°) as $\kappa$ increases. The effect of $\kappa$ is significant when it is below 0.3. However, when $\kappa$ exceeds 0.3, the influence of $\kappa$ on the shear strength is less noticeable and the strength for $\kappa$ = 1 is almost identical to that when no limit is set in the rotational resistance model. Considering the volumetric response which is shown in Figure 6.27 (c), while the NRR sample is contractive overall, the RR samples initially contract but then dilate and are dilative overall. The magnitude of dilation increases with increasing $\kappa$ when $\kappa$ is below 0.3, however, for $\kappa$ higher than 0.3, the samples behave less dilatively as $\kappa$ increases and the volumetric response for $\kappa$ = 1 is close to that for the case when no limit is set for the rotational resistance. Therefore, it is recommended to restrict $\kappa$ to be below 0.3.

Figure 6.28 illustrates the influence of $\kappa$ on the micro-scale measures. As Figure 6.28 (a) shows, while the coordination number ($Z$) increases initially with axial strain and then decreases for the NRR simulation, $Z$ decreases consistently with axial strain when the rotational resistance model is switched on. The $Z$ values decrease as $\kappa$ is increased and $Z$ becomes less sensitive to $\kappa$ when $\kappa$ exceeds 0.3. Similar observations can be made for the mechanical coordination number ($Z_m$). In contrast, the fabric anisotropy in terms of the deviatoric fabric ($\Phi_1 - \Phi_3$) increases with increasing $\kappa$ as shown in Figure 6.28 (c). The influence of $\kappa$ on the structural anisotropy is more significant for $\kappa$ < 0.3, and the deviatoric fabric becomes almost identical when $\kappa$ exceeds 0.3. The lower coordination number and

higher structural anisotropy indicate that the strong force chains are more self-stable and less reliant on the lateral supports when rotational resistance is introduced.

The effect of $\kappa$ on the proportion of the plastic contacts is presented in Figure 6.29. The sliding fraction is increased when rotational resistance is introduced but the oscillations are more obvious in the sliding fraction when rotational resistance is considered. The sliding fraction seems to increase with increasing $\kappa$ as the sliding fraction for $\kappa$ = 0.1 is slightly lower than that for $\kappa$ = 0.3 and 1. Plastic yielding of the rolling and twisting springs is considered separately. As shown in Figure 6.29 (b), the rolling fraction decreases dramatically from 0.59 to 0.02 as $\kappa$ is increased from 0.1 to 1. The twisting fraction also decreases as $\kappa$ increases. The rolling fraction is higher than the twisting fraction when $\kappa$ is smaller than 0.3, while for $\kappa$ =1.0, the twisting fraction becomes slightly higher than the rolling fraction. Figure 6.29 reveals that when $\kappa$ is low, the rotational behaviour is dominant while the opposite is true when $\kappa$ exceeds 0.3.

The contacts can be further categorised into eight subgroups according to which type of plastic limit (rolling, twisting and sliding) is reached, considering the contact as elastic when none of these plastic limits are attained. The classifications are given as following: **PR**: pure rolling; **PT**: pure twisting; **PS**: pure sliding; **Elastic**: no rolling, no twisting and no sliding; **R-T**: rolling and twisting; **R-S**: rolling and sliding; **T-S**: twisting and sliding; **R-S-T**: rolling, sliding and twisting. Figure 6.30 presents the effect of $\kappa$ on the elastic-plastic configurations of the contacts considering three $\kappa$ values ($\kappa$=0.1, 0.3 and 1). For the three $\kappa$ values considered, the following observations can be made:

- the fraction of the elastic contacts decreases, while the number of the plastic contacts increases immediately after loading commences
- the number of contacts at which only one type of plastic limit is reached is significantly higher than the number of contacts at which more than one type of plastic limit are attained

In particular, when $\kappa$ is low ($\kappa$ = 0.1), the percentage of the PR contacts is the most dominant case, while the fraction of the contacts which remain elastic is the second-most significant case. The number of the PS contacts is higher than the number of the PT contacts. The larger proportion of PR contacts than PT contacts indicates anisotropy in the rotational motion when the rotational resistance is introduced. Considering that the contact normals are more likely to orient in the loading direction, the anisotropy in the rotational motion actually indicates the concentration of rotation along the horizontal direction. At the intermediate $\kappa$ value considered, about 53% of the contacts are elastic, the number of the PR contacts is

close to the number of the PS contacts and the difference between the number of the PR contacts and the number of PT contacts diminishes. When a $\kappa$ value as high as 1 is used, most of the contacts are elastic. This explains the more significant oscillations in the stress-strain behaviour (Figure 6.27) as the harmonic motion at the contacts will be dominant as $\kappa$ increases. The number of the PS contacts surpasses the number of either PR or PT contacts. The number of PT contacts exceeds the number of PR contacts, which is due to the decreasing constraints acting on the particles that participate in force transmission as a consequence of the reduced number of lateral supports. Obviously, there is a transition from rolling to sliding at the contacts as $\kappa$ increases. The sample becomes 'stickier' at the contacts as $\kappa$ increases.

*(b) Effect of $\delta$*

The influence of $\delta$ on the stress–strain behaviour is presented in Figure 6.31. All the samples had an identical initial states ($e_0$=0.646, $\sigma'_3$=100 kPa) but different $\delta$ (1, 3, 5, 8 and 10) values were applied during shearing. As shown in Figure 6.31 (a), the deviatoric stress increases when $\delta$ is increased but the effect of $\delta$ is nonlinear. The deviatoric stress increases more rapidly when $\delta$ is below 5, while when $\delta$ exceeds 5, the effect of $\delta$ on the deviatoric stress is less marked. The oscillations in the stress-strain curve are more obvious for higher $\delta$ values than for lower $\delta$ values. This may be attributable to the increasing frequency of the harmonic motion with increasing $\delta$ as indicated in Figure 6.17. Similar observations can be made for the angle of shearing resistance ($\phi'$) as shown in Figure 6.31 (b). It is worth noticing that $\phi'$ at critical state is still below the value for the real Toyoura sand (31°). Figure 6.31 (c) illustrates the influence of $\delta$ on the volumetric response. For all the $\delta$ values considered, the numerical sample initially contracts followed by dilation. The maximum contractive volumetric strain decreases with increasing $\delta$, while the numerical sample becomes more dilative as $\delta$ increases. However, when $\delta$ exceeds 5, the influence of $\delta$ is no longer obvious. Comparing with the evolution of the deviatoric stress, the evolution of the volumetric strain is smoother.

### 6.4.3 Position of the CSL

Figure 6.32 shows the effect of $\delta$ on the critical-state loci obtained in both $e$-log($p'$) and $q$-$p'$ spaces for $\kappa$=1. The CSL obtained in Chapter 5 when the rotational resistance is not activated (indicated by the black dashed line) and the CSL for the real Toyoura sand (Verdugo & Ishihara, 1996) are superimposed in Figure 6.32. As Figure 6.32 (a) shows, the void ratio at the critical state when rotational resistance is considered is higher than that when rotational resistance is absent. The void ratio at the critical state increases with increasing $\delta$ and the

effect of $\delta$ becomes negligible when $\delta$ exceeds 3. This agrees with Figure 6.31. It should also be noticed that when $\delta$ exceeds 5, the void ratio at the critical state initially increases with increasing $p'$ when $p'$ is below 1,600 kPa. Similar to the cases when $\mu \geq 0.5$, this observation is at odds with what is expected within the framework of CSSM and is also attributed to the increasing number of floating particles due to the increased stability of strong force chains. On the other hand, despite the capacity of rotational resistance to increase the void ratio at the critical state, the effect is limited and the obtained critical-state void ratio remains below that obtained for real Toyoura sand.

It can be observed in Figure 6.32 (b) that the slope of the CSL in $q$-$p'$ space increases as $\delta$ increases. The effect of $\delta$ is significant when $\delta$ is below 3, however, when $\delta$ exceeds 3, the effect is negligible in accordance with Figure 6.31 (b). Similar to the observation made for the position of the CSL in $e$-log($p'$) space, the effect of $\delta$ is limited and the slope of the CSL is unable to reach the value of real Toyoura sand using the current $\mu$ value.

## 6.5 Summary

In this Chapter, a rotational resistance model has been developed to investigate the influence of particle shape on the behaviour of granular materials. The new model was derived in an attempt to capture as closely as possible the physical origin of the interlocking effect. Different scenarios for which the particle motion can be determined analytically were used to verify the implementation of the model. The effectiveness of rotational resistance in capturing the influence of particle shape on the mechanical behaviour was explored.

In the new rotational resistance model, both the rolling and twisting motions are considered. The rolling stiffness was derived considering the uneven distribution of normal contact force while the twisting resistance was obtained by integrating the contribution of annular shear flow to the torque with respect to the contact centre due to the relative twisting motion. Two additional parameters were introduced into the traditional DEM: the strength index, $\kappa$, which reflects the strength of asperities and $\delta$ which is related to the surface roughness. Different post-yield options have been considered: the rotational resistances can remain constant or drop to zero when the plastic limit is reached. The former assumes perfect elasto-plastic behaviour for the asperities while the latter assumes brittle elasto-plastic response for the asperities.

Rotational resistance affects the packing density after isotropic compression. The void ratio after isotropic compression increases nonlinearly with both $\kappa$ and $\delta$. The effect of $\delta$ is more pronounced compared to the effect of $\kappa$. Both $\kappa$ and $\delta$ have significant effects on the stress-

strain behaviour of the numerical assemblies when subjected to triaxial shearing. The strength increases with both $\kappa$ and $\delta$. While the dilative volumetric strain increases consistently with increasing $\delta$, this is only true for $\kappa \leq 0.3$: when $\kappa$ exceeds 0.3, the numerical sample behaves less dilatively. In general, the effect of both $\kappa$ and $\delta$ is limited and the critical-state strength obtained when rotational resistance is considered is still below that of the real Toyoura sand. The transition from rolling to sliding at the contacts in the presence of rotational resistance was identified, following a converse trend when rotational resistance is absent. Specifically, rolling is dominant when $\kappa$ is small while sliding surpasses rolling when $\kappa$ is further increased. This is opposite to the influence of $\mu$ as having been discussed in Chapter 4.

A comparison of the critical-state loci in both $q$-$p'$ and $e$-log($p'$) spaces shows that the strength and the void ratio at the critical state are affected by rotational resistance. In particular, the slope of the CSL in $q$-$p'$ space is increased as $\delta$ increases. Rotational resistance yields higher void ratios at critical state than the traditional DEM simulations and the critical-state loci in $e$-log($p'$) space move upwards as $\delta$ increases. However, the effect of rotational resistance is limited and cannot yield a CSL that is similar to the real Toyoura sand in either $q$-$p'$ or $e$-log($p'$) space. The strength and dilatancy of the simulations results may be increased by increasing the interparticle friction coefficient, $\mu$. However, as discussed in Chapter 4, the effect of increasing $\mu$ is limited. In this sense, it seems that to quantitatively investigate the behaviour of real sand using DEM, non-spherical particles should be adopted rather than using a rotational resistance model. Despite this limitation, this Chapter reveals that rotational resistance resistance can qualitatively capture the influence of particle shape on the mechanical behaviour of sand to a certain extent. Furthermore, the current rotational resistance model also enables the underlying mechanism of the effect of particle shape to be revealed at the contact level, i.e., an increase in the number of elastic contacts and transition from rolling to sliding at the contacts.

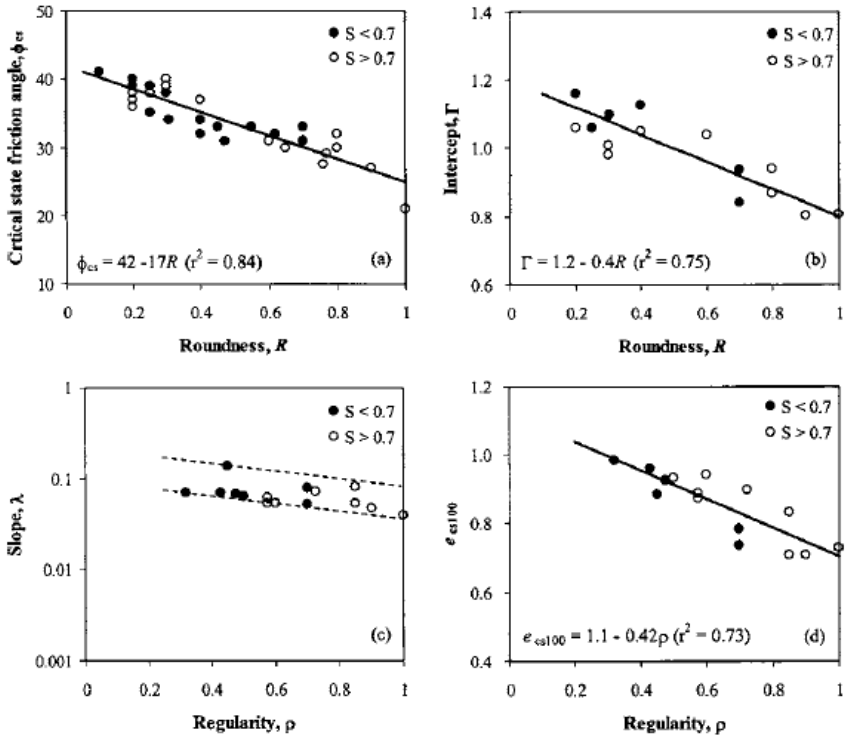



Figure 6.1 Effect of particle shape on critical state parameters where S represents sphericity (Cho et al., 2006)

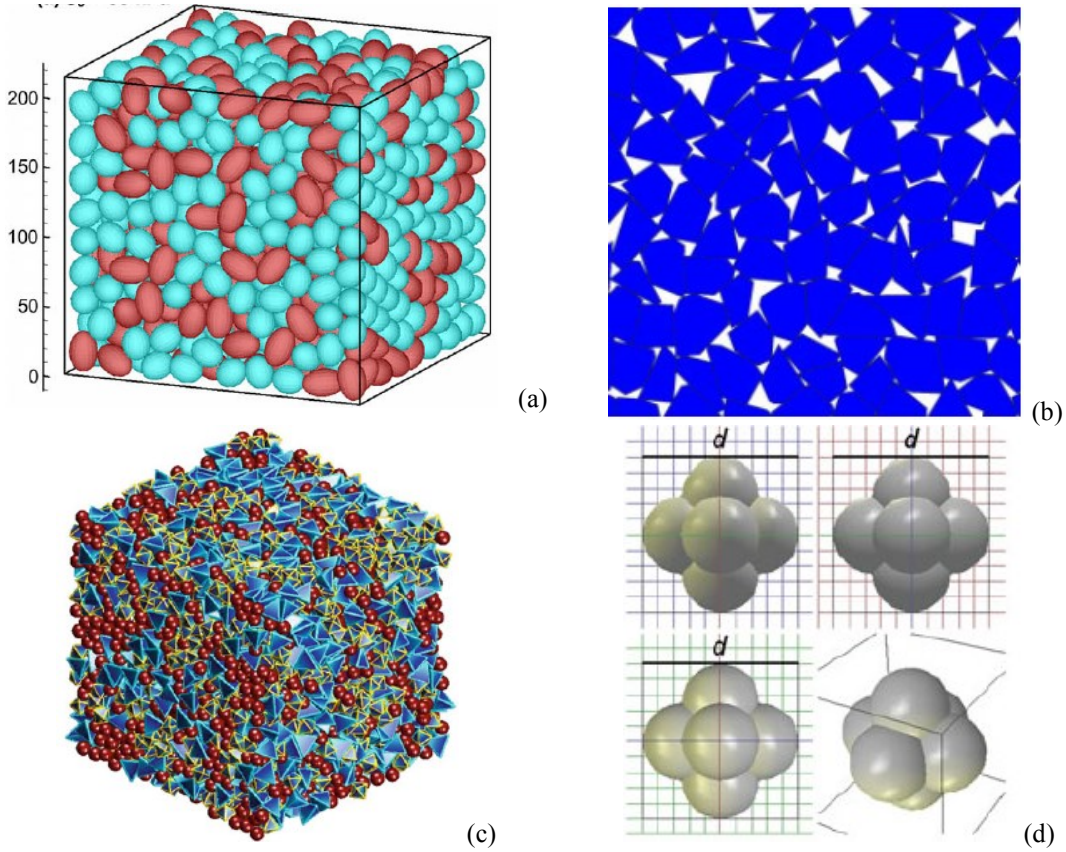
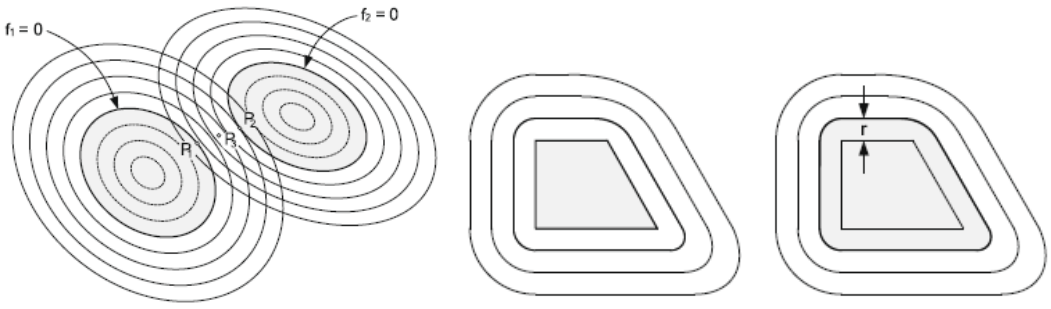
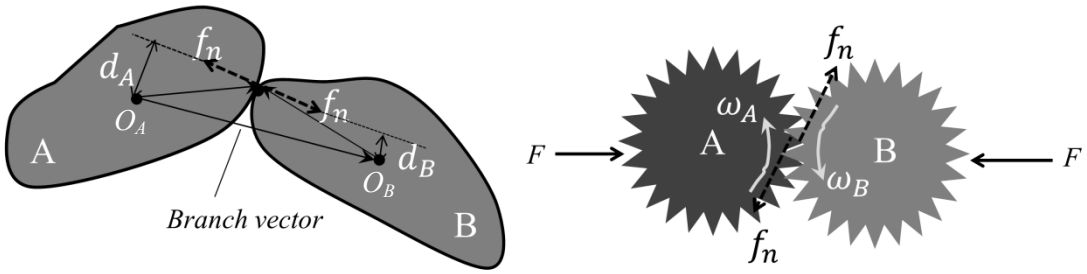



Figure 6.2 Different techniques used to consider the effect of particle shape in DEM simulations: (a) Ellipsoids (Ng, 2009); (b) Polygons (Peña et al., 2008); (c) Polyhedrons (Langston et al., 2013); (d) Clumps (Kozicki et al., 2012)




(a) (b)

Figure 6.3 (a) Illustration of the concept of 'potential' particles (Houlsby, 2009); (b) Potential particles with different shapes




(a) (b)

Figure 6.4 Illustration of physical origin of rotational resistance: (a) Noncoincidence between the branch vector direction and the contact normal direction; (b) Interlocking effect

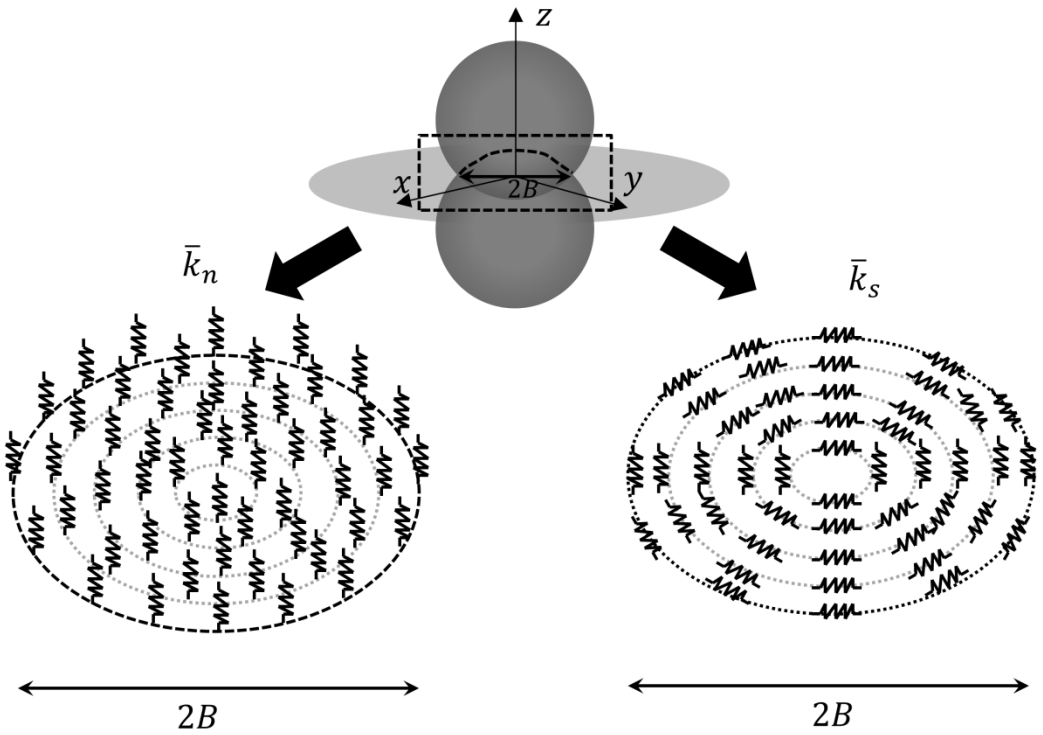



Figure 6.5 Discretisation of the contact springs

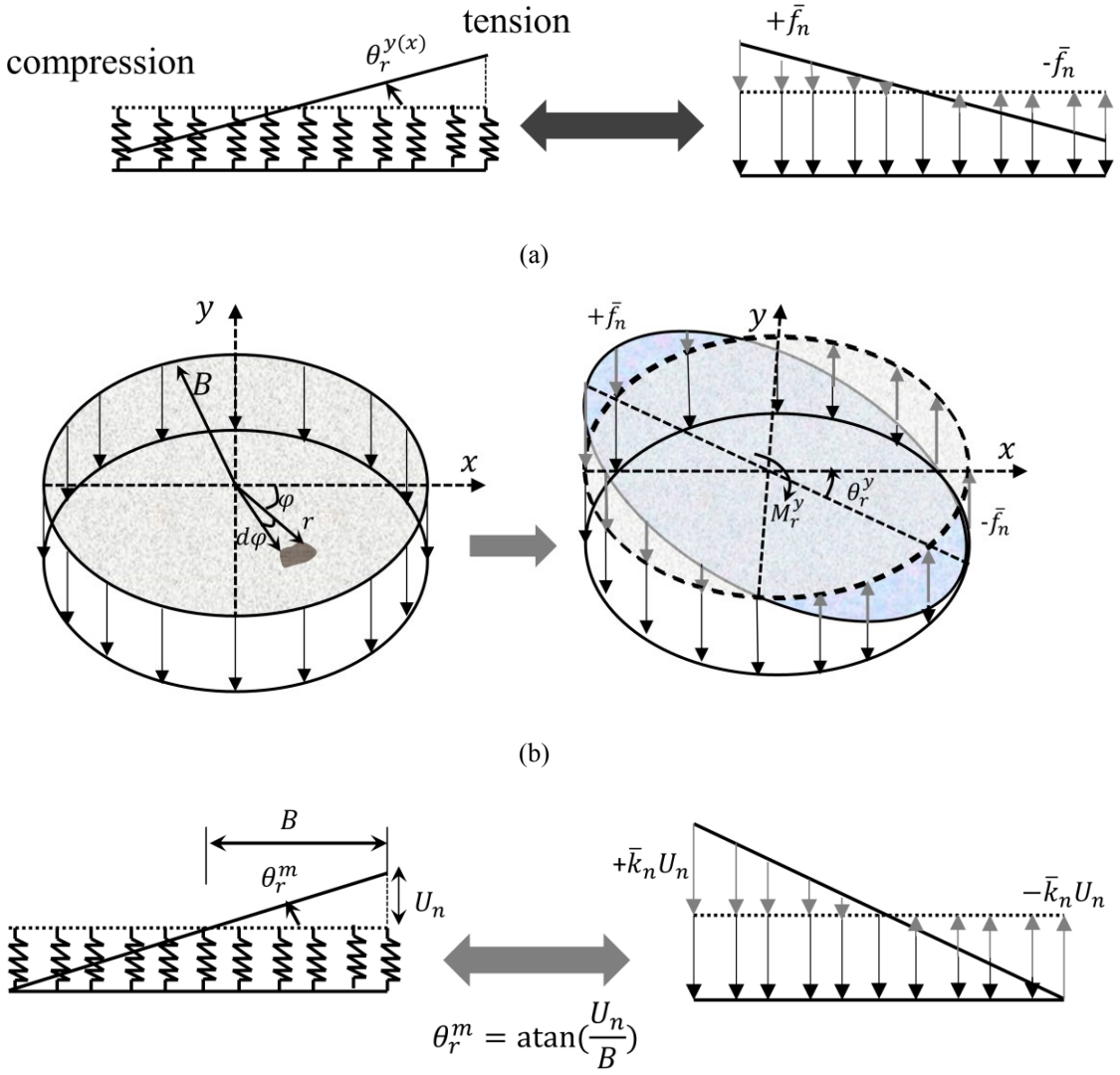



Figure 6.6 Assumed mechanism of rolling resistance: (a) 2D illustration; (b) 3D illustration of contact force redistribution due to rolling about the y axis; (c) Limit of the rolling resistance prior to the opening of the contact

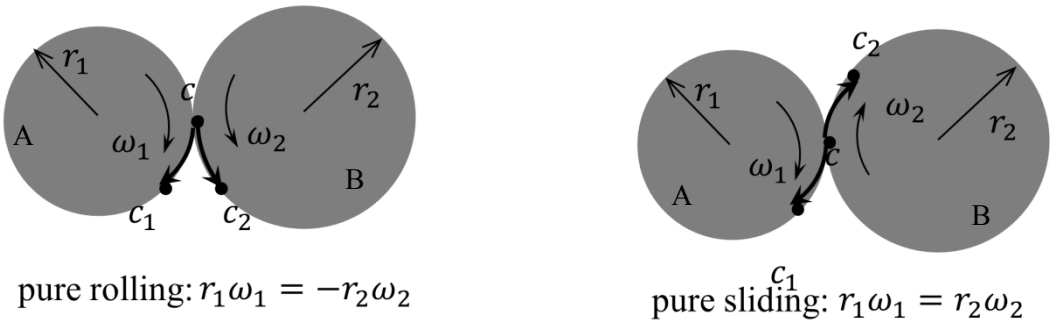



Figure 6.7 Illustration of pure rolling and pure sliding in the absence of rigid-body rotation

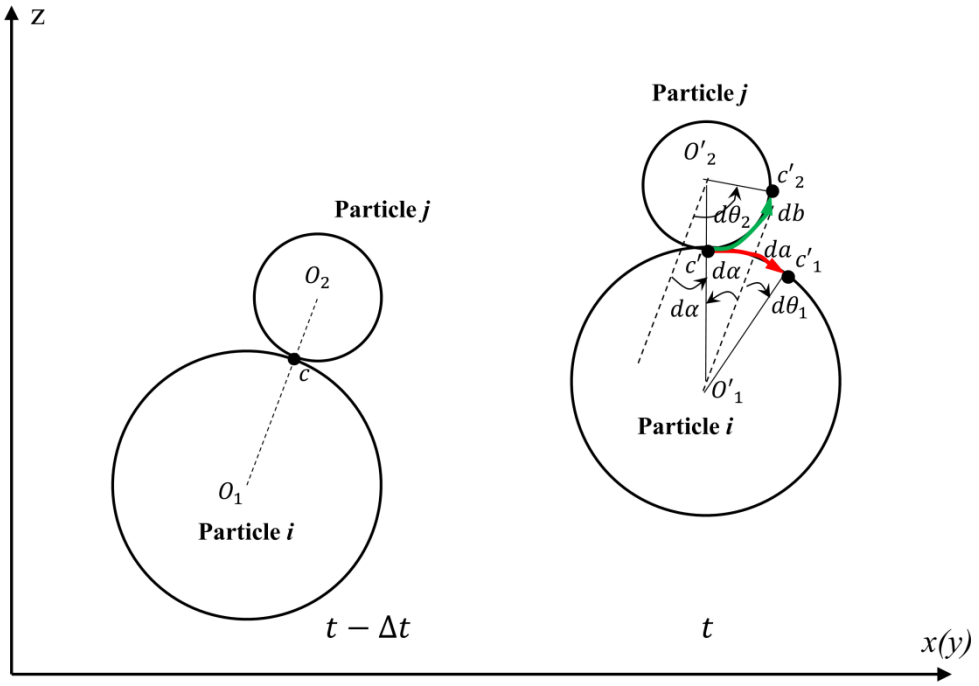



Figure 6.8 Kinematics of two particles in contact over a single timestep projected in a local coordinate system (After Jiang et al. (2005))

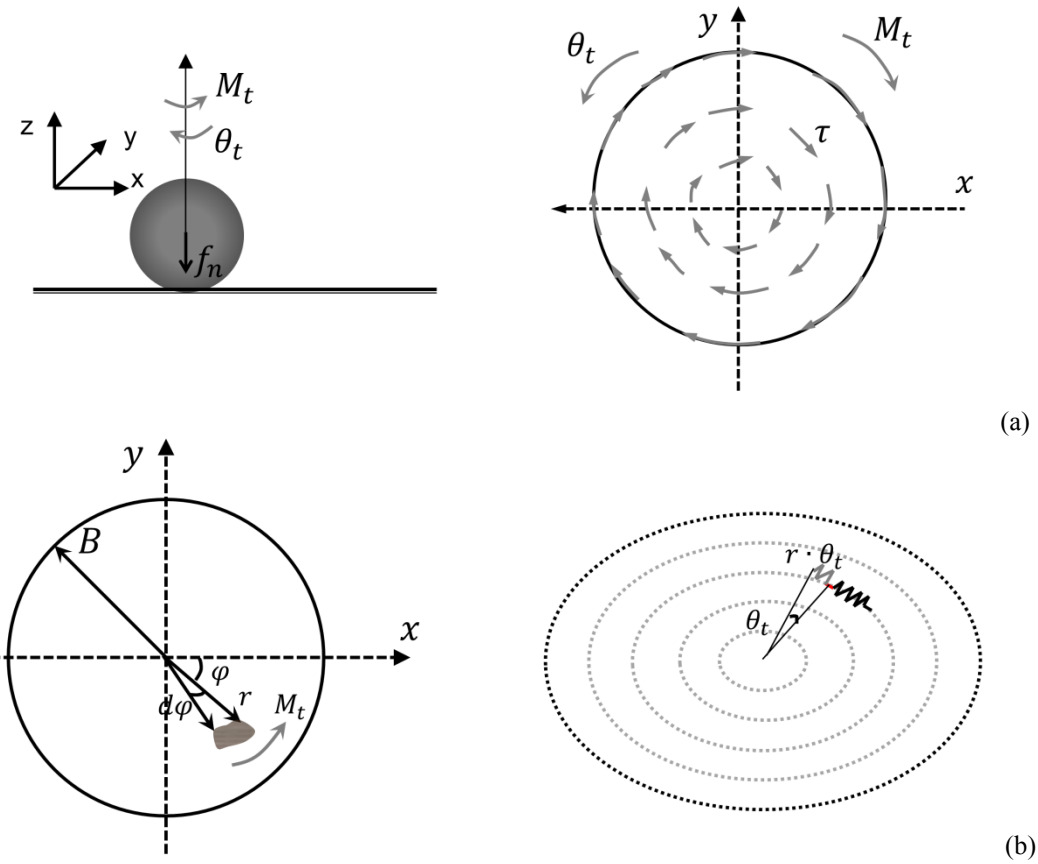
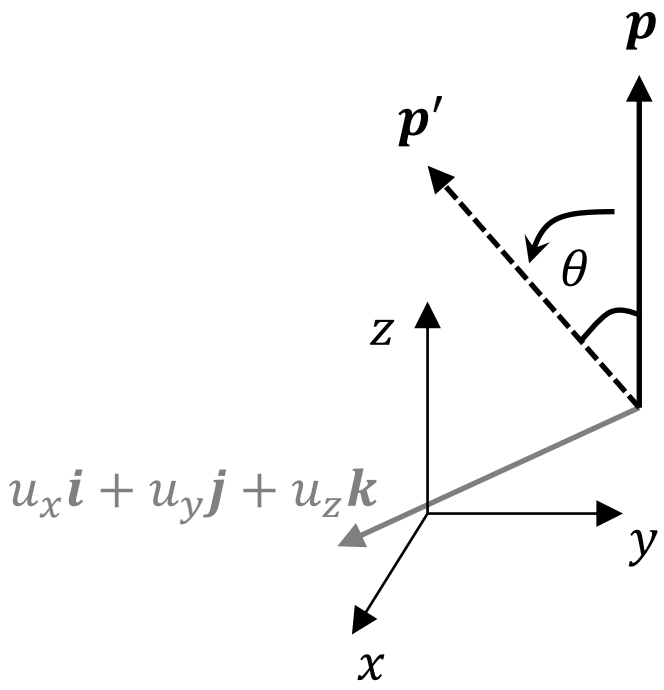
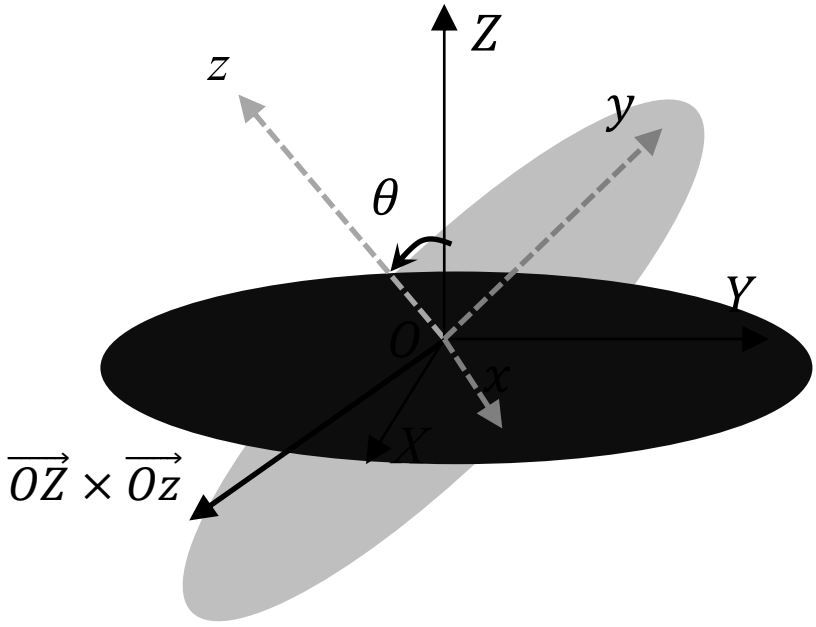



Figure 6.9 Assumed mechanism for the twisting/torque resistance model: (a) Illustration of the annular shear stress flow on the contact plane; (b) Calculation of the annular shear stress




(a)




(b)

Figure 6.10 Applying quaternions to perform spatial rotation: (a) Rotation of a single vector around an arbitrary axis; (b) Rotation of a coordinate system around an axis that is orthogonal to the z axes of the old and new coordinate system

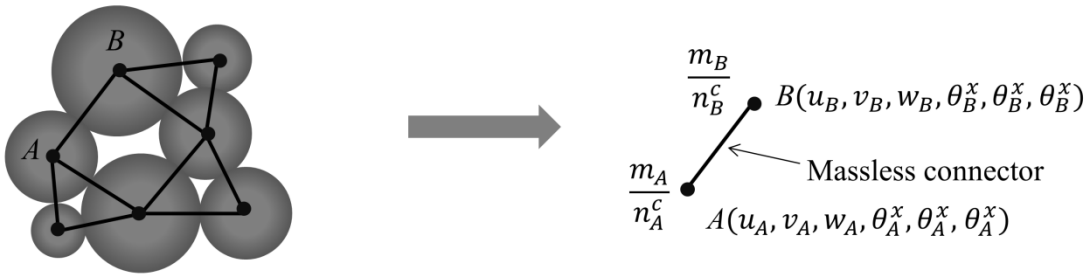



Figure 6.11 Illustration of the construction of the lumped mass matrix

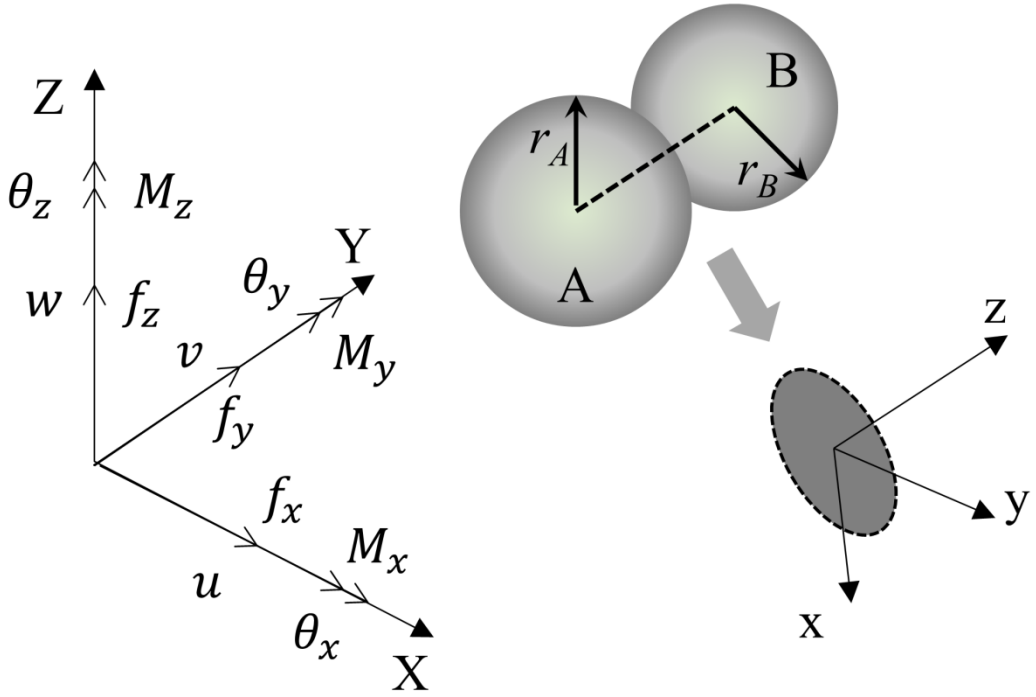



Figure 6.12 Illustration of the local and global coordinate system for two particles in contact

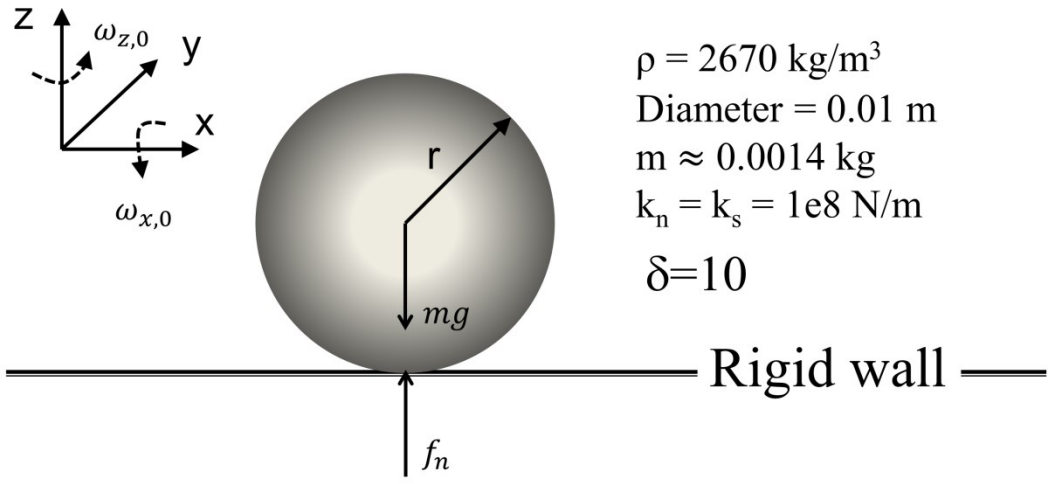
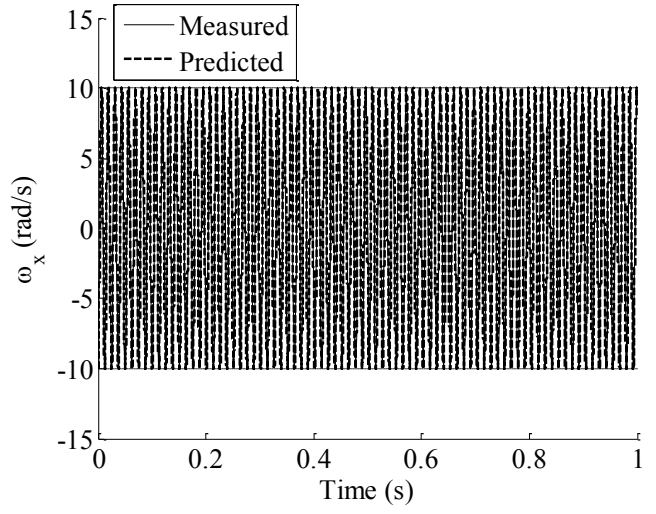
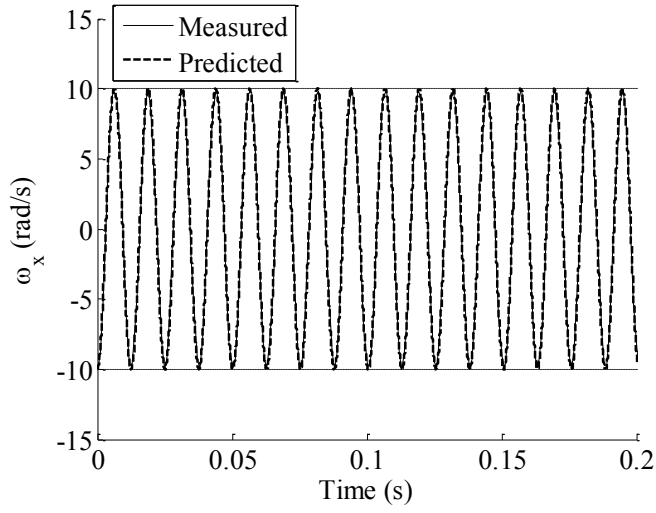


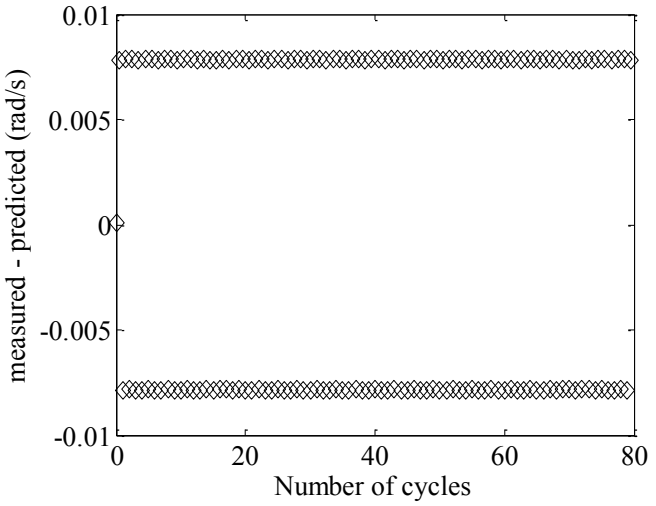

Figure 6.13 A single particle spins on a flat rigid wall




(a)

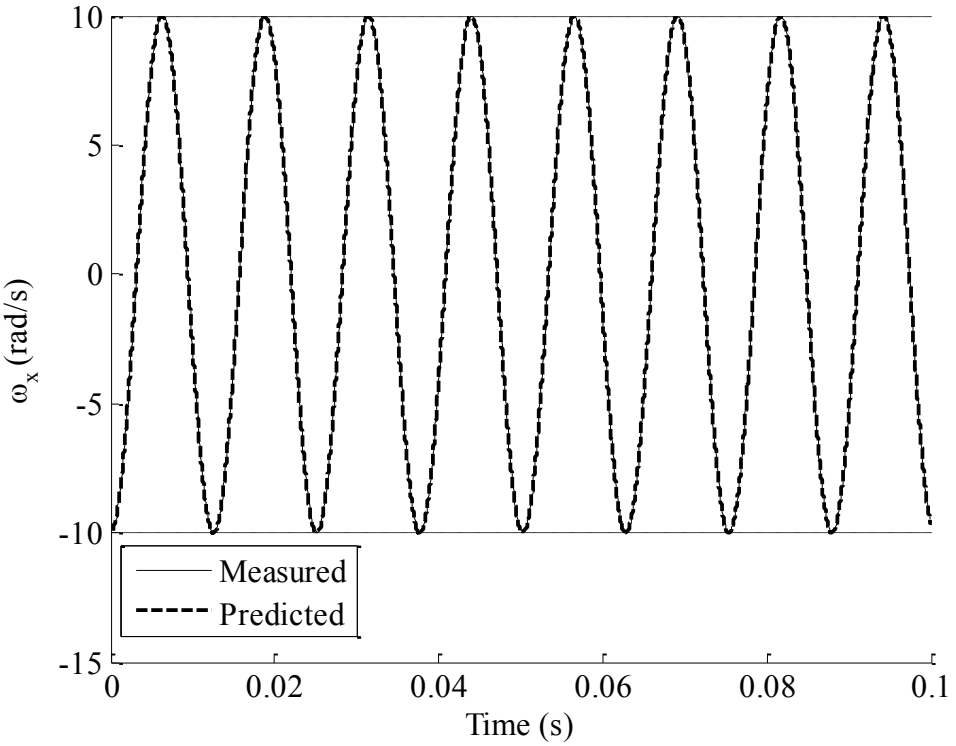



(b)

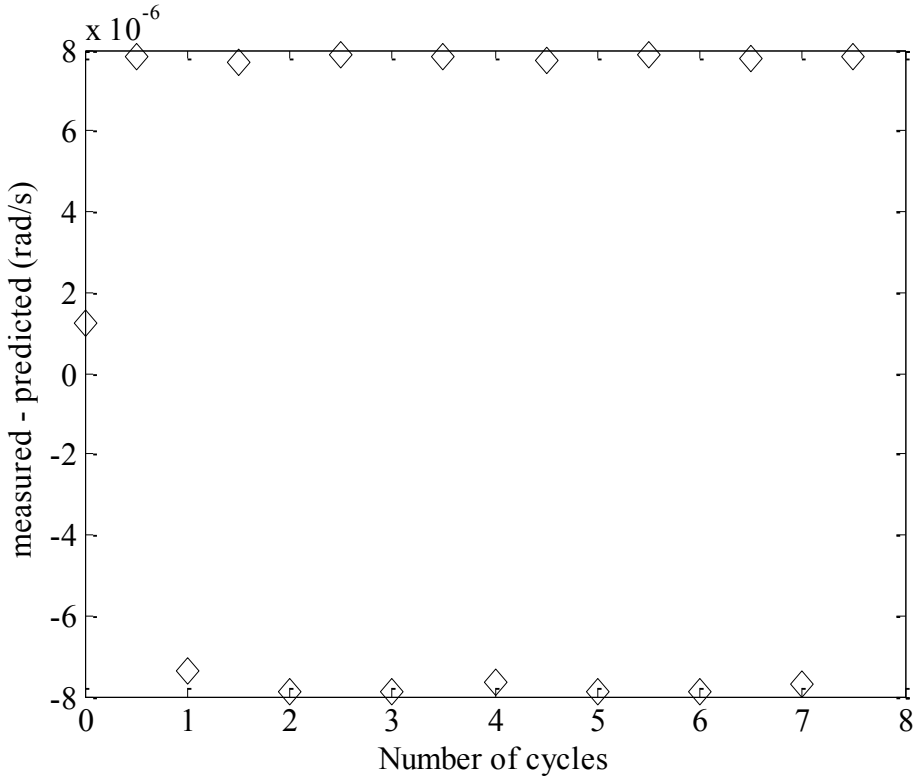



(c)

Figure 6.14 Comparison between the measured motion and the analytical harmonic motion ($\Delta t$ = 1e-6, no limit on the rolling resistance): (a) between 0 and 1 s; (b) Small scale (between 0 and 0.2 s); (c) Difference between the measured $\omega_x$ and the predicted $\omega_x$ at the peak and the valley

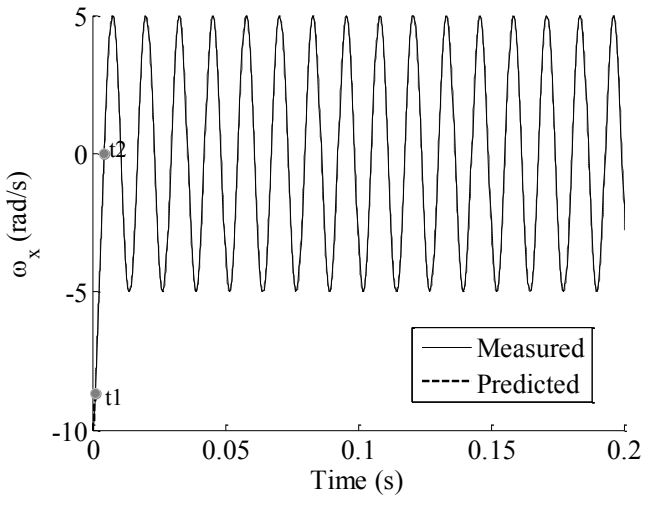



(a)

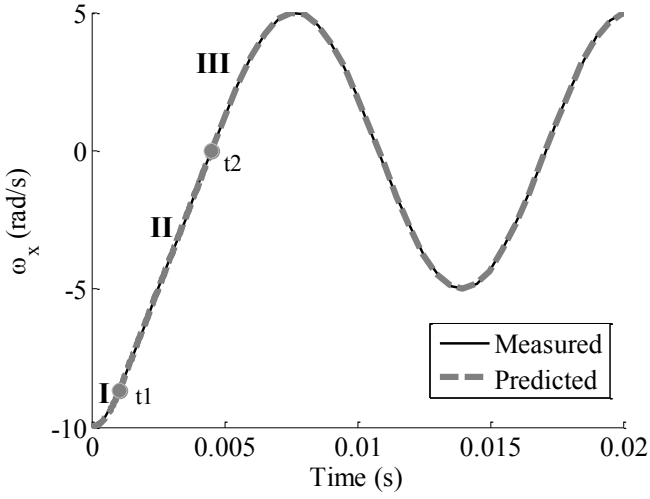



(b)

Figure 6.15 Comparison between the measured motion and the analytical harmonic motion ($\Delta t$ = 1e-9, no limit on the rolling resistance): (a) between 0 and 0.1 s; (b) Difference between the measured $\omega_x$ and the predicted $\omega_x$ at the peak and the valley




(a)




(b)

Figure 6.16 Comparison between the measured motion and the theoretically-derived motion when the rolling resistance is bounded by a limit ($\Delta t$ = 1e-9, $\kappa$=0.5): (a) between 0 and 0.2 s; (b) between 0 and 0.02 s

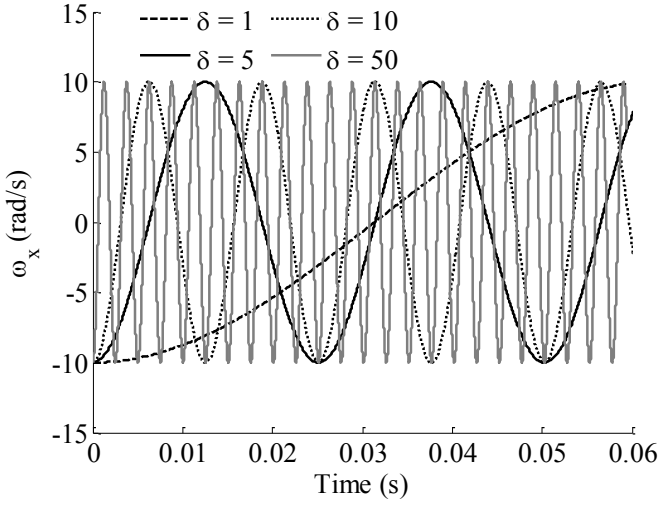



Figure 6.17 Effect of $\delta$ on the angular motion ($\Delta t$ = 1e-9, no limit)

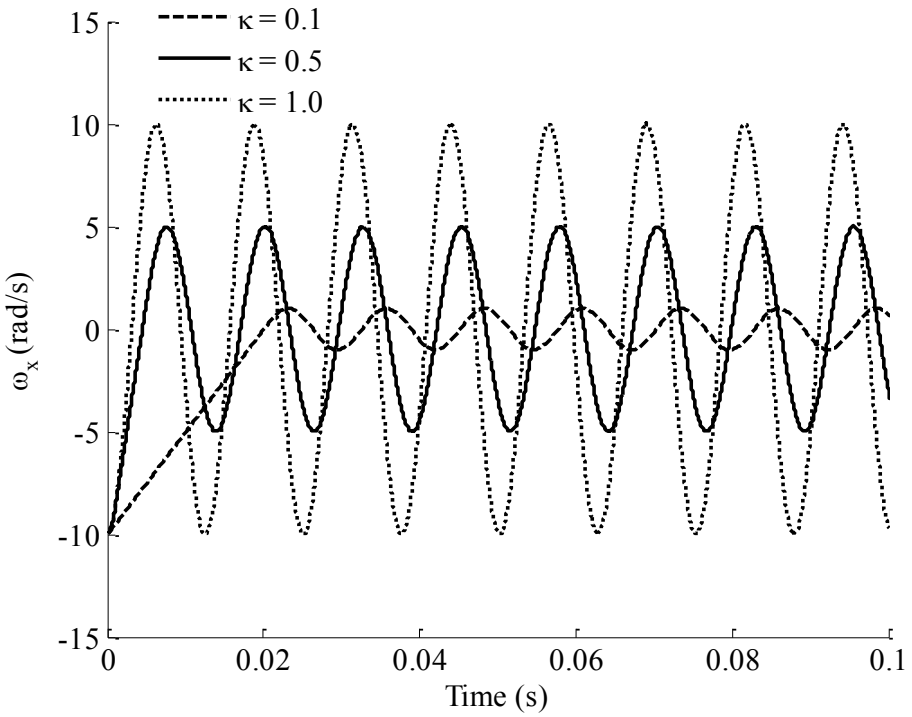



Figure 6.18 Influence of κ on the angular motion (Δt = 1e-9)

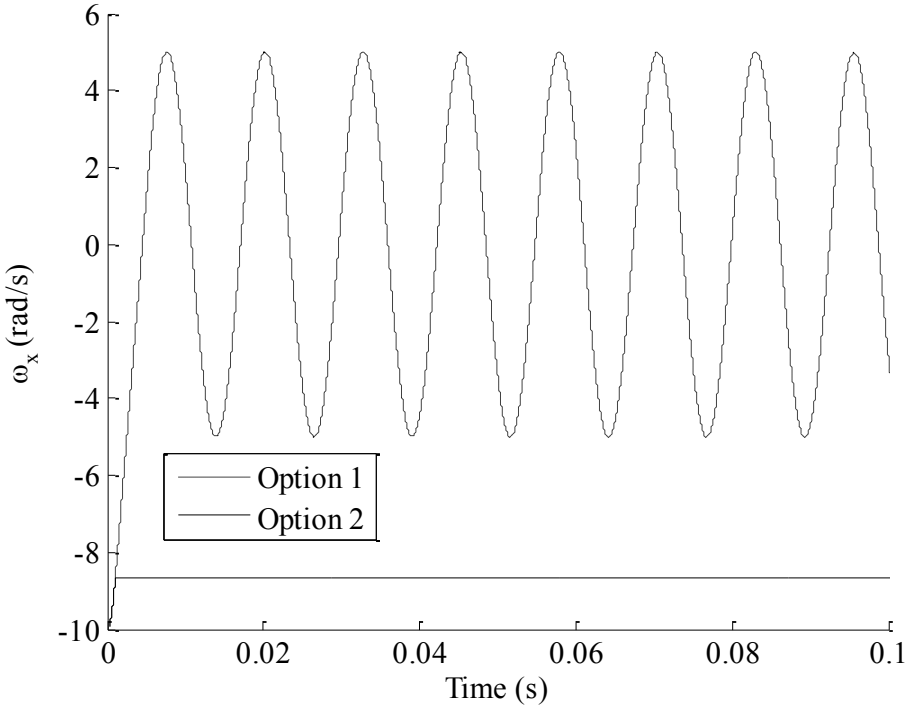



Figure 6.19 Comparing the influence of different options after the limiting value for the rolling resistance is attained (Δt = 1e-9, κ=0.5) (Option 1: the rolling resistance is maintained at the limiting value; Option 2: The rolling resistance drops to zero.)

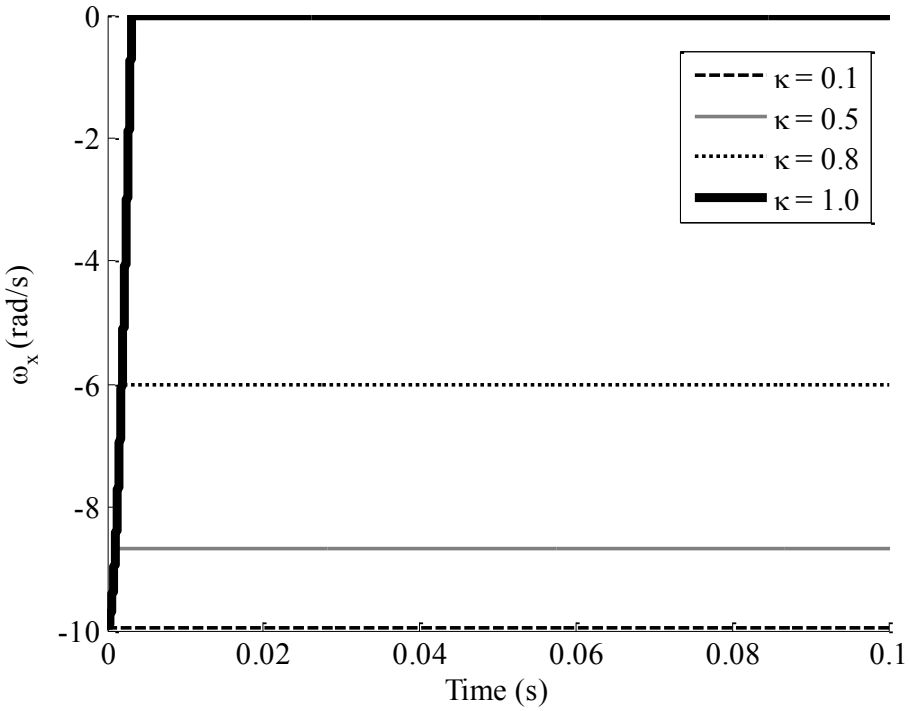
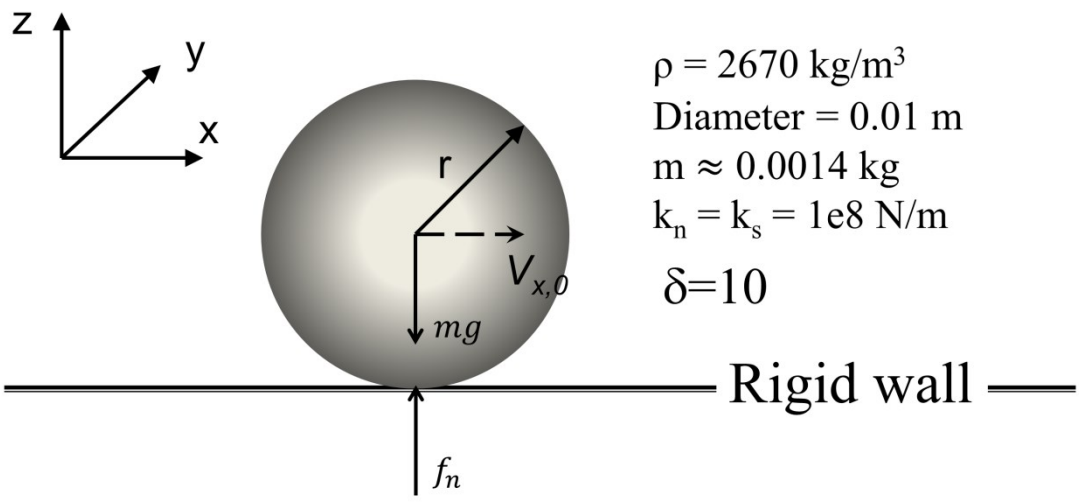
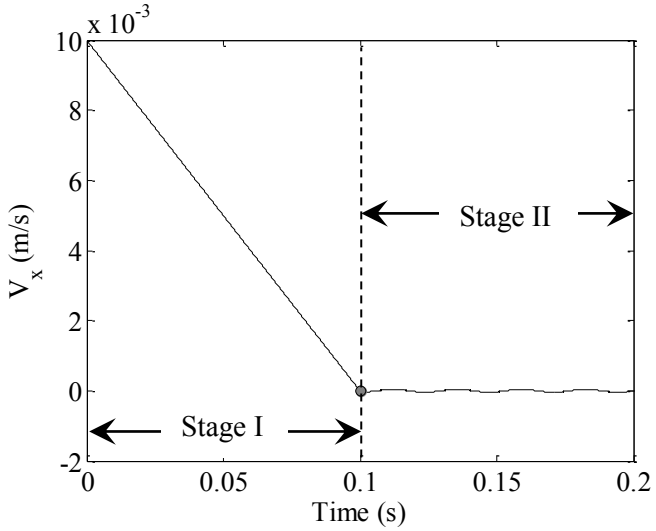


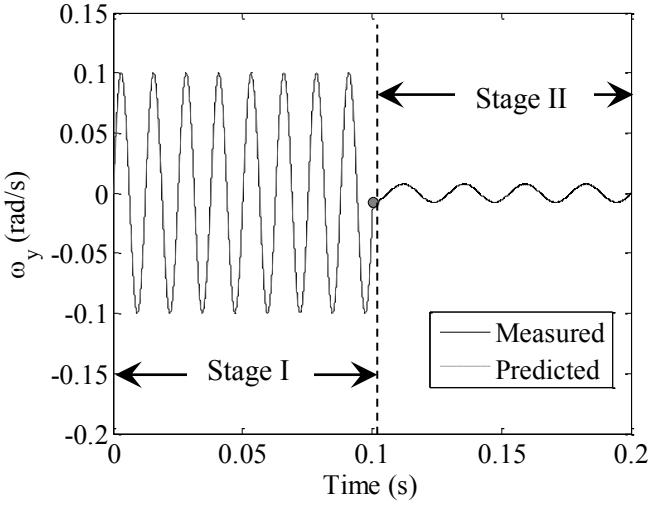

Figure 6.20 Influence of κ on the angular motion when Option 2 is adopted after the limit of the rolling resistance is attained




(a)




(b)




(c)

Figure 6.21 The kinematics of a single ball moving along a flat wall with initial translational velocity: (a) Illustration of the model; (b) Translational velocity; (c) Rotational velocity

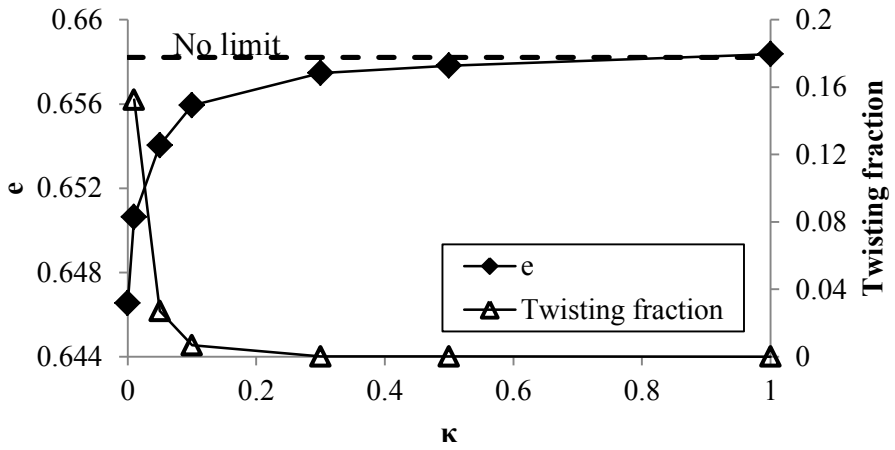



Figure 6.22 Influence of $\kappa$ on the packing density after isotropic compression ($\sigma'_3$=100 kPa, $\delta$ =1,$\mu$ = 0.25, dashed line indicates the value without limit set for the rotational resistance)

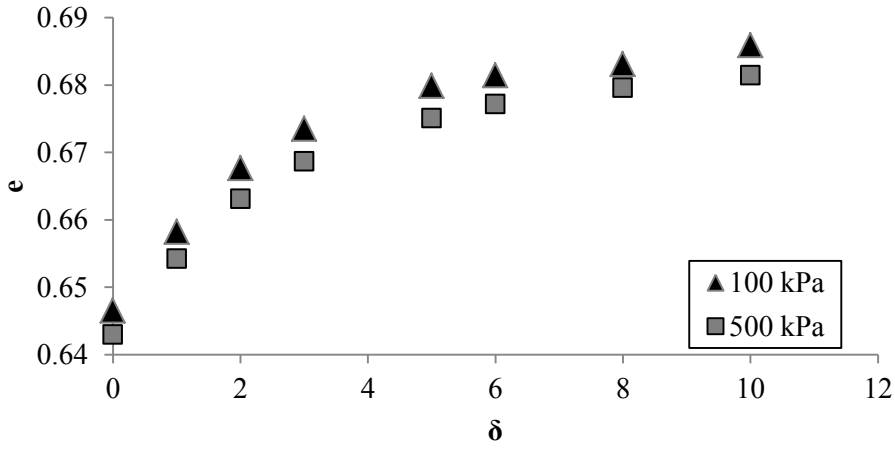



Figure 6.23 Influence of $\delta$ on the packing density after isotropic compression ($\mu$ = 0.25, no limit for the rotational resistance)

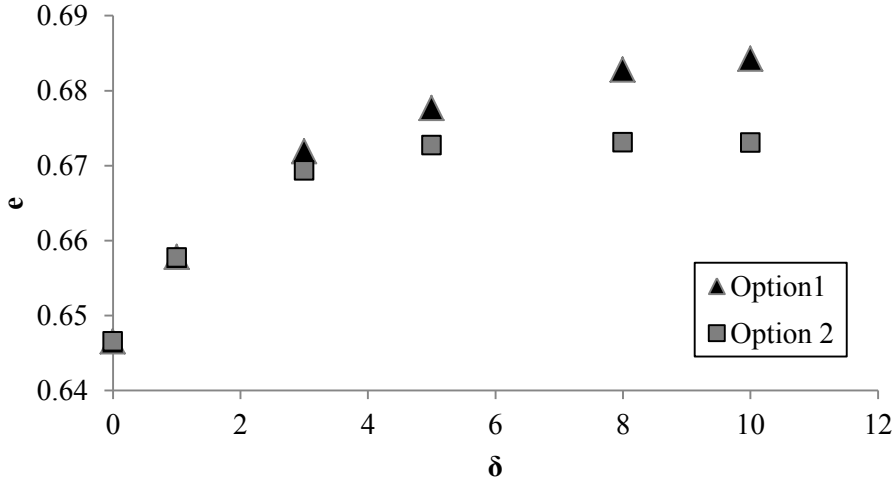



Figure 6.24 Comparing the packing density after isotropic compression for different post-limit options ($\sigma'_3$=100 kPa, $\kappa$ =0.5, $\mu$ = 0.25. Option 1: $M_r = M_r^m$post limit; Option 2: $M_r$ = 0 post limit)

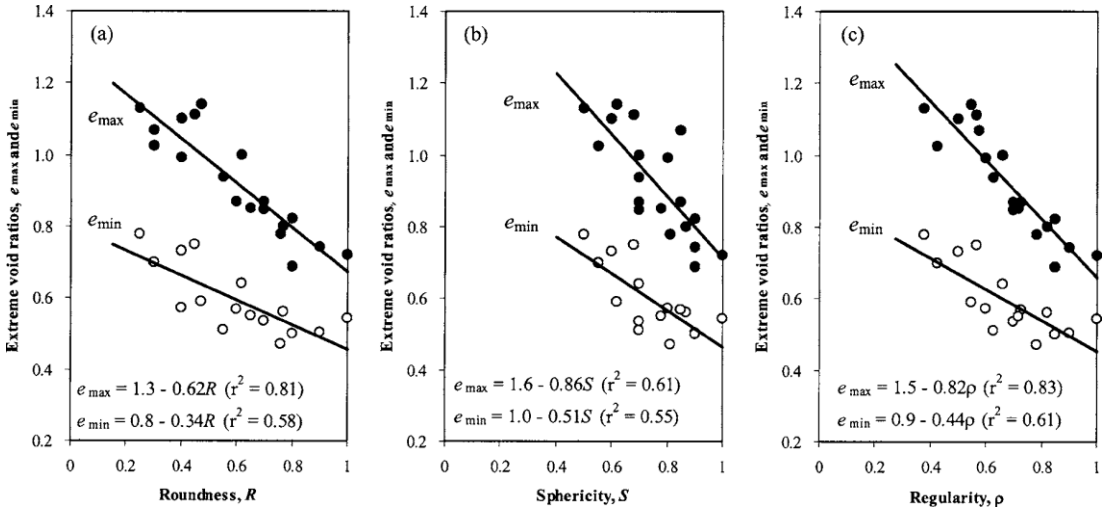
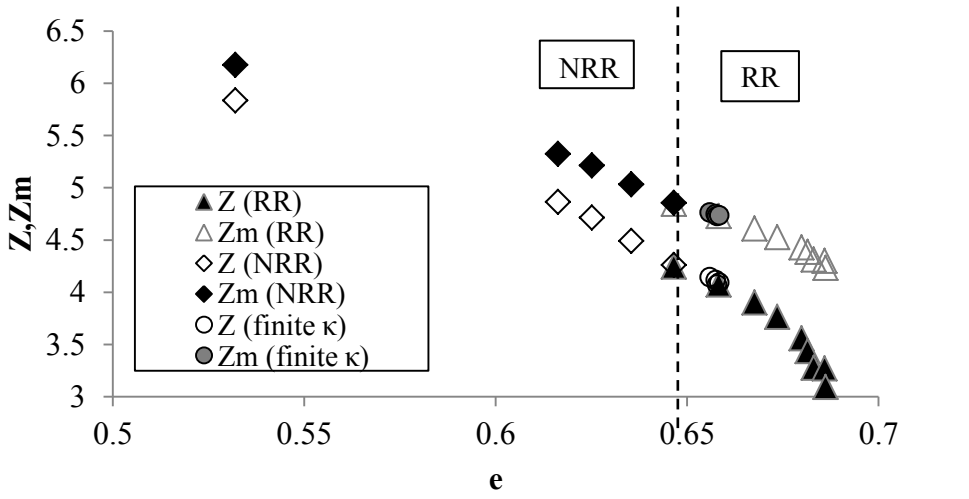
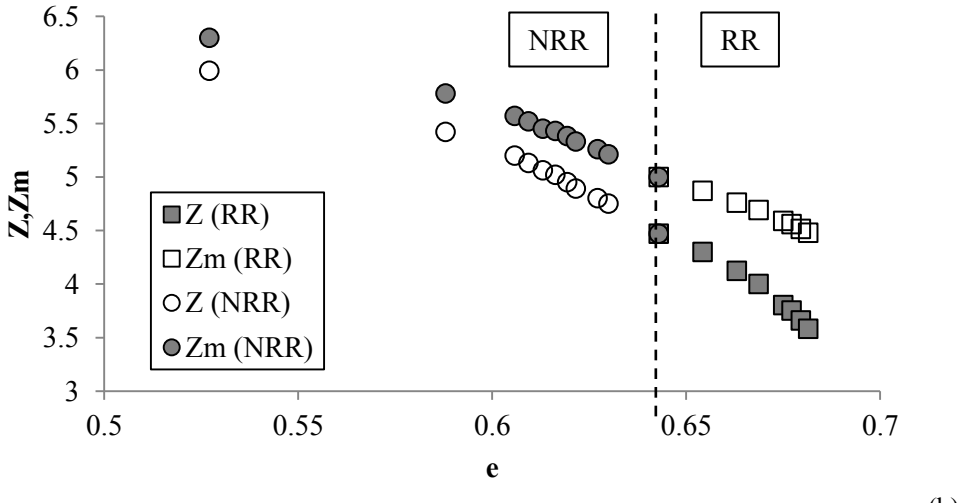



Figure 6.25 Influence of particle shape on the packing density ($e_{max}$ and $e_{min}$) (Cho et al., 2006)

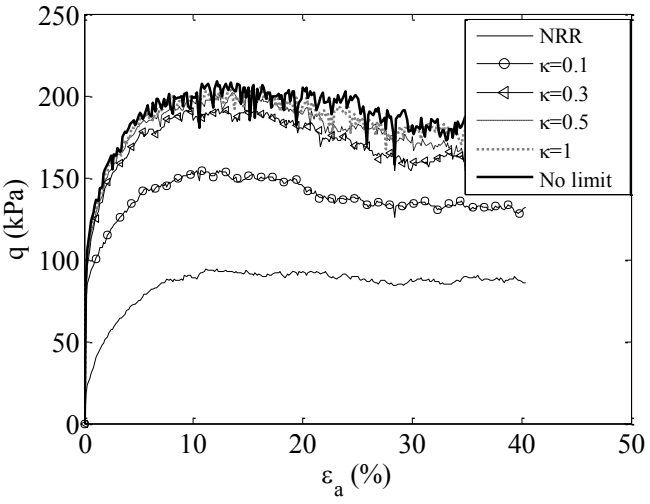



(a)

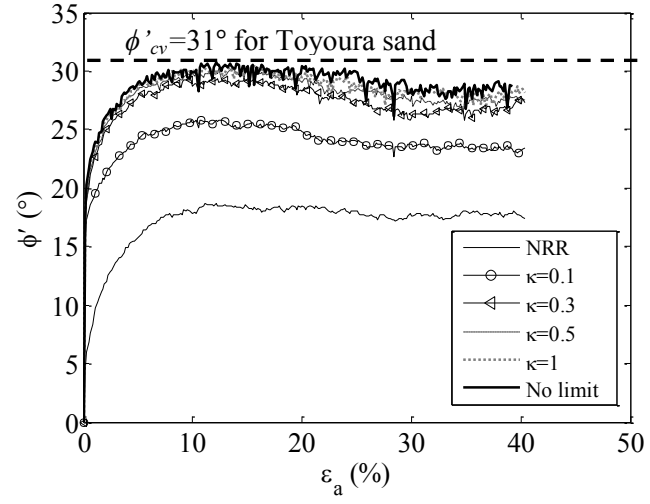



(b)

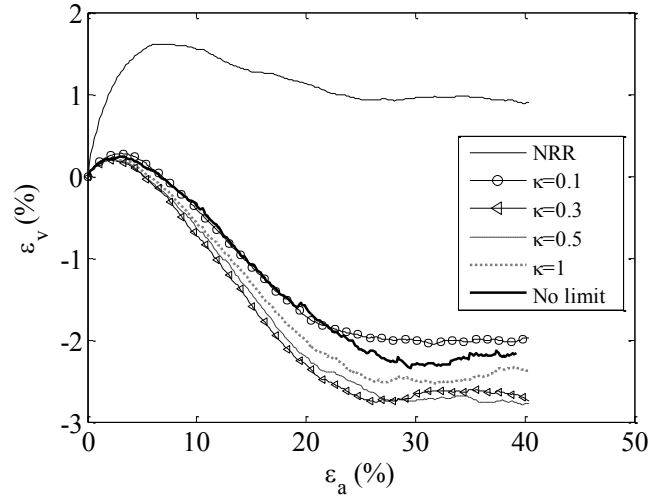
Figure 6.26 Correlations between the void ratio and the coordination number ($Z$) and between the void ratio and the mechanical coordination number ($Z_m$) after isotropic compression: (a) 100 kPa; (b) 500 kPa (RR: With rotational resistance; NRR: No rotational resistance)




(a)

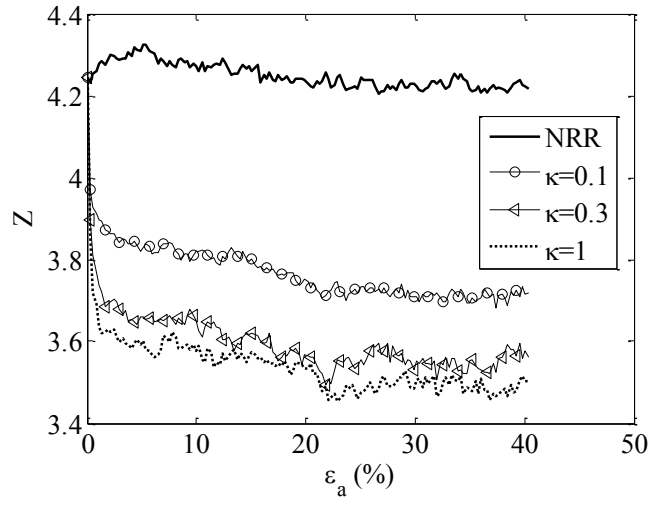



(b)

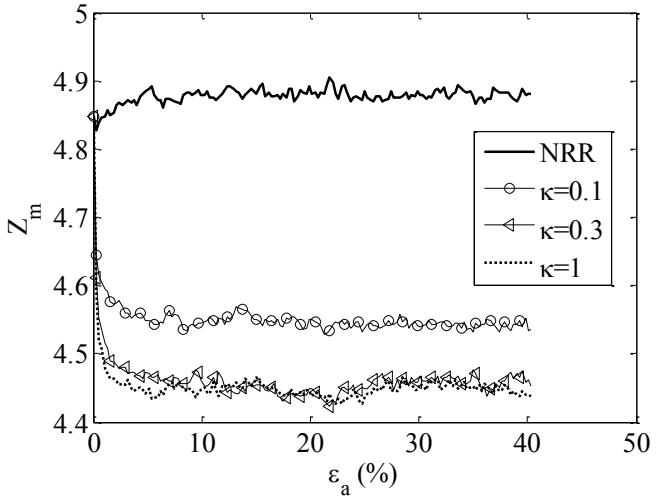



(c)

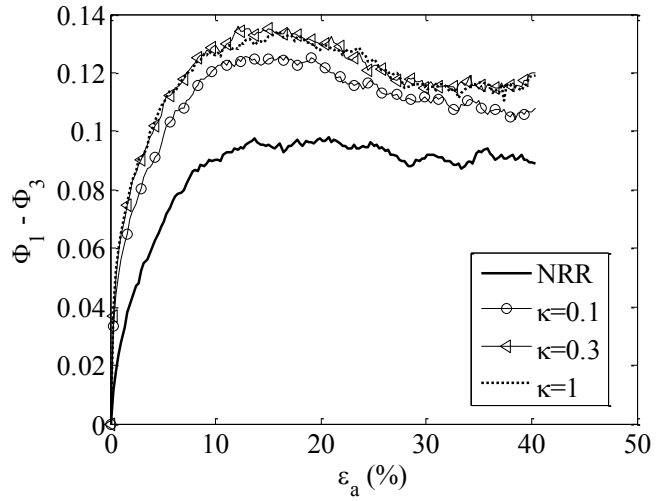
Figure 6.27 Influence of $\kappa$ on the mechanical behaviour ($e_0$=0.646, $\sigma'_3$=100 kPa): (a) Deviatoric stress vs axial strain; (b) Angle of shearing resistance vs axial strain; (c) Volumetric strain vs axial strain




(a)

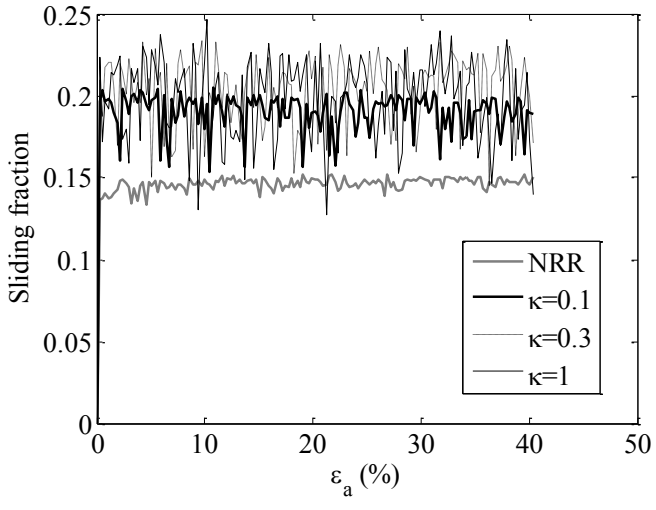



(b)

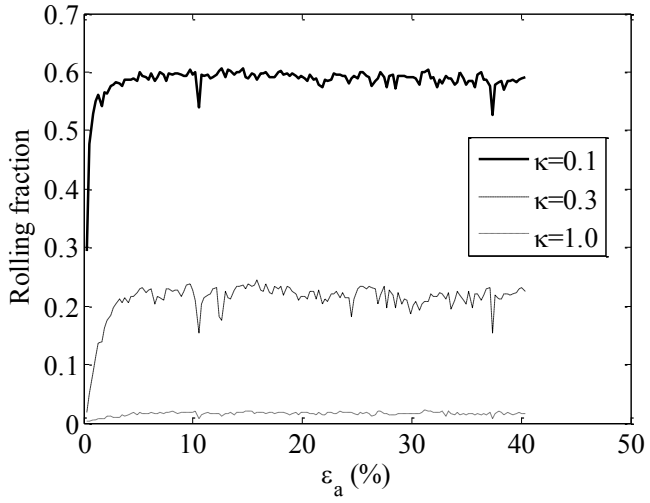



(c)

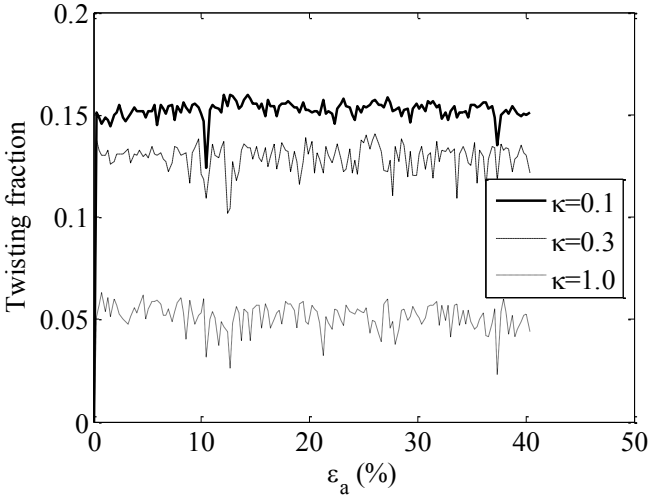
Figure 6.28 Influence of $\kappa$ on the particle-scale measures ($e_0$=0.646, $\sigma'_3$=100 kPa): (a) Coordination number; (b) Mechanical coordination number; (c) Deviatoric fabric




(a)

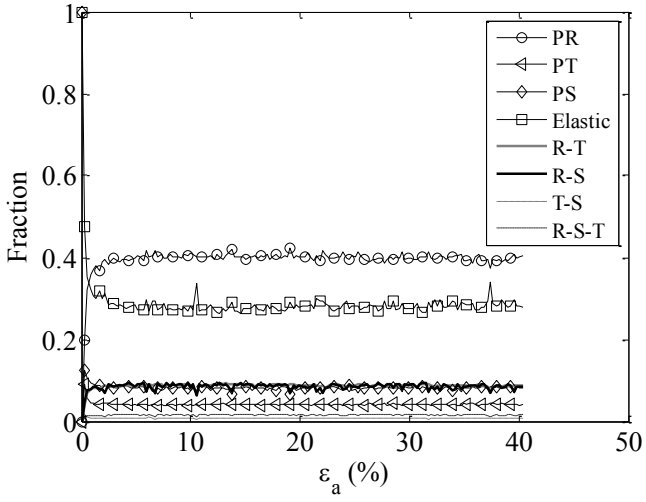



(b)

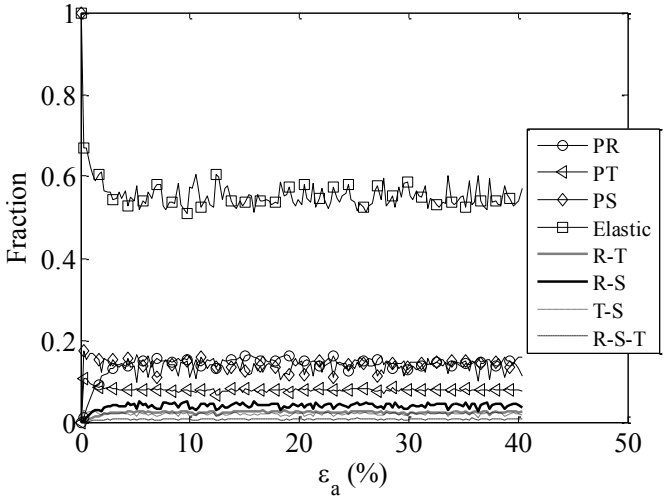



(c)

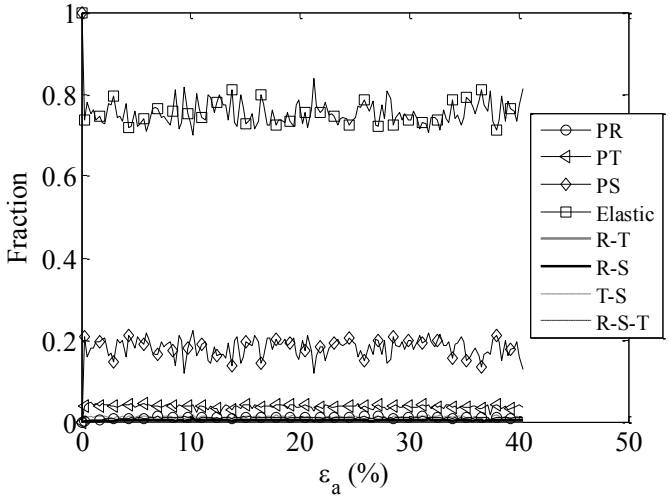
Figure 6.29 Influence of $\kappa$ on the fraction of the contacts that reach the plastic limit: (a) Sliding fraction; (b) Rolling fraction; (c) Twisting fraction




(a)

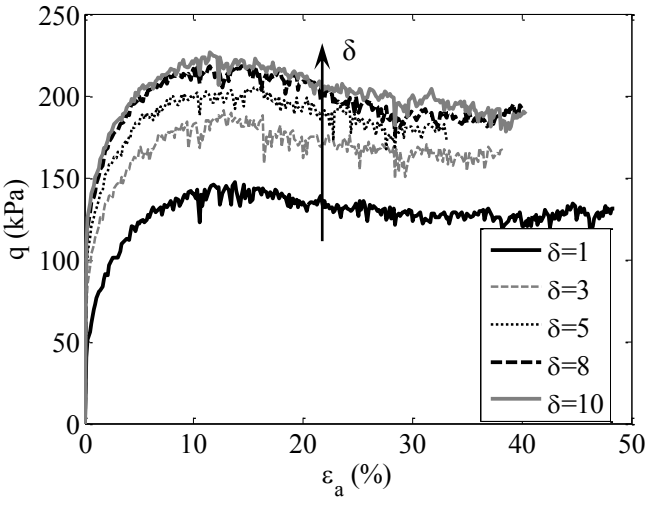



(b)

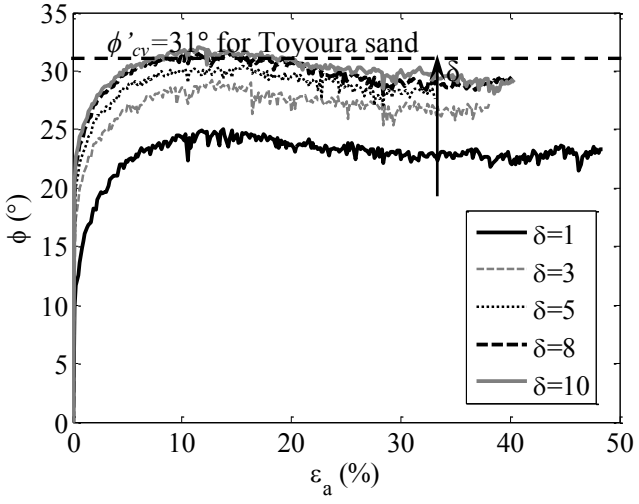



(c)

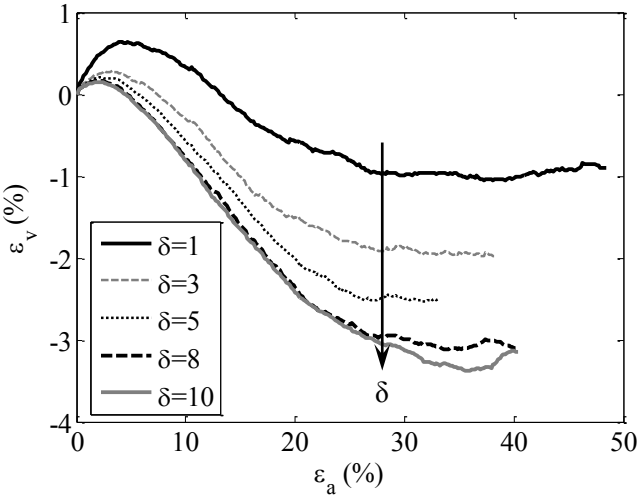
Figure 6.30 Effects of $\kappa$ on the elastic and plastic configurations of the contacts: (a) $\kappa$=0.1; (b) $\kappa$=0.3; (c) $\kappa$=1 (**PR**: pure rolling; **PT**: pure twisting; **PS**: pure sliding; **Elastic**: no rolling, no twisting and no sliding; **R-T**: rolling and twisting; **R-S**: rolling and sliding; **T-S**: twisting and sliding; **R-S-T**: rolling, sliding and twisting)




(a)

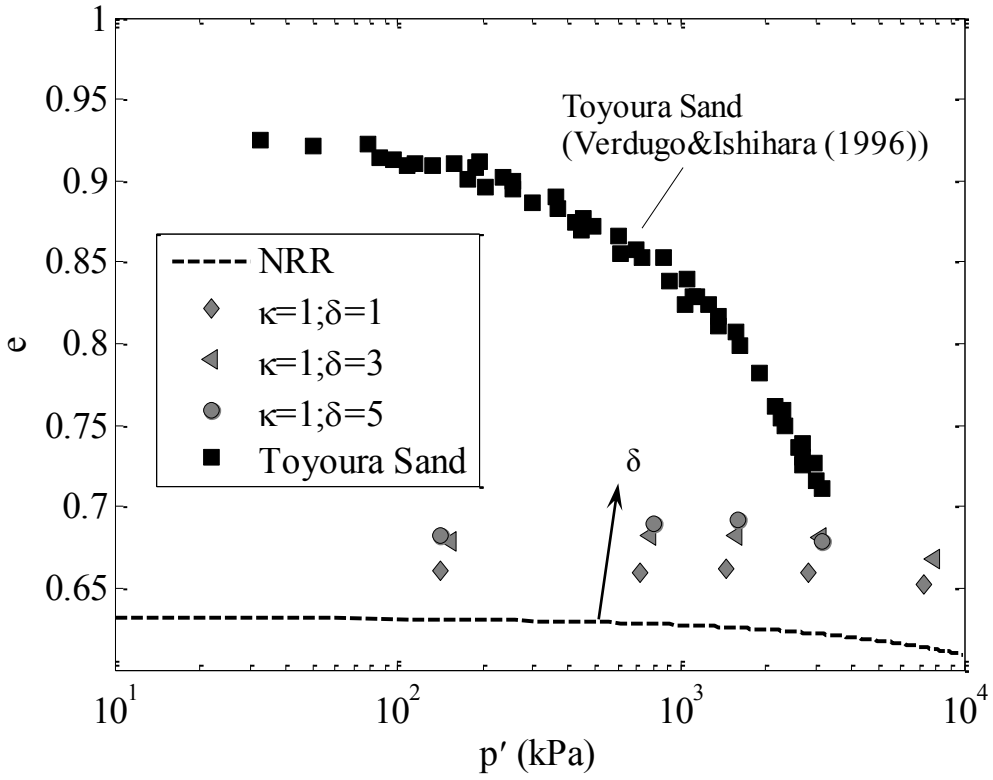



(b)

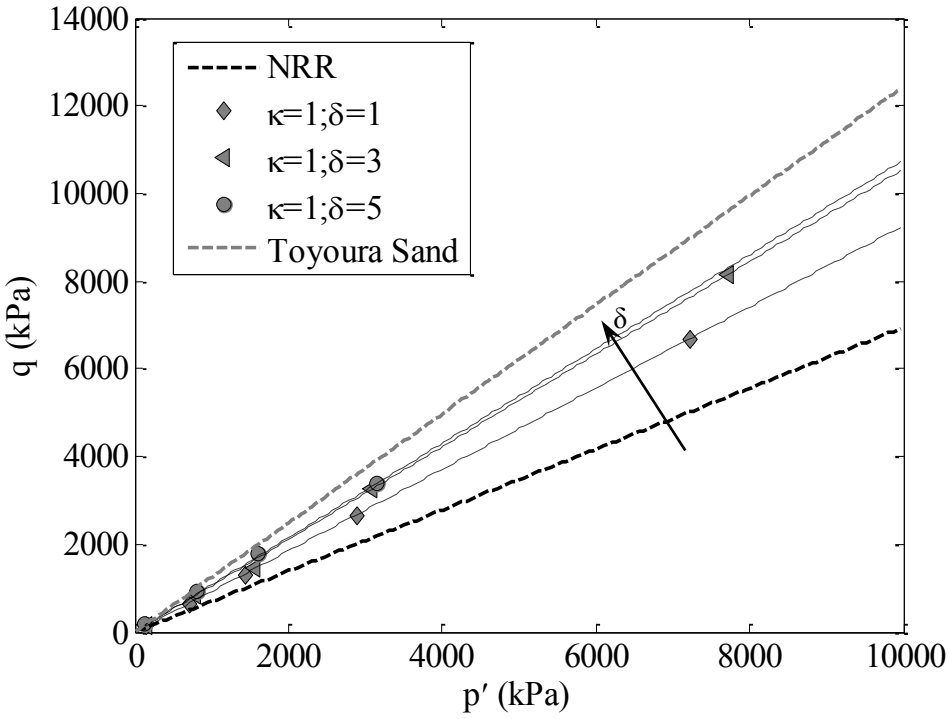



(c)

Figure 6.31 Influence of $\delta$ on the mechanical behaviour ($e_0$=0.646, $\sigma'_3$=100 kPa, $\kappa$=1): (a) Deviatoric stress vs axial strain; (b) Angle of shearing resistance vs axial strain; (c) Volumetric strain vs axial strain




(a)




(b)

Figure 6.32 Effect of rotational resistance on the position of the critical state lines: (a) *e*-log*(p')* space; (b) *q-p'* space

# Chapter 7 Conclusions

## 7.1 Summary

This work has investigated the mechanical behaviour of granular materials under generalised three-dimensional loading conditions using DEM and considering the framework of critical state soil mechanics (CSSM). The particle size distribution of the numerical samples is representative of the grading of Toyoura sand. A large database containing over 150 simulations has been established with the aid of the cx1 high-performance-computing facility at Imperial College.

Chapter 2 explained in detail the modifications made to the original LAMMPS code including different types of servo-control schemes that simulate different laboratory testing conditions. The modified code was verified by comparing the simulation results with the analytical solutions for the peak stress ratios at failure derived for face-centred-cubic assemblies by Thornton (1979).

The first objective, which was to show the usefulness of the CSSM framework to assess the validity of DEM simulations of soil behaviour, was fulfilled in Chapters 3 and 4. Specifically, Chapter 3 explored the origin of the sample size effect observed in DEM simulations using rigid-wall boundaries. Numerical assemblies containing different numbers of particles were generated and subjected to triaxial shearing. The homogeneity of the numerical assemblies was evaluated by considering the spatial distributions of void ratio and contact density. The size of the zone of influence of the rigid walls was identified. When interpreting the critical-state data, the homogeneous interior region excluding the zone of influence of the rigid walls was considered separately from the whole assembly.

A parametric study to assess the influence of the interparticle friction coefficient ($\mu$) on the mechanical behaviour of granular materials was carried out in Chapter 4. Numerical assemblies with the same initial state were sheared under drained triaxial loading conditions with different $\mu$ values. The observed variations of the peak and critical-state strengths with $\mu$ were compared with different analytical solutions. The shape of the critical state line (CSL) in $e$-log($p'$) space was found to be dependent on $\mu$. Most notably, for high values of $\mu$, the void ratio at the critical state increases with increasing mean effective stress ($p'$) at small stress levels. This behaviour does not agree with our understanding of soil behaviour from the CSSM framework and was considered non-physical. To determine the origin of this non-physical behaviour, extensive particle-scale analyses were conducted and linked to the macro-scale responses. The fundamental mechanisms were identified by considering the

influence of $\mu$ on the buckling strength of a simple conceptual force chain. A transition from sliding-dominant to rolling-dominant contact behaviour was identified and related to the variation of strength in response with $\mu$.

The second objective, i.e., to explore the extent to which DEM can capture the behaviour of sand within the CSSM framework and the extent to which DEM can extend our understanding of soil behaviour, was addressed in Chapters 5 and 6. In Chapter 5, different axisymmetric triaxial loading conditions were considered: constant $\sigma'_3$, constant $p'$ and constant volume (to simulate undrained conditions). Drained true triaxial simulations were also performed to investigate the influence of the intermediate stress ratio ($b$) on the overall response of granular materials. The failure mechanism under true triaxial loading conditions was discussed. The uniqueness of the CSL was evaluated considering the influence of $b$. Relationships between the state parameter and soil stress-deformation characteristics proposed by Jefferies and Been (2006) were investigated and were extended to 3D loading conditions. NorSand, an isotropic critical-state-based constitutive model, was calibrated to model the DEM data.

A new rolling/twisting resistance model with a rational physical basis was developed for use with spherical particles to investigate the effect of interlocking between irregular soil grains in Chapter 6. In this model, individual particles are assumed to contact each other through an evenly-distributed spring system over a finite circular contact area rather than through a single spring in both normal and tangential directions. The resistance to relative rolling is assumed to originate from the uneven redistribution of contact force when relative rolling motion takes place which generates a contact moment that is opposite to the direction of relative rolling. The origin of the twisting resistance is attributed to the distortion of tangential contact springs due to the relative spinning motion around the contact normal. The model was verified using several simple scenarios for which the particle motion can be determined analytically. The effectiveness of the new model in capturing the influence of particle shape on the mechanical behaviour of soils, in particular, the critical-state behaviour, was presented. The associated underlying mechanism was also discussed.

## 7.2 Major findings

The key findings derived in this research include following aspects. More detailed conclusions may be found at the end of each Chapter.

(a) Origin of sample size effects in DEM simulations with rigid-wall boundaries

The sample size effect is attributed to the geometrical constraints imposed by the rigid wall boundaries to the kinematic movements of particles. These constraints lead to a higher void ratio and a lower contact density in the region that extends to approximately $2D_{50}$ away from the rigid walls. When considering the entire sample, the critical-state locus in $e$-log($p'$) space was found to depend on the sample size. This is contradictory to experimental observations and violates the CSSM framework. However, when the zone of influence of rigid walls was excluded in the calculation of stresses and void ratio, the critical-state loci of the rigid-wall samples became coincident and approached the critical state line (CSL) of the homogeneous periodically-bounded sample, indicating that the interior parts of rigid-wall-bounded samples are the most representative of the real material behaviour.

(b) Selection of an appropriate interparticle friction coefficient ($\mu$)

The influence of $\mu$ on the mechanical behaviour of granular materials is limited. Both the macro-scale and micro-scale responses are nonlinearly related to $\mu$. It was found that when $\mu$ exceeds 0.5 the stress-deformation characteristics of granular materials is no longer sensitive to $\mu$. When $\mu$ higher than 0.5 is used, the void ratio at the critical state initially increases with increasing mean effective stress at low stress levels. This is caused by the increasing number of rattlers in the numerical assembly as a consequence of increasing stability of the strong force chains due to the increasing $\mu$. The observed $e$-log($p'$) relationship does not agree with what is observed in physical experiments. Therefore, a $\mu$ value below 0.5 is recommended for DEM simulations of soil behaviour.

(c) Failure mechanism for granular materials subjected to three-dimensional loading

None of the prior analytical solutions which assumed sliding as the chief failure mechanism could give good agreement with the observed dependency of overall strength on $\mu$. In the low $\mu$ region, where contact sliding is indeed likely, they underestimated the shearing strength by ignoring the contribution from the lateral contacts supporting the strong force chains, while they overestimate the shearing strength for high $\mu$ values because these expressions do not consider the transition from sliding to rolling at the contacts. The failure of granular materials was attributed to the buckling of strong force chains which carry the majority of applied load. DEM data showed that the strength of granular materials initially increases with increasing $b$ followed by a decrease in strength beyond a certain $b$ value. This is in good agreement with prior failure criteria developed for three-dimensional loading and has been explained by the transition from column-like (two-dimensional) buckling to plate-like (one-dimensional) buckling of strong force chains as $b$ increases.

(d) Insight into the critical state

For each intermediate stress ratio considered, the critical state loci collapsed to unique relationships in both $q$-$p'$ and $e$-log($p'$) spaces. However, the positons of the critical state line (CSL) in both $q$-$p'$ and $e$-log($p'$) spaces was shown to depend on the intermediate stress ratio ($b$). The slope of the CSL in $q$-$p'$ space decreases consistently with increasing $b$, while the CSL in $e$-log($p'$) space moves upwards as $b$ increases. Particle-scale studies showed that while the coordination number at the critical state is insensitive to $b$, the internal structures at critical state represented by the deviatoric fabric are affected by $b$. The higher position of the CSL in $e$-log($p'$) space at higher $b$ values is attributable to more anisotropic fabric that develops at the critical state as $b$ increases.

(e) The capacity of DEM to capture the state-dependent nature of soil behaviour

The dependency of soil responses on the initial stress state and packing density under both drained and undrained loading conditions was also observed in DEM simulations. Moreover, the DEM data showed that the relationships between the state parameter and strength and between the state parameter and dilatancy that were reported by Jefferies and Been (2006) are not restricted to axisymmetric loading conditions but are also applicable to three-dimensional loading. The relationship between the initial state parameter and the dilatancy-induced strength and the relationship between the initial state parameter and dilatancy at peak were shown to be independent of the intermediate stress ratio. NorSand, an isotropic constitutive model that was proposed based on experimental data was shown to be able to satisfactorily model the behaviour of DEM samples under three-dimensional loading conditions. This shows the potential of DEM to be used as a tool to aid the development of advanced soil constitutive models.

(f) Effectiveness of the rotational resistance model

By incorporating a new rotational resistance model for spherical particles, it was shown that the new model can qualitatively capture the influence of particle shape on the mechanical behaviour of sand. Particularly, the strength and dilatancy increase with the increasing shape parameter ($\delta$) which is considered to represent the non-spherical shape of particles. In particular, the slope of the critical state line in $q$-$p'$ space increases and the position of the critical-state data in $e$-log($p'$) space moves upwards as $\delta$ increases. The impact of the strength index ($\kappa$) which is related to the strength of the asperities is less significant in comparison to $\delta$. However, the capacity of rotational resistance to replicate the effect of particle shape is limited. Therefore, to quantitatively compare the DEM simulation results with laboratory testing data, it is necessary to use nonspherical particles. Despite the limitation, the underlying mechanism of the effect of particle shape can be revealed when

rotational resistance is considered, i.e., transition from rolling to sliding at the contacts as the irregularity in particle shape increases.

## 7.3 Limitations and Recommendations for further work

### 7.3.1 Limitations

The stress level considered in the current study is beyond the normal range that would be considered in laboratory tests. Under such circumstances, particle crushing is unavoidable and may dominate the overall stress-deformation response. However, such a mechanism was absent in the current study. The second limitation resides in the idealisation of particle geometry. Only spherical particles were used while the irregular topology of real soil grains was ignored. While a rotational resistance model has been incorporated, as discussed in Chapter 6, the extent to which the rotational resistance model can simulate the real particle shape effect is limited. In order to enable quantitative comparison between the DEM simulations and the laboratory tests, it is necessary to consider irregular particles with morphology accurately described in the future simulations.

### 7.3.2 Recommendations for further work

(a) State-dependent behaviour of granular materials

Although various correlations between the state parameter and the stress-deformation responses that are similar to real sand have been identified, these observations were made only for two uniform materials. To confirm that DEM simulations can be in broad agreement with the laboratory evidence, extended studies are necessary to consider materials with differing gradings, e.g., well-graded or gap-graded materials.

Since this study was restricted to initially isotropic samples, it is important to investigate the influence of initial/inherent anisotropy to complete our understanding of the state-dependent nature of granular materials. This can be achieved by using non-spherical particles following the techniques described in Section 6.1 and adhering to the same sample generation procedures used in laboratory tests. If the critical state is indeed independent of the initial fabric as observed by other researchers, e.g., Yan & Zhang (2013), the relationships between the initial state parameter and the strength and between the initial state parameter and dilatancy would not agree with what has been identified in the current study. If this is indeed true, the scatter in the laboratory data collected by Jefferies & Been (2006) can be soundly explained by different degrees of inherent anisotropy for different samples involved in their dataset. The initially more contractive response under triaxial extension than under triaxial

compression was shown to be less obvious in the DEM simulations than in laboratory tests. This was attributed to the rapid convergence of the principal stress direction and the principal fabric direction as a consequence of the initially isotropic structure in the current study. Introducing a certain degree of initial anisotropy will allow this idea to be explored.

Recent research showed that the liquefaction resistance under cyclic loading conditions is also a function of the state parameter (Yang & Sze, 2011). It will be interesting to look at the behaviour of granular materials subjected to cyclic loading using DEM and see whether DEM can reproduce this observation and uncover the underlying mechanism.

(b) Soil constitutive modelling

The preliminary attempt presented in the current study indicated that DEM can be used as an effective tool for the development of soil constitutive models. Apart from the loading conditions considered in this study, other more sophisticated laboratory testing conditions, e.g., hollow cylinder tests, can also be simulated using DEM. This capacity enables DEM to provide data sources for the development of advanced constitutive models. On the other hand, particle-scale information obtained in DEM simulations may be used to assess the reasonability of the micro-macro correlations embedded in some of the existing constitutive models. For example, the anisotropic critical state theory (ACST) (Li & Dafalias, 2012) provides a framework to consider the evolution of internal structure in soil constitutive models. Within this framework, an anisotropic index is introduced into the stress-dilatancy law (flow rule) and different expressions have been proposed (e.g., Gao et al., 2013; Li & Dafalias, 2012). However, due to the lack of particle-scale information, these correlations were arbitrarily defined. It will be useful to assess these models using the DEM simulation results and see whether or not the assumed mechanisms can be reproduced. With the available particle-scale information, physically more rigorous correlations may be proposed. Moreover, DEM also allows different definitions of fabric anisotropy to be assessed so that the one that is most closely related to the macro-scale responses may be identified for inclusion in soil constitutive models.

# References


Ai, J., Chen, J.-F., Rotter, J.M. & Ooi, J.Y. (2011) Assessment of rolling resistance models in discrete element simulations. *Powder Technology*. 206 (3), 269–282.

Antony, S. & Kruyt, N. (2009) Role of interparticle friction and particle-scale elasticity in the shear-strength mechanism of three-dimensional granular media. *Physical Review E*. 79 (3), 1–9.

ASTM (2011) *Standard Test Method for Consolidated Drained Triaxial Compression Test for Soils*. doi:10.1520/D7181.

Atkinson, J. (2007) *The Mechanics of Soils and Foundations*. 2nd edition. Taylor and Francis.

Azéma, E. & Radjaï, F. (2012) Force chains and contact network topology in sheared packings of elongated particles. *Physical Review E*. 85 (3), 1–12.

Bagi, K. (1996) Stress and strain in granular assemblies. *Mechanics of Materials*. 22, 165–177.

Bardet, J.P. & Huang, Q. (1993) Rotational stiffness of cylindrical particle contacts. In: *Powders and Grains 93*. pp. 39–43.

Barreto, D. (2009) *Numerical and Experimental Investigation into the behaviour of granular materials under gerneralised stress states*. PhD thesis. Univ. of London (Imp. Coll. of Sci., Technol. & Med.), UK.

Barreto, D. & O'Sullivan, C. (2012) The influence of inter-particle friction and the intermediate stress ratio on soil response under generalised stress conditions. *Granular Matter*. 14, 505–521.

Been, K. & Jefferies, M.G. (1985) A state parameter for sands. *Géotechnique*. 35 (2), 99–112.

Been, K., Jefferies, M.G. & Hachey, J. (1991) The critical state of sands. *Géotechnique*. 41 (3), 365–381.

Behringer, R.P., Daniels, K.E., Majmudar, T.S. & Sperl, M. (2008) Fluctuations, correlations and transitions in granular materials: statistical mechanics for a non-conventional system. *Philosophical transactions. Series A, Mathematical, physical, and engineering sciences*. 366 (1865), 493–504.

Belheine, N., Plassiard, J.-P., Donzé, F.-V., Darve, F., et al. (2009) Numerical simulation of drained triaxial test using 3D discrete element modeling. *Computers and Geotechnics*. 36 (1-2), 320–331.

Belytschko, T. (1983) An overview of semidiscretization and time integration procedures. In: T.J.R. Belytschko, T. and Hughes (ed.). *Computational Methods for Transient Analysis, Computational Methods in Mechanics Series*. North Holland, New York, NY.

Bishop, A.W. (1954) Discussion on “Shear Characteristics of a Saturated Silt, Measured in Triaxial Compression.” *Géotechnique*. (1), 43–45.

Bishop, A.W. (1971) Shear strength parameters for undisturbed and remoulded soil specimens. In: *Proceedings of the Roscoe Memorial Symposium*. 1971 Cambridge, UK. pp. 65–78.

Bolton, M.D. (1986) The strength and dilatancy of sands. *Géotechnique*. 36 (1), 65–78.

Brilliantov, N., Spahn, F., Hertzsch, J. & Pöschel, T. (1996) Model for collisions in granular gases. *Physical review. E, Statistical physics, plasmas, fluids, and related interdisciplinary topics*. 53 (5), 5382–5392.

Bulson, P.S. (1970) *The Stability of Flat Plates*. London, UK, Chatto & Windus.

Calvetti, F. & Emeriault, F. (1999) Interparticle forces distribution in granular materials : link with the macroscopic behaviour. *Mechanics of cohesive-frictional materials*. 4, 247–279.

Caquot, A. (1934) *Equilibre des Massifs a Frottement Interne. Stabilite des Terres pulverents et Coherentes*. Paris, Gauthier Villars.

Carrera, A., Coop, M.R. & Lancellotta, R. (2011) Influence of sample preparation techniques and stress path followed on the location of the Critical State Line : an example of a silty-sandy tailing. In: *International Symposium on Deformation Characteristics of Geomaterials*. 2011 pp. 526–532.

Casagrande, A. (1936) Characteristics of cohesionless soils affecting the stability of earth fills. *Journal of Boston Society of Civil Engineering. Reprinted in Contributions to soil mechanics 1925-1940*.

Chan, S.K. & Ng, K.M. (1986) Geometrical characteristics of a computer-generated three-dimensional packed column of equal and unequal sized spheres—with special reference to wall effects. *Chemical Engineering Communications*. 48 (4-6), 215–236.

Chantawarangul, K. (1993) *Numerical simulations of three-dimensional granular assembles*. PhD thesis. The University of Waterloo.

Cho, G., Dodds, J. & Santamarina, J. (2006) Particle shape effects on packing density, stiffness, and strength: natural and crushed sands. *Journal of Geotechnical and Geoenvironmental Engineering*. 132 (5), 591–602.

Collop, A.C., McDowell, G.R. & Lee, Y.W. (2006) Modelling dilation in an idealised asphalt mixture using discrete element modelling. *Granular Matter*. 8 (3-4), 175–184.

Cui, L. & O’Sullivan, C. (2003) Analysis of a triangulation based approach for specimen generation for discrete element simulations. *Granular Matter*. 5 (3), 135–145.

Cui, L., O’Sullivan, C. & O’Neill, S. (2007) An analysis of the triaxial apparatus using a mixed boundary three-dimensional discrete element model. *Géotechnique*. 57 (10), 831–844.

Cundall, P.A. (2001) A discontinuous future for numerical modelling in geomechanics? *Geotechnical Engineering*. 149 (1), 41–47.

Cundall, P.A. & Strack, O.D.L. (1979) A discrete numerical model for granular assemblies. *Géotechnique*. 29 (1), 47–65.

Drescher, A. & De Josselin De Jong, G. (1972) Photoelastic verification of a mechanical model for the flow of a granular material. *Journal of the Mechanics and Physics of Solids*. 20, 337–351.

Duran, J. (2000) *Sands, Powders, and Grains: An introduction to the Physics of Granular Materials*. New York, NY, USA, Springer.

Estrada, N., Taboada, A. & Radjaï, F. (2008) Shear strength and force transmission in granular media with rolling resistance. *Physical Review E*. 78 (2), 021301.

Ferellec, J.-F. & McDowell, G.R. (2010) A method to model realistic particle shape and inertia in DEM. *Granular Matter*. 12 (5), 459–467.

Finno, R.J., Harris, W.W., Mooney, M.A. & Viggiani, G. (1996) Strain localization and undrained steady state of sand. *Journal of Geotechnical Engineering*. 122 (6), 462–473.

Finno, R.J. & Rechenmacher, A.L. (2003) Effects of Consolidation History on Critical State of Sand. *Journal of Geotechnical and Geoenvironmental Engineering*. 129 (4), 350–360.

Fu, P. & Dafalias, Y.F. (2011) *Fabric evolution within shear bands of granular materials and its relation to critical state theory*. 35, 1918–1948.

Gajo, A. & Wood, D.M. (1999) Severn–Trent sand: a kinematic-hardening constitutive model: the q–p formulation. *Géotechnique*. 49 (5), 595–614.

Gao, Y., Wang, Y. & Su, J.C.P. (2013) Mechanisms of Aging-Induced Modulus Changes in Sand under Isotropic and Anisotropic Loading. *Journal of Geotechnical and Geoenvironmental Engineering*. 139 (3), 470–482.

Gao, Z., Zhao, J., Li, X. & Dafalias, Y.F. (2013) A critical state sand plasticity model accounting for fabric evolution. *International Journal for Numerical and Analytical Method in Geomechanics*. 38 (4), 370–390.

Golub, G.H. & Van Loan, C.F. (1983) *Matrix-Computations*. Oxford, North Oxford Academic.

Göncü, F. & Luding, S. (2013) Effect of particle friction and polydispersity on the macroscopic stress–strain relations of granular materials. *Acta Geotechnica*. 8 (6), 629–643.

Gong, G. (2008) *DEM simulations of drained and undrained behaviour*. PhD thesis. The University of Birmingham.

Green, G.E. & Bishop, A.W. (1969) A note on the drained strength of sand under generalized strain conditions. *Géotechnique*. 19 (1), 144–149.

Gu, X., Huang, M. & Qian, J. (2014) DEM investigation on the evolution of microstructure in granular soils under shearing. *Granular Matter*. 16 (1), 91–106.

Guo, N. & Zhao, J. (2013) The signature of shear-induced anisotropy in granular media. *Computers and Geotechnics*. 471–15.

Gutierrez, M. & Ishihara, K. (2000) Non-coaxiality and energy dissipation in granular materials. *Soils and Foundations*. 40 (2), 49–59.

Hasan, A. & Alshibli, K.A. (2010) Experimental assessment of 3D particle-to-particle interaction within sheared sand using synchrotron microtomography. *Géotechnique*. 60 (5), 369–379.

Head, K.H. (1994) *Manual of soil laboratory testing. Vol.2: Permeability, shear strength and compressibility tests*. 2nd edition. London, UK, Pentech Press.

Horne, M.R. (1969) The behaviour of an assembly of rotund , rigid , cohesionless particles . III *. *Proceedings of the Royal Society A: Mathematical, Physical and Engineering Sciences*. 310 (1500), 21–34.

Horne, M.R. (1965a) The Behaviour of an Assembly of Rotund, Rigid, Cohesionless Particles. I. *Proceedings of the Royal Society A: Mathematical, Physical and Engineering Sciences*. 286 (1404), 62–78.

Horne, M.R. (1965b) The Behaviour of an Assembly of Rotund, Rigid, Cohesionless Particles. II. *Proceedings of the Royal Society A: Mathematical, Physical and Engineering Sciences*. 286 (1404), 79–97.

Houlsby, G.T. (2009) Computers and Geotechnics Potential particles : a method for modelling non-circular particles in DEM. *Computers and Geotechnics*. 36 (6), 953–959.

Hunt, G.W., Tordesillas, A., Green, S.C. & Shi, J. (2010) Force-chain buckling in granular media: a structural mechanics perspective. *Philosophical transactions. Series A, Mathematical, physical, and engineering sciences*. 368 (1910), 249–262.

*Imperial College High Performance Computing Service*. http://www.imperial.ac.uk/ict/services/teachingandresearchservices/highperformancecomputing.

Ishihara, K. (1993) Liquefaction and flow failure during earthquakes. *Géotechnique*. 43 (3), 351–451.

Itasca Consulting Group (2007) *PFC3D Version 4.0 User Manual*. Minneapolis, MN, USA., Itasca Consulting Group.

Iwashita, K. & Oda, M. (2000) Micro-deformation mechanism of shear banding process based on modified distinct element method. *Powder Technology*. 109 (1-3), 192–205.

Iwashita, K. & Oda, M. (1998) Rolling resistance at contacts in simulation of shear band development by DEM. *Journal of Engineering Mechanics*. 124 (3), 285–292.

Jefferies, M. & Shuttle, D. (2011) On the operating critical friction ratio in general stress states. *Géotechnique*. 61 (8), 709–713.

Jefferies, M.G. (1993) Nor-Sand : a simple critical state model for sand. *Géotechnique*. 43 (1), 91–103.

Jefferies, M.G. & Been, K. (2006) *Soil liquefaction: a critical state approach*. Taylor and Francis.

Jefferies, M.G., Been, K. & Hachey, J.E. (1990) The influence of scale on the constitutive behaviour of sand. In: *Proceedings of 43rd Canadian Geotechnical Conference*. 1990 Quebec City, Canada. pp. 263–273.

Jefferies, M.G. & Shuttle, D.A. (2002) Dilatancy in general Cambridge-type models. *Géotechnique*. 52 (9), 625–638.

Jefferies M.G. and Shuttle D.A. (2005) NorSand: Calibration and Use. *11th Conference of the International Association for Computer Methods and Advances in Geomechanics*, 2005 Turin, 19-24 See http://www.civil.ubc.ca/research/geotech/download_software.php. Accessed 10/11/2013

Jiang, M.J., Konrad, J.M. & Leroueil, S. (2003) An efficient technique for generating homogeneous specimens for DEM studies. *Computers and Geotechnics*. 30 (7), 579–597.

Jiang, M.J., Yu, H.-S. & Harris, D. (2005) A novel discrete model for granular material incorporating rolling resistance. *Computers and Geotechnics*. 32 (5), 340–357.

Johnson, K. (1985) *Contact Mechanics*. 1st edition. Cambridge, United Kingdom, Cambridge University Press.

Ke, T. & Bray, J. (1995) Modeling of particulate media using discontinuous deformation analysis. *Journal of Engineering Mechanics*. 121 (11), 1234–1243.

Ko, H.Y. & Scott, R.F. (1967) A new soil testing apparatus. *Géotechnique*. 17, 40–57.

Kozicki, J. & Donzé, F.-V. (2008) A new open-source software developed for numerical simulations using discrete modeling methods. *Computer Methods in Applied Mechanics and Engineering*. 197, 4429–4443.

Kozicki, J., Tejchman, J. & Mróz, Z. (2012) Effect of grain roughness on strength, volume changes, elastic and dissipated energies during quasi-static homogeneous triaxial compression using DEM. *Granular Matter*. 14 (4), 457–468.

Kruyt, N.P. & Rothenburg, L. (2009) Plasticity of Granular Materials: a Structural-mechanics View. *AIP Conference Proceedings*. 1073 (1), 1073–1076.

Kruyt, N.P. & Rothenburg, L. (2006) Shear strength, dilatancy, energy and dissipation in quasi-static deformation of granular materials. *Journal of Statistical Mechanics: Theory and Experiment*. 2006 (07), 1–13.

Kuhn, M.R. & Bagi, K. (2009) Specimen Size Effect in Discrete Element Simulations of Granular Assemblies. *Journal of Engineering Mechanics*. 135 (6), 485–492.

Kwok, C.-Y. & Bolton, M.D. (2010) DEM simulations of thermally activated creep in soils. *Géotechnique*. 60 (6), 425–433.

Lade, P. V. (1993) Initiation of static instability in the submarine Nerlerk berm. *Canadian Geotechnical Journal*. 30, 895–904.

Lade, P. V. & Duncan, J.M. (1975) Elastoplastic Stress-Strain Theory for Cohesionless Soil. *Journal of the Geotechnical Engineering Division*. 101 (10), 1037–1053.

Lamarche, F. & Leroy, C. (1990) Evaluation of the volume of intersection of a sphere with a cylinder by elliptic integrals. *Computer Physics Communications*. 59, 359–369.

Lamei, M. & Mirghasemi, A.A. (2011) A discrete element model for simulating saturated granular soil. *Particuology*. 9 (6), 650–658.

Langston, P., Ai, J. & Yu, H.-S. (2013) Simple shear in 3D DEM polyhedral particles and in a simplified 2D continuum model. *Granular Matter*. 15 (5), 595–606.

Li, X. (2006) *Micro-scale investigation on the quasi-static behavior of granular material*. PhD thesis. The Hong Kong University of Science and Technology.

Li, X.S. (2002) A sand model with state-dependent dilatancy. *Géotechnique*. 52 (3), 173–186.

Li, X.S. & Dafalias, Y.F. (2012) Anisotropic Critical State Theory : Role of Fabric. *Journal of Engineering Mechanics*. 138 (3), 263–275.

Li, X.S. & Dafalias, Y.F. (2002) Constitutive Modeling of Inherently Anisotropic Sand Behavior. *Journal of Geotechnical and Geoenvironmental Engineering*. 128 (10), 868–880.

Li, X.S. & Dafalias, Y.F. (2000) Dilatancy for cohesionless soils. *Géotechnique*. 50 (4), 449–460.

Li, X.S. & Wang, Y. (1998) Linear representation of steady-state line for sand. *Journal of Geotechnical and Geoenvironmental Engineering*. 124 (12), 1215–1217.

Luding, S. (2008) Cohesive, frictional powders: contact models for tension. *Granular Matter*. 10 (4), 235–246.

Maeda, K., Fukuma, M. & Nukudani, E. (2009) Macro and micro critical states of granular materials with different grain shapes. *AIP Conference Proceedings*. 1145, 829–832.

Maeda, K., Sakai, H., Kondo, A., Yamaguchi, T., et al. (2010) Stress-chain based micromechanics of sand with grain shape effect. *Granular Matter*. 12 (5), 499–505.

Magnanimo, V., Ragione, L. La, Jenkins, J.T., Wang, P. & Makse, H.A. (2008) Characterizing the shear and bulk moduli of an idealized granular material. *EPL (Europhysics Letters)*. 81 (3), 34006.

Mahmood, Z. & Iwashita, K. (2011) A simulation study of microstructure evolution inside the shear band in biaxial compression test. *International Journal for Numerical and Analytical Methods in Geomechanics*. 35, 652–667.

Majmudar, T.S. & Behringer, R. (2005) Contact force measurements and stress-induced anisotropy in granular materials. *Nature*. 435 (23), 1079–1082.

Manzari, M.T. & Dafalias, Y.F. (1997) A critical state two-surface plasticity model for sands. *Géotechnique*. 47 (2), 255–272.

Marketos, G. & Bolton, M. (2010) Flat boundaries and their effect on sand testing. *International Journal for Numerical and Analytical Methods in Geomechanics*. 34, 821–837.

Matsuoka, H. & Nakai, T. (1974) Stress-deformation and strength characteristics of soil under three different principal stresses. *Proceedings of JSCE*. (232), 59–70.

Minh, N.H., Cheng, Y.P. & Thornton, C. (2014) Strong force networks in granular mixtures. *Granular Matter*. 16 (1), 69–78.

Mohamed, A. & Gutierrez, M. (2010) Comprehensive study of the effects of rolling resistance on the stress–strain and strain localization behavior of granular materials. *Granular Matter*. 12 (5), 527–541.

Mollon, G. & Zhao, J. (2014) 3D generation of realistic granular samples based on random fields theory and Fourier shape descriptors. *Computer Methods in Applied Mechanics and Engineering*. *279, 46-65.*

Mollon, G. & Zhao, J. (2012) Fourier–Voronoi-based generation of realistic samples for discrete modelling of granular materials. *Granular Matter*. 14 (5), 621–638.

Morgan, J.K. (1999) Numerical simulations of granular shear zones using the distinct element method 2 . Effects of particle size distribution and interparticle. *Journal of Geophysical Research*. 104 (B2), 2721–2732.

Munjiza, A. (2004) *The combined finite-discrete element method*. Chichester, UK, John Wiley & Sons Ltd.

Murthy, T.G., Loukidis, D., Carraro, J.A.H., Prezzi, M., et al. (2007) Undrained monotonic response of clean and silty sands. *Géotechnique*. 57 (3), 273–288.

Newland, P.L. & Allely, B.H. (1957) Volume changes in drained triaxial tests on granular materials. *Géotechnique*. 7 (1), 17–34.

Ng, T.-T. (2004a) Macro- and micro-behaviors of granular materials under different sample preparation methods and stress paths. *International Journal of Solids and Structures*. 41 (21), 5871–5884.

Ng, T.-T. (2004b) Shear strength of assemblies of ellipsoidal particles. *Géotechnique*. 54 (10), 659–669.

Ng, T. -T. (2009a) Discrete Element Method Simulations of the Critical State of a Granular Material. *International Journal of Geomechanics*. 9 (5), 209–216.

Ng, T.-T. (2009b) Shear strength and micro-descriptors of bidisperse ellipsoids under different loading paths. *Mechanics of Materials*. 41 (6), 748–763.

Ní Bhreasail, Á. (2014) *An investigation of the micromechanical response of soil to one dimensional compression in varied thermal conditions*. PhD thesis. Imperial College London.

O'Sullivan, C. (2014) Advancing geomechanics using DEM. In: Kenichi Soga (ed.). *The International Symposium on Geomechanics from Micro to Macro (IS-Cambridge 2014)*. 2014 Cambridge, UK, CRC Press/Balkema.

O'Sullivan, C. (2011) *Particulate discrete element modelling: A geomchanics Perspective*. London, Taylor and Francis.

O'Sullivan, C. & Bray, J.D. (2004) Selecting a suitable time step for discrete element simulations that use the central difference time integration scheme. *Engineering Computations*. 21 (2/3/4), 278–303.

O'Sullivan, C., Bray, J.D. & Riemer, M.F. (2002) Influence of Particle Shape and Surface Friction Variability on Response of Rod-Shaped Particulate Media. *Journal of Engineering Mechanics*. 128 (11), 1182–1192.

O'Sullivan, C. & Cui, L. (2009) Micromechanics of granular material response during load reversals: Combined DEM and experimental study. *Powder Technology*. 193 (3), 289–302.

O'Sullivan, C., Wadee, M.A., Hanley, K. & Barreto, D. (2013) Use of DEM and elastic stability analysis to explain the influence of the intermediate principal stress on soil shear strength. *Géotechnique*. 63 (15), 1298–1309.

Oda, M. (1977) Coordination number and its relationship to shear strength of granular material. *Soils and Foundations*. 17 (2), 29–42.

Oda, M. & Kazama, H. (1998) Microstructure of shear bands and its relation to the mechanisms of dilatancy and failure of dense granular soils. *Géotechnique*. 48 (4), 465–481.

Oda, M., Konishi, J. & Nemat-Nasser, S. (1982) Experimental micromechanical evaluation of strength of granular materials: effects of particle rolling. *Mechanics of Materials*. 1, 269–283.

Ogawa, S., Mitsui, S. & Takemure, O. (1974) Influence of the intermediate principal stress on mechanical properties of a sand. In: *Proceedings of the 29th Annual Meeting of JSCE,Part 3*. 1974 pp. 49–50.

Ouadfel, H. & Rothenburg, L. (2001) `Stress–force–fabric' relationship for assemblies of ellipsoids. *Mechanics of Materials*. 33 (4), 201–221.

Parkin, A.K. (1965) On the strength of packed spheres. *Journal of the Australian Mathematical Society*. 5, 443–452.

Peña, A.A., Lizcano, A., Alonso-Marroquin, F. & Herrmann, H.J. (2008) Biaxial test simulations using a packing of polygonal particles. *International Journal for Numerical and Analytical Methods in Geomechanics*. 32, 143–160.

Plassiard, J.-P., Belheine, N. & Donzé, F.-V. (2009) A spherical discrete element model: calibration procedure and incremental response. *Granular Matter*. 11 (5), 293–306.

Plimpton, S. (1995) Fast parallel algorithms for short-range molecular dynamics. *Journal of Computational Physics*. 117, 1–19.

Potyondy, D.O. & Cundall, P.A. (2004a) A bonded-particle model for rock. *International Journal of Rock Mechanics and Mining Sciences*. 41, 1329–1364.

Proubet, J. & Bardet, J.P. (1991) A numerical investigation of the structure of persistent shear bands in granular media. *Géotechnique*. 41 (4), 599–613.

Radjai, F., Jean, M., Moreau, J. & Roux, S. (1996) Force Distributions in Dense Two-Dimensional Granular Systems. *Physical review letters*. 77 (2), 274–277.

Radjai, F., Wolf, D.E., Jean, M. & Moreau, J. (1998) Bimodal Character of Stress Transmission in Granular Packings. *Physical Review Letters*. 80 (1), 61–64.

Rechenmacher, A.L., Abedi, S. & Chupin, O. (2010) Evolution of force chains in shear bands in sands. *Géotechnique*. 60 (5), 343–351.

Rechenmacher, A.L. (2006) Grain-scale processes governing shear band initiation and evolution in sands. *Journal of the Mechanics and Physics of Solids*. 54 (1), 22–45.

Rennie, B.C. (1958) On the strength of sand. *Journal of the Australian Mathematical Society*. 1, 71–79.

Riemer, M.F. & Seed, R.B. (1997) Factors affecting apparent position of steady-state line. *Journal of Geotechnical and Geoenvironmental Engineering*. 123 (3), 281–288.

Roller, K. & Trepmann, C.A. (2011) Stereo 32 V1.0.3 help. Ruhr-University, Bochum,Germany.

Roscoe, K.H., Schofield, A.N. & Wroth, C.P. (1958) On the yielding of soils. *Géotechnique*. 8 (1), 22–53.

Rothenburg, L. & Kruyt, N.P. (2004) Critical state and evolution of coordination number in simulated granular materials. *International Journal of Solids and Structures*. 41, 5763–5774.

Rowe, P.W. (1962) The Stress-Dilatancy Relation for Static Equilibrium of an Assembly of Particles in Contact. *Proceedings of the Royal Society A: Mathematical, Physical and Engineering Sciences*. 269 (1339), 500–527.

Satake, M. (1975) Consideration of yield criteria from the concept of metric space. *The Technology reports of Tohoku University*. 40 (2), 521–530.

Satake, M. (1982) Fabric tensor in granular materials. In: P.A. Vermeer & H.J. Luger (eds.). *IUTAM Symposium on Deformations and Failure of Granular Materials*. 1982 Rotterdam:Balkema. pp. 63–68.

Sayão, A. & Vaid, Y.P. (1996) Effect of intermediate principal stress on the deformation response of sand. *Canadian Geotechnical Journal*. 33, 822–828.

Sazzad, M. & Suzuki, K. (2011) Effect of Interparticle Friction on the Cyclic Behavior of Granular Materials Using 2D DEM. *Journal of Geotechnical and Geoenvironmental Engineering*. 137 (5), 545–549.

Sazzad, M.M. & Suzuki, K. (2013) Density dependent macro-micro behavior of granular materials in general triaxial loading for varying intermediate principal stress using DEM. *Granular Matter*. 15 (5), 583–593.

Schofield, A. & Wroth, P. (1968) *Critical State Soil Mechanics*. London, UK, McGraw-Hill.

Senetakis, K., Coop, M.R. & Todisco, M.C. (2013) Tangential load–deflection behaviour at the contacts of soil particles. *Géotechnique Letters*. 3 (2), 59–66.

Shin, H. & Santamarina, J.C. (2013) Role of Particle Angularity on the Mechanical Behavior of Granular Mixtures. *Journal of Geotechnical and Geoenvironmental Engineering*. 139 (2), 353–355.

Shire, T. (2014) *Micro-scale Modelling of Granular Filters*. PhD thesis. Imperial College London.

Simmons, G. & Brace, W.F. (1965) Comparison of Static and Dynamic Measurements of Compressibility of Rocks. *Journal of Geophysical Research*. 70 (22), 5649–5656.

Sitharam, T.G. & Vinod, J.S. (2009) Critical state behaviour of granular materials from isotropic and rebounded paths: DEM simulations. *Granular Matter*. 11 (1), 33–42.

Skinner, A.E. (1969) A note on the influence of interparticle friction on the shearing strength of a random assembly of spherical particles. *Géotechnique*. 19 (1), 150–157.

Suiker, A.S.J. & Fleck, N. a. (2004) Frictional Collapse of Granular Assemblies. *Journal of Applied Mechanics*. 71 (3), 350–358.

Suzuki, K. & Yanagisawa, E. (2006) Principal Deviatoric Strain Increment Ratios for Sand Having Inherent Transverse Isotropy. *International Journal of Geomechanics*. 6 (5), 356–366.

Taylor, D.W. (1948) *Fundamentals of soil mechanics*. New York, NY, USA, Wiley.

The MathWorks Inc. (2011) *MATLAB7.13(R2011b)*. Natick, Massachusetts, The MathWorks Inc.

Thevanayagam, S. & Mohan, S. (2000) Intergranular state variables and stress - strain behaviour of silty sands. *Géotechnique*. 50 (1), 1–23.

Thornton, C. (2000) Numerical simulations of deviatoric shear deformation of granular media. *Géotechnique*. 50 (1), 43–53.

Thornton, C. (1979) The conditions for failure of a face-centered cubic array of uniform rigid spheres. *Géotechnique*. 29 (4), 441–459.

Thornton, C. & Antony, S.J. (2000) Quasi-static shear deformation of a soft particle system. *Powder Technology*. 109, 179–191.

Thornton, C. & Zhang, L. (2010) On the evolution of stress and microstructure during general 3D deviatoric straining of granular media. *Géotechnique*. 60 (5), 333–341.

Tordesillas, A. (2007) Force chain buckling, unjamming transitions and shear banding in dense granular assemblies. *Philosophical Magazine*. 87 (32), 4987–5016.

Tordesillas, A. & Muthuswamy, M. (2009) On the modeling of confined buckling of force chains. *Journal of the Mechanics and Physics of Solids*. 57 (4), 706–727.

Tordesillas, A. & Walsh, D.C.S. (2002) Incorporating rolling resistance and contact anisotropy in micromechanical models of granular media. *Powder Technology*. 124 (1-2), 106–111.

Vaid, Y.P., Chung, E.K.F. & Kuerbis, R.H. (1990) Stress path and steady state. *Canadian Geotechnical Journal*. 27, 1–7.

Vaid, Y.P. & Sasitharan, S. (1991) The strength and dilatancy of sand. *Canadian Geotechnical Journal*. 29 (10), 522–526.

Vaid, Y.P. & Thomas, J. (1995) Liquefaction and Postliquefaction Behavior of Sand. *Journal of Geotechnical Engineering*. 121 (2), 163–173.

Vasquez, A. & Dobry, R. (1988). The behavior of undrained contractive sand and its effect on the seismic liquefaction flow failure of earth structures. *Report of Rensselaer Poly technic Institute*.

Verdugo, R. (1992) Discussion on The critical state of sands. *Géotechnique*. 42 (4), 655–663.

Verdugo, R. & Ishihara, K. (1996) The steady state of sandy soils. *Soils and Foundations*. 36 (2), 81–91.

Wanatowski, D. (2007) Undrained instability of loose sand under plane-strain conditions and its engineering application. *Foundations of Civil and Environmental Engineering*. (10), 131–141.

Wanatowski, D. & Chu, J. (2007) Static liquefaction of sand in plane strain. *Canadian Geotechnical Journal*. 44, 299–313.

Wang, Z.-L., Dafalias, Y.F., Li, X.-S. & Makdisi, F.I. (2002) State Pressure Index for Modeling Sand Behavior. *Journal of Geotechnical and Geoenvironmental Engineering*. 128 (6), 511–519.

Wikipedia (Accessed on July 16, 2014) *Buckling*. http://en.wikipedia.org/wiki/Buckling.

Wikipedia (Accessed on July 24, 2014) *Gimbal lock*. http://en.wikipedia.org/wiki/Gimbal_lock#Solutions.

Wood, D.M., Belkheir, K. & Liu, D.F. (1994) Strain softening and state parameter for sand modelling. *Geotechnique*. 44 (2), 335–339.

Yan, W.M. & Dong, J. (2011) Effect of Particle Grading on the Response of an Idealized Granular Assemblage. *International Journal of Geomechanics*. 11 (4), 276–285.

Yan, W.M. & Zhang, L. (2013) Fabric and the critical state of idealized granular assemblages subject to biaxial shear. *Computers and Geotechnics*. 49, 43–52.

Yang, J. (2002) Non-uniqueness of flow liquefaction line for loose sand. *Géotechnique*. 52 (10), 757–760.

Yang, J. & Sze, H.Y. (2011) Cyclic behaviour and resistance of saturated sand under non-symmetrical loading conditions. *Géotechnique*. 61 (1), 59–73.

Yang, J. & Wei, L.M. (2012) Collapse of loose sand with the addition of fines : the role of particle shape. *Géotechnique*. 62 (12), 1111–1125.

Yang, Z.X., Yang, J. & Wang, L.Z. (2012) On the influence of inter-particle friction and dilatancy in granular materials: a numerical analysis. *Granular Matter*. 14 (3), 433–447.

Zhang, H. & Makse, H. (2005) Jamming transition in emulsions and granular materials. *Physical Review E*. 72, 011301.

Zhao, J. & Guo, N. (2014) Rotational resistance and shear-induced anisotropy in granular media. *Acta Mechanica Solida Sinica*. 27 (1), 1–14.

Zhao, J. & Guo, N. (2013) Unique critical state characteristics in granular media considering fabric anisotropy. *Géotechnique*. 63 (8), 695–704.

Zhao, X. & Evans, T.M. (2011) Numerical analysis of critical state behaviors of granular soils under different loading conditions. *Granular Matter*. 13 (6), 751–764.

Zhou, Y.C., Wright, B.D., Yang, R.Y., Xu, B.H., et al. (1999) Rolling friction in the dynamic simulation of sandpile formation. *Physica A: Statistical Mechanics and its Applications*. 269 (2-4), 536–553.